Gary Hodes (Editor)

Electrochemistry of Nanomaterials

Related titles from Wiley-VCH

Janos H. Fendler (Ed.)

Nanoparticles and Nanostructured Films

ISBN 3-527-29443-0

A. E. Kaifer, M. Gómez-Kaifer

Supramolecular Electrochemistry

ISBN 3-527-29597-6

Rüdiger Memming

Semiconductor Electrochemistry

ISBN 3-527-30147-X

Gary Hodes (Ed.)

Electrochemistry of Nanomaterials

Weinheim – New York – Chichester – Brisbane – Singapore – Toronto

Editor

Dr. Gary Hodes
Dept. of Materials and Interfaces
Weizman Institute of Science
Rehovot, 76100
Israel

First Edition 2001
First Reprint 2002
Second Reprint 2005

This book was carefully produced. Nevertheless, authors, editors and publisher do not warrant the information contained therein to be free of errors. Readers are advised to keep in mind that statements, data, illustrations, procedural details or other items may inadvertently be inaccurate.

Library of Congress Card No.: applied for

British Library Cataloguing-in-Publication Data:
A catalogue record for this book is available from the British Library.

Die Deutsche Bibliothek –
CIP-Cataloguing-in-Publication Data
A catalogue record for this book is available from Die Deutsche Bibliothek

© WILEY-VCH Verlag GmbH
D-69469 Weinheim, 2001

All rights reserved (including those of translation in other languages). No part of this book may be reproduced in any form – by photoprinting, microfilm, or any other means – nor transmitted or translated into machine language without written permission from the publishers. Registered names, trademarks, etc. used in this book, even when not specifically marked as such, are not to be considered unprotected by law.

printed in the Federal Republic of Germany
printed on acid-free paper

Composition K+V Fotosatz GmbH,
D-64743 Beerfelden
Printing Strauss Offsetdruck GmbH,
D-69509 Mörlenbach
Bookbinding J. Schäffer GmbH & Co. KG,
D-67269 Grünstadt

ISBN 3-527-29836-3

Preface

One of the cornerstones of the push toward future improvements in present-day electronic technology, and the research and development generated by this push, is the decrease in size of the various components making up the device. Nowhere is this more evident than in computer technology, where progress has been summed up by Moore's empirical (but surprisingly accurate and still valid) law that the density of transistors on a chip doubles every 18 months. Increasing computing speed and memory density are directly dependent on reducing the size of the discrete components making up the computers. Smaller components mean not only a higher density of these components; smaller units (and the leads should be included here) means smaller capacitance, C, and therefore higher speed of operation (low RC if resistance, R, is low). Also, the lower currents and possibly lower voltages mean lower power consumption and less heating (which would offset the increased density).

Although computers may be the most obvious manifestation of this drive to miniaturization, there are many more applications for which miniaturization is desirable or necessary, not only in the electronics and optoelectronics industries, but more generally in the quest for new functional and smart materials. Such materials depend, to a large extent, on the possibility of controlling the formation of the material at the nanoscopic scale, whether it be a single material or a composite in which each component material has a well-defined geometrical arrangement relative to the others.

Electrodeposition is a technique that is conceptually well-suited to the preparation of nanostructures. There are several reasons for this. One is that it is usually a low-temperature technique (high-temperature molten salt electrodeposition, a not so common variation, being the exception). This discourages crystal growth (electrodeposited materials tend to have a very small grain size as deposited). Another important property of electrodeposition is the very precise control of the amount of material deposited through Faraday's law, which relates the amount of material deposited to the amount of charge passed:

96500 Coulombs (= A.s) of charge results in $1/n$ g-mole of deposit where n is the number of electrons transferred/molecule of product.

Thus, a known number of Coulombs passed will result in a defined amount of material deposited. This assumes 100% current efficiency, absence of side reac-

tions, and (possibly relevant for very small amounts of charge passed) ignores double layer charging. These loss factors can, however, usually be measured and allowed for.

It is also only fair to mention that electrodeposits are often non-homogeneous, both on the macroscale and on the nanoscale. Typical of the former is the preferential deposition on the edges of electrodes, because of a combination of enhanced diffusion and electric fields. The latter can lead to nanocrystalline deposits rather than coherent coverage. Whether this is considered a disadvantage or is desirable depends on what is required from the deposit.

Electrodeposition of metal nanostructures, outside the scope of this book, is nonetheless closely related to electrodeposition of semiconductor nanostructures. Examples include pulsed electrodeposition of metal multilayers [1, 2] (deposition of metal multilayers is reviewed in Switzer's chapter) and porous membrane-templated electrodeposition of gold nanotubes [3] and Ni nanowires [4] (this technique has also been successfully used for electrodeposition of semiconductors (e.g. Ref. [5]). Composites of nanocrystalline semiconductors with non-semiconductors (usually metals) have also been electrodeposited by incorporation of the semiconductor phase from solution into the electrodepositing metal [6, 7]. The absence of all these topics from this book emphasizes the lack of any intention, from the beginning, of trying to cover the field comprehensively. Rather the contributions cover chosen topics to give readers a broad cross-section of the field.

The above might cause the reader to understand that the subject of this book is electrochemical *preparation* of nanostructures. Although this is true for the first half of the book, the second half deals with electrochemical *properties* of nanostructures which *might* have been made by a totally different method. Below a certain size scale, the electrochemical properties of electrodes can change discontinuously and dramatically. One well-known example is the large increase in limiting current densities at very small electrodes and electrode arrays. There are other properties which become apparent only below a certain size scale. The quantum size effect, the most obvious manifestation of which is an increase in the bandgap of the nanocrystalline semiconductor (or quantum dot), is probably the best-known example. One consequence of this effect is the change in the spectral sensitivity of semiconductor photoelectrodes. Another size-related property, featured prominently in a number of chapters in this book, is the absence of a space-charge layer in many nanocrystalline films. In general, devices based on a space-charge layer cannot be very small because of the relatively large size of the space-charge layer; small nanoparticles, unless they are very highly doped, cannot support an appreciable space-charge layer. Tunneling devices can be smaller, because of high doping, and the width of the space-charge layer can, therefore, be as low as ca. 10 nm. Can we talk about normal doping in a nanoparticle, however, when a single dopant (which may be located either in the bulk or on the surface, and might behave differently in the two cases) will drastically change the properties of that nanoparticle? Porous nanocrystalline semiconductor layers are an important subject well-represented in this book. The ability of an electrolyte to penetrate the pores and thereby make contact with the very high real surface area of the semiconductor is critical to the operation of devices based on these films.

The contributions in this book can be divided into the preparation of nanostructures (the first five chapters) and their properties (the last four chapters). Although this division is not strict – there is often considerable discussion of properties in the first section of the book and the later chapters often describe preparative aspects – this division is generally valid.

Chapter 1

Penner describes a method of electrodeposition of semiconductor nanocrystals (ZnO, CuI, and CdS) on graphite by first depositing metal nanocrystals, then chemically converting the metal into oxides/hydroxides and, finally, by either liquid or gas phase reactions, to the desired semiconductors. Because the chemical conversion occurs on a particle-by-particle basis, the size and size distribution of the semiconductor nanocrystals is determined by the properties of the metal nanocrystals. The metal nanocrystals can be electrodeposited with controllable size and good size distribution and the reasons for this are discussed in terms of electrochemical Volmer-Weber nucleation and growth. CdS and CuI were epitaxially deposited on the graphite. In all the materials, the nanocrystals were strongly luminescent, despite their direct proximity to the graphite substrate. Even more notable, band-gap emission and the absence of sub-band-gap luminescence were apparent in all the luminescence spectra.

Chapter 2

In describing their work on electrodeposition of semiconductor quantum dots, Hodes and Rubinstein cover both 'thick' films of aggregated nanocrystals and the electrodeposition of isolated quantum dots. The electrodeposition is performed from a dimethyl sulfoxide solution of a metal salt (usually Cd) and elemental chalcogen (Te, which is insoluble in dimethyl sulfoxide, is complexed with an alkyl phosphine). This technique leads naturally to small crystal size. This size, and the spatial distribution of the nanocrystals, can, however, be tuned over a considerable range by a variety of means. Particular attention is paid to the role of semiconductor-substrate lattice mismatch, which enables size control of epitaxially-deposited quantum dots through the lattice mismatch strain. Not only size, but also shape and crystal phase can be altered in this way. The interaction between semiconductor and substrate is also shown to be an important factor in determining the growth mode.

Chapter 3

Switzer describes pulsed electrodeposition of superlattices and multilayers. After reviewing the literature on metallic and magnetic multilayers, he turns to modu-

lated oxide layers. Oxides of many metals have been deposited either by redox change (oxidation of metal ion usually results in more readily hydrolysis to the hydroxide) or local pH change (e.g. by hydrogen evolution or oxygen reduction, which increase the pH at the electrode). Lead oxide-thallium oxide superlattice electrodeposition is an example where, because of the small lattice mismatch between the two oxides, two-dimensional layered growth is favored over three-dimensional growth. Thallium oxide-defect chemistry superlattices are described; in these the cation interstitials or oxygen vacancies (therefore oxide doping) were controlled by the overpotential. Alternating layers of Cu and Cu_2O, with highly anisotropic properties, were deposited by spontaneous potential oscillations in the deposition system. Large-mismatch semiconductor-metal layers were grown epitaxially by relative rotation of the two lattices.

Chapter 4

Kelly and Vanmaekelbergh give a comprehensive review of the formation (mainly by (photo)electrochemical etching) and characterization of porous semiconductors in general. They discuss various mechanisms of pore formation and follow this with a comprehensive review of the formation of porous semiconductors. This review naturally includes silicon, but deals in detail with many other semiconductors: Si-Ge alloys, SiC, III–V semiconductors (gallium nitride, phosphide and arsenide, and InP), CdTe and ZnTe as II–VI materials and TiO_2. They also describe various photoelectrochemical techniques used to characterize these porous semiconductors, such as impedance measurements, photoelectrochemical photocurrent characterization, luminescence properties, and intensity-modulated photocurrent spectroscopy (IMPS), which has been successfully exploited to study charge transport in the porous structures.

Chapter 5

Because the great bulk of work on electrochemical formation of porous semiconductors is on porous silicon (p-Si), the next chapter, by Green, Létant, and Sailor, deals almost exclusively with this material. They discuss, in detail, the mechanisms involved in the electrochemical formation of p-Si in HF solutions, including the effect of illumination on the etching process. The ability to control the pore size, and therefore the effective dielectric constant of the p-Si, enables construction of optical elements, such as periodic layers of differing dielectric constant, with tuned reflection spectra. The great interest in p-Si is largely because of its relatively efficient photo- and electroluminescence, in strong contrast to bulk Si; this luminescence is discussed in terms of quantum effects, surface species, and carrier lifetimes. Surface modification of the p-Si by organic functional groups is described with particular emphasis on enhancement of chemical stability.

Chapter 6

Lindquist, Hagfeldt, Södergren, and Lindström discuss photogenerated charge transport in porous nanostructured semiconductor films. The emphasis is on charge generated by supra-band-gap light absorption, although dye-sensitized charge-injection is also treated. After describing the steps involved in charge generation and transport in these films, they discuss the breakdown of the Schottky (space charge layer) model in such small semiconductor units. The experimental techniques used to study the charge transport – photocurrent spectroscopy, transient photocurrent, and intensity-modulated photocurrent(voltage) spectroscopy – are treated in detail and the conclusions obtained from these experiments discussed. The role of charge transport in the electrolyte is also treated in depth. Attention is given to the controversy over the importance of any electric field existing at the semiconductor-back contact.

Chapter 7

Whereas the previous chapter emphasizes charge transport in nanostructured electrodes in which light is absorbed in the semiconductor, Cahen, Grätzel, Guillemoles and Hodes, confine their chapter to dye-sensitized nanocrystalline films. The emergence of the dye-sensitized solar cell (DSSC) has triggered a very large effort in understanding the various factors – fundamental and experimental – involved in this system. Although our understanding of the DSSC has increased considerably in recent years as a result of this intensive study, there are still questions and disagreements concerning cell operation. This chapter discusses present day thinking on cell operation. It considers the different parts of the cell and looks at how each part contributes to cell operation. In contrast with previous studies, which have mostly concentrated on electron transport through the porous semiconductor film, this chapter tries to balance all the components of cell performance, including the source of the photovoltage generated and factors which affect the cell-fill factor.

Chapter 8

The photochromic, electrochromic, and electrofluorescent properties of films of nanostructured semiconductors, either by themselves or combined with surface-linked chromophores or fluorophores, are described by Kamat. The preparation of nanostructured films is discussed first, with emphasis on formation from colloidal suspensions. Photochromic and electrochromic properties of these films, usually involving a transition from colorless to blue resulting from trapped electrons, are discussed. Nanostructured semiconductors can also be used as substrates for active dye and redox chromophores which are linked through suitable

reactive groups to the semiconductor surface. These modified films can be switched from colored to colorless or vice versa by application of an external potential. In a similar manner, potential-controlled electrochemically modulated photoluminescence can be obtained by linking fluorescent molecules to the semiconductor surface.

Chapter 9

Cassagneau and Fendler describe chemical self-assembly of different monolayers of polymers (conducting, insulating, and semiconducting) and polyelectrolytes, sometimes together with metal and semiconductor nanoparticles, and show how various devices based on charge transport and storage can be built from these units. These include rectifying diodes made from doped semiconducting polymer layers and from combinations of semiconducting polymers and semiconductor nanoparticles; light-emitting diodes from nanostructured polymer films or alternate anionic and cationic polyelectrolyte layers; single electron transport in self-assembled polymer and nanoparticle films; and photo- or electrochromic displays utilizing self-assembled polyoxometallates with polycations. Self-assembly of layers with different functions has mimicked natural photosynthesis. Self-assembly has been used to produce oxidized graphite and polyethylene oxide films with good Li^+ intercalation properties for use in lithium-ion batteries.

References

1 J. Yahalom, *Surface and Coatings Technology* **1998**, *105*, VII.

2 T. Cohen, J. Yahalom, W. D. Kaplan, *Rev. Anal. Chem.* **1999**, *18*, 279.

3 C. R. Martin, D. T. Mitchell, in: *Electroanalytical Chemistry*, Vol. 21 (Eds. A. J. Bard, I. Rubinstein); Marcel Dekker, New York Basel, **1999**, p. 1.

4 L. Sun, P. C. Searson, C. L. Chien, *Appl. Phys. Lett.* **1999**, *74*, 2803.

5 D. Routkevitch, T. Bigioni, M. Moskovits, J. M. Xu, *J. Phys. Chem.* **1996**, *100*, 14037.

6 M. Zhou, N. R. de Tacconi, K. Rajeshwar, *J. Electroanal. Chem.* **1997**, *421*, 111.

7 P. M. Vereecken, I. Shao, P. C. Searson, *J. Electrochem. Soc.* **2000**, *147*, 2572.

Contents

1 **Hybrid Electrochemical/Chemical Synthesis of Semiconductor Nanocrystals on Graphie** *1*
Reginald M. Penner
1.1 Introduction *1*
1.1.1 Dimensional Control in Materials Electrodeposition: The State of the Art *2*
1.1.2 The Electrochemical/Chemical Synthesis of Semiconductor Quantum Dots *3*
1.2 Size-Selective Electrodeposition of Metal Nanoparticles *5*
1.3 Understanding Particle Size Dispersion in Electrochemical Volmer-Weber Growth *8*
1.4 Converting Metal Nanoparticles into Semiconductor Quantum Dots *13*
1.4.1 A Metal Oxide Intermediate *13*
1.4.2 Conversion from Metal Oxide to Metal Salt and Characterization *14*
1.5 Photoluminescence Spectroscopy of E/C Synthesized Materials *17*
1.6 An Application for E/C Synthesized Quantum Dots: Photodetection Based on a New Principle *20*
References *23*

2 **Electrodeposition of Semiconductor Quantum Dot Films** *25*
Gary Hodes and *Israel Rubinstein*
2.1 Introduction *25*
2.1.1 General *25*
2.1.2 Some Specific Issues Relevant to Characterization of Nanocrystalline Materials *27*
2.2 Electrodeposition of Thick Films of Semiconductors from DMSO Solutions *29*
2.2.1 CdS and CdSe *29*
2.2.2 Miscellaneous Sulfides and Selenides *32*
2.2.3 CdTe *33*
2.3 Ultrathin Films and Isolated Nanocrystal Deposition *35*
2.3.1 Effect of Substrate on Non-aqueous Deposited Films *35*
2.3.2 Epitaxy *36*

2.3.3 Variation of Semiconductor 37
2.3.3.1 CdSe on Au 37
2.3.3.2 Cd(Se,Te) on Au 42
2.3.3.3 (Cd,Zn)Se on Au 43
2.3.3.4 CdS on Au 43
2.3.4 Variation of Substrate 45
2.3.4.1 CdSe on Pd 45
2.3.4.2 CdS on Pd 47
2.3.4.3 CdSe on Au-Pd Alloy 47
2.3.4.4 CdSe on Au-Cd Alloy; Rocksalt CdSe 48
2.4 Electronic Characterization of Electrodeposited Semiconductor Nanoparticle Films 50
2.4.1 Scanning Probe Current-Voltage Spectroscopy 50
2.4.2 Photoelectrochemical (PEC) Photocurrent Spectroscopy 58
2.5 Potential Applications of Electrodeposited Nanocrystalline Semiconductor Films 62
References 64

3 Electrodeposition of Superlattices and Multilayers 67
Jay A. Switzer
3.1 Background on Superlattices and Multilayers 67
3.1.1 Introduction 67
3.1.2 Quantum Confinement in Multiple Quantum Wells 68
3.1.3 Spin-dependent Transport 70
3.1.4 Mechanical Properties of Layered Nanostructures 71
3.2 Electrodeposition of Superlattices and Multilayers 72
3.2.1 Introduction 72
3.2.2 Single and Dual Bath Electrodeposition of Superlattices and Multilayers 72
3.2.3 Electrodeposition of Metallic Multilayers and Superlattices 76
3.2.4 Electrodeposition of Semiconductor and Ceramic Multilayers and Superlattices 78
3.2.4.1 Electrodeposition of Compound Semiconductor Films 79
3.2.4.2 Electrodeposition of Metal Oxide Ceramic Films 81
3.2.4.3 Electrodeposition of Ceramic Superlattices and Multilayers 83
3.3 Characterization of Superlattices and Multilayers 88
3.3.1 X-ray Diffraction 88
3.3.2 Scanning Tunneling Microscopy 93
3.3.3 Transmission Electron Microscopy 93
3.4 Recent Developments and Future Work 95
References 98

4 Porous-etched Semiconductors: Formation and Characterization 103
J.J. Kelly and *D. Vanmaekelbergh*
4.1 Introduction 103

4.2 Semiconductor-etching Mechanisms *104*
4.3 Mechanisms of Porous Etching *107*
4.4 Review of Porous-etched Semiconductors *109*
4.4.1 Silicon *109*
4.4.1.1 Electrochemistry *109*
4.4.1.2 Morphology (Micro-/mesoporous) *111*
4.4.1.3 Morphology (Macroporous) *111*
4.4.1.4 Stain Etching *113*
4.4.2 IV–IV Materials *113*
4.4.2.1 $Si_{1-x}Ge_x$ Alloys *113*
4.4.2.2 SiC *114*
4.4.3 III–V Materials *115*
4.4.3.1 GaP *115*
4.4.3.2 GaAs *116*
4.4.3.3 InP *119*
4.4.3.4 GaN *120*
4.4.4 II–VI Materials *120*
4.4.4.1 CdTe *120*
4.4.4.2 ZnTe *121*
4.4.5 Titanium Dioxide *121*
4.5 Photoelectrochemical Characterization *122*
4.5.1 Electrical Impedance *122*
4.5.2 Photocurrent *126*
4.5.3 Luminescence *129*
4.5.4 Electron Transport in Porous Semiconductors *132*
4.6 Applications of Porous-etched Semiconductors *134*
4.7 Conclusions *135*
References *136*

5 Electrochemical Formation and Modification of Nanocrystalline Porous Silicon *141*
Will H. Green, Sonia Létant and *Michael J. Sailor*
5.1 Introduction *141*
5.2 Synthesis of Nanocrystalline Porous Si, Ge, GaAs, GaP, and InP *142*
5.3 Junction Properties of Si-Electrolyte Interfaces *143*
5.3.1 Chemistry of Silicon in Aqueous HF *146*
5.3.2 Electrochemical Formation of Porous Si *147*
5.3.3.1 Photoelectrochemically Patterned Porous Si *151*
5.3.3.2 Porous Si Layers and Multilayers *152*
5.4 Properties of Porous Si *154*
5.4.1 Structural Properties of Porous Si *155*
5.4.2 Luminescence Properties of Porous Si *156*
5.4.3 Electrical Properties of Porous Si *158*
5.5 Electroluminescence from Porous Si *158*
5.6 Electrochemical Functionalization *160*

5.7 Applications 161
References 162

6 Charge Transport in Nanostructured Thin-film Electrodes 169
Sten-Eric Lindquist, Anders Hagfeldt, Sven Södergren, and *Henrik Lindström*
6.1 Introduction 169
6.2 From Single Crystal to Quantum Dots 170
6.2.1 Nanostructured Film Electrodes 170
6.3 Limitations of Charge Transport 172
6.4 The Breakdown of the Schottky Barrier Model 174
6.5 Action Spectra Analysis 176
6.5.1 Technique and Definitions 176
6.5.2 The Zones of Efficient Charge Separation 177
6.5.2.1 Action Spectra of TiO_2 Film Electrodes 178
6.5.2.2 Photocurrent Action Spectra from Porous CdSe and CdS Films 179
6.5.2.3 Scavengers in the Electrolyte 180
6.6 The Diffusion Model 181
6.7 Laser-pulse-induced Current Transients 183
6.8 The Influence of Traps 185
6.9 Charge Transport in the Electrolyte 186
6.9.1 Liquid Electrolytes 186
6.9.2 "Solid Electrolytes" 188
6.10 Intensity-modulated Photocurrent and Photovoltage Spectroscopy 189
6.11 Ambipolar Diffusion of Carriers Nanostructures 192
6.12 The Electrical Field at the Nanostructured SC-Back-contact Interface 192
6.13 Ballistic Electron Transport 195
6.14 Charge Transport and Applications of Nanostructured Electrodes 195
6.15 Summary 196
References 197

7 Dye-sensitized Solar Cells: Principles of Operation 201
David Cahen, Michael Grätzel, Jean Francois Guillemoles, and *Gary Hodes*
7.1 General Description of DSSC Systems 201
7.1.1 Solar Cells, How do They Work? 201
7.1.1.1 General 201
7.1.1.2 p/n Solid-state Cells 202
7.1.1.3 Photoelectrochemical Cells 203
7.1.1.4 Photogalvanic Cells 203
7.1.1.5 Summary 204
7.1.2 Comparison of Dye-sensitized Solar Cells with Other Types 204
7.1.2.1 Description of DSSC 204
7.1.2.2 General Model of Cell Action 204
7.1.2.3 What are the Special Features of a DSSC? 205
7.2 Detailed Description of Dye-sensitized Solar Cells 206
7.2.1 Dye Chemistry and Photochemistry: General Presentation 206

7.2.1.1 Dye Molecules *208*
7.2.2 Nanocrystalline Semiconductor Film *209*
7.2.3 Electron Injection from Dye to TiO_2 *211*
7.2.4 The Importance of the Porous Nanocrystalline Structure of Semiconductor Film *211*
7.2.4.1 Space Charge Layer Effects *212*
7.2.4.2 Particle Charging *215*
7.2.5 Traps and Discrete Charge Effects *215*
7.2.5.1 Trapping *217*
7.2.6 Importance of Redox Potential and of the HOMO Level of the Dye *217*
7.3 DSSC Output Parameters *218*
7.3.1 Photocurrent *218*
7.3.2 Photovoltage *219*
7.3.3 Fill Factor *219*
7.3.4 DSSCell Performance *220*
7.4 Further Comments on the Mode of Action of the DSSC *221*
7.5 Modeling the DSSC *223*
7.5.1 Energy Diagrams *223*
7.5.1.1 Effective Medium Picture [42, 53]: Advantages, Limitations and Uses *224*
7.6 Comparison of Liquid Electrolytes and Solid-state DSSCs *226*
7.7 Potential Applikations *227*
References *227*

8 Electrochromic and Photoelectrochromic Aspects of Semiconductor Nanostructure-Molecular Assembly *229*
Prashant V. Kamat
8.1 Introduction *229*
8.2 Preparation and Characterization of Nanostructured Semiconductor Thin Films *230*
8.2.1 From Colloidal Suspensions *230*
8.2.2 Electrochemical Deposition *231*
8.2.3 Self-assembled Layers *232*
8.3 Photochromic Effects *232*
8.4 Electrochromic Effects *234*
8.4.1 Nanostructured Metal Oxide Films *234*
8.4.2 Nanostructured Oxide Films Modified with Dyes and Redox Chromophores *236*
8.4.2.1 From Colorless to Colored Films under the Application of an Electrochemical Bias *238*
8.4.2.2 From a Colored to Colorless Window using Reverse Bias *238*
8.4.3 Surface-Bound Fluoroprobes *239*
8.5 Concluding Remarks *242*
References *243*

9 Electron Transfer and Charge Storage in Ultrathin Films Layer-by-layer Self-assembled from Polyelectrolytes, Nanoparticles, and Nanoplatelets *247*
Thierry P. Cassagneau and *Janos H. Fendler*
9.1 Introduction *247*
9.1.1 Importance of Electron Transfer and Charge Storage *247*
9.1.2 Principles of the Layer-by-layer Self-assembly *247*
9.1.3 Scope of the Review *249*
9.2 Self-assembled Light-emitting Diodes (LEDs) and Photochromic and Electrochromic Display Devices *250*
9.2.1 LEDs Based on Nanostructured Polymers Films *250*
9.2.2 LEDs Based on Redox Polymer Films *252*
9.2.3 Photochromic and Electrochromic Display Devices *256*
9.3 Self-assembled Rectifying Diodes *258*
9.3.1 p-n Junctions *260*
9.3.2 Schottky Diodes *268*
9.4 Single-electron Conductivity – Self-assembled Coulomb Blockade Devices *269*
9.5 Photoinduced Energy and Electron Transfer in Self-assembled Multilayers *273*
9.6 Self-assembled Electrodes for Lithium Storage Batteries *276*
9.7 Conclusions and Perspectives *281*
References *282*

Index *287*

List of Symbols *299*

List of Abbreviations *307*

Electrochemistry of Nanomaterials
by *Gary Hodes (Ed.)*
© WILEY-VCH Verlag GmbH, 2001

1
Hybrid Electrochemical/Chemical Synthesis of Semiconductor Nanocrystals on Graphite

Reginald M. Penner

Abstract

Electrochemically deposited metal nanocrystals can be chemically converted into semiconductor nanocrystals, or quantum dots. This hybrid "electrochemical/chemical" or "E/C" synthesis typically involves two chemical transformations: Oxidation of the metal nanoparticles to the metal oxide, $MO_{n/2}$ (where n is the oxidation state of the metal) and displacement of the oxide with an anion, X, to form the semiconducting salt MX_n (in the case where the anion is univalent). Surprisingly, the transformation from metal to metal oxide to metal salt occurs on a particle-by-particle basis. Consequently, the mean size and size dispersion of metal salt nanoparticles produced by an E/C synthesis is directly determined by the corresponding properties of the metal nanoparticles deposited in the first step of the synthesis.

To date, three materials have been synthesized using the E/C approach: ZnO (E_{BG}=3.50 eV), β-CuI (E_{BG}=2.92 eV), and CdS (E_{BG}=2.50 eV). In all three of these examples, the synthesis has been carried out on the (0001) surface of graphite. The use of graphite facilitates the analysis of products and intermediates via selected area electron diffraction (SAED). Single crystal SAED patterns are obtained for ensembles of β-CuI and CdS nanocrystals proving that these two materials are epitaxially deposited on graphite. In addition, we have found that high quality photoluminescence spectra may be obtained from E/C synthesized nanocrystals on graphite. For all three of the above-mentioned materials, synthesis conditions have been identified which yield nanocrystals which are luminescent at the band edge and for which emission from trap states in the gap is negligible.

1.1
Introduction

Over the last fifteen years, a small number of electrochemists have infringed on the domain of materials scientists by developing electrochemical methods for synthesizing electronic materials including semiconductors [1–7], metal oxides [8–10], metal nitrides [11, 12], porous silicon [13, 14], and a variety of layered compo-

sites [15–17]. As a consequence of their successes, an exciting new sub-discipline of electrochemistry – materials electrodeposition – has emerged. Some of the most striking successes have involved the synthesis of compositionally complex materials containing two or more elements and possessing a particular crystal structure. Examples include the synthesis of cubic δ-BiO_2 [18] and wurtzite phase CdX (X = S, Se, Te) [19]. An unsolved problem in materials electrodeposition involves *controlling the dimensions* of electrodeposited structures. Dimensional control and the ability to create *dimensionally uniform* nanometer-scale structures is important because the fabrication of device structures such as quantum wells and quantum dots requires nanometer scale-dimensional control in addition to composition control. In this chapter we will describe a new hybrid electrochemical/chemical (or E/C) method in which electrochemical and chemical operations are combined to obtain semiconductor nanocrystals that are strongly luminescent, and which have high dimensional uniformity.

1.1.1
Dimensional Control in Materials Electrodeposition: The State of the Art

The current state of the art with respect to dimensional control in materials electrodeposition is represented by recent work from the research groups of Stickney and Switzer, and the collaboration of Hodes and Rubinstein. Stickney and coworkers have developed a solution phase analog to molecular beam epitaxy (MBE) called electrochemical atomic layer epitaxy or ECALE. In an ECALE synthesis of CdTe, for example, atomic layers of tellurium and cadmium are alternatively electrodeposited to build up a thin layer of wurtzite phase CdTe [7, 20–22]. The necessary atomic-level control over the electrodeposition of these two elements is obtained by depositing both elements using under-potential deposition (UPD) schemes. The thickness of the CdTe layer prepared by ECALE can be specified by controlling the number of Cd and Te layers that are deposited, and Stickney's research group has automated the tedious layer-by-layer deposition process.

Switzer and coworkers [23, 24] have recently demonstrated a novel electrochemical method for obtaining multiple quantum well structures consisting of alternating Cu_2O and Cu^0 layers. These layered nanocomposites are obtained during galvanostatic deposition from copper plating solutions using specified conditions of pH and temperature that produce an oscillating potential during growth. Switzer has shown that these oscillations of the potential are produced by the alternating deposition of Cu^0 and Cu_2O layers having dimensions of nanometers [23]. The frequency of the potential oscillations, and hence the thickness of a Cu_2O-Cu^0 period in these superlattice structures, is adjustable via the deposition conditions. The resulting superlattice structures exhibit a variety of novel electronic properties including a profoundly anisotropic electrical resistance, and a negative differential resistance for conduction along the growth direction [25].

Hodes and Rubinstein have shown that CdSe and $CdSe_xTe_{1-x}$ can be epitaxially electrodeposited as nanometer-scale islands on to Au(111) surfaces [26–28]. This process – which mimics the formation of quantum dots by molecular beam epi-

taxy (MBE) – produces islands having a preferred diameter based on the degree of lattice mismatch between the island and the Au(111) surface: the larger the lattice mismatch, the smaller the equilibrium island diameter. This research group has demonstrated that the diameter of CdSe islands, for example, is increased by replacing selenium with tellurium since the resulting ternary $CdSe_xTe_{1-x}$ possesses a better lattice match to the Au(111) surface than CdSe [29, 30]. An important advantage of electrochemistry for materials synthesis – especially from the standpoint of dimensional control – is the ability to precisely control the reaction rate via the applied voltage (or current). In all three of the preceding examples, the ability to precisely control the reaction rate was essential to achieving dimensional control of the electrodeposited structures.

The research groups of Charles Martin [31, 32], Martin Moskovits [33–35], and Peter Searson [36–38] have demonstrated an intriguing alternative strategy involving the use of porous matrices to "template" the growth of nanostructures. In a typical experiment, the porous "host" material (e.g., a polycarbonate filtration membrane with cylindrical pores) is brought into contact with an electrode surface and the electrodeposition of a material into the voids of this host is carried out. As a final step, the matrix may be removed by dissolution to expose the electrodeposited structures. Because porous templates having extremely uniform pores of variable diameter (down to a few nanometers) are obtainable, highly dimensionally uniform nanostructures have been synthesized using this method. A clear advantage of this "template synthesis" strategy is its generality: template synthesis has been applied to the electrodeposition of a wide variety of materials including semiconductors, superconductors, metals, and polymers.

1.1.2 The Electrochemical/Chemical Synthesis of Semiconductor Quantum Dots

A new method for synthesizing semiconductor "quantum dots" (QDs) on graphite surfaces, called the electrochemical/chemical method, is described in this chapter. In essence, quantum dots are semiconductor particles having diameters that are smaller than 100 Å or so. Such semiconductor "nanoparticles" exhibit a bandgap that depends on the particle diameter – the smaller the nanoparticle, the larger the bandgap. Because QDs possess a "size-tunable" bandgap, these diminutive particles have potential applications as transducers which inter-convert light and electricity in detectors [39, 40], light-emitting diodes [39], electroluminescent devices [41, 42], and lasers [43, 44].

Before the unique properties of QDs can be exploited, physicists and chemists must produce QDs having certain attributes: Chemical and thermal stability are obviously important. It also must be possible to synthesize QDs that are size monodisperse over a range of mean particle diameters (so that the optical properties can be tuned). Finally, QDs can not function as transducers unless each QD has an electrical connection to the outside world. Existing methods for synthesizing semiconductor nanocrystals (e.g., molecular beam epitaxy (MBE), solution phase precipitation) satisfy some, but not all, of these requirements. We have

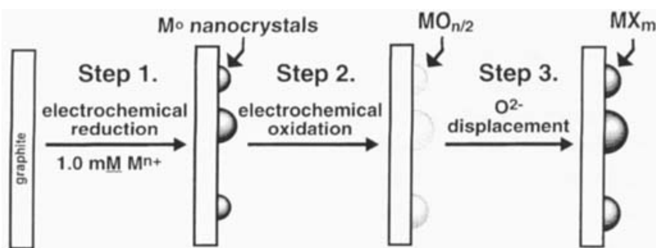

Scheme 1.1 The electrochemical/chemical method.

demonstrated that quantum dots composed of copper(I) iodide or cadmium sulfide produced using the electrochemical/chemical can possess all of these desirable attributes.

The essential features of the E/C Method are depicted in Scheme 1.

The first step of the synthesis involves the electrodeposition of metal nanoparticles onto a graphite surface from a solution containing ions, M^{n+}, of the corresponding metal. Then M^0 nanoparticles are electrochemically oxidized to yield a metal oxide, $MO_{m/2}$, in which the oxidation state of the metal, $+m$, matches the oxidation state in the final product. Finally, metal oxide nanoparticles are converted into nanoparticles of a semiconducting salt, MX_m (provided the anion is univalent), via a displacement reaction in which oxide or hydroxide is replaced by the anion X. This conversion from M^0 to $MO_{m/2}$ to MX_m occurs on a particle-by-particle basis. In other words, each M^0 nanoparticle deposited in the first step of the E/C synthesis is converted into a MX_m nanoparticle in the final step of the synthesis. Consequently, the properties of the MX_m nanoparticles – especially the mean diameter and the size monodispersity of these particles – are decided by the properties of the metal nanoparticle dispersion produced in Step 1. As we shall see, the salient features of the E/C mechanism represented in Scheme 1 are confirmed by tracking the structure and composition of the nanoparticles during synthesis using X-ray photoelectron spectroscopy and electron diffraction.

Five E/C synthesis schemes are shown in Scheme 2.

The E/C syntheses of β-CuI (a I–VII semiconductor) [45], CdS (a II–VI) [46, 47], and ZnO (a II–VI) [48] represent published procedures for the E/C syntheses of these materials. Also shown is a proposed E/C synthesis for InN, a III–V semiconductor. This technologically important material has not yet been electrosynthesized and we are currently in the process of searching for displacement conditions that permit conversion of the intermediate In_2O_3 to InN. It is important to note that the final displacement step of an E/C synthesis can be carried out either in a polar liquid phase, in which case it has the character of an ion exchange reaction, or in the gas phase. In the case of one material, CdS, we have found both solution [46] and gas phase [47] conditions which permit displacement of OH^- from the intermediate oxide, $Cd(OH)_2$, by S^{2-}.

In this monograph, we deconstruct the "E/C" and individually examine each of the three steps that comprise an E/C synthesis. The optical properties of E/C

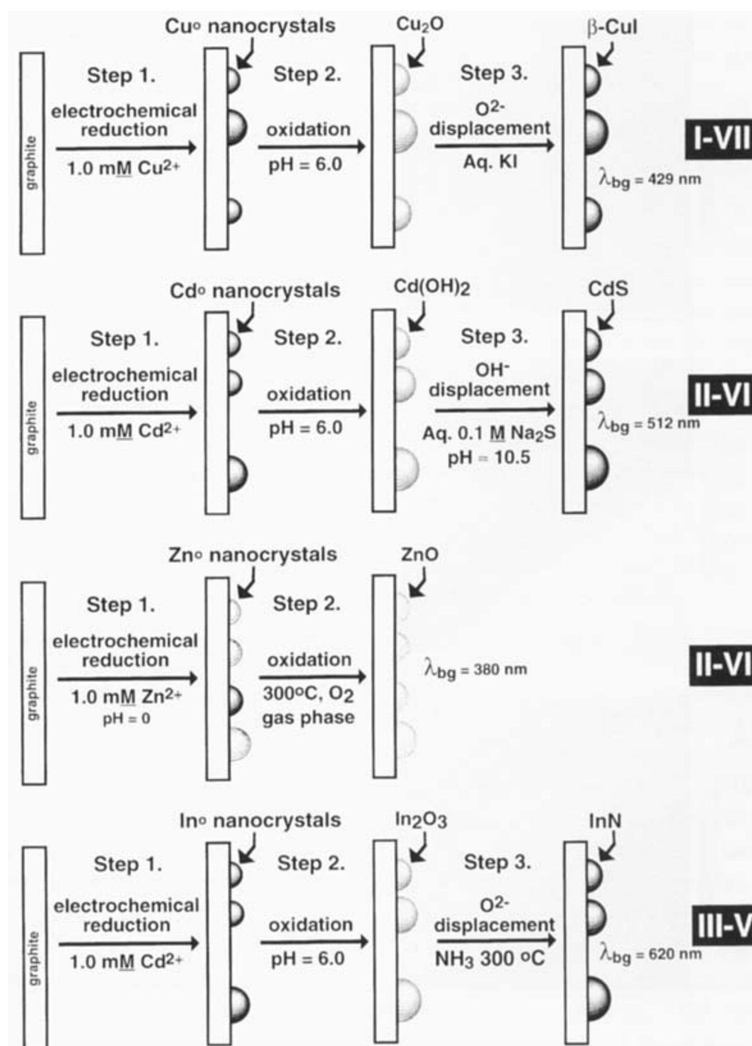

Scheme 1.2 E/C synthesis schemes for four semiconducting materials.

synthesized materials, and the application of these materials in devices, are also discussed.

1.2
Size-Selective Electrodeposition of Metal Nanoparticles

The E/C synthesis of semiconductor NCs begins with the electrodeposition of metal nanoparticles onto a graphite surface. Because of the particle-by-particle nature of the oxidation and displacement steps which follow metal deposition, disper-

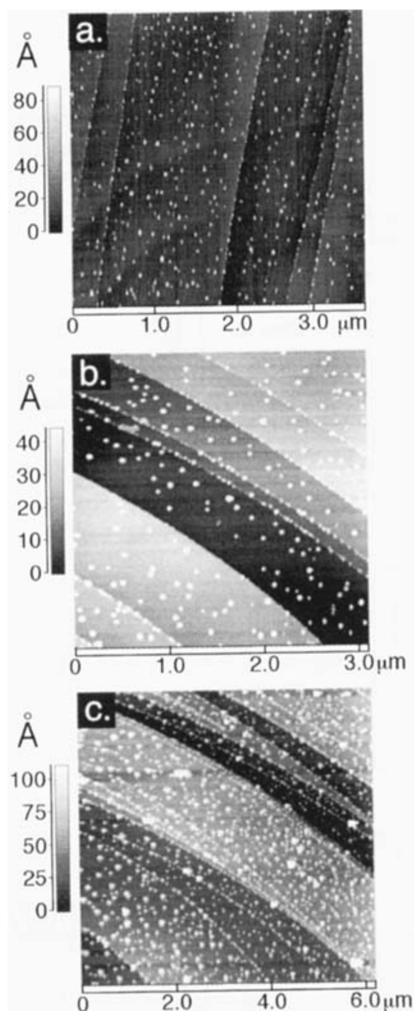

Fig. 1.1 Non-contact atomic force microscope (NC-AFM) images of the graphite basal plane surface following the deposition of platinum nanocrystals. (a) A 3.4 μm×3.4 μm area after the application of a 10 ms plating pulse which yielded a deposition charge of 4.84 μC cm^{-2} corresponding to 0.0050 equivalent platinum atomic layers (assuming an adsorption electrovalence of 4.0). (b) A 3.0 μm×3.0 μm area after a 50 ms plating pulse which yielded a deposition charge of 37.6 μC cm^{-2} corresponding to 0.039 equivalent platinum atomic layers. (c) A 6.0 μm×6.0 μm area after a 100 ms plating pulse which yielded a deposition charge of 77.1 μC cm^{-2} corresponding to 0.080 equivalent platinum atomic layers.

sions of semiconductor nanoparticles possessing a high degree of dimensional uniformity can only be obtained from metal nanoparticle dispersions that are dimensionally uniform. How can these metal nanoparticle dispersions be prepared?

The electrochemical Volmer-Weber [49] growth of metal nanoparticles on graphite surfaces was discovered in 1995 by Jim Zoval, a graduate student in our lab. Using a non-contact atomic force microscope (NC-AFM), Jim examined graphite surfaces on which minute quantities of silver – less than the equivalent of a single silver atomic layer – had been electrodeposited [50]. These surfaces were prepared by plating silver from an aqueous solution containing 1.0 mM Ag^+ using a large overpotential of –500 mV for 10–100 ms. Following the application of a single plating pulse, Jim removed and rinsed the graphite surface and examined it

ex-situ by NC-AFM. His images of the surface revealed that on each square micron of the graphite surface, between 1 and 10 silver nanoparticles were present (corresponding to a "nucleation density" of 10^8–10^9 silver nanoparticles cm^{-2}). These particles had not been detected in prior work because these weakly physisorbed metal clusters could not be seen by conventional repulsive mode AFM or by STM since the probe tip interacted too strongly with these particles and displaced them from the surface during imaging. Jim's data demonstrated that both silver and platinum (from $PtCl_6^{2-}$) deposited via a Volmer-Weber mechanism [49] in which three dimensional clusters of metal formed immediately. Jim's data also supported the conclusion that silver particles nucleated very non-selectively on the graphite surface: Silver nanoparticles were present both at defects, such as step edges, and on atomically smooth terraces. Since 1995, we have discovered that platinum [51], copper [45], cadmium [46, 47], and zinc [48] also grow via this Volmer-Weber mechanism on graphite and that silver may be deposited onto hydrogen-terminated silicon surfaces [52] by a similar mechanism. Representative NC-AFM images of several types of nanoparticles are shown in Fig. 1.

The electrodeposition of all of these metals apparently share two other important similarities. First, the nucleation of metal particles ceases to occur within a few milliseconds following the application of a plating pulse to the surface. Relative to the 10–100 ms duration of plating, then, nucleation is said to be "instantaneous" [53]. Experimentally, then, NC-AFM images of graphite surfaces reveal a nucleation density that is independent of the plating duration, and in the range indicated above.

Secondly, the dimensional uniformity of the metal nanoparticles is degraded as the duration of the plating pulse, and the mean diameter of the particles which are obtained, increases. A quantitative measure of the particle size monodispersity is the standard deviation of the diameter, σ_{dia}, and the relative standard deviation, RSD_{dia} ($RSD = \sigma_{dia}/\langle dia \rangle$, where $\langle dia \rangle$ is the mean particle diameter). This trend is apparent in the particle size distributions for platinum nanoparticles shown in Fig. 2.

The smallest platinum nanoparticles examined in that study were produced by a 10 ms plating pulse and possessed a mean diameter of 25 Å with $\sigma_{dia} = 9$ Å corresponding to an RSD_{dia} of ca. 25%. The dimensional uniformity of these nanoparticles was quite good, and in other experiments, nanoparticles having larger mean diameters up to 50 Å had RSD_{dia} which were approximately at this level. However for larger platinum nanoparticles, produced by plating pulses longer than 100 ms, the nanoparticles became increasing heterogeneous in size. Particles produced by a 100 ms plating pulse, shown in Fig. 1c, for example, possessed a mean diameter of 75 Å, σ_{dia} = 35 Å and $RSD_{dia} \approx$ 50–60%. We have found that the degradation of the particle size monodispersity of the metal nanoparticles produced by "long" deposition pulses is an absolutely general observation for many different metals.

Metal nanoparticle dispersions having a mean size of less than 50 Å (and reasonably good size monodispersity) are ideally suited to the production of semiconductor nanoparticles using the E/C method, and we discuss the details of several

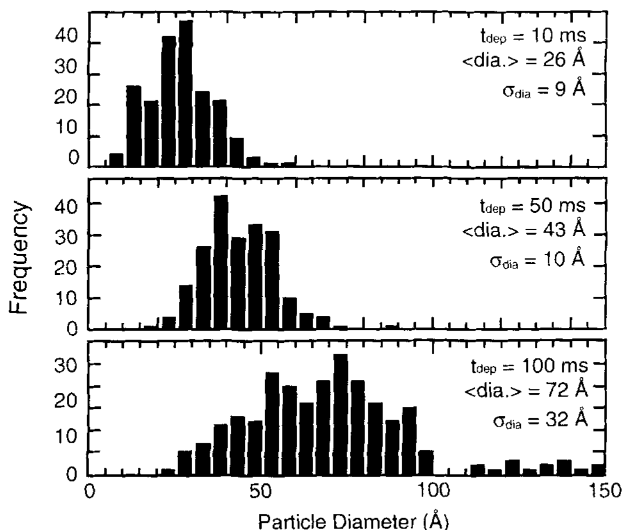

Fig. 1.2 Histograms of platinum particle heights for the same three surfaces shown in the NC-AFM images of Figure 1.

syntheses in Section 1.4. In Section 1.3, however, we describe the origin for the development of size dispersion in metal nanoparticles produced by electrodeposition on graphite. This digression can be skipped by the reader who is primarily interested in the E/C synthesis technique.

1.3 Understanding Particle Size Dispersion in Electrochemical Volmer-Weber Growth

We have demonstrated that dispersions of metal (e.g., platinum [51], silver [50], copper [45], cadmium [46, 47], and zinc [48]) nanoparticles can be electrodeposited onto graphite and silicon electrode surfaces from dilute metal plating solutions. Now we ask, 'What factors are responsible for controlling the size monodispersity of these nanoparticles?'

Two experimental facts are germane to this question: First, we have indicated that a high density of metal nanoparticles is obtained by applying a large overpotential of approximately –500 mV during the deposition of metal. Under these conditions, the metal reduction reaction at the electrode surface occurs at the planar diffusion-controlled rate predicted by the Cottrell equation [8]. Secondly, for the growth of noble metal (Ag [50] and Pt [51]) nanocrystals on graphite surfaces, we have shown that nucleation occurs during the first few milliseconds following the application of the voltage pulse to the electrode surface and then ceases. Thus, relative to the total duration of growth, nucleation is instantaneous [50, 51].

For particles growing in a colloidal suspension, the combination of instantaneous nucleation- and diffusion-controlled growth is known [54, 55] to produce

narrow particle size distributions which become even narrower as the growth duration increases. In recently published work, Ngo and Williams [56] concluded that the situation is fundamentally the same for particles that are confined during growth to a two-dimensional surface (as in electrodeposition). In fact, these workers concluded that instantaneous nucleation leads to very narrow particle size distributions for any growth duration irrespective of the rate law which applies (e.g., particle radius, $r^n \propto t$ where $n=2$, 3, and 4) provided every particle on the surface grows according to the *same* rate law [56]. If nucleation is not instantaneous, then the *RSD* of the island radii is expected to decrease as a function of time for virtually any rate law [56]. However as we have seen, this "convergent growth" mode is not seen for metal particles growing on electrode surfaces: While metal nanoparticles with a mean diameter smaller than 50 Å prepared using growth pulses of ca. 10 ms *are* narrowly dispersed in diameter (e.g., for platinum [51], $RSD \leq 35\%$), both the standard deviation and the relative standard deviation *increase* as a function of the deposition time.

We have recently reported a Brownian dynamics simulation study [57] of the growth of nanoparticle ensembles. In these simulations, ensembles of up to 200 metal particles were grown in a large simulation volume at diffusion control from single atoms to mean diameters of 3 nm from a 10^{-3} M "solution" of metal ions. Since the number of nuclei in each simulation is fixed at the beginning of the simulation, nucleation is rigorously instantaneous. Each metal particle in these ensembles was explicitly modeled so that the development of size dispersion for the ensemble could be monitored as a function of the deposition time. The behavior of "random" ensembles of nanoparticles and hexagonal arrays were compared across a range of experimentally relevant nucleation densities.

The central result of this work is illustrated by the plots shown in Fig. 1.3.

Here the deposition current and the standard deviation of the particle diameter are plotted for depositions having a duration of 0.5 ms. In each of these plots, open circles indicate the deposition current, and filled circles show the standard deviation of the particle diameter, σ_{dia}. Several trends are apparent from these data: First, a peak exists in the current versus time plot. As shown in Scheme 1.3, this peak occurs at $\tau_{peak} = r^2/2D$, where r is one-half the mean distance between nearest neighbors on the surface. The origin of this peak is shown in Scheme 1.3.

At the onset of metal deposition (Scheme 1.3a), the hemispherical layers surrounding each nanoparticle that are depleted of metal ions are well separated from one another and, on average, the growth of a metal particle is not influenced by the growth of neighboring particles. In this "weak interaction" limit, the current at an ensemble of particles equals the current for a single, isolated particle multiplied by the number of particles, N, growing on the surface [58]:

Eq. (1) predicts that the current in this time domain increases and is proportional to $t^{1/2}$. At long times (Scheme 1.3d), depletion layers at adjacent particles merge and an approximately planar diffusion layer blankets the entire geometric surfaces area of the electrode. The current in this "strong interaction" limit is exactly the same as that at a planar electrode having the same geometric area, A, and is given by the familiar Cottrell equation [59]:

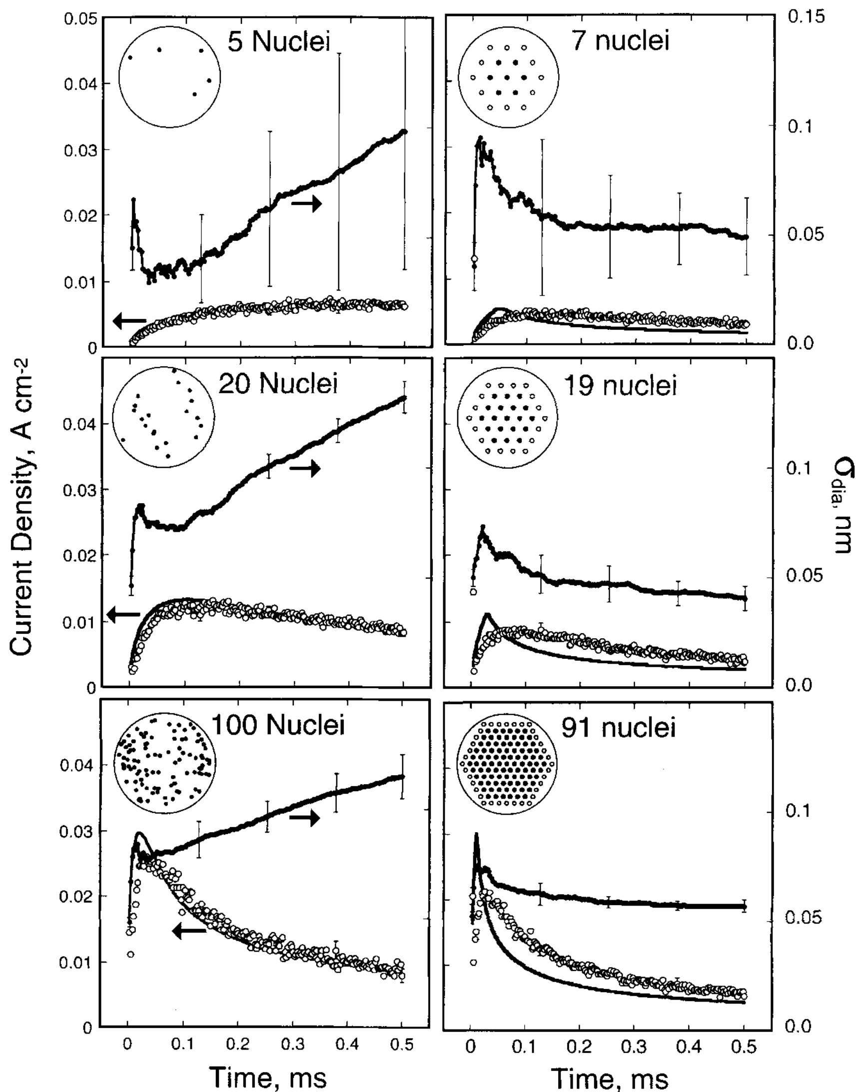

Fig. 1.3 Current density (open circles) and the standard deviation of the particle diameter, σ_{dia}, (solid circles) as a function of time for three random ensembles (shown at left) and three hexagonal ensembles (shown at right). Each of these six data sets represent the mean of three simulations, each of which involved a different silver plating "solution", and different positions for nuclei on the surface. The standard deviation of the current and σ_R are indicated by the error bars ($\pm$ 1σ) which are shown at five times. Data sets are labeled with the nucleation density in units of 10^9 cm^{-2}.

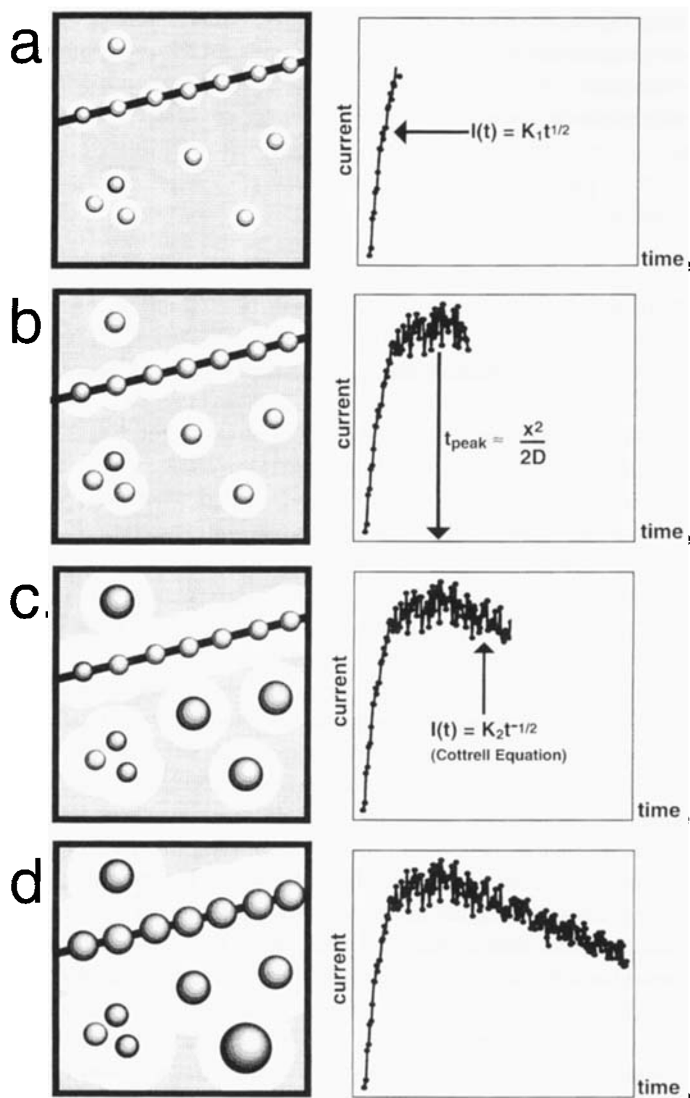

Scheme 1.3 The development of particle size polydispersity in metal nanoparticles growing under diffusion control on a surface.

$$i(t) = \frac{\pi F N (2 D_{Ag^+} C^*_{Ag^+})^{3/2} (M_{Ag} t)^{1/2}}{\rho_{Ag}^{1/2}} \quad (1)$$

Eq. (2) predicts that the current decays with time and is proportional to $t^{1/2}$. The presence of a peak in the current time plot is therefore required to connect the increasing current at short times with the decaying current which is observed at

long times. As shown in Scheme 1.3c, "cross-over" from weak to strong interaction occurs at a time, t_{peak}, which depends on the proximity of particles to one another, and hence on the nucleation density. If the mean distance between nearest neighbors on the surface is $2x$, then $t_{peak} \approx x^2/2D$.

$$i(t) = \frac{nFAD_{Ag^+}^{1/2} C_{Ag^+}^*}{(\pi t)^{1/2}} \qquad (2)$$

With this information in hand, let us focus attention on results for random ensembles of particles shown at left in Fig. 1.3. Data for three particle densities, corresponding to 5, 20 and 100 nanoparticles on a surface having a total area of 10^{-9} cm^{-2}, are presented. Three temporal domains can be distinguished in the σ_{dia} versus time transients: First, σ_{dia} rapidly increases and peaks at ca. 100 μs, then σ_{dia} decreases until the peak in the current-time transient is observed (a "convergent growth" time domain); and finally at longer times, σ_{dia} increases approximately linearly (a "divergent growth" domain). The origin of this behavior for σ_{dia} has been discussed in detail [57], however Scheme 1.3 shows qualitatively what is occurring on the electrode surface. The convergent growth time domain which is observed for $t > 100$ μs mimics the behavior of nanoparticles growing in three-dimensional solution (i.e., dr/dt increases as a function of particle diameter; small particles therefore 'catch up to' larger ones resulting in distribution narrowing).

Following t_{peak} and the transition to a planar depletion layer, the flux of metal ions per unit area on the surface is spatially uniform. Nuclei are randomly located on the surface, however, and the nucleation density is locally variable. Densely nucleated areas can therefore be expected to grow more slowly than regions of the same size (and sharing the same planar flux) but encompassing a smaller number of nanoparticles. This mechanism should lead to a recognizable correlation between the mean radius of nearest neighbors on the surface and the distance separating them, and a statistical analysis of the data confirm [57] that this correlation exists. A second independent check on this explanation is provided by Brownian dynamics simulations of hexagonal arrays for which the nearest neighbor distance for every particle on the surface is identical, and the mechanism of size distribution broadening mentioned above can not operate. Representative examples of simulations for hexagonal arrays are shown at right in Fig. 1.3 and it is immediately apparent that the increase in σ_{dia} seen for random arrays is absent. Not shown in Scheme 1.3 is the origin of the initial rapid increase in polydispersity which we have shown [57] is caused by stochastic processes which play the dominant role when the nanoparticles consist of a few atoms.

Once the mechanism by which size dispersion develops in a growing ensemble of particles is understood, the growth conditions for metal nanoparticles can be engineered to yield improved size monodispersity. For example, a clear prediction of these BD simulation results is that particle size monodispersity can be improved by locating nucleation sites in a two-dimensional geometric array. Unfortunately, this regularity is not characteristic of nucleation processes in nature. If, as

is usually the case, metal nanoparticles nucleate randomly, the size monodispersity of growing nanoparticles can be improved by slowing the growth rate since development of the depletion layer responsible for coupling neighboring particles on the surfaces will be retarded. A second possibility involves inducing nanoparticles to move on the surface during growth (temporal fluctuations of the interparticle nearest neighbor spacing – for all of the particles on a surface – is almost as beneficial as growing stationary particles in a regular array). We have recently confirmed that both of these strategies can be successful.

1.4 Converting Metal Nanoparticles into Semiconductor Quantum Dots

As shown in Schemes 1 and 2, the conversion of electrodeposited metal nanoparticles into nanoparticles of a semiconducting metal salt generally requires two steps: 1. electrochemical oxidation, and 2. displacement of oxide (or hydroxide) by another anion. We discuss these two operations next.

1.4.1 A Metal Oxide Intermediate

A metal oxide intermediate is not a requirement for a successful E/C synthesis based on thermodynamic grounds. Rather, metal oxide formation is inevitable for metal nanoparticles subjected to air exposure. We have found this to be true, at least, for all metals we have examined with the exception of platinum [51]. Strictly speaking, it would not be necessary to subject metal nanoparticles to atmosphere if it were not desirable to characterize them by selected area electron diffraction (SAED) which (at UCI) requires that samples be transferred through air into a transmission electron microscope equipped to perform SAED measurements. Although oxidation of the metal particle is not detrimental, the oxidation conditions must be selected to produce a metal oxide in which the metal has the same oxidation state as in the targeted semiconducting salt. This is because the oxidation state of the metal will not normally change during the final displacement step.

Because a particular metal oxide is required, the oxidation process is usually carried out electrochemically in the metal plating solution immediately following the electrodeposition of metal. The selection of appropriate oxidation conditions (pH and potential) is guided by the Pourbaix diagram [60] for the metal of interest. Pourbaix diagrams appropriate for zinc, copper, and cadmium at a concentration of 10^{-3} M are shown in Fig. 4.

All three of these metals can be electrodeposited at $pH<6$ without resorting to complexing agents. The deposition potentials which we have employed are indicated in Fig. 4 by solid circles. Following deposition, the metal deposit is either permitted to spontaneously oxidize at open circuit (for Zn and Cd), or the oxidation is carried out potentiostatically at the potential indicated by the open circle (Cu). The Pourbaix diagram, however, does not always accurately predict the product of these

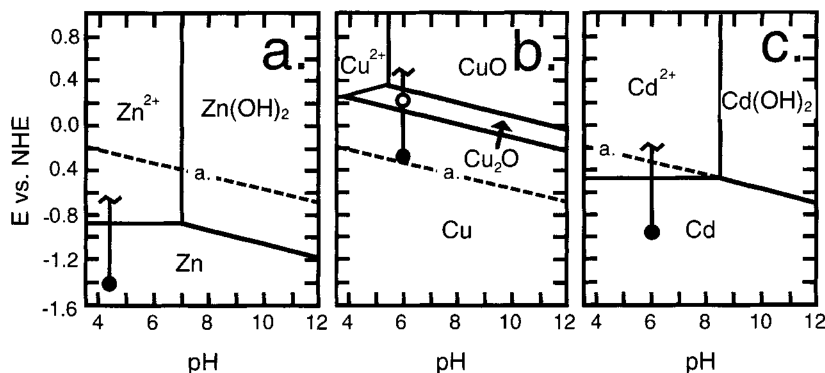

Fig. 1.4 Pourbaix diagrams for zinc (a), copper (b), and cadmium (c) indicating typical deposition and oxidation conditions employed for steps 1 and 2 of the E/C synthesis of ZnO, β-CuI, and CdS, respectively. In these diagrams, the tilde represents the initial potential and pH for each deposition, and the filled circle represents the metal deposition potential and pH. An open circle in the copper Pourbaix diagram marks the potential employed for the potentiostatic oxidation of Cu^0 to Cu_2O.

oxidation processes. In the case of zinc, for example, the Pourbaix diagram of Fig. 1.4 predicts that the thermodynamically favored product for the oxidation of zinc metal at pH = 4.5 is Zn^{2+} however we observe the formation of ZnO under these conditions [48]. Oxidation of metallic Cu and Cd at pH = 6.0 yields Cu_2O and $Cd(OH)_2$ which are suitable for conversion in the final step of the E/C synthesis to Cu(I)I and CdS [45, 47]. The identities of the metal oxides obtained upon oxidation are established using selected area electron diffraction analysis (SAED).

1.4.2
Conversion from Metal Oxide to Metal Salt and Characterization

The displacement of OH^- or O^{2-} from the intermediate oxide formed in step 2 of the E/C synthesis occurs upon exposure to the anion of interest. We have found that this transformation may be carried out either in the gas phase (e.g. via H_2S at 300°C in the case of $Cd(OH)_2$) [47] or in the liquid phase (e.g. via I^- in the case of Cu_2O) [45]. Again, SAED analysis guides the selection of the displacement conditions and permits the composition of the metal salt nanocrystallites to be determined. In addition, the formation of epitaxial nanocrystals can be unambiguously detected from the SAED pattern. Fig. 1.5, for example, shows typical SAED patterns for graphite surfaces on which nanocrystals of ZnO, β-CuI and CdS have been deposited. Wurtzite phase ZnO (Fig. 1.5 a) is identified based on two diffuse diffraction rings at d-spacings that match the [110] and [100] spacings for this compound [48].

Rings of diffracted electron intensity are observed indicating that ZnO particles have no preferential azimuthal orientation on the graphite surface. SAED patterns for copper iodide and cadmium sulfide, on the other hand, consist of diffraction

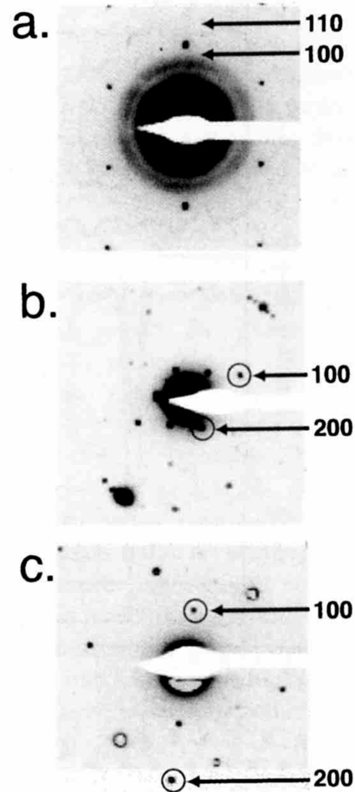

Fig. 1.5 Selected area diffraction patterns (SAED) for E/C-synthesized materials: (a) 100 Å ZnO film; (b) 50–100 Å diameter β-CuI NCs; (c) 18 Å diameter CdS NCs. In each case a 10 μm diameter regior of the surface was sampled. Assignments of key diffraction spots associated with each of these products is as indicated. In addition, a hexagonal array of diffraction spots assignable to graphite is visible in each pattern.

spots that are superimposed on the hexagonal diffraction pattern for the graphite surface. Because a 10 μm diameter region of the graphite surface encompassing hundreds of nanocrystals is probed in an SAED measurement, the spot patterns seen for β-CuI and CdS must be generated by diffraction from ensembles of nanocrystals which are crystallographically identical [45, 47]. Because individual NCs on the graphite surface are well separated from one another, this orientational uniformity can only be produced if nanocrystals adopt a preferred orientation with respect to the hexagonal graphite lattice.

It is worthwhile to ask *why* NCs of β-CuI and CdS adopt epitaxial orientations on the graphite surface and NCs of ZnO do not. In order to answer this question, we have calculated the energy of a rigid, two layer thick island of the metal salt (containing 182 atoms) on a rigid HOPG(0001) surface (containing 1882 atoms in two layers) as a function of the azimuthal orientation of the island on the surface [47, 48, 61]. This calculation involves summing the pairwise interactions between all atoms in the island with all atoms in the surface using a generic Lennard-Jones (L-J) 6–12 potential. Since a L-J potential parameterized for these materials does not exist (as far as we are aware), in Fig. 1.6 we have normalized the calculated interaction energy, E, using the well-depth of the L-J 6–12 potential, ε_0.

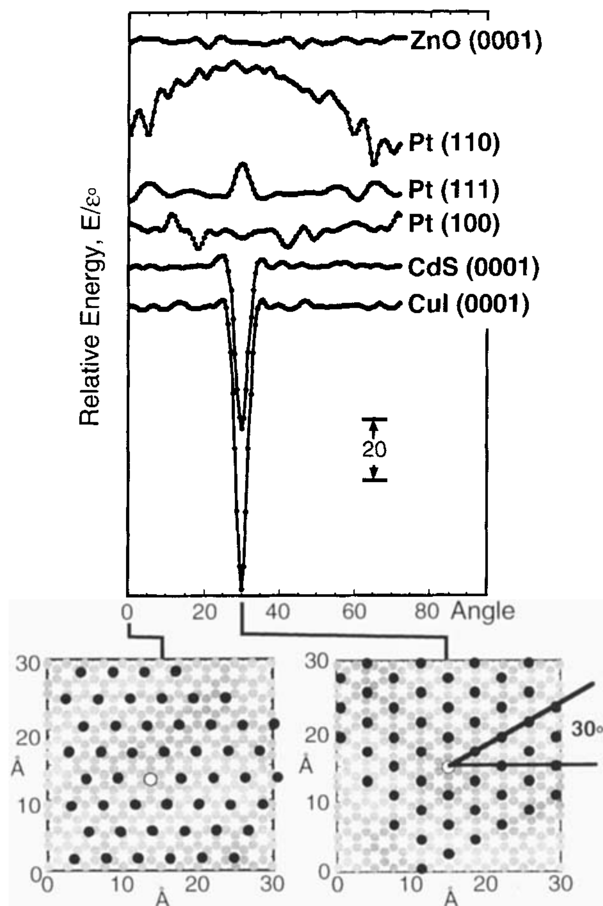

Fig. 1.6 Plot of the calculated interfacial energy, $E/4_0$, against angle calculations for the interface of six different materials with graphite (0001) surface. In each of these calculations, the absolution interfacial energy, E, has been normalized by the well depth of the Lennard-Jones pairwise potential, ε_0. Each island was approximately 25 Å in diameter and consisted of 126 atoms partitioned into two layers of equal size. The graphite surface consisted of 1882 atoms also partitioned into two layers. At bottom left is shown the configuration for the CdS-graphite calculation corresponding to 0°, and at bottom right is shown the configuration for this system corresponding to the energy minimum at 30°.

We have performed these calculations assuming that the (0001) surface of the hexagonal metal salt contacts the graphite surface since the c-axis orientation determined from SAED requires this orientation [45, 47]. Fig. 1.6 shows the calculated energy of an island as a function of its angle with respect to the graphite surface. For both β-CuI and CdS, significant energetic wells are seen for a 60° rotation of the (0001) β-CuI and the (0001) CdS lattices on the hexagonal graphite surface (relative to the arbitrary starting point shown at the bottom of Fig. 1.6). These energetic wells correspond to coincidences between the lattice of the NC,

and that of the graphite surface, as shown schematically for CdS at the bottom of Fig. 1.6 [47]. In contrast, no significant energetic minima are seen for the (0001) surface of wurtzite phase ZnO indicating that this interface is badly mismatched at all angles [48]. Thus no energetic reason exists for ZnO NCs to adopt a preferential orientation on the graphite surface, and a SAED powder pattern like that seen in the experimental data of Fig. 1.5a are expected. Data for the three low-index faces of platinum are also shown in Fig. 6 for purposes of comparison. Especially for [100] and [111] (the likely termination faces for a platinum NC), pronounced energy minima are absent. Experimentally we have found that platinum NCs, like ZnO, have no orientational preference (data not shown) [51]. Thus, the relatively simple calculation depicted in Fig. 1.6 correctly predicts the epitaxial nature of the E/C deposition for both β-CuI and CdS, and it predicts the absence of epitaxy for NCs of ZnO and platinum metal on graphite.

It is nevertheless surprising that NCs of β-CuI and CdS possess sufficient mobility on the graphite surface to locate their minimum energy orientations. This is particularly true since transmission electron microscopy (TEM) images [45, 47] reveal that no center of mass motion occurs for nanoparticles on the graphite surface during the transformation from metal oxide to metal salt. The microscopic mechanism by which this final displacement step of the E/C mechanism occurs is incompletely understood at present. Collectively, the SAED data coupled with TEM images of β-CuI and CdS NCs convincingly demonstrate that metal oxide nanoparticles are converted on a particle-by-particle basis into semiconducting metal salt particles thereby supporting the "E/C paradigm" set forth in the schematic diagrams of Schemes 1.1 and 1.2.

1.5 Photoluminescence Spectroscopy of E/C Synthesized Materials

Gregor Hsiao, a graduate student in the group, acquired the first PL spectra for the β-CuI NCs he synthesized in 1996 [45]. At that time, we were astonished that purple luminescence ($h\nu_{fluor}=2.9$ eV) – visible to the naked eye at room temperature – could be seen for less than a monolayer of β-CuI NCs on the conductive graphite surface. The surprising part is that this photoluminescence isn't quenched [62] by the graphite surface. Since then, we have obtained PL spectra for E/C synthesized ZnO and CdS on graphite (albeit usually at low temperature), and it can only be concluded that, relative to a metal, graphite (a semi-metal) is an inefficient quencher of the charge-separated state for all of these materials. This is fortuitous since it has permitted us to acquire PL spectra for E/C synthesized materials with a minimum of post-synthesis manipulation.

PL spectra for ZnO [48], β-CuI [45], and CdS [47] are compiled in Fig. 1.7. Shown in Fig. 1.7a is the PL spectrum for a ZnO film a few hundred angstroms in thickness.

Nanoparticles of this material have been synthesized using the E/C approach, however we have not obtained emission spectrum from them since the absorption

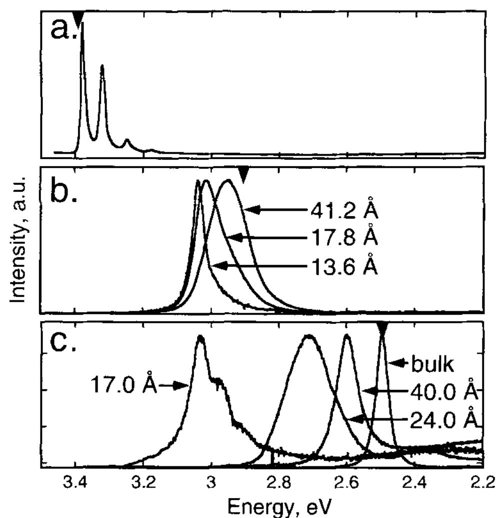

Fig. 1.7 Photoluminescence (PL) emission spectra for E/C synthesis materials. In all three cases, PL was excited using the 351 nm line of an Ar^+ laser. (a) ZnO film approximately 100 Å in thickness. $T=20$ K. (b) β-CuI nanocrystals of three radii as labeled. $T=295$ K. (c) Sulfur-passivated CdS nanocrystals of three radii as labeled. $T=20$ K.

edge for these quantum dots, which is blue-shifted to beyond 3.5 eV, can not be assessed using our present lasers. The ZnO PL spectrum of Fig. 1.7a is notable for two reasons [48]: First, the progression of emission lines which are observed derive from phonon loss transitions in which an integer number of phonons have been excited in the course of emission. The energy separating these emission lines ($\approx$ 76 meV) corresponds to the energy of a single LO phonon in this material, and the presence of 6 phonon loss lines in this spectrum is consistent with an extremely low defect density for this material. Secondly, the low energy region of the PL spectrum in Fig. 1.7a from 3.2 (UV) to 2.2 eV (green) is absolutely devoid of emission. Emission from mid-gap states derived from impurities and defects has been an absolutely ubiquitous feature of the PL spectrum for ZnO synthesized using other methods [48]. The absence of this emission in the spectrum of Fig. 1.7a points to the high purity, and crystallinity, of E/C synthesized ZnO.

PL spectra for β-CuI and CdS quantum dots possessing a range of sizes are shown in Fig. 1.7b and c, respectively. In this figure, the arrow along the top of each frame indicates the energy of the band-gap for these two materials. Emission from the E/C synthesized nanocrystals of β-CuI and CdS are blue-shifted from this energy and the magnitude of this shift is inversely related to the nanoparticle radius, indicating that photogenerated electrons and holes in these nanoparticles are quantum-confined. However the energy shift seen for CdS NCs having a radius of 17 Å ($\approx$ 500 meV) is much greater than for β-CuI NCs with a radius of 13.6 Å ($\approx$ 120 meV). The greater "sensitivity" of CdS to the NC radius derives from the smaller hole effective mass in this material (0.8 m_0 compared with 1.4 m_0 for CuI). Because the dielectric constants of β-CuI and CdS are similar (4.58 compared with 5.4), the lighter reduced effective mass of CdS possess larger wavefunctions than their counterparts in CuI and the Bohr radius for an exciton in CdS is therefore proportionately larger.

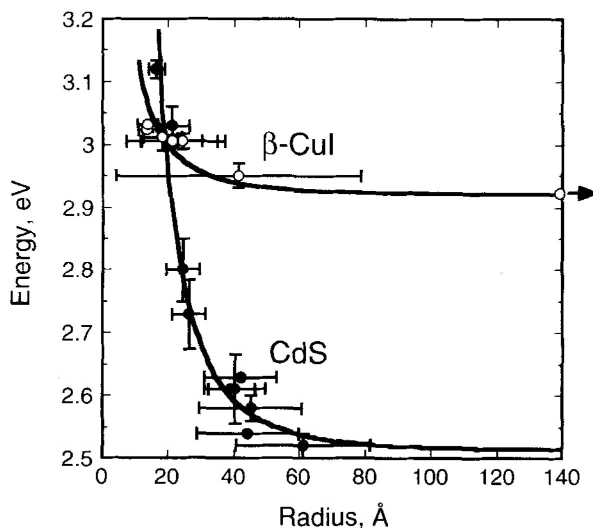

Fig. 1.8 Plots of the energy of maximum emission versus the radius for nanocrystals of β-CuI (open circles) and CdS (filled circles). Error bars represent the dispersion (i.e. $\pm 1\sigma$) in the energy and the nanoparticle radius for a series of measurements at different locations on the graphite surface. Solid lines represent the calculated bandgap energy as a function of radius for these two materials [45, 47].

Plots of PL energy against radius for β-CuI and CdS are shown in Fig. 1.8 (data points). Also plotted in Fig. 8 are calculations of the bandgap energy as a function of the NC radius for these two materials (solid lines).

The agreement between the calculated bandgap and the experimentally observed PL indicates that photoexcited electrons at the conduction band edge recombine directly with holes at the valence band edge. This process results in the emission of a PL photon having an energy equal to that of the bandgap. A competing process involves the thermalization of electrons and holes into trap states existing within the bandgap. These traps are the inevitable consequence of defects and impurities, and the recombination of trapped electron and holes generates photons having an energy smaller than that of the bandgap. Little evidence for this "trap state" emission exists in the form of red-shifted emission in the spectra shown in Fig. 1.7. We say that these QDs are "optically intrinsic".

Collectively, the data shown in Figs. 1.7 and 1.8 permit the following conclusions: 1) E/C-synthesized nanocrystals of β-CuI and CdS on graphite surfaces are luminescent, 2) luminescence from these NCs derives from the band-to-band recombination of photogenerated electron and holes; this transition does not involve "deep" trap states. This fact suggests that the crystal quality and purity of these materials are both high, and 3) the PL emission energy can be smoothly tuned by adjusting the NC radius using the E/C synthesis conditions (i.e., the radius of the metal nanocrystals deposited in Step 1).

1.6
An Application for E/C Synthesized Quantum Dots: Photodetection Based on a New Principle

We have recently demonstrated [40] the feasibility of electrically detecting the absorption of light by a submonolayer coverage of cadmium sulfide QDs supported on a graphite surface. The device structure shown in Scheme 1.4 was the first to enable the absorption of light by semiconductor nanocrystallites to be directly detected as an electrical signal.

To construct these photodetectors [40] a 10–100 nm thick layer of the insulating polymer, Formvar, was deposited by first dissolving the Formvar in chloroform, then floating a few drops of this solution on to the surface of Nanopure water in a beaker, and finally pulling the immersed graphite surface, on which CdS QDs had been deposited, through the floating polymer film. Following the evaporation of solvent from this film, a Scotch tape mask with a 5 mm diameter aperture was applied to the sample as a contact pad, then a thin semitransparent (10–15 nm) silver top electrode was evaporated onto the surface of the Scotch tape and the exposed Formvar film.

The principle of operation is shown schematically in Fig. 1.9a. Photoexcited electrons (or holes) in a quantum dot can be transferred into unfilled (or filled) states of the graphite surface. The probability with which this transfer occurs is likely to be different for electron and holes because the density of states in graphite is a strongly varying function of energy near the Fermi level. Provided these two "quenching" rates are unequal, the absorption of a photon by an ensemble of millions of quantum dots will result in an excess of either electrons or holes at

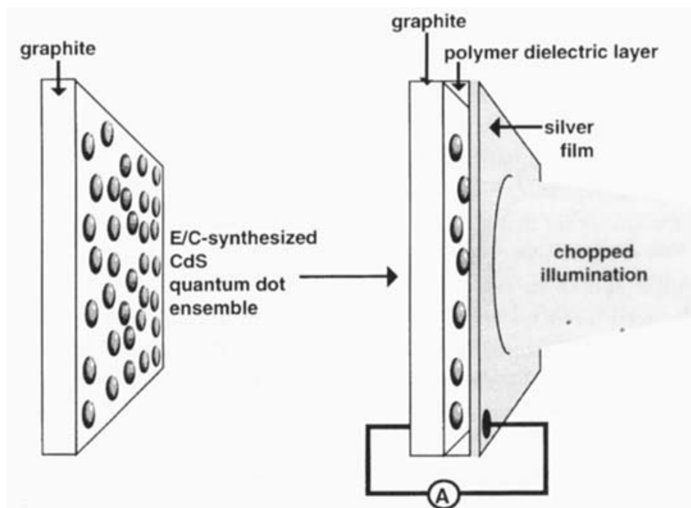

Scheme 1.4 Schematic diagram of the construction of a photodetector based on E/C-synthesized CdS nanocrystals on graphite.

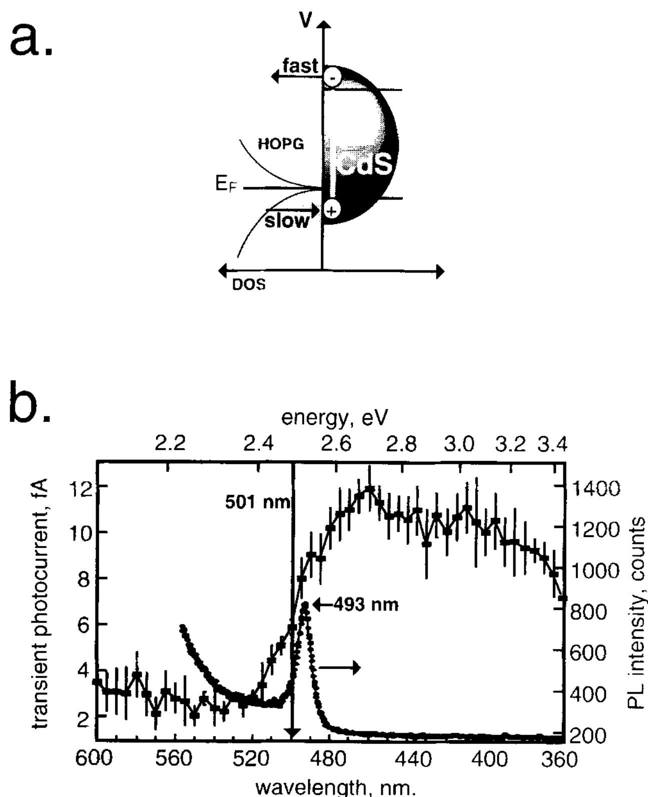

Fig. 1.9 Proposed mechanism of operation for the photodetector of Scheme 4. Experimental data for a photodetector having the construction shown in Scheme 4. Both photoluminescence spectra (acquired at 20 K using $h\nu_{ex}$=3.51 eV; solid circles) and device response spectra (acquired at 298 K; solid squares) are shown. The device response was measured by chopping the incident illumination and synchronously measuring the resulting difference between anodic and cathodic charging transients using a fast ammeter in conjunction with a lock-in amplifier [40]. Error bars represent the dispersion of these photocurrent measurements.

the graphite surface, and this excess can be directly measurable as a transient current in the device shown in Fig. 1.9a.

Low temperature PL spectra and transient photo-current device response spectra are compared in the plot of Fig. 1.9b for a device which was constructed using r=40 Å CdS QDs [40]. The PL spectrum for this device shows a slight blue-shift of the emission maximum to 493 nm, qualitatively as expected for 40 Å CdS QDs. The absorption edge seen in the device spectrum was likewise blue-shifted to 501 nm proving that the photocurrent measurement is sensitive to the nanoparticle band gap even at room temperature. Control devices, with the construction shown in Scheme 1.4 but without QDs (i.e., using clean graphite surfaces) exhibited no photocurrent peaks above background.

Two advantages of this detector are the tunability of its response (imparted by the identity of the quantum dots and their radii), and the fact that the detection of light involves no space-charge region (as in conventional photodiodes and charge-coupled devices). In principle, then, a detector having the construction shown in Scheme 1.4 could be a few microns in total thickness.

Summary

The electrochemical/chemical method is a fundamentally new route to semiconductor quantum dots. Although QDs can be obtained using solution phase chemical methods, and by molecular beam epitaxy, the E/C method has the following attributes: 1) Semiconductor nanocrystals prepared using the E/C method possess *a high degree of size monodispersity.* 2) *Functionalization of the surface of QDs is not required* to prevent aggregation since the interaction of each incipient QD with the graphite surface during the E/C synthesis eliminates the lateral motion of particles on the surface. 3) The mean particle diameter is fixed by the diameter of the metal nanoparticles which are deposited in the first step of the synthesis. Therefore, *a range of mean particle diameters can be prepared and adjusting the mean particle diameter is straightforward.* 4) *The E/C method has excellent versatility.* We have so far demonstrated E/C syntheses for three materials including a metal oxide (ZnO), a material from the I–VII family (CuI), and a II–VI material (CdS). It is conceivable that, in the future, III–V materials such as InN will be accessible using E/C procedures such as that shown in Scheme 1.2. 5) The semiconductor materials obtained using the E/C method can possess *excellent photoluminescence emission properties* in which emission from the band-to-band transition dominates the emission spectrum and trap-state emission is virtually non-existent. 6) QDs of selected materials can be *epitaxially deposited* using the E/C method. 7) QDs prepared using the E/C method are disposed in *intimate electrical contact with the graphite surface.* This fact makes possible the fabrication of the photodetector described above which requires electrical communication between the QDs and the surface. Finally, 8) Relative to competing methods, the E/C method is fast and inexpensive.

The primary disadvantage of the E/C method is its dependence on the technologically irrelevant graphite surface. Although we have demonstrated that devices based on graphite, such as the optical detector discussed above, can be constructed there is a strong motivation to extend the E/C synthetic protocols to the technologically relevant Si(100) surface. Because graphite and hydrogen-terminated silicon both have a very low surface free energy and defect density, one might expect the deposition of metals to occur via a similar mechanism on these two surfaces. We have recently demonstrated [52] that for silver, this is indeed the case. The growth of silver on hydrogen-terminated Si(100) occurs via a Volmer-Weber mechanism and the deposition of size-similar silver NCs is possible [52]. Based on this result, there is every reason to believe that it will be possible in the future to carry out the E/C synthesis of QDs on silicon.

Acknowledgments

Presently, semiconductor synthesis investigations in the author's laboratory are funded by the National Science Foundation (#DMR-9876479) and the Petroleum Research Fund of the American Chemical Society (#33751-AC5). The author also gratefully acknowledges an A.P. Sloan Foundation Fellowship and a Camille Dreyfus Teacher-Scholar award. RMP thanks current and former coworkers. Finally, the work described here would have been much more expensive without the generosity of Dr. Art Moore of Advanced Ceramics who has provided my group with graphite for the past 9 years.

References

1 G. Hodes, in: *Physical Electrochemistry: Principles, Methods and Applications*; I. Rubinstein, Ed.;, Marcel Dekker, **1995**, 515.
2 B. W. Gregory, J. L. Stickney, *J. Electroanal. Chem.* **1991**, 300, 543.
3 B. W. Gregory, M. L. Norton, J. L. Stickney, *J. Electroanal. Chem.* **1990**, 293, 85.
4 F. Cerdeira, I. Torriani, P. Motisuke, V. Lemos, F. Decker, *Appl. Phys.* **1988**, 46, 107.
5 G. Hodes, S. J. Fonash, A. Heller, B. Miller, in *Advances in Electrochemistry and Electrochemical Engineering*; Gerischer, H., Ed.; J. Wiley & Sons: New York, **1985**, Vol. 13, 113.
6 A. M. Kressin, V. V. Doan, J. D. Klein, M. J. Sailor, *Chem. Mat.* **1991**, 3, 1015.
7 D. W. Suggs, I. Villegas, B. W. Gregory, J. L. Stickney, *J. Vac. Sci. Technol. A* **1992**, 10, 886.
8 B. E. Breyfogle, C. J. Hung, M. G. Shumsky, J. A. Switzer, *J. Electrochem. Soc.* **1996**, 143, 2741.
9 T. D. Golden, M. G. Shumsky, Y. C. Zhou, R. A. Vanderwerf, J. L. Switzer, *Chem. Mat.* **1996**, 8, 2499.
10 R. A. Van Leeuwen, C. J. Hung, D. R. Kammler, J. A. Switzer, *J. Phys. Chem.* **1995**, 99, 15247.
11 T. Wade, J. M. Park, E. G. Garza, C. B. Ross, R. M. Crooks, *J. Am. Chem. Soc.* **1992**, 114, 9457.
12 T. Wade, C. B. Ross, R. M. Crooks, *Chem. Mat.* **1997**, 9, 248.
13 J. M. Lauerhaas, G. M. Credo, J. L. Heinrich, M. J. Sailor, *J. Am. Chem. Soc.* **1992**, 114, 1911.
14 V. Doan, M. J. Sailor, *Appl. Phys. Lett.* **1992**, 60, 619.
15 J. A. Switzer, M. J. Shane, R. J. Phillips, *Science* **1990**, 247, 444.
16 J. A. Switzer, C. J. Hung, B. E. Breyfogle, M. G. Shumsky, *Science* **1994**, 264, 1573.
17 T. D. Golden, R. P. Raffaelle, J. A. Switzer, *Appl. Phys. Lett.* **1993**, 63, 1501.
18 J. Switzer, M. Shumsky, E. Bohannan, *Science* **1999**, 284, 293.
19 L. Colletti, B. Flowers, J. Stickney, *J. Electrochem. Soc.* **1998**, 145, 1442.
20 D. W. Suggs, I. Villegas, B. W. Gregory, J. L. Stickney, *J. Vac. Sci. Technol. A* **1992**, 10, 886.
21 D. W. Suggs, J. L. Stickney, *Surf. Sci.* **1993**, 290, 362.
22 D. W. Suggs, J. L. Stickney, *Surf. Sci.* **1993**, 290, 375.
23 E. Bohannan, L. Huang, F. Miller, M. Shumsky, J. Switzer, *Langmuir* **1999**, 15, 813.
24 J. Switzer, C. Hung, L. Huang, E. Switzer, D. Kammler, T. Golden, E. Bohannan, *J. Am. Chem. Soc.* **1998**, 120, 3530.
25 J. A. Switzer, B. M. Maune, E. R. Baub, E. W. Bohannan, *J. Phys. Chem. B* **1999**, 103, 395.
26 Y. Golan, B. Alperson, J. L. Hutchison, G. Hodes, I. Rubinstein, *Adv. Mat.* **1997**, 9, 236+.
27 Y. Golan, L. Margulis, I. Rubinstein, G. Hodes, *Langmuir* **1994**, 8, 749
28 Y. Golan, L. Margulis, G. Hodes, I. Rubinstein, J. L. Hutchison, *Surface Science* **1994**, 311, L633

29 Y. Golan, G. Hodes, I. Rubinstein, *J. Phys. Chem.* **1996**, 100, 2220

30 Y. Golan, J. L. Hutchison, I. Rubinstein, G. Hodes, *Adv. Mat.* **1996**, 8, 631

31 J. Hulteen, C. Martin, *J. Mat. Chem.* **1997**, 7, 1075

32 C. R. Martin, *Science* **1994**, 266, 1961

33 D. Routkevitch, T. L. Haslett, L. Ryan, T. Bigioni, C. Douketis, M. Moskovits, *Chemical Physics* **1996**, 210, 343

34 D. Routkevitch, T. Bigioni, M. Moskovits, J. M. Xu, *J. Phys. Chem.* **1996**, 100, 14037

35 D. Almawlawi, C. Z. Liu, M. Moskovits, *J. Mat. Res.* **1994**, 9, 1014

36 K. Liu, C. Chien, P. Searson, Y. Kui, *Appl. Phys. Lett.* **1998**, 73, 1436

37 P. D. Searson, R. C. Cammarata, C. L. Chien, *J. Electron. Mat.* **1995**, 24, 955

38 L. Sun, P. Searson, C. Chien, *Appl. Phys. Lett.* **1999**, 74, 2803

39 N. C. Greenham, X. G. Peng, A. P. Alivisatos, *Phys. Rev. B* **1996**, 54, 17628

40 G. Erley, S. Gorer, R. M. Penner, *Appl. Phys. Lett.* **1998**, 72, 2301

41 V. L. Colvin, M. C. Schlamp, A. P. Alivisatos, *Nature* **1994**, 370, 354

42 B. O. Dabbousi, M. G. Bawendi, O. Onitsuka, M. F. Rubner, *Appl. Phys. Lett.* **1995**, 66, 1316

43 H. Shoji, K. Makai, N. Ohtsuka, M. Sugawara, T. Uchida, H. Ischikawa, *IEEE Photon. Technol. Lett.* **1995**, 7, 1385

44 N. Kirstaedter, N. N. Ledentsov, M. Grundmann, D. Bimberg, V. M. Ustimov, S. S. Ruvimov, P. S. Maximov, *Electron. Lett.* **1994**, 30, 1416

45 G. S. Hsiao, M. G. Anderson, S. Gorer, D. Harris, R. M. Penner, *J. Am. Chem. Soc.* **1997**, 119, 1439

46 M. Anderson, S. Gorer, R. M. Penner, *J. Phys. Chem.* **1997**, 101, 5895

47 S. Gorer, J. A. Ganske, J. C. Hemminger, R. M. Penner, *J. Am. Chem. Soc.* **1998**, 120, 9584

48 R. M. Nyffenegger, B. Craft, M. Shaaban, S. Gorer, R. M. Penner, *Chem. Mat.* **1998**, 10, 1120

49 A. Zangwill, Physics at Surfaces; Cambridge University Press, Cambridge, **1988**

50 J. V. Zoval, R. M. Stiger, P. R. Biernacki, R. M. Penner, *J. Phys. Chem.* **1996**, 100, 837

51 J. V. Zoval, J. Lee, S. Gorer, R. M. Penner, *J. Phys. Chem.* **1998**, 102, 1166

52 R. Stiger, B. Craft, R. M. Penner, *Langmuir* **1999**, 15, 790

53 The Fundamentals of Metal Deposition; J. A. Harrison, H. R. Thirsk, Eds.; Marcel Dekker: New York, **1971**, Vol. 5

54 J. T. G. Overbeek, *Adv. Coll. Int. Sci.* **1982**, 15, 251

55 T. Sugimoto, *Adv. Coll. Interface Sci.* **1987**, 28, 65

56 T. T. Ngo, R. S. Williams, *Appl. Phys. Lett.* **1995**, 66, 1906

57 J. L. Fransaer, R. M. Penner, *J. Phys. Chem. B* **1999**, 103, 1643

58 P. A. Bobbert, M. M. Wind, J. Vlieger, *Physica A* **1987**, 146, 69

59 A. J. Bard, L. R. Faulkner, Electrochemical Methods: Fundamentals and Applications; John Wiley & Sons, New York, **1980**

60 M. Pourbaix, *Atlas of Electrochemical Equilibria in Aqueous Solutions*, Pergammon Press, New York, **1966**

61 S. Gorer, G. S. Hsiao, M. G. Anderson, R. M. Stiger, J. Lee, R. M. Penner, *Electrochim. Acta* **1998**, 43, 2799

62 R. R. Chance, A. Prock, R. Silbey, *J. Chem. Phys.* **1974**, 2184, 2744

Electrochemistry of Nanomaterials
by *Gary Hodes (Ed.)*
© WILEY-VCH Verlag GmbH, 2001

2
Electrodeposition of Semiconductor Quantum Dot Films

Gary Hodes and *Israel Rubinstein*

2.1
Introduction

2.1.1
General

The field of nanophase materials is one which covers a wide and active area of research. Various properties of these materials, including mechanical, optical, electrical and structural, are often very different from the same materials in the bulk phase.

Quantum dots are nanoparticles which are sufficiently small that their electronic energy structure is changed from that of bulk material. The size regime of quantum dots varies from only several atoms up to nearly 100 nm in size, depending on the material properties. For metals, the size where quantum size effects are appreciable tends toward the lower limit of this range, while for semiconductors, it can vary over the whole range, depending mainly on the effective masses of the electronic charges (electrons and holes) in the semiconductor; typically it ranges from a few nm up to a few tens of nm. While quantum dots do not necessarily need to be crystalline (amorphous materials also possess an energy structure), virtually all examples studied to date are crystalline.

As outlined in the preface of this book, electrodeposition normally leads to small particle size, largely because it is a low temperature technique, thereby minimizing grain growth. Other factors also contribute to limitations of grain size and will be discussed in this chapter. This characteristic of low temperature is shared by other low-temperature chemical methods, in particular by chemical solution deposition, which also commonly yields nanocrystalline materials. Electrodeposition, however, possesses the additional feature of a very high degree of control over the amount of deposited material through Faraday's law, which relates the amount of material deposited to the deposition charge (see Preface). This feature is particularly desirable when isolated nanocrystals are to be deposited on a substrate.

Many different techniques have been used to electrodeposit semiconductors; a number of reviews of semiconductor electrodeposition exist which describe the

various methods used [1–4]. While the deposits are usually crystalline there is no shortage in the literature of references to electrodeposited amorphous semiconductor deposits [5–7]. The designation of the term 'amorphous' is usually based on X-ray diffraction (XRD) experiments where either a very weak or no pattern was observed. In our own experience, a careful repeat of some of these experiments, acquiring the XRD spectra at very slow scan speeds, showed that the electrodeposits were definitely crystalline and sometimes with a relatively large crystal size. (For our purposes, the use of the term 'large' when describing crystal size refers to crystals which are too large to exhibit quantum size effects – usually considerably greater than 10 nm.). In fact, the description of a deposit as being 'amorphous' based on XRD data (or rather, lack of it) is in itself a useful pointer to locating materials in the previous literature which are nanocrystalline, although not explicitly (and often even not implicitly) described as such.

Among the various techniques employed to electrodeposit semiconductors, the one which appears to result in the smallest crystal size is cathodic deposition from non-aqueous solutions containing elemental chalcogen (S, Se) and a metal salt, first described by Baranski and Fawcett [8]. This technique was quite extensively used by many groups after it was first reported. Particularly notable about this technique was the blue shift often measured in the spectra (either directly or inferred from the reported color). There are many examples of such spectral shifts in the literature; three representative ones are reproduced below to illustrate the point.

"The reason for the discrepancy between the estimate of E_g for CdSe deposited from dimethyl sulfoxide (DMSO) (1.94 eV) and from aqueous solutions (1.74 eV) is unclear, but it probably results from the great structural difference between the two materials. Moreover, the estimated band-gaps for all the CdS_xSe_y films are larger than expected on the basis of previously reported data for mixed films [4, 5]. This result is probably due to the amorphous character of the electrodeposited material and may also reflect some incorporated impurities..." [7].

"Values in the 1.35–1.43 eV range were obtained. These are somewhat higher than the band-gap values quoted in previous work..." [9] (for SnS).

"The optical absorption spectrum of CdS films obtained in DMSO and DEG are shown ...From this data was calculated the band-gap ... Their values were: 2.57 eV ... and 2.45 eV ... This latter value is more in accordance with the 2.4 eV of the Literature. Nevertheless, the former can be considered acceptable and the discrepancies attributed to experimental errors..." [10].

Either no explanation or incorrect ones were forwarded to explain these spectral shifts. As with the 'amorphous' deposits usefulness in tracing nanocrystalline materials, these shifts were an excellent indicator of size quantization which turned out to explain the shifts.

The nonaqueous electrodeposition method, which is the subject of this chapter, has been extensively studied, by other groups as well as by ourselves, from various points of view. At the outset, it must be admitted that the mechanism for this deposition is still unclear. A review of the literature, including discussion of the possible mechanisms of this deposition has been made [4]. Two main mecha-

nisms are considered for the deposition: a) deposition of metal (e.g., Cd) followed by chemical reaction with elemental chalcogen in solution, and b) reduction of chalcogen to (poly)chalcogenide followed by ionic reaction between chalcogenide and metal cations. It seems likely that the former predominates at the beginning of the deposition. In fact, the very beginning of the deposition, when the substrate is a metal with a strong affinity for chalcogen (such as Au) is characterized by an underpotential prepeak in the voltammetry characteristics. Since the first stage of this deposition is often on a chalcogen-covered surface (depending on the affinity of the substrate for the chalcogen), it is probable that, in such cases, it involves underpotential deposition of metal on the chalcogen to give the metal chalcogenide. Whether deposition of the metal chalcogenide on to itself occurs by the same mechanism or by reduction of elemental chalcogen to chalcogenide (reaction (b) above) is still an open question. The balance between the two mechanisms may depend, not only on the amount of material already deposited, but also on the specific system and on the deposition parameters.

2.1.2 Some Specific Issues Relevant to Characterization of Nanocrystalline Materials

Before describing the electrodeposits using this technique, some comments on the experimental techniques used to characterize them, with emphasis on their nanocrystallinity are in order. The three most common techniques used are transmission electron microscopy (TEM) together with electron diffraction (ED); X-ray powder diffraction (XRD) and optical absorption (or transmission) spectroscopy.

TEM is used to image nanocrystal (lateral) size, shape and size distribution. ED provides information on the composition of the deposit, crystal phase and orientation. XRD also provides similar information on composition (more accurately than ED) and phase as well as crystallite orientation. In the latter, ED is superior in many ways, since a much smaller area can be selected (selected area diffraction, SAD) and, in addition, azimuthal lattice alignment between deposit and substrate (epitaxy) can be determined from ED but not from XRD; the latter reveals texturing (one particular crystal face parallel to the substrate for all crystals for perfect texturing) but not orientation (crystal lattices in any direction parallel to the substrate of all crystals aligned in the same way).

One very important use of XRD when dealing with nanocrystals is to estimate crystal dimensions through the Debye-Scherrer relationship:

$$\text{Crystal diameter} = \frac{1.3\lambda}{\Delta(2\theta)\cos\theta}$$

where λ is the X-ray wavelength (0.15418 nm for CuKα radiation), $\Delta(2\theta)$ is the peak full width at half maximum (FWHM) in radians and θ is the peak position. The shape of the crystal can also modify this relationship, which is valid for a spherical (close to the shape often encountered) crystal.

As a rough and useful rule of thumb, a peak FWHM of 1° at an angle of $2\theta = 25°$ means a crystal size of 10 nm (for CuKα radiation), and the size is inversely proportional to the FWHM. Actually, to be more precise, what is measured is not necessarily crystal size but coherence length, the length over which the periodicity of the crystal is complete. An example of a coherence length smaller than the crystal size is a twinned crystal: XRD measures the size of each individual twin. Another cause of XRD peaks being broader than expected based on crystal size is the presence of defects, such as strain in the crystal or dislocations which destroy the long range lattice order. Thus, the interpretation of XRD peak broadening should be carried out with care and preferably using complementary TEM measurements. The opposite case, where the peaks are narrower than expected based on crystal size, does not occur; a narrow peak means a (relatively) large coherence length and therefore crystal size. However, even here, interpretation is not always straightforward. For example, the XRD pattern of a deposit of tall cylinders of small cross-section will give a peak width characteristic of the height but not of the cross-section (the latter will be seen in TEM images). Thus the TEM and XRD sizes will necessarily be different in such a case. Another example is where there is a mixture of large and small crystals. Even if the large crystals constitute a relatively small fraction of the total material, they may, in some cases, dominate the XRD pattern since peak heights decrease with decreasing crystal size (due to increase of peak width and (ideally) constant peak area for the same quantity of material).

Since the most apparent effect of very small crystal size is the increasing band-gap due to size quantization (the effect is visible to the eye if the band-gap is in the visible region of the spectrum), absorption (or transmission) optical spectroscopy is clearly a fast and simple pointer to crystal size, since band-gap-size correlations have been made for a number of semiconductor colloids and films. The problem here is in extracting an estimate of the band-gap from the spectrum. For bulk semiconductors, the relationship between spectrum and band-gap is given by:

$$(ah\nu)^n = C\,(h\nu - Eg)$$

where n is 2 for a direct transition and 0.5 for an indirect one, and C is a constant. A plot of $(\alpha h\nu)^n$ against $h\nu$ should then give a straight line (over much of the absorption onset region) which extrapolates at a zero value of $(\alpha h\nu)^n$ to the band-gap. This calculation is based on the density of states in the valence and conduction bands of the bulk semiconductor [11]. For semiconductors in the quantum size regime, however, the density of states may be quite different than in the bulk. In practice, however, this extrapolation often appears to be valid. We find that a useful approximation for films with a fairly sharp absorption onset is that the band-gap lies one third up the edge of the absorption spectrum (or one third down the edge of the transmission spectrum). Since the shape of the absorption and transmission spectra are not identical, this approximation is not exact: however, taking into account that there is invariably a distribution of crystal sizes –

and therefore of band-gaps if the material is in the quantum size regime – any measurement is clearly only an estimate, since there is not one single band-gap.

For spectra where the absorption onset is gradual, this one-third approximation is totally invalid. In that case, $(\alpha h\nu)^n$ should be plotted against $h\nu$, and n chosen to give a best linear fit. In this case, we have less experience with the validity of the measurement. An example, as will be shown later, is CdSe deposited from DMSO solutions. Although CdSe is normally direct, the spectra of these deposits often behave in between a direct and indirect material with the best value of $n=1$. This value has sometimes been observed for reportedly amorphous semiconductors (ZnSe [12] and $CuInSe_2$ [13]).

2.2 Electrodeposition of Thick Films of Semiconductors from DMSO Solutions

Because much of this chapter will be involved with ultrathin films or, more accurately, with deposits of non-connected nanocrystals, by thick films we mean more than about 10 nm in average thickness (we will come back to the concept of average thickness when dealing with "thin" films, as it is more relevant in that case). The films to be discussed in this section will, in most cases, be between several tens and a hundred nm in thickness.

2.2.1 CdS and CdSe

Fig. 2.1 shows transmission spectra of such CdS and CdSe films. The band-gap values estimated from the spectra are shown by the vertical lines intersecting the spectra. It can be seen that the CdSe onset is considerably less steep than for the CdS and while the latter gives a linear plot of $(\alpha h\nu)^n$ against $h\nu$ for n close to 2 ($n=2$ for a bulk direct band-gap semiconductor), the value of the exponent, n, for the CdSe is 1. We have no convincing explanation for this difference and have not attempted to study it further. The CdSe is clearly crystalline, as seen in dark field TEM [14] and high resolution transmission electron microscopy (HRTEM) lattice imaging (unpublished). One possible explanation could be the rather wide size distribution which would smear out the spectrum. If this were the case, then the value of unity for n would be purely coincidental.

The blue shifts of these spectra compared with the bulk ones are evident and correspond to increases in the band-gap of ca. 0.2 eV. TEM measurements of these films have shown lateral crystal sizes of typically 5 nm [14, 15]. XRD, on the other hand, shows larger dimensions, particularly for the CdS, where the coherence length in the direction perpendicular to the basal plane (the preferred growth direction) is ca. 15 nm, resulting in short quantum wires [16]. In spite of this, the size quantization is appreciable.

This quantization has been put to use by depositing the CdS, formed in this way, as a window layer on $CuInS_2$ and $CuInSe_2$ photovoltaic cells instead of the

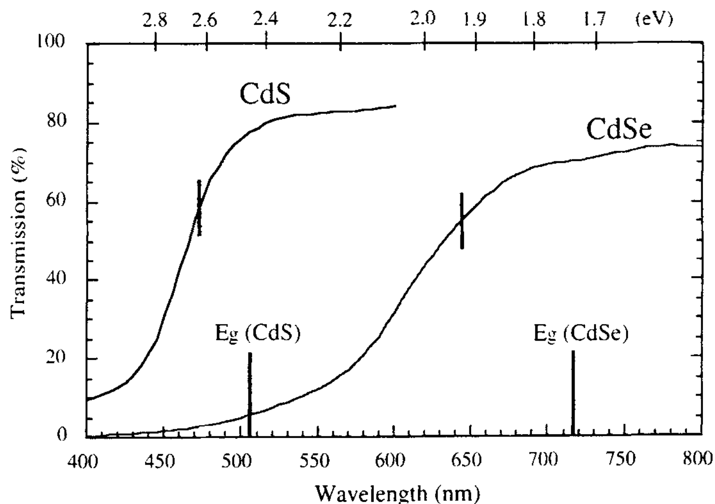

Fig. 2.1 Transmission spectra of CdS and CdSe films electrodeposited from DMSO solutions containing $CdCl_2$ and S or Se at ca. 100 °C. Film thicknesses 100–200 nm. The band-gaps of the films, estimated from the spectra, are shown as vertical lines cutting the spectra. The vertical lines on the Wavelength axis show the bulk band-gap values of Wurtzite CdS and CdSe.

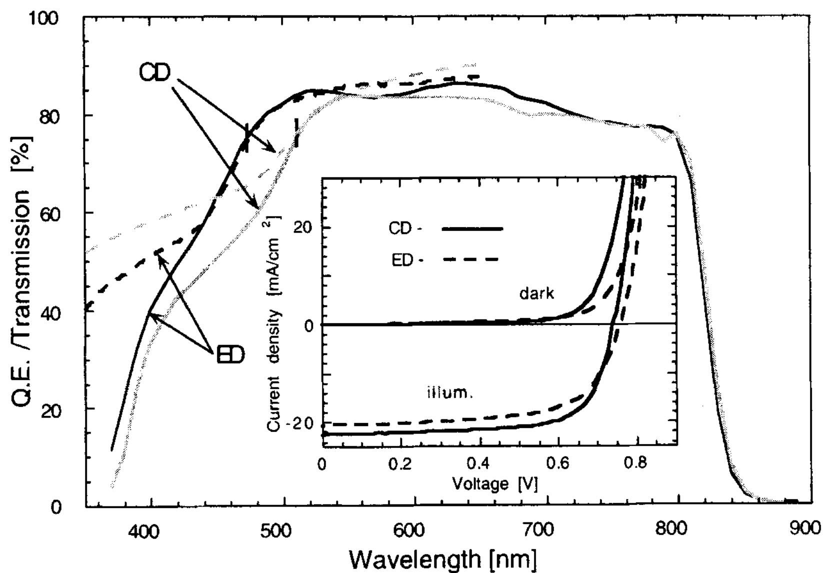

Fig. 2.2 Photocurrent spectra (solid lines) of $CdS/CuInS_2$ photovoltaic cells with the CdS deposited by electrodeposition (ED, black line) and chemical deposition (CD, gray line). Transmission spectra of the ED and CD CdS on glass (CD) or SnO_2 conducting glass (ED) are shown by the respective broken lines. The current-voltage characteristics are shown in the inset.

conventional chemical solution-deposited CdS (which is not size quantized as normally deposited) [16]. The rationale was that, since most of the light absorbed by the CdS in these cells is lost by recombination, a higher band-gap CdS should allow more short wavelength light to reach the $CuInS(Se)_2$ resulting in higher photocurrents. This was indeed found to be the case, as seen in Fig. 2.2 which shows the spectral responses of cells prepared with chemically deposited and electrodeposited CdS along with the absorption spectra of the two different layers of CdS deposited on conducting glass and the output characteristics of the two cells. In this case, the wire structure of the CdS may even be an advantage since it means that there will be fewer grain boundaries in the CdS layer in the direction of current flow and therefore less probability of resistance losses. The subject of resistance loss is interesting in itself. It might be expected that size quantization would imply high resistance (effective charge localization). The CdS layers are resistive in the dark but are photoconductive. The fact that quantization occurs in the directions where current flow is not important, but presumably does not in the direction where it is (i.e., normal to the substrate) may be a critical feature.

Of particular importance in this electrodeposition technique is the nature of the anion of the metal salt, in contrast to aqueous electrodeposition of semiconductors where it is usually not important. There are two reasons for this sensitivity.

One is the fact that many salts are unstable in hot DMSO containing dissolved chalcogen. Cd salts of carboxylic acids (such as acetate or formate) decompose to form CdS, probably due to the reducing action of these anions [17]. The nitrate decomposes to a white solid (the composition of which was not investigated) while the sulfate is insoluble. The perchlorate and halides are both soluble and stable (the fluoride also decomposes, but very slowly indeed and many electrodepositions can be carried out from the same solution if the solution temperature is not too high). The methylsulfonate and borofluoride salts of Cd, ($Cd(CH_3SO_3)_2$ and $Cd(BF_4)_2$, have also been successfully used for CdS deposition [18, 19].

The other reason that the anion is important is that it affects the structure of the film and in particular the crystal size. Baranski and Fawcett found a strong dependence of crystal texturing on the anion (Cl^- or ClO_4^-) [20] and explained the difference by varying adsorption of Cl^- on different crystal faces of the CdS [19]. We do not find clear cut differences in texture when using Cl^- and ClO_4^- although it should be noted that such differences may depend on experimental variables and, in particular, on the nature of the substrate. More important for our purposes is that there is a pronounced difference in the crystal sizes (and therefore on the band-gaps) of CdS and CdSe deposited from solutions of the two anions. Films deposited from Cl^- solutions exhibit band-gaps between 0.1 and 0.2 eV higher than those of the same compound deposited from ClO_4^- solutions [14]. More recent and detailed studies indicate that this difference is due to adsorption of the more strongly-adsorbed Cl^- on the growing CdX surface, preventing further crystal growth (capping) [21]. In particular, F^- behaves like ClO_4^- and not like the other halides in this respect (Fig. 2.3 gives transmission spectra of CdS films which show a spectral shift due to size quantization for the Cl^- but not for the ClO_4^- or F^-). This is expected based on halide adsorption; unlike the other halides, F^- does not normally adsorb on electrodes.

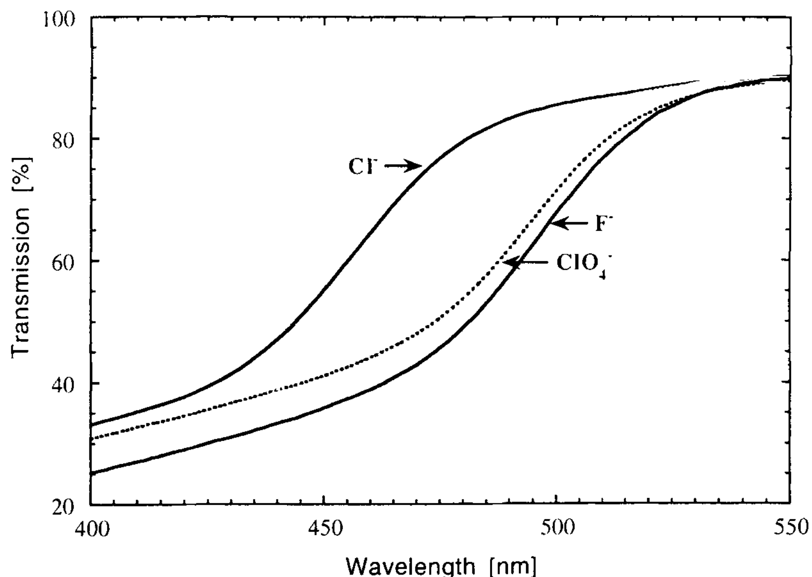

Fig. 2.3 Transmission spectra of CdS layers deposited on SnO_2-coated glass from DMSO solution containing S and different Cd salts (perchlorate, fluoride and chloride). The spectra are corrected for specular reflection.

2.2.2
Miscellaneous Sulfides and Selenides

While CdS and CdSe have been the most studied examples of this electrodeposition technique, other materials have been reported, including Bi_2S_3 [22] and SnS [9]. In addition, solid solutions can be deposited using mixtures of either S and Se and/or different metal cations in solution. Cd(S,Se) has been deposited with varying S:Se ratios [7]. The XRD peaks of the films became weaker as the Se:S ratio increased but the peak width did not increase (Se-rich films were found to be amorphous while the S-rich ones were crystalline). We find that CdSe is always crystalline using this technique, but the vertical dimensions (measured by XRD) are indeed smaller than those of CdS. We have reported deposition of $CuInS_2$ films from mixtures of Cu and In; the stoichiometry was, however, very difficult to control [23]. A range of (Cd,Zn)Se films were deposited varying from pure CdSe to almost pure ZnSe from mixtures of Cd and Zn perchlorates [24]. Since CdSe deposits much more readily than ZnSe, a very small concentration of Cd and a much higher one of Zn were used and the composition of the deposit controlled by the deposition current density. At low current densities, Cd-rich films are obtained. However, as the current density is increased, the Cd is increasingly depleted and higher percentages of Zn are deposited, as seen from the transmission spectra and compositions in Fig. 2.4.

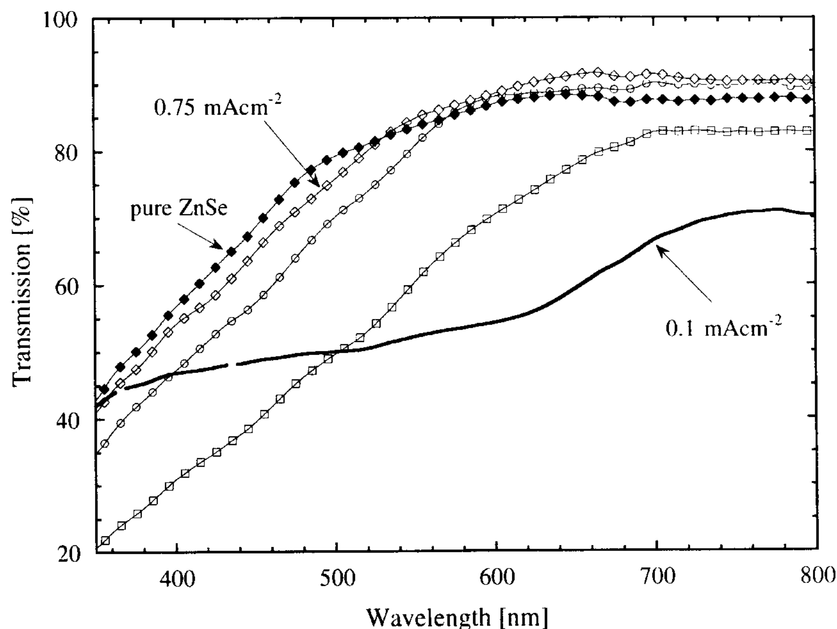

Fig. 2.4 Transmission spectra of $Cd_xZn_{1-x}Se$ layers deposited on SnO_2-coated glass from DMSO solution containing 0.1 M $LiClO_4$, $Zn(ClO_4)_2$ (50 mM), $Cd(ClO_4)_2$ (0.1 mM) and Se (saturated; 10 mM added Se) at 150 °C. The current densities used for the samples (in the direction of decreasing wavelength) were: 0.1, 0.2, 0.4, 0.75 $mA cm^{-2}$. The corresponding values of x, measured by XPS, were: 0.75, 0.56, 0.46, 0.24, 0.20. The ZnSe film is pure ZnSe (no Cd in the electrolyte). The spectra are corrected for specular reflection.

2.2.3 CdTe

The deposition of CdTe by the same method has been reported using elemental Te and the deposit crystallinity was found to be very dependent on the current density, although the crystal size appeared to be much larger, at least under some conditions, than those described above for the sulfides and selenides [25]. Our own attempts to deposit CdTe in this manner have been totally unsuccessful – we have been unable to dissolve even very small amounts of elemental Te in DMSO under any conditions, except to a small extent when elemental Se is also present, in which case Cd(Se,Te) with a small fraction of Te is deposited.

A related method to deposit CdTe has been described by Cocivera et al. [6, 26]. They dissolved elemental Te in tri-*n*-butylphosphine (TBP) which reacts with Te to form TBP telluride. This compound, together with a Cd salt dissolved in propylene carbonate, was the electrolyte from which CdTe was cathodically electrodeposited. The as-deposited films were reported to be X-ray amorphous, a fact that suggested to us that they may in fact be polycrystalline as discussed previously. We modified this technique and simplified it, in particular by using a one-step technique to prepare the solution [27]. In this case, DMSO was found to be the only

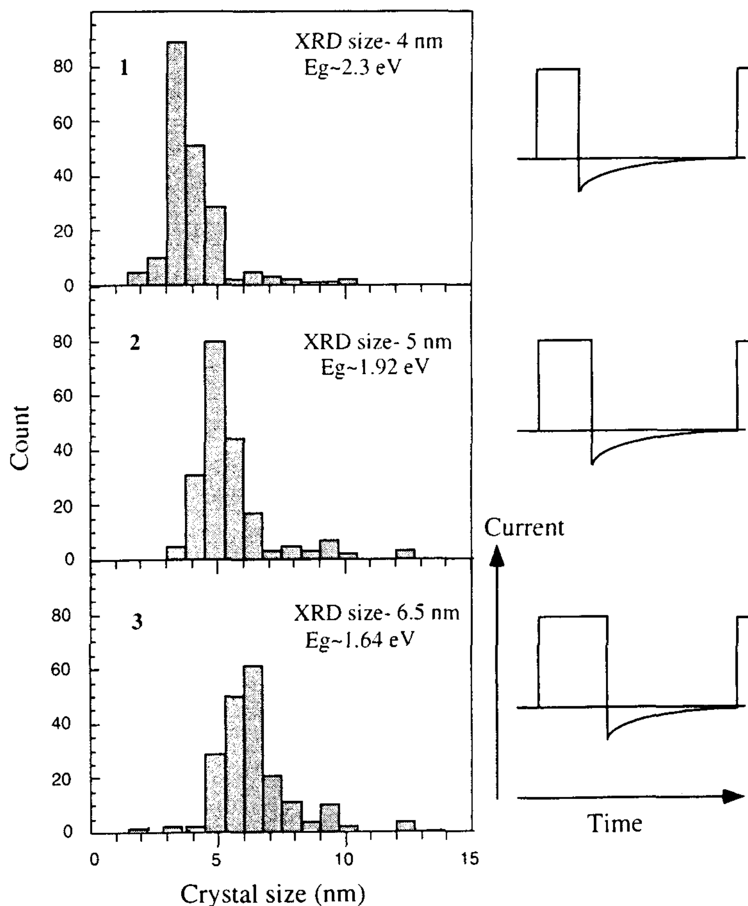

Fig. 2.5 Pulse electrodeposited CdTe films on SnO_2-coated glass from DMSO solution containing 4 mM $Cd(ClO_4)_2$, 60 mM tributyl phosphine and 20 mM Te at 100 °C. The size distributions are shown, measured by TEM imaging. The size measured by XRD peak broadening and the band-gaps estimated from the transmission spectra are also given. The pulse plating regime is shown (time axis to scale) to the right of the distributions. The pulse frequency was 1 Hz. The deposition was carried out potentiostatically at −1100 mV (relative to the SCE) deposition pulse and −550 mV stripping pulse.

solvent (among the several we tried) which would give satisfactory deposits using the one-step technique. The CdTe was found to be nanocrystalline with a wide size distribution varying from several nm up to tens of nm. In addition, the films were generally non-stoichiometric with excess Te or Cd depending on the deposition potential. It was difficult to deposit close-to-stoichiometric film. To improve the stoichiometry, we employed reverse pulse deposition. The rationale for this was that CdTe would be deposited during the cathodic pulse and any excess Cd or Te would be stripped during the anodic pulse (which was not sufficiently anodic to strip also the CdTe). This technique indeed resulted in stoichiometric films. No

less important, however, was its effect on the crystal size and size distribution. Fig. 2.5 shows size distributions, measured from TEM micrographs, of three films deposited under the same conditions except that the pulse regime (shown on the right of the figure) was varied. The crystal sizes measured from the XRD spectra are given and agree with the TEM measurements. The CdTe band-gaps, measured from the transmission spectra, are also shown and the increase in band-gap with decrease in crystal size is clear.

The average crystal size decreases as the duration of the cathodic pulse becomes shorter and that of the anodic pulse longer. There are two factors to which this effect can be attributed. Pulse plating is known to result in smaller crystal size for metallic electrodeposits. The normal conditions for pulse plating are very high current densities which result in rapid nucleation; such high current densities cannot be maintained under DC conditions because of electrolyte depletion. Since the current densities employed here were not particularly high (mostly $<1\,mA\,cm^{-2}$), this effect is not expected to be very strong, although it might have an effect. The second factor is the capping effect of the TBP. Phosphines are known to adsorb strongly to Cd chalcogenides and to block crystal growth – the capping effect [28–30]. In this case, the longer the time between depositions (the anodic pulses), the more opportunity there is for capping to occur and the more efficient it should be. Thus the shorter cathodic pulses result in less crystal growth and the longer anodic ones ensure that the following cathodic pulse will renucleate CdTe rather than grow on an existing crystal.

Colyer and Cocivera used the same basic method to deposit films of (Cd,Hg)Te [31]. From XRD spectra, a crystal size of ca. 5 nm could be estimated which grew through 7.5 nm (200 °C) to 22 nm (300 °C) on annealing. Optical absorption spectra of these films could be explained by size quantization [4].

2.3 Ultrathin Films and Isolated Nanocrystal Deposition

2.3.1 Effect of Substrate on Non-aqueous Deposited Films

Most of the rest of this chapter deals with the effect of the substrate and the substrate-semiconductor lattice mismatch on the semiconductor crystal size and structure. First, however, we review the sparse previous literature, not necessarily connected with crystal size, on the effect of substrate on the semiconductor electrodeposited from these nonaqueous solutions.

The deposition of CdS on metals with an affinity for sulfur (Au, Pt, Hg) exhibited similar current-voltage voltammograms insomuch as a prepeak – corresponding to about a monolayer – occurred at potentials positive of the main deposition wave. Two explanations were offered for this peak: underpotential deposition of Cd on the metal surface [32] (more probably on the S-covered surface) or reduction of the sulfide formed by chemisorption of S on the metal surface [18, 19].

This prepeak was not observed on non-reactive substrates such as glassy carbon where chemisorption of S presumably does not occur [19].

The crystallographic texture of CdS films was found to depend on, among other parameters, the substrate material [33]. Differing degrees of texturing were found on Cd/Cr/glass and SnO_2-glass substrates, while little texture was found on steel substrates. Also, the deposition current density affected the texture of the deposit. Based on XRD, the crystal size was estimated to be ca. 15–20 nm. It was suggested that the crystallographic differences were connected with the nucleation sites on the various substrates. In the absence of crystallographic data on the bare substrates, it is difficult to explain these crystallographic effects.

2.3.2
Epitaxy

We now turn to the effect of lattice mismatch between the substrate and electrodeposited semiconductor. We begin with a brief description of epitaxy and types of epitaxial crystal growth.

Epitaxy refers to the growth of one material on another such that the lattice of the deposited material has the same orientation – in the plane of the substrate – as that of the substrate itself. In this case, the crystal planes of the deposit will all also be facing in the same direction: (as described in the description of techniques at the beginning of the chapter, the planes may all face the same direction without the individual crystals all having the same azimuthal direction). Epitaxy is favored by close matching of the lattice plane distances of semiconductor overlayer and substrate. This match extends to matching of various ratios of lattice distances and of the match when one lattice is rotated with respect to the other. Examples of both will be given later.

There are three main forms of growth when a material is deposited on a substrate, shown schematically in Fig. 2.6. When the interaction between semiconductor overlayer and substrate is strong – stronger than that between molecules of the semiconductor itself, a layered growth is likely (Frank-van der Merwe growth, a), assuming the lattice match is good. The opposite case, when the interaction between the semiconductor and substrate is weak, leads to island growth (Volmer-Weber growth, b). Stranski-Krastanow growth (c), where an initial layered growth turns to an island growth, is an intermediate type of growth.

The growth of nanostructures of one semiconductor on another where the size is controlled by the lattice mismatch has been extensively studied for vapor phase deposition techniques, mainly molecular beam epitaxy and metal-organic vapor phase epitaxy. Ref. [34] gives a review of this field. The principle of the control of crystal size is that the growing crystal is subjected to increasing strain due to the lattice mismatch (mismatch strain) until eventually it is energetically more favorable for the crystal to stop growing and for a new one to nucleate in another position. In most of the reported studies the growth mode appears to be the Stranski-Krastanow one. The island sizes typically range from tens to hundreds of nm (lateral dimensions) and several nm to several tens of nm in height depending on the

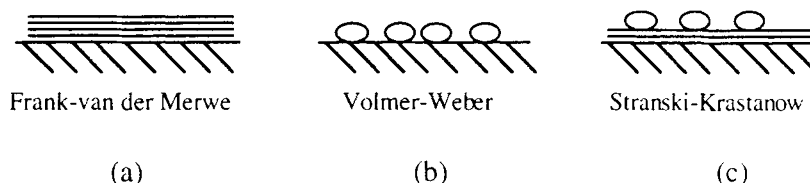

Fig. 2.6 Epitaxial growth modes.

system and the conditions. However, the island size distributions are usually narrow, which is explained by the mismatch strain mechanism, whereby the islands stop growing when a certain strain has been reached. They usually exhibit well-defined geometric shapes, often pyramidal. It should also be noted that these deposition techniques are usually carried out at substrate temperatures of at least 500 °C: the high temperatures appear to be necessary to obtain epitaxy due to diffusion of the atomic species to the most stable position. This type of growth, where the crystal size, and sometimes also the geometry of the distribution, is determined by built-in properties of the system rather than externally imposed, e.g. by lithography, is often termed self-organized growth.

2.3.3 Variation of Semiconductor

2.3.3.1 CdSe on Au

We have studied such self-organized growth of Cd chalcogenide semiconductor nanoparticles, although with some fundamental differences with those discussed in Ref. [34]. A general schematic of this system is shown in Fig. 2.7 for the case of CdSe on Au. Au (30–35 nm thick) is evaporated on to a glass or mica substrate. The films are annealed for 3 h at 250 °C to form {111}-textured films with a grain size up to several hundred nanometers. The importance of the annealing step is mainly to enhance the Au grain size so as to allow selected area electron diffraction (SAD) to be carried out on a single Au grain.

CdSe was cathodically electrodeposited onto these Au films from hot (90–120 °C) DMSO containing Cd^{2+} (usually $Cd(ClO_4)_2$ but sometimes $Cd(Cl)_2$) and elemental Se. A glassy carbon plate was used as the anode (for more experimental details, see Refs [35–37]). Because of the poor adhesion of Au to glass, the Au, together with the CdSe deposit, could be easily separated from the glass on the

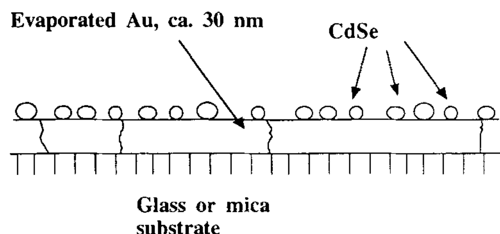

Fig. 2.7 Schematic diagram of electrodeposited CdSe nanocrystals on a Au film.

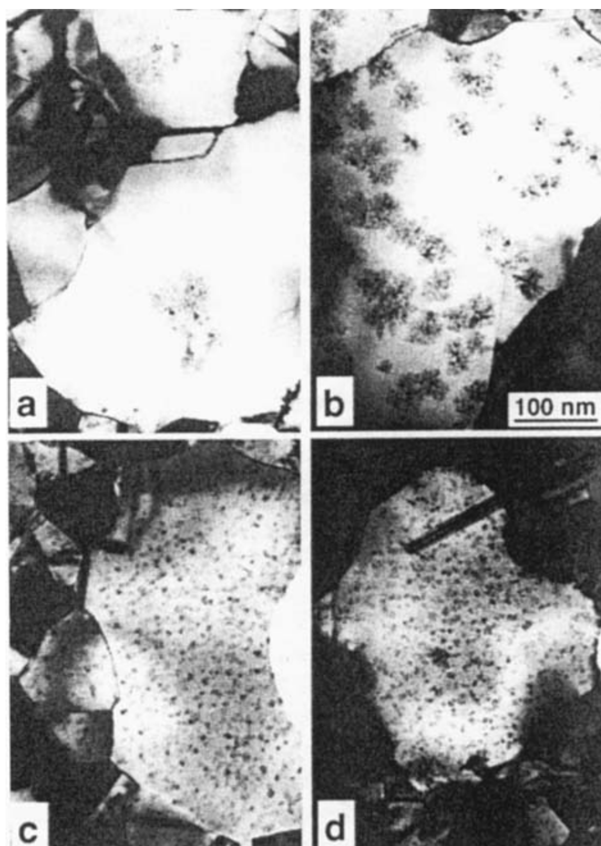

Fig. 2.8 TEM images of CdSe nanocrystals electrodeposited on Au. (a–c), current density=0.1 $mA\,cm^{-2}$ for 7 s; temperatures (a) 150 °C, (b) 120 °C, (c) 90 °C; (d) 0.7 $mA\,cm^{-2}$ for 1 s at 120 °C.

surface of 5% aqueous HF (the HF did not come in contact with the CdSe) for TEM observation.

The amount of CdSe deposited could be calculated from the plating charge, the CdSe density and Faraday's equation as explained in the preface. Based on a 2-electron transfer and assuming 100% current efficiency, at the plating current density used here (0.1 $mA\,cm^{-2}$ unless stated otherwise), each five seconds of deposition is equivalent to a homogeneous deposit 0.8 nm thick. Since our deposits are not homogeneous, but, as seen below, comprised of nanocrystals, either isolated or aggregated, we use the term "nominal thickness" to refer to the thickness which would be obtained if the deposit was homogeneous and non-porous. For example, a deposition time of 15 s would give a nominal thickness of ca. 2.5 nm. For a nanocrystal height of 4–5 nm, this would be equivalent to a little more than half a monolayer coverage of crystals.

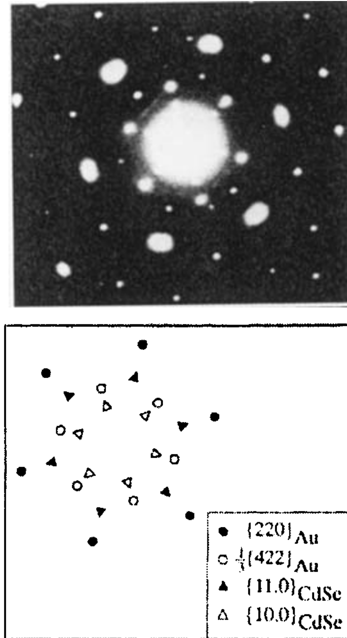

Fig. 2.9 Selected area electron diffraction (SAD) pattern of many CdSe crystals on a single Au grain. Assignment of the various reflections is given in the lower part. From Golan et al., [36].

The distribution of the CdSe electrodeposit on the Au is shown in Fig. 2.8 for various deposition temperatures and current densities. In all cases, the lateral crystal sizes are similar (4–5 nm), but the degree of aggregation varies greatly. Decreasing temperature (a–c) and increasing current density (d) favor decreased aggregation, i.e. more isolated crystals. This behavior is not surprising since higher temperatures or longer times (lower current densities for the same charge) should favor increased aggregation due to mobility of the CdSe. In this respect, it should be noted that samples of isolated nanocrystals similar to those in Fig. 8c and d are stable at room temperature and do not aggregate even after a year.

A SAD pattern of a single Au grain with hundreds of CdSe nanocrystals, together with assignment of the pattern, is shown in Fig. 2.9. The single crystal spot pattern of the Au with {220} and 1/3{422} reflections is evident. The CdSe reflections ({11.0} and {10.0}), although formed by many crystals, also form a sharp spot pattern. This means that all the CdSe crystals are aligned in the same direction and the correspondence between the Au and CdSe spots shows that the deposit is epitaxial with the Au in a {111}Au||{00.2}CdSe and ⟨110⟩Au||⟨11.0⟩CdSe orientation relationship. The epitaxy can be understood from the close lattice match between the two lattice spacings: d-$\{110\}_{Au}$ (the smallest interatomic distance in the {111} plane of the fcc lattice) and $a_{0(CdSe)}$ (the smallest interatomic distance in the basal plane of the hexagonal lattice). The literature values of the lattice spacings are d-$\{110\}_{Au}=0.2884$ nm and $a_{0(CdSe)}=0.4299$ nm, which, in a ratio of 3:2, correspond to a mismatch of –0.6%.

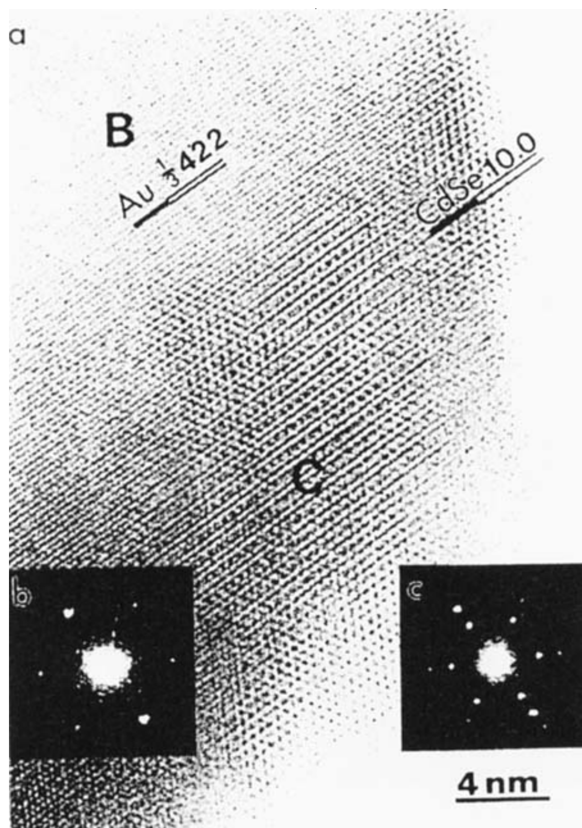

Fig. 2.10 (a) HRTEM image of an aggregate of CdSe nanocrystals on Au. The optical diffraction patterns were obtained from the area marked "B" in the image corresponding to the Au only (b) and from the area marked "C" showing alignment between CdSe and Au reflections (c). From Golan et al., [36].

HRTEM and optical diffraction of HRTEM images confirmed this epitaxial relationship, and showed that the quantum dots exhibit essentially perfect crystal structure [36]. Fig. 2.10 shows a HRTEM image of a cluster of CdSe crystals (the aggregate boundaries are often not evident in HRTEM). The identities of the CdSe and Au are clearly shown by the optical nanodiffraction patterns (b and c) and the identical alignment of the CdSe and Au lattices is clearly seen, verifying the SAD pattern in Fig. 2.9. The 3:2 lattice match is prominently seen as superstructure lines superimposed on the CdSe and Au lattice images.

The above discussion applies to a monolayer or less of crystals. When more CdSe than this is deposited, the epitaxy is gradually lost and the crystal size becomes larger. For deposition from $Cd(ClO_4)_2$, the crystal size increases by up to several times between the first crystal layer and subsequent ones. This can be seen in the TEM micrograph of a 15 nm thick film (Fig. 2.11). The loss in epitaxy

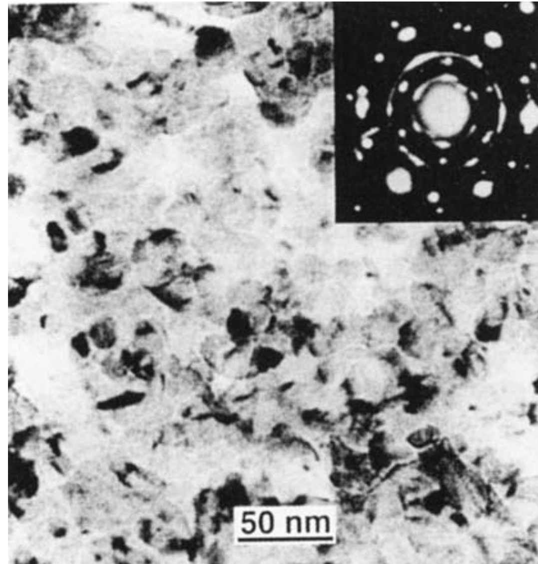

Fig. 2.11 TEM image of CdSe deposit (nominal thickness 15 nm) on Au. Inset: SAD of deposit on a single Au grain.

of these films is clear from the ED pattern as the point pattern of the epitaxial deposit changes into a ring pattern characteristic of a non-oriented deposit.

The epitaxy between the CdSe and Au can be explained by their small (–0.6%) lattice mismatch. However, as noted above for the vapor-deposited 'self-assembled' islands, a consequence of the mismatch strain is a relatively narrow size distribution. This also occurs in the electrodeposited nanocrystals as can be seen by a typical size distribution histogram (shown in Fig. 2.20). If this is indeed the correct reason for the particular crystal size, then this size should be controllable by choice of the semiconductor and substrate lattice parameters: the larger the mismatch, the smaller the crystal size and vice versa. To test this hypothesis, we studied a range of different electrodeposited semiconductor-substrate combinations.

Tab. 2.1 Lattice parameters of the materials considered in this paper. The parameter of the semiconductors and Cd (all of the hexagonal (Wurtzite) structure) is the cell 'a' distance (the smallest interatomic distance in the basal plane) whereas that of the cubic metals (Au, Pd) is the equivalent distance in the (111) plane, the spacing between {110} planes.

Material	*Lattice parameter (nm)*
CdS	0.4136
CdSe	0.4299
CdTe	0.4578
ZnSe	0.4008
Au	0.2884
Pd	0.2752
Cd	0.2980

Table 1 shows the lattice parameters of relevant semiconductors and metals used in this study. It should be noted that the lattice parameters of many alloys – semiconductors as well as metals – vary approximately linearly with composition (assuming no change of phase occurs), a relationship known as Vegard's law.

2.3.3.2 **Cd(Se,Te) on Au**

An obvious strategy would be to obtain perfect lattice match in the expectation of obtaining an epitaxial layer of the semiconductor. This was not attained for various reasons as will be seen below. The first attempt in this direction was to deposit an alloy of $CdSe_xTe_{1-x}$. From the values of lattice parameters in Table 1 and applying Vegard's law, which has been shown to be valid for these solid solutions, a value of $x=0.88$ (12% Te) should result in such a perfect match. It may be remembered that we could not dissolve Te in DMSO. However, small amounts of Te could be dissolved in the presence of dissolved Se (this could be seen visually from a change in the color of the DMSO from the orange characteristic of dissolved Se to yellow when Te was added, suggesting some complex formation between the Se and Te in the DMSO [38]. While we do not know the concentration of Te in the electrolyte (it was almost certainly <1 mM), we could qualitatively vary the amount of Te in the deposit by varying the deposition current density and temperature. Relatively high current densities resulted in severe depletion of the Te near the cathode thereby favoring the more concentrated Se in the deposit, in the same manner as the Zn concentration was varied in the (Cd,Zn)Se deposits described below. In the same way, higher deposition temperatures increased the concentration of Te at the cathode and therefore in the deposit.

Fig. 2.12 shows a series of TEM micrographs of Cd(Se,Te) deposits on Au. In all cases the same amount of charge was passed and the differences are due to combinations of current density and temperature. SAD showed that the deposits were epitaxial as for the pure CdSe (this was found for all the deposits). The maximum concentration of Te (relative to Se) in the deposit (Fig. 2.12f) was measured by XPS to be 2.5% and semiquantitatively by Raman spectroscopy to be closer to 10%. We assume a value ca. 5% which is a sufficiently good indication of the actual amount for our purposes. In any case, it is still below the 12% required for perfect lattice match. In addition, it is a fair assumption that, both due to the small amount of Te as well as the chemical similarity of Se and Te, any differences between CdSe and Cd(Se,Te) will be due to lattice variations rather than to chemical effects between semiconductor and substrate.

The qualitative increase in average lateral dimension with increasing Te concentration from pure CdSe (4–5 nm) up to the ca. 5% Te compound (18 nm) clearly shows the results anticipated from the mismatch strain principle. The crystal height, measured by XRD, also increased with increasing Te content up to 12 nm [38]. This means that the larger crystals had larger lateral dimensions than the vertical one – i.e., they were more disk-shaped than pure CdSe whose average vertical and lateral dimensions were similar. However, this increase in crystal height is also influenced to an extent by deposition conditions (current density and temperature) and therefore should not be correlated with Te content directly.

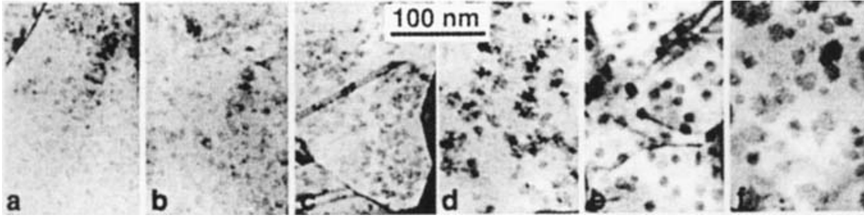

Fig. 2.12 TEM images of: (a) (Te free) CdSe nanocrystals on Au. (b–f) Cd(Se,Te) nanocrystals with increasing average size from 6 (b) to 18 (f) nm. All the images in this figure are shown at the same magnification, and were all electrodeposited using the same amount of electrical charge ($0.70\,mC\,cm^{-2}$). Deposition parameters: (a) $0.100\,mA\,cm^{-2}$, 7 s, 90°C (Te free); (b) $0.100\,mA\,cm^{-2}$, 7 s, 120°C; (c) $0.100\,mA\,cm^{-2}$, 7 s, 150°C; (d) $0.015\,mA\,cm^{-2}$, 47 s, 120°C; (e) $0.005\,mA\,cm^{-2}$, 140 s, 130°C; (f) $0.015\,mA\,cm^{-2}$, 47 s, 170°C. Deposition solutions: (a) 50 mM $Cd(ClO_4)_2 6H_2O$ + 12 mM elemental Se in DMSO; (b–f) 25 mM $Cd(ClO_4)_2 6H_2O$ + 0.3 mM elemental Se + 1.0 mM elemental Te (excess – not all dissolved) in DMSO.

Also evident from Fig. 2.12 is that the crystal size distribution increases in general with increasing average size (Te content), although Fig. 2.12e is an interesting exception. It is possible that this is due to variations in composition from one crystal to another. Since the measured estimates for the Te concentrations are average ones, the largest crystals in the distribution should then have a higher Te content than this average value.

2.3.3.3 (Cd,Zn)Se on Au

To obtain smaller crystals (greater mismatch), we chose the (Cd,Zn)Se system, using the same principle as described above for thicker films of this material (low Cd and high Zn concentrations). Fig. 2.13 shows the size distribution histogram measured from a TEM image of such a deposit. The lateral measurements are smaller than those of CdSe, as expected. XRD gave a crystal height of 5 nm – more than twice the average lateral dimension [39]. The crystals can therefore be considered as short quantum wires rather than quantum dots. The SAD pattern of this deposit (inset of Fig. 2.13) shows that epitaxy is maintained. These results show very clearly the same effect of mismatch strain, but in the opposite direction that was obtained for the Cd(Se,Te).

2.3.3.4 CdS on Au

As our final example of variation in semiconductor composition, we consider CdS on Au [40]. The mismatch in this case is –4.5% – large compared with our previous values. The properties of the deposit in this case are very dependent on the amount deposited. The progression of crystal size and orientation with deposit amount is seen in Fig. 2.14. For small amounts of deposit, the crystals are predominantly epitaxial (although not perfectly so as for CdSe on Au, seen as arcs in the SAD patterns). The average lateral crystal dimension grows and the degree of

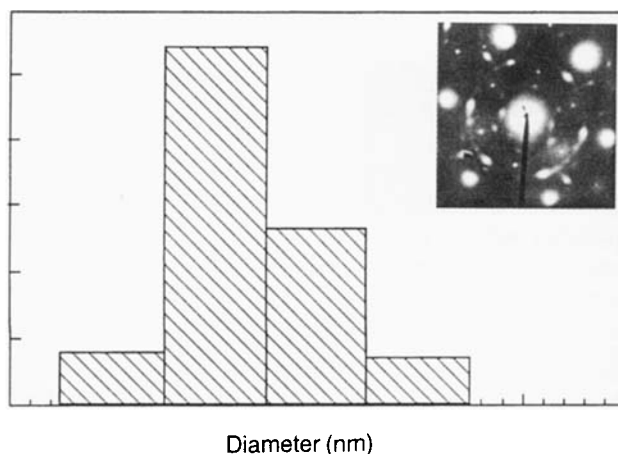

Fig. 2.13 Size distribution of $Cd_xZn_{1-x}Se$ ($x \approx 0.8$) electrodeposited on Au, measured from TEM image. Inset: SAD of deposit on a single Au grain.

orientation decreases as the amount of deposit increases. The crystal height for the nominally 5 nm deposit was found to be 3 nm – similar to the lateral dimension (this was measured by scanning force microscopy, since no XRD pattern could be seen on the thinner deposits).

There is a number of observations to be made when comparing the CdS deposition to other depositions described above. First, considering the 5 nm sample, where the crystal height is 3 nm, this should correspond to more than one monolayer of CdS crystal; yet Fig. 2.14 clearly shows that less than one layer of crystals has been formed. This suggests that the current efficiency of this deposition is less than for the CdSe deposition. An XPS study of this deposition has shown that the efficiency at the beginning of the deposition is indeed very low, and that CdS only begins to deposit after a 'nominal' deposition of 2 nm has occurred [40]. This means that the actual amounts of CdS deposited are at least 2 nm less than the nominal values. For example, the 5 nm film is no more than 3 nm average thickness, i.e. ≤ a monolayer of crystals. Another difference is the higher current densities used for the CdS deposition ($0.5\,mA\,cm^{-2}$) compared with the $0.1\,mA\,cm^{-2}$ typical for CdSe. Since S is much more soluble in DMSO than is Se (100 mM was used in these experiments), higher current densities were used. This may or may not be important: for CdSe on Au/Pd alloys, it is an important factor (see below) while for CdSe on Au, current density does not appear to affect the epitaxy.

Since the mismatch strain argument relies on an epitaxial growth, the partial loss of this epitaxy for CdS on Au means that the argument is not valid or only partially so. The loss of epitaxy is reasonable, based on the relatively large mismatch. For the 8 and 10 nm films, there may either be new layers of crystals or the crystals in the first layer may grow in the lateral direction (since TEM mea-

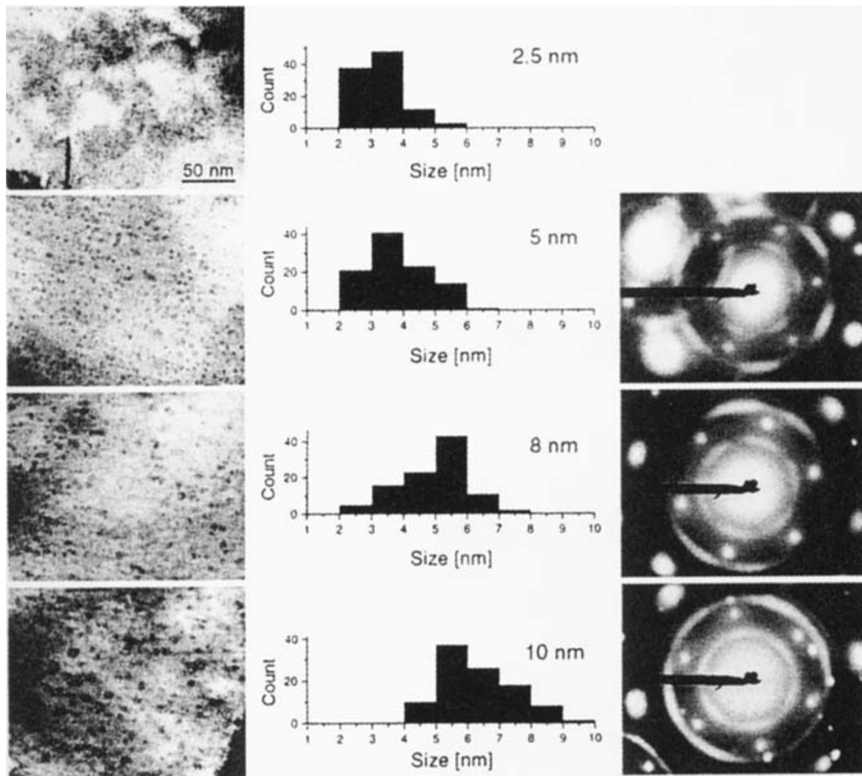

Fig. 2.14 TEM micrographs (left side), crystal size distribution histograms (center) and SAD patterns (no pattern was seen for the 2.5 nm sample) (right side) of CdS deposited on Au at 90 °C and a plating current density of 0.5 mA cm^{-2} for plating times of 3.5 s (nominal thickness 2.5 nm); 7 s (5 nm); 11 s (8 nm) and 14 s (10 nm). The scale marker shown on the top TEM micrograph applies to all micrographs. From Behar et al., [40].

sures lateral dimensions – they can also grow in the vertical direction, and apparently do so, as seen by XRD measurements of the thicker films). The former seems more likely, both because there is not much space on the substrate for the crystals to grow laterally after the 5 nm deposit and, more important, the reasonably oriented crystals in the first layer would have to rotate in order to lose this orientation as the crystal size grows – an unlikely occurrence.

2.3.4
Variation of Substrate

2.3.4.1 CdSe on Pd

Up to now, we have varied the semiconductor-substrate mismatch by changing the semiconductor. We now look at several examples where the substrate is varied.

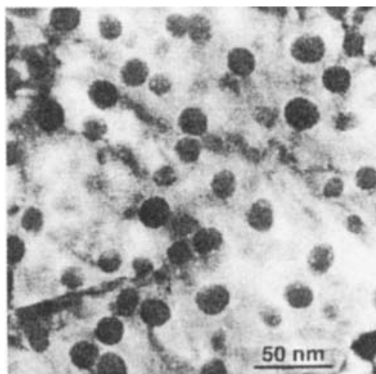

Fig. 2.15 TEM image of CdSe electrodeposited on Pd at 120 °C and a constant current of 0.10 mA cm^{-2} for 10 s.

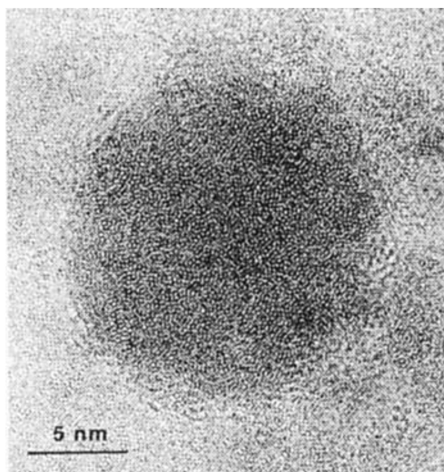

Fig. 2.16 HRTEM of part of the deposit from Figure 15.

The most extensively studied system using a substrate other than Au is CdSe on Pd [37, 41]. Pd has the same fcc structure as Au; the lattice spacing, however, is almost 5% smaller than that of Au, with the result that the mismatch between CdSe and Pd is +4.1%. This is close to the mismatch between CdS and Au, but in the opposite direction, i.e., the CdSe should be compressed instead of stretched.

Fig. 2.15 shows a TEM view of a CdSe deposit on Pd (nominal thickness ca. 1.5 nm). The deposit is very different than the one obtained on Au. There are particles of ca. 10–20 nm with a size distribution larger than that shown by CdSe on Au. On further deposition, these particles grow larger, up to at least 100 nm. Additionally, the whole surface of the Pd appears to be covered by deposit. This is seen better in a HRTEM image (Fig. 2.16) which shows one particle and the surrounding region. The Pd lattice is not seen even in the thin surrounding region. Superficial investigation of this image suggests that the deposit is amorphous. Slow scan XRD showed no diffraction pattern, which would seem to support such a conclusion. However, careful examination of the HRTEM image reveals the pres-

ence of many regions showing short range order, often with hexagonal symmetry. An in-depth analysis of this short range order showed the presence of irregular structures of ordered CdSe, ca. 1 nm in size, surrounded by disordered CdSe. Furthermore, Fourier analysis of HRTEM images showed some degree of preferential orientation of the ordered structures relative to the Pd lattice, but rotated 30° to the Pd [41]. Subsequent modeling of the superimposed CdSe-Pd lattices showed that this 30° rotation indeed resulted in an improved lattice match compared with the aligned lattices [37].

The very small ordered structures are in qualitative agreement with the mismatch strain argument which predicts very small crystals in this case. This argument is only valid for these ordered regions, and then only to a certain extent because of the lack of full epitaxy. It will not, of course, apply to the disordered regions since there is no epitaxy and therefore no long-range mismatch strain – any local strain can be easily accommodated by variations in local bonding.

The growth behavior of CdSe on Au and Pd is very different. This is not likely to be a simple lattice effect but also connected with the chemical interaction between CdSe and substrate (or Se-coated substrate). Se itself reacts more strongly with Au than with Pd as shown by XPS analyses [37]. However, while CdSe forms a complete wetting layer on Pd, it does not on Au, where only islands are formed. Pd has a higher surface energy than Au which may play a role here. It should be noted, however, that the adsorption of S on Pd is strong enough to form surface chemical species corresponding to Pd-S_x [42, 43].

2.3.4.2 CdS on Pd

CdS has only a small mismatch with Pd – +0.17% (2:3 ratio). However, our attempts to obtain thin electrodeposits of CdS on Pd were unsuccessful. Small particles (ca. 2 nm) were obtained; however the identity of these particles was unknown – XPS analysis showed almost total absence of Cd. In this case, chemical interaction between S and Pd probably dominates the surface.

2.3.4.3 CdSe on Au-Pd Alloy

Because the 3×Au lattice spacing is slightly larger than the 2×CdSe one, while the Pd is smaller, an obvious question is: what if an alloy of Au-Pd is used, where the lattice parameter can be varied at will and can also be made identical to that of the CdSe (at a content of ca. 12% Pd)? The alloy films were prepared by evaporating previously alloyed Au and Pd in the correct proportions. XRD and XPS analyses showed that the metal film composition was close to that of the starting material. A range of alloys up to 26% Pd were made and CdSe electrodeposited on the alloy films.

The character of the deposits, in terms of crystal size and orientation, did not behave as predicted from the mismatch theory. Instead of increase in crystal size and perfect epitaxy as the Pd concentration increases up to the theoretical perfect

match, the orientation was gradually reduced as the Pd content increased, although not lost entirely, even for the 26% Pd film. However, if the deposition current was reduced from 0.1 to 0.01 $mA cm^{-2}$, the epitaxy was greatly improved, and even the 26% alloy was almost perfectly epitaxial [39]. It appears that kinetic factors are important in the orientation.

The variation of crystal size with Pd content was not reproducible. While there was a general tendency for crystal size to increase somewhat (and to become more faceted compared with the CdSe on Au), the size distribution was considerably wider than on pure Au and a range of sizes from less than 2 nm up to 10 nm was found [39]. XRD, used to measure crystal height, was not very useful as the peaks became weaker with increasing Pd content. This could be due to defects in the crystals which would reduce the coherence length.

While the mismatch theory appears to fail in this case, some consideration must be given to the assumption that the alloys behave like the pure metals, only with differing lattice constants. Surface enrichment of Au has been found to occur at the (113) face of Au_3Pd alloys using low angle ion scattering [44]. This does not explain our results since we would still expect perfect epitaxy (at 0.1 $mA cm^{-2}$) just as occurs on pure Au. Another and more likely possibility is that the surface is disordered, as might be expected for a material with differing bond lengths positioned at random. A third option is that the surface interaction effects between CdSe and (Se)alloy dominate the behavior.

2.3.4.4 **CdSe on Au-Cd Alloy; Rocksalt CdSe**

To try and separate chemical effects from lattice mismatch, we have carried out some studies of an alloy of Cd with Au containing 3% Cd. Cd was chosen due to its strong interaction with Se. The change in lattice spacing due to the 3% of Cd is very small (+0.07%) and therefore we can reasonably attribute any change in CdSe properties to differences in chemical interaction (taking into account what we suggested above concerning disorder in the surface of alloys). No measurable difference in the XRD peak position was found between the Cd-Au and pure Au, as might be expected for such a small difference.

The structure of the CdSe, deposited under standard conditions on to this alloy, was very different from that on pure Au. Fig. 2.17a shows a TEM image of a CdSe film (nominal thickness 1.5 nm) deposited on the Cd-Au. While the crystal size (ca. 5 nm) is similar to that on pure Au, the coverage of the substrate is almost complete compared with the relatively small coverage of the pure Au using similar deposition conditions (see Fig. 2.8). This implies that the crystals are thinner than those on Au. However, more surprising is the SAD pattern of this deposit (Fig. 2.17b). The deposit is epitaxial with the substrate, like that of CdSe on pure Au (compare with Fig. 2.9). However there is an additional reflection near the CdSe (11.0) wurtzite/(220) zincblende one, with a 5% smaller (220) spacing (farther from the center) than the normal wurtzite/zincblende one.

This additional reflection has been shown to originate from rocksalt (RS) CdSe [45]. CdSe (and CdS) are known to undergo a phase transition from the wurtzite

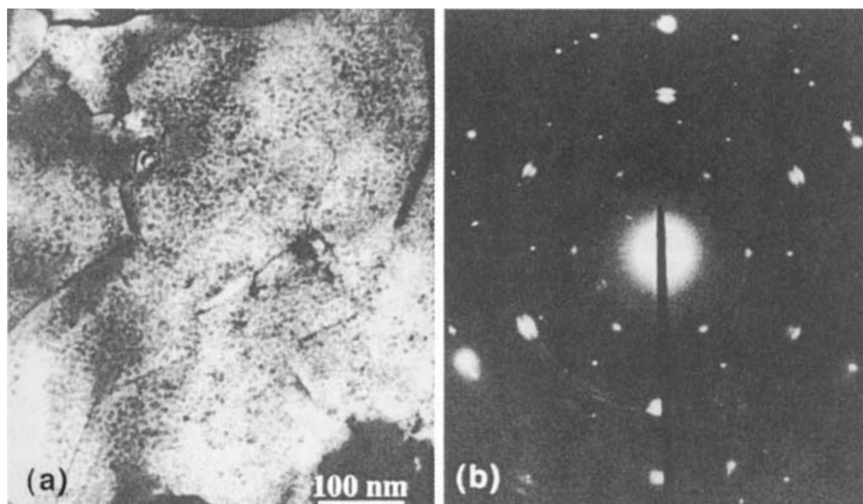

Fig. 2.17 (a) TEM micrograph of CdSe electrodeposited on a 3% Cd/Au alloy film on a glass substrate at 0.1 $mA\,cm^{-2}$ for 8 s at 110 °C. (b) SAD pattern of part of the above sample showing spots due to both rocksalt (RS) and wurtzite/zincblende (W/ZB) phases with the same crystal orientation.

(W) structure to a RS phase under high pressure and to revert to a mixture of W and zincblende (ZB) upon release of the pressure. CdSe nanocrystals were shown to undergo the W-to-RS transition at higher pressures than bulk CdSe [46, 47]. The differences between solid-solid phase changes in bulk and nanocrystalline materials have been discussed in terms of two main factors [46, 48]: the absence of defects in nanocrystals (phase change in bulk material is usually initiated at defects), and the large effect of surface energies in the thermodynamics of nanocrystal phase transformations. These studies conclude that nanocrystals can be metastable under ambient conditions where bulk crystals of the same material would be unstable. Two studies have indeed shown the existence of RS CdS under ambient conditions: nanocrystals ca. 2 nm in diameter biosynthesized in yeasts [49] and large (ca. 100 nm) crystals synthesized in polymer films in the presence of certain surfactants [50].

An additional difference between the SAD in Fig. 2.17b and that of CdSe on pure Au is the reversal of the intensity ratio between the CdSe (10.0) and (11.0) reflections. The theoretical electron diffraction pattern of W CdSe predicts an intensity ratio of 10 (10.0): 7 (11.0), as has been seen qualitatively in ED patterns of electrodeposited CdSe on Au [35]. On the Cd-Au substrate, the (11.0) reflection is always more intense, although this reverse intensity ratio is occasionally found on pure Au as well. This reversal suggests the presence of ZB CdSe, since the ZB 1/3 (422) reflection with the same lattice spacing as W(10.0), is forbidden. HRTEM images of the CdSe deposits on Cd-Au have confirmed the coexistence of RS, ZB and W phases [45].

For thicker films, the RS reflections disappear. Also the ED pattern corresponds more closely to that of W CdSe, i.e., the (11.0) intensity is greater than that of the (11.0) reflection. Although the common crystal phase in such films is W, we find that the RS structure often forms in the early stages of deposition and converts to a mixed W/ZB structure as the deposition proceeds and is stable over long periods of time in very thin films.

Since the mismatch strain is expected to stretch the CdSe, it is difficult to see why the high pressure RS phase, which is normally formed under compressive forces, is formed. It was suggested that the surface tension of the growing crystal compresses the crystal [45]. This is probably also connected with the strong interaction between the growing crystal and the substrate. Since >30% of the crystal atoms are surface atoms, this effect can be large. For thicker crystals, such as those showing the W or ZB structure, the surface effects will be correspondingly smaller. In view of the disappearance of the RS reflection with thicker films, the initial RS phase transforms into the ZB/W phases as the crystal becomes thicker and the surface-to-volume ratio decreases, resulting in a decreased compressive force.

2.4 Electronic Characterization of Electrodeposited Semiconductor Nanoparticle Films

One of the most common measurements made on size-quantized semiconductors – both colloids and films – is optical transmission (absorption) spectroscopy to measure the band-gap. This can then be correlated with the semiconductor crystal size, usually measured by TEM and/or XRD. This technique works well in most cases for films on transparent substrates (conducting glass for electrodeposited films). However, for many of the samples described above, which are on metal film substrates with low optical transmission, this simple technique is of limited usefulness. This limitation is severely compounded by the very small amount of material often present on these substrates – as little as an average thickness of 2 nm or even less.

Because of these limitations, we turned to other, less obvious techniques to extract values of Eg for these samples. We were able to measure these values to a reasonable approximation in most cases. Apart from this relatively mundane measurement, however, we found interesting properties of the samples, some of them not related to quantum size effects. The two methods described here are scanning probe current-voltage spectroscopy and photoelectrochemical photocurrent spectroscopy.

2.4.1 Scanning Probe Current-Voltage Spectroscopy

This method uses the tip of a scanning probe microscope – either a scanning force microscope (SFM) with an electrically conducting tip or a scanning tunneling microscope (STM). The tip contacts, either directly (SFM) or via a tunneling

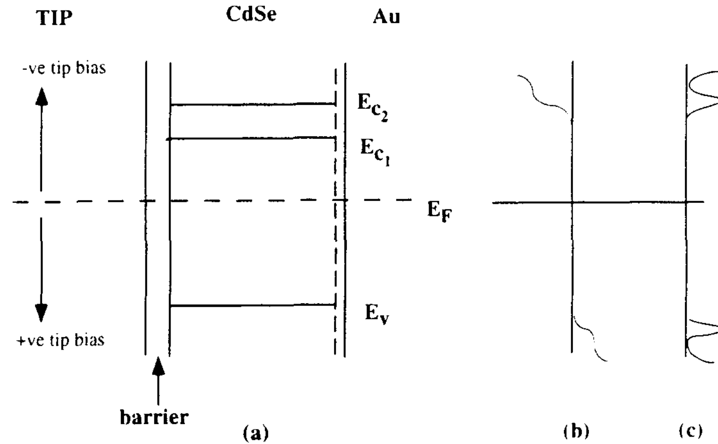

Fig. 2.18 (a) Energy diagram of scanning probe tip – CdSe nanocrystal – Au substrate showing one valence level and two conduction levels. (b) Corresponding current-voltage (*i–V*) characteristic, where the horizontal axis is the current axis. (c) Corresponding conductivity–voltage plot, where the horizontal axis is the conductivity (d*I*/d*V*) axis.

gap (STM), the semiconductor nanocrystals which are deposited on the conducting substrate, forming a metal-semiconductor-metal or metal-tunneling barrier-semiconductor-metal junction, respectively. A potential sweep is applied to the two metal contacts and the current measured as a function of the applied bias – hence the designation current-voltage (*i-V*) spectroscopy. This method has been used to measure band-gaps of semiconductors, both bulk and size-quantized [51–53].

The basis of the technique is shown in Fig. 2.18. When a negative bias is applied to the tip, its Fermi level moves up with respect to the semiconductor energy levels in the energy diagram (a). As long as there is no empty level to accept electrons from the tip (the situation ideally in the gap), no current will flow. Current will flow when the tip Fermi level reaches the first empty conduction level (E_{c_1}). Similarly, when the tip is positively biased, its Fermi level moves down and again no current flows until resonance is established between the tip Fermi level and the top filled valence level (E_V). The zero current region, shown in Fig. 2.18b, can then be identified with the semiconductor band-gap.

This description is oversimplified for a number of reasons. To be valid, it requires that all of the applied bias falls across the tip-semiconductor barrier. If all the bias falls across an assumed semiconductor-substrate barrier (shown in Fig. 2.18a between the vertical broken line and the Au substrate surface), the zero current region will be the same, since a negative (positive) tip bias will result in the substrate Fermi level moving down (up) with respect to the tip level, resulting in the same spectrum. The problem arises if both barriers are comparable: in that case only some of the applied bias will fall across the larger barrier. The zero current region will then probably be larger than the band-gap (it could possibly be smaller if the Fermi level in the semiconductor is close to one of the edges).

Another important (and interesting) factor that must be taken into account in this model is the charging energy of the nanocrystal. The energy (voltage) required to inject an electron into a material separated from the source by a barrier is given by:

$$E = e^2/2C \, (V = e/2C)$$

where e is the electronic charge and C is the capacitance of the material. In most cases, C is sufficiently large such that this energy is much lower than the thermal energy and the charging effect is not observed. If very low temperatures are employed, these effects can be observed (since the thermal energy is very small) and are seen as discrete steps in the current-voltage spectra (the single electron tunneling effect) [54]. For the very small semiconductor structures described here, where C is often less than 10^{-18} F and the voltage required to inject a single electron is given in tens of an eV, these effects can be seen at room temperature. This charging affects the current-voltage spectra in two ways. First, the zero current region only gives an approximate value of E_g. More accurately, E_g is given by the difference in energy between the first conductivity peaks at +ve and –ve bias, minus twice the above charging energy, i.e. e^2/C (twice, since charge is injected in both bias directions, once electrons and once holes). Second, in the region where current flows, every additional electron injected into, or removed from, the nanocrystal will require an additional voltage of e/C, resulting in plateaus in the i-V spectrum (Fig. 2.18b) or peaks in the conductivity (di/dV) spectrum, as seen in Fig. 2.18c. The peak separation in the conductivity spectrum can arise not only from single electron charging but also from charge transfer via higher energy levels (such as E_{c_2} in Fig. 2.18a). If the peak separation can be attributed to charging, then subtraction of this separation from the zero current voltage span will give the band-gap. (Note that this band-gap differs from the optical band-gap by the difference between the charging energy and the electron-hole coulomb energy: this difference is small in our samples – probably no more than tens of meV, and is ignored here, since the accuracy of these measurements is less than this difference.)

Fig. 2.19 gives an example of such spectra – current–voltage and conductivity – taken at room temperature using a Pd/Au-coated AFM tip for electrodeposited CdSe on Au on mica with a CdSe coverage of ca. 25%. Mica is used rather than glass as it is smoother and therefore more suitable for scanning probe measurements. The conductivity spectrum, which may be obtained either directly or by mathematical manipulation of the current-voltage spectrum (in this case the latter is employed), shows the features more sharply. The zero current region of ca. 2.2 V is prominent in both spectra. It should be stressed that many of the spectra taken on this (and similar) samples with a relatively low coverage of nanocrystals show an almost vertical line representing direct contact between the tip and Au substrate; this shows that the spectra such as shown here are not merely artifacts of the measurement.

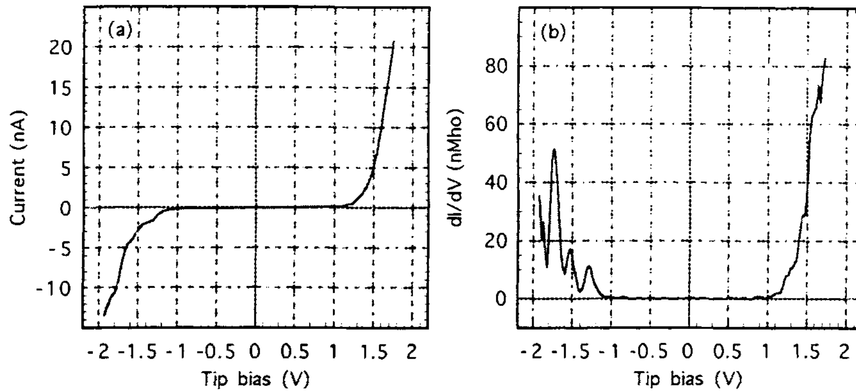

Fig. 2.19 Current-voltage (a) and conductance (b) spectra of electrodeposited CdSe quantum dots (less than a monolayer coverage of dots) on Au.

A feature of these spectra which can complicate the interpretation is the frequent appearance of a small peak in the conductivity spectrum close to the main peaks (such a peak is not seen in Fig. 2.19). This peak could be either due to tunneling into a surface state close to the first conduction level or it could give the position of the conduction level itself. We believe the former is more likely for a number of reasons. The small size of the peak indicates a slow rate of increase of current with bias, suggesting poor coupling between tip and semiconductor states. Such poor coupling is not unexpected for tunneling into surface states which are localized and may be physically more distant from the tip. (In a few cases, this first peak may be large enough to lead to an ambiguous interpretation of the spectrum.) Also, the energy separation between this first small peak and the next one is very different (larger) than that between the other peaks. The energy separations between the three main peaks in the conduction levels have been attributed to Coulomb charging [55]; thus the small peak probably represents a different level. Thirdly, the band-gaps measured by this technique correlate well with the measured sizes [55] while if the small peak was assumed to be the position of the first conduction level, this correlation would not hold. Finally, surface states have been identified in chemically deposited CdSe quantum dots [56–58] as well as in similarly-electrodeposited CdSe quantum dots [59].

Based on the above, a value of the band-gap for the CdSe specimen in Fig. 2.19 is estimated at 2.25±0.05 eV, corresponding to a size of 3.4±0.4 nm [30]. The voltage separation between peaks (e/C, assuming the peak structure is due to charging) is ca. 0.19 V on average.

Looking at the three peaks in the negative bias region of the conductivity spectrum, which are assumed to correspond to a total of three electrons in the first unoccupied level ($1S_e$), one might ask the question: how can there be three electrons in a level which should only hold two (the S level is doubly degenerate). Because surface states are known to exist on these nanocrystals (as noted above) and the lifetime of electrons in these states is almost certainly much longer than in

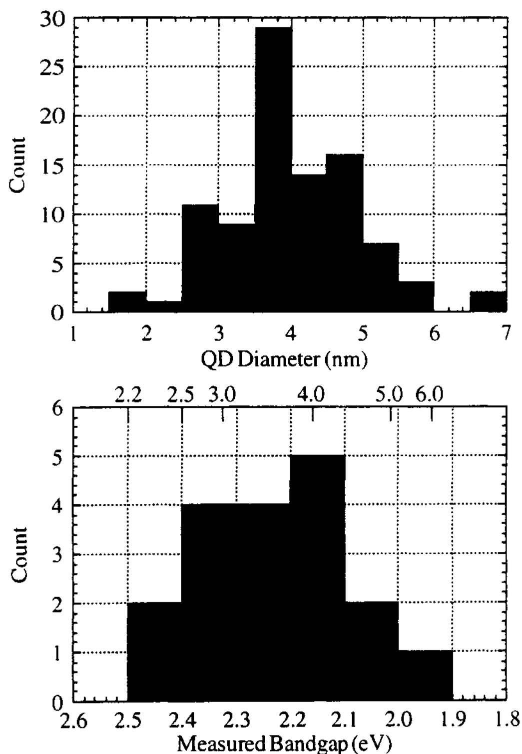

Fig. 2.20 Upper histogram: Size distribution of CdSe nanocrystals on Au measured by TEM imaging. Lower histogram: Distribution of band-gap measurements from conductance spectra (bottom scale) together with experimental results (from Ref. [30]) of CdSe quantum dot size corresponding to these band-gaps (top scale). It should be noted, in comparing the updated band-gap distribution shown here with that in Ref. [55], that the band-gap values in the latter were underestimated by ca. 0.2 eV (in that reference, twice the charging peak separation, i.e., $2e^2/C$, was subtracted from the zero current region rather than $2(e^2/2C)$.

the delocalized states, it is quite possible that the electrons which tunnel into the delocalized states are trapped before the next electron enters the same state. This will not affect the charging spectrum fundamentally (there may be secondary effects due to the different spatial distribution of electrons in the nanocrystals resulting in some changes in capacitance), but will affect the occupation of levels.

Owing both to the relatively poor lateral resolution of the SFM tip as well as to the thermal drift of the specimen relative to the tip for these room temperature measurements, the nanocrystal size and spectrum could not be measured together and a direct correlation could not be made between size and spectrum. To overcome this limitation, we originally compared the band-gap distribution, measured by current-voltage spectroscopy, with the size distribution, measured by direct TEM imaging, of a sample prepared in an identical manner. This correlation is shown in Fig. 2.20 together with the nanocrystal size, calculated from our measured band-gaps and the band-gap-size relationship described by Murray et al. [30]. The good correspondence between the distribution measured by TEM and that measured by current-voltage spectroscopy attests to the validity of the technique.

More recently, we have been able to measure individual QD size and spectrum using low temperature STM [60]. The low temperature (4.2 K) prevents appreciable thermal drift and the STM tip allows better resolution, the two factors which previously prevented us from carrying out these measurements together, as noted

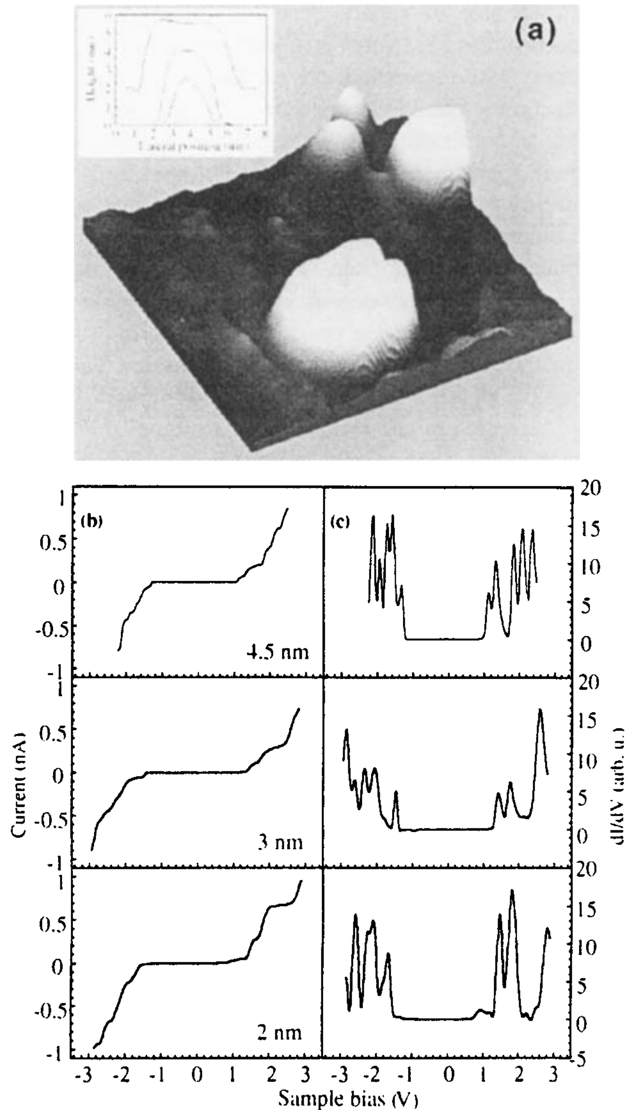

Fig. 2.21 (a) STM topography image (12×12 nm^2) showing four individual CdSe quantum dots electrodeposited on Au. Inset: cross-sections of the three lower quantum dots, for which current-voltage spectroscopy is shown in (b) and conductance spectroscopy in (c). From Alperson et al., [60].

above. Fig. 2.21a shows the STM topographies of four different CdSe quantum dots electrodeposited on Au together with three line scans in the *z*-direction (inset). The current-voltage and conductivity spectra of three of the dots of average diameter 2.0, 3.0 and 4.5 nm are shown in Fig. 21b and c respectively. The increase in band-gap and in peak spacing of the conductivity spectra with decrease

in dot size are clearly apparent. While the general features are similar to those seen in the SFM room temperature spectra (Fig. 2.19), there is one striking difference. While typically three equally-spaced conductivity peaks are seen in the conduction levels, the largest dot in the low temperature STM experiments (the sample where most peaks could be seen, as expected due to its smaller band-gap and peak spacings) shows a doublet followed by a triplet in the conduction level bias direction. The peak spacings within the doublet and triplet have been attributed to Coulomb charging while the spacing between the doublet and triplet was explained as arising from two different energy levels – the $1S_e$ and $1P_e$ levels. The $1S_e$ level is doubly degenerate while the $1P_e$ level is sixfold degenerate (only three of the six degenerate peaks are seen here; in similar, subsequent measurements on QDs of the low band-gap InAs (the low band-gap allowing accession of more peaks), all six of the $1P_e$ peaks have been seen in the spectrum [61]).

According to our previous explanation of the triplet peak in the conduction level side of the SFM spectra (trapping in surface states), this difference suggests that such trapping is less important in the low temperature STM experiments than in the room temperature SFM ones. We note that room temperature SFM spectra carried out in a dry ambient (normally, these room-temperature measurements are carried out in normal – i.e., humid – surroundings) clearly show the presence of conductivity peaks in the band-gap region corresponding to surface states [59] while these peaks are absent when carried out in the normal humid atmosphere. In the STM measurements, which are carried out in vacuum, and therefore necessarily water-free environment, such surface state peaks are not normally seen, except to a slight extent in very small dots (such as the 2 nm dot in Fig. 2.21). Water has previously been shown to partially passivate surface states on chemically deposited CdSe QDs [56, 57]. Therefore we conclude that the effect of surface states in the room temperature SFM measurements is connected with either the temperature and/or with the specific technique and not with an effect of measurement ambient. Further experiments will hopefully shed light on this effect.

The above studies have been carried out on CdSe. Clearly it is of interest to extend them to other semiconductors with different band-gaps. We have also studied electrodeposited CdS on Au using SFM current-voltage spectroscopy [40]. While these spectra are similar to those of CdSe, with the larger band-gap expected from CdS, there are also important differences. Before discussing the spectra, we recall the main size characteristics of the CdS crystals on Au discussed above.

The size of the CdS nanocrystals depends on the amount of deposit. Essentially no CdS was formed during the initial stages of deposition, corresponding to a theoretical average thickness of 2 nm. For a theoretical (nominal) thickness of 5 nm (=ca. 3 nm average thickness), the average crystal lateral size was 4 nm with a height of 3 nm while for a theoretical thickness of 10 nm (8 nm average), the average size increased to 6.3 nm with a height of 6–8 nm. The 3 nm (average thickness) film was made up of somewhat less than a monolayer of crystals while the 8 nm film was comprised – at least to a considerable extent – of larger crystals on top of smaller ones.

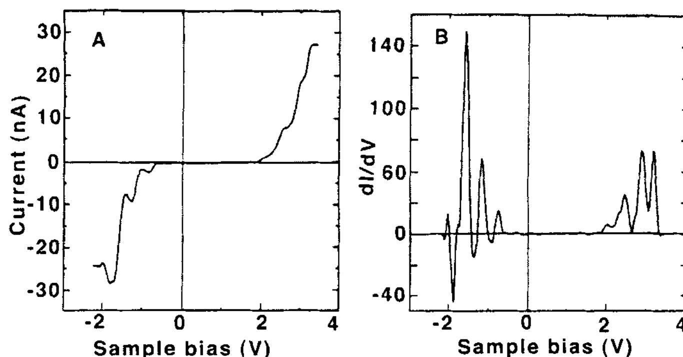

Fig. 2.22 Current-voltage (a) and conductivity-voltage (b) plots of a 5 nm (nominal thickness) CdS on Au taken using a SFM with a B-doped conducting diamond tip. From Behar et al., [40].

Fig. 2.22 shows current-voltage and corresponding conductivity spectra of a (nominal) 5 nm CdS film. The measurements were carried out as for the corresponding CdSe spectra, except that a boron-doped conducting diamond tip was used instead of a Pd/Au-coated tip. The zero current region and structure in the regions of current flow in both bias directions can be seen. These are the same qualitative characteristics of the equivalent CdSe spectra. A statistical distribution of the width of the zero current region over a number of measurements gives an average value of 2.8 eV. After correcting for Coulomb charging of ca. 0.2 eV (the conductivity peak spacing), the average band-gap is 2.6 eV. This value is expected for 4–5 nm CdS quantum dots and is clearly larger than the corresponding values for the smaller band-gap CdSe.

For thicker films, the zero current region becomes larger, although the opposite might be expected since the crystal size is greater (therefore loss in size quantization). However, for thicker films, we are no longer measuring one nanocrystal, but rather (probably) two in series – one on top of the other. The grain boundary between the two crystals constitutes an additional barrier for applied voltage to drop across; therefore the zero current region no longer gives a measure of the band-gap.

An important difference between the current-voltage spectra for CdS and CdSe is the lack of symmetry of the zero current region of the CdS about the zero bias value. For CdSe, the zero bias is symmetrical in almost all cases (see Fig. 2.19) while for CdS, the zero bias is usually much closer to what is believed to be the conduction level, as seen in Fig. 2.22. In the case of CdSe QDs, the symmetry is believed to be due to the intrinsic nature of the CdSe (Fermi level near midgap). For the CdS QDs, however, XPS valence band spectroscopy has shown that the Fermi level is considerably closer to the conduction level than to the valence level. This can explain the difference in symmetry. It should be mentioned, however, that other factors may influence the symmetry, in particular the presence of external charges near the nanocrystal.

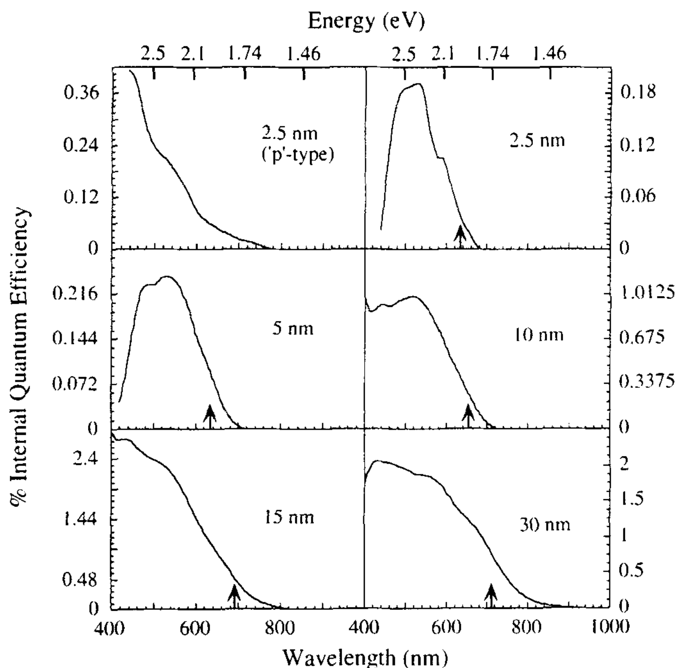

Fig. 2.23 PEC photocurrent spectra of various nominal thicknesses (given in the figure) of CdSe QDs electrodeposited from a $Cd(ClO_4)_2$ solution on gold. 2.5 nm is equivalent to half a monolayer of QDs; 5 nm is a full monolayer; 15 nm is a little more than two layers, and 30 nm is at least three. The 'p-type' spectrum shown in the top left was observed with a sample which behaved as 'p-type' (in contrast to the usual 'n-type' behavior). The quantum efficiency was corrected for thickness differences. Arrows indicate the estimated band-gap value. Energy (in eV) is given in the top scale.

Regarding the peaks in the conductance spectra, while Coulomb charging can explain the structure to a considerable extent, it is probable that energy level spacing also plays a role to some extent. This is discussed in Ref. [40].

2.4.2
Photoelectrochemical (PEC) Photocurrent Spectroscopy

When a semiconductor is immersed in an appropriate electrolyte, electrically connected to a second (counter) electrode (often platinum or carbon) and illuminated with supra-band-gap light, a current may flow between the two electrodes. This is the basis of photoelectrochemical (or liquid junction) solar cells. Essentially, the cell behaves much as a metal-semiconductor junction; the semiconductor-electrolyte junction (analogous to the semiconductor-metal junction) causes formation of a space charge layer in the semiconductor which separates photogenerated electrons and holes that react with the electrolyte, and results in current flow on illumination. For nanocrystalline semiconductor films, the charge separation may be due not to a space charge layer in the semiconductor but to differential trapping

of electrons and holes at the nanocrystal surface [56]. However, for our present purposes, this difference in mechanism of photocurrent generation is not essential. The main issue is that since (ideally) only supra-band-gap light results in photocurrent, the band-gap can be measured from the photocurrent spectrum (photocurrent against illumination energy or wavelength) much as it is measured from an absorption spectrum [62]. In practice, PEC spectroscopy is often very sensitive to surface state adsorption: this can be an advantage (by giving information on surface states) or a disadvantage (by masking the true band-gap photocurrent onset).

We have used a chopped monochromatized source of illumination incident on the specimen. The (short circuit) photocurrent is fed through a current-to-voltage converter to a lock-in amplifier. This set-up can measure $<10^{-13}$ A, an important factor when measuring very tiny amounts of material (down to 2.5 nm average thickness of CdSe on Au). The electrolyte used was an aqueous solution of sodium selenosulfite ($Na_2SO_3 + Se$). This solution is colorless in the visible region (absorption begins at ca. 400 nm) and can be both readily oxidized and reduced.It therefore served as a moderately stabilizing electrolyte (at the low monochromatic levels of illumination used) for CdSe as well as preventing excessive polarization of the counter electrode (important since a two electrode set-up was used; a three electrode arrangement, using a potentiostat, was noisier and therefore less sensitive).

Photocurrent spectra were measured for CdSe electrodeposited on Au from $Cd(ClO_4)_2$ electrolyte. The spectra for different nominal thicknesses of CdSe are shown in Fig. 2.23. The band-gaps, estimated by extrapolating the square of the photoresponse to zero, are shown in the figure by vertical arrows. Ignoring, for the moment, the top, left spectrum (2.5 nm 'p'-type), the shift in band-gap from 1.95 eV for the 2.5 nm film to the bulk value of 1.73 eV for the 30 nm one reflects the increase in crystal size with increasing deposit thickness described above for the current-voltage spectroscopy. It does not do so very quantitatively, however, particularly for the 2.5 and 5 nm films. The average crystal diameter of the 2.5 nm films is ca. 5 nm. According to the results of Murray et al. [30], the band-gap values should be ca. 2.1 eV for the 2.5 and 5 nm films. We explained this discrepancy by the distribution of crystal sizes, and therefore of band-gaps in the films, resulting in domination of the current onset by the larger crystals in the distribution [63].

There are a number of other features in these spectra. Of particular interest is the large increase in internal quantum efficiency between the first (5 nm film) and second (10 nm and thicker) layers of CdSe crystals. It should be noted that the real internal quantum efficiency is considerably higher (by about an order of magnitude) than the numbers given in Fig. 2.23. The numbers are based on the measured quantum efficiency of the 30 nm film (which absorbs ca. 10% in the strongly absorbing region) and corrected for the film thickness by multiplying the measured quantum efficiency by the ratio between 30 (nm) and the thickness of the film measured.

The sharp increase in quantum efficiency between the first and second layers of crystals can be explained by two different mechanisms. In one (charge transfer),

carriers photogenerated in the first layer of crystals are very likely to undergo recombination at the Au, while those generated in the second (and subsequent) layers are much less likely to suffer this fate since, to do so, both charges would have to cross the grain boundary between the first and subsequent crystal layers. In the second mechanism (energy transfer), the recombination is strongly dependent on the distance of the photogenerated carriers from the Au; carriers generated in the second layer of crystals will be further from the Au than those in the first layer, and will therefore be less subject to recombination by energy transfer. At present, we cannot distinguish between these two mechanisms.

The 30 nm film exhibits a relatively strong sub-band-gap response. Such sub-band-gap responses in PEC spectroscopy have been attributed to absorption in intra-band-gap states [64–66]. For the nanocrystals discussed here, it is likely that such states are surface states and that they would be more dominant due to the large surface-to-volume ratio. In fact, the thinner films with smaller crystal size might be expected to be even more dominated by sub-band-gap absorption, which is not apparently the case. It should be kept in mind, however, that if the surface state absorption is very strong, it might be difficult to separate it from the supra-band-gap absorption, which could also explain the apparent lower than expected measured band-gaps of the thin films.

The final feature, which we mention only briefly, due to its speculative nature, is the peak in the response at ca. 2.4 eV for the 2.5 and 5 nm films. This has been explained by hot hole generation whereby higher energy holes are more likely to recombine, either through the charge transfer or energy transfer mechanisms. The *increase* in the photocurrent in the spectrum of the 2.5 nm 'p'-type sample supports this suggestion in the charge transfer mechanism, since the lower probability of hole transfer to the electrolyte will increase the response whereas it decreases it for the (normal) n-type response [63].

Since the CdSe crystals deposited from chloride electrolyte are appreciably smaller than those deposited from perchlorate, this should be reflected in the photocurrent spectra. This has been seen for chloride-deposited films [63], particularly for thicker films, where the chloride acts as a capping agent to limit crystal growth [21]. These spectra, shown in Fig. 2.24, are also qualitatively similar to the perchlorate ones in Fig. 2.23 in the large difference between quantum efficiencies of the first and second crystal layers (for the chloride samples, the difference is even larger) and the peak response of the very thin films. The quantum efficiencies of the thicker (two or more crystal layers) chloride films are greater (by a factor of 3) than the corresponding perchlorate ones although no clear explanation for this effect can be proposed.

The CdSe/Pd system, discussed above, is interesting from the characterization aspect since it contains very tiny 'crystals' (ca. 1 nm) which are in direct contact with disordered (amorphous) CdSe. The measured band-gap is expected to be essentially that of the amorphous CdSe (which forms the main constituent of the deposit). Even if the nanocrystals were to make up a major part of the deposit, quantization effects are expected to be small since the 'crystals' are in intimate contact with the amorphous CdSe, resulting in small, if any, size quantization.

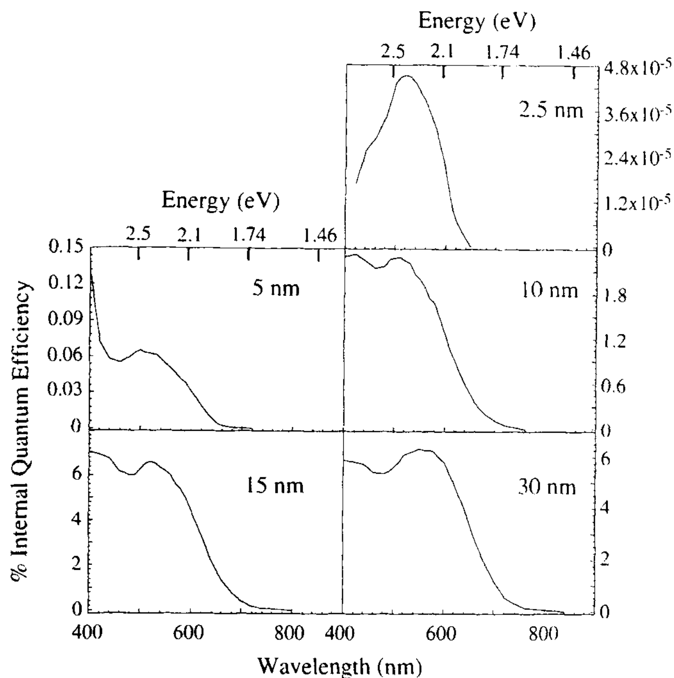

Fig. 2.24 PEC photocurrent spectra of various nominal thicknesses (given in the figure) of CdSe QDs electrodeposited from a $CdCl_2$ solution on gold. In all cases the quantum efficiency was corrected for thickness differences. Top scale shows the energy (in eV).

The photocurrent spectra of CdSe deposits on Pd with five different nominal thicknesses are shown in Fig. 2.25. The spectra are normalized at their peak intensities in order to compare their spectral shapes. The three thinnest films (2.5, 5 and 10 nm) all have essentially the same photocurrent onset at 720–740 nm. This may be at first sight unexpected, since quantization in the vertical direction is expected in the 2.5 and 5 nm films (assuming a similar effective mass for amorphous CdSe as for crystalline CdSe). However, this assumption is probably incorrect. We do not know of studies of size quantization in amorphous semiconductors; however, effective masses in disordered materials are likely to be greater than in the same substance which is ordered, resulting in smaller quantum effects. The thicker films (15 and 30 nm) show increasing red shifts. Since we do not know the band-gap of amorphous CdSe, we cannot make a direct comparison. It is likely that the onsets of the thicker films represent the mobility edge of the amorphous CdSe.

The relative photocurrents can be obtained by the sensitivity factors of the spectra in Fig. 2.25. As with the crystalline CdSe on Au, the very thin sample (2.5 nm) has a very low photocurrent yield which increases greatly with increasing initial thickness and then to a lesser extent. The reason for this is likely to be related to the morphology of these deposits: initially a thin CdSe layer completely covering the Pd (hence electron/hole generation very close to the substrate) which develops into relatively large particles of CdSe with increasing deposit thickness.

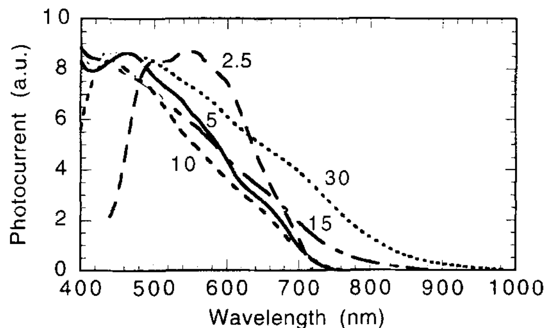

Fig. 2.25 PEC photocurrent spectra of various nominal thicknesses (given in the figure in nm) of CdSe electrodeposited on Pd (evaporated film on glass). The spectra are normalized to give the same peak heights. The relative photocurrents can be obtained from the sensitivity factors (and the sensitivity factors corrected for differing thicknesses) which are: 2.5 nm: ×150 (12.5); 5 nm: ×28 (4.7); 10 nm: ×5 (1.7); 15 nm: ×5.3 (2.6); 30 nm: ×1 (1) (B. Alperson, I. Rubinstein, G. Hodes, unpublished results).

Finally, we briefly mention some photocurrent spectra of CdS (this has been dealt with more fully in Ref. [40]). Referring to the nominal CdS thicknesses on Au discussed above and in Ref. [40], the samples varied from an average crystal size of <4 nm (5 nm nominal thickness), through 5 (8) to 6.3 nm (10 nm). Considering only the shapes of the spectra and, specifically, the band-gap values estimated from these spectra, the 5 and 8 nm (nominal thickness) films gave identical band-gaps of 2.65 eV while the 10 nm (and thicker – 15 and 20 nm) samples all gave bulk band-gaps of 2.45 eV, as expected for crystals of this size. The larger band-gap for the 5 and 8 nm samples is qualitatively as expected form size quantization. The 5 nm sample would actually be expected to have a larger band-gap. The discrepancy can be explained by either the predominance of the larger crystals in the distribution (more specifically, a small fraction of larger crystals sitting on top of underlying ones) and/or the very small signal from the 5 nm sample, resulting in greater inaccuracies [40]. The former seems to be the more likely explanation.

As with the CdSe/Au, the very thin (one layer of crystals) deposit gave very poor photoresponse which increased greatly with deposition of the second layer of crystals; this can be explained in the same way, either by charge transfer through grain boundaries or energy transfer variation with distance.

2.5
Potential Applications of Electrodeposited Nanocrystalline Semiconductor Films

In this concluding section, we attempt to predict potential applications for the materials discussed in this chapter. This is done with the obvious caveats that (a) some of these suggestions will never come to fruition, and more important (b) applications that have not yet been conceived may arise.

An obvious actual use has already been mentioned early in this chapter: size-quantized CdS as a window layer for $CuInS_2$ solar cells, using the increased band-gap of the CdS to allow greater light absorption resulting, therefore, in higher photocurrents.

The current-voltage spectroscopic studies of the various isolated nanocrystals suggests application in obtaining devices with tailored current-voltage characteristics. The device size would be only a few nm (conveniently ignoring the size of contacts to the nanocrystal). There are many features in the current-voltage characteristics, some of which can already be reasonably-well controlled. One of these is the zero current region voltage span together with the symmetry of this region about the zero bias. The zero current region can be controlled over a larger range by combination of choice of semiconductor or crystal size (i.e. band-gap) or by more layers of crystals (additional barriers which increase the width of this region). The factors which control symmetry are not well understood at present, but this can be varied almost over the complete zero current region (only part of our experimental data on this subject have been mentioned here). Other features which are amenable (to a greater or lesser extent at present) to control are the shapes and spacings of the current flow regions and the appearance of negative differential resistance features.

Thicker films of nanocrystals are porous to some extent. Porous, nanocrystalline semiconductor layers, in particular those of TiO_2, have been applied to several different devices, in particular to the dye-sensitized solar cell [67] and various "pollution cleanup" systems [68]. While TiO_2 is admittedly an ideal semiconductor for many of these purposes, the use of electrodeposition to prepare such films of semiconductors in general (and also TiO_2 in particular) is an option. Control of porosity, of considerable importance in most of these applications, is an issue which has been essentially ignored in these electrodeposited films. It is likely that this property, as with many other properties of the deposits, can be controlled. One possibility is to co-deposit another, readily-dissolvable phase with the semiconductor which can subsequently be dissolved away (e.g., metallic Zn). Another is to deposit under diffusion-limiting conditions which tends to give dendritic deposits.

There are many methods to prepare nanocrystals, with new techniques or modifications of old ones continually appearing. Each technique has its advantages and disadvantages. Also, many properties (optical, photo(electro)chemical, electrical, mechanical, magnetic, etc.) of the nanocrystals are either size dependent and/or surface area dependent. Many applications have emerged recently in the field of photocatalysis. Undoubtedly, many more will follow in this and in other fields.

Acknowledgments
This research was supported by the US Office of Naval Research, the Israel Ministry of Science and the United States-Israel Binational Science Foundation.

References

1 G. F. FULOP, R. M. TAYLOR, *Ann. Rev. Mater. Sci.* **1985**, *15*, 197.
2 C. D. LOKHANDE, S. H. PAWAR, *Phys. Status Solidi (a)* **1989**, *111*, 17.
3 R. C. DEMATTEI, R. S. FEIGELSON, in: *Electrochemistry of Semiconductors and Electronics*, edited by J. McHardy and F. Ludwig, Noyes, Park Ridge, NJ, **1992**.
4 G. HODES, in: *Physical Electrochemistry: Principles, Methods, and Applications*, edited by I. Rubinstein, Marcel Dekker, **1995**, p. 515.
5 M. P. R. PANICKER, M. KNASTER, F. A. KROGER, *J. Electrochem. Soc.* **1978**, *125*, 566.
6 A. DARKOWSKI, M. COCIVERA, *J. Electrochem. Soc.* **1985**, *132*, 2768.
7 A. S. BARANSKI, W. R. FAWCETT, K. GATNER, A. C. MCDONALD, J. R. MACDONALD, M. SELEN, *J. Electrochem. Soc.* **1983**, *130*, 579.
8 A. S. BARANSKI, W. R. FAWCETT, *J. Electrochem. Soc.* **1980**, *127*, 766.
9 K. MISHRA, K. RAJESHWAR, A. WEISS, M. MURLEY, R. D. ENGELKEN, M. SLAYTON, H. E. MCCLOUD, *J. Electrochem. Soc.* **1989**, *136*, 1915.
10 E. FATAS, P. HERRASTI, T. GARCIA, F. ARJONA, E. GARCIA CAMARERO, *Mater. Chem. and Phys.* **1985**, *13*, 497.
11 J. I. PANKOVE, *Optical Processes in Semiconductors*, Dover Publications, New York, **1971**.
12 P. K. LIM, D. E. BRODIE, *Canad. J. Phys.* **1977**, *55*, 1641.
13 H. NEUMANN, B. PERLT, N. A. K. ABDUL-HUSSEIN, R. D. TOMLINSON, A. E. HILL, *Solid State Commun.*, **1982**, *42*, 855.
14 G. HODES, T. ENGELHARD, A. ALBU-YARON, A. PETTFORD-LONG, in: *Mat. Res. Soc. Symp.*, **1990**, p. 81.
15 G. HODES, A. ALBU-YARON, in: *Optical, Structural and Photoelectrochemical Properties of Quantum Box Semiconductor Films*, **1988**, p. 298.
16 D. GAL, G. HODES, D. HARISKOS, D. BRAUNGER, H.-W. SCHOCK, *Appl. Phys. Lett.* **1998**, *73*, 3135.
17 R. ELBAUM, S. VEGA, G. HODES, *Submitted.*
18 A. S. BARANSKI, W. R. FAWCETT, A. C. MCDONALD, *J. Electroanal. Chem.* **1984**, *160*, 271.
19 A. S. BARANSKI, W. R. FAWCETT, *J. Electrochem. Soc.* **1984**, *131*, 2509.
20 A. S. BARANSKI, M. S. BENNETT, W. R. FAWCETT, *J. Appl. Phys.* **1983**, *54*, 6390.
21 Y. MASTAI, D. GAL, G. HODES, *J. Electrochem. Soc.*, in press.
22 A. S. BARANSKI, W. R. FAWCETT, C. M. GILBERT, *J. Electrochem. Soc.* **1983**, *130*, 2423.
23 G. HODES, D. CAHEN, *Solar Cells* **1986**, *16*, 245.
24 D. GAL, G. HODES, *J. Electrochem. Soc.*, in press.
25 A. C. RASTOGI, K. S. BALAKRISHNAN, *J. Electrochem. Soc.* **1989**, *136*, 1502.
26 J. VON WINDHEIM, M. COCIVERA, *J. Electrochem. Soc.* **1987**, *134*, 440.
27 Y. MASTAI, G. HODES, *J. Phys. Chem.* B, **1997**, *101*, 2685.
28 Y. NOSAKA, K. YAMAGUCHI, H. MIYAMA, H. HAYASHI, *Chem. Lett.* **1988**, 605.
29 M. L. STEIGERWALD, A. P. ALIVISATOS, J. M. GIBSON, T. D. HARRIS, R. KORTAN, A. J. MULLER, A. M. THAYER, T. M. DUNCAN, D. C. DOUGLASS, L. E. BRUS, *J. Am. Chem. Soc.* **1988**, *110*, 3046.
30 C. B. MURRAY, D. J. NORRIS, M. G. BAWENDI, *J. Amer. Chem. Soc.* **1993**, *115*, 8706.
31 C. L. COLYER, M. COCIVERA, *J. Electrochem. Soc.* **1992**, *139*, 406.
32 D. K. ROE, L. WENZHAO, H. GERISCHER, *J. Electroanal. Chem.* **1982**, *136*, 323.
33 K. S. BALAKRISHNAN, A. C. RASTOGI, *Sol. Energy Mater.* **1990**, *20*, 417.
34 R. NÖTZEL, *Semicond. Sci. Technol.* **1996**, *11*, 1365.
35 Y. GOLAN, L. MARGULIS, I. RUBINSTEIN, G. HODES, *Langmuir* **1992**, *8*, 749–752.
36 Y. GOLAN, L. MARGULIS, G. HODES, I. RUBINSTEIN, J. L. HUTCHISON, *Surf. Sci.* **1994**, *311*, L633.
37 Y. GOLAN, G. HODES, I. RUBINSTEIN, *J. Phys. Chem.* **1996**, *100*, 2220.
38 Y. GOLAN, A. HATZOR, J. L. HUTCHISON, I. RUBINSTEIN, G. HODES, *Isr. J. Chem.* **1997**, *37*, 303.

39 G. Hodes, Y. Golan, D. Behar, Y. Zhang, B. Alperson, I. Rubinstein, in: *Nanoparticles and Nanostructured Films*, edited by J. H. Fendler, Wiley-VCH, **1998**, pp. 1–22.

40 D. Behar, I. Rubinstein, G. Hodes, S. Cohen, H. Cohen, *Superlatt. Microstruct.* **1999**, *25*, 601.

41 Y. Golan, E. Ter-Ovanesyan, Y. Manassen, L. Margulis, G. Hodes, I. Rubinstein, E. G. Bithell, J. L. Hutchison, *Surf. Sci.* **1996**, *350*, 277.

42 C. H. Patterson, R. M. Lambert, *Surf. Sci.* **1987**, *187*, 339.

43 J. A. Rodriguez, S. Chaturvedi, T. Jirsak, *Chem. Phys. Lett.* **1998**, *296*, 421.

44 G. Piaszenski, M. Aschoff, S. Speller, W. Heiland, *Nucl. Instr. Meth. B.* **1998**, *135*, 331.

45 Y. Zhang, G. Hodes, I. Rubinstein, E. Grünbaum, R. Nayak, J. L. Hutchison, *Adv. Mater.* **1999**, *11*, 1437.

46 S. H. Tolbert, A. P. Alivisatos, *Science* **1994**, *265*, 373.

47 C.-C. Chen, A. B. Herhold, C. S. Johnson, A. P. Alivisatos, *Science* **1997**, *276*, 398.

48 L. E. Brus, J. A. W. Harkless, F. H. Stillinger, *J. Am. Chem. Soc.* **1996**, *118*, 4834.

49 C. T. Dameron, R. N. Reese, R. K. Mehra, A. R. Kortan, P. J. Carroll, M. L. Steigerwald, L. E. Brus, D. R. Winge, *Nature* **1989**, *338*, 596.

50 J. Lin, E. Cates, P. A. Bianconi, *J. Am. Chem. Soc.* **1994**, *116*, 4738.

51 R. M. Feenstra, P. Mårtensson, *Phys. Rev. Lett.* **1988**, *61*, 447–450.

52 X. K. Zhao, L. D. McCormick, J. H. Fendler, *Langmuir* **1991**, *7*, 1255–1260.

53 S. Ogawa, F.-R. F. Fan, A. J. Bard, *J. Phys. Chem.* **1995**, *99*, 11182–11189.

54 U. Meirav, E. B. Foxman, *Semicond. Sci. Technol.* **1995**, *10*, 255.

55 B. Alperson, S. Cohen, I. Rubinstein, G. Hodes, *Phys. Rev. B.* **1995**, *52*, R17017.

56 L. Kronik, N. Ashkenasy, M. Leibovitch, E. Fefer, Y. Shapira, S. Gorer, G. Hodes, *J. Electrochem. Soc.* **1998**, *145*, 1748.

57 E. Lifshitz, I. Dag, I. Livtin, G. Hodes, S. Gorer, R. Reisfeld, M. Zelner, H. Minti, *Chem. Phys. Lett.* **1998**, *288*, 188–196.

58 E. Lifshitz, I. Dag, I. D. Litvin, G. Hodes, *J. Phys. Chem. B* **1998**, *102*, 9245.

59 B. Alperson, I. Rubinstein, G. Hodes, *Phys. Rev. B*, **2000**, in press.

60 B. Alperson, I. Rubinstein, G. Hodes, D. Porath, O. Millo, *Appl. Phys. Lett.* **1999**, *75*, 1751.

61 U. Banin, Y. W. Cao, D. Katz, O. Millo, *Nature* **1999**, *400*, 542.

62 Y. Mirovsky, R. Tenne, G. Hodes, D. Cahen, *Thin Solid Films* **1982**, *91*, 348–355.

63 B. Alperson, H. Demange, I. Rubinstein, G. Hodes, *J. Phys. Chem. B* **1999**, *103*, 4943.

64 D. Laser, S. Gottesfeld, *J. Electrochem. Soc.* **1979**, *126*, 475–478.

65 J.-N. Chazalviel, *J. Electrochem. Soc.* **1980**, *127*, 1822–1826.

66 F. Iranzo Marin, M. A. Hamstra, D. Vanmaekelbergh, *J. Electrochem. Soc.* **1996**, *143*, 1137–1142.

67 B. O'Regan, M. Grätzel, *Nature* **1991**, *353*, 737.

68 A. Fujishima, K. Hashimoto, T. Watanabe, *TiO_2 Photocatalysis: Fundamentals and Applications*; BKC, Tokyo, **1999**.

© WILEY-VCH Verlag GmbH, 2001

3
Electrodeposition of Superlattices and Multilayers

Jay A. Switzer

3.1
Background on Superlattices and Multilayers

3.1.1
Introduction

The intense interest in nanometer-scale materials stems from the fact that their optical electrical, magnetic, or mechanical properties can be tuned by changing the physical dimensions of the material. Superlattices and multilayers are especially well suited for device applications, since the confinement dimension (i.e., the individual layer thicknesses) can be kept in the nanometer range for films that are quite thick. A schematic for both multilayers and superlattices is shown in Fig. 3.1. They are composed of alternating layers of material A and B, with a bilayer thickness called the modulation wavelength, Λ. Superlattices are a particular type of crystalline multilayer structure in which there is coherent stacking of

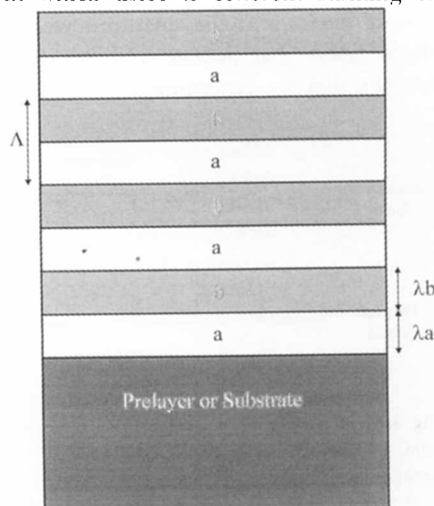

Fig. 3.1 Schematic of a superlattice or multilayer. The modulation wavelength, Λ, is the bilayer thickness. The individual layers do not need to be equal, as long as the structure is periodic. Superlattices are a particular type of crystalline multilayer structure in which there is coherent stacking of atomic planes, and periodic modulation of the structure or composition, or both. The crystallographic orientation of the superlattice is determined by the orientation of the substrate or prelayer. Superlattices or multilayers can be grown electrochemically with layers that are only a few atoms thick.

atomic planes, and periodic modulation of the structure or composition, or both [1–3]. Multilayers and superlattices are both modulated materials, but superlattices have the additional constraint that they are crystallographically coherent. Because of this constraint, superlattices are usually produced with alternating layers of materials with very low lattice mismatch, while multilayers can be produced using even amorphous materials. The substrate in Fig. 3.1 is typically a single crystal for a superlattice, and the crystallographic orientation of the superlattice is determined by the orientation of the substrate. That is, the superlattices are epitaxial. In this section of the chapter, we will discuss some of the desirable properties of superlattices and multilayers that arise from the small layer thickness. In later sections we will discuss the electrodeposition and characterization of these nanometer-scale multilayered materials.

3.1.2
Quantum Confinement in Multiple Quantum Wells

The emphasis in the area of nanometer scale-layered materials has concentrated on semiconductor-based materials. This field of work began when Esaki and Chang reported resonant tunneling across barriers in superlattices grown by molecular beam epitaxy [4], and when Dingle reported optical verification of quantum confinement in semiconductor quantum wells. A quantum well is produced when a smaller band-gap material such as GaAs is sandwiched between layers of a larger band-gap material like GaAlAs [5]. A schematic for a quantum well structure is shown in Fig. 3.2.

Carriers confined in the quantum well behave like quantum-mechanical particles in a box [6–8]. Since this early work, there has been explosive growth in the area of layered nanostructures. This growth has been driven both by the basic scientific interest in quantum physics, and in the development of useful devices [6–10]. Examples of actual devices are the high electron mobility transistor (HEMT), tunnel diode, and the quantum well laser. The nanoscale dimensions produce diode lasers that operate at lower threshold currents, and emit light at wavelengths that are determined by the layer thickness. Hence, a normally intrinsic

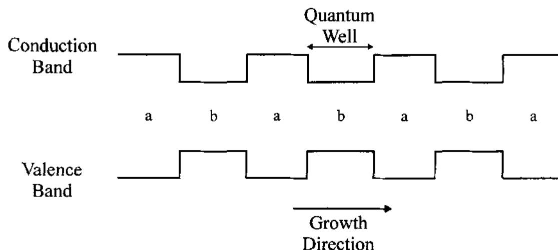

Fig. 3.2 Schematic of a quantum well structure. A quantum well is produced when a smaller band-gap material (layer b in the figure) such as GaAs (E_g=1.4 eV) is sandwiched between a larger band-gap material (layer a in the figure) like GaAlAs ($E_g \approx 1.8$ eV). Carriers confined in the quantum well behave like quantum-mechanical particles in a box.

property of the material can be tuned (band-gap engineering) by simply changing the layer thickness. For example, there is typically a blue shift in the absorption and emission spectra of the quantum-well semiconductor as the layer thickness decreases. Bound states are generated in the valence and conduction bands of the quantum well semiconductors that are shifted relative to the valence and conduction band edges as shown in Eq. (1):

$$\Delta E = \hbar^2 \pi^2 n^2 / (2 m m_0 L^2) \tag{1}$$

where ΔE is the displacement of the bound state either positive of the conduction band or negative of the valence band (J), $\hbar$ (1.055×10^{-34} J s) is equal to $h/2\pi$, n is a quantum number that labels the states ($n=1, 2, 3, \ldots$), m is the effective mass of the electron or hole (dimensionless), m_0 is the free electron mass (9.109×10^{-31} kg), and L is the confinement dimension (m). The confinement dimension is typically the thickness of the semiconductor with the smaller band-gap (i.e., the quantum well layer).

Both the band-gap and the lattice parameters of the semiconductors must be considered when constructing a multiple quantum well superlattice. The band-gaps and lattice parameters of selected materials are presented in Table 1 [11, 12].

Tab. 3.1 Band-gaps and lattice parameters of selected materials.

Material	*Band-gap at 300 K (eV)*	*Direct (D) or Indirect (I)*	*Lattice parameters (Å)*	
			a	*c*
Si	1.12	I	5.43095	
Ge	0.66	I	5.64613	
C (diamond)	5.47	I	3.56683	
α-SiC	3.00	I	3.086	15.117
AlSb	1.58	I	6.1355	
BN	7.5	I	3.6150	
GaN	3.36	D	3.189	5.185
GaSb	0.72	D	6.0959	
GaAs	1.42	D	5.6533	
GaP	2.26	I	5.4512	
AlAs	2.16	I	5.6605	
InP	1.35	D	5.8686	
InAs	0.36	D	6.0584	
InSb	0.17	D	6.4794	
PbS	0.41	D	5.9362	
PbSe	0.26	D	6.124	
PbTe	0.29	D	6.4620	
ZnO	3.35	D	3.2496	5.2065
Cu_2O	1.93	I	4.266	
CdS	1.93	D	5.8320	
CdSe	1.70	D	6.050	
CdTe	1.56	D	6.482	

For each material it is also indicated whether the lowest energy optical transition is indirect or direct. Direct transitions are vertical transitions in which $\Delta k=0$, where k is the wavevector (or reciprocal lattice vector). Direct gap materials (e.g., GaAs) are preferred for optical applications, since optical absorption and emission processes are allowed for these materials, and therefore occur with higher efficiency than with indirect gap materials (e.g., Si). Semiconductors are chosen so that there is a large difference in band-gap between the layers, but a small difference in lattice parameters. Usually, the lattice mismatch between alternating layers is chosen to be less than 1% for semiconductor superlattices. For systems with larger mismatch the strain induces three-dimensional growth instead of the two-dimensional growth that is desired for superlattices. If the thickness of the alternating layers is maintained below a critical thickness, however, it is possible to produce strained-layer superlattices such as the Si/Ge system [13, 14], in which the strain from the lattice mismatch is further used to tune the properties of the resulting layered structure. The lattice mismatch in the Si/Ge system is about 4%. If the layer thicknesses exceed a critical value, island formation occurs. Strain-induced island formation in systems of large lattice mismatch is another way to produce nanometer-scale structures such as self-assembled quantum dots [15–19].

3.1.3
Spin-dependent Transport

If the layered materials in the superlattice or multilayer are magnetic, it is possible to construct devices based on spin-dependent transport [20]. Magnetoelectronic devices based on spin-dependent transport are receiving increasing attention for use in magnetic recording and in nonvolatile memories. Ferromagnetic materials which serve as a source of spin-polarized carriers are at the heart of such devices. Ferromagnetic materials can be layered with nonmagnetic materials such as conductors or tunnel barriers, for example, to produce giant magnetoresistance (GMR) devices or spin valves. These devices respond to a magnetic field by giving a low resistance when the spins of the ferromagnetic layers are parallel and high resistance when the spins are antiparallel [21]. A schematic of a device exhibiting spin-dependent transport is shown in Fig. 3.3. The emphasis of work in this area has been on metallic ferromagnets. However, the spin polarization in these materials is relatively low. For example, the spin polarization in elemental Fe is only 44% [22]. There is interest in using materials such as magnetite, Fe_3O_4, for these applications, because this material was shown to be half-metallic, with 100% spin polarization at the Fermi level [23]. There is also interest in integrating devices based on spin-polarized transport with traditional semiconductor devices [24]. An issue to be addressed in the production of these hybrid ferromagnetic-semiconductor structures is the processing temperature. This is especially true for structures based on metal oxide ferromagnets. The processing temperatures must be kept below about 1000 °C to prevent reaction with the semiconductor. The use of electrochemical processing to prepare these structures at or near room temperature is especially appealing.

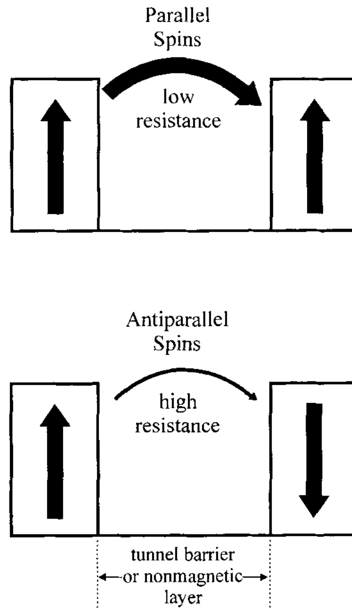

Fig. 3.3 Schematic of a device exhibiting spin-dependent transport. Ferromagnetic materials are layered with nonmagnetic materials such as conductors or tunnel barriers to produce giant magnetoresistance (GMR) devices which respond to a magnetic field by giving a low resistance when the spins of the ferromagnetic layers are parallel and high resistance when the spins are antiparallel.

3.1.4
Mechanical Properties of Layered Nanostructures

A final reason for interest in superlattices and multilayers is their enhanced mechanical properties. Multilayered materials are being considered for protective coatings, since the hardness of the multilayers greatly exceeds the values for comparable bulk alloys [25–29]. For multilayers with two alternating phases, the resistance to plastic deformation and hardness increase as the modulation wavelength decreases [25]. Although much of this work has focused on metallic multilayers, single-crystal TiN/VN strained-layered superlattices with extremely high mechanical hardness have been produced by reactive magnetron sputtering [30]. At a modulation wavelength of 5.2 nm the multilayer had a hardness that was more than 2.5 times larger than that of TiN, VN, or a $Ti_{0.5}V_{0.5}N$ alloy. Tench and White have used electrodeposition to prepare Ni-Cu multilayers with an ultimate tensile strength (1300 MPa) that was almost a factor of three greater than that measured for pure Ni metal, and more than a twice as large as the value for the corresponding alloy of Ni and Cu [31].

3.2
Electrodeposition of Superlattices and Multilayers

3.2.1
Introduction

Most of the work performed on the fabrication of nanometer-scale superlattices and multilayers has focused on the use of chemical and physical vapor phase deposition processes in an ultra-high vacuum. For materials such as GaN, that cannot be formed by simple electrochemical reactions in aqueous solution, vapor phase methods will continue to be preferred. When electrodeposition can be applied to the synthesis of a material, it has several distinct advantages [32, 33]: the low processing temperature (often room temperature) of electrodeposition minimizes interdiffusion, the film thickness can be controlled by monitoring the delivered charge, composition and defect chemistry can be controlled through the applied overpotential, films can be deposited on to complex shapes, non-equilibrium phases can be deposited, the driving force can be precisely controlled, the technique is not capital intensive, the current-time transient following a potential step provides in-situ information on the kinetics and dimensionality of growth, and the method is also amenable to in-situ characterization tools such as the scanning probe microscope and the electrochemical quartz microbalance. Possible disadvantages of electrodeposition are the requirement that the substrate and film have reasonable electrical conductivity, and that there is the possibility of contamination of the film from the solution. The contamination issue can often be circumvented by pre-electrolyzing in the solution to remove any undesired contaminants.

3.2.2
Single and Dual Bath Electrodeposition of Superlattices and Multilayers

The electrodeposition of compositionally-modulated nanostructures such as superlattices and multilayers has been reviewed by other authors [34, 35]. Useful reviews on the general electrochemical synthesis and modification of materials, including metal oxide ceramics, are also available [36, 37]. There are two general techniques for electrochemically depositing superlattices and multilayers: dual bath and single bath deposition. Dual bath deposition is the simpler of the two methods to design, but the more difficult to implement for architectures with a large number of layers, or with very small modulation wavelengths. The electrode is alternated between two deposition solutions containing the chemical precursors of the two different layers. The technique is simple, and it is possible to deposit pure alternating layers of different materials, but it is generally only applied to the deposition of superlattices and multilayers with a limited number of alternating layers. In single bath deposition, the precursors for both layers are in the same deposition solution. Single bath deposition requires much more attention to the chemistry of the system, but it is ideal for producing nanostructures with a nearly unlimited number of layers. Also, the electrode is not exposed to the atmo-

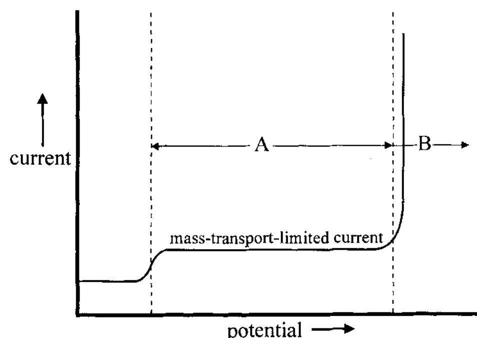

Fig. 3.4 Expected linear sweep voltammogram for a single-bath solution used to electrodeposit superlattices or multilayers with alternating layers A and B. The concentrations of the precursors for layers A and B are small and large, respectively. At low overpotentials the deposition of material A is mass-transport-limited, and at high overpotentials the deposition of material B is kinetically controlled. If the concentration of the precursor for layer A is small enough, the mass-transport-limited current is much smaller than the kinetically-controlled current, and the layer deposited at high overpotential is almost pure B.

sphere between deposition cycles, and potential control can be maintained throughout the process.

The usual trick for single bath deposition is to use a very low concentration of the precursor for the layer that is deposited at low overpotential (layer A) and a high concentration of the precursor for the layer that is deposited at higher overpotentials (layer B). Therefore, at low overpotentials, pure material A is deposited, and at higher overpotentials an alloy which is predominately material B is deposited. The higher the applied current density during the high overpotential pulse, the higher the concentration of B in that layer. The expected linear sweep voltammogram for a typical system for the electrodeposition of superlattices or multilayers with alternating layers A and B is shown in Fig. 3.4. At high overpotentials the deposition of material B is kinetically controlled, and the current increases exponentially as the overpotential is increased. At low overpotentials the deposition of material A is mass-transport-controlled, and the limiting current, i_L, is independent of overpotential. If the concentration of the precursor for layer A is small enough, the mass-transport-limited current is much smaller than the kinetically-controlled current, and the layer deposited at high overpotential is almost pure B. The superlattice or multilayer is deposited by pulsing either the applied potential or current. Fig. 3.5 shows a schematic of superlattice or multilayer growth in a single bath. Another approach that has received little attention is to modulate the mass-transport to the electrode surface using a rotating disk electrode with a modulated rotation rate.

An advantage of electrodeposition over vapor deposition methods, such as CVD or sputtering for the assembly of superlattices, is that the thicknesses of layers A and B in the superlattice (λ_a, λ_b) depend on the deposition times at the respective current densities for each layer. In vapor deposition methods the layer thickness

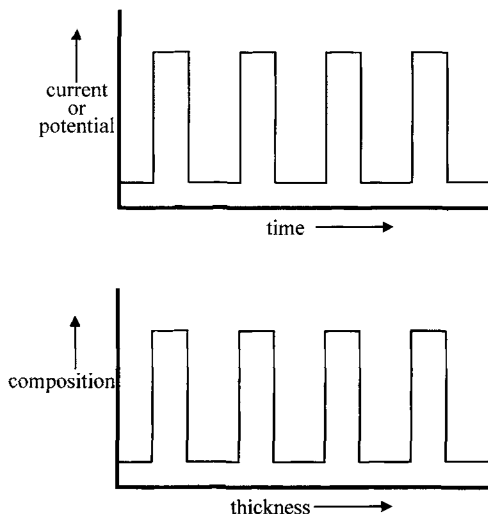

Fig. 3.5 Applied current/time or potential/time waveforms used to deposit a superlattice or multilayer from a single bath (top). The profile of composition against thickness is shown in the bottom of the figure.

is normally found in a trial and error manner. The layer thicknesses for electrodeposited superlattices are calculated from Faraday's law according to Eq. (2), and the modulation wavelength (Λ) is calculated from Eqs (3) and (4). For galvanostatic deposition, the charge of the individual layers (Q) is replaced by the product of current and time (it) which results in Eq. (5):

$$\lambda = MQ/nFA\rho \quad (2)$$

$$\Lambda = \lambda_a + \lambda_b \quad (3)$$

$$\Lambda = 1/nFA(Q_a M_a/\rho_a + Q_b M_b/\rho_b) \quad (4)$$

$$\Lambda = 1/nFA(i_a t_a M_a/\rho_a + i_b t_b M_b/\rho_b) \quad (5)$$

where M is the formula weight, Q is the charge, n is the number of electrons transferred, F is Faraday's number, A is the electrode area, i is the applied current, t is the dwell time, and ρ is the density. These equations assume 100% current efficiency, and a density for the electrodeposited material that is equal to the crystallographic density.

Work in our group has shown that multilayers and superlattices grown from a single bath may not have the simple square-wave composition profile that is normally assumed based on the applied potential-time waveform [38]. Since the deposition of species A during the high overpotential pulse is diffusion limited, the composition is graded throughout the layer with a $(\text{time})^{-1/2}$ dependence. The identity of the diffusion-limited component can be determined by applying the Cottrell equation to the current-time decay. The Cottrell equation is:

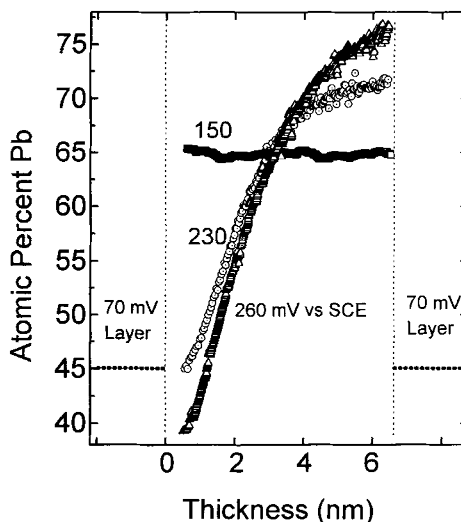

Fig. 3.6 Composition profiles calculated from the current-time transients during the electrodeposition of Pb-Tl-O superlattices grown by pulsing the potential between 70 mV and 150, 230, and 260 mV relative to the SCE. This method can be used both to calculate and tailor composition profiles from graded to very abrupt in real time during the deposition process (from Ref. [38]).

$$i = nFAD^{1/2}C^{*}\pi^{-1/2}t^{-1/2}$$

where i is the current, n is the number of electrons transferred, F is Faraday's number, A is the electrode area, D is the diffusion coefficient, C^{*} is the bulk concentration of the diffusion-limited component, and t is the time.

The composition profiles can then be calculated by analyzing the current-time transients during potentiostatic deposition [38]. Superlattices grown at lower potentials, in which the reactants for both layers are deposited under activation control, have square composition profiles. Hence, it is possible to use the current-time transients to both estimate and tune the composition profiles during deposition. This is a distinct advantage of electrodeposition over vapor phase deposition methods. The calculated profiles are shown in Fig. 3.6 for three Pb-Tl-O superlattices that were grown by pulsing between 70 mV and 150, 230, or 260 mV relative to the SCE in a solution of 0.005 M Tl(I) and 0.1 M Pb(II) in 5 M NaOH. Thallium-rich layers are deposited at low overpotentials, while lead-rich layers are deposited at higher overpotentials. As can be seen in Fig. 3.6, the composition of the 150 mV layer is relatively constant at 64% Pb, while the Pb content of the 260 mV layer varies from 39 to 76% through the layer. The graded composition may be desirable for some applications. For example, grading the composition and lattice parameter may inhibit misfit dislocation formation in strained-layer superlattices. In semiconductor devices for optical or electronic applications, however, it may be desirable to have square composition profiles. The important point is that the electrochemical method is ideal for both measuring and tailoring the interface symmetry and composition profile in real time on a nanometer scale.

3.2.3
Electrodeposition of Metallic Multilayers and Superlattices

Multilayered metallic structures were first produced by Blum in 1921 by depositing alternating Cu and Ni layers using the dual bath method [39]. The layers were fairly thick ($\geq 24\ \mu m$), and the films were explored for their higher tensile strengths than the corresponding pure metals or alloys. Brenner first used single bath deposition in 1963 to produce multilayers of Cu and Bi [40]. Several years later in 1987 Cohen et al. produced multilayers of Ag and Pd by pulsing either the current or potential in a single plating bath [41]. Multilayers with layers as thin as 50 nm were characterized by scanning electron microscopy and Auger depth profiling. In the same time period several groups used single bath deposition to prepare multilayers of Cu and Ni [31, 42, 43]. The Cu/Ni system has received a lot of attention, because it has low lattice mismatch (2.6% mismatch), and the electrochemical irreversibility is nearly ideal. The Ni layer becomes passive and does not re-dissolve during the lower-potential deposition of Cu [44, 45].

In 1988, Lashmore and Dariel demonstrated that multilayers of Cu and Ni deposited using a triple galvanostatic pulse were superlattices [46]. These results were important, because earlier work by other researchers had only shown that samples were layered, but the layered structures were not necessarily crystallographically coherent. Lashmore and Dariel demonstrated the coherent nature of the superlattices by X-ray diffraction. Superlattices were deposited on to single crystal copper substrates and cold-rolled copper sheet from a nickel sulfamate electrolyte containing 90 g L^{-1} Ni, 0.9 g L^{-1} Cu in the form of copper sulfate, and 30 g L^{-1} boric acid at a pH ranging from 3 to 3.5. The triple cycle consisted of a short, high current density pulse (12–20 mA cm^{-2}) to deposit essentially pure Ni; a short zero current pulse designed to improve the sharpness of the Ni-Cu interface; and, finally, a lengthy, low current density pulse (0.3 mA cm^{-2}) for depositing the pure Cu layer. Superlattices with alternating layers as thin as 2–3 nm were characterized by X-ray diffraction. First-order satellites due to the composition modulation were observed in the X-ray patterns.

Moffat has shown that Cu-Ni multilayers deposited on to single-crystal Cu(100) are in fact strained-layer superlattices with a strong in-plane orientation [47]. This was an important result, because most of the work on the electrodeposition of layered nanostructures has been on columnar, textured films with an out-of-plane orientation, but no in-plane orientation. Hence, these results pushed the field closer to the work that is done in ultra-high vacuum. The superlattices were produced from a single plating bath composed of 1.5 M $Ni(SO_3NH_2)_2$, 0.5 M H_3BO_3, and 0.009 M $CuSO_4$. The Cu/Ni superlattices were deposited using potentiostatic control. Copper was deposited under diffusion control at –0.270 V relative to the SCE, and nickel was grown under charge transfer control at –1.0 V relative to the SCE. The copper layer grew at a quasi-steady-state value of 0.15 mA cm^{-2}, which corresponds to 1/3 of a monolayer per second or 0.06 nm s^{-1}, while the nickel layer grew at a rate of about 33 monolayers per second or 5.81 nm s^{-1}. It was estimated that the nickel-rich layer contained about 1 at% copper. Superlattices were

produced with modulation wavelengths ranging from 2.6 to 70 nm, with specimen areas of 2.5 cm^2, and total film thicknesses of 2.4 to 4.7 μm. X-ray patterns of the superlattices showed several orders of superlattice satellites, and an out-of-plane orientation that followed the (100) substrate. The in-plane orientation of the superlattices was verified by electron channeling. The channeling patterns had fourfold symmetry, consistent with the (100) in-plane orientation.

Although most of the research on the electrodeposition of superlattices and multilayers has been done using the single bath method, there have been several studies on dual bath deposition since Blum's initial work in 1921 [39]. Cu/Ni multilayers were produced galvanostatically by Celis, Haseeb and Roos by manually transferring the working electrode between two beakers containing the precursors for the Cu and Ni layers [48]. Layers with individual thicknesses ranging from 5 to 100 nm were produced. Quite high current densities of 5–50 mA cm^{-2} for the Cu layer and 20 mA cm^{-2} for the Ni layer were used.

A dual bath method was developed by the Spaepen group at Harvard University which automatically transfers the working electrode between the two deposition solutions [49]. The films were made by automatically exposing a circular substrate to two electrolytes as it rotated. The system resembles a multi-target sputtering system in concept. Jets of the two electrolytes were directed upwards against the substrate, and made contact with it in two wedge-shaped regions defined by the plating nozzles. Cross contamination of the electrolytes was minimized by cleaning with jets of distilled water or N_2 gas, or by rubber wipers that pressed up against the substrate as it rotated. The modulation wavelength of the resulting multilayer was controlled by varying the deposition current density or the substrate rotation speed. This technique was used to make Ni/NiP_x [50], NiP_x/NiP_y [51], and Cu/Ni [50] multilayers.

Although the initial interest in metallic multilayers and superlattices was based on their superior mechanical properties relative to pure metals or alloys, recent emphasis in this area has been on the synthesis of devices for spin-dependent transport. Ferromagnetic materials can be layered with nonmagnetic materials to produce giant magnetoresistance (GMR) devices or spin valves [20, 21, 24, 52–57]. The immediate interest in these materials is in read heads for hard disk data storage. There has been extensive work on the electrochemical synthesis of metallic multilayers and superlattices for GMR applications [58–72]. The field has been reviewed by Schwarzacher and Lashmore [58]. Resistance changes of up to 55% and sensitivities of up to 0.07%/Oe have been reported in electrodeposited Co(-Cu)/Cu [59] and Co-Ni-Cu/Cu [60] superlattices, respectively, at room temperature. These results compare very well with those obtained on superlattices grown by sputtering, and the electrodeposition process is simpler and less expensive. A disadvantage of the electrodeposited superlattices, however, is that they are typically deposited on to metallic, conductive substrates. The high conductivity of the substrate makes it difficult to utilize the GMR properties of the thin multilayer films. The standard procedure to eliminate this problem is to dissolve the substrate. The superlattices are typically deposited on to Cu substrates, and the Cu is selectively dissolved using a sulfuric acid/chromic acid etch. Shima et al. have made a big

step towards eliminating this problem by electrodepositing Co/Cu multilayers on to Si(001) wafers with a 20 nm Cu seed layer that was deposited by electron beam evaporation [68]. The sample exhibited both structural and magnetic fourfold symmetry. Azimuthal X-ray scans showed that the multilayer was rotated 45° relative to the Si substrate. The misfit between the superlattice and the Si substrate is 34%, but this misfit is reduced to 7% with the 45° rotation. The coherent nature of the $[Co\ (2\ nm)/Cu\ (3\ nm)]_{100}$ superlattice has been shown by X-ray diffraction. First-order satellites were observed around the (002) Bragg peak. Rocking curve analysis indicated that the multilayer had a mosaicity of only 1.8° (FWHM) about the (002) pole. Co-Ni-Co/Cu multilayers have also been directly deposited on to an n-Si wafer without a seed layer, but the multilayer did not grow epitaxially on the Si(001) [69]. There is intense interest in electrodepositing epitaxial superlattices directly on to Si substrates without seed layers.

Another important advance in the electrodeposition of metallic multilayers and superlattices for GMR applications was the electrodeposition of magnetic multilayered nanowires [70–72]. Multilayer nanowires have not been produced by line-of-sight vapor deposition methods. The nanowires were electrodeposited into the nanometer-scale pores of a track-etched polycarbonate membrane, following the template synthesis pioneered by Chuck Martin [73]. The Cu/Co multilayers had a diameter of about 40 nm and a length of about 10 μm, and included 500 periods of approximately 10 nm Co-rich and 10 nm Cu-rich layers. Besides the obvious novelty of producing multilayer nanowires, there is also considerable technological incentive. Most GMR multilayers and superlattices are characterized in the CIP (current in the planes) geometry, because of the very low resistance in the CPP (current perpendicular to the planes) geometry. It is expected that the GMR effect will be much larger in the CPP geometry, but experimental tests of these predictions have been hampered by the difficulties with the CPP geometry for films. The multilayered nanowires, however, can be measured in this geometry. Magnetoresistance ratios higher than 20% at ambient temperatures have been reported [72] in magnetic multilayered nanowires.

An area of research that has not received attention is the electrodeposition of metal oxides for GMR applications. Thousandfold changes in resistivity have been observed in magnetoresistive La-Ca-Mn-O films [56, 57]. Epitaxial films grown on $LaAlO_3$ substrates by laser ablation exhibited magnetoresistance values of 127 000% near 77 K and 1300% near room temperature. So far, no work has been done on the electrodeposition of metal oxide magnetoresistance materials. The electrodeposition of nonmagnetic ceramic superlattices is covered in the next section of this chapter.

3.2.4
Electrodeposition of Semiconductor and Ceramic Multilayers and Superlattices

Although the vast majority of work on the electrodeposition of multilayers and superlattices has been based on metals, research has been done on the deposition of multilayers and superlattices of semiconductors and metal oxide ceramics.

Most of the work in this area has focused on nanomodulated metal oxide ceramics. We will begin this section with a discussion of the deposition of films of semiconductors and oxides, and end with a discussion of work from the author's laboratory on the electrodeposition of ceramic superlattices.

3.2.4.1 Electrodeposition of Compound Semiconductor Films

Semiconductor films can be electrodeposited either by co-deposition [74–85] or by electrochemical atomic layer epitaxy or ECALE [86–94]. A recent review of ECALE by Stickney [86] is an excellent source of references on both co-deposition and electrochemical atomic layer epitaxy of compound semiconductors, since it contains over 400 references to work in this area. Co-deposition and ECALE are similar to the single-bath and dual-bath techniques, respectively, that we described previously for the deposition of metallic superlattices. In co-deposition, a single solution must be designed which will allow the deposition of all of the components of a semiconductor at a fixed potential. Great care must be exercised to adjust solution concentrations, pH, and potential to ensure that all of the components assemble at the same time. ECALE is the electrochemical version of atomic layer epitaxy (ALE), because a material is assembled monolayer at a time using surface-limited reactions. ECALE usually uses a flow cell to alternately expose the surface to solutions from which monolayers of the elements of the semiconductor are deposited. The alternating monolayers are deposited by underpotential deposition (UPD). The UPD layers form at a potential prior to the bulk deposition potential due to the free energy of formation of the surface compound. The UPD layers are expected to grow two dimensionally rather than three dimensionally. Co-deposition and ECALE could be compared, respectively, to analog and digital electronics. Of the two methods, ECALE is the most chemically elegant, but it is also the most difficult method to use to grow films of appreciable (e.g., micrometer) thickness. Recently, the Stickney group has used ECALE to produce bulk films of InAs [94].

Most of the research on co-deposition of compound semiconductors has been on Group II–VI compound semiconductors of metal chalcogenides such as CdS, CdSe, CdTe, and $Hg_{1-x}Cd_xTe$. Both anodic and cathodic processes have been used to deposit metal chalcogenides. In the anodic process the metal is electrochemically oxidized in the presence of chalcogenide ions. The technique is simple, but it does not allow the deposition of the metal chalcogenide on to substrates other than metals. The cathodic process is a true deposition process, since both components of the film are deposited from solution precursors. In this case, higher-valence metal and chalcogenide ions (for example, Cd^{2+} and $HTeO_2^+$) are electrochemically reduced to the elements at the electrode surface, where they combine to form the metal chalcogenide. These reactions are summarized in Eqs (6)–(10):

Cathodic Deposition

$$Cd^{2+} + 2e^- = Cd \quad (6)$$

$$HTeO_2^+ + 4e^- + 3H^+ = Te + 2H_2O \quad (7)$$

$$Cd + Te = CdTe \quad (8)$$

Anodic Deposition

$$Cd = Cd^{2+} + 2e^- \quad (9)$$

$$Cd^{2+} + Te^{2-} = CdTe \quad (10)$$

Rajeshwar has shown that the cathodic reactions shown above are a simplification of the actual deposition process [79]. The reduction of $HTeO_2^+$ according to Eq. (7) is thought to be a crucial step, followed by the subsequent assimilation of Cd into the Te layer in a two-electron process, as shown in Eq. (11), below. The Te electrodeposition is also very complex, and the six electron reduction product, H_2Te, may also participate in the precipitation of CdTe according to Eq. (12). A further complication in the deposition process is that homogeneous chemical reactions between electrogenerated species can lead to impurities in the film. The homogeneous reaction in Eq. (13), for instance, will lead to Te impurities.

$$Cd^{2+} + 2e^- + Te = CdTe \quad (11)$$

$$Cd^{2+} + H_2Te = CdTe + 2H^+ \quad (12)$$

$$2H_2Te + HTeO_2^+ = 3Te + 2H_2O + H^+ \quad (13)$$

Despite of the complexity of the co-deposition process for metal chalcogenide semiconductors, these electrodeposited materials have been shown to compete very successfully with vapor-deposited materials for optoelectronic applications such as photovoltaic solar cells, infrared detectors, and "smart" goggles [74, 79]. Photovoltaic conversion efficiencies in the 8–10% range have been observed [79]. Rajeshwar has also produced multilayers of metal chalcogenides by pulsing the potential during growth [79]. No evidence was given that these multilayers were also superlattices.

Although the majority of work on the co-deposition of metal chalcogenides has been on the electrodeposition of polycrystalline films, Lincot et al. have recently shown that single crystal films of CdTe can be epitaxially grown on to single-crystal InP substrates [85]. This was a significant advance in the field. The deposition was carried out in an aqueous solution at pH 2 with 1 M $CdSO_4$, 5×10^{-4} M TeO_2, a deposition temperature of 85 °C, and a deposition rate of 0.7 μm h^{-1}. Epitaxy was confirmed by five-circle X-ray diffraction and reflection high-energy electron

diffraction (RHEED). The epitaxy was found to exhibit higher perfection when the InP was covered with a thin film (20–30 nm) of epitaxial CdS grown by chemical bath deposition.

3.2.4.2 **Electrodeposition of Metal Oxide Ceramic Films**

Films of metal oxide ceramics can be electrodeposited from aqueous solution using either a redox change method or the electrochemical generation of base [37, 95–97]. In both cases the source of oxygen is water. The methods are similar to co-deposition that was described in the previous section, except that water coordinated to the metal ion undergoes hydrolysis to an hydroxide, which dehydrates to form the metal oxide. It is not necessary (or, perhaps, not even possible) to co-deposit the oxygen and metal in atomic form, as in the co-deposition of metal chalcogenides.

In the redox method, a metal ion or complex is placed in a solution at a pH in which the starting oxidation state is stable, but the oxidized (or reduced) form of the ion undergoes hydrolysis to form the oxide. Since coordinated water molecules are generally more acidic for metal ions in higher oxidation states, the majority of the redox schemes involve oxidation of the metal ion or complex. Cuprous oxide, Cu_2O, is an exception, since it is formed by electrochemically reducing Cu(II) in alkaline solution [97–102]. Some representative overall reactions for the synthesis of metal oxides by the redox change method are shown in Eqs (14)–(19).

Electrodeposition of Ceramics by the Redox Change Method

$$2Tl^{+} + 6OH^{-} = Tl_2O_3 + 3H_2O + 4e^{-} \quad (14)$$

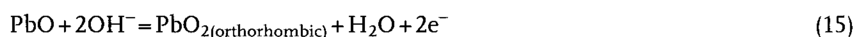

$$PbO + 2OH^{-} = PbO_{2(\text{orthorhombic})} + H_2O + 2e^{-} \quad (15)$$

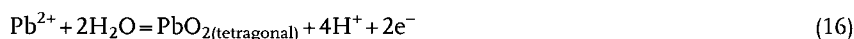

$$Pb^{2+} + 2H_2O = PbO_{2(\text{tetragonal})} + 4H^{+} + 2e^{-} \quad (16)$$

$$3Fe^{2+} + 4H_2O = Fe_3O_4 + 8H^{+} + 2e^{-} \quad (17)$$

$$Ag^{+} + H_2O = AgO + 2H^{+} + e^{-} \quad (18)$$

$$2Cu(OH)_2 + 2e^{-} = Cu_2O + 2OH^{-} + H_2O \quad (19)$$

In Eqs (15) and (19) the precursors are shown as solids, because this is the standard representation in tables of standard reduction potentials. In practice, however, the reactions are run under conditions in which the precursors are soluble. For example, at high pH PbO dissolves to form the plumbite ion, and the Cu(II) in Eq. (19) is usually complexed with lactate, acetate, or tartrate ions. Notice that the orthorhombic polymorph of PbO_2 is formed in alkaline solution, while the tetragonal form is produced in acidic solution. All of the reactions shown are simply

overall reactions, and do not imply any details of the reaction mechanism, except that the source of oxygen in the oxides is the water or hydroxide from solution. The formation of Tl_2O_3 in Eq. (14) is a good example of the redox method. The Tl^+ ion is similar chemically to K^+, and is therefore very stable in strong base. The ion exists as a hydrated complex with negligible hydrolysis. The Tl^{3+} ion is readily hydrolyzed in basic solution to form Tl_2O_3. Aqueous Tl^{3+} is formed when Tl^+ is electrochemically oxidized in strongly acidic solution, while black films of Tl_2O_3 are formed if the oxidation is run at a pH greater than ca. 10.

We have used the redox method to produce films of Tl_2O_3 [95, 103–107], PbO_2 [108], AgO [109], Cu_2O [98, 99], the oxy salt $Ag(Ag_3O_4)_2NO_3$ [108], δ-Bi_2O_3 [110, 111], Fe_3O_4 [112], superlattices in the Pb-Tl-O system [1, 38, 113–116], defect-chemistry superlattices based on Tl_2O_3 [117], and layered nanocomposites based on Cu and Cu_2O [118–122]. Matsumoto et al. have used the redox method to photoelectrochemically deposit epitaxial films of PbO_2 on to single-crystal TiO_2 and $SrTiO_3$ substrates [123].

In the electrogenerated base method, cathodic processes are used to increase the pH at the electrode surface by generating base (or depleting protons). In this case the metal ions are already in a high oxidation state. The metal ions or complexes are then hydrolyzed by the electrogenerated base. The process is essentially a pH titration, but it occurs only at the electrode surface. Sample base generation reactions are shown in Eqs (20)–(23). A reaction is chosen after considering the reduction potential, electrochemical kinetics, and whether gas evolution (e.g., hydrogen gas evolution) is desired. For example, hydrogen evolution reactions might be desired to produce powders or even porous films, while reactions like the reduction of dissolved oxygen or hydrogen peroxide might be preferred for the synthesis of films. Also, the reduction of nitrate ion is known to occur on Ni electrodes, and has been used to produce $Ni(OH)_2$, but the reaction may be kinetically sluggish on other electrode surfaces. We have used the electrogenerated base method to prepare nanoscale CeO_2 [95, 124] and ZrO_2 [125]. Pauporte and Lincot have produced epitaxial ZnO films on GaN [126], Mitchell and Wilcox used the method to produce preshaped ceramic bodies [127], and Redepenning has deposited brushite and hydroxyapatite on to prosthetic alloys [128].

Reduction Reactions Used to Generate Base

$$2H_2O + 2e^- = H_2 + 2OH^- \tag{20}$$

$$O_2 + 2H_2O + 4e^- = 4OH^- \tag{21}$$

$$H_2O_2 + 2H^+ + 2e^- = 2H_2O \tag{22}$$

$$NO_3^- + H_2O + 2e^- = NO_2^- + 2OH^- \tag{23}$$

3.2.4.3 Electrodeposition of Ceramic Superlattices and Multilayers

In 1990, we used single-bath deposition to prepare compositional superlattices in the Pb-Tl-O system [1, 113–116]. The Pb-Tl-O system is ideal for superlattice deposition, because the composition can be controlled by varying the applied current or potential, the Pb-rich layer does not strip when the Tl-rich layer is deposited at less positive potentials, the oxides are highly conducting, and the oxides in the alternating layers have very similar crystal structures and lattice parameters. The superlattices were electrodeposited from a solution of 0.005 M $TlNO_3$ and 0.1 M $Pb(NO_3)_2$ in 5 M NaOH by pulsing either the applied potential or current. These solution conditions were chosen because the standard reduction potentials for the two end members of the system, Tl_2O_3 and PbO_2, are 0.02 V and 0.28 V, respectively, relative to the standard hydrogen electrode (NHE). Hence, in a 1 M NaOH solution containing both Tl^+ and Pb^{2+} under standard conditions, Tl_2O_3 should be produced at potentials greater than 0.02 V relative to the NHE (or –0.22 V relative to the SCE), and PbO_2 should be produced at potentials greater than 0.28 V relative to the NHE (or 0.04 V relative to the SCE). The Tl^+ concentration is kept low, so that deposition of Tl_2O_3 should become mass-transport-limited at the higher potentials when PbO_2 deposition occurs. That is, referring to Fig. 3.4, deposition of Tl_2O_3 films should occur in region A of the figure, and mixed Pb-Tl-O materials should be deposited in region B, with the Pb content of the film increasing as the potential is increased. The deposition process is not as simple as this discussion would suggest, since the films contain Pb at potentials negative of the PbO_2 standard reduction potential. Apparently, the formation of Pb-Tl-O compounds shifts the standard potentials negative of those observed for the deposition of pure materials. As can be seen in Table 3.2, the composition of the films can be controlled through either the applied potential or current. Thallium-rich films are deposited at low potentials or currents, and lead-rich films are deposited at high potentials or currents.

The crystal structures of the alternating layers of the Pb-Tl-O superlattice were very similar [108]. Superlattices were typically deposited by pulsing the applied current density between 0.05 and 5.0 mA cm^{-2}. The lattice mismatch between films grown under these conditions was only about 0.3%. The materials have a fluorite structure with space group Fm3m. The end members of the series have different crystal structures. Thallic oxide has a bcc bixbyite structure with a = 1.054 nm, and lead dioxide deposited from alkaline solution is orthorhombic

Tab. 3.2 Composition and lattice parameters of Pb-Tl-O films as a function of applied potential or current density [116].

Potential (mV vs SCE)	*Current density (mA cm^{-2})*	*Pb content (atom%)*	*Tl content (atom%)*	*Lattice parameter (nm)*
70	0.05	54	46	0.5328
150	1.0	68	32	0.5338
230	5.0	79	21	0.5342

with $a=0.4938$ nm, $b=0.5939$ nm, and $c=0.5486$ nm. There is also a high pressure polymorph of PbO_2 which has an fcc fluorite structure with a = 0.5349 nm. The Pb-Tl-O system undergoes a transition from a bcc Bravais lattice, like that of Tl_2O_3, to an fcc Bravais lattice at a lead content of greater than 40%. It appears that the substitution of Pb(IV) for Tl(III) in Tl_2O_3 stabilizes the fcc fluorite structure by the addition of oxygen. The bixbyite structure of Tl_2O_3 is often described in terms of a distorted fcc fluorite structure with one-quarter of the oxygen atoms missing. In the fluorite structure the coordination number of the oxygens is four, and the coordination number of the metals is eight. In the bixbyite structure the oxygen still has a coordination number of four, but the metal coordination number becomes six. Also, there are two types of metal sites. The missing oxygens for one-quarter of the metals are at the ends of the body diagonal, and for the remainder of the metals the missing oxygens are at the ends of the face diagonal. As Pb(IV) is substituted into thallium(III) oxide, the $MO_{1.5}$ formula of bcc bixbyite approaches the MO_2 formula of fcc fluorite. We have included this discussion of the structures to emphasize the point that it is necessary to pay close attention to crystal structure and lattice mismatch when assembling materials as superlattices. Low mismatch is required so that the alternating layers grow two dimensionally. As we will discuss in the last section of this chapter, it is possible to deposit epitaxial systems with high mismatch, provided that a low-mismatch coincidence lattice is accessible [110].

The Pb-Tl-O superlattices grew epitaxially on oriented prelayers with either a [100] or [210] texture [113, 116]. The superlattices had a fiber texture. That is, they were oriented out-of-plane but not in-plane. The out-of-plane texture was maintained throughout the growth of the superlattice. X-ray diffraction (XRD) showed the films to be superlattices by the presence of satellites around the main Bragg reflections. There was good agreement between XRD and scanning tunneling microscopy (STM) for the measurement of modulation wavelengths, Λ, from 3 to 150 nm [1, 114, 116]. Partial relaxation of coherency was observed for modulation wavelengths exceeding about 20 nm.

A new type of nanoscale material called a defect chemistry superlattice was electrodeposited in our laboratory [117]. These nanometer-scale layered structures based on thallium(III) oxide were electrodeposited in a beaker at room temperature by pulsing the applied potential during deposition. The conducting metal oxide samples had layers as thin as 6.7 nm. The superlattices are similar in concept to doping superlattices that are based on compound semiconductors. The defect chemistry was a function of applied overpotential: high overpotentials favored oxygen vacancies, whereas low overpotentials favored cation interstitials. The transition from one defect chemistry to another in this non-equilibrium process occurred in the same overpotential range (100–120 mV) in which the back electron transfer reaction became significant (as evidenced by deviation from linearity in a Tafel plot). The epitaxial structures have the high carrier density and low dimensionality of high temperature superconductors. They also have very interesting near-IR optical properties because of their high carrier density. The materials exhibit a plasma resonance in the near-IR at about 1500 nm, and the optical band-

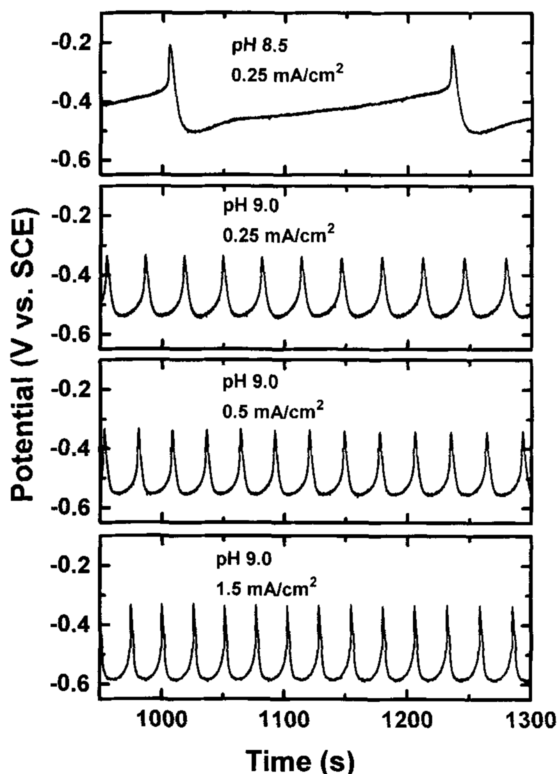

Fig. 3.7 Spontaneous potential oscillations observed during the growth of copper/cuprous oxide-layered nanostructures. The solution was 0.6 M $CuSO_4$ and 3 M lactate ion at 30°C. The oscillation period was a strong function of pH, but was relatively independent of the applied current density.

gap is blue shifted by up to 1.1 eV by the Moss-Burstein shift owing to the high free carrier concentration [106]. The superlattices were characterized by XRD and scanning tunneling microscopy.

Although all of the superlattices or multilayers that have been discussed so far in this section of the chapter have been produced by pulsing either the applied current or potential, our group has discovered a system which assembles itself into a layered structure by undergoing *spontaneous* potential oscillations. The layered nanostructures were based on copper metal and cuprous oxide (Cu_2O), and were deposited from an aqueous solution of 0.6 M Cu(II) and 3 M lactate ion at a pH between 8 and 10. The electrode potential oscillated when a fixed current density was applied. Fig. 3.7 shows potential oscillations that were observed at pH 8.5 and 9 for applied current densities of 0.25 to 1.5 mA cm^{-2}. The oscillation period, layer thickness, and phase composition was a strong function of the solution pH. At an applied current density of 0.25 mA cm^{-2}, the oscillation period was 230 s at pH 8.5, but decreased to 31 s at pH 9.0. At pH 9.0, the oscillation period remained in the 25–31 s range, even though the current density was varied from 0.25 to 1.5 mA cm^{-2}.

Evidence for layering in the Cu_2O system was provided by Auger depth profiling (see Fig. 3.8), cross-sectional STM and SEM, and in-situ electrochemical

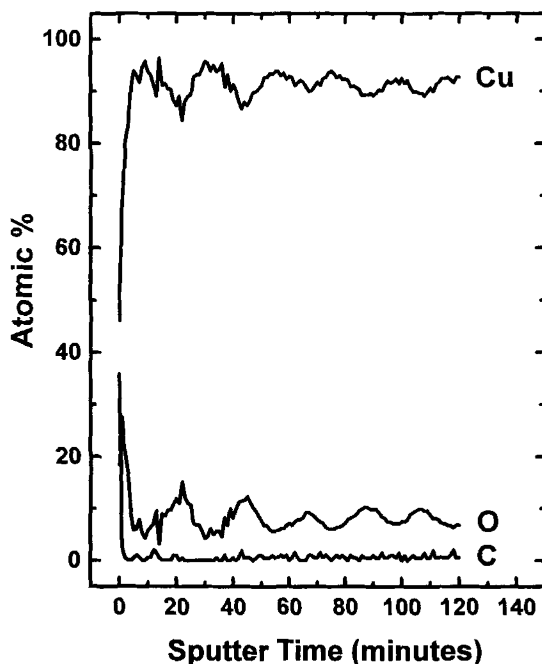

Fig. 3.8 Auger depth profile for an electrodeposited copper/cuprous oxide-layered nanostructure showing modulation of the Cu and O contents. The film was grown from a solution of 0.6 M $CuSO_4$ and 3 M lactate ion at a pH of 8.5 and an applied current density of 0.25 mA cm^{-2} (from Ref. [119]). Evidence for layering was also obtained by cross-sectional STM and SEM.

quartz crystal microbalance (EQCM) studies. The EQCM showed that the materials consisted of very thin layers of Cu_2O that were formed during the positive-going spike in the potential-time oscillations, and a nanocomposite of Cu and Cu_2O were formed in the more negative plateau region of the oscillations. Fig. 3.9 shows the oscillation in potential (A) and equivalent weight (B), and the proposed nanostructure (C) for a film that was electrodeposited at pH 9 and a current density of 2.0 mA cm^{-2} as measured in real time with the EQCM. The Cu_2O layer was estimated to be 1.5 nm thick, and the Cu/Cu_2O layer was estimated to be 15 nm thick and to consist of approximately 82 mol% Cu. The Cu_2O layers could be made thinner by decreasing the applied current at fixed pH, or by increasing the pH at fixed current density.

Because of the layered structure of the Cu_2O/Cu nanostructures, and the p-type semiconducting behavior of Cu_2O, the electrical properties were highly anisotropic. For a film grown at a current density of 1.5 mA cm^{-2} the resistivity was 1.4×10^{-4} Ω cm when measured parallel with the layers, but 4.3×10^{5} Ω cm when measured perpendicular to the layers. Percolation behavior was observed when the transport was measured parallel with the layers, and negative resistance, suggestive of resonant tunneling, was observed when transport was measured perpendicular to the layers. The percolation behavior is shown in Fig. 3.10. The resistivity varied by over ten orders of magnitude from approximately 10^{-4} Ω cm at high Cu contents to greater than 10^{6} Ω cm at low Cu contents. There was an abrupt decrease in resistivity at Cu contents exceeding 9.8 vol.%. The curve in Fig. 3.10 is a fit to the data using percolation theory.

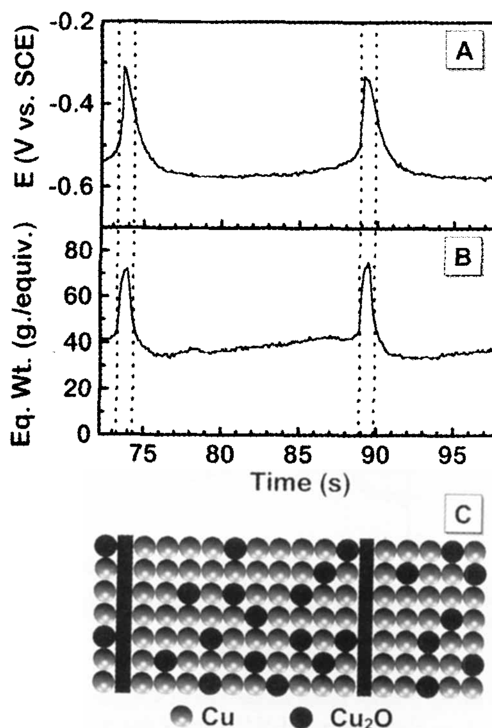

Fig. 3.9 Real-time monitoring of the deposition of a copper/cuprous oxide-layered nanostructure using the electrochemical quartz crystal microbalance (EQCM). (A) Potential oscillations that are observed during the deposition of a film at a current density of 2.0 mA cm^{-2} at a pH of 9.0 directly on to a 0.2 cm^2 platinum-coated EQCM oscillator. (B) Equivalent weight of the deposit calculated from the change in frequency of the quartz oscillator. (C) Proposed nanostructure for the film. The Cu_2O layer is estimated to be 2.5 nm thick, and the Cu/Cu_2O layer is estimated to be 15 nm thick and to consist of approximately 82 mol% Cu [122].

Evidence for quantum confinement in the cuprous oxide layer was seen in perpendicular transport measurements on the Cu/Cu_2O-layered nanostructures [119, 122]. Fig. 3.11 shows the current-voltage curve for perpendicular transport through a Cu/Cu_2O-layered nanostructure with 554 layers. The sample was deposited on to a copper substrate, and a point contact with an area of 1×10^{-5} A cm^{-2} was made to the top of the surface. The Cu_2O layer thickness was estimated to be 2.4 nm. A sharp negative differential resistance (NDR) feature was observed on both the positive and negative scans at +0.17 V and –0.18 V, respectively. The slope of the curve becomes negative at biases exceeding the NDR maximum, and the differential conductance and resistance are negative in this region. The current density flowing through the point contact was in the 40000–50000 A cm^{-2} range.

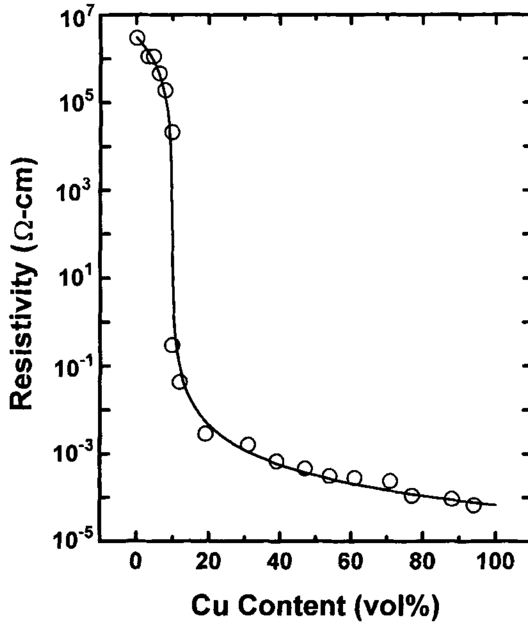

Fig. 3.10 Dependence of parallel resistivity on Cu content for a series of Cu/Cu_2O-layered nanostructures. The Cu content was controlled by varying the applied current. The solid line is a fit to the date using percolation theory, with a percolation threshold of 9.8 vol% Cu [119].

The observation of NDR does not prove that the system is quantum confined. It is necessary to show that the position of the NDR maximum shifts with layer thickness as predicted by Eq. (1). Fig. 3.12 shows that the NDR signature shifts to higher bias as the Cu_2O layer is decreased from 2.5 to 0.8 nm. The maximum in the NDR curve shifts with a $1/L^2$ dependence (Fig. 3.13), consistent with quantum confinement [122]. The interest in resonant tunneling devices stems from the fact that they can be made both small and fast, since tunneling is not limited by carrier mobilities in the semiconductor. Resonant tunneling diodes based on group III–V semiconductors such as GaAs/GaAlAs and InAs/AlSb have been produced which operate at frequencies up to 712 GHz [129, 130].

3.3 Characterization of Superlattices and Multilayers

3.3.1 X-ray Diffraction

The best evidence for a superlattice is the observation of satellites around the Bragg reflection in X-ray diffraction (XRD) [131–143]. Since the structures are crystallographically coherent, and follow the orientation of the substrate or prelayer, the Bragg peaks that are observed are determined by the substrate or prelayer. The satellites are caused by the superperiodicity in the system, because the

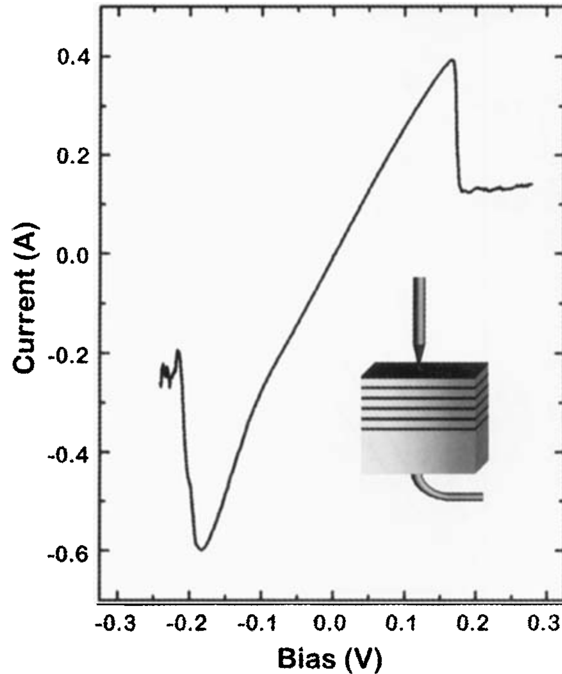

Fig. 3.11 Perpendicular transport at room temperature through a Cu/Cu_2O film with 554 layers. The Cu_2O layer is estimated to be 2.4 nm thick. The slope of the *i–V* curve becomes negative at biases exceeding the negative differential resistance (NDR) maximum, and the differential conductance and resistance are negative in this region. Inset cartoon shows the configuration used to make the perpendicular transport measurement. The point contact area is approximately 1×10^{-5} cm^2, so the current density is in the 40000 to 50000 A cm^{-2} range [122].

X-ray pattern is the Fourier transform of the product of the lattice and modulation functions convoluted with the basis. The periodic variation can be represented as a waveform. For waveforms that vary sinusoidally, only first order satellites are expected, since only one Fourier term is needed to describe a sine wave. As the waveform becomes more square, higher order Fourier terms are necessary, and higher order satellites are observed. For a perfect square wave (rarely observed), only odd orders of satellites are expected. When the lattice spacing and composition both vary periodically, the intensities of like orders of satellites are not equal. The scattering factor is said to be convoluted with the lattice spacing variation.

It is very straightforward to determine the bilayer thickness or modulation wavelength, Λ, from the satellite spacing in an X-ray diffraction pattern. For superlattices with large Λ the satellites are close to the Bragg peak, and as Λ becomes smaller the satellites move further away from the Bragg peak. In a superlattice the modulation wavelength creates an artificial spacing that is not present in the bulk materials. These planes scatter X-rays similar to a bulk crystal, where the

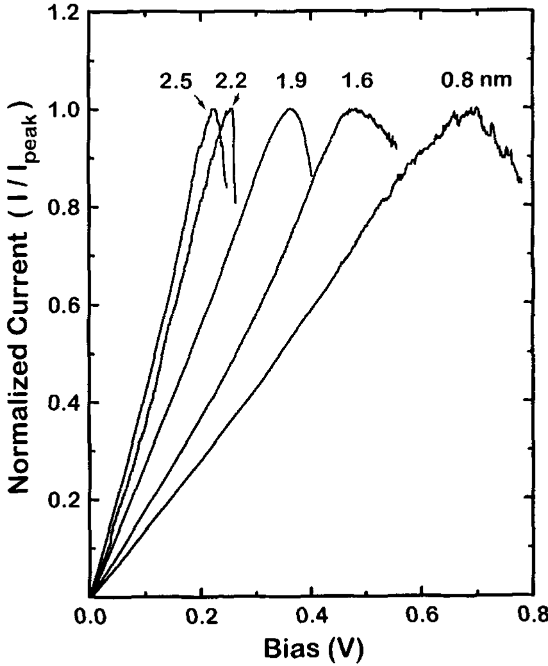

Fig. 3.12 Negative differential resistance (NDR) curves for layered Cu/Cu_2O nanostructures as a function of the Cu_2O layer thickness. The NDR maximum shifts to higher applied bias for samples with thinner Cu_2O layers [122].

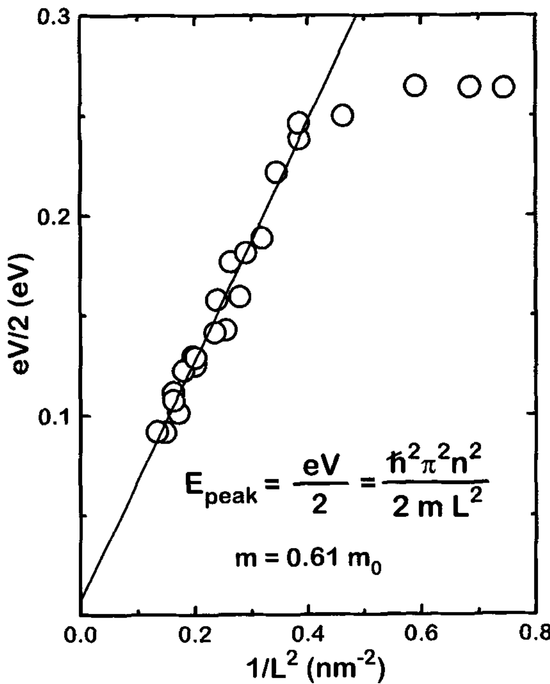

Fig. 3.13 Evidence for quantum confinement in Cu/Cu_2O-layered nanostructures. Demonstration that the NDR signature shifts with the Cu_2O layer thickness (L) with a $1/L^2$ dependence, as would be expected according to Eq. (1). The effective mass calculated from the slope of the line is 0.61 m_0, indicating that holes in the valence band are the quantum-confined carriers [122].

scattering from the ith plane can be represented by Eq. (24), a modification of Bragg's law.

$$L_i\lambda = 2\Lambda \sin \theta_i \tag{24}$$

For two planes i and j separated by a distance Λ, the path distance is:

$$(L_i - L_j)\lambda = 2\Lambda(\sin \theta_i - \sin \theta_j) \tag{25}$$

or, in terms of the modulation wavelength:

$$\Lambda = (L_i - L_j)\lambda / \ 2(\sin \theta_i - \sin \theta_j) \tag{26}$$

where L_i and L_j are the satellite orders, θ_i and θ_j are the angles corresponding to the positions of the satellites, and λ is the wavelength of the X-ray radiation. Eq. (26) is usually used to calculate Λ from the positions of the satellites. The X-ray data will also be cast in reciprocal space using the scattering vector **Q**, defined in Eq. (27):

$$\mathbf{Q} = 2\pi/d = 4\pi \sin \theta/\lambda \tag{27}$$

For a superlattice, the fundamental, or Bragg peak, will be at $\mathbf{Q} = 2\pi/\langle d\rangle$, where $\langle d\rangle$ is the average d spacing for the A and B layers, and the harmonics or satellites will be located at $\Delta\mathbf{Q} = 2\pi n/\Lambda$, where n is the order of the harmonic or satellite. **Q** has units of $Å^{-1}$, and the harmonics are usually designated as $\mathbf{Q}^{+n}$ and $\mathbf{Q}^{-n}$.

Even if a structure is a multilayer instead of a superlattice, it can also be characterized by X-rays. An example would be a layered material in which at least one of the alternating materials is amorphous. In this case, low-angle X-ray reflectivity is used [131]. A series of interference fringes is observed, with the spacing determined by the modulation wavelength. Again, the smaller the modulation wavelength, the larger the spacing between the peaks in the reflectivity spectrum.

Examples of X-ray diffraction patterns of Pb-Tl-O superlattices are shown in Figures 14 and 15. The superlattices in Fig. 3.14 were grown by single-bath deposition by pulsing the applied current density between 0.05 mA cm^{-2} for 82 s and 5 mA cm^{-2} for 1.2 s in a solution of 0.005 M Tl(I) and 0.1 Pb(II) in 5 M NaOH. The superlattice in Fig. 3.14 A was deposited on to a [100]-oriented prelayer of Tl_2O_3, and the superlattice in Fig. 3.14 B was deposited on to a [210] oriented prelayer of a Pb-Tl-O material that was deposited from the same solution as the superlattice at a fixed current density of 5 mA cm^{-2}. Notice that both of the superlattices have a strong preferred orientation, since the out-of-plane orientation of the prelayers was maintained throughout the growth of the superlattice. Only first order satellites were observed for the two samples. The satellites correspond to modulation wavelengths of 13.3 and 11.8 nm for the [100]- and [210]-oriented superlattices, respectively. For comparison, an X-ray diffraction pattern of a Pb-Tl-O superlattice that was produced using potential control is shown in Fig. 3.15.

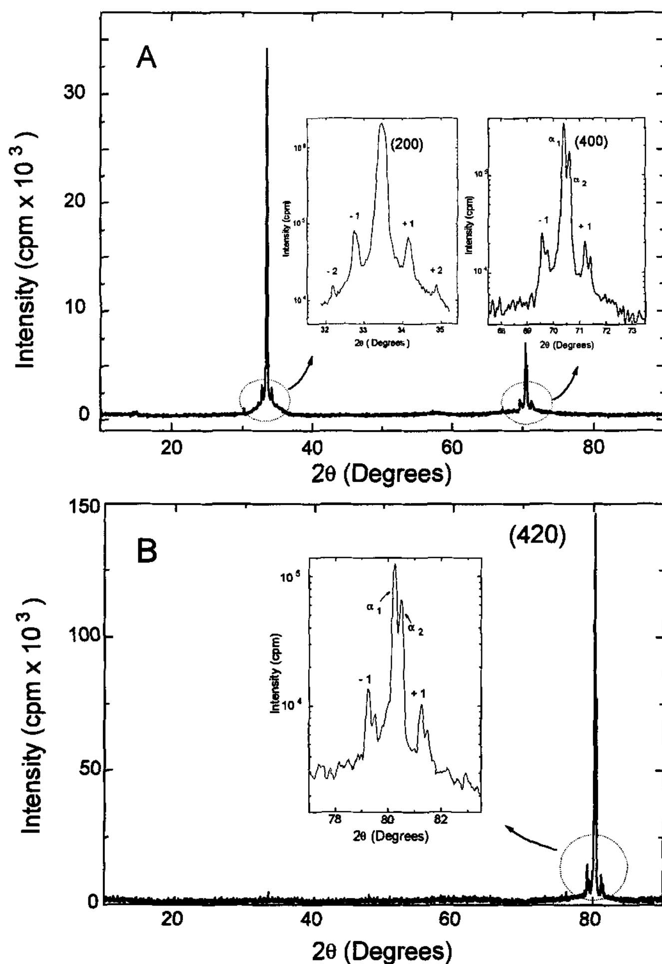

Fig. 3.14 X-ray diffraction patterns of two electrodeposited Pb-Tl-O compositional superlattices. The top superlattice has a strong [100] orientation and a modulation wavelength of 13.3 nm, and the bottom superlattice has a strong [210] orientation and a modulation wavelength of 11.8 nm. The superlattices are epitaxial structures that follow the crystallographic orientation of the prelayer. The spacing of the satellites around the Bragg peaks is used to determine the modulation wavelength according to Eq. (26) [116].

The superlattice was produced by applying a short potential pulse at 242 mV and a long potential pulse at 52 mV relative to the SCE. The modulation wavelength was 13.4 nm. In this case, the XRD pattern showed superlattice satellites out to fourth order, consistent with a more square composition profile. These results were consistent with scanning tunneling microscopy studies of superlattices grown under potential and current control [1].

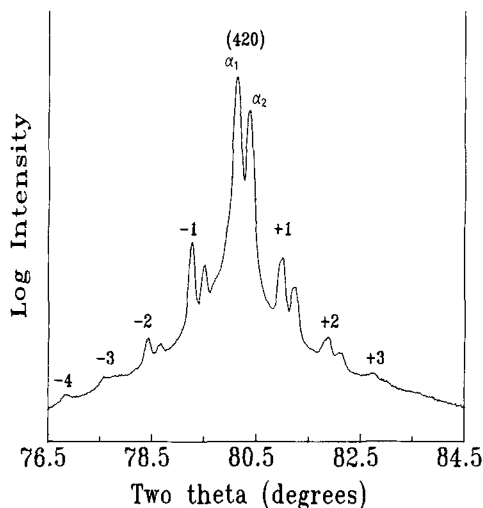

Fig. 3.15 X-ray diffraction pattern of a Pb-Tl-O superlattice produced using potential control. Superlattice satellites out to fourth order are seen around the (420) Bragg reflection. The modulation wavelength calculated from the satellite spacing is 13.4 nm. The X-ray radiation is CuK_α. The splitting of the peaks is caused by the presence of α_1 and α_2 radiation [1].

3.3.2 Scanning Tunneling Microscopy

Another way to characterize superlattices is by scanning tunneling microscopy (STM). The technique does not require the detailed sample preparation that is necessary for transmission electron microscopy (TEM). Cleaved cross-sections of both compositional and defect chemistry superlattices can be readily imaged in the STM [1, 114, 115]. A cross-sectional STM image of a Pb-Tl-O superlattice grown with potential control is shown in Fig. 3.16. Cross-sections of the Cu/Cu_2O-layered nanostructures have also been imaged, following an etch in dilute nitric acid to enhance the contrast between the layers [119]. The modulation wavelength can be determined using Fourier analysis of the STM images [115]. The STM is especially well suited to the measurement of modulation wavelengths that are too large to measure by X-ray diffraction but too small to measure by scanning electron microscopy. The STM can also give qualitative information about the composition profile in electrodeposited superlattices. For example, Pb-Tl-O superlattices grown under current control have nearly sinusoidal profiles, while superlattices grown under potential control have more abrupt profiles [1].

3.3.3 Transmission Electron Microscopy

Transmission electron microscopy (TEM) can provide detailed information about the interfaces between the layers in a superlattice. It is an especially valuable tool to use when trying to understand the mechanical properties of superlattice, or the relief of strain in strained-layer superlattices. The main problem with the technique is the difficulty in preparing samples. Although the superlattice nanowires

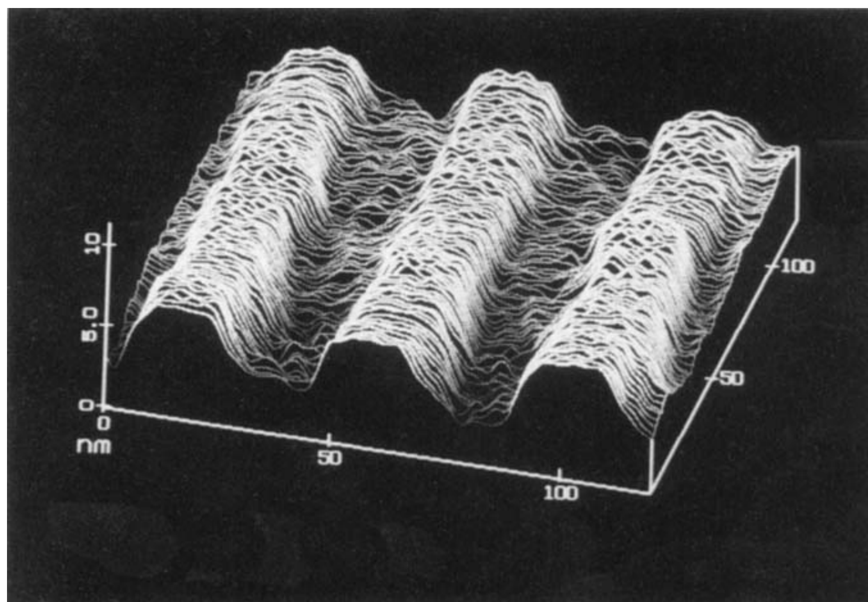

Fig. 3.16 Cross-sectional STM image of a Pb-Tl-O superlattice that was grown using potential control. Both layers of the superlattice were designed to be 25 nm thick (adapted from Ref. [1]).

[70–72] discussed earlier can be imaged directly, most samples need to be thinned to electron transparency.

Lashmore and Thomson have studied cracks and dislocations in fcc metallic multilayers based on Cu and Ni [144]. Samples for TEM were fabricated by overcoating the sample with about 4 mm of Cu by electrodeposition followed by sectioning the sample in a direction normal to the growth direction with a slow-speed diamond saw to produce a foil containing the superlattice. The foil was then thinned to electron transparency in a two-stage process. The first step consisted of metallographically polishing the foil to a thickness of about 50 μm, and the second step consisted of thinning in a cold stage ion milling instrument. The superlattices had very flat layers and uniform modulation wavelengths. Lashmore and Thomson found that the superlattices had coherent interfaces if the modulation wavelength was in the 10 nm range, but that at wavelengths above about 60 nm the interfaces became incoherent. They analyzed dislocations produced in a cracked sample and found that the dislocations had strong interactions with alternating interfaces in the superlattice. Their results suggested that these materials should be ductile and have high toughness.

3.4 Recent Developments and Future Work

Most research on the electrodeposition of superlattices and multilayers has used polycrystalline materials or oriented prelayers as substrates. The superlattices and multilayers are typically columnar, textured films with an out-of-plane orientation, but no in-plane orientation. An important area of future work will be the electrodeposition of single-crystal superlattices on single-crystal substrates. As discussed in Section 2.3, Moffat has shown [47] that Cu-Ni strained-layer superlattices can be electrodeposited directly on to single-crystal Cu(100). The superlattices had both an in-plane and out-of-plane orientation. More work of this type needs to be done, especially as quantum-confined electronic devices are produced electrochemically as competitors for semiconductor devices produced by UHV vapor deposition methods. The work by Stickney et al. on electrochemical atomic layer epitaxy of semiconductors is moving nicely in this direction [86].

There have been some recent developments in the electrodeposition of epitaxial films that may prove important for future work on the electrodeposition of single-crystal superlattices. Epitaxial films of CdSe on InP [85], ZnO on GaN [126], and δ-Bi_2O_3 [110, 111], Cu_2O [99], Tl_2O_3 [107], PbS [145], and Fe_3O_4 [112] on single-crystal Au have been deposited. PbO_2 has been photoelectrochemically deposited on to single-crystal TiO_2 [123]. All of these films have both in-plane and out-of-plane orientations that are determined by the single-crystal substrate, and they should serve as an excellent foundation for the electrodeposition of layered nanostructures such as multilayers or superlattices. For example, the Cu/Cu_2O-layered nanostructures that were discussed in Section 2.4.3 were deposited on to polycrystalline substrates. It would be most interesting to extend this work to the deposition on to single crystal Au, Cu, or Si substrates.

The in-plane and out-of-plane orientation of an epitaxial film relative to the single-crystal substrate can be determined by X-ray diffraction. A powder diffractometer fitted with a texture goniometer is adequate for most work. The Bragg (θ), tilt (χ), azimuthal (ϕ), and rocking (ω) angles used in the measurements are shown in Fig. 3.17. The out-of-plane orientation is determined in the Bragg-Brentano configuration by standard θ-θ scans. The out-of-plane mosaicity can be determined by rocking the sample about the ω axis. The in-plane orientation can be probed by pole figures and azimuthal scans. It is necessary in this case to bring other planes besides those which are parallel with the surface into the Bragg condition. In a pole figure the sample is tilted about the χ axis in small steps and the sample is rotated about the azimuthal axis, ϕ, at each tilt angle. Azimuthal scans (ϕ) are two-dimensional sections at a fixed tilt angle (χ) of a three-dimensional pole figure. They show the in-plane orientation of the film in relation to the substrate.

A surprising result that has been obtained in this work so far is the demonstration that it is possible to grow epitaxial systems with very large mismatch. Although small mismatch is still desired for the two-dimensional growth of superlattices with nanometer-scale layers, we have shown that several systems will grow

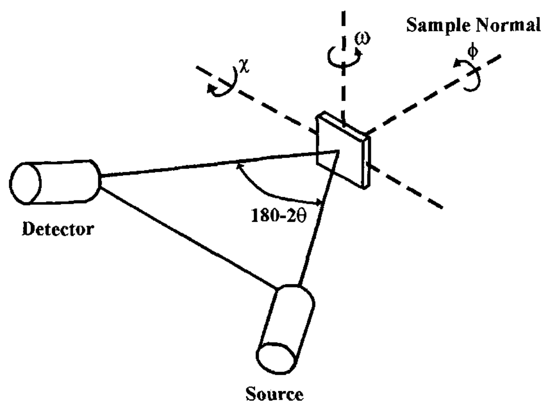

Fig. 3.17 Schematic of the experimental set-up to determine the in-plane and out-of-plane orientation of epitaxial films. The out-of-plane orientation is determined in the Bragg-Brentano configuration by standard θ-θ scans. The mosaicity can be determined by rocking the sample about the ω axis. The in-plane orientation can be probed using pole figures and azimuthal scans. In a pole figure the sample is tilted about the χ axis in small steps and the sample is rotated 360° about the azimuthal axis, ϕ, at each tilt angle. Azimuthal scans (ϕ scans) are two-dimensional sections at a fixed tilt angle of a three-dimensional pole figure. They show the orientation of the film in relation to the substrate.

epitaxially in spite of very large lattice mismatch. The large mismatch in the δ-Bi_2O_3/Au (35.3%) and PbS/Au (45.5%), Tl_2O_3/Au (29.1%) systems was accommodated by the formation of coincidence lattices, in which the film was rotated relative to the Au substrate. The mismatch in the Cu_2O/Au system was only 4.4%, and no rotation was observed. Evidence for a coincidence lattice for δ-Bi_2O_3 deposited on to Au(110) is shown in Fig. 3.18. The Bi_2O_3 peaks in the azimuthal scan are rotated 90° relative to the Au(110) substrate, consistent with the (1×1)δ-Bi_2O_3(110) [110]//(2×1)Au(110) [100] coincidence lattice shown in Fig. 3.18C. The mismatch in this coincidence lattice is only –4.4%, compared to the +35.3% mismatch for a commensurate system. A step towards the electrodeposition of single-crystal superlattices is the recent demonstration that it is possible to grow a Cu_2O/PbS-epitaxial heterojunction on single-crystal Au(100) [146].

Another important area of future work will be the electrodeposition of layered materials based on magnetic oxides for GMR applications. Although all of the work so far has focused on depositing layered structures based on metallic materials [58–72], the highest known GMR effects have been observed with oxides such as La-Ca-Mn-O [56, 57]. Thousandfold changes in resistivity have been observed in these materials. Since it is possible to electrodeposit ferromagnetic materials such as Fe_3O_4 epitaxially on to single-crystal gold [112], it should be possible to extend this work to the electrodeposition of layered nanostructures, in which the ferromagnetic material is layered with a nonmagnetic metal oxide. The low temperatures of electrodeposition may allow the deposition of these nanostructures on to semiconductors, permitting the integration of spin-dependent trans-

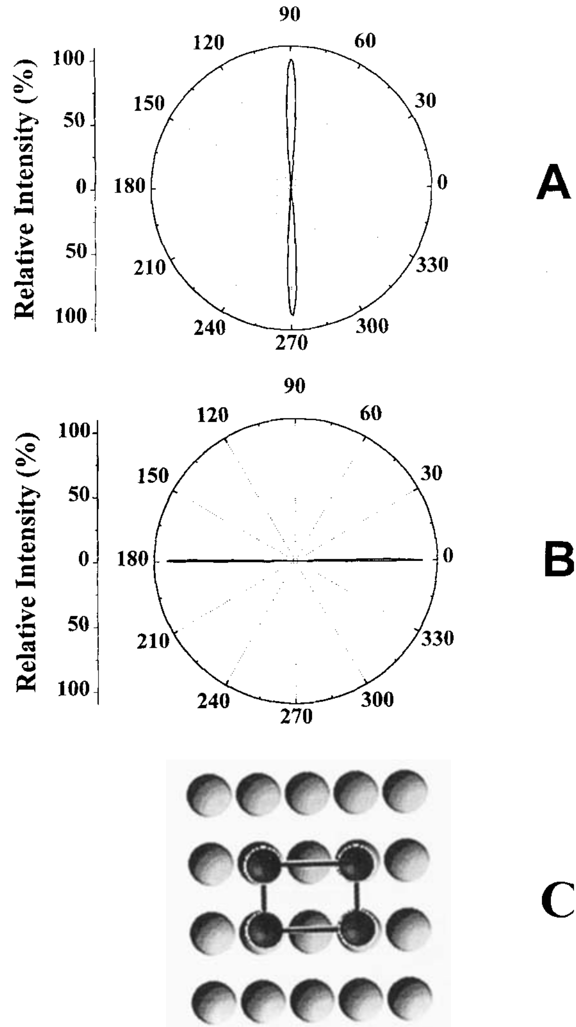

Fig. 3.18 Evidence for in-plane orientation for δ-Bi_2O_3 electrodeposited onto single-crystal Au(110). Parts A and B show azimuthal X-ray scans for the δ-Bi_2O_3 film and Au(110) substrate, respectively. For both azimuthal scans the sample was tilted at $\chi=45°$ to bring the (200) reflections into the Bragg condition. Notice that the peaks for the δ-Bi_2O_3 are rotated 90° relative to those of Au. Part C shows an interface model for epitaxial growth of δ-Bi_2O_3 on Au(110). The δ-Bi_2O_3 overlayer (bismuth atoms represented as dark balls) is rotated 90° relative to the Au substrate. The rotation reduces the lattice mismatch from 35.4% to –4.2%.

port devices with traditional electronic devices. The direct electrodeposition of epitaxial architectures on single-crystal silicon will be a major breakthrough in this area.

Acknowledgments

The author would like to acknowledge the hard and enthusiastic work of a large number of graduate and postdoctoral students whose names are in the references. He would also like to acknowledge financial support of his work on the deposition of nanomaterials by National Science Foundation grants DMR-9020026, DMR-9202872, DMR-9704288, CHE-9816484, DMR-0071365, and DMR-0076338, Office of Naval Research grants N00014-91-1-1499, N00014-94-1-0917, and N00014-96-0984, the Foundation for Chemical Research, and the University of Missouri Research Board.

References

1 J. A. Switzer, R. P. Raffaelle, R. J. Phillips, C.-J. Hung, T. D. Golden, *Science 258*, 1918 (1992).
2 I. K. Shuller, *Phys. Rev. Lett. 44*, 1597 (1980).
3 I. K. Shuller, H. Homma, *MRS Bulletin*, March 17, 1987, p. 18.
4 L. Esaki, L. L. Chang, *Phys. Rev. Lett. 33*, 495 (1974).
5 R. Dingle, W. Wiegmann, C. H. Henry, *Phys. Rev. Lett. 33*, 827 (1974).
6 J. H. Davies, *The Physics of Low-Dimensional Semiconductors*; Cambridge University Press: Cambridge, 1998.
7 M. J. Kelley, *Low-Dimensional Semiconductors*; Oxford University Press: Oxford, 1995.
8 C. Weisbuch, B. Vinter, *Quantum Semiconductor Structures*; Academic Press: San Diego, 1991.
9 L. Esaki, *IEEE J. Quantum Electron., QE-33*, 1611 (1986).
10 R. P. Andres et al., *J. Mater. Res. 4*, 704 (1989).
11 S. M. Sze, *Physics of Semiconductor Devices*; John Wiley & Sons: New York, 2nd edn, pp. 848–849, 1981.
12 J. I. Pankove, Optical Processes in Semiconductors; Dover: New York, pp. 412–413, 1971.
13 G. C. Osbourn, *IEEE J. Quantum Electron. QE-22*, 1677 (1986).
14 R. People, *IEEE J. Quantum Electron. QE-22*, 1696 (1986).
15 D. J. Eaglesham, M. Cerullo, *Phys. Rev. Lett. 64*, 1943 (1990).
16 G. Medeiros-Ribeiro, A. M. Bratkovski, T. I. Kamins, D. A. A. Ohlberg, R. S. Williams, *Science 279*, 353 (1998).
17 F. Liu, F. Wu, M. G. Lagally, *Chem. Rev. 97*, 1045 (1997).
18 F. M. Ross, R. M. Tromp, M. C. Reuter, *Science 286*, 1931 (1999).
19 R. S. Williams, G. Medeiros-Ribeiro, T. I. Kamins, D. A. A. Ohlberg, *Acc. Chem. Res. 32*, 425 (1999).
20 G. A. Prinz, *Science 282*, 1660 (1998).
21 M. M. Baibich, J. M. Broto, A. Fert, F. Nguyen van Dau, F. Petroff, P. Etienne, G. Creuzet, A. Friedrich, J. Chazeles, *Phys. Rev. Lett. 61*, 2472 (1988).
22 P. M. Tedrow, R. Meservey, *Phys. Rev. B 7*, 318 (1973).
23 S. F. Alvarado, W. Eib, F. Meier, D. T. Pierce, K. Sattler, H. C. Siegmann, J. P. Remeika, *Phys. Rev. Lett. 34*, 319 (1975).
24 G. A. Prinz, *Science 250*, 1092 (1990).
25 T. P. Weihs, T. W. Barbee, Jr., M. A. Wall, *Acta Mater. 45*, 2307 (1997).
26 G. S. Was, T. Foedke, *Thin Solid Films 286*, 1 (1996).
27 K. K. Shih, D. B. Dove, *Appl. Phys. Lett. 61*, 654 (1992).
28 P. B. Mirkarimi, L. Hultman, S. A. Barnett, *Appl. Phys. Lett. 57*, 2654 (1990).
29 R. C. Cammarata, T. E. Schlesinger, C. Kim, S. B. Qadri, A. S. Edelstein, *Appl. Phys. Lett. 56*, 1862 (1990).
30 U. Helmersson, S. Todorova, S. A. Barnett, J.-E. Sundgren, L. C. Market, J. E. Greene, *J. Appl. Phys. 62*, 481 (1987).
31 D. Tench, J. White, *Metallurg. Trans. A 15A*, 2039 (1984).
32 J. A. Switzer, "Electrodeposition of Superlattices and Nanocomposites," in:

Nanoparticles and Nanostructured Films, J. H. Fendler, editor; Wiley–VCH: Weinheim, **1998**, Chapter 3.

33 J. A. Switzer, "Electrodeposition of Nanoscale Architectures," in: *Handbook of Nanophase Materials*, A. N. Goldstein, editor; Marcel Dekker: New York, **1997**, Chapter 4.

34 C. A. Ross, *Annu. Rev. Mater. Sci. 24*, 159 (**1994**).

35 A. Haseeb, J. P. Celis, J. R. Roos, *Trans. Met. Finish. Assoc. India 1*, 15 (**1992**).

36 P. C. Searson, T. P. Moffat, *Crit. Rev. in Surface Chem. 3*, 171 (**1994**).

37 G. H. A. Therese, P. V. Kamath, *Chem. Mater. 12*, 1195 (2000).

38 J. A. Switzer, R. J. Phillips, T. D. Golden, *Appl. Phys. Lett. 66*, 819 (**1995**).

39 W. Blum, *Trans. Am. Electrochem. Soc. 40*, 307 (**1921**).

40 A. Brenner, *Electrodeposition of Alloys*; Academic Press: New York, Vol. 2, p. 589, **1963**.

41 U. Cohen, F. B. Koch, R. Sard, *J. Electrochem. Soc. 138*, 1987 (**1983**).

42 C. Ogden, *Plating Surface Finishing 5*, 133 (**1986**).

43 J. Yahalom, O. Zadok, *J. Mater. Sci. 22*, 499 (**1987**); U.S. Patent 4,652,348 (**1987**).

44 S. Menezes, D. P. Anderson, *J. Electrochem. Soc. 137*, 440 (**1990**).

45 A. R. Despic, V. D. Jovic, S. Spaic, *J. Electrochem. Soc. 136*, 1651 (**1989**).

46 D. S. Lashmore, M. P. Dariel, *J. Electrochem. Soc. 135*, 1218 (**1988**).

47 T. P. Moffat, *J. Electrochem. Soc. 142*, 3767 (**1995**).

48 J. P. Celis, A. Haseeb, J. R. Roos, *Trans. Inst. Metal Finish 70*, 123 (**1992**).

49 L. M. Goldman, C. A. Ross, W. Ohashi, D. Wu, F. Spaepen, *Appl. Phys. Lett. 55*, 2182 (**1989**).

50 C. A. Ross, L. M. Goldman, F. Spaepen, *J. Electrochem. Soc. 140*, 91 (**1993**).

51 L. M. Goldman, B. Blanpain, F. Spaepen, *J. Appl. Phys. 60*, 1374 (**1986**).

52 G. Binasch, P. Grünberg, F. Saurenbach, W. Zinn, *Phys. Rev. B 39*, 4828 (**1989**).

53 S. S. P. Parkin, R. Bhadra, K. P. Roche, *Phys. Rev. Lett. 66*, 2152 (**1991**).

54 P. M. Levy, *Solid State Phys. 47*, 367 (**1994**).

55 P. M. Levy, *Science 256*, 972 (**1992**).

56 S. Jin, T. H. Tiefel, M. McCormack, R. A. Fastnacht, R. Ramesh, L. H. Chen, *Science 264* (**1994**).

57 C. N. R. Rao, A. K. Cheetham, *Science 272*, 369 (**1996**).

58 W. Schwarzacher, D. S. Lashmore, *IEEE Transactions on Magnetics 32*, 3133 (**1996**).

59 K. D. Bird, M. Schlesinger, *J. Electrochem. Soc. 142*, L65 (**1995**).

60 S. Z. Hua, D. S. Lashmore, L. Salamanca-Riba, W. Schwarzacher, L. J. Swartzenruben, R. D. McMichael, L. H. Bennett, R. Hart, *J. Appl. Phys. 76*, 6519 (**1994**).

61 M. Alper, K. Attenborough, R. Hart, S. J. Lane, D. S. Lashmore, C. Younes, W. Schwarzacher, *Appl. Phys. Lett. 63*, 2144 (**1993**).

62 M. Alper, K. Attenborough, V. Baryshev, R. Hart, D. S. Lashmore, W. Schwarzacher, *J. Appl. Phys. 75*, 6543 (**1994**).

63 R. D. McMichael, U. Atzmony, C. Beauchamp, L. H. Bennett, L. J. Swartzenruber, D. S. Lashmore, L. T. Romankiw, *J. Magn. Magn. Mater. 113*, 149 (**1992**).

64 S. Z. Hua, D. S. Lashmore, L. Salamanca-Riba, W. Schwarzacher, L. J. Swartzenruber, R. D. McMichael, L. H. Bennet, *J. Appl. Phys. 76*, 6519 (**1994**).

65 K. Attenborough, R. Hart, S. J. Lane, M. Alper, W. Schwaracher, *J. Magn. Magn. Mater. 148*, 335 (**1995**).

66 G. Nabiyouni, W. Schwarzacher, *J. Magn. Magn. Mater. 156*, 355 (**1996**).

67 I. Bakonyi, E. Toth-Kakar, T. Becsei, J. Toth, T. Tarnoczi, A. Cziraki, I. Gerocs, G. Nabiyouni, W. Schwarzacher, *J. Magn. Magn. Mater. 156*, 347 (**1996**).

68 M. Shima, L. Salamanca-Riba, T. P. Moffatt, R. D. McMichael, L. J. Swartzenruber, *J. Appl. Phys. 84*, 1504 (**1998**).

69 A. P. O'Keefe, O. I. Kasyutich, W. Schwarzacher, L. S. de Oliveira, A. A. Pasa, *Appl. Phys. Lett. 73*, 1002 (**1998**).

70 L. Piraux, J. M. George, J. F. Despres, C. Leroy, E. Ferain, R. Legras, K. Ounadjela, A. Fert, *Appl. Phys. Lett. 65*, 2484 (1994).

71 A. BLONDEL, J. P. MEIER, B. DOUDIN, J.-PH. ANSERMET, *Appl. Phys. Lett.* *65*, 3019 (1994).

72 A. BLONDEL, J. MEIER, B. DOUDIN, J.-PH. ANSERMET, K. ATTENBOROUGH, P. EVANS, R. HART, G. NABIYOUNI, W. SCHWARZACHER, *J. Magn. Magn. Mater.* *148*, 317 (1995).

73 C. R. MARTIN, *Science* 266, 1961 (1994).

74 G. HODES, *Physical Electrochemistry*, I. Rubinstein, editor; Marcel Dekker: New York, p. 515, 1995.

75 F. A. KROGER, *J. Electrochem. Soc.* *125*, 2028 (1978).

76 R. D. ENGELKEN, *J. Electrochem. Soc.* *135*, 834 (1988).

77 G. F. FULOP, R. M. TAYLOR, *Ann. Rev. Mater. Sci.* *15*, 197 (1985).

78 R. C. DEMATTEI, R. S. FEIGELSON, *Electrochemistry of Semiconductors and Electronics, Processes and Devices*, J. McHardy and F. Ludwid, editors; Noyes Publications: Park Ridge, NJ, p. 1, 1992.

79 K. RAJESHWAR, *Adv. Mater.* *4*, 23 (1992).

80 R. K. PANDEY, S. N. SAHU, S. CHANDRA, *Handbook of Semiconductor Electrodeposition*, A. M. Hermann, editor; Marcel Dekker: New York, 1996.

81 M. W. VERBRUGGE, C. W. TOBIAS, *J. Electrochem. Soc.* *132*, 1298 (1985).

82 G. HODES, J. MANASSEN, D. CAHEN, *Nature* *261*, 403 (1976).

83 M. P. R. PANICKER, M. KNASTER, F. A. KROGER, *J. Electrochem. Soc.* *125*, 566 (1978).

84 B. MILLER, S. MENEZES, A. HELLER, *J. Electroanal. Chem.* *94*, 85 (1978).

85 D. LINCOT, A. KAMPMANN, B. MOKILI, J. VEDEL, R. CORTES, M. FROMENT, *Appl. Phys. Lett.* *67*, 2355 (1995).

86 J. L. STICKNEY, "Electrochemical Atomic Layer Epitaxy," in: *Electroanalytical Chemistry, A Series of Advances*; Marcel Dekker: New York, p. 75 (1999).

87 B. E. BOONE, C. SHANNON, *J. Phys. Chem.* *100*, 9480 (1996).

88 U. DEMIR, C. SHANNON, *Langmuir* *10*, 2794 (1994).

89 L. P. COLLETTI, D. TEKLAY, J. L. STICKNEY, *J. Electroanal. Chem.* *369*, 145 (1994).

90 U. DEMIR, C. SHANNON, *Langmuir* *12*, 594 (1996).

91 T. E. LISTER, L. P. COLLETTI, J. L. STICKNEY, *Isr. J. Chem.* *37*, 287 (1997).

92 B. M. HUANG, L. P. COLLETTI, B. W. GREGORY, J. L. ANDERSON, J. L. STICKNEY, *J. Electrochem. Soc.* *142*, 3007 (1995).

93 I. VILLEGAS, J. L. STICKNEY, *J. Electrochem. Soc.* *139*, 686 (1992).

94 T. L. WADE, L. C. WARD, C. B. MADDOX, U. HAPPEK, J. L. STICKNEY, *Electrochem. Soc. Solid State Lett.* *2*, 616 (1999).

95 J. A. SWITZER, *Am. Ceram. Soc. Bull.* *66*, 1521 (1987).

96 R. T. COYLE, J. A. SWITZER, "Electrochemical Synthesis of Ceramic Films and Powders, U.S. Patent No. 4,882,014, issued November, 1989.

97 D. TENCH, L. F. WARREN, *J. Electrochem. Soc.* *130*, 869 (1983).

98 T. D. GOLDEN, M. G. SHUMSKY, Y. ZHOU, R. A. VANDERWERF, R. A. VAN LEEUWEN, J. A. SWITZER, *Chem. Mater.* *8*, 2499 (1996).

99 E. W. BOHANNAN, M. G. SHUMSKY, J. A. SWITZER, *Chem. Mater.* *11*, 2289 (1999).

100 A. K. MUKHOPADHYAY, A. K. CHAKRABORTY, A. P. CHATTERJEE, S. K. LAHIRI, *Thin Solid Films* *209*, 92 (1992).

101 A. P. CHATTERJEE, A. K. MUKHOPADHYAY, A. K. CHAKRABORTY, R. N. SASMI, S. K. LAKIRI, *Mater. Lett.* *11*, 358 (1991).

102 A. E. RAKHSHANI, J. VARGHESE, *Thin Solid Films* *157*, 87 (1991).

103 J. A. SWITZER, *J. Electrochem. Soc.* *133*, 722 (1986).

104 R. J. PHILLIPS, M. J. SHANE, J. A. SWITZER, *J. Mater. Res.* *4*, 923 (1989).

105 R. J. PHILLIPS, T. D. GOLDEN, M. G. SHUMSKY, J. A. SWITZER, *J. Electrochem. Soc.* *141*, 2391 (1994).

106 R. A. VAN LEEUWEN, C.-J. HUNG, D. R. KAMMLER, J. A. SWITZER, *J. Phys. Chem.* 99, 15247 (1995).

107 A. A. VERTEGEL, M. G. SHUMSKY, J. A. SWITZER, *Electrochimica Acta* *45*, 3233 (2000).

108 B. E. BREYFOGLE, R. J. PHILLIPS, J. A. SWITZER, *Chem. Mater.* 4, 1356 (1992).

109 B. E. BREYFOGLE, C.-J. HUNG, M. G. SHUMSKY, J. A. SWITZER, *J. Electrochem. Soc.* *143*, 2741 (1996).

110 J. A. SWITZER, M. G. SHUMSKY, E. W. BOHANNAN, *Science* *284*, 293 (1999).

111 E. W. Bohannan, C. C. Jaynes, M. G. Shumsky, J. K. Barton, J. A. Switzer, *Solid State Ionics 131*, 97 (**2000**).
112 M. P. Nikiforov, A. A. Vertegel, M. G. Shumsky, J. A. Switzer, *Adv. Mater. 12*, 1351 (**2000**).
113 J. A. Switzer, M. J. Shane, R. J.. Phillips, *Science 247*, 444 (**1990**).
114 J. A. Switzer, T. D. Golden, *Adv. Mater.* 5, 474 (**1993**).
115 T. D. Golden, R. P. Raffaelle, J. A. Switzer, *Appl. Phys. Lett. 63*, 1501 (**1993**).
116 R. J. Phillips, T. D. Golden, M. G. Shumsky, E. W. Bohannan, J. A. Switzer, *Chem. Mater.* 9, 1670 (**1997**).
117 J. A. Switzer, C.-J. Hung, B. E. Breyfogle, M. G. Shumsky, R. Van Leeuwen, T. D. Golden, *Science 264*, 1573 (**1994**).
118 J. A. Switzer, C.-J. Hung, E. W. Bohannan, M. G. Shumsky, T. D. Golden, D. C. Van Aken, *Adv. Mater. 9*, 334 (**1997**).
119 J. A. Switzer, C.-J. Hung, L.-Y. Huang, E. R. Switzer, D. R. Kammler, T. D. Golden, E. W. Bohannan, *J. Am. Chem. Soc. 120*, 3530 (**1998**).
120 J. A. Switzer, C.-J. Hung, L.-Y. Huang, F. S. Miller, Y. Zhou, E. R. Raub, M. G. Shumsky, E. W. Bohannan, *J. Mater. Res. 13*, 909 (**1998**).
121 E. W. Bohannan, L.-Y. Huang, F. S. Miller, M. G. Shumsky, J. A. Switzer, *Langmuir, 15*, 813 (**1999**).
122 J. A. Switzer, B. M. Maune, E. R. Raub, E. W. Bohannan, *J. Phys. Chem. B. 103*, 395 (**1999**).
123 Y. Matsumoto, M. Fujisue, T. Sasaki, J. Hombo, M. Nagata, Appl. Phys. Lett. 369, 251 (**1994**).
124 Y. Zhou, R. J. Phillips, J. A. Switzer, *J. Am. Ceram. Soc. 78*, 981 (**1995**).
125 J. A. Switzer, R. J. Phillips, *Mat. Res. Soc. Symp. Proc. 121*, 111 (**1988**).
126 T. Pauporte, D. Lincot, *Appl. Phys. Lett. 75*, 3817 (**1999**).
127 P. J. Mitchell, G. D. Wilcox, *Nature 357*, 395 (1992).
128 J. Redepenning, J. P. McIsaac, *Chem. Mater. 2*, 625 (**1990**).
129 E. R. Brown, J. R. Söderström, C. D. Parker, L. J. Mahoney, K. M. Molvar, T. C. McGill, *Appl. Phys. Lett. 58*, 2291 (**1991**).
130 V. J. Goldman, D. C. Tsui, J. E. Cunningham, *Phys. Rev. Lett. 58*, 1256 (**1987**).
131 G. Burns, A. M. Glazer, *Space Groups for Solid State Scientists*; Academic Press: San Diego, CA, 2nd edition, **1990**, pp. 313.
132 D. B. McWhan, in *Synthetic Modulated Structures*, L. L. Chang, B. C. Giessen, editors; Academic Press: Orlando, FL, **1985**, Chapter 2.
133 E. E. Fullerton, I. K. Schuller, Y. Bruynseraede, *J. Mater. Educ. 14*, 251 (**1992**).
134 A. Segmüller, A. E. Blakeslee, *J. Appl. Cryst. 6*, 19 (**1973**).
135 A. Segmüller, P. Krisha, L. Esaki, *J. Appl. Cryst. 10*, 1 (**1977**).
136 Ch. Morawe, A. Abromeit, N. Metoki, P. Sonntag, H. Zebel, *J. Mater. Res. 9*, 570 (**1994**).
137 I. K. Schuller, C. M. Falco, *Surf. Sci. 113*, 443 (**1982**).
138 W. M. Paulson, J. E. Hilliard, *J. Appl. Phys. 48*, 2117 (**1977**).
139 M. Takano, T. Terashima, Y. Bando, H. Ikeda, *Appl. Phys. Lett. 51*, 205 (1987).
140 D. A. Neumann, H. Zabel, H. Morkoc, *Appl. Phys. Lett. 43*, 59 (**1983**).
141 R. M. Fleming, D. B. McWhan, A. C. Gossard, W. Wiegmann, R. A. Logan, *J. Appl. Phys. 51*, 357 (**1980**).
142 F. J. Lamelas, H. D. He, R. Clarke, *Phys. Rev. B. 43*, 12296 (**1991**).
143 D. Buttard, D. Bellet, T. Baumbach, *Thin Solid Films 276*, 69 (**1996**).
144 D. S. Lashmore, R. Thomson, *J. Mater. Res. 7*, 2379 (**1992**).
145 A. A. Vertegel, M. G. Shumsky, J. A. Switzer, *Angew. Chem. Int. Ed. 38*, 316 (**1999**).
146 A. A. Vertegel, M. G. Shumsky, J. A. Switzer, *Chem. Mater. 12*, 596 (**2000**).

Electrochemistry of Nanomaterials
by *Gary Hodes (Ed.)*
© WILEY-VCH Verlag GmbH, 2001

4
Porous-etched Semiconductors: Formation and Characterization

J.J. Kelly and *D. Vanmaekelbergh*

In this chapter we review the porous etching of a range of crystalline semiconductors including Si, TiO_2 and IV–IV, III–V and II–VI materials. Mechanisms are considered for a number of electrochemical methods such as (photo)anodic dissolution, electroless etching and photoetching. The photoelectrochemical characterization of these and other porous electrodes is described. Some applications of porous-etched semiconductors are considered.

4.1
Introduction

When Uhlir performed his pioneering experiments on the anodic etching of silicon in HF solution [1], it was not clear to him that he had formed a porous semiconductor. He described his results as follows: "Instead of being shiny, the surfaces have a matte black, brown or red deposit...tentatively supposed to be a silicon suboxide". Memming and Schwandt [2] suggested that the layer was amorphous silicon resulting from the disproportionation of divalent silicon formed electrochemically. Subsequent experiments [3] showed that, in fact, a porous matrix is formed and the crystallinity of the solid is maintained. Since a sub-surface porous structure is seldom evident to the naked eye, porosity arising from etching experiments probably often went undetected.

The unusual properties of porous silicon were quickly recognized. Because of its very open structure, porous silicon can be thermally oxidized at a high rate under mild conditions [4]. If the porosity is properly chosen, a completely compact oxide layer is obtained. This has resulted in applications in silicon-on-insulator (SOI) technology. Again, because of its porosity, the etch rate of porous silicon in solution is much higher than that of the non-porous single crystal. As a result, the porous semiconductor can be used as sacrificial layer in micromechanical device technology [5]. The very large internal surface area makes porous silicon interesting for sensor applications [6]. Perhaps the most spectacular property, strong luminescence in the visible spectral range, went unnoticed until Canham "rediscovered" it in 1990 [7, 8]. The unusual optical properties have regenerated interest

in the material. An obvious aim of such work is to produce devices in which both electronic and optical functions can be integrated [9].

A second development that stimulated interest in porous semiconductor systems was the report by Grätzel and O'Regan [10] of a photoelectrochemical solar cell based on a dye-sensitized nanoparticulate TiO_2 electrode. This system offers the possibility of relatively high light-to-current conversion efficiencies at low cost. These developments also demonstrated the advantages of porous matrices for other applications such as rapid intercalation in battery and electrochromic systems [11, 12].

The field of porous semiconductors has become a research area in its own right presenting many challenging issues. These include the preparation of both random and ordered (crystalline) porous structures, the characterization of the unusual chemical and physical properties of such systems and the application of these systems in device technology and fabrication. In this chapter we shall consider mainly the first two of these topics.

There are various ways of making porous semiconductors. These include deposition from colloidal suspensions (by dipcoating, spincoating or "smearing"), sol-gel techniques, deposition from the vapor phase, chemical bath deposition and electrodeposition. Strictly speaking, only the latter falls within the scope of the present volume. Because a number of contributors will be describing electrodeposition elsewhere in this volume, in this chapter we shall consider a different approach, i.e. the porous etching of crystalline semiconductors. In the second part of the chapter devoted to characterization and properties we again concentrate on porous-etched systems but, where relevant, we consider results obtained with other types of porous layers.

Before discussing the special features of porous etching we first consider briefly general mechanisms for semiconductor dissolution (Section 2). The first of the two main topics, porous etching of single-crystal semiconductors, is dealt with in Sections 3 and 4. The second main theme of the chapter, the photoelectrochemical characterization of porous semiconductors, forms the basis for Section 5. In the final section current and potential applications of these systems are considered.

4.2
Semiconductor-etching Mechanisms

Etching of a semiconductor generally requires the localization of valence-band holes in surface bonds [13, 14]. When all back bonds are broken, the oxidized surface atom goes into solution as a soluble product. For example, in the case of a III–V semiconductor such as GaAs six charge carriers are required for the oxidation of one formula unit and trivalent products are formed [13, 14]

$$GaAs + 6\,h^{+}\,(VB) \rightarrow Ga\,III + As\,III. \quad (1)$$

The nature of the products depends on the solution composition and the etching conditions [13].

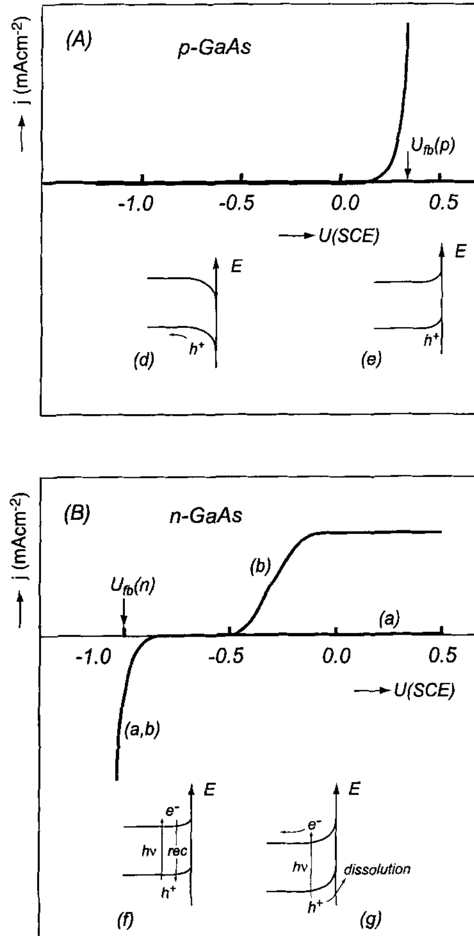

Fig. 4.1 Current–potential curves for GaAs in H_2SO_4 solution. The p-type electrode dissolves anodically in the dark (A) whereas illumination is required to dissolve the n-type electrode (curve (b), Fig. 4.1 B). At negative potentials hydrogen is evolved at the n-type semiconductor in the dark (curve (a), Fig. 4.1 B). The band bending for each case is shown in an inset.

On this basis one expects a p-type semiconductor to dissolve anodically in the dark when the surface hole concentration is appreciable, i.e. at potentials close to or more positive than the flat-band potential U_{fb} (Fig. 4.1A). On the other hand, n-type semiconductors do not dissolve anodically in the dark (Fig. 4.1B, curve (a)). Illumination is necessary to generate minority carriers. Under conditions in which the minority carriers can reach the surface without recombination (see inset, Fig. 4.1B), an anodic photocurrent is observed as a result of oxidative dissolution (Fig. 4.1 B, curve (b)). In general, electrochemical dissolution gives rise to surfaces with a roughness on a scale ranging from 10 to 1000 nm. It is possible to choose "polishing" conditions to give a mirror-like finish [13]. In certain cases an atomically flat surface can even be obtained [15].

When an n-type electrode is subjected to a very positive potential an anodic current may be observed, even in the dark [16]. Surface electrons can tunnel from

the top of the valence band (or from electronic states in the band-gap) through the space-charge layer to the conduction band; the resulting holes cause dissolution of the solid. The tunnel distance depends on the width of the space-charge layer, which is inversely proportional to the square root of the doping density. Consequently, a tunneling mechanism is more likely for highly doped (n^+) electrodes [16]. Since at very positive potentials there is a strong electric field present within the semiconductor at the interface, avalanche breakdown or impact ionization can also occur, generating holes in the valence band [16, 17]. The breakdown potential decreases strongly with increasing donor concentration. Avalanche breakdown and impact ionization mechanisms very often depend on the state of the surface, e.g. on crystallographic defects and surface impurities. Consequently, anodic etching is strongly localized [17, 18], in contrast to the uniform dissolution usually observed with p-type material.

In anodic etching, holes are supplied to the electrode interface by means of a current in the external circuit. Holes can also be created by reducing an oxidizing agent via the valence band of the semiconductor. The oxidant extracts electrons from, i.e. injects holes into, the band. For example, the $Fe(CN)_6^{3-}$ ion can inject holes into GaAs from a solution of high pH

$$Fe(CN)_6^{3-} \rightarrow Fe(CN)_6^{4-} + h^+. \quad (2)$$

The holes produced in this way can be used to oxidize surface atoms; the semiconductor dissolves under open-circuit conditions.

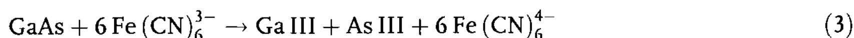

$$GaAs + 6\,Fe(CN)_6^{3-} \rightarrow Ga\,III + As\,III + 6\,Fe(CN)_6^{4-} \quad (3)$$

This form of dissolution, which occurs for both p-type and n-type materials in the dark, is generally referred to as "electroless etching". A prerequisite for open-circuit etching is that the electron acceptor levels of the redox system have an energy distribution which shows overlap with that of the valence band of the solid. Electroless etching of semiconductors has been widely studied with electrochemical and other techniques [13, 14].

A semiconductor can be photoetched under open-circuit conditions in a solution containing an oxidizing agent capable of "scavenging" electrons from the conduction band [13]. The acceptor levels in this case have an energy distribution overlapping the bottom of the conduction band. Photons generate electron-hole pairs; the electrons reduce the oxidizing agent from solution and the holes oxidize surface atoms. The mechanism should work for both p-type and n-type materials. For photoetching to be effective the kinetics of the oxidation and reduction reactions must be more favorable than those of electron-hole recombination. For simple redox systems this is seldom the case. An exception is the photoetching of InP in aqueous $FeCl_3$ solution, reported by Gomes and coworkers [19].

Semiconductors can also be etched by a surface reaction that does not involve free charge carriers (holes). In this case valence electrons are exchanged directly between the oxidizing agent in solution and the surface bond. For example, in the

$GaAs/H_2O_2$ system electron exchange between HO-OH and Ga-As bonds leads to rupture of existing bonds and formation of new bonds [20]

(4)

This mechanism, which is referred to as "chemical etching", does not result in porosity. However, the oxidizing agents that are used in such systems give rise to interesting effects when the semiconductor is illuminated locally with supra-bandgap light under open-circuit conditions [21, 22]. We shall return to these results when discussing porous etching of GaAs in Section 4.

4.3 Mechanisms of Porous Etching

Depending on the etching conditions, dissolution of a semiconductor may or may not be spatially uniform. Localized attack on the surface can give rise to the development of porosity. A IUPAC convention [23] distinguishes three cases: "macroporous" refers to systems with pore diameters larger than 100 nm while microporous describes the range below about 2 nm. Since in the latter case the dimensions of the unetched structures can be similar to the radius of the Bohr exciton, effects due to quantum confinement may be expected for many semiconductors. The term "mesoporous" is used for intermediate cases. Since the starting point for almost all the examples given in this chapter is a semiconductor single crystal, the etched solid is a "porous single crystal" without grain boundaries. Most other methods, such as those mentioned in Section 1, give polycrystalline porous matrices.

There are two important aspects to porous etching: pore initiation and pore propagation. The mechanisms of these processes can differ for the different cases defined above. In addition, one can distinguish between systems in which pore formation is random or is crystallographically determined.

For the macroporous case pores often nucleate at defects such as surface dislocations [24]. Artificial defects can be introduced deliberately by using photolithography to generate an etch pit pattern on the surface [25]. In certain cases pore initiation has been attributed to the localized breakdown of a surface-passivating layer [17]. In a similar way, "pitting" of oxidized aluminum can give rise to a highly porous metal. In the case of localized photoetching or photoanodic etching, the light pattern can generate a pattern of holes in the semiconductor [26, 27].

Propagation of macropores during anodic etching of n-type semiconductors can be due to enhanced dissolution as a result of the much higher electric field at the pore tip. This idea, first postulated by Theunissen [3], was extended by Beale [28]. The Beale model has been widely used. Parkhutik and coworkers adapted a model they developed for porous oxide formation on aluminum to describe pore growth in silicon [29, 30]. The model is based on two competitive processes: the forma-

tion of a passive layer at the bottom of each pore and electrochemical dissolution of the oxide. The rates of both processes depend on electric field; their relative contribution to the resulting porous structure depends on the anodisation regime, i.e. on potential or current density. The model allows for various morphologies including ordered and disordered arrays of pores similar to those observed experimentally [30, 31]. Smith and coworkers [28] developed a diffusion-limited model which explains pore formation in terms of diffusion of holes to or electrons from the silicon surface. Computer simulations based on this model reproduce quite well the structures actually observed in TEM. Erlebacher et al. [32] included biased hole motion to the nearest pore tip in Monte Carlo simulations in order to mimic local electric field effects. Several morphological features encountered in porous silicon are seen in their simulations; these include highly directional pores, steady-state pore spacing and a smooth pore front. The pore spacing and degree of side branching were dependent on bias and hole concentration, as in actual experiments. Since anodic etching of n-type semiconductors, either under illumination or as a result of breakdown, requires the electric field of a depletion layer, pore growth may stop when depletion layers from adjacent pores overlap [24].

As in the macroporous case, pore propagation in microporous etching has been attributed to electric field enhancement at the pore tips and diffusion control [28, 33]. The mechanism responsible for pore initiation is the subject of debate. The pore density is generally much too high to link nucleation to surface defects. Kooij and Vanmaekelbergh [34] have suggested a kinetic mechanism to explain various experimental results observed for photoanodic etching of n-type silicon. Their model assumes that the chemical oxidation of an Si(II) surface intermediate to an Si(IV) product, which is accompanied by the formation of a hydrogen molecule, is catalyzed by a mobile Si(I) intermediate. The authors suggest that this "autocatalytic" mechanism can account for pore initiation.

On the other hand Chazalviel and coworkers [35] attribute pore formation to the morphological instability of the dissolution process. Their model takes into account transport of charge carriers across the space charge layer and the silicon/solution interface. Using linear stability analysis they link the occurrence of micropore and macropore formation in a sinusoidally perturbed p-type silicon surface to the relative resistivities of the semiconductor and the electrolyte solution. An instability parameter a is defined on the basis of the resistivities and the wavenumber of the perturbation, q. When a is plotted as a function of q, regions of micro-instability, macro-stability and macro-instability can be distinguished.

For microporous silicon with its nanometre-sized structures quantum-size effects can influence strongly the dissolution reaction. Such ideas have led to quantum models for porous silicon formation [36]. The widening of the band-gap as a result of quantum confinement leads to a mismatch of the bandedges at the interface with bulk silicon and thus to a decrease in the concentration of charge carriers in confined structures. In this way smaller crystallites are protected against further etching.

4.4
Review of Porous-etched Semiconductors

In this section we review the literature on single-crystal semiconductors made porous by etching. The aim is to give some details of the etching technique and to describe the morphology and some of the physical properties. The photoelectrochemical investigation of a number of these systems is reserved for Section 5.

There has been a huge amount of work done on the porous etching of silicon, too much to cover completely in this chapter, and in any case, this will be dealt with in more detail in Chapter 5. Aspects of this work and some results on two IV–IV compound semiconductors are described. Various other compound semiconductors, III–V and II–VI materials and TiO_2, are also considered.

4.4.1
Silicon

Silicon can be made porous by anodic dissolution in HF solutions [28, 33]. Unlike almost all other semiconductors this occurs under normal etching conditions, i.e. for p-type in the dark, for n-type under illumination. In addition, porous silicon can be produced by electroless etching in a HF solution containing an oxidizing agent [37]. Because of these rather unusual properties we begin this section with a short description of silicon electrochemistry. Drawing on previous reviews [28, 33] we summarize the types of morphology (micro, meso and macro) that can be obtained. Finally, a short description of porous electroless etching ("stain etching") is presented.

4.4.1.1 Electrochemistry
Fig. 4.2 A shows a typical current-potential curve for p-type silicon in HF solution. At potentials more positive than the open-circuit value the current rises exponentially with increasing potential. The semiconductor is dissolved; the dissolution mechanism is complex [38]. Only two holes are required to remove each silicon atom to solution while one molecule of hydrogen is formed. Hydrogen is assumed to result from reaction of protons or HF with an intermediate of the silicon oxidation reaction, e.g. Si II $+ 2H^+ \rightarrow$ Si IV $+ H_2$. The total anodic reaction can be represented simplistically by:

$$Si + 6\,HF + 2\,h^+ \rightarrow SiF_6^{2-} + H_2 + 4H^+ \qquad (5)$$

and porous silicon is formed. At higher potential a current peak is observed after which the current becomes weakly dependent on potential. In this range an oxide is formed on the semiconductor and the anodic current is controlled by mass-transport of fluoride species in solution. As a result, silicon is electropolished [38].

As expected, the dark current of moderately doped n-type silicon in HF solution is low (Fig. 4.2 B, curve (a)). Under illumination, a photocurrent is observed whose limiting value depends on the light intensity (curves (b) and (c)). At low in-

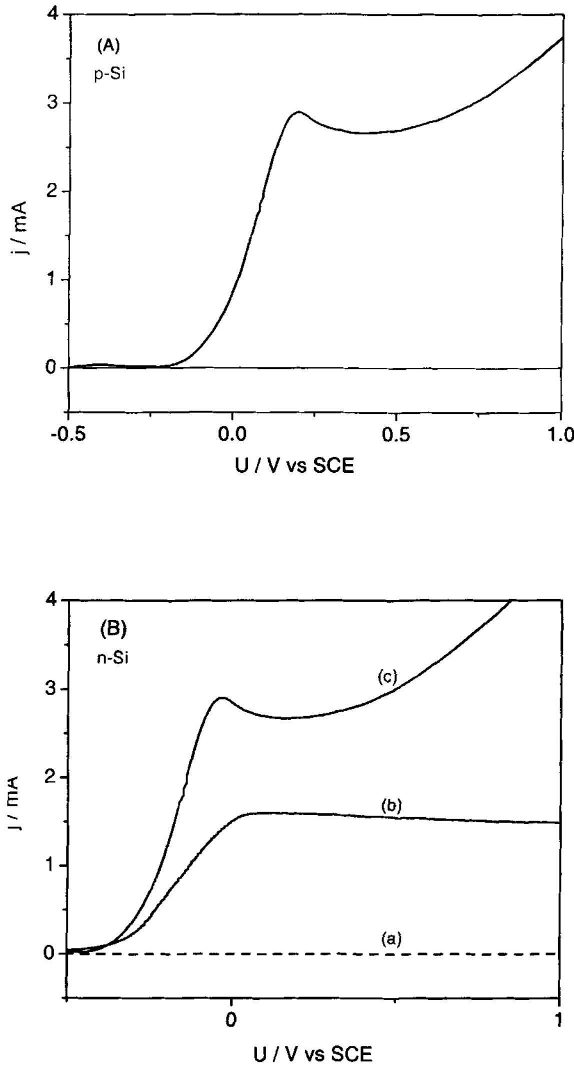

Fig. 4.2 Anodic current–potential curves for p-type silicon in the dark (A) and n-type silicon (B) in the dark (curve a) and under illumination at low and high light intensities (curves b and c, respectively) in 1 M HF solution.

tensity, the oxidation of silicon is controlled by the surface reaction involving holes and porous silicon is formed in the whole potential range (Fig. 4.2 B, curve (b)). At high light intensity (Fig. 4.2 B, curve (c)) the reaction becomes mass-transport controlled and the form of the photocurrent-potential curve resembles that of the "dark curve" for p-type silicon. In the porous etching regime the dissolution

mechanism is again complex being further complicated by electron injection into the conduction band from silicon dissolution intermediates [34].

Highly doped n-type (n^+) silicon shows dark current-potential characteristics similar to those of p-type silicon as a result of electron tunneling. Breakdown mechanisms operating at higher potentials can give anodic current in lower doped n-type silicon in the dark. In both cases (n and n^+), porous layers are formed [28].

4.4.1.2 **Morphology (Micro-/mesoporous)**

The morphology of porous-etched silicon depends on the dopant type and doping density and on the etching conditions. The rich variety in microstructure has been reviewed by a number of authors [28, 33]. Smith and Collins [28] classify morphologies according to four types (n, p, n^+ and p^+) based on the dopant density. For p-type silicon both the pore diameters and interpore spacings are extremely small (1–5 nm) and the porous network is highly interconnected and uniform. The pore diameters and interpore spacings increase slightly as the dopant density increases, leading to channel formation for p^+ material. The pore morphologies of n^+ silicon are similar to those of the p^+ semiconductor.

For n-type silicon there is a strong tendency for anisotropic pores to form (Smith and Collins refer to this as "piping"). This is considered below under macroporous silicon. In contrast to p-type silicon the pore diameters and average interpore spacings decrease with increasing dopant concentration. The pore diameters in n-type silicon are considerably larger than in p-type.

In general, the pore structure at low current densities is random and the pores are filament-like. At potentials approaching the electropolishing range pore growth tends to become anisotropic giving "pipe" geometries (see below). Chuang et al. [39] have used TEM and electron diffraction to demonstrate that pore propagation occurs in $\langle 100 \rangle$ directions for both p-type and n-type silicon.

4.4.1.3 **Morphology (Macroporous)**

In a series of papers starting in 1990 [25, 40, 41] Lehmann and coworkers described very elegant work on macropore formation in silicon. Highly anisotropic pores could be formed by photoanodic etching of n-type (100) silicon whose surface had first been provided with etch pits, e.g. by dark etching at high potential (Fig. 4.3). The wafers were illuminated from the back side. Pore widths ranged from 0.5 to 10 μm while a pore depth of 200 μm could be readily achieved. By starting with an ordered array of pits, produced by anisotropic etching through a photolithographically masked pattern, a perfectly ordered two-dimensional array of pores could be produced. Such lattices are interesting for photonic applications. The orientation of the primary pores is crystallographically determined; they grow in the $\langle 100 \rangle$ direction. Lehmann described macropore formation in n-type silicon as a self-adjusting mechanism characterized by a specific current density at the pore tip. At this current density dissolution changes from a charge-transfer-lim-

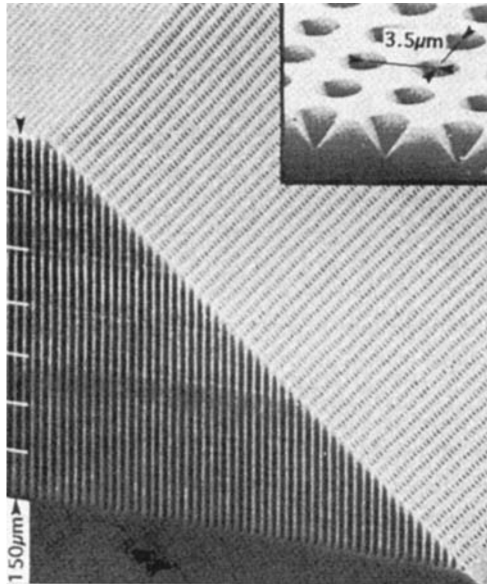

Fig. 4.3 Surface, cross section, and a 45° bevel of an n-type silicon sample (10^{15} cm^{-3} phosphorous doped) showing a predetermined pattern of macropores (3 V, 350 min, 2.5% HF). Pore growth was induced by a regular pattern of pits produced by standard lithography and subsequent alkaline etching (inset upper right). To measure the depth dependence of the growth rate, the current density was periodically kept at 5 mA cm^{-2} for 45 min and then reduced to 3.3 mA cm^{-2} for 5 min. This reduction results in a periodic decrease of the pore diameter, as marked by white labels in the figure (from Ref. [25]).

ited to a mass-transport-limited regime. Passivation of the pore walls is attributed to a depletion of the minority carriers.

Föll and coworkers [42] extended earlier work with Lehmann by studying the dependence of macropore formation on the substrate orientation. Samples were cut from a large silicon crystal in various orientations between {100} and {111}. The growth direction of the photoanodically formed macropores was found to be ⟨100⟩ and ⟨103⟩ with a switch over at a critical angle of 43°. Surprisingly, pores obtained by breakdown at high field without illumination always grow in the ⟨100⟩ direction. The reason for such differences is not clear.

Levy Clement and coworkers [43] have investigated the influence of doping density on the microstructure. Marked differences were observed between the morphologies of strongly and lightly doped silicon, especially in the initial stages of photoanodic etching. The results are explained by a model previously used for II–VI compound semiconductors. A breakdown field near surface dopant atoms is postulated. In this, as in previous work, it is clear that the macroporous layer is often formed beneath a micro- or mesoporous layer.

Kang and Jorné [44, 45] have performed a morphological stability analysis on the photoelectrochemical etching of n-type silicon, illuminated from the back of the wafer. They concluded that, while porous silicon is formed when the dissolution process is controlled by the supply of holes, the porous structure depends on both the semiconductor material properties and the process conditions.

Recent work [35, 46] has shown that macropores can also be formed in low-doped p-type silicon in HF solution in the dark. This may seem surprising. Space-charge effects should not be important in this case since etching occurs close to

flat-band conditions. It is also unlikely that in aqueous HF solution the silicon surface will be passivated. The explanation based on morphological instability put forward by Chazalviel and coworkers (see Section 3) has been questioned by Lehmann and Rönnebeck [46] who suggested an alternative mechanism involving charge-transfer mechanisms across the Schottky barrier. Ponomarev and Lévy-Clément [47] have shown that macropores can also be formed in solutions of HF in acetonitrile and dimethylformamide.

4.4.1.4 **Stain Etching**

Silicon can be made microporous by electroless etching in solutions containing HF and HNO_3 [37, 48]; this process is generally referred to as "stain etching". Nitric acid acts as oxidizing agent injecting into the valence band the holes required for the oxidation of the semiconductor. The composition of the solution is important for obtaining porosity. The mechanism of the reaction is complicated; HNO_3 reduction occurs via an autocatalyzed reaction [49]. An induction period is often observed before etching starts [48]. Microporous silicon, produced by staining, also shows photoluminescence in the visible spectral range [37, 48]. The fact that external contacts are not required, makes this method attractive for certain device applications.

Zhang and coworkers [50] have recently reported a novel open-circuit etching method. Si p/p$^+$ epitaxial wafers with the (111) orientation were hydrothermally etched in a 7:6 (by volume) mixture of 40% HF and 0.3 M $Fe(NO_3)_3$ aqueous solution. The reaction was conducted at 142 °C for 45 min. Porous layers prepared in this way showed photoluminescence which, in contrast to that of anodically etched or stain-etched silicon, was stable over a period of many months. The authors attribute this effect to a passivation of the surface by Fe, possibly via the formation of Si-Fe bonds on the porous surface.

4.4.2 IV–IV Materials

4.4.2.1 **$Si_{1-x}Ge_x$ Alloys**

Pike et al. [51, 52] studied the microstructure of stain-etched $Si_{1-x}Ge_x$ alloys ($0.06 \leq x \leq 0.25$) using TEM, chemical microanalysis and photoluminescence. The alloy samples, grown by molecular beam epitaxy on Si (100) substrates, had a thickness of 0.75 μm and a boron-doping density of 10^{17}–10^{18} cm^{-3}. The etchant was 4:1:4 HF-HNO_3-H_2O. The porous layers were mainly composed of amorphous material with some crystallites at the substrate interface. All layers had a porosity of between 70% and 80% and were substantially richer in Ge than the unetched material. The visible photoluminescence from the porous layers dropped off sharply with increasing Ge content of the stain-etched alloy. The emission maximum did not vary with the composition. Luminescence was attributed to small "active units" containing a limited number of silicon atoms.

Schoisswohl et al. [53] have made $Si_{1-x}Ge_x$ porous by anodic etching in HF-H_2O-ethanol solution. Both an intense red luminescence and a weak blue luminescence were observed with the porous alloy.

4.4.2.2 SiC

Electrochemically, SiC resembles Si in a number of respects. An oxide layer protects the semiconductor very effectively from anodic attack in most solutions. Like Si, p-type SiC can be anodically dissolved in HF solution in the dark, while the n-type material dissolves under illumination [54]. The valence-band edge of SiC is, however, at an energy much lower than that of Si [54]; consequently, hole injection from an oxidizing agent in aqueous solution does not occur so that electroless etching is, under normal conditions, not possible.

In 1993 Shor et al. [55, 56] reported for the first time the porous etching of SiC. They used good quality n-type 6H single crystal wafers with a doping density of 3×10^{18} cm^{-3}. Photoanodic dissolution was carried out in aqueous 2.5% HF solution at potentials between 0 and 4 V relative to the SCE. The photocurrent density ranged from 10–30 mA cm^{-2}. A simple test showed that a thick porous layer is formed under such conditions. The anodized SiC samples were thermally oxidized in a steam ambient for 4 hours at 1150 °C. For bulk SiC this should result in a surface oxide layer with a thickness of less than 60 nm. However, after a short HF dip to remove the oxide, cavities several microns deep were observed, indicating that a highly porous layer had been oxidized and removed. As in the case of Si, anodisation of p-type SiC in HF solution in the dark resulted in porosity. TEM revealed a porous structure with pore sizes in the range 10–30 nm and with interpore spacings of 5–150 nm. A selected area diffraction analysis showed the etched layer to be single crystal 6H SiC. The authors give two suggestions for pore initiation: defects present in sublimation growth 6 H SiC or variations in surface chemistry.

Konstantinov et al. [57] and van de Lagemaat et al. [58] found that porous etching also occurs with n-type SiC in HF solutions in the dark at strongly positive potentials (4–5 V and 20–25 V, respectively). On the other hand, high-quality crystals from Cree Research Inc. showed only very low anodic dark current up to 60 V [54]. This absence of dissolution proves the importance of defects for the breakdown phenomena required for anodic dissolution of n-type semiconductors in the dark. Konstantinov et al. showed that the morphology of the porous layer depends on the anodisation conditions [57]. The average wall thickness for dark-etched SiC is much larger (0.5–1 μm) than that of photoanodically etched material (< 50 nm). They reject quantum confinement as a mechanism for protecting the very thin "fibers" formed under illumination. Instead, they suggest a model involving Fermi-level pinning which leads to a greatly increased resistivity. Shin et al. [31] describe a change in microstructure of n-type 6H SiC from fibrous to dendritic as the anodic photocurrent density increases from 20 to 60 mA cm^{-2}. They use the Parkhutik model based on a passivating oxide at the pore tip [30] to model the change in microstructure.

4.4.3 III–V Materials

4.4.3.1 GaP

In what, to the average electrochemist, would seem a rather extreme experiment, Chase and Holt in 1972 used a chlorine/methanol solution and a potential difference of 120 V (!) to thin GaP anodically [59]. The (111) Ga surface was exposed to the solution. A tungsten counter-electrode was incorporated into a jet with which the semiconductor surface could be sprayed locally with the solution. An orange surface film was formed. Transmission electron microscopy (TEM) showed that a porous layer had been formed with high density networks of tunnels about 30 nm in diameter. The tunnels ran in the ⟨111⟩ direction, "in the polar sense from the gallium to the phosphorus atom along a chemical bond". No relation was found with any preexisting defects in the material that could be seen with TEM (the tunnel density was much higher than the dislocation density). The authors suggested avalanche breakdown of the depletion layer as a result of the very high electric field to explain tunnel formation.

Porous GaP was "rediscovered" in 1995 by two groups. Anedda et al. [60] produced a 3 μm thick light-yellow layer on n-type (100) material by anodic etching at 20 mA cm^{-2} in 50% solution of HF in ethanol. The electrolyte was probably chosen because of its success in producing luminescent porous silicon. A porous layer was obvious in scanning electron micrographs; the GaP skeleton consisted of walls of nanometre dimensions. Erné et al. [24, 61] also etched n-type (100) GaP in the dark but at a constant potential (5–10 V relative to the SCE) in 0.5 M H_2SO_4 solution (Fig. 4.4). Sub-micron pits, 10–30 μm apart, were first formed at the surface. Below the largely unetched surface the pits acted as nuclei for pores. The initial pits were attributed to a breakdown mechanism at defects. Pit propagation was linked to electric field enhancement at the tip. Secondary pores were found to branch radially from the primary pores and these gave rise to porous domains. Pore widths and pore wall thicknesses were about 100 nm. In contrast to the results of Chase and Holt for (111) GaP, the pores did not propagate along crystallographically defined directions. Secondary pore growth stopped when pore fronts from adjacent domains met; this was explained by overlap of the depletion layers of pore fronts. Etching via "primary" pores continued to very large depths (> 100 μm). These layers had a porosity of ca. 35%.

Schuurmans et al. [62] showed that the porosity could be increased to ca. 50% by means of a novel etching process. The dark-etched GaP is subjected to a photoanodic etching procedure in a H_2O-H_2SO_4-H_2O_2 electrolyte solution. Sub-band-gap light from a HeNe laser is used (the band-gap of GaP is 2.24 eV, the photon energy is 1.96 eV). Photons are absorbed by a transition of an electron from the top of the valence band to an interfacial state 0.3 eV below the conduction band edge. This is followed by thermal release of the interfacial electron into the conduction band. The hole in the valence band causes oxidation and dissolution of the surface. Because of the weak absorption of light (due to its sub-band-gap energy) the etch rate is constant across the porous network and the sample is etched

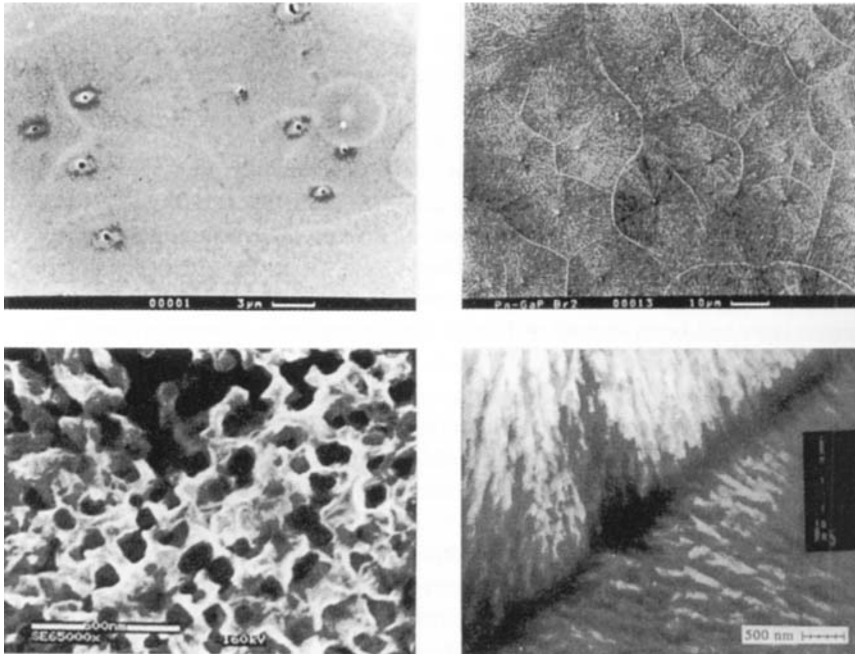

Fig. 4.4 Electron micrographs of an n-GaP electrode after anodic etching: 16 C cm^{-2} charge was passed, equivalent to the removal of 30 μm in the case of uniform etching. (a, top left) SEM micrograph of the surface of the electrode, showing a low density of submicron pits. (b, top right) SEM micrograph after removal of a top layer of less than 0.5 μm using a chemical etchant. Porous domains have become visible with nuclei which lie directly below the spots at which pits are seen at the surface of the electrode. Dark areas indicate the absence of GaP material. (c, bottom left) High resolution SEM micrograph taken along the propagation direction of the pores. Pore diameters and pore wall thicknesses are ca. 100 nm. (d, bottom right) TEM micrograph of the wall of a porous domain. In contrast to the SEM micrographs, the dark areas now indicate the presence of GaP material. The nonporous wall is 100 to 150 nm thick (from Ref. [24]).

uniformly resulting in a uniform decrease in wall thickness and increase in porosity over the whole layer.

4.4.3.2 GaAs

In the paper of Chase and Holt on porous GaP [59], there is a reference to earlier work on GaAs. However, with the upsurge of interest in porous semiconductors in the nineties, a number of groups have been working on the formation of porous n-type GaAs in the dark. There is also somewhat older work on the use of focussed lasers or patterned light beams to generate pores either by open-circuit or anodic photoetching. Here, we review briefly the results with the various approaches.

Schmuki et al. [17, 18] studied pitting, pore initiation and growth in (100) GaAs. Localized dissolution of the p-type material was only observed in chloride solution when a passivating film was present on the surface. Otherwise, uniform dissolution of the semiconductor was observed. This case is similar to that of aluminum where oxide breakdown by chloride ions causes pitting. Pore initiation and propagation were found in n-type GaAs at sufficiently positive potentials in the dark. Clearly, depletion layer breakdown is responsible in this case. Interestingly, the onset potential for pore formation is reduced when chloride ions are present in solution; the potential decreases as the chloride concentration increases. This shows that chloride ions, by participating in the dissolution mechanism, influence pitting. A SEM study of the porous n-type GaAs revealed microstructure with dimensions in the submicron range. From cross-section SEM it was clear that the porous layer had a "needle-like" appearance. The authors report preferential attack perpendicular to the (100) direction, i.e. along ⟨011⟩. The pitting process was not influenced by surface roughness but was promoted by mechanical damage of the surface, e.g. scratching. The latter result suggested to the authors that pitting could be due to surface defects such as dislocations and to differences in reactivity of different crystal planes exposed to the electrolyte.

Oskam and coworkers [63] carried out an extensive study of the porous etching of (100) GaAs. The n-type semiconductor was anodically etched in the dark in concentrated HF solution (see GaP). The pore density, the pore dimensions and the structure of the porous layer depended on the doping density and the crystallographic orientation of the surface. The pore morphology was independent of the current. The pore front velocity was linearly dependent on the current and the porous layer could be grown to any thickness. Transmission electron microscopy and small-angle neutron scattering were used to study the structure. The primary pores grow in the ⟨111⟩a direction and have triangular or hexagonal cross-sections. The pore diameters increase from 80 nm for highly doped GaAs to 400 nm for the undoped semiconductor. The authors suggest a depletion layer breakdown mechanism to explain pore propagation.

In a subsequent paper [64] crystallographic aspects were considered in more detail (Fig. 4.5). A model was developed based on two assumptions: firstly, etching occurs more rapidly at sharply curved pore tips where the electric field is strongest and, secondly, atoms are removed preferentially from surface kink sites; the reactivity of these sites is assumed to be highest as their coordination to the lattice is lowest. With this model some essential differences in the porous etching of GaAs and Si could be highlighted. For Si the model suggests that, after nucleation of a pore by a surface pit, etching proceeds by the removal of kink atoms from [11-2]-type steps on {111} planes. The flow of steps away from the tip generates a pore with a square cross-section and {110} pore walls. In GaAs the geometry of pores is controlled by the propagation of a tetrahedral vertex into the lattice sustained by the flow of [11-2] type steps from the vertex to the pore wall. The angle which these steps make to the propagation direction leads to a higher etch rate at the center of the walls and explains why the pore cross-section is a distorted hexagon.

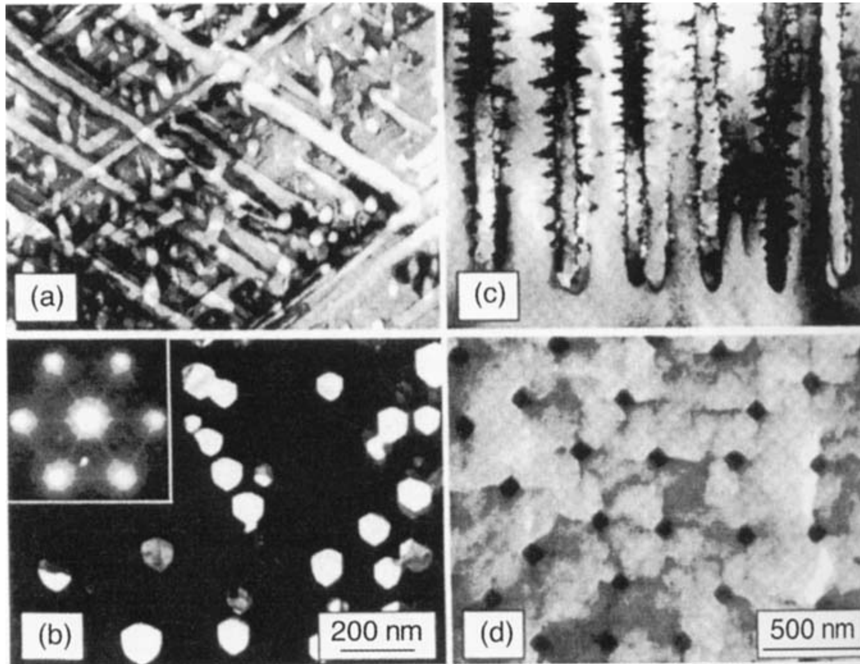

Fig. 4.5 (a) Bright-field TEM image of an ion-milled cross-section with [110] orientation showing the structure of pores formed in 2×10^{18} cm^{-3} n-type (001) GaAs after etching in 49% HF for 60 min at 10 mA cm^{-2}. The growth direction is from top to bottom. Two sets of pores can be seen in the plane of the foil while the other two are inclined. Images (a), (c) and (d) are at the same magnification. (b) Higher-magnification bright-field image of a crushed fragment of the same specimen as in (a), viewed down one of the ⟨111⟩ pore propagation directions. The inset is a diffraction pattern showing streaking in ⟨011⟩ direction. (c) Bright-field image of an ion-milled cross-section tilted slightly off the [110] orientation showing pores formed in 9×10^{16} cm^{-3} n-type (001) Si after etching in 20% HF (EtOH) for 10 min at 50 mA cm^{-2}. Side branching is visible. (d) Plan-view SEM image of the same specimen as in (c), showing the ⟨100⟩ side branches and the {110} pore wall orientation (from Ref. [64]).

Osgood and coworkers have produced quite spectacular results with UV-induced open-circuit etching of n-type GaAs single crystals [26, 65–67]. A focussed, frequency-doubled argon-ion laser (257 nm) was used to generate vertical, high aspect features such as grooves and through-holes, 2 μm wide with a depth of over 200 μm. Etch rates of 10 μm min^{-1} were achieved at laser intensities of 10 W cm^{-2} in H_2SO_4-H_2O_2-H_2O solution. The extreme anisotropy observed in this work is attributed to effective waveguiding of the light within the etched features. This approach using a focussed laser can obviously be used to generate any arbitrary pattern of deep holes or grooves in the semiconductor. In principle, a high intensity uniform light source could be used with a patterned mask for the same purpose.

The mechanism of open-circuit etching in such systems has been investigated by van de Ven and Nabben [21, 22]. In the illuminated area the laser beam generates electron/hole pairs. In n-type GaAs the majority carriers, the electrons, equilibrate very rapidly and are available for reduction of the oxidizing agent over the whole surface (illuminated and unilluminated). Since H_2O_2 has been shown to chemisorb on III–V semiconductors, it can effectively capture electrons from the conduction band. Since the whole surface is available for this reaction, kinetic and mass-transport limitation of the reduction is avoided. The holes generated by the beam are held at the surface by the electric field of the depletion layer. The holes cause oxidation and dissolution of the solid. Being majority carriers, photogenerated holes in p-type GaAs are not localized effectively within the beam area and, consequently, the photoetch rate is much lower than for n-type material.

Rauh and coworkers [27, 68] demonstrated the importance of doping density and mask orientation for determining photoanodically-etched features in (100) n-GaAs. Structures etched along the ⟨001⟩ direction produced V-grooves, showing that the (111) Ga surface is a "stop plane" with regard to oxidation by photogenerated holes. Other orientations etch more isotropically. Undercutting of the mask edge is attributed to the lateral diffusion of holes due to slow kinetics of the interfacial reaction. This effect is minimized in highly doped crystals where high quality vertical walled gratings were produced with aspect ratios of more than 10:1 using visible light.

4.4.3.3 **InP**

Takizawa et al. [69] formed a vertical porous n-type InP structure with an aspect ratio larger than 100 by anodisation in the dark of a (111) A-oriented n-InP substrate in a HCl solution. Etching was carried out galvanostatically (15 mA cm^{-2}). SEM revealed small pores with a diameter of around 50 nm randomly distributed on the surface. In cross section, a high-density pillar structure was clear with a depth of about 2 μm. A similar etching procedure with a (100)-oriented n-type InP surface produced pores aligned along ⟨111⟩ and ⟨–1-11⟩ directions with a depth of about 5 μm. Clearly, the ⟨111⟩ direction is preferred for pore propagation. By initiating the etching of the (111) A surface through SiO_2-defined masked windows a uniform high-density structure was fabricated. The shape of the pores was determined crystallographically and did not reflect the shape of the holes in the SiO_2 mask. The unetched pillars were triangular and the sides corresponded to the cleaved facets [1-10], perpendicular to the (111) A surface. The pillar height was 1.5 μm and a space filling factor of around 50% was achieved. These structures are very interesting for electrical and optical measurements [69].

Ferreira et al. [70] showed that the surface of n-type InP (100) could be textured by photoelectrochemical etching in HCl solution. Elongated etch pits were observed. Hamamatsu et al. [71] produced porous InP by photoelectrochemical anodisation of n-type (100) material, again in HCl solution. In this case the electrode was polarized at potentials at which passivation (oxide formation) occurred (2–7 V relative to the SCE). ⟨001⟩-oriented nanometer-sized straight pores without

branches were formed. The pore diameter, wall thickness and pore length could be changed in the ranges 110–250 nm, 16–50 nm and 17–80 μm, respectively, by changing the anodisation potential. A combination of the Beale and diffusion-limited models was used to explain pore formation. Widening of the pores stops when the pore walls become so thin they are completely depleted of charge carriers.

Deep holes and grooves can also be photoetched in InP at open-circuit. Lowes and Cassidy [72] used a focussed argon-ion laser to etch n-type (100) InP in dilute H_3PO_4 solution. The light was chopped at a frequency between 15 and 3.2 Hz and a duty cycle of 5% to 100% was used. Photoetch rates of up to 7 $\mu m\ min^{-1}$ could be achieved for a light intensity of 250 $W\ cm^{-2}$. The etched depth increased linearly with time. As in the work described above for GaAs, very deep holes a few microns wide could be produced, again pointing to the importance of a self-propagating waveguide. In this work it is not clear which reduction reaction is responsible for removal of the photogenerated electrons (see Section 2). Probably oxygen, naturally present in aqueous solution, scavenges the electrons. As in the case of GaAs the photoetch rate of p-type InP is much lower than that of the n-type material.

4.4.3.4 GaN

Youtsey et al. [73] describe an unusual mechanism for obtaining a porous semiconductor. Photoelectrochemical etching of n-type MOCVD GaN in dilute KOH solution at light intensities of 5–10 $mW\ cm^{-1}$ resulted in whisker formation. The whiskers had typical diameters of 25 nm and could be up to a micron long. The surface density was high ($2\times10^9\ cm^{-2}$). The authors show that whiskers arise around dislocations; the material between the defects is selectively removed. A correlation between the etched features and threading dislocations in the unetched film was confirmed with TEM studies. Clearly, enhanced electron-hole recombination at defects protects the surrounding area from photoanodic attack.

4.4.4 II–VI Materials

While etch-pit formation is widely known for II–VI semiconductors [74, 75], porosity has only been reported recently.

4.4.4.1 CdTe

Erné et al. [76] described how p-type $Cd_{0.95}Zn_{0.5}Te$ becomes porous on anodic treatment in acidic solution. Prolonged anodisation gives porous layers up to 100 μm thick. Coulometry and XPS analysis showed the pore walls to be covered by a film of elemental tellurium.

$$CdTe + 2h^+ \rightarrow Cd^{2+} + Te^0 \quad (6)$$

The Te^0 can be further oxidized to $HTeO_2^+$ (see ZnTe below). The authors propose a mechanism involving non-uniform hole collection to explain porous etching. Etch pits are formed with a crystallographically determined shape, implying surface diffusion of holes to sites where hole collection is kinetically favored. Dislocations and inhomogeneities are suggested as sites for this initial attack. The tellurium film grows on the remaining surface, preventing further dissolution. Pore propagation is explained in terms of space charge limitation, enhancement of the electric field and hole depletion in the porous layer.

4.4.4.2 ZnTe

Electrochemical etching of p-type ZnTe in HNO_3: HCl: H_2O solution gives rise to patterns several microns deep in (111) and (110) surfaces [77]. A surface enlargement of a factor of 50 could be observed. By performing etching at higher potential, tellurium formation on the surface is avoided

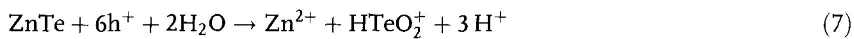

$$ZnTe + 6h^+ + 2H_2O \rightarrow Zn^{2+} + HTeO_2^+ + 3\,H^+ \quad (7)$$

Etching was found to nucleate at specific defects, possibly dislocations, and to proceed by the growth of etch pits displaying the symmetry of the surface. Etching along the ⟨100⟩ directions occurs at the fastest rates; (100)-oriented surfaces therefore remain smooth and etch pits are found only if there is a misorientation in which case large rectangular etch pits with smooth terrace-like bottoms are observed. In contrast, etching in the (111) and (110) orientations produced deep pits. These exhibit the typical threefold symmetry for (111) surfaces while a pattern of rectangular pits is obtained for the (110) orientation. Lateral growth of the pits proceeds until the edges meet. Further etching results in a deepening of the pits. A columnar structure several microns deep results, with walls of 25–700 nm.

4.4.5 Titanium Dioxide

Although TiO_2 had been considered the prime example of a stable photoanode, Nakato et al. [78] showed that prolonged illumination in sulfuric acid solution at positive potentials causes etching; in fact, deep pores are formed. A very interesting microstructure was reported by Sugiura et al. [79]. They used sintered pellets, formed by press-molding of TiO_2 powder in vacuo. The pellets were fired at 1300 °C for 6 h in a nitrogen atmosphere and then slightly reduced by heating at 700 °C for 4 h under a stream of 10% hydrogen to obtain n-type semiconductivity. Etching was performed under potentiostatic conditions in 0.1 M H_2SO_4 solution with light from a high pressure mercury lamp. The morphology depended on the applied potential. At a potential just positive of the onset of the photocurrent the grains were selectively dissolved while the grain boundaries were left untouched; this created a "skeleton" structure. This is probably the same effect (enhanced recombination) as that observed with GaN (see Section 4.3). Under strong anodic

polarization corresponding to photocurrent saturation the grain boundaries were selectively attacked and a characteristic etching pattern appeared on each grain surface. The Faradaic efficiency of the photoetching reaction was approximately 3%, independent of the applied potential; oxygen evolution accounts for most of the current.

The etched TiO_2 consisted of quadrangular cells with uniform size (100–200 nm) and a depth of up to 5 μm. The authors call this unique morphology a "nanohoneycomb" structure. Selected area diffraction showed that photoetching proceeded along the c axis and, consequently, the entire interior surface of the honeycomb consisted of a (110) crystal face. Quadrangular cells were also found when the (001) surface of a rutile single crystal was etched in the same way as the sintered sample. Photoetching takes place preferentially on the (001) face, thus creating a cell surrounded by four equivalent thin walls with (110) crystal faces connected vertically with each other. The authors attribute the relative stability of the (110) face to the larger number of Ti-O bonds that must be broken when photoetching occurs.

4.5 Photoelectrochemical Characterization

In this section we describe the characterization of porous semiconductors by a number of photoelectrochemical techniques. Impedance measurements (Section 5.1) give information mainly about the potential distribution which depends on the morphology of the layer. Photocurrent (Section 5.2) and luminescence measurements (Section 5.3) and intensity-modulated photocurrent spectroscopy (IMPS) (Section 5.4) give information on the charge carrier dynamics. IMPS is particularly suitable for studying transport of charge carriers in porous media.

4.5.1 Electrical Impedance

In an extrinsic bulk-semiconductor electrode three potential regimes can be defined with respect to the flat-band condition [13, 14]. In this and the subsequent sections we take an n-type semiconductor as an example. At potentials more positive than the flat-band value U_{fb} a depletion layer is formed in which the majority carrier concentration at the surface is lower than in the bulk ($n_s < n_b$). The thickness of the depletion layer, W, is determined by the band bending, U_{sc}:

$$W = \sqrt{\frac{2\varepsilon\,\varepsilon_0\,U_{sc}}{eN_D}} \qquad (8)$$

where ε is the dielectric constant of the solid and N_D is the donor density. If a change in applied potential leads only to a change in band bending then $U_{sc}=|U-U_{fb}|$, where U is the electrode potential. The capacitance associated with

the depletion layer C_{sc} can be calculated from Mott–Schottky theory [13] and is usually plotted as:

$$\frac{1}{C_{sc}^2} = \frac{2}{\varepsilon \varepsilon_0 N_D e}\left(U_{sc} - \frac{kT}{e}\right). \qquad (9)$$

At strong band bending inversion may occur. In this case the concentration of minority carriers at the surface exceeds that of the majority carriers ($p_s > n_s$). However, since minority carriers generally react at the interface at a rate higher than the rate of thermal generation, this situation is not common in semiconductor electrochemistry. Instead, deep depletion is observed.

At potentials negative with respect to U_{fb}, an accumulation layer is formed in which the surface concentration of the majority carriers is larger than the bulk concentration ($n_s > n_b$). The width of the accumulation layer is much smaller than that of the depletion layer. As the electrode potential is made negative, the Fermi level E_F passes through the conduction band edge at the surface and the semiconductor becomes quasi-metallic. This usually results in a change of the potential drop across the Helmholtz layer and, in the case of an n-type semiconductor, an upward shift of the band edges at the surface.

The formation of a depletion or accumulation layer in a porous electrode depends not only on the applied potential but also on the dimensions of the microporous or macroporous structures in relation to the dimensions of the space-charge layer. Obviously we need to distinguish between depletion and accumulation conditions.

In microporous and mesoporous systems the typical dimensions of the solid structures are too small to sustain a depletion layer. Consequently, in the case of porous p-type silicon the impedance measured is that of the substrate/electrolyte interface at the base of the porous layer [80]. On the other hand, with a macroporous electrode a depletion layer is expected when its width (W) is smaller than the typical dimensions (D) of the porous structure. In such a case the inner edge of the depletion layer can follow the internal surface of the porous layer; this is shown schematically in Fig. 4.6(a).

As a result, the depletion layer capacitance, which is directly proportional to the surface area, is very large. Since the width of the depletion layer increases with increasing potential (Eq. 8), the porous structures can become completely depleted as the bias is increased and W becomes comparable to $D/2$. The inner edge of the space-charge layer is no longer located within the porous structure but is shifted to the interface between the porous layer and its substrate (Fig. 4.6b). Such effects are illustrated in the results of Konstantinov et al. [57] obtained with n-type SiC. The upper straight line in Fig. 4.7 is the Mott-Schottky plot (see Eq. 9) for the unetched single crystal while the lower curve was measured with the macroporous electrode. Between the flat-band potential (at ca. –1 V) and a bias of +1 V (indicated by A in the figure), the space-charge layer capacitance is greatly increased ($1/C_{sc}^2$ is very small). This corresponds to the range of incomplete depletion. At higher bias the porous layer becomes completely depleted (range B, Fig. 4.7). The

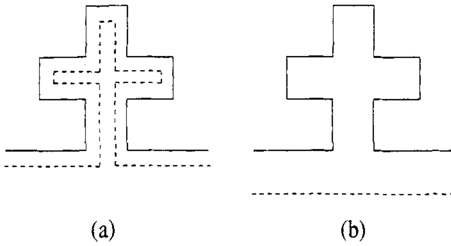

Fig. 4.6 Schematic representation of a porous structure under depletion conditions. In case (a) the depletion layer width W is less than half the typical dimension D of the structure. The inner edge of the depletion layer follows the contours of the porous layer and the space charge layer capacitance is very large. (b) The porous structure is completely depleted ($W > D/2$). The depletion layer edge is not located within the porous layer but at the interface between the porous layer and the substrate. In this case the space charge layer capacitance is similar to that of a flat electrode.

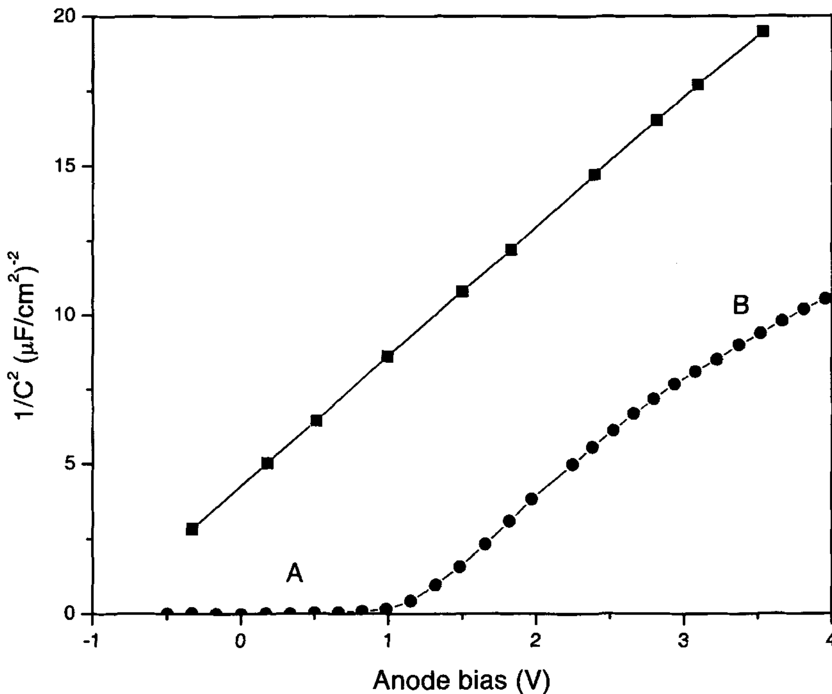

Fig. 4.7 Capacitance-voltage characteristics of the semiconductor/electrolyte interface for single-crystal SiC (diamonds) and for porous-etched SiC (circles) (from Ref. [57]).

same two ranges are clear in the capacitance-potential plot of Fig. 4.8 for the macroporous n-type GaP/electrolyte system [24, 61]. As the charge passed during porous etching increases on going from curves 2 to 8, the capacitance in range A increases by more than two orders of magnitude. A similar result has been found

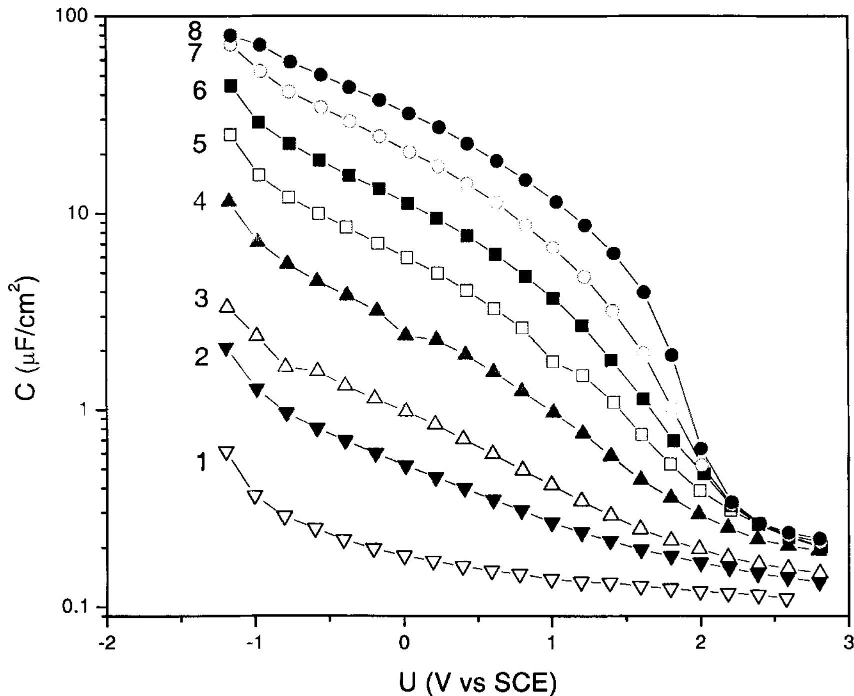

Fig. 4.8 The capacitance of the n-GaP/H_2SO_4 (aq) interface as a function of potential at various stages of anodic porous etching. Curve 1 is the unetched surface. In curves 2–8 the charge density passed during etching increases from 0.1 to 10 C cm^{-2}.

for n-type GaP/Au [81] and for n-type SiC/electrolyte interfaces [58]. The transition from the high to low capacitance ranges in Fig. 4.8 is not abrupt. This is mainly due to the fact that the pores are not monodisperse. This and the fact that the electric field within the space charge layer depends on the local geometry of the surface complicates the modeling of such systems.

Shen et al. [82] showed that the depletion layer impedance of photoelectrochemically etched n-type silicon, measured in an non-aqueous electrolyte, was almost identical to that of the smooth substrate. This is surprising since the authors report that the etched layer on which the measurements were performed is macroporous (with pore dimensions of the order of 1 μm); the microporous top layer could be dissolved in KOH solution and its removal did not influence the impedance results. The authors explain their results by complete depletion of the macropore walls. This must mean that the walls are very thin, a result supported by SEM measurements.

Under accumulation conditions porous silicon shows quasi-metallic properties and the interfacial capacitance is dominated by the Helmholtz double layer. Peter et al. [83] describe a novel application of this result for monitoring "in-situ" the internal surface area of an n-type substrate during anodic formation of the porous layer. The interfacial capacitance was determined from the current response to a

triangular voltage-wave form. The capacitance and thus the area was found to be linearly dependent on the anodic charge passed during etching and independent of the current density used. From these results conclusions were drawn regarding the morphology of the porous layer.

Using the same approach Peter and Wielgosz [84] measured the capacitance of a porous p-type silicon electrode illuminated from the back of the wafer at potentials corresponding to depletion of a bulk electrode. The value found ($750\ \mu F\ cm^{-2}$) is several orders of magnitude larger than that of bulk n-type silicon under accumulation conditions ($\sim 1\ \mu F\ cm^{-2}$). Obviously, electrons photogenerated in the substrate accumulate in the porous layer and give rise to a capacitance directly proportional to the internal surface area.

4.5.2
Photocurrent

The photocurrent measured with a semiconductor electrode depends on the dynamics of photogenerated charge carriers and on the kinetics of the surface reactions. In order to understand the possible effects of porosity on the photocurrent quantum yield it is useful first to consider the situation at a non-porous electrode. The processes of importance are: generation of electrons and holes (by light absorption); their separation (by migration and diffusion); recombination (in the bulk and at the surface); transfer of minority carriers across the interface; and transport of majority carriers to the back contact.

To illustrate the interplay of these factors we consider the case of an n-type semiconductor which is illuminated through a solution containing an efficient hole acceptor. The generation rate of electrons and holes at a depth x is given by $-d\phi(x)/dx$ where $\phi(x)=\phi(0)e^{-\alpha(\lambda)x}$, $\phi(0)$ is the photon flux at the electrode surface ($x=0$), $\phi(x)$ is the flux at a depth x and $\alpha(\lambda)$ is the absorption coefficient for light of wavelength λ. The penetration depth of the light $L(\lambda)$ is usually defined as $L(\lambda)=1/\alpha(\lambda)$. As shown in Fig. 4.9 two processes contribute to the spatial separation of the photogenerated charge carriers. Electron-hole pairs created within the depletion layer (of width W) are separated by the strong electric field. The minority carriers (holes) migrate to the surface, the majority carriers (electrons) to the bulk; this occurs extremely fast, on a picosecond time scale [80]. Because of the effective charge separation within the depletion layer, the concentration of minority carriers at the bulk edge of this layer is low. Minority carriers generated in the bulk can diffuse over a distance L_p to the depletion layer edge and so reach the solution interface. The distance $W+L_p$ can be considered a retrieval length for minority carriers. Electrons and holes created by photons deeper in the solid recombine and hence do not contribute to the photocurrent.

The quantum efficiency Q, defined as the number of charge carriers measured in the external circuit for each photon absorbed, is determined by the flux of minority carriers arriving at the surface j_p and by losses due to surface recombination of electrons and holes. For the case in which surface recombination can be disre-

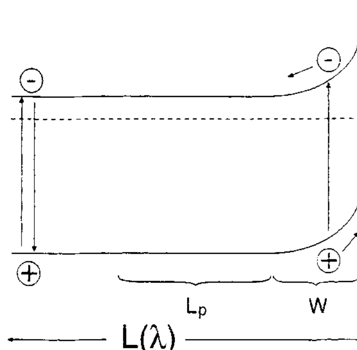

Fig. 4.9 Band diagram showing a depletion layer in an n-type semiconductor at a solution interface. The depletion layer width is given by W, and the minority carrier diffusion length by L_p. $L(\lambda)$ is the penetration depth of the light.

garded, the Gärtner model [80] describes the dependence of the quantum efficiency on the widths of the depletion and absorption layers:

$$Q = \frac{j_p}{e\phi(0)} = 1 - \frac{e^{-\alpha(\lambda)W}}{1 + \alpha(\lambda) L_p}. \tag{10}$$

From this equation it follows that, to ensure a significant quantum efficiency, it is necessary that $1/\alpha(\lambda) < W$ or $1/\alpha(\lambda) < L_p$. To illustrate the importance of these parameters we consider a semiconductor such as TiO_2 or GaP with an indirect band-gap. In this case the absorption coefficient for photon energies just above the fundamental absorption edge is small. For example, the band-gap of GaP is 2.24 eV, corresponding to a wavelength of 554 nm. For λ=514 nm, $\alpha(\lambda)$ is 10^3 cm^{-1} giving $L(\lambda)$ = 10 µm. A typical value for L_p in GaP is 50 nm [24, 61]. The depletion layer width at a band bending of 1 eV is of the order of 50 nm for a moderate doping level. Consequently the retrieval length of minority carriers ($W + L_p$) is only 100 nm which is much smaller than $L(\lambda)$. A quantum efficiency of only about 1% is found in this case (this is in agreement with Eq. 10) [24, 61]. Most of the electron-hole pairs recombine in the bulk of the semiconductor. At higher photon energies corresponding to the direct band-gap in GaP, the absorption coefficient is much larger and the penetration depth of the light smaller. This results in a more effective electron-hole separation and a higher quantum efficiency.

Porosity can affect in two ways the optical properties of a photoelectrode, thus enhancing the quantum efficiency. Losses due to reflection of the incident supra-band-gap light at the interface may be reduced. If the typical dimensions of the porous structures are of the same order of magnitude as the wavelength, then light is scattered in the layer. In this way the effective absorption coefficient can be considerably higher than the corresponding value for the non-porous solid as a result of the increase in optical path length.

Because of the limited dimensions of the porous structures and the enhanced absorption in the porous layer, the minority carrier is generally created close to the interface with the contacting medium within the pores. Consequently, the minority carrier is much more likely to reach the interface. This important effect was first pointed out by Hodes et al. [85] in a paper on photoelectrochemical cells

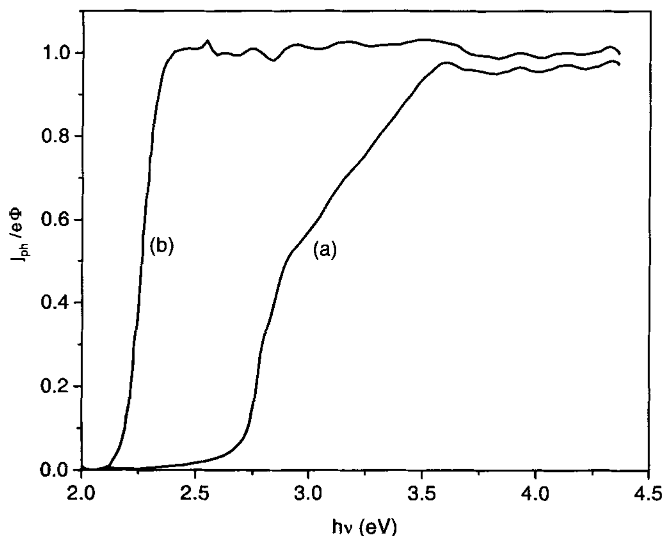

Fig. 4.10 The quantum efficiency $i_{ph}/e\phi$ at + 1 V (SCE) as a function of the photon energy for a polished n-type (100) GaP electrode (curve a) and for the same electrode after anodic dissolution at +10 V (SCE) in the dark for the time needed to pass 16 C cm^{-2} (curve b). The indirect optical transition is at 2.24 eV and the direct transition at 2.76 eV (from Ref. [24]).

based on nanocrystalline CdS and CdSe electrodes. Two cases can be distinguished. If the nanostructures are too small to support a depletion layer, then the minority carrier must reach the interface by diffusion. This requires a diffusion length comparable to the halfwidth of the nanostructure ($D/2 < L_p$). With larger nanostructures, as in macroporous layers, a depletion layer can be formed which follows the internal surface of the porous matrix (see Section 5.1). In this case if the minority carrier is to reach the interface then the halfwidth of the nanostructures must be smaller than the sum of the diffusion length and the space-charge layer thickness ($D/2 < L_p + W$). The photocurrent quantum efficiency is determined ultimately by competition between transfer of the minority carrier across the interface and surface recombination with a majority carrier. If the kinetics of charge transfer are more efficient, then a high quantum efficiency can be obtained, even for a light penetration depth which in a non-porous electrode would give a negligible efficiency.

Results obtained with etched single-crystalline n-type GaP [24, 61], described in Sections 4.3 and 5.1, constitute a spectacular example of the second case ($D/2 < L_p + W$). Curve (a) of Fig. 4.10 shows the spectral response of a non-porous electrode. The quantum efficiency for photons with energy just above the fundamental absorption edge (2.24 eV) is low because, as already pointed out, the penetration depth $L(\lambda)$ of the light is much larger than the retrieval length ($W + L_p$) of the minority carriers. As the photon energy (and thus $\alpha(\lambda)$) is increased, $L(\lambda)$ de-

creases leading to a gain in efficiency. A strong increase is observed at 2.76 eV, which corresponds to the first direct optical transition in GaP. On the other hand, the quantum efficiency of the macroporous electrode (Fig. 4.10, curve b) reaches a value of one for photons of energy close to the fundamental absorption edge. Since the dimensions of the structural units are in the 100 nm range and the minority carrier diffusion length is 50 nm, the criterion for ensuring high efficiency is met for the potential range in which surface recombination is negligible ($U_{sc} > 0.5$ V). Similar results were obtained with porous n-type SiC electrodes [58]. Nanoparticulate TiO_2 electrodes with particle sizes of 30 nm are an example of the case in which $D/2 < L_p$ [86]. With an efficient hole scavenger such as methanol in solution, surprisingly high quantum efficiencies can be realized. The nanocrystalline CdS and CdSe electrodes described by Hodes et al. [85] also correspond to this case.

As far as we are aware there is no evidence for photocurrent originating directly from microporous or mesoporous silicon. Only a very small photocurrent is observed when the porous layer of a p-type electrode in indifferent electrolyte solution is illuminated with light absorbed by the quantized semiconductor [87, 88]. Possibly because of the poor kinetics for the hydrogen evolution reaction, photogenerated electrons and holes are not effectively separated (with the electron reacting at the interface). Instead, they recombine and visible luminescence is observed. The photocurrent measured with p-type and n-type porous silicon electrodes originates from the depletion layer at the interface between the bulk semiconductor and solution. The porous layer acts as a filter for short wavelength light [87, 88]. However, two groups have shown that a thin porous layer can improve the photocurrent-potential characteristics of silicon photoelectrodes: n-type in concentrated HI solution [89] and p-type in a cobalticinium ion/cobatocene (CoC_p^+/CoC_p) solution in acetonitrile [90]. This improvement is attributed to two effects: reduced reflection of the incident light and a decrease in surface recombination as a result of the hydrogen-terminated surface which is produced by anodic etching in HF. The etched electrodes also proved to be markedly more stable. A similar improvement in the photocurrent quantum efficiency as a result of porous etching has been reported for ZnTe [77].

4.5.3 Luminescence

The photoluminescence (PL) of porous silicon has been extensively studied and there has been much discussion regarding the origin of the visible emission [91]. Although complete consensus has not been reached, it is widely accepted that the visible luminescence is due to radiative recombination in quantum-confined structures. While there have been claims on the basis of PL for quantum confinement in porous-etched GaP [60] and GaAs [92], these conclusions have also been disputed [93, 94] and the emission attributed to surface oxides in the porous layer.

In this section we consider in-situ luminescence studies of etched single crystals, both PL and electroluminescence (EL).

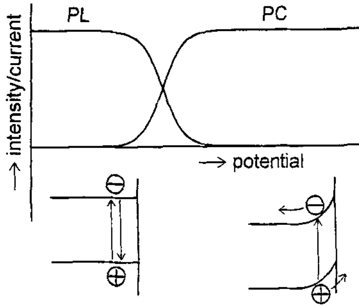

Fig. 4.11 Schematic representation of the potential dependence of the photocurrent (PC) and the photoluminescence intensity (PL) of an n-type semiconductor in an indifferent electrolyte solution. Energy band diagrams are shown for the illuminated semiconductor under flat band and depletion conditions.

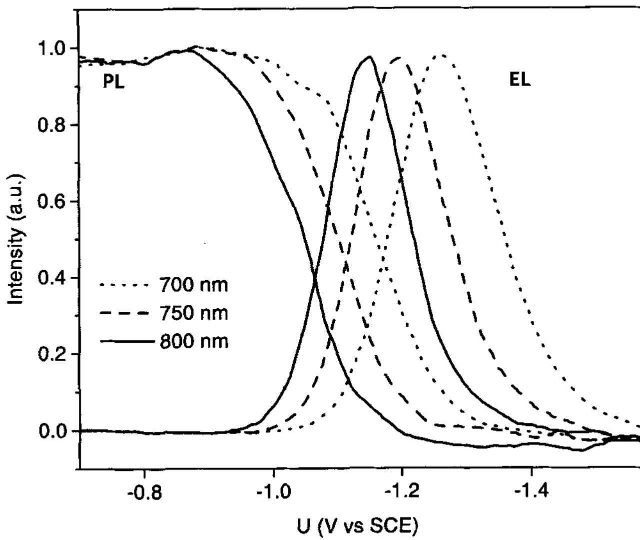

Fig. 4.12 The potential dependence of the emission intensity from a porous n-type silicon electrode in H_2SO_4 solution. Three emission wavelengths are shown. For the photoluminescence (PL) measurements an argon-ion laser was used as excitation source. Electroluminescence (EL) was excited by reduction of peroxydisulfate, added to the H_2SO_4 solution (from Ref. [96]).

In a non-porous electrode, photogenerated electron-hole pairs recombining radiatively in the bulk will give rise to photoluminescence (PL) [95]. According to the Gärtner model the PL intensity, I_{PL}, is given by:

$$I_{\mathrm{PL}} = \frac{\kappa\phi(0)}{1 + a(\lambda)L_{\mathrm{p}}} e^{-a(\lambda)W} \tag{11}$$

where κ is the ratio of the rate of radiative recombination to the total recombination rate. Clearly, the potential-dependence of the emission (as contained in Eq. 11) is different from that of the photocurrent (Eq. 9). Both are shown schema-

tically in Fig. 4.11. As the potential is decreased from positive values towards the flat-band potential the photocurrent decreases to zero while the PL intensity increases to a maximum ($W = 0$, $I_{max} = \kappa\phi(0)/(1 + a(\lambda)L_p)$.

The general features of the I_{PL}-U curve for a macroporous electrode, in which $D/2 > L_p$, are not expected to be markedly different from those of a flat electrode. However, since the space-charge region of the porous electrode is much less uniform, as is clear from the capacitance measurements described in Section 5.1, and the exciting light is more effectively absorbed in the layer, one might expect to see some differences. As far as we are aware such effects have not been studied.

The potential dependence of the strong PL of microporous and mesoporous silicon observed in indifferent electrolyte solution is, on the other hand, markedly different from that of a bulk electrode. Under conditions corresponding to depletion in a non-porous electrode, potential-independent emission is observed (Fig. 4.12a). Charge carriers generated within nanocrystallites are not spatially separated but recombine. The photoluminescence is quenched at potentials negative with respect to U_{fb}, a process that has been attributed to Auger recombination [96] or to hydrogen-mediated recombination [97]. The potential at which the PL intensity decreases depends on the wavelength of the emitted light: emission at lower energy (i.e. from larger crystallites) is quenched at more positive potentials than the high energy emission (from the smallest crystallites). This has been attributed to a higher barrier for transfer of an electron from bulk silicon to small, more confined particles than to larger particles [96].

There are numerous ways in which electron-exchange reactions can generate EL in porous silicon electrodes; these have been reviewed recently [95]. Here we confine the discussion to visible light emission due to simple minority carrier injection. For example, the methylviologen radical cation in solution can inject electrons into the conduction band of porous p-type silicon. If, under accumulation conditions, majority carriers (holes) are supplied to the porous layer from the substrate, visible EL is observed. Similarly, when holes are injected from solution into porous n-type silicon and electrons are supplied from the substrate, visible emission is also observed. The most efficient and widely studied system is that in which peroxydisulfate ($S_2O_8^{2-}$) is used as oxidizing agent. The potential dependence of the integrated emission is shown in Fig. 4.12(b). Onset of luminescence is at a potential negative with respect to the onset potential for reduction of $S_2O_8^{2-}$. The emission passes through a maximum and is quenched at negative potential. Quenching is attributed to the same mechanisms as proposed for PL quenching. An interesting aspect of the emission from this system is its "voltage tunability": the emission maximum shifts to shorter wavelength as the potential is made more negative [96]. It has been suggested that this effect is also due to quantum confinement. Because of band edge mismatch supply of majority carriers to porous structures depends on their size, a more negative potential is required to "feed" smaller structures with electrons; these electrons are required for the first step of the $S_2O_8^{2-}$ reduction and the subsequent hole injection reaction.

4.5.4 Electron Transport in Porous Semiconductors

Because of the permeation of the semiconducting solid phase by the electrolyte solution on a 1 to 100 nm scale, photogenerated minority carriers are transferred effectively to the solution. As we have seen, this feature leads to an enhanced photocurrent quantum yield. It also opens the possibility for the study of electron transport, since photogenerated electrons have to travel over macroscopic distances through the porous system to reach the conducting phase at the back side.

The study of electron transport in porous semiconductors has attracted the interest of groups in several fields, from statistical physics to solar physics and chemical catalysis [10, 61, 85, 86, 98–105]. Preliminary work showed that the transport of photogenerated electrons through a porous electrode is very slow [98–100]. The characteristic transit time is in the 10^{-3} s range. For comparison, the time it takes a charge carrier to travel across the depletion layer (about 100 nm in width) present at the interface of a bulk single crystalline semiconductor electrode is 10^{-9} s, i.e. six orders of magnitude faster. This suggests that the motion of charge carriers in porous semiconductors is strongly attenuated. This might be due to the presence of grain boundaries, to electrical interactions between the traveling electron and dipole molecules in the electrolyte and to trapping of electrons in localized levels in the band-gap. Study of the attenuation of electron flow in porous systems is also of practical importance: a long residence time of the photogenerated electrons in the porous structure may lead to electron back-transfer to an oxidized species in the electrolyte, hence to electron-hole recombination via the permeated electrolyte phase [10, 61, 85, 104, 105]. This is a loss mechanism in photoelectrochemical solar cells.

The flow of a photocurrent in the external circuit implies that there is a directed electron flux in the porous system, though there is, a priori, no electric field in the main direction of electron motion, i.e. towards the conducting contact (the electron sink). The motion of electrons from where they are generated to the sink is due to diffusion. The statistical driving force behind this directed electron flux corresponds to the gradient of the electrochemical potential [Fermi-level] of the free electrons. Vanmaekelbergh and de Jongh showed that the electrochemical potential of the free electrons decays by one to a few kT over the width of the porous layer (denoted d) [106]. The driving force is hence about kT/d, and was shown to be independent of the incident light intensity (photogeneration rate). From a thermodynamic point of view, the decay of the electrochemical potential in the porous system leads to a loss in the work that can be performed in the external circuit by the photogenerated electrons. This is the price that must be paid for a statistically directed electron flow.

The characteristic time that electrons take to travel through the porous system (i.e. transit time) cannot be obtained from the steady-state photocurrent. Instead, the transient photocurrent response in the external circuit upon a perturbation of the light intensity must be analyzed. This method has been extensively used in the study of electron transport in disordered, i.e. amorphous, semiconductors

[107–112]. When a strong light pulse is used, the photocurrent response is often typical of a dispersive transport process. This means that the transport is not characterized by an average transit time characteristic for the majority of the photogenerated electrons. Thus, the transport of individual electrons takes a time that can vary over many orders of magnitude. Strong light pulses have also been applied to porous photoelectrodes, but a consistent interpretation of the photocurrent transients remains a matter of debate [98–100].

In contrast, the study of electron transport in porous semiconductor electrodes under steady-state conditions, using a small harmonic light intensity modulation superimposed on the background light intensity, has proved to be very successful [86, 101–103]. This method is referred to as Intensity Modulated Photocurrent Spectroscopy (IMPS). The reason that electron transport is regular (i.e. non-dispersive) under steady-state conditions has been discussed by Vanmaekelbergh and de Jongh [113]. It has been shown by several groups that the characteristic time of the opto-electrical transfer function $\tilde{j}(\omega)/e\tilde{\Phi}(\omega)$, where $\tilde{j}(\omega)$ is the modulated photocurrent and $\tilde{\Phi}(\omega)$ the modulated light intensity, gives the average transit time τ_d of the electrons through the system, when the lifetime of the electrons for recombination is considerably longer than τ_d. The spectrum of the opto-electrical transfer function $\tilde{j}(\omega)/e\tilde{\Phi}(\omega)$ is measured as a function of important parameters such as the thickness of the porous layer, temperature and background light intensity. Electron transport has been investigated with the IMPS technique in a variety of porous electrodes, including bare and dye-sensitized particulate TiO_2, nanoparticulate ZnO and macroporous random networks of GaP [86, 101–103]. A characteristic and almost general feature is a transit time τ_d that decreases considerably with increasing steady-state light intensity; i.e. $\tau_d \propto \phi^{-\gamma}$ where γ is between 1/2; and 1, depending on the system studied. This feature is indicative of multiple trapping of the electrons in localized electron levels with energy located in the band-gap. Under steady-state conditions, the attenuation of electron transport is mainly due to trapping in states close to the Fermi-level [86, 101–103, 114]. It can be shown that the transit time is given by the average number of trapping events times the localization time in levels close to the Fermi-energy. Interestingly, it has been shown that all types of levels attenuate electron transport in the same way. The only important parameter is the energetic distribution of the electron levels (the density of states or DOS). Since the position of the Fermi-level in the band-gap can be shifted by variation of the background light intensity, it is possible to map the DOS. Presumably, the electron levels are localized at the internal semiconductor/electrolyte interface. Thus, measurement of the transport characteristics of porous electrodes with IMPS may also be considered as a photoelectrochemical characterization technique. However, studies presented in the literature focus mainly on the fundamental aspects of the transport characteristics, not on the mapping of band-gap states [86, 101–103]. A wide public does not yet seem to recognize the potential of IMPS as a physical and photoelectrochemical characterization method.

4.6 Applications of Porous-etched Semiconductors

The "oldest" of the porous-etched semiconductors, silicon, is clearly the one most widely used in practice. Reports on two recent meetings devoted to "Porous Semiconductors – Science and Technology" [114, 115] give a good impression of the wide range of applications of porous silicon. One of the first of these was in semiconductor-on-insulator (SOI) technology [4]. A new approach in this field, ELTRAN (Epitaxial Layer TRANsfer), allows the transfer of epitaxial layers for SOI structures and reuse of the seed wafers [115, 116]. Porous silicon can serve as sacrificial layer in microelectromechanical systems (MEMS) [117]. Müller et al. [115] describe a novel approach based on the high perfection of macroporous silicon with billions of identical pores on one wafer for fabricating particle pumps. Macroporous silicon is also being considered as a material for the integration of capacitors in circuit technology [118]. Mesoporous silicon can serve as a membrane in separation technology [119] and can be used for local thermal isolation in devices such as gas-flow sensors based on thermal detection [120].

The discovery of visible luminescence from mesoporous and microporous silicon [7, 8] seemed to herald a new era of optoelectronics. While interesting light-emitting devices have been fabricated [9, 115, 121] there are still problems to be solved before the technology can be considered viable. These include the chemical stability of the porous material and the low electroluminescence efficiency.

On the other hand, porous silicon is finding application in a number of new fields such as microphotonics [122] and solar cells [123, 124]. Lérondel et al. [125] describe the intriguing possibility of making three-dimensional photonic structures in silicon by prepatterning the surface of the wafer and modulating the porosity by periodic modulation of the current density during anodic etching. A recent development in sensor applications involves the use of interferometric detection techniques which allow for extremely high sensitivity [115, 126].

Of particular interest is the use of silicon for applications in the field of biology [115]. Porous silicon has been shown to provide an excellent coupling matrix for enzymes in micro-bioreactors [127]. Porous silicon has been used as a substrate for culturing neurons [115, 128] and for making biosensors [129]. Such applications profit from the enormous internal surface area of the semiconductor. In addition, since silicon is biocompatible, devices based on porous silicon can be used for in-vivo monitoring [115, 129]. An added attraction may be the fact that porous silicon is biodegradable so that components, once no longer needed, do not have to be surgically removed from the body [115]; in a physiological environment silicon is resorbed and the resorbability can, in principle, be tuned over weeks or years.

In contrast to silicon there are at present few reported applications for other porous-etched semiconductors. However, there are certainly many potential uses both in actual devices and in fabrication technology. The success of such applications will probably depend on the reproducibility of the etching process.

SiC is closest to Si in its electrochemical properties. Porous SiC can, like porous Si, be thermally oxidized under relatively mild conditions [55]. This process could

be interesting for electrical insulation in devices or for making components with a high capacitance [54, 57]. Shor and coworkers have shown that SiC can be patterned by thermally oxidizing a patterned porous layer and subsequently dissolving the oxide in HF solution [55]. Such possibilities make SiC an interesting material for MEMS applications.

The potential applications of porous-etched III–V and II–VII materials would appear to be mainly in the fields of optics and optoelectronics. For example, Takizawa and coworkers [69, 130] have made high-density patterns of ordered, anisotropic, monodisperse pores in InP by anodic etching of the (111)A face. The authors show that these materials are birefringent at wavelengths used for optical communication. The materials can be easily integrated into optoelectronic systems [130]. The process of anisotropic porous etching is also attractive for the fabrication of high-density quantum wire and box structures with a low size fluctuation [130].

Schmuki et al. [131, 132] have shown how porous etching can be used to make visible light-emitting micropatterns in GaAs by a direct writing process. A focused beam is used to implant Si^{2+} ions into an n-type wafer. Under anodic polarization the areas damaged by implantation are etched selectively to give a porous layer. The porous material shows visible photoluminescence at green-yellow wavelengths. In principle, patterns with a spatial resolution of 100 nm could be possible with this approach making the system suitable for novel light-emitting devices.

Porous-etched semiconductors may be interesting for photonic applications. Macroporous GaP, produced by photoanodic etching, is the most strongly scattering material for visible light reported to date [62]. There is evidence for the onset of Anderson localization in this material [133]. This property would make porous GaP a candidate for applications such as diffusive totally reflecting mirrors.

As outlined in Section 5.2 porous etching can greatly enhance the quantum efficiency of semiconductor devices which convert light into electrical energy (photodiodes, solar cells). The most significant improvement is expected for semiconductors with an indirect band-gap and/or a small value of the minority carrier diffusion length. Such effects have been demonstrated for GaP [24], SiC [58] and TiO_2 [134] but have not yet been incorporated into actual devices based on porous-etched single crystal or polycrystalline semiconductors.

4.7 Conclusions

This review, though not exhaustive, shows that many single-crystalline semiconductors can be made porous by anodic etching. Both Si and SiC become porous under "normal" etching conditions, i.e. the p-type semiconductor is anodically dissolved in the dark while the n-type semiconductor undergoes photoanodic decomposition. In most other cases depletion layer breakdown in n-type electrodes is required to generate porosity. There have been reports of porous etching in p-type GaAs and CdTe, associated with layer formation. There is no satisfactory explana-

tion for the essential difference between the (photo)electrochemical properties of Si and SiC and those of other compound semicoconductors.

The morphology of porous silicon has been studied in depth, that of III–V semiconductors to a lesser extent. In Si, the pores grow in the ⟨100⟩ directions while, for the III–V materials, pores in the ⟨111⟩ direction are generally observed. Much less attention has been devoted to the morphology of other porous semiconductors.

Various models are available for describing pore initiation and propagation. These have been used in a somewhat "ad hoc" fashion and are rather simplistic. Ross and coworkers [64] have been successful in explaining the striking differences between Si and GaAs by assuming that etching is favored by the high electric field at pore tips and that atoms are removed preferentially from surface kink sites. However, despite the elegance of their results, the authors admit that the predictive power of their model is limited. More sophisticated models combined with simulation are clearly required.

Porous semiconductors show a wide range of interesting chemical, optical, electrical and optoelectrical properties. Models aimed at describing the relationship between morphology and physical properties are, in general, still at a primitive stage. There is clearly a host of possible applications for such systems. Up to now, the emphasis has been mainly on porous silicon. However, we foresee interesting applications for other porous-etched semiconductors.

References

1 A. Uhlir Jr., *Bell Systems Techn. J.* **1956**, *35*, 333.
2 R. Memming, G. Schwandt, *Surf. Sci.* **1966**, *4*, 109.
3 M. J. J. Theunissen, *J. Electrochem. Soc.* **1972**, *119*, 351.
4 Y. Kato, T. Ito, A. Hiraki, *Appl. Surf. Sci.* **1989**, *41/42*, 614.
5 P. Steiner, A. Richter, W. Lang, *J. Micromech. Microeng.* **1993**, *3*, 32.
6 M.T. Kelly, J. K. M. Chun, A. B. Bocarsly, *Science* **1996**, *382*, 215.
7 L. T. Canham, *Appl. Phys. Lett.* **1990**, *57*, 1046.
8 A. G. Cullis, L. T. Canham, *Nature* **1991**, *353*, 335.
9 K. D. Hirschman, L. Tsybeskov, S. P. Duttagupta, P. M. Fauchet, *Nature* **1996**, *384*, 338.
10 B. O'Regan, M. Grätzel, *Nature* **1991**, *353*, 737.
11 R. Cinnsealach, G. Boschloo, S. N. Rao, D. Fitzmaurice, *Solar Energy Materials and Solar Cells* **1998**, *55*, 215.
12 R. van de Krol, A. Goossens, E. A. Meulenkamp, *J. Electrochem. Soc.* **1999**, *146*, 3150.
13 P. H. L. Notten, J. E. A. M. van den Meerakker, J. J. Kelly, Etching of III–V Semiconductors. An Electrochemical Approach, *Elsevier Advanced Technology*, Oxford, **1991**.
14 J. J. Kelly, D. Vanmaekelbergh, *Chapter 3 of "Semiconductor Micromachining" Vol. 1 Fundamental Electrochemistry and Physics*, Wiley, Chichester **1998**.
15 M. Koinuma, K. Uosaki, *Surf. Sci.* **1994**, *311*, L737.
16 J. C. Tranchart, L. Hollan, R. Memming, *J. Electrochem. Soc.* **1978**, *125*, 1185.
17 P. Schmuki, J. Fraser, C. M. Vitus, M. J. Graham, H. S. Isaacs, *J. Electrochem. Soc.* **1996**, *143*, 3316.
18 P. Schmuki, L.E. Erickson, D. J. Lockwood, B. F. Mason, J. W. Fraser, G. Champion, H. J. Labbé, *J. Electrochem. Soc.* **1999**, *146*, 735.

19 I. E. Vermeir, K. Van den Kerchove, W. P. Gomes, *J. Electroanal. Chem.* **1991**, *313*, 141.

20 B. P. Minks, D. Vanmaekelbergh, J. J. Kelly, *J. Electroanal. Chem.* **1989**, *273*, 133.

21 J. van de Ven, H. J. P. Nabben, *J. Electrochem. Soc.* **1990**, *137*, 1603.

22 J. van de Ven, H. J. P. Nabben, *J. Electrochem. Soc.* **1999**, *138*, 144.

23 T. J. Barton, L. M. Bull, W. G. Klemperer, D. A. Loy, B. McEnaney, M. Misono, P. A. Monson, G. Pez, G. W. Scherer, J. C. Vartuli, O. M. Yaghi, *Chem. Mater.* **1999**, *11*, 2633.

24 B. H. Erné, D. Vanmaekelbergh, J. J. Kelly, *J. Electrochem. Soc.* **1996**, *143*, 305.

25 V. Lehmann, *J. Electrochem. Soc.* **1993**, *140*, 2836.

26 R. M. Osgood, Jr, A. Sanchez-Rubio, D. J. Ehrlich, V. Daneu, *Appl. Phys. Lett.* **1982**, *40*, 391.

27 M. M. Carrabba, N. M. Nguyen, R. D. Rauh, *J. Electrochem. Soc.* **1987**, *134*, 1857.

28 R. L. Smith, S. D. Collins, *J. Appl. Phys.* **1992**, *71*, R1.

29 V. P. Parkhutik, V. I. Shershulsky, *J. Phys. D: Appl. Phys.* **1992**, *25*, 1258.

30 V. P. Parkhutik, J. M. Albella, J. M. Martinez-Duart, J. M. Gómez-Rodriguez, A. M. Baró, V. I. Shershulsky, *Appl. Phys. Lett.* **1993**, *62*, 366.

31 W. Shin, T. Hikosaka, W.-S. Seo, H.S. Ahn, N. Sawaki, K. Kuomoto, *J. Electrochem. Soc.* **1998**, *145*, 2456.

32 J. Erlebacher, K. Sieradzki, P. C. Searson, *J. Appl. Phys.* **1994**, *76*, 182.

33 G. Bomchil, A. Halimaoui, I. Sagnes, P. A. Badoz, I. Berbezier, P. Perret, B. Lambert, G. Vincent, L. Garchery, J. L. Regolini, *Appl. Surf. Sci.* **1993**, *65/66*, 394.

34 E. S. Kooij, D. Vanmaekelbergh, *J. Electrochem. Soc.* **1997**, *144*, 1296.

35 R. B. Wehrspohn, F. Ozanam, J.-N. Chazalviel, *J. Electrochem. Soc.* **1999**, *146*, 3309.

36 V. Lehmann, U. Gösele, *Appl. Phys. Lett.* **1991**, *58*, 856.

37 J. N. Kidder, Jr, P. S. Williams, T. P. Pearsall, D. T. Schwartz, B. Z. Nosho, *Appl. Phys. Lett.* **1992**, *61*, 2896.

38 M. J. Eddowes, *J. Electroanal. Chem.* **1990**, *280*, 297.

39 S.-F. Chuang, S. D. Collins, R. L. Smith, *Appl. Phys. Lett.* **1989**, *55*, 675.

40 V. Lehmann, H. Föll, *J. Electrochem. Soc.* **1990**, *137*, 653.

41 S. Ottow, V. Lehmann, H. Föll, *J. Electrochem. Soc.* **1996**, *143*, 385.

42 S. Rönnebeck, J. Carstensen, S. Ottow, H. Föll, *Electrochem. Solid State Lett.* **1999**, *2*, 126.

43 E. Galun, C. Reuben, S. Matlis, R. Tenne, C. Lévy-Clément, *J. Phys. Chem.* **1995**, *99*, 4132.

44 Y. Kang, J. Jorné, *J. Electrochem. Soc.* **1993**, *140*, 2258.

45 Y. Kang, J. Jorné, *Appl. Phys. Lett.* **1993**, *62*, 2224.

46 V. Lehmann, S. Rönnebeck, *J. Electrochem. Soc.* **1999**, *146*, 2968.

47 E. A. Ponamarev, C. Lévy-Clément, *Electrochem. Solid State Lett.* **1998**, *1*, 42.

48 L. A. Jones, Ö. Yüksekeŕ, D. F. Thomas, *J. Vac. Sci. Technol. A* **1996**, *14*, 1505.

49 E. S. Kooij, K. Butter, J. J. Kelly, *Electrochem. Solid State Lett.* **1999**, *2*, 178.

50 Y. H. Zhang, X. J. Li, L. Zheng, Q. W. Chen, *Phys. Rev. Lett.* **1998**, *81*, 1710.

51 W. T. Pike, A. Ksendzov, R. W. Fathauer, T. George, *J. Vac. Sci. Technol. B* **1993**, *11*, 1401.

52 A. Ksendzov, R. W. Fathauer, T. George, W. T. Pike, R. P. Vasquez, *Appl. Phys. Lett.* **1993**, *63*, 200.

53 M. Schoisswohl, M. Rosenbauer, J. L. Cantin, S. Lebib, H. J. von Bardeleben, J. L. Fave, J. Cernogora, G. Amato, A. Rossi, *J. Appl. Phys.* **1996**, *79*, 9301.

54 J. van de Lagemaat, D. Vanmaekelbergh, J. J. Kelly, *J. Appl. Phys.* **1998**, *83*, 6089.

55 J. S. Shor, I. Grimberg, B.-Z. Weiss, A. D. Kurtz, *Appl. Phys. Lett.* **1993**, *62*, 2836.

56 J. S. Shor, L. Bemis, A. D. Kurtz, I. Grimberg, B. Z. Weiss, M. F. MacMillan, W. J. Choyke, *J. Appl. Phys.* **1994**, *76*, 4045.

57 A. O. Konstantinov, C. I. Harris, E. Janzén, *Appl. Phys. Lett.* **1994**, *65*, 2699.

58 J. van de Lagemaat, M. Plakman, D. Vanmaekelbergh, J. J. Kelly, *Appl. Phys. Lett.* **1996**, *69*, 2246.

59 B. D. Chase, D. B. Holt, *J. Electrochem. Soc.* **1972**, *119*, 314.

60 A. Anedda, A. Serpi, V.A. Karavanskii, I. N. Tiginyanu, M. V. Ichizli, *Appl. Phys. Lett.* **1995**, *67*, 3316.

61 B. H. Erné, D. Vanmaekelbergh, J. J. Kelly, *Adv. Mater.* **1995**, *7*, 739.

62 F. J. P. Schuurmans, D. Vanmaekelbergh, J. van de Lagemaat, A. Lagendijk, *Science* **1999**, *284*, 141.

63 G. Oskam, A. Natarajan, P. C. Searson, F. M. Ross, *Appl. Surf. Sci.* **1997**, *119*, 160.

64 F. M. Ross, G. Oskam, P. C. Searson, J. M. Macauley, J. A. Liddle, *Phil. Mag. A* **1997**, *75*, 525.

65 D. V. Podlesnik, H. H. Gilgen, R. M. Osgood, Jr., *Appl. Phys. Lett.* **1984**, *45*, 563.

66 D. V. Podlesnik, H. H. Gilgen, A. E. Wilmer, R. M. Osgood, Jr., *J. Opt. Soc. Am. B* **1986**, *3*, 775.

67 D. V. Podlesnik, H. H. Gilgen, R. M. Osgood, Jr., *Appl. Phys. Lett.* **1986**, *48*, 496.

68 M. M. Carrabba, N. M. Nguyen, R. D. Rauh, *Mat. Res. Soc. Symp.* **1987**, *75*, 665.

69 Takizawa, S. Arai, M. Nakahara, *Jpn. J. Appl. Phys.* **1994**, *33*, L643.

70 N. G. Ferreira, D. Soltz, F. Decker, L. Cescato, J. *Electrochem. Soc.* **1995**, *142*, 1438.

71 A. Hamamatsu, C. Kaneshiro, H. Fujikura, H. Hasegawa, *J. Electroanal. Chem.* **1999**, *473*, 223.

72 T. D. Lowes, D. T. Cassidy, *J. Appl. Phys.* **1990**, *68*, 814.

73 C. Youtsey, L. T. Romano, I. Adesida, *Appl. Phys. Lett.* **1998**, *73*, 797.

74 R. Tenne, G. Hodes, *Surf. Sci.* **1983**, *135*, 453.

75 R. Tenne, H. Flaisher, R. Triboulet, *Phys. Rev. B* **1984**, *29*, 5799.

76 B. H. Erné, A. Million, J. Vigneron, C. Mathieu, C. Debiemme-Chouvy, A. Etcheberry, *Electrochem. Solid State Lett.* **1999**, *2*, 619.

77 F. Zenia, C. Lévy-Clement, R. Triboulet, R. Könenkamp, K. Ernst, M. Saad, M. C. Lux-Steiner, *Appl. Phys. Lett.* **1999**, *75*, 531.

78 Y. Nakato, H. Akanuma, J. Shimizu, Y. Magari, *J. Electroanal. Chem.* **1995**, *396*, 35.

79 T. Sugiura, T. Yoshida, H. Minoura, *Electrochem. Solid State Lett.* **1998**, *1*, 175.

80 J. J. Kelly, D. Vanmaekelbergh, *Electrochim. Acta* **1998**, *43*, 2773.

81 D. Vanmaekelbergh, A. Koster, F. Iranzo Marin, *Adv. Mater.* **1997**, *9*, 573.

82 W.-M. Shen, M. Tomkiewicz, C. Lévy-Clement, *J. Appl. Phys.* **1994**, *76*, 3635.

83 L. M. Peter, D. J. Riley, R. I. Wielgosz, *Appl. Phys. Lett.* **1995**, *66*, 2355.

84 L. M. Peter, R. I. Wielgosz, *Appl. Phys. Lett.* **1996**, *69*, 806.

85 G. Hodes, I. D. J. Howell, L. M. Peter, *J. Electrochem. Soc.* **1992**, *139*, 3136.

86 P.E. de Jongh, D. Vanmaekelbergh, *J. Phys. Chem.* **1997**, *101*, 2716.

87 H. Noguchi, T. Kondo, K. Uosaki, *J. Phys. Chem. B* **1997**, *101*, 4978.

88 B. Gelloz, A. Bsiesy, *Electrochem. Soc. Proc.* **1997**, *97-7*, 92.

89 C. Lévy-Clément, A. Lagoubi, M. Neumann-Spallart, R. Rodot, R. Tenne, *J. Electrochem. Soc.* **1991**, *138*, L69.

90 D. Mao, K. J. Kim, Y. S. Tsuo, A. J. Frank, *J. Phys. Chem.* **1995**, *99*, 3643.

91 A. G. Cullis, L. T. Canham, P. D. J. Calcott, *J. Appl. Phys.* **1997**, *82*, 909.

92 P. Schmuki, D. J. Lockwood, H. J. Labbé, J.W. Fraser, *Appl. Phys. Lett.* **1996**, *69*, 1620.

93 A. Meijerink, A. A. Bol, J. J. Kelly, *Appl. Phys. Lett.* **1996**, *69*, 2801.

94 X. Li, P. W. Bohn, *J. Electrochem. Soc.* **2000**, *147*, 1740.

95 J. J. Kelly, E. S. Kooij, E. A. Meulenkamp, *Electrochim. Acta* **1999**, *45*, 561.

96 L. M. Peter, D. J. Riley, R. I. Wielgosz, P. A. Snow, R. V. Penty, I. H. White, E. A. Meulenkamp, *Thin Solid Films* **1996**, *276*, 123.

97 J. J. Kelly, E. S. Kooij, D. Vanmaekelbergh, *Langmuir* **1999**, *15*, 3666.

98 K. Schwarzburg, F. Willig, *Appl. Phys. Lett.* **1991**, *58*, 2520.

99 F. Cao, G. Oskam, G. J. Meijer, P. C. Searson, *J. Phys. Chem.* **1996**, *100*, 17021.

100 A. Solbrand, H. Linström, H. Rensmo, A. Hagfeldt, S.-E. Lindquist, S. Södergren, *J. Phys. Chem. B* **1997**, *101*, 2514.

101 D. Vanmaekelbergh, F. Iranzo Marín, J. van de Lagemaat, *Ber. Bunsenges. Phys. Chem.* **1996**, *100*, 616.

102 P. E. de Jongh, D. Vanmaekelbergh, *Phys. Rev. Lett.* **1996**, *77*, 3427.

103 L. Dloczik, O. Ileperuma, I. Lauermann, L. M. Peter, E. A. Ponomarev, G. Redmond, N. J. Shaw, I. Uhlendorf, *J. Phys. Chem. B* **1997**, *101*, 10281.

104 U. Bach, D. Lupo, P. Comte, J. E. Moser, F. Weissörtel, J. Salbeck, H. Spreitzer, M. Grätzel, *Nature* **1998**, *395*, 583 (and references therein).

105 A. Köhler et al., *Nature* **1998**, *392*, 903.

106 D. Vanmaekelbergh, P. E. de Jongh, *J. Phys. Chem. B* **1999**, *103*, 747.

107 R. A. Street, "Hydrogenated Amorphous Silicon" Ed. R. W. Cahn, E. A. Davis, I. M. Ward, *Cambridge Solid State Science Series*, Cambridge, **1991**.

108 H. Scher, M. F. Schlesinger, J. T. Bendler, *Physics Today* **1991**, 26.

109 H. Scher, E. W. Montroll, *Phys. Rev. B* **1975**, *12*, 2455.

110 B. Hartenstein, H. Bässler, A. Jakobs, K. W. Kehr, *Phys. Rev. B* **1996**, *54*, 8574.

111 A. F. Seynhaeve, R. P. Barclay, G. J. Adriaenssens, J. M. Marshall, *Phys. Rev. B* **1989**, *39*, 10196.

112 A. Jakobs, K. W. Kehr, *Phys. Rev. B* **1993**, *48*, 8780.

113 D. Vanmaekelbergh, P. E. de Jongh, *Phys. Rev. B* **2000**, *61*, 4699.

114 A collection of papers presented at the First International Conference on Porous Semiconductors – Science and Technology, held at Mallorca, Spain **1998** published in *J. Porous Mat.* **2000**, *7*, 9–414.

115 Extended Abstracts of the Second International Conference on Porous Semiconductors – Science and Technology, Madrid, Spain **2000**.

116 T. Yonehara, K. Sakaguchi, N. Sato, *Appl. Phys. Lett.* **1994**, *64*, 2108.

117 P. Steiner, A. Richter, W. Lang, *J. Micromech. Microeng.* **2000**, *3*, 32.

118 J. E. A. M. van den Meerakker, R. J. G. Elfrink, F. Roozeboom, J. F. C. M. Verhoeven, *J. Electrochem. Soc.* **2000**, *147*, 2757.

119 R. W. Tjerkstra, J. G. E. Gardeniers, M. C. Elwenspoek, A. van den Berg, Proc. MTAS '98, **1998**, 133.

120 K. Kaltsas, A. G. Nassiopoulou, *Sensors and Actuators A* **1999**, *76*, 133.

121 H. A. Lopez, P. M. Fauchet, *Appl. Phys. Lett.* **1999**, *75*, 3989.

122 F. Müller, A. Birner, U. Gösele, V. Lehmann, S. Ottow, H. Föll, *J. Porous Mat.* **2000**, *7*, 201.

123 P. Menna, S. Tsuo, in: Properties of Porous Silicon, Ed. L. Canham, EMIS Datareviews Series No 18, INSPEC London, **1997**, 384.

124 S. P. Duttagupta, P. M. Fauchet, A. C. Ribes, H. F. Tiedje, S. Damas-Kinos, T. E. Dixon, D. E. Brodie, S. K. Kurinec, *Solar Energy Materials and Solar Cells* **1998**, *52*, 271.

125 G. Lérondel, T. Yao, Abstract 0-54 of Ref. [115].

126 S. E. Létant, M. J. Sailor, *Adv. Mater.* **2000**, *12*, 355.

127 J. Drott, K. Lindstrom, K. Rosengren, L. Laurell, *J. Micromech. Microeng.* **1997**, *7*, 14.

128 S. C. Bayliss, L. D. Buckberry, Fletcher, M. J. Tobin, *Sensors and Actuators A* **1999**, *74*, 139.

129 L. T. Canham, *Adv. Mater.* **1995**, *7*, 1055.

130 E. Kikuno, M. Amiotti, T. Takizawa, S. Arai, *Jpn. J. Appl. Phys.* **1995**, *34*, 177.

131 P. Schmuki, L. E. Erickson, D. J. Lockwood, J. W. Fraser, G. Champion, H.J. Labbé, *Appl. Phys. Lett.* **1998**, *72*, 1039.

132 P. Schmuki, L. E. Erickson, D. J. Lockwood, B. F. Mason, J. W. Fraser, G. Champion, H. J. Labbé, *J. Electrochem. Soc.* **1999**, *146*, 735.

133 F. J. P. Schuurmans, M. Megens, D. Vanmaekelbergh, A. Lagendijk, *Phys. Rev. Lett.* **1999**, *83*, 2183.

134 A. Tsujiko, T. Kisumi, Y. Magari, K. Murakoshi, Y. Nakato, *J. Phys. Chem. B* **2000**, *104*, 4873.

Electrochemistry of Nanomaterials
by *Gary Hodes (Ed.)*
© WILEY-VCH Verlag GmbH, 2001

5
Electrochemical Formation and Modification of Nanocrystalline Porous Silicon

Will H. Green, Sonia Létant and *Michael J. Sailor*

5.1
Introduction

The development of silicon-integrated circuit technology during this century ranks as one of the most important events in modern history and its impact on science and society has been incredible. Despite the tremendous amount known about Si and SiO_2, our ability to manipulate and modify these materials continues to improve and there is every indication that this trend will persist for quite some time. Visible light emission from a Si electrode in an electrochemical cell was first reported in 1960 by Gee at Texas Instruments [1]. It would be another three years before the same company produced an integrated circuit containing four silicon transistors. Over the next thirty years, intensive research and development efforts would result in silicon circuits containing 10^6 transistors per chip, yet, surprisingly, Gee's discovery was largely overlooked during this same time period. In 1990, the light emitting properties of Si were rediscovered when Leigh Canham reported efficient room temperature photoluminescence (PL) from anodically etched Si in an HF electrolyte [2]. The electrochemically etched material is known as porous Si, and it consists of a matrix of nanocrystalline Si domains. The visible light emission was attributed to quantum confinement effects in the nanocrystallites. Canham's report sparked an intense period of research by workers in many disciplines with the aim of incorporating silicon optoelectronic functions into conventional silicon microelectronics.

This article reviews aspects of the electrochemistry of nanocrystalline porous Si. We will begin with an introduction to semiconductor electrochemistry leading to a description of the electrochemical reactions responsible for the formation of nanocrystalline porous Si. We will discuss some of the interesting layered and patterned structures that can be fabricated from porous Si by manipulation of the electrochemical conditions. As Gee showed in 1960, electrochemical reactions can be used to induce light emission from the material, and the electrochemical reactions involved in electrochemiluminescence will be discussed. We will then present electrochemical reactions that have been used to modify the surface properties of porous Si. We will finish with a discussion of potential applications for this material.

5.2 Synthesis of Nanocrystalline Porous Si, Ge, GaAs, GaP, and InP

In 1956, during a study of electropolishing on silicon single crystals in aqueous hydrofluoric acid (HF), Uhlir [3] observed that under particular current conditions an insoluble brown-red layer formed. Memming and Schwandt [4] demonstrated in 1965 that these films were porous. Seven years after, Theunissen [5] showed that porous Si was produced by a localized dissolution of the semiconductor that creates an array of pores. In 1990, Canham reasoned that if the pores in these films were allowed to grow large enough until they overlapped, the remaining isolated wires of silicon might be small enough to display quantum confinement effects [2]. Canham reported an intense, broad, visible photoluminescence from his films under UV excitation. Electroluminescence from these films was discovered by Halimaoui et al. [6] a year later. Since that date, much work has been carried out in order to characterize and understand the promising properties of this new material.

Porous Si layers are generally etched electrochemically. In this process, the monocrystalline Si substrate is anodized in an electrochemical cell with a mixture of HF, water and ethanol. The characteristics of the porous Si layer obtained are determined by the electrochemical parameters used during the etching process, which have been extensively reviewed [7, 8]. The morphology of both pores and crystallites depends on the doping type and level of the initial Si substrate, the porosity depends primarily on the combination of HF concentration and current density, and the thickness is proportional to the duration of the etch. Chemical reactions, commonly called "stain etches", have also been used to produce porous Si [9]. The chemical dissolution is usually carried out in a mixture of HF and a strong oxidizing agent such as HNO_3. Porous Si has also been fabricated using a dry spark-erosion process [10–15]. These techniques are not generally as flexible or reproducible [16] as the electrochemical technique. By modifying and adapting the formation parameters, porous Si chips can be used in various applications: for example, homogeneous p- or n-type layers presenting an array of nanometer-sized pores and crystallites are well suited for gas phase sensors, and p^{++} layers with macropores (with diameters above 100 nm) are required for liquid phase sensors of large biological molecules.

Porous germanium can also be prepared [17, 18] using a similar anodization process as is used for porous Si. The germanium crystallites present a nanowire shape (with diameters under 50 nm), but the surface roughness of the samples is generally on the micron scale. A red photoluminescence is also observed, which is less intense than is observed for porous Si.

Pore formation has more recently been achieved on direct band-gap GaAs [19]. Samples are electrochemically etched in aqueous solutions containing HCl. The crystallite size ranges from micrometer to nanometers and two photoluminescence bands are observed at room temperature: one in the infrared centered at 840 nm, and the other one in the green, centered at 540 nm. The authors mention that all their samples show a certain degree of inhomogeneity with respect to morphology, surface chemistry and photoluminescence. Porous GaP [20], pre-

pared under identical conditions, consists of crystallites with diameters ranging between 20 and 50 Å which exhibit blue and violet PL. Gudino-Martinez et al. [21] reported recently the first preparation of photoluminescent spark-processed porous InP. The technique consists of the application of high voltage discharges (50 kV, 20 Hz) on the substrate in air or in an argon atmosphere for several hours. The size of the active InP core is 42 Å and the PL, which is weak at room temperature, occurs between 400 and 500 nm.

Although porous semiconductor structures have been realized with various substrates, the most reproducible samples have been obtained with silicon. Moreover, different electrochemical preparation conditions lead to different morphologies, porosities and thicknesses, which are well controlled and useful for different applications. By way of introduction to the next section, it should be noted that many of the unique properties of porous Si stem directly from the electrochemical nature of its synthesis and are difficult to understand without a good appreciation of this process. Thus, it is useful to look at the electrochemistry of semiconductor electrodes with a view toward a better understanding of porous Si and its potential uses.

5.3 Junction Properties of Si-Electrolyte Interfaces

The properties of semiconductor/electrolyte interfaces have been extensively reviewed [22, 23], but a short discussion here is appropriate. When a semiconductor is brought into contact with an electrolyte and the interface attains equilibrium, the Fermi energy in the two phases must become equal. Thermodynamically, the Fermi level is the average energy of the mobile charge carriers in a solid and is

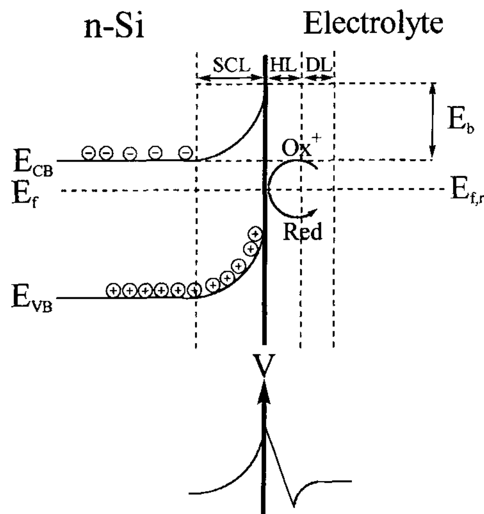

Fig. 5.1 The energy levels and potential distribution across an n-Si–electrolyte interface. $E_{f,r}$ is the electrochemical potential of the electrolyte, E_f is the Fermi level in the semiconductor, E_{CB} and E_{VB} are the energies of the conduction and valence band edges respectively and E_b is the band bending. SCL, HL and DL refer to the space charge layer, the Helmholtz layer and the diffuse layer respectively. The widths of these regions are not drawn to scale. The bottom illustration shows how the potential is distributed across the interface.

analogous in definition to the Nernst potential of a redox couple in solution. The mechanism by which equilibrium is established involves charge transfer between the semiconductor bands and the redox species in solution. This process is shown schematically in Fig. 5.1 for an n-type Si electrode in contact with a solution containing a reversible redox couple.

Charge transfer with a semiconductor electrode can take place through the conduction band by electron transfer, or through the valence band by hole transfer, depending on the position of the Fermi level with respect to the potential of the redox couple (Eqs 1–4):

$$Ox^+ + e^-_{(CB)} \rightarrow Red \quad (1)$$

$$Red \rightarrow Ox^+ + e^-_{(CB)} \quad (2)$$

$$Ox^+ \rightarrow Red + h^+_{(VB)} \quad (3)$$

$$Red + h^+_{(VB)} \rightarrow Ox^+. \quad (4)$$

The situation illustrated in Fig. 5.1 shows that electrons are depleted from the surface while positively charged holes are drawn to the surface by the electric field gradient in the space charge region. Accordingly, in the vicinity of the electrode the solution acquires a negative charge. The net result of the redistribution of charge at the interface is the formation of an electric double-layer with three distinct zones; the space charge layer (SCL), the Helmholtz layer (HL) and the diffuse layer (DL) as shown in Fig. 5.1. The space charge layer is the region that lies entirely within the semiconductor and where the electric field felt by a charge carrier is a function of its distance from the surface. On the electrolyte side of the interface, the opposite charge accumulates through the specific adsorption of ions and polarized solvent molecules to form the Helmholtz layer which includes the first monolayer of adsorbed species on the electrode. Finally, the diffuse layer is defined as the region extending from the Helmholtz layer to the bulk electrolyte where the ion concentrations deviate from their nominal bulk values.

An externally applied potential controls the position of the Fermi level of the semiconductor with respect to a reference. The potential distribution across the junction is determined by the density of charges on either side of the interface. The charge density of a 0.1 M electrolyte solution is around 10^{20} cm^{-3} whereas a typical semiconductor has a dopant concentration of 10^{15}–10^{19} cm^{-3}. Therefore, most of the potential drop is felt by the semiconductor in the space charge region. Under an applied bias, the energy of a charge carrier in the bulk differs from the carriers at the surface by an amount equal to the band bending energy. Band bending can be positive, negative or zero and reflects the different concentrations of carriers at the surface and in the bulk. As seen in Fig. 5.1, band bending causes the majority carriers (electrons) at the surface to move toward the bulk of the semiconductor while holes are attracted to the surface. The electrode pictured here is said to be in depletion mode because electrons have been depleted

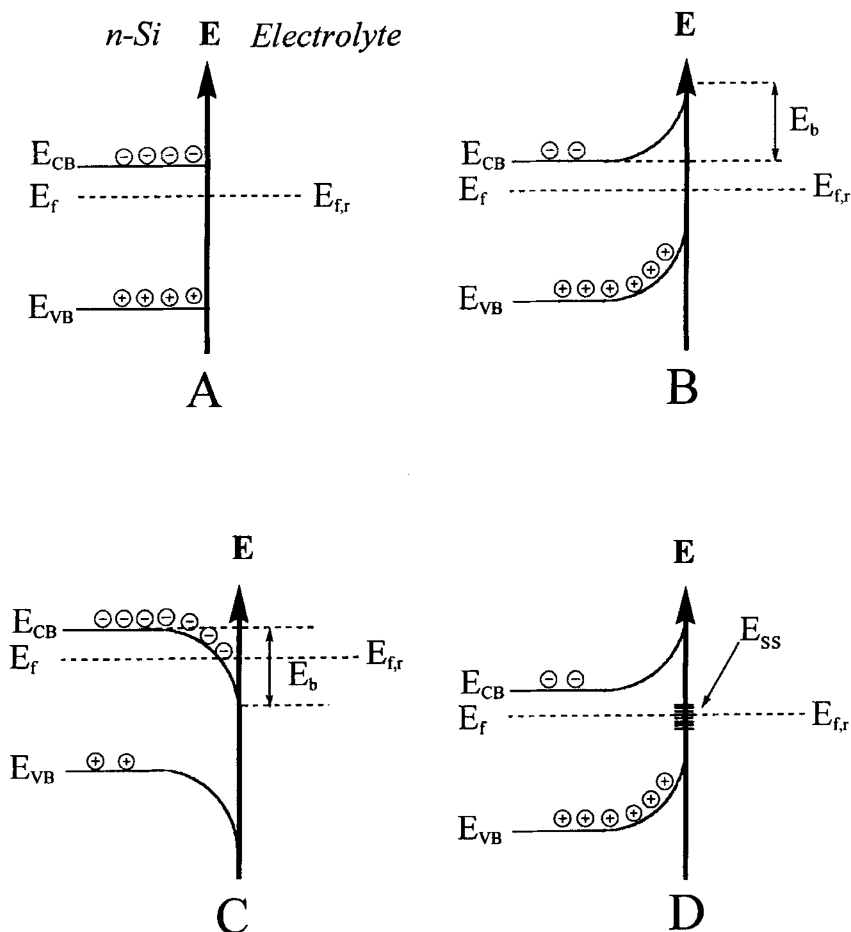

Fig. 5.2 Different types of band bending at an n-type Si electrode in equilibrium with a solution redox couple. (A) Flat band potential. (B) Inversion. (C) Accumulation. (D) Fermi level pinning by surface states. E_{VB} is the valence band energy, E_{CB} is the conduction band energy, E_f is the Fermi level in the semiconductor, $E_{f,r}$ is the Nernst potential of the redox couple in solution, E_b is the band bending energy and E_{ss} is the surface state energy.

from the surface. A quantity of particular importance in semiconductor electrochemistry is the flat band potential (E_{fb}) or the potential at which there is no space charge layer and hence no band bending at the interface (Fig. 5.2 A). Knowledge of the flat band potential allows one to predict the extent of overlap between the valence and conduction bands of the semiconductor and the donor and acceptor levels of a redox species in solution. In other words, the flat band potential is essential if the semiconductor band edges are to be referenced to an electrochemical energy scale, such as the normal hydrogen electrode (NHE).

There are important exceptions to the usual situation where the potential drop is felt mostly in the space charge region of the semiconductor. When a doped (n-

or p-type) semiconductor is forward biased by a sufficiently large applied potential, the Fermi level can approach and penetrate the conduction or valence band producing very high concentrations of majority carriers at the surface (Fig. 5.2C). Under these conditions, the semiconductor is said to be in accumulation mode and the electrode behaves as if it were metallic. It follows that any further increase in electrode potential will be felt across the Helmholtz layer. Obviously, the magnitude of the potential at which this occurs depends strongly on the dopant concentration in the semiconductor. The second exception arises when surface states are present with energies in the band-gap (Fig. 5.2D). Surface states are energy levels associated with distinct chemical species either physically or chemically bound to the electrode surface. Adsorbates, reaction intermediates, oxides, lattice defects and dangling bonds can all produce surface states, and when present in sufficiently high concentrations, will introduce large uncertainties in how the potential is distributed across the interface. This is most likely to be the case during the electrochemical corrosion of Si. When the Fermi level in the semiconductor becomes isoenergetic with the surface states, charge transfer between the redox couple and semiconductor will take place through these levels. Thus, the occupancy and charge state of the surface becomes dependent on the applied potential. If the charge density associated with surface states is greater than the charge density in the space charge region, the Fermi level will no longer be representative of the energy of electrons in the semiconductor, but rather, becomes fixed at the energy of the surface states. This condition is called Fermi level pinning because the band bending is fixed and the band edges appear to vary with applied potential. Charging and discharging of surface states can occur through redox species or charge carriers in the semiconductor, situations that in practice are difficult to distinguish. The practical consequence of surface states is that they introduce uncertainty into the potential distribution across the junction and therefore the charge transfer rate of any reaction occurring at the surface. As will be discussed in more detail below, knowledge of the potential distribution at the Si-HF interface turns out to be of critical importance in formulating reasonable models for this reaction and the formation of porous Si.

5.3.1
Chemistry of Silicon in Aqueous HF

Thermodynamic considerations show that Si is a strong reducing agent, forming hydrogen gas and silane (SiH_4) upon reaction with water. Silane subsequently decomposes in the presence of water to form SiO_2. Everyday experience, however, shows silicon is quite unreactive towards water. The main reason stems from the passivating nature of the silicon oxide layer. In addition, the excellent matching of the thermal expansion coefficients of Si and SiO_2 means the surface is mechanically and chemically very resistant towards further attack by the oxidizing agent. In fact, HF is one of the few substances that can dissolve SiO_2 at room temperature. Silicon's propensity for combining with oxygen and the thermodynamic stability of SiO_2 also explains why silicon is rarely found without an oxide layer un-

der ambient conditions. An important exception to this rule is the hydride-terminated silicon surface formed upon reaction of silicon with aqueous hydrofluoric acid. Analysis of the chemical composition of the surface of Si after exposure to HF shows predominantly silicon hydride species and very little oxide or fluoride [24–27]. This is somewhat surprising considering the energies of Si-F and Si-O bonds are larger than Si-H bonds (129.3, 88.2, and 70.4 kcal mol^{-1}, respectively). Kinetic and electronic factors are more important than thermodynamic ones in this reaction. The main reason for the stability of Si-H over Si-F and Si-O bonds on Si surfaces comes from the electronegativities of the elements; highly electronegative elements like F and O polarize the Si surface atoms, making them more susceptible to nucleophilic attack.

5.3.2
Electrochemical Formation of Porous Si

As was mentioned above, porous Si can be formed from single crystal Si by a number of methods, although the mostly widely used is an electrochemical etch in ethanolic HF solution. A two electrode cell consisting of a Si working electrode and a Pt counter electrode is commonly employed and the reaction is carried out at constant current. The corrosion of crystalline Si requires a supply of valence band holes at the surface, thus, p-type Si can be etched in the dark while n-type Si requires illumination to supply photogenerated holes. Using relatively high concentrations of HF and etching at low overpotentials ensures the formation of a porous layer rather than an electropolished surface. The exact morphology of the porous layer, however, is very sensitive to many experimental variables, such as the doping density of the Si substrate, the type of dopant, the current density and the duration of the etch [28–32]. To ensure that reasonable comparisons can be made between different porous Si samples, identical etch conditions must be used. As will be discussed later, certain properties of porous Si such as the emission wavelength and quantum efficiency of the photoluminescence are very sensitive to the formation conditions.

There is a general consensus among those who have studied the formation mechanism of porous Si, that once initiated, pores propagate through the material under the combined influence of the electric field, the hole concentration and the preference of certain crystallographic planes [30, 33–35]. It is supposed that initiation of the porous structure occurs at localized regions on the Si surface where random defects create minute concave depressions [36]. The potential distribution between the Si and the electrolyte depends on the band bending at the interface, which is lower at the tip of a growing pore [7]. Since the band bending represents a barrier for charge transfer with the electrolyte, the lower the barrier, the faster the etch. The electric field is also enhanced at the pore tips, which attracts and concentrates valence band holes in this region. Although the pores are self-propagating once started, their dimension, in addition to the path they take through the crystal, will be determined by other factors. For example, it is thought that as the crystallite domains reach the quantum confinement regime they are

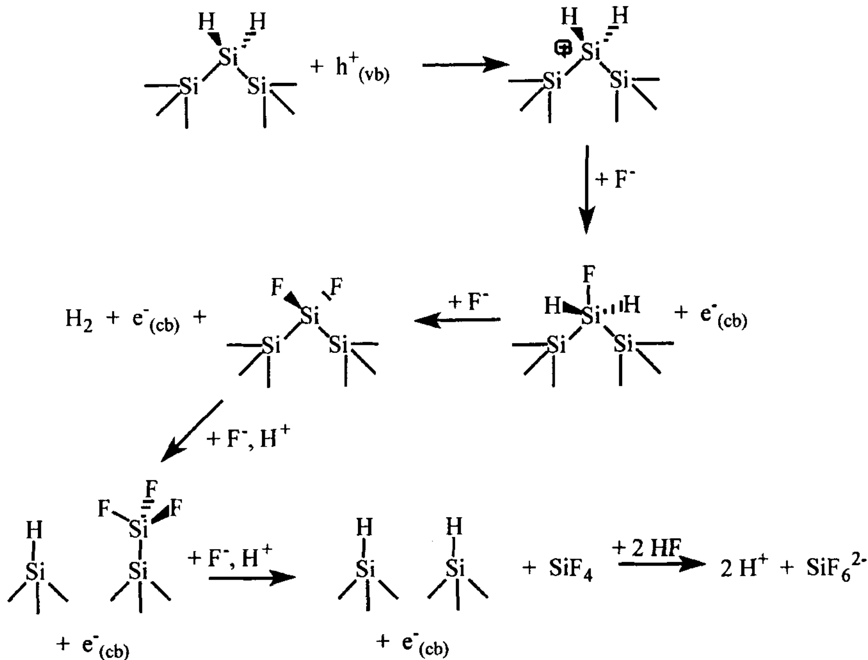

Fig. 5.3 A proposed mechanism of oxidation of n-type Si in HF electrolyte (after Ref. [29]).

depleted of charge and the corrosion reaction is suppressed [28, 37]. There is still considerable debate over what controls the final morphology of the porous layer.

Despite the considerable effort made to unravel the mechanism of the Si/HF electrochemical reaction, there is still uncertainty as to the intermediates and reaction steps involved. Part of the problem lies in the complexity of the reaction, which is known to involve chemical as well as electrochemical steps and whose mechanism changes with HF concentration and overpotential [38].

Fig. 5.3 shows a reaction mechanism for the oxidation of n-type Si in aqueous HF [29]. The reaction is cyclic in that there is an alternation between hydride- and fluoride-terminated surfaces as each Si atom is removed into solution. Starting with the hydride terminated surface, the first step involves capture of a photogenerated hole by a Si-Si bond. The hole can then migrate on to a Si-H bond thus releasing a proton. Attack of the Si radical by fluoride causes electron injection into the Si conduction band and the formation of a Si-F bond. The next few steps involve the sequential replacement of hydrogen with fluorine on the more highly oxidized Si, with the concurrent injection of an electron into the conduction band. The final step is a chemical reaction in which HF adds across the one remaining Si–Si bond to release SiF_4 into solution. At the same time, the surface-bound silicon is terminated with a hydride. As seen in Fig. 5.3, for every photogenerated hole that is consumed at the surface three electrons are injected into the conduction band resulting in a photocurrent quantum yield of 4. The SiF_4 species that

was released into solution quickly adds two additional fluoride anions to form SiF_6^{-2} which, interestingly enough, is one of the few silicon fluorine compounds that is stable towards hydrolysis in aqueous solution. Was this product not soluble or stable, HF would probably act like most other oxidizing agents towards Si and simply form a layer of SiO_2 on the surface.

As described, this mechanism is thought to be operative at low overpotentials and high HF concentrations in the regime where porous Si is formed [29]. However the exact mechanism is dependent on light intensity and under high light flux, hydrogen gas is evolved and the photocurrent quantum yield falls to 2 (i.e., for every photogenerated hole consumed only one electron is injected). At high overpotentials and low HF concentrations, the reaction mechanism changes again and the surface is electropolished rather than etched. The mechanism of oxidation in this regime is much more complex and will not be covered in detail. For instance, there are many reports of current-voltage oscillations, chaos and other non-linear behavior during the electropolishing of Si [39, 40]. The current consensus is that there are at least two coupled reactions occurring at the surface at the same time; one is SiO_2 formation and the other is the chemical dissolution of this oxide by HF [38, 41]. The interaction between these competing reactions is equivalent to positive feedback, a known requirement for nonlinear behavior [42].

The *i-V* characteristic of an n-type Si/HF junction at small overpotentials closely follows that of a Schottky diode when measured in the dark. The relevant relationship [43] is given by the ideal diode law, Eq. (5):

$$j = j_0 \left[\exp\left(-\frac{qV}{AkT} \right) - 1 \right] \tag{5}$$

where j is the current density, j_0 is the reverse-bias saturation current density, q is the charge of an electron, A is the diode quality factor, k is the Boltzmann constant, and T is temperature. Under reverse bias, the junction passes only a small current, called the saturation current (j_0), but when forward biased the current increases exponentially with potential. This is the basis for the rectifying nature of a Schottky junction. Both n- and p-type Si are stable to dissolution under negative bias and behave as typical semiconductor electrodes in HF solutions (i.e., Schottky diode behavior, reduction of water with hydrogen evolution). It is only under positive polarization that Si dissolves. However, depending on the magnitude of the applied overpotential, very different surface morphologies can result.

There are three main potential regimes for anodic dissolution of Si in HF, shown in Fig. 5.4 for a p-type Si electrode [44]. At potentials slightly positive of the dissolving potential (–0.1 V relative to the SCE; region A in Fig. 5.4) the surface is dissolved in an irregular, fractal-like manner leaving behind a highly porous layer of nanometer-sized structures composed of hydride-terminated crystalline Si. At higher overpotentials (region B in Fig. 5.4) the *i-V* curve departs from Schottky diode behavior and a transition region between pore formation and electropolishing occurs. In this potential region, pore formation competes with electropolishing to control the surface morphology. Electropolishing (region C in

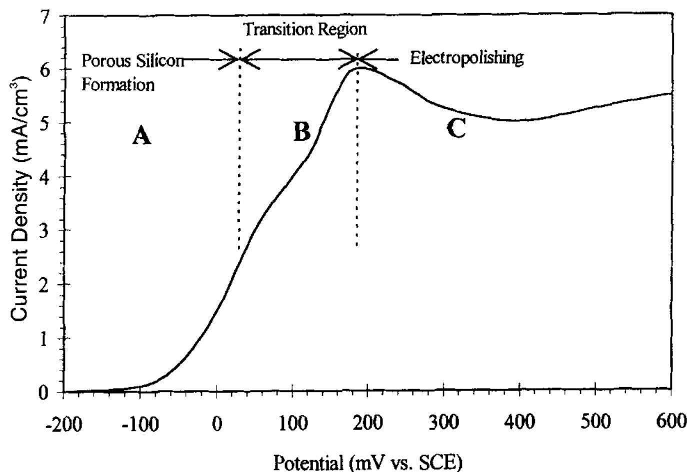

Fig. 5.4 Current-voltage curve of p-type Si in 1% HF solution. The three lines separating regions A, B, and C indicate a change in the reaction mechanism that results in the dissolution of Si surface [44].

Fig. 5.4) begins at still more positive potentials. This region is characterized by its planarizing action on the Si, leaving behind a mirror-like surface with excellent conventional electronic properties. In order to suggest a mechanism by which such radically different surface morphologies can result from relatively small changes in overpotential, one must first propose an appropriate potential distribution across the junction by specifying a rate-limiting step. Viewed another way, accurate measurement of the relative potential drops across the space charge layer and the Helmholtz layer allows reasonable rate-limiting steps to be proposed for high and low overpotentials. The literature on this topic is not in agreement. For instance, based on a Tafel slope of 60 mV for region A of Fig. 5.4, Zhang et al. [44] came to the conclusion that the kinetics were under Helmholtz-layer control ($RT/\beta nF$) while Ronga et al. [45] used the same slope to argue for space charge layer control (kT/q).

Electrochemical impedance spectroscopy has helped to clarify some of the controversy over the potential distribution at the Si/HF interface, as these measurements allow determination of the flat band potential and capacity of the space charge layer [35]. Knowing where the flat band potential lies relative to the applied potential allows one to determine the magnitude and direction of band bending at the semiconductor surface and hence the concentration of free carriers available for reaction. The most common way of determining V_{fb} is by measuring the junction capacitance, C_{sc}, as a function of applied potential and plotting the data according to the Mott-Schottky relationship [43] (Eq. 6):

$$\frac{1}{C_{sc}^2} = \frac{2}{qA_s^2 \varepsilon_s N_D}\left(|V - V_{fb}| - \frac{kT}{q}\right) \tag{6}$$

where A_s is the electrode area, ε_s is the dielectric constant of the semiconductor, N_D is the dopant density and V is the applied potential. A plot of the reciprocal square of capacitance against voltage yields the flat-band potential.

It is generally assumed that the measured junction capacitance reflects the space charge capacitance because it is in series with the Helmholtz and diffuse layer capacitances, both of which are much larger (10–100 $\mu F\,cm^{-2}$) than the capacity of the space charge region. The Mott-Schottky equation is only valid when the space charge layer is in mild depletion (Fig. 5.2B) and interface states are not present. Deviations from linearity are often observed, however, indicating an alternate method should be used to find V_{fb}. For purposes of characterizing the Si/HF system, obtaining a linear Mott-Schottky plot and showing that the semiconductor is in depletion is taken as good evidence for space charge control of the reaction. In the region of pore formation this is largely true; however for n-type Si, some authors have reported that linear behavior was only observed on the first sweep, where little or no pore formation occurs [46]. Other authors have shown a clear dependence of rate on the concentration of HF, which implies Helmholtz layer control [41]. The results appear to conflict if one assumes that the reaction must be controlled by either the space charge or the Helmholtz layer, but not by both. The postulation of a global mechanism explaining the kinetics and chemistry of the Si/HF electrochemical reaction as well as the morphology obtained has remained elusive due to the complex electrochemical behavior shown by this system.

5.3.3.1 **Photoelectrochemically Patterned Porous Si**

To a first approximation, Si in contact with a hydrofluoric acid etching solution behaves like a solid-state Schottky junction; corrosion of p-type Si occurs in the forward-bias direction, while corrosion of n-type Si occurs under reverse-bias conditions. Just as in a Schottky photodiode, current induced by light can add to or subtract from the corrosion current passing through the Si, depending on the majority carrier type present in the Si wafer. This is why n-type Si wafers will not readily electrocorrode unless they are illuminated, and the corrosion reaction is suppressed by illumination of p-type electrodes [47–49]. Thus porous Si can be patterned by projecting an image onto the Si surface during electrochemical etch [47, 48]. The intensity of light at a given spot on the wafer locally modulates the etch rate, resulting in porosity gradients in both the in-plane [47, 48] and z-directions [49] of the porous Si layer [50]. Photoluminescent layers can be fabricated which have surfaces ranging from matte black to so reflective that they display optical cavity modes [48, 50, 51]. This photoelectrochemical procedure also allows control of the intensity and wavelength of photoluminescence that can be obtained from porous Si [52].

Photochemical and photoelectrochemical patterning has also been used to selectively derivatize porous Si surfaces [53–55]. For example, photoelectrochemical oxidation of luminescent porous Si in carboxylic acids produces a silyl ester-modified surface, which can be photopatterned by illuminating the surface through a mask

during the derivatization procedure [53]. Photoluminescence from the ester-modified surface is reversibly quenched by H_2O vapor, while photoluminescence from the original Si-H surface is much less sensitive to H_2O vapor. This demonstrates the ability to pattern porous Si surfaces to impart specific chemical sensing properties, important in generating high density multifunctional sensor arrays [56].

5.3.3.2 Porous Si Layers and Multilayers

If the size of the pores is smaller than the wavelength of light, films of porous Si often display optical interference [48, 51]. If the films are assumed to be optically transparent, the optical reflectivity spectrum can be modeled using the Fabry-Pérot relationship (Eq. 7):

$$Y = \frac{2}{\pi}\left(\cos\frac{2nL\pi}{\lambda}\right)^3\left(\sin\frac{2nL\pi}{\lambda}\right) + \frac{1}{\pi}\left(\cos\frac{2nL\pi}{\lambda}\right)^2\left(4\pi - \sin\frac{4nL\pi}{\lambda}\right) \quad (7)$$

where Y is the intensity of reflected light of wavelength λ, L is the thickness of the film, and n is the refractive index of the film. The equation results in a series of maxima, equally spaced in energy, corresponding to the condition for constructive interference in the film. The maximum of each fringe is given by Eq. (8) for light incident normal to the porous Si surface [57]:

$$m\lambda = 2nL \quad (8)$$

where m is an integer corresponding to the spectral order of the fringe.

The determining physical parameters for the reflectivity of the film are the refractive index (n) and the thickness (L). The quantity $2nL$ is commonly referred to as the effective optical thickness of the film. The values of n and L are both determined and well controlled by the electrochemical parameters used in the synthesis, and thin films with given optical parameters can be etched in a reproducible way. Fig. 5.5 gives an example of a high quality Fabry-Pérot interferometer film made from porous Si. The high contrast observed in the optical fringes is a signature of the formation of two planar and parallel interfaces. A shift in these fringes occurs upon analyte binding in the pores, which provides a sensitive transduction modality for chemical sensing, discussed in more detail below.

It is possible to fabricate more sophisticated optical devices from porous Si films. In 1995 Pavesi and Mazzoleni [58] reported the first microcavity made entirely out of porous Si. These structures are planar microcavities based on an active medium (luminescent porous Si) sandwiched between two distributed Bragg reflectors. Chemical sensing using Bragg mirrors of porous Si was first demonstrated by Snow and coworkers [59].

Porous Si multilayers are prepared by periodically varying the current density during the etching process; a current versus time profile can be transferred to a porosity, i.e. refractive index, versus depth profile. The HF concentration of the electrolyte and the current densities are adjusted to allow formation of layers of

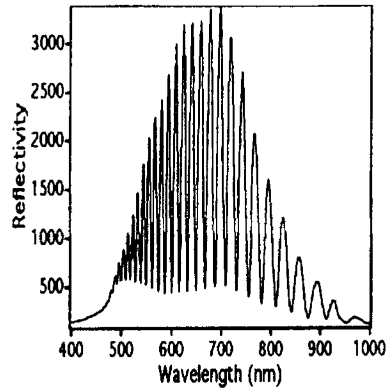

Fig. 5.5 Optical reflection spectrum (normal incidence) showing the interference fringes obtained on a porous Si thin film. The position of the optical fringes is highly dependent on the refractive index of the material filling the pores, and this phenomenon can be used for chemical sensing.

the appropriate refractive indices, and the etch times are adjusted to control layer thicknesses. The multilayers display the properties of Bragg mirrors when both refractive indexes n_1 and n_2 and thickness of the layers L_1 and L_2 satisfy the following relationship:

$$m\lambda = n_1 L_1 = n_2 L_2 \quad (9)$$

Fig. 5.6 shows an example of a $\lambda/4$ Bragg stack formed electrochemically from porous Si.

The reflectivity spectrum of the Bragg stack of Fig. 5.6 shows a Bragg plateau (or photonic band-gap) centered at 680 nm with a FWHM of 60 nm. These two optical properties can be tuned by adjusting the electrochemical parameters of the etch.

If the periodicity of the Bragg structure is broken by the introduction of a $\lambda/2$ central layer, a mode is opened in the reflectivity of the Bragg plateau. The spectrum then displays a sharp transmission peak in the middle of the forbidden

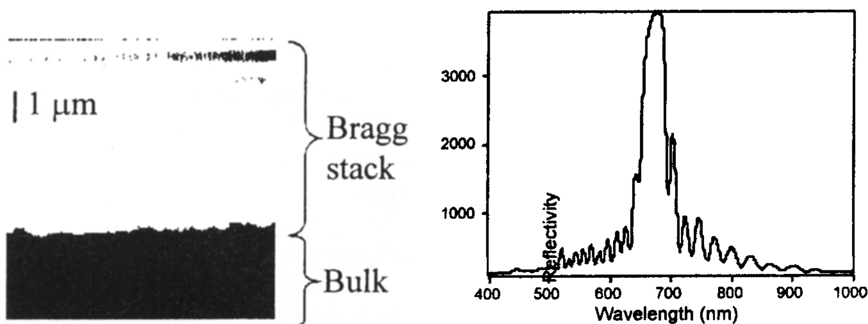

Fig. 5.6 A multilayer porous Si Bragg stack (ten repeats) with $n_1 \approx 1.1$, $L_1 \approx 0.75$ μm and $n_2 \approx 1.4$, $L_2 \approx 0.59$ μm. On the left is an electron micrograph image of the cross section, and on the right is shown the reflectivity spectrum of the structure.

band and constitutes a Fabry-Pérot filter for any luminescence coming from the central layer. Once again, the spectral position of the mode can be tuned by modifying the electrochemical parameters of formation.

Cavity effects on the luminescence of the central active porous Si layer, or on the luminescence of dyes introduced in the porous structure, have been observed [60–64]. Reduction of the photoluminescence line width from 130 to 15 nm and a strong directionality of the emission along the axis normal to the surface is observed. No lasing has been reported yet, certainly because of the low quantum efficiency of the porous Si luminescence and because of the losses in the structure arising from absorption and interface roughness. However, recently Fauchet and coworkers demonstrated femtomolar-level detection of single-stranded DNA using a similar porous Si optical microcavity structure that had been modified with the complementary DNA strand [65].

5.4 Properties of Porous Si

As the electrochemical etch that forms porous Si proceeds, the size of the crystallites carved out of the substrate is reduced. The fraction of atoms identified as surface atoms increases. As a consequence, many of the properties of porous Si are determined by these surface atoms; the high radius of curvature induces strain in the films; the surface atoms become more reactive than atoms at the surface of flat Si; and their electronic properties are highly perturbed. A lot is happening at the surface, and chemical transformations of the surface can generate surface states on porous Si that are more or less accessible chemically and energetically.

In addition to the higher relative density of surface electronic states, which may have a distinctive chemical nature as depicted in Fig. 5.7, there are other photophysical mechanisms that may be operative in nanocrystals that are not available to bulk solids. Since the surface-free energy is a significant term in determining

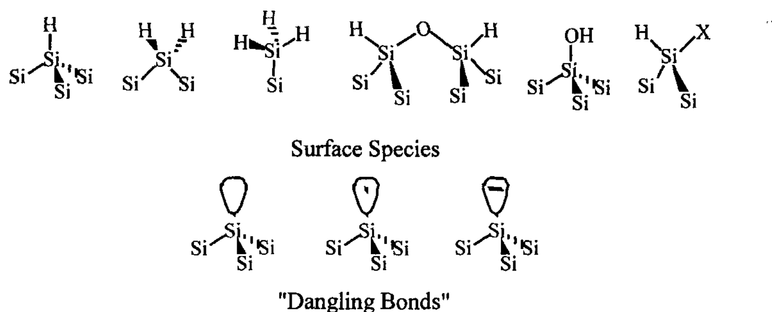

Fig. 5.7 Some of the species known to be present on the surface of porous Si. The species "X" can be a variety of intentionally or unintentionally introduced chemical moieties.

the overall thermodynamics of nanoparticles, surface strain can have a large effect on their electronic properties. For example, Alivisatos and coworkers have shown that the phase diagram for II–VI nanocrystals is very different from the bulk material, and that both the kinetics and thermodynamics of phase transitions can be size-dependent [66, 67]. One of the distinctive characteristics of porous Si is that its properties are limited by surface chemistry. In particular, any modification of the surface energy may affect the size, shape, and lattice parameter of the nanocrystals and any modification of the surface states may affect their band structure.

5.4.1 Structural Properties of Porous Si

The first issue we will discuss is the effect on the atomic arrangement in the lattice when the size of the solid semiconductor is reduced. On porous Si it has been shown [68] that the electrochemical formation of pores on an initially crystalline substrate does not lead to any loss in crystallinity. Indeed, the X-ray diffraction rocking curves [69] of supported porous Si layers clearly show two sharp Bragg peaks coming from the Si substrate and from the porous Si layer respectively. The difference in the angular position of these peaks is directly correlated to the lattice mismatch (Δa) along the normal direction of the sample surface. No modification of the lattice parameter has been detected in the parallel direction of the sample surface. The authors measured a lattice expansion ($\Delta a/a$) of 30×10^{-4} on p-type PSi films of 65% porosity (the expansion is proportional to the porosity), which is attributed to the reconstructed Si-H_x surface. This result is in good agreement with the simulations of Ito et al. [70], which indicated an increase of the Si-Si distance when the surface of Si clusters is covered with hydrogen. It has also been observed that the lattice parameter expands when the films are oxidized [71]. The stress derives from the large volume increase (factor of 2.3) when bulk Si is converted into silica. Lattice expansion also occurs when porous Si is wetted by adsorption of alkanes [72].

A dependence of the lattice parameter on crystallite size has also been observed with II–VI based semiconductors. Bawendi and coworkers [73] have synthesized CdS, CdSe and CdTe quantum dots with diameters ranging from 115 to 12 Å. The X-ray powder diffraction spectra of the dots exhibit the wurtzite crystal structure with the lattice parameters of the bulk materials. As the diameter decreases, a size broadening of the reflections appears, indicating an enhancement of the number of stacking faults. The diffraction pattern from the 12 Å-diameter particles is very different from the other sizes. In that case, the clusters possess too few atoms to define a core crystal structure. The authors also mention the possibility of surface reconstruction and a contribution from the capping groups to the diffraction pattern. Goldstein et al. [67] have evidenced a contraction of the lattice parameter of CdS quantum dots as their diameter is reduced. The surface tension increases from $0.750\ \mathrm{N\,m^{-1}}$ for bulk CdS to $1.74\ \mathrm{N\,m^{-1}}$ for capped nanocrystals and to $2.50\ \mathrm{N\,m^{-1}}$ for bare ones. As the dimensions are reduced, the contribution

of the surface tension to the free energy of the crystal increases, and the thermodynamic parameters of the nanocrystals appear to be modified. The melting point of CdS quantum dots with diameters ranging from 24 to 80 Å was studied by TEM [67]: a decrease of the melting temperature from 1200 K (80 Å diameter) to 600 K (24 Å diameter) is observed, whereas the melting temperature of the bulk material is 1680 K. Another example of the size effect on the thermodynamic properties of nanocrystals is provided in the study of a solid-solid phase transition performed by Tolbert et al. on CdSe quantum dots [66]. Indeed, bulk CdSe undergoes a phase transition from a wurtzite to a rock salt structure at 2 GPa, and the authors report an evolution of the transition pressure from 3.6 to 4.9 GPa when the radius of the nanocrystals decreases from 21 to 10 Å.

5.4.2
Luminescence Properties of Porous Si

The optical properties of nanocrystalline porous Si have been the subject of extensive investigations during the past 10 years. Indeed, for both porous semiconductors and semiconductor quantum dots, efficient visible photoluminescence has been reported. For porous Si, electroluminescence has also been observed in solid-state [74–77] and liquid junctions [6, 78]. Although the visible emission of these nanocrystals under UV excitation is the property that has been studied the most, the recognition that electrically stimulated emission would most likely lead to practical optoelectronic applications has resulted in a significant amount of effort focussed on electroluminescence phenomena. In recent years the passive optical properties of thin porous Si films and multilayers, which we have already discussed, have received increased attention.

The reduction in size of a crystal to the nanometer range often results in the occurrence of quantum confinement effects, which will principally affect the value of the band-gap and the electron-hole recombination rate. The loss of long-range periodicity and the presence of surface states will also play important roles. Porous Si was at first considered a material comprised of quantum wires, although now it is thought of more as a matrix of interconnected quantum dots [79, 80]. The semiconductor physics representation of such a system is a well of potential in which the carriers are more or less trapped, depending on the height of the potential barrier. The energy levels in the well are quantized, and their positions are strongly affected by the size of the nanocrystal. If the three dimensions of the nanocrystal are respectively L_x, L_y and L_z, the confinement energy, E_c, will depend on these values as $(1/L_x^2 + 1/L_y^2 + 1/L_z^2)$. If the bulk semiconductor has a band-gap E_g, the nanocrystalline semiconductor will have a band-gap $E_{g'} = E_g + E_c$. The relationship between the gap and the size of the crystallites in porous Si has been modeled in various ways, but all the calculations lead to a relation $\Delta E_g \approx D^{-\alpha}$, with D the diameter of the crystallite and α a coefficient. The α parameter depends on the model, $\alpha = 2$ for infinite potential barriers, $\alpha = 1.64$ for finite oxide barriers in the effective mass approximation [81], and $\alpha = 1.39$ for the LCAO method on spherical clusters passivated by hydrogen [82]. These models show a good

correlation with the average spectral positions of the emission data. However, the spectra usually display linewidths much larger than those seen in the spectra of "conventional" quantum dots based on II–VI materials. For II–VI quantum dots it is not unusual to observe spectral linewidths of <50 nm and fine structure corresponding to higher order transitions [83], while the photoluminescence spectra of porous Si have linewidths that are typically 150 nm and featureless.

The time-resolved photoluminescence spectra are somewhat difficult to interpret, displaying non-exponential decays that tend to range from a few microseconds on the high energy end of the emission spectrum to a hundred microseconds on the low energy end [84]. Fishman et al. [81] have shown that the steady-state spectra can be fit using a Gaussian distribution of crystallite diameters. The time-resolved data are usually fit with a stretched exponential [85, 86] or a semi-quantitative "average" lifetime based on the half-life of the decay curve [87]. This distribution complicates the interpretation of the kinetics for energy or charge transfer at porous Si interfaces significantly [87].

Concerning the lifetime of radiative recombination, one can expect that the break in the crystalline symmetry makes transitions that are formally forbidden in the bulk material allowed, and the long lifetimes associated with an indirect gap material would shorten to resemble a direct gap semiconductor. Moreover, the simple fact that the carriers are spatially localized increases the probability of recombination. Thus, the lifetimes are usually shorter for radiative recombination in nanocrystals than for radiative recombination in the parent semiconductors. For quantum dots, the lifetimes are typically in the range of 100 ns [88] and multi-exponential. As already mentioned, larger diameters induce longer lifetimes. For porous Si, the very long (microsecond) lifetimes indicate that the indirect character of the semiconductor is conserved. Experimental verification of the indirect nature of the radiative transition was first reported by Calcott et al. [89], who clearly observed the TO and TA phonon-assisted transitions under resonant excitation at 2 K.

Unlike the generally well-isolated quantum dots based on II–VI materials [83], the interconnected nature of the porous Si matrix results in partial overlap of wavefunctions between adjacent nanocrystalline domains. This property manifests itself in two main electronic features: first, it provides a pathway for current transport in the matrix, and second, it provides a low energy route for migration of excited carriers and for their non-radiative recombination [90]. The quantum efficiency for emission depends on the rate of radiative recombination relative to the rate of non-radiative recombination. When the size of a nanocrystal decreases, localization increases and the effect of surface traps and dangling bonds is magnified. Indeed, in as far as the wavefunctions of the carriers occupy the whole particle, one defect is sufficient to kill the luminescence of a nanocrystallite. Passivation techniques like the core-shell structures for quantum dots [91, 92] and oxidation or surface derivatization for porous Si [93, 94] have been shown to lead to good improvement of the quantum yields. Typical values are around 5% for porous Si and around 50% for quantum dots.

5.4.3 Electrical Properties of Porous Si

Much of the interest generated by Canham's first report of photoluminescence from porous Si stemmed from the idea that it would be easy to inject electrons and holes into the nanocrystals with an electrical contact. The interconnected nature of the material and the fact that its synthesis relies on electrical injection of holes from the Si substrate means that the material should readily lend itself to electroluminescent device structures, and the first demonstrations of such devices appeared within a few years of Canham's discovery [6, 74, 76–78, 95–100]. Nevertheless, it took quite a long time to get stable, efficient contacts on porous Si [101–111], and good porous Si LEDs have only recently been realized [103, 112]. One reason for this is that efficient luminescence is correlated with high spatial localization of holes and electrons while transport involves motion of carriers over macroscopic distances. The problem has been successfully addressed with the II–VI nanoparticles by imbedding them in conducting polymer matrices [91, 106]. The organic materials have a lower density of states than conventional metals or semiconductors, so the probability of interfacial recombination events is reduced. Transport studies on the interconnected crystallites in porous Si have led to a better understanding of the conduction processes, and have been key to achieving efficient devices with this material.

The resistivity of nanoporous Si has been reported to be a few orders of magnitude higher than microporous Si [113]. Typical values of the resistivity are 10^{10}–$10^{12}\,\Omega\,\text{cm}$ at room temperature and can increase to 10^{16}–$10^{17}\,\Omega\,\text{cm}$ when the samples are oxidized. The conductivity is thermally activated, with an activation energy in the range of 0.3–0.7 eV [114]. Among different models proposed to explain the conductivity of porous Si, a hopping mechanism seems to explain most of the observed experimental facts [115, 116]. An electron at the Fermi level can jump from its equilibrium position in a crystallite while leaving a positive trap behind. Under these conditions, the higher the energetic barrier, the lower the probability of hopping. This explains quite well the fact that conductivity decreases with increasing porosity (higher confinement energy), with increasing oxidation (higher barrier), and with decreasing temperature (no activation energy available to jump the barrier). The point which needs to be stressed is that efficient luminescence and efficient conductivity are orthogonal phenomena, and that increasing the efficiency of confinement in the nanocrystallites strongly increases both photoluminescence and resistivity of the porous material.

5.5 Electroluminescence from Porous Si

A significant obstacle encountered in fabrication of LEDs from porous Si has been the generation of a low resistance, stable electrical contact to the porous layer. A number of approaches have been reported, including thin metal films [100, 117], sputtered indium tin oxide (ITO) [97, 118], and conducting polymers

[101, 119, 120]. Liquid junctions, although not practical, have also been extensively studied as they provide an intimate electrical contact to the porous layer [121–123]. Chemical corrosion is a problem with any electrochemical system and substrate oxidation tends to occur readily in most solvents [38]. Despite the drawbacks, liquid contacts allow flexibility in studying charge transport processes at the interface, and they provided the initial impetus for the study of electrochemical reactions at porous Si surfaces. A fundamental distinction between solid-state and liquid junctions should be made here. Electroluminescence generally refers to the solid-state process. If a chemical reaction is involved in the electrical generation of light, the process is usually referred to as electrochemiluminescence. Because the energy produced as light contains a contribution from the free energy released in the making and breaking of chemical bonds, electrochemiluminescence can occur at applied voltages lower than would be possible for production of the same energy of light by electroluminescence.

Despite the fact that crystalline Si (c-Si) has an indirect band-gap in the near infrared, visible electroluminescence has been observed from this material under a variety of experimental conditions [124–128]. For example, when a high voltage is applied to a Si p-n junction, avalanche breakdown can occur, resulting in the emission of a broadband spectrum with photon energies considerably greater than the band-gap energy of bulk Si [127]. Although it is now widely accepted that quantum confinement effects are responsible for the efficient visible emission from freshly prepared porous Si, there is evidence that molecular species or defect states may also play a role, particularly in aged or oxidized samples [129–132].

The high surface area of porous Si combined with its known sensitivity to molecular adsorbates makes contamination of the surface an important consideration in the photophysics. As suggested by Canham, the accumulation of organic material may be responsible for the appearance of a blue emission band in the PL spectrum of aged porous Si [133]. The density of defects formed during oxidation of porous Si should be much higher than a similar oxide grown on flat Si. Silicon-oxygen-related defects, such as the non-bonding oxygen hole center (NBOHC) [134], P_b [135–137] and E′ centers [138, 139], have been characterized and studied extensively because of their importance in the fabrication of high-quality Si/SiO_2 junctions for microelectronic circuits. Although the assignment of PL bands to specific defects is difficult, there is general agreement that many defects commonly found in amorphous silica (a-SiO_2) and at Si/SiO_2 junctions can give rise to visible emission [138, 139]. For example, the NBOHC is strongly associated with a broad red emission at 1.9 eV [140] and the P_b and E′ centers are also reported to have emission bands in the red portion of the spectrum [134, 141–143]. Silanol or suboxide groups have been correlated with fast, blue PL in both a-SiO_2 [132] and rapidly oxidized porous Si [144]. It is becoming increasingly clear that the model describing the electroluminescent properties of oxidized porous Si must include contributions from quantum-confined crystalline Si and from defect states localized in the oxide layer or at the nanocrystalline Si/SiO_2 interface.

Visible EL from SiO_2 has been well documented in studies concerning the transport of energetic carriers through metal-oxide-semiconductor (MOS) struc-

tures [145–150]. It is generally accepted that electronic transitions of hot electrons are responsible for the emission from MOS structures subjected to high electric fields [145–151]. Although less thoroughly studied, visible electrochemiluminescence has been observed from oxidized Si anodes in aqueous and non-aqueous electrolytes under conditions of very high applied over-potentials (greater than +50 V) [152, 153]. For example, Hasegawa [154] observed visible electrochemiluminescence from oxidized a-Si(H) and crystalline Si anodes and ascribed the phenomenon to electronic transitions occurring at the SiO_2/Si interface and in the bulk SiO_2 film. With porous Si, the electrochemiluminescence process often produces interfacial oxides or oxide-related species that can act as emissive centers. For example, electrochemiluminescent porous Si/formic acid junctions slowly produce mixed oxide and formate ester species at the interface [123]. This oxide layer, which can also be generated at flat Si, is highly photoluminescent. Stable electrochemiluminescence has not been achieved on porous Si, although the product of the electrochemical reaction can often produce a species bonded to the surface that is useful for other applications. A variety of electrochemical reactions have now been found that are of some utility in the modification of porous Si surfaces.

5.6 Electrochemical Functionalization

Pristine porous Si has a hydride-terminated surface that is prone to oxidation and corrosion. In recent years there has been much effort to chemically modify porous Si and hydride-terminated crystalline Si with organic moieties in order to stabilize the surface or to impart some specific chemical property. The electrochemiluminescence reaction involving formic acid that was described above works with a variety of carboxylic acids [53, 54, 155]. The covalently attached Si esters are readily removed, and they provide a convenient starting point for chemical modification reactions (Eq. 10). Such surfaces have been used to impart chemical specificity to porous Si for gas sensor applications [53]. Alkoxy groups can similarly be electrochemically attached to Si [156].

Much more chemically adherent layers can be formed using Si-C bonds to link the organic group to the Si surface. Covalently attached (Si-C) layers have been formed at Si and porous Si surfaces using Grignard and alkyl- or aryllithium reagents [157–164]. Similar results have been obtained by thermal [158, 165], photochemical [55, 162] and Lewis acid catalyzed [166] hydrosilylation reactions. Electrochemical oxidation of methyl-Grignards [167] on porous Si and electrochemical reduction of phenyldiazonium salts [168] on single crystal Si have been shown to yield dense monolayers of methyl and phenyl groups, respectively. Electrochemical reduction of organohalides (Eq. 11) has also been demonstrated as an effective grafting technique [169]. In many cases, the organic functionalization dramatically improves the chemical stability of porous Si [170, 171], which has spurred interest in this material for sensor, display, and photoelectrochemical conversion applications.

The reductive electrolysis of organoiodides and organobromides (Eq. 11) is a fast and highly efficient

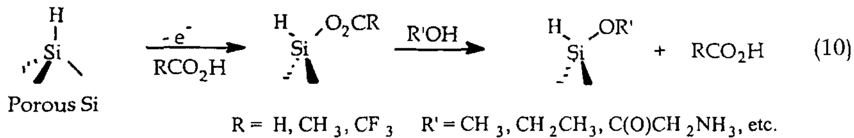

electrochemical method for surface functionalization of n- and p-type porous Si [169]. This method provides high surface coverage, while requiring only very short (< 2 min) reaction times. Widely available mono- and bifunctional organo halide reagents with low to moderate reactivity make this method convenient to use and generally applicable. The reductions are performed in 0.2 M to 0.4 M solutions of the organo halides in an acetonitrile electrolyte. Application of a cathodic current (2 to 10 mA cm^{-2}) for 30–120 s leads to high coverage of the porous Si surface with organic species. As-formed alkyl layers are stable in ethanolic HF, which has become a litmus test to determine if grafting proceeds through formation of covalent Si-C bonds [160, 166]. Si-O bonds are rapidly dissolved under these conditions.

5.7 Applications

Obtaining efficient electroluminescence was a key milestone on the path to integrating porous Si-based optoelectronic functionality on a Si microcircuit chip. The requirements for light emitting diodes used in displays are a bit more stringent: a quantum efficiency higher than 1%, three colors (blue, green, and red) with a spectral width about 0.1 eV, a turn-on threshold below 5 V, and a stability greater than 10^5 h [172]. Until recently, such requirements presented a serious obstacle for porous Si devices, which showed typical electroluminescence efficiencies around 0.1% and stability under one month. Gelloz et al. [103] have reported an enhancement of the quantum efficiency using an anodic passivation process. They obtain an electroluminescence efficiency of 0.21% at emission wavelengths around 640 nm and an applied bias of under –30 V. The device is made of porosified n+type Si contacted with indium tin oxide. This advance has made porous Si-based light emitters a viable option for optical switching applications. Another approach for is to couple passive porous Si optical devices like Bragg reflectors and microcavities with porous Si LEDs. The first attempt was realized by Araki et al. in 1996 with a device composed of a thin gold film, a light-emitting porous Si layer, a multilayer porous Si mirror, a p-type substrate and an ohmic contact [173]. The main advantage of this device is that the Bragg mirror filters the emission of the porous Si to provide a narrow linewidth. The authors report a FWHM of about 0.1 eV. Recently, Chan et al. sandwiched a highly luminescent p+ type porous Si layer between two porous Si Bragg mirrors contacted with gold [112]. The

electroluminescence threshold is about 30 V, the emission is narrow (FWHM around 20 nm), tunable (between 750 and 670 nm), and directional (30 degree cone around the normal axis of the device), demonstrating the potential use of porous Si microcavities for flat-panel displays, although three-color operation has not yet been achieved. Despite the fact that different groups [61–63, 112] reported band narrowing and directionality effects, lasing in porous Si structures has also not been observed yet.

The open pore structure and large specific surface area (a few hundred m^2 per cm^3, corresponding to about a thousand times the surface of the polished Si wafer) make porous Si a convenient material for sensitive detection of liquid and gaseous analytes. The ability to electrochemically tune the pore diameters [174] and to chemically modify the surface [175–177] provides control over the size and type of molecules adsorbed. These properties have been exploited to develop porous Si sensors for detection of toxic gases [178, 179], solvents [59, 180, 181], explosives [182, 183], DNA [65, 184], and proteins [174, 185, 186]. The main techniques investigated to achieve signal transduction are capacitance [187], resistance [188], photoluminescence [189], and reflectivity [51]. Detection limits of at least a few ppb have been demonstrated for some of these [56].

Silicon has an advantage over other crystalline semiconductors in that it is inexpensive and easy to integrate in electronic devices. Porous Si films can be prepared to be luminescent [2], to have a measurable conductivity [115] and to show interference fringes in reflectivity [190]. Sophisticated passive optical structures like Bragg reflectors, microcavities [191], gratings and waveguides [192] have been demonstrated. In-vitro studies have shown the material to be very biocompatible [193–195]. Applications in smart drug delivery systems and temporary medical implants have been proposed [193]. There is little doubt that porous Si will see increased use in practical devices as the field develops. As this occurs, electrochemical control of the surface and morphology will become crucial.

References

1 A. Gee, *J. Electrochem. Soc.* **1960**, *107*, 787.
2 L. T. Canham, *Appl. Phys. Lett.* **1990**, *57*, 1046–1048.
3 A. Uhlir, *Bell System Tech. J.* **1956**, *35*, 333.
4 R. Memming, G. Schwandt, *Surface Sci.* **1965**, *4*, 109–115.
5 M. J. J. Theunissen, *J. Electrochem. Soc.* **1972**, *119*, 351–358.
6 A. Halimaoui, C. Oules, G. Bomchil, A. Bsiesy, F. Gaspard, R. Herino, M. Ligeon, F. Muller, *Appl. Phys. Lett.* **1991**, *59*, 304–306.
7 R. L. Smith, S. D. Collins, *J. Appl. Phys.* **1992**, *71*, R1–R22.
8 L. Canham, *Properties of Porous Silicon*; Short Run Press, London, **1997**, Vol. 18.
9 K. H. Beckmann, *Surface Sci.* **1965**, *3*, 314.
10 D. Ruter, W. Bauhofer, *J. Luminesc.* **1993**, *57*, 19–23.
11 R. E. Hummel, S. Chang, *Appl. Phys. Lett.* **1992**, *61*, 1965–1967.
12 R. E. Hummel, A. Morrone, M. Ludwig, S. S. Chang, *Appl. Phys. Lett.* **1993**, *63*, 2771–2773.

13 R. E. Hummel, M. Ludwig, S. S. Chang, G. Latorre, *Thin Sol. Films* **1995**, *255*, 219–223.

14 R. E. Hummel, M. Ludwig, S. S. Chang, *Sol. St. Comm.* **1995**, *93*, 237–241.

15 M. Ludwig, R. E. Hummel, S. S. Chang, *J. Vac. Sci. Technol. B* **1994**, *12*, 3023–3026.

16 R. W. Fathauer, T. George, A. Ksendzov, R. P. Vasquez, *Appl. Phys. Lett.* **1992**, *60*, 995–997.

17 S. Bayliss, Q. Zhang, P. Harris, *Appl. Surface Sci.* **1996**, *102*, 390–394.

18 S. Miyazaki, K. Sakamoto, K. Shiba, M. Hirose, *Thin Sol. Films* **1994**, *255*, 99–102.

19 D. J. Lockwood, P. Schmuki, H. J. Labbé, J. W. Fraser, *Physica E* **1999**, *4*, 102–110.

20 K. Kuriyama, K. Ushiyama, K. Ohbora, Y. Miyamoto, S. Takeda, *Phys. Rev. B* **1998**, *58*, 1103–1105.

21 A. Gudino-Martinez, E. Rosendo, H. Navarro-Contretas, M. A. Vidal, *Thin Sol. Films* **1998**, *322*, 282–289.

22 N. S. Lewis, *J. Phys. Chem. B* **1998**, *102*, 4843–4855.

23 N. S. Lewis, *Electrochem. Soc. Interface* **1996**, *5*, 28–31.

24 V. A. Burrows, Y. J. Chabal, G. S. Higashi, K. Raghavachhari, *Appl. Phys. Lett.* **1988**, *53*, 998–1000.

25 Y. J. Chabal, G. S. Higashi, K. Raghavachhari, V. A. Burrows, *J. Vac. Sci. Technol. A* **1989**, *7*, 2104–2109.

26 G. S. Higashi, Y. J. Chabal, G. W. Trucks, K. Raghavachhari, *Appl. Phys. Lett.* **1990**, *56*, 656–658.

27 G. W. Trucks, R. Krishnan, G. S. Higashi, Y. J. Chabal, *Phys. Rev. Lett.* **1990**, *65*, 504–507.

28 V. Lehmann, U. Gosele, *Adv. Mater.* **1992**, *4*, 114–116.

29 V. Lehmann, U. Gosele, *Appl. Phys. Lett.* **1991**, *58*, 856–858.

30 P. C. Searson, J. M. Macaulay, F. M. Ross, *J. Appl. Phys.* **1992**, *72*, 253–258.

31 R. Herino, in: *Properties of Porous Silicon* (Ed. L. Canham); EMIS Datareviews, Vol. 18, Short Run Press, London, **1997**, pp. 89–96.

32 A. G. Cullis, L. T. Canham, P. D. J. Calcott, *J. Appl. Phys.* **1997**, *82*, 909–965.

33 J. Erlebacher, K. Sieradzki, P. C. Searson, *J. Appl. Phys.* **1994**, *76*, 182–187.

34 X. G. Zhang, *J. Electrochem. Soc.* **1991**, *138*, 3750–3756.

35 D. Vanmaekelbergh, P. C. Searson, *J. Electrochem. Soc.* **1994**, *141*, 697–702.

36 R. L. Smith, S.-F. Chuang, S. D. Collins, *J. Electron. Mater.* **1988**, *17*, 533–541.

37 S. Fronhoff, M. Marso, M. G. Berger, M. Thonissen, H. Luth, H. Munder, *J. Electrochem. Soc.* **1995**, *142*, 615.

38 H. Foll, *Appl. Phys. A* **1991**, *53*, 8–19.

39 J. Stumper, R. Greef, L. M. Peter, *J. Electroanal. Chem.* **1991**, *310*, 445.

40 C. C. Yeh, K. Y. J. Hsu, P. C. Chen, H. L. Hwang, *Appl. Surf. Sci.* **1993**, *65/66*, 415–422.

41 M. Matsumura, S. R. Morrison, *J. Electroanal. Chem.* **1983**, *147*, 157–166.

42 J. Cleick, *Chaos: Making a New Science*; Penguin Books, New York, **1988**.

43 S. M. Sze, *Physics of Semiconductor Devices*; John Wiley & Sons: New York, **1981**, pp. 250–311.

44 X. G. Zhang, S. D. Collins, R. L. Smith, *J. Electrochem. Soc.* **1989**, *136*, 1561.

45 I. Ronga, A. Bsiesy, F. Gaspard, R. Herino, M. Ligeon, F. Muller, *J. Electrochem. Soc.* **1991**, *138*, 1403–1407.

46 F. Gaspard, A. Bsiesy, M. Ligeon, F. Muller, R. Herino, *J. Electrochem. Soc.* **1989**, *136*, 3043–3046.

47 V. V. Doan, M. J. Sailor, *Appl. Phys. Lett.* **1992**, *60*, 619–620.

48 V. V. Doan, M. J. Sailor, *Science* **1992**, *256*, 1791–1792.

49 C. Levy-Clement, A. Lagoubi, M. Tomkiewicz, *J. Electrochem. Soc.* **1994**, *141*, 958–967.

50 M. J. Sailor, V. V. Doan, in: University of California, San Diego: US Patent, **1994**.

51 C. L. Curtis, V. V. Doan, G. M. Credo, M. J. Sailor, *J. Electrochem. Soc.* **1993**, *140*, 3492–3494.

52 V. V. Doan, R. M. Penner, M. J. Sailor, *J. Phys. Chem.* **1993**, *97*, 4505–4508.

53 E. J. LEE, T. W. BITNER, J. S. HA, M. J. SHANE, M. J. SAILOR, *J. Am. Chem. Soc.* **1996**, *118*, 5375–5382.

54 E. J. LEE, T. W. BITNER, A. P. HALL, M. J. SAILOR, *J. Vac. Sci. Technol. B* **1996**, *14*, 2850–2854.

55 M. P. STEWART, J. M. BURIAK, *Angew. Chem. Int. Ed. Engl.* **1998**, *37*, 3257–3260.

56 M. J. SAILOR, in: *Properties of Porous Silicon* (Ed. L. Canham); EMIS Datareviews, Vol. 18, Short Run Press, London, **1997**, pp. 364–370.

57 B. ROSSI, *Optics*; Addison-Wesley: Reading, MA, **1957**, pp. 125.

58 C. MAZZOLENI, L. PAVESI, *Appl. Phys. Lett.* **1995**, *67*, 2983–2985.

59 P. A. SNOW, E. K. SQUIRE, P. S. J. RUSSELL, L. T. CANHAM, *J. Appl. Phys.* **1999**, *86*, 1781–1784.

60 V. PELLEGRINI, A. TREDICUCCI, C. MAZZOLENI, L. PAVESI, *Phys. Rev. B (Condens. Matt.)* **1995**, 52, R14328–R14331.

61 L. PAVESI, R. GUARDINI, C. MAZZOLENI, *Sol. St. Commun.* **1996**, *97*, 1051–1053.

62 L. PAVESI, C. MAZZOLENI, A. TREDICUCCI, V. PELLEGRINI, *Appl. Phys. Lett.* **1995**, *67*, 3280–3282.

63 S. SETZU, P. SOLSONA, S. LÉTANT, R. ROMESTAIN, J. C. VIAL, *Eur. Phys. J. Appl. Phys.* **1999**, *7*, 59–63.

64 S. SETZU, S. LÉTANT, P. SOLSONA, R. ROMESTAIN, J. C. VIAL, *J. Lumin.* **1998**, *80*, 129–132.

65 S. CHAN, P. M. FAUCHET, in: *Porous Semiconductors*, Science and Technology International Conference, **2000**, pp. 104–105.

66 S. H. TOLBERT, A. P. ALIVISATOS, *Science* **1994**, *265*, 373–376.

67 A. N. GOLDSTEIN, C. M. ECHER, A. P. ALIVISATOS, *Science* **1992**, *256*, 1425–1427.

68 D. BELLET, G. DOLINO, *Thin Sol. Films* **1996**, *276*, 1–6.

69 D. BUTTARD, D. BELLET, G. DOLINO, T. BAUMBACH, *J. Appl. Phys.* **1998**, *83*, 5814–5822.

70 T. ITO, H. KIYAMA, T. YASUMATSU, H. WATABE, A. HIRAKI, *Physica B* **1991**, *170*, 535–539.

71 K. H. KIM, G. BAI, M. A. NICOLET, A. VENEZIA, *J. Appl. Phys.* **1991**, *69*, 2201–2205.

72 D. BELLET, G. DOLINO, *Phys. Rev. B* **1994**, *50*, 17162–17165.

73 C. B. MURRAY, D. J. NORRIS, M. G. BAWENDI, *J. Am. Chem. Soc.* **1993**, *115*, 8706–8715.

74 N. KOSHIDA, H. KOYAMA, *Appl. Phys. Lett.* **1992**, *60*, 347–349.

75 N. KOSHIDA, H. KOYAMA, Y. YAMAMOTO, G. J. COLLINS, *Appl. Phys. Lett.* **1993**, *63*, 2655–2657.

76 F. KOZLOWSKI, M. SAUTER, P. STEINER, A. RICHTER, H. SANDMAIER, W. LANG, *Thin Sol. Films* **1992**, *222*, 196–199.

77 P. STEINER, F. KOZLOWSKI, W. LANG, *Appl. Phys. Lett.* **1993**, *62*, 2700–2702.

78 L. T. CANHAM, W. Y. LEONG, M. I. J. BEALE, T. I. COX, L. TAYLOR, *Appl. Phys. Lett.* **1992**, *61*, 2563–2565.

79 P. D. T. CALCOTT, K. J. NASH, L. T. CANHAM, M. J. KANE, D. BRUMHEAD, *J. Phys. Cond. Mater.* **1993**, 5, L91–L98.

80 I. MIHALCESCU, J. C. VIAL, R. ROMESTAIN, *J. Appl. Phys.* **1996**, *80*, 2404–2411.

81 G. FISHMAN, I. MIHALCESCU, R. ROMESTAIN, *Phys. Rev. B* **1992**, *48*, 1454–1468.

82 C. DELERUE, G. ALLAN, E. MARTIN, M. LANOO, in: *Porous Silicon Science and Technology* (Eds. J. C. Vial, J. Derrien). Les editions de physique, Springer, Berlin, **1994**, pp. 91–101.

83 M. G. BAWENDI, *Solid State Commun.* **1997**, *107*, 709.

84 Y. H. XIE, W. L. WILSON, F. M. ROSS, J. A. MUCHA, E. A. FITZGERALD, J. M. MACAULAY, T. D. HARRIS, *J. Appl. Phys.* **1992**, *71*, 2403–2407.

85 M. C. KO, G. J. MEYER, *Chem. Mater.* **1995**, *7*, 12–14.

86 M. C. KO, G. J. MEYER, *Chem. Mater.* **1996**, *8*, 2686–2692.

87 J. H. SONG, M. J. SAILOR, *J. Am. Chem. Soc.* **1997**, *119*, 7381–7385.

88 M. A. HINES, P. GUYOT-SIONNEST, *J. Phys. Chem.* **1996**, *100*, 468–471.

89 P. D. J. CALCOTT, K. J. NASH, L. T. CANHAM, M. J. KANE, D. BRUMHEAD, *J. Lumin.* **1993**, *57*, 257–269.

90 S. FELLAH, R. B. WEHRSPOHN, N. GABOUZE, F. OZANAM, J.-N. CHAZALVIEL, *J. Lumin.* **1999**, *80*, 109–113.

91 M. C. SCHLAMP, X. PENG, A. P. ALIVISATOS, *J. Appl. Phys.* **1997**, *82*, 5837–5842.

92 B. O. Dabbousi, J. Rodriguez-Viejo, F. V. Mikulec, J. R. Heine, H. Mattoussi, R. Ober, K. F. Jensen, M. G. Bawendi, *J. Phys. Chem. B* **1997**, *101*, 9463–9475.

93 I. Mihalcescu, M. Ligeon, F. Muller, R. Romestain, J. C. Vial, *J. Lumin.* **1993**, *57*, 111–115.

94 V. Petrova-Koch, T. Muschik, A. Kux, B. K. Meyer, F. Koch, V. Lehmann, *Appl. Phys. Lett.* **1992**, *61*, 943–945.

95 A. Bsiesy, F. Muller, F. Ligeon, R. Gaspard, R. Herino, R. Romestain, J. C. Vial, *Phys. Rev. Lett.* **1993**, *71*, 637–640.

96 A. Bsiesy, F. Muller, M. Ligeon, F. Gaspard, R. Herino, R. Romestain, J. C. Vial, *Appl. Phys. Lett.* **1994**, *65*, 3371–3373.

97 W. Lang, P. Steiner, F. Kozlowski, *J. Lumin.* **1993**, *57*, 341–349.

98 E. A. Meulenkamp, P. M. M. C. Bressers, J. J. Kelly, *Appl. Surf. Sci.* **1993**, *64*, 283–295.

99 F. Muller, R. Herino, F. Ligeon, R. Gaspard, R. Romestain, J. C. Vial, A. Bsiesy, *J. Lumin.* **1993**, *57*, 283–292.

100 R. Sabet-Dariani, N. S. McAlpine, D. Haneman, *J. Appl. Phys.* **1994**, *75*, 8008–8011.

101 A. Bsiesy, Y. F. Nicolau, A. Ermolieff, F. Muller, F. Gaspard, *Thin Sol. Films* **1995**, *255*, 43–48.

102 P. M. Fauchet, *J. Lumin.* **1996**, *70*, 294–309.

103 B. Gelloz, T. Nakagawa, N. Koshida, *Appl. Phys. Lett.* **1998**, *73*, 2021–2023.

104 S. Lazarouk, P. Jaguiro, S. Katsouba, G. Masini, S. L. Monica, G. Maiello, A. Ferrari, *Appl. Phys. Lett.* **1996**, *68*, 2108–2110.

105 A. Loni, A. J. Simons, T. I. Cox, P. D. J. Calcott, L. T. Canham, *Electron. Lett.* **1995**, *31*, 1288–1289.

106 H. Mattoussi, L. H. Radzilowski, B. O. Dabbousi, B. O. Thomas, M. G. Bawendi, M. F. Rubner, *J. Appl. Phys.* **1998**, *83*, 7965–7974.

107 L. Pavesi, R. Guardini, P. Bellutti, *Thin Sol. Films* **1996**, *297*, 272–276.

108 P. Steiner, F. Kozlowski, W. Lang, *Thin Sol. Films* **1995**, *255*, 49–51.

109 L. Tsybeskov, S. P. Duttagupta, P. M. Fauchet, *Sol. St. Comm.* **1995**, *95*, 429–433.

110 B. Unal, S. C. Bayliss, *J. Appl. Phys.* **1996**, *80*, 3532–3539.

111 Y. H. Xu, T. Fujino, H. Naito, T. Dohmaru, K. Oka, H. Sohn, R. West, *Jpn. J. Appl. Phys.* **1999**, *38*, 6915–6918.

112 S. Chan, P. M. Fauchet, *Appl. Phys. Lett.* **1999**, *75*, 274–276.

113 R. C. Anderson, R. S. Muller, C. W. Tobias, *J. Electrochem. Soc.* **1991**, *138*, 3406–3411.

114 M. Ben-Chorin, in: *Properties of Porous Silicon* (Ed. L. Canham); EMIS Datareviews, Vol. 18, Short Run Press, London, **1997**, pp. 165–175.

115 M. Ben-Chorin, F. Moller, F. Koch, W. Schirmacher, M. Eberhard, *Phys. Rev. B* **1995**, *51*, 2199–2210.

116 E. Lampin, C. Delerue, M. Lanoo, G. Allan, *Phys. Rev. B* **1998**, *58*, 12044–12048.

117 R. Laiho, A. Pavlov, *Thin Sol. Films* **1995**, *255*, 276–278.

118 H. Mimura, T. Matsumoto, Y. Kanemitsu, *Appl. Surf. Sci.* **1996**, *92*, 598–605.

119 K.-H. Li, D. C. Diaz, Y. He, J. C. Campbell, C. Tsai, *Appl. Phys. Lett.* **1994**, *64*, 2394–2396.

120 L. Zhang, J. L. Coffer, Y. G. Rho, R. F. Pinizzotto, *J. Electrochem. Soc.* **1996**, *143*, L42–L44.

121 P. C. Searson, S. M. Prokes, O. J. Glembocki, *J. Electrochem. Soc.* **1993**, *140*, 3327–3331.

122 P. M. M. C. Bressers, J. W. J. Knapen, E. A. Meulenkamp, J. J. Kelly, *Appl. Phys. Lett.* **1992**, *61*, 108–110.

123 W. H. Green, E. J. Lee, J. M. Lauerhaas, T. W. Bitner, M. J. Sailor, *Appl. Phys. Lett.* **1995**, *67*, 1468–1470.

124 R. Newman, W. C. Dash, R. N. Hall, W. E. Burch, *Phys. Rev. A* **1955**, *98*, 1536.

125 T. Figielsky, A. Torun, *Proc. Int. Conf. Phys. Semiconductors* **1962**, 853.

126 J. R. Haynes, W. C. Westphal, *Phys. Rev. B* **1955**, *101*, 1676–1678.

127 A. L. Lacaita, F. Zappa, S. Bigliardi, M. Manfredi, *IEEE Trans. Electron Devices* **1993**, *40*, 577–582.

128 J. Shewchun, L. Y. Wei, *Solid-State Electron.* **1965**, *8*, 485–493.

129 S. M. Prokes, W. E. Carlos, *J. Appl. Phys.* **1995**, *78*, 2671–2674.

130 H. J. von Bardeleben, M. Chamarro, A. Grosman, V. Morazzani, C. Ortega, J. Siejka, S. Rigo, *J. Lumin.* **1993**, *57*, 39–43.

131 M. Schoisswohl, H. J. von Bardeleben, V. Morazzani, A. Grosman, C. Ortega, S. Frohnhoff, M. G. Berger, H. Munder, *Thin Sol. Films* **1995**, *255*, 123–127.

132 H. Tamura, M. Ruckschloss, T. Wirschem, S. Veprek, *Thin Sol. Films* **1995**, *255*, 92–95.

133 L. T. Canham, A. Loni, P. D. J. Calcott, A. J. Simons, C. Reeves, M. R. Houlton, J. P. Newey, K. J. Nash, T. I. Cox, *Thin Sol. Films* **1996**, *276*, 112–115.

134 S. Munekuni, T. Toshihisa, Y. Shimogaichi, K. Nagasawa, Y. Hama, *J. Appl. Phys.* **1990**, *68*, 1212–1217.

135 E. Cartier, J. H. Stathis, *Appl. Phys. Lett.* **1996**, *69*, 103–105.

136 D. Goguenheim, M. Lannoo, *Phys. Rev. B* **1991**, *44*, 1724–1733.

137 E. H. Poindexter, G. J. Gerardi, M.-E. Rueckel, P. J. Caplan, N. M. Johnson, D. K. Biegelsen, *J. Appl. Phys.* **1984**, *56*, 2844–2849.

138 W. L. Warren, E. H. Poindexter, M. Offenberg, W. Muller-Warmuth, *J. Electrochem. Soc.* **1992**, *139*, 872–880.

139 D. L. Griscom, *J. Ceram. Soc. Jap. Int. Ed.* **1991**, 99, 899–916.

140 L. Skuja, *J. Non-Cryst. Sol.* **1994**, *179*, 51–69.

141 A. Anedda, G. Bongiovanni, M. Cannas, F. Congiu, A. Mura, M. Martini, *J. Appl. Phys.* **1993**, *74*, 6993–6995.

142 K. Mukasa, M. Ono, R. Wakabayashi, K. Ishii, K. Ohki, H. Nishikawa, *J. Phys. D* **1997**, 30, 283–285.

143 A. R. Silin, L. N. Skuja, A. N. Trukhin, *J. Non-Cryst. Sol.* **1980**, *38/39*, 195–200.

144 L. Tsybeskov, J. V. Vandyshev, P. M. Fauchet, *Phys. Rev. B* **1994**, *49*, 7821–7824.

145 A. J. Pepe, W. Chen, M. Oyler, *J. Electrochem. Soc.* **1993**, *140*, 1090–1093.

146 D. J. DiMaria, J. R. Kirtley, E. J. Pakulis, D. W. Dong, T. S. Kuan, F. L. Pesavento, T. N. Theis, J. A. Cutro, S. D. Brorson, *J. Appl. Phys.* **1984**, *56*, 401–416.

147 D. J. DiMaria, M. V. Fishetti, *Appl. Surf. Sci.* **1987**, *30*, 278–297.

148 R. A. Gdula, *J. Electrochem. Soc.* **1976**, *123*, 42–47.

149 E. H. Nicollian, C. N. Berglund, P. F. Schmidt, J. M. Andrews, *J. Appl. Phys.* **1971**, *42*, 5654–5664.

150 J. N. Bradford, S. Woolf, *J. Appl. Phys.* **1991**, *70*, 490–492.

151 D. J. DiMaria, D. W. Dong, C. Falcony, T. N. Theis, J. R. Kirtley, J. C. Tsang, D. R. Young, F. L. Pesavento, S. D. Brorson, *J. Appl. Phys.* **1983**, *54*, 5801–5827.

152 A. P. Baraban, P. P. Konorov, S. A. Bota, J. R. Morante, *Mat. Res. Soc. Symp. Proc.* **1993**, *298*, 253–258.

153 G. Zhou, Y. Nakanishi, Y. Hatanaka, *J. Electrochem. Soc.* **1993**, *140*, 1468–1471.

154 H. Hasegawa, S. Arimoto, J. Nanjo, H. Yamamoto, H. Ohno, *J. Electrochem. Soc.* **1988**, *135*, 424–431.

155 E. J. Lee, J. S. Ha, M. J. Sailor, *J. Am. Chem. Soc.* **1995**, *117*, 8295–8296.

156 M. Warntjes, C. Vieillard, F. Ozanam, J.-N. Chazalviel, *J. Electrochem. Soc.* **1995**, *142*, 4138–4142.

157 M. R. Linford, C. E. D. Chidsey, *J. Am. Chem. Soc.* **1993**, *115*, 12631–12632.

158 M. R. Linford, P. Fenter, P. M. Eisenberger, C. E. D. Chidsey, *J. Am. Chem. Soc.* **1995**, *117*, 3145–3155.

159 J. Terry, M. R. Linford, C. Wigren, R. Cao, P. Pianetta, C. E. D. Chidsey, *J. Appl. Phys.* **1999**, *85*, 213–221.

160 J. H. Song, M. J. Sailor, *J. Am. Chem. Soc.* **1998**, *120*, 2376–2381.

161 J. H. Song, M. J. Sailor, *Inorg. Chem.* **1999**, *38*, 1498–1503.

162 J. Terry, M. R. Linford, C. Wigren, R. Cao, P. Pianetta, C. E. D. Chidsey, *Appl. Phys. Lett.* **1997**, *71*, 1056–1058.

163 C. Vieillard, M. Warntjes, F. Ozanam, J.-N. Chazalviel, in: *Proc. Electrochem. Soc.* (Eds. D. J. Lockwood, P. M. Fauchet, N. Koshida, S. R. J. Brueck); Vol. 95-25, **1996**, pp. 250–258.

164 A. Bansal, X. Li, I. Lauermann, N. S. Lewis, S. I. Yi, W. H. Weinberg, *J. Am. Chem. Soc.* **1996**, *118*, 7225–7226.

165 A. B. Sieval, A. L. Demirel, J. W. M. Nissink, M. R. Linford, J. H. van der-Maas, W. H. de Jeu, H. Zuilhof, E. J. R. Sudholter, *Langmuir* 1998, *14*, 1759–1768.

166 J. M. Buriak, M. J. Allen, *J. Am. Chem. Soc.* **1998**, *120*, 1339–1340.

167 T. Dubois, F. Ozanam, J.-N. Chazalviel, in: *Proc. Electrochem. Soc.* (Ed. P. Schmuki, D. J. Lockwood, H. Isaacs, A. Bsiesy); Vol. 97-7, **1997**, pp. 296–311.

168 C. H. de Villeneuve, J. Pinson, M. C. Bernard, P. Allongue, *J. Phys. Chem. B* **1997**, *101*, 2415–2420.

169 C. Gurtner, A. W. Wun, M. J. Sailor, *Angew. Chem. Int. Ed.* **1999**, *38*, 1966–1968.

170 A. Bansal, N. S. Lewis, *J. Phys. Chem. B* **1998**, *102*, 4058–4060.

171 J. M. Buriak, M. J. Allen, *J. Lumin.* **1998**, *80*, 29–35.

172 T. I. Cox, in: *Properties of Porous Silicon*, (Eds. L. T. Canham); EMIS Datareviews, Vol. 18, Short Run Press, London, **1997**, pp. 290–310.

173 M. Araki, H. Koyama, N. Koshida, *Appl. Phys. Lett.* **1996**, *69*, 2956–2958.

174 A. Janshoff, K.-P. S. Dancil, C. Steinem, D. P. Greiner, V. S.-Y. Lin, C. Gurtner, K. Motesharei, M. J. Sailor, M. R. Ghadiri, *J. Am. Chem. Soc.* **1998**, *120*, 12108–12116.

175 M. J. Sailor, J. L. Heinrich, J. M. Lauerhaas, in: *Semiconductor Nanoclusters: Physical, Chemical, and Catalytic Aspects*, (Eds. P. V. Kamat, D. Meisel); Studies in Surface Science and Catalysis, Vol. 103, Elsevier Science, Amsterdam, **1997**, pp. 209–235.

176 T. F. Harper, M. J. Sailor, *J. Am. Chem. Soc.* **1997**, *119*, 6943–6944.

177 J. M. Buriak, *Adv. Mater.* **1999**, *11*, 265–267.

178 S. Létant, M. J. Sailor, *Adv. Mater.* **2000**, *12*, 355–359.

179 H. Sohn, S. Létant, M. J. Sailor, W. C. Trogler, *J. Am. Chem. Soc.* **2000**, *122*, 5399–5400.

180 J. M. Lauerhaas, G. M. Credo, J. L. Heinrich, M. J. Sailor, *J. Am. Chem. Soc.* **1992**, *114*, 1911–1912.

181 S. Zangooie, R. Jansson, H. Arwin, *J. Appl. Phys.* **1999**, *86*, 850–858.

182 S. Content, W. C. Trogler, M. J. Sailor, *Chem. Europ. J.*, in press **2000**.

183 M. J. Sailor, W. C. Trogler, S. Content, S. Létant, H. Sohn, Y. Fainman, P. E. Shames, in: *SPIE Meeting on Unattended Ground Sensor Technologies and Applications* (Eds. E. M. Carapezza, D. B. Law, K. T. Stalker); SPIE, **2000**, to be published.

184 V. S. Lin, K. Motesharei, K. S. Dancil, M. J. Sailor, M. R. Ghadiri, *Science* 1997, *278*, 840–843.

185 K.-P. S. Dancil, D. P. Greiner, M. J. Sailor, *J. Am. Chem. Soc.* **1999**, *121*, 7925–7930.

186 S. Zangooie, R. Bjorklund, H. Arwin, *Thin Sol. Films* **1998**, *313/314*, 825–830.

187 R. C. Anderson, R. S. Muller, C. W. Tobias, *Sens. Actuat.* 1990, *A21–A23*, 835–839.

188 M. Ben-Chorin, A. Kux, I. Schechter, *Appl. Phys. Lett.* **1994**, *64*, 481–483.

189 J. M. Lauerhaas, M. J. Sailor, *Science* **1993**, *261*, 1567–1568.

190 K.-P. S. Dancil, D. P. Greiner, M. J. Sailor, in: *Mat. Res. Soc. Symp. Proc.* (Eds. L. T. Canham, M. J. Sailor, K. Tanaka, C.-C. Tsai); Vol. 536, **1999**, pp. 557–562.

191 M. Thonissen, M. G. Berger, in: *Properties of Porous Silicon* (Eds. L. Canham); EMIS Datareviews, Vol. 18, Short Run Press, London, **1997**, pp. 30–37.

192 H. F. Arrand, T. M. Benson, P. Sewell, A. Loni, R. J. Bozeat, R. Arenz-Fisher, M. Kruger, H. Luth, *IEEE Journal of Selected Topics in Quantum Electronics* **1998**, *4*, 975–982.

193 L. T. Canham, *Adv. Mater.* **1995**, *7*, 1033–1037.

194 L. T. Canham, J. P. Newey, C. L. Reeves, M. R. Houlton, A. Loni, A. J. Simmons, T. I. Cox, *Adv. Mater.* **1996**, *8*, 847–849.

195 L. T. Canham, C. L. Reeves, A. Loni, M. R. Houlton, J. P. Newey, A. J. Simons, T. I. Cox, *Thin Sol. Films* **1996**, *297*, 304–307.

Electrochemistry of Nanomaterials
by *Gary Hodes (Ed.)*
© WILEY-VCH Verlag GmbH, 2001

6
Charge Transport in Nanostructured Thin-film Electrodes

Sten-Eric Lindquist, Anders Hagfeldt, Sven Södergren, and *Henrik Lindström*

6.1
Introduction

The properties of mesoscopic nanoporous-nanocrystalline, frequently named nanostructured, thin-film electrodes, have been extensively studied. Such porous films immersed in an electrolyte show surprisingly good ability to accommodate photogenerated electrons in the conduction band (CB) of the semiconductor (SC) and deliver a current to a conducting support (back contact). We know from solid-state semiconductor physics that disordered structures in, e.g., polycrystalline film electrodes normally have a relatively poor performance compared with electrodes made from highly ordered materials such as single crystals. This raises several questions. How it is possible to collect electrons and transport them so efficiently through such a poor and disordered structure as a nanostructured thin-film electrode? What are the mechanisms of charge transport? Although extensive work has been performed, there still remain questions to be answered and the mechanism of charge transport in mesoporous electrodes is currently under intense debate in the literature [1–8] and will probably be so for some time to come. Slowly a clearer picture of the factors affecting the transport of charge carriers in nanostructured electrodes is emerging. The object of this chapter is to review the recent work on charge transport in mesoscopic (particulate) nanostructured film electrodes. This review of the field will be accompanied by a discussion which aims to pinpoint eventual inconsistencies and reveal areas where we still have limited knowledge.

There are a few earlier reviews of charge transport in nanostructured electrodes. Peter et al. [5, 9] have recently reviewed the properties of "nanocrystalline electrodes" with particular emphasis on electron transport in dye-sensitized nanocrystalline photovoltaic cells. Some information concerning charge transport in nanostructured electrodes is also found in a paper by Miller et al. [10]. Recent papers by Hagfeldt and Grätzel [11], Hagen [12], and Cahen et al. [13] are also of great value as sources of information for the discussion.

Most of the work presented in this chapter will relate to papers published during the last decade. This is for the simple reason that before the appearance of the paper "A low-cost, high-efficiency solar cell based on dye-sensitized colloidal ti-

tanium dioxide films" by O'Regan and Grätzel in Nature 1991 [14], little attention was paid to the properties of nanostructured electrodes in photoelectrochemistry. In the early fundamental work on dye-sensitized SC electrodes by Gerischer, Tributsch, Willig [15–19], Memming [20], and others, well-defined single crystal electrodes were used. The dye was attached as a monolayer (or less) at a defined flat surface at the electrode-electrolyte interface. The potential distribution in the semiconductor could then correctly be described as a Schottky barrier using the Gärtner-Butler approximation [21]. When polycrystalline and apparently porous large inner area electrodes were used as support for dyes (see, e.g., Refs [22] and [23] and references cited therein) the Schottky barrier was still frequently adopted to describe the potential distribution in the semiconductor. Today's dye-sensitized electrodes are almost exclusively nanostructured *wide band-gap* oxide semiconductor thin films in liquid electrolytes. The absorption of the SC is in the UV while the effective absorption of the dye is in the visible region.

The most extensively studied material so far is TiO_2. The first studies of the charge transport in nanostructured electrodes were made on bare (no adsorbed dye) SC film electrodes [24, 25]. Investigations on dye-sensitized films subsequently were more commonly studied. Different experimental procedures to study where in the SC film efficient separation of photoinduced charge takes place will be presented in this chapter. Thus, photostationary as well as photocurrent transient measurements will be treated. Results from intensity-modulated photocurrent spectroscopy (IMPS) and intensity-modulated photovoltage spectroscopy (IMVS) will be described and discussed [5, 7, 26–33] and attempts to model the charge transport through the films will be reviewed. As we will see, the transport of charge carriers in the porous films and transport of the ions in the electrolyte-filled pores are interrelated. Effects of different morphologies of the nanostructured films will also be briefly addressed. The aim is to elucidate what is known and understood today in this rapidly developing field.

6.2
From Single Crystal to Quantum Dots

6.2.1
Nanostructured Film Electrodes

What is commonly called in the literature today a mesoporous or nanostructured electrode is a porous electrode built up from interconnected semiconductor particles of nanometer size. (An overview of nanostructured materials, methods of preparation of nanoparticles and films, and optical and electronic properties are given in Chapter 7 and by Hagfeldt and Grätzel [34] as well as in other chapters in this book. We will here only point out a fast and cost-efficient method recently introduced for on-line fabrication of thin nanostructured films [35].) Most workers use films that have a relatively homogenous distribution of particles and pores. Typically particle size is in the range of 5–50 nm, and the porosity is normally around 50%. The films

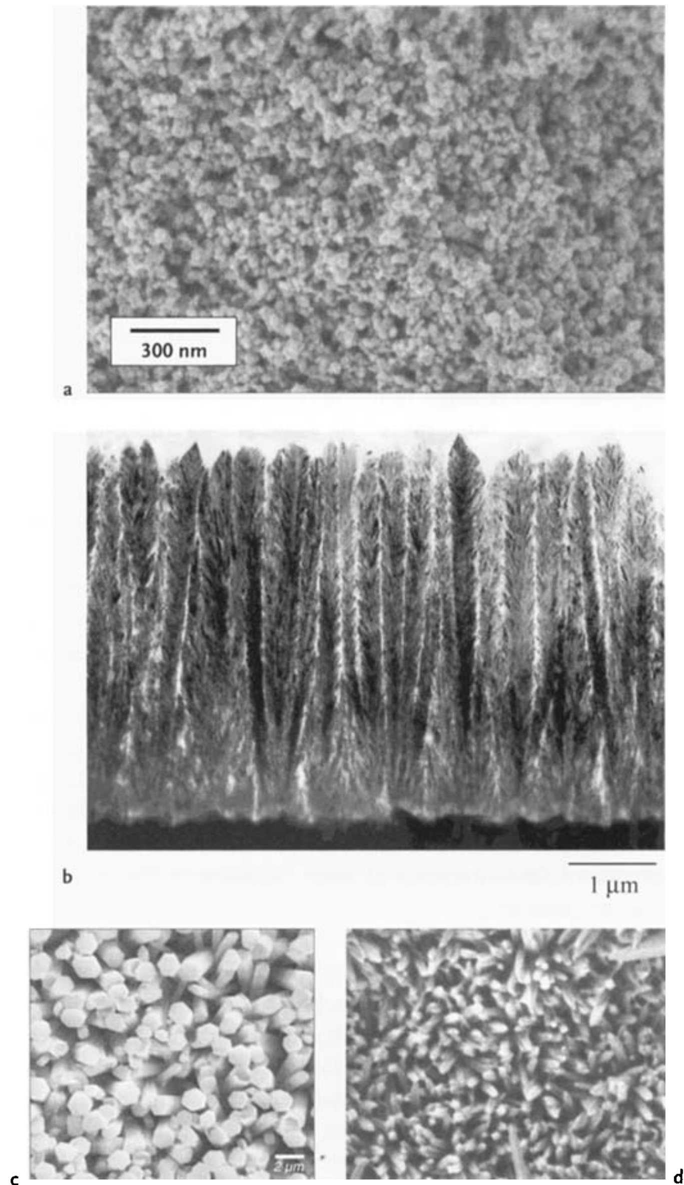

Fig. 6.1 Some examples of different morphologies of nanostructured film electrodes: (a) Isotropic nanostructured TiO_2 from Degussa P 25 powder on a conducting $SnO_2(F)$ film on glass prepared by the press technique [35]. (b) TEM cross-section of a reactively sputtered highly non-isotropic TiO_2 film. The film is porous and allows dye molecules and electrolyte to penetrate the film all the way up to the $SnO_2(F)$ back contact [41]. (c) SEM picture of hexagonal ZnO rods in a film formed by chemical deposition from a solution. (d) SEM picture of a hematite (α-Fe_2O_3) fiber film [39, 40].

are often described as randomly-packed spheres (see, e.g., Ref. [36]) although for many materials, the nanoparticles are highly crystalline and show distinct crystal facets. The vocabulary used for these films varies from author to author and words like nanocrystalline, nanoporous-nanocrystalline, particulate and even microporous are used. An important parameter for the charge transport in porous film electrodes is also their morphology. Most of the work has been done on more or less isotropic films of nanoparticles, but highly non-isotropic films with etched pores in solid single crystals [37], nanorods or rod-like nanoparticles parallel, or perpendicular to the plane of the back contact have been prepared and investigated [38–41]. Even the Langmuir-Blodgett technique [42] and self-assembly and subsequent self-organization of a semiconductor nanocrystallite to form superlattices have been used [43]. A few examples of the different film morphologies are given in Fig. 6.1. As can be expected, such changes in morphology will have major impact on the charge transport properties of the films [40]. Another morphological change with an impact on the charge transport properties is a gradually changing porosity with film depth. From these examples, it is obvious that modeling of porous film electrodes must include aspects of morphology. So far only models for uniform, isotropic, nanostructured film electrodes have been presented. But many other morphologies are currently under investigation [39]. Many of these non-isotropically structured electrode materials (TiO_2, Fe_2O_3, GaP, SiC) often show enhanced efficiencies for conversion of light to photocurrent compared to their isotropically nanostructured counterpart [37, 40, 44].

Independent of morphology, nanostructured film electrodes are characterized by a large inner surface area – often several orders of magnitude larger than the geometric area of the support they are attached to. A 10 μm thick film has typically a geometric-to-inner surface area ratio of 1:1000. In an electrochemical or photoelectrochemical device, this inner film electrode area is the site of the interfacial chemistry. One advantage of porous film electrodes is that slow interfacial kinetics can be compensated by a large number of turnovers at this inner surface area. Another advantage is utilized in the dye-sensitized solar cells and also recently developed colored displays [44–50], where the large inner area allows a large number of dye molecules to be attached to the surface of the SC. Thus only a monolayer of molecules at the interface will result in a high absorption of light per unit area of illuminated film. Independent of morphology, a common feature of all nanostructured electrodes seems to be that transport of the charge carriers is slow.

6.3 Limitations of Charge Transport

To picture the main elements affecting the charge transport in a nanostructured electrode, we have to consider the whole system, that is the transport of carriers in the SC and in the electrolyte. The transport of electrons in the SC, and ions and redox species in the electrolyte are intimately related. Under steady state conditions, one electron leaving the electrode at the back contact of a photoanode

means a corresponding positive charge passing the interface of the nanostructure at the electrolyte side of the electrode. But that is not all. The SC and electrolyte must be looked upon as one effective medium [13]. The redistribution of ions and dipoles between the solution in the pores and the surface of the nanostructured SC strongly affects charge separation and kinetics at the nanostructured semiconductor electrode-electrolyte interface (NSEI) [51], as well as the charge transport. Any excess electron in a SC particle is screened by a corresponding image charge by ions and dipoles in the solution.

Let us list the important steps in the charge transport after a light-induced charge separation in an n-type nanostructured film electrode sandwiched with a counter electrode:

1. absorption of a photon and excitation of an electron from the valence band (VB) to the conduction band (CB);
2. transfer of a hole over the NSEI;
3. a hole-hole acceptor reaction (an oxidation step) in the electrolyte at the NSEI;
4. electron transport of electrons through the SC nanoparticle film;
5. transport of a corresponding positive charge out of the nanostructure towards the CE;
6. transport of the electron through the outer circuit to the CE; and
7. electron transfer and redox chemistry at the CE.

(In a DSC the same steps are present, with the difference being that the dye absorbs the photon (excitation from HOMO to LUMO level) and the electron in the LUMO level is injected into the CB, thus leaving the dye with an excess positive charge – a "hole".)

Step one is fast but in principle any one of the other steps can be rate limiting. We will in the following focus on the transport of charges in the nanostructured film, that is, steps 4 and 5. As will be discussed below, step 4 can eventually be divided into two processes: transport through the nanostructure up to the interfacial region close to the back contact, and the transport from this region into the back contact. The latter is related to a discussion concerning the existence of a junction in the vicinity of the back contact (vide infra). Whenever discussing the charge transport, we have to keep in mind all steps, and consider which is rate-limiting. While step 1, as well as the electron injection in the case of a dye-sensitized system, have been proven to be extremely fast [52–60], in most systems studied, the reaction over the NSEI (step 3) will depend on the interfacial rates of reaction between the charge carrier passing over the NSEI (hole or electron) and accepting species in the electrolyte. This reaction is strongly system dependent. E.g. in an n-type nanostructure, an efficient hole-accepting species in the solution can speed up the interfacial reaction. The reaction rates for the reduction of the dye with an electron donor in the electrolyte, as well as for step 7, are extremely important in the solar cell device, but this is outside the scope of this paper.

It should also be noted that step 4 is further complicated by trapping-detrapping [7, 8, 61–63] of electrons in intrinsic SC and/or surface states and by different electron back reactions across the NSEI. As noted above, the charge transport is also affected by the intimate relation between carriers in the SC and dipoles

and ions in the electrolyte. The net flux of charge through a nanostructured electrode is a function of material parameters such as particle and pore size, morphology and properties of the SC, as well as the concentration of supporting electrolytes and redox components in the solution. It will also depend on experimental conditions. Thus, the generation rate (step 1) of charge carriers is an important parameter, since the properties of the nanostructured electrodes may change with increasing concentration of electrons in the CB. Also the interfacial reactions are a dynamic function of the concentration and distribution of free and trapped carriers in the system [5, 28, 30, 64].

6.4
The Breakdown of the Schottky Barrier Model

As mentioned above, the traditional manner of describing the behavior of semiconducting electrodes stems from solid state semiconductor physics. It is well known that when a crystalline (with crystal size of at least hundreds of nanometers) semiconducting electrode is brought in contact with a solution, a Schottky barrier is (usually) formed in the semiconductor at the liquid-SC interface. The energetics in the system is described by the positions of the conduction band and valence band and the relative positions of the Fermi levels (E_F) in the semiconductor and the electrolyte. A schematic of the energetics and relevant equations are shown and described for an n-type SC in Fig. 6.2 and the figure legend. This figure provides the basis for the generally used Gärtner-Butler equation (Eq. 1) [21, 65] giving the net photocurrent density i_{ph} as a function of the absorption coefficient, α, the diffusion length, L_p, of the minority carrier in the semiconductor, the photon flux Φ_0 incident on the electrode and depletion layer w (Eq. 2). The latter is expressed as a function of the electrode potential, U, the flat band potential, U_{FB}, the relative dielectric constant, ε, the permittivity of free space, ε_0, the donor concentration in the SC, N_D, and the elementary charge, q, as shown by Eq. (2). Because, in the following text, we will deal the monochromatic or "incident photon to current efficiency" $IPCE = \phi_\lambda = i_{ph}/q\Phi_0$, Eq. (1) has been rearranged to give Eq. (3). Thus $IPCE$ (or ϕ_λ, quantum efficiency, *vide infra*, page 177) is a function of the wavelength λ of the incident light. We will in the following also consider backwall illumination of nanostructured film electrodes, therefore the equation for a solid semiconductor electrode for backwall (SE) illumination as derived by Lindquist et al. [66] is given (Eq. 4), for comparison. In Eq. (4) the thickness, d, of the film (as defined in Fig. 6.2) becomes an important parameter.

When we substitute the single crystal with a particulate porous semiconductor electrode, the conditions for charge separation and charge transport become even more complex. For the sake of the discussion, let us look at this transformation in a process in which the macroscopic solid semiconductor electrode is gradually broken up into smaller and smaller, physically and electrically interconnected particles. What we will observe is not only an electrode that is penetrated by the liquid electrolyte and gradually increases its interfacial area. At a certain point we

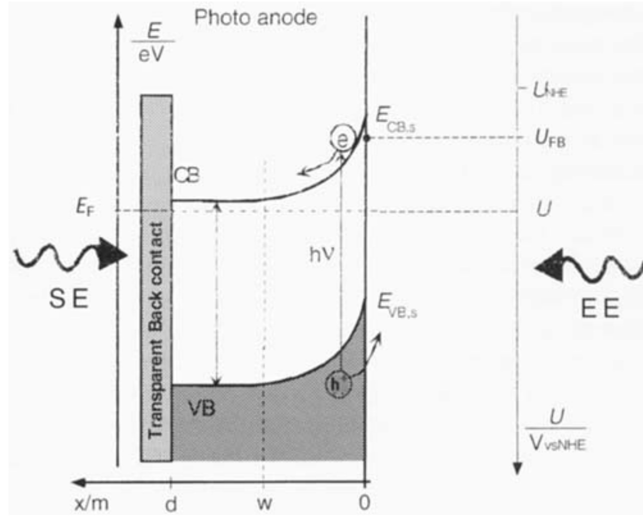

Fig. 6.2 The energetics of an n-type, compact solid state SC electrode in contact with an electrolyte. The direction of illumination is defined EE or "front wall" and SE "back wall" are defined in the figure. Gärtner-Butler equation:

$$i_{ph} = q\Phi_0 \left[1 - \frac{\exp(-\alpha w)}{1 + \alpha L_p} \right] \tag{1}$$

where

$$w = \left(\frac{2\varepsilon\varepsilon_0}{eN_D} \right)^{1/2} (U - U_{FB})^{1/2} = w_0 (U - U_{FB})^{1/2} \tag{2}$$

is for EE illumination expressed by:

$$\phi_{EE} = 1 - \frac{1}{1 + \alpha L_p} \exp(-\alpha w) \tag{3}$$

and for SE illumination by:

$$\phi_{SE} = \frac{1}{1 - \alpha L_p} \exp[-\alpha(d - w)] - \exp[-\alpha d] \tag{4}$$

Symbols are explained in the text, and in [66].

will also have to accept a breakdown of the Gärtner-Butler formalism described above. The reason is that the particle size becomes so small, that it can no longer support an effective depletion layer [67, 68]. Therefore the band model description will no longer be applicable. Moreover, as the particle size approaches a few nanometers or less, the number of atoms in the particles becomes so small that they start to show "molecular properties". The particles become "quantum dots" or

"quantum rods", subject to the quantum size effect [69–76]. This change in size of the particles in the electrode can be observed spectroscopically as a blue shift of the absorption edge, which is a consequence of an increase of the band-gap (see, e.g., Ref. [77]). More or less distinct bands also appear in the absorption spectra due to separation of the energy levels in the bands. Another change is related to scattering of light. The simple interfacial specular reflection at the interfaces of a perfect single crystal electrode turns into a pattern of scattered light. We have to consider the diffusely transmitted and reflected light. A *porous* mesoscopic SC film with a band-gap > 3 eV (and subsequently with no absorption in the visible region) will in ambient daylight if the particles (nanocrystals, aggregates of nanocrystals, amorphous particles, etc.) are large enough, appear white due to scattered visible light and the transmitted light appears brownish, because of the loss of scattered blue light. As the particles approach the size of a few nanometers or smaller, the scattered light shifts into the UV region and the semiconductor nanoparticle films become transparent in the visible region again. It should here be emphasized that if nanocrystals form aggregates, it is rather the size of the aggregates than the size of the nanocrystals that determines the spectral distribution of the scattered light.

As already stated, with decreasing size of the particles, the concept of a Schottky barrier [21, 65] will be increasingly invalid. A depletion region, w, at the semiconductor-electrolyte interface (SEI), commonly assumed for single crystal and solid polycrystalline electrodes, will normally not be formed. Unless the doping density is very high, such small particles cannot sustain a depletion layer of any magnitude [2, 34]. Furthermore, as the electrolyte penetrates the electrode all the way to the back contact, and we have to consider the total inner nanostructured semiconductor electrode-electrolyte interface, the following questions arise: Where does the efficient charge separation take place in a nanostructured electrode, and how are the charge carriers separated? How can we explain the photocurrent and photovoltage in a nanostructured electrode, when employed as the photoactive electrode in a sandwich wet-solar-cell, and how can we explain efficiency as high as 10–11% in dye-sensitized solar cells [1, 11, 78, 79]? All these questions relate to some extent to the mechanism of charge transport in nanostructured electrodes. A first handle in the search for answers to these questions was given by action spectra analysis.

6.5 Action Spectra Analysis

6.5.1 Technique and Definitions

Action spectra analysis can be a powerful tool in the investigations of the photoelectrochemical properties of SC thin-film electrodes. The electrodes are illuminated with continuous monochromatic light under potentiostatic conditions in a three-electrode system. The photocurrent is registered and displayed as a function

of wavelength. As the output power per unit area (P) of light from the monochromator varies with wavelength, the "incident photon to current efficiency" $IPCE$ (or ϕ_λ) is calculated from:

$$IPCE = \phi_\lambda = \frac{hc}{q}\frac{i_{ph}}{P\lambda} \qquad (5)$$

where h is Planck's constant, and c the velocity of light.

$IPCE$ and ϕ_λ are used synonymously in the literature. During the last decade, $IPCE$ has become predominant, and will be used in this chapter. Normally, $IPCE$ is not corrected for losses of light by absorption in solutions, glass substrates and transparent back contacts as well as for reflection losses at interfaces, etc. For comparison of experimentally collected data with theoretical expressions, such corrections are important. In solar cell devices, these corrections are not always carried out, as the performance of the complete device as assembled is of interest. Different workers practice different conventions. Occasionally the *quantum yield* or "absorbed photon to current efficiency" ($APCE$) is calculated

$$APCE = IPCE/A_\lambda \qquad (6)$$

where A_λ is the absorption. $APCE$ is the number of electrons collected at the back contact per photon absorbed in the SC. That is, a correction is also made for the transmitted light.

$APCE$ is a measure of how many electrons leave the electrode at the back contact per photon absorbed. For dye-sensitized electrode and cells, the following expression is often used

$$IPCE = LHE\phi_{inj}\eta_{esc} \qquad (7)$$

where ϕ_{inj} is the quantum yield for the injection of electrons (or holes), η_{esc} is the charge separation probability, and LHE is the light harvesting efficiency (and identical with A_λ). Apparently $APCE = \phi_{inj}\eta_{esc}$.

6.5.2
The Zones of Efficient Charge Separation

Shortly after the Nature paper of Grätzel and O'Regan [14] was published in 1991, the photocurrent action spectra of nanostructured CdS and CdSe were recorded by Hodes and Peter [24]. At the same time, $IPCE$ actions spectra for nanostructured TiO_2 [25, 80] electrodes were registered by Hagfeldt et al. A common feature of these experiments was that film electrodes were deposited on a transparent conducting substrate, so action spectra could be recorded both with the light incident on the substrate-electrode interface (SE-illumination) or on the electrolyte–electrode interface (EE-illumination). By tradition from earlier PEC work, "front wall" (EE) and "back wall" (SE) illuminations are still used by many workers. For definitions see Fig. 6.2 and corresponding text.

6.5.2.1 **Action Spectra of TiO_2 Film Electrodes**

Action spectra of nanostructured TiO_2 film electrodes were recorded in the UV region [25] and compared with similar measurements performed on compact TiO_2 thin films with transparent back contacts [66]. There was a distinct difference in the spectral distribution of ϕ_λ (= *IPCE*) of the nanostructured TiO_2 film electrodes, when compared with the same type of action spectra recorded at the compact TiO_2 thin films presented almost ten years earlier. The spectral distributions were very much the same. Agreement between the two spectra could be obtained if the indices EE and SE were shifted. That is, the EE action spectrum for the nanostructured electrode was similar to the SE action spectrum of the solid film electrode and vice versa. The results are shown in Figure 6.3 a and b. The SE and EE illumination action spectra of compact TiO_2 thin-film electrodes were satisfactory explained by applying the Gärtner-Butler model [66] for a Schottky barrier at

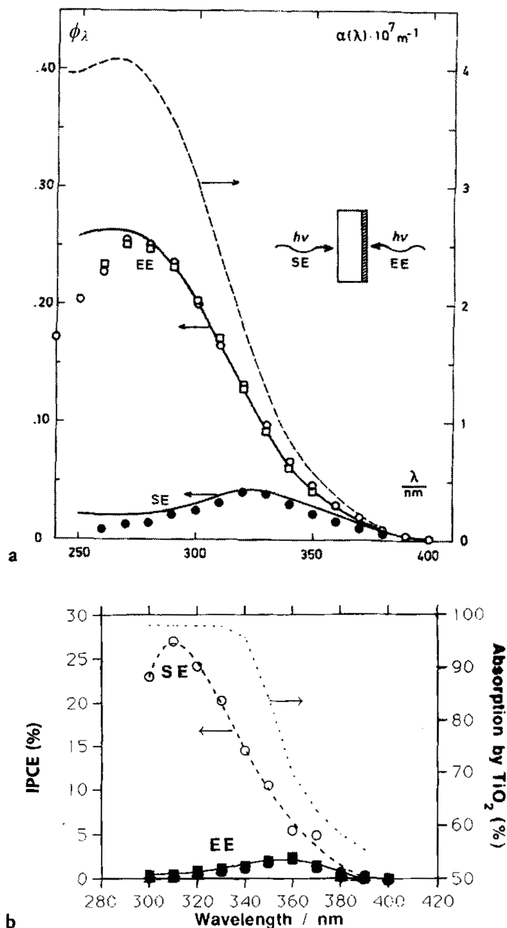

Fig. 6.3 (a) The action spectrum for SE and EE illumination for a 70 nm amorphous compact TiO_2 film. The dashed curve shows the spectrum of the absorption coefficient. Best fits to experimental data using the Gärtner-Butler model are shown by the solid curves [66]. (b) The action spectrum for SE and EE illumination for a 7-μm thick nanostructured TiO_2 film. The dashed upper curve shows the absorption spectrum [25, 80].

the electrode-electrolyte interface (Eqs. 1–4). The action spectra of the nanostructured TiO_2 electrodes were in direct contradiction to what had been observed for solid thin films [25, 80]. Thus, using the penetration depth of the monochromatic light at different wavelengths as a probe, from the comparison of the two sets of action spectra, it could be concluded that the most efficient charge separation in the nanostructured electrodes took place in a zone close to the back contact.

6.5.2.2 **Photocurrent Action Spectra from Porous CdSe and CdS Films**

From similar backwall (SE) and frontwall (EE) photocurrent (i_{ph}) action spectra analyses for nanocrystalline porous CdS and CdSe thin films, Hodes et al. [24] came to a similar conclusion: "Charge separation in these photoelectrodes occurs at the semiconductor-electrolyte interface which occurs throughout the thickness of the porous film, and not in a built-in space charge field. Relatively low recombination loss is due to rapid removal of one of the charges (holes) allowing electrons to pass through a number of grain boundaries with a small chance of meeting a hole on its journey to the substrate", this explanation emphasizes the interfacial kinetics. That is, the rapid loss of one of the charge carriers in the SC (in the present example, the hole) at the electrolyte-nanoparticle interface. Implicitly, it also points to another important parameter: The long lifetime of the other charge carrier, the electron in the CB – allowing this carrier to reach the back contact without recombining either with holes or by reductive back reactions with components in the electrolyte (see below). This new information indeed indicated that the normal description valid for ideal single crystals and compact thin solid film electrodes was not valid for the porous SC electrodes. These experiments also announced another important property of nanostructured electrodes: The fact that a porous electrode, composed of small interconnected particles, so that the electrolyte could penetrate the electrode all the way to the back contact, could efficiently transfer electrons to the back contact.

A number of investigations followed and similar SE and EE action spectra characteristics were found for different nanostructured dye-sensitized [81, 82] as well as bare electrodes [51, 83]. Almost all materials investigated, mainly large bandgap metal oxides, showed "n-type behavior". That is, the electrons in the conduction band were transferred to the back contact, just as in an n-doped single crystal semiconductor with a Schottky barrier at the electrode-electrolyte interface. Normally n-type behavior indicates that the SC material is n-doped. However, if the assumption that the interfacial kinetics and the lifetime of the different carriers in the nanostructure determines the direction of the current is correct, then the type of doping should be of less importance. Actually non-doped (close to intrinsic) TiO_2 seems to work very well. In their CdS and CdSe electrodes, Hodes et al. observed a transition from n- to "p-type behavior" [84] explained by change in the interfacial kinetics, which was subsequently related to preferential charge trapping of electrons or holes at the nanocrystalline CdSe surface [69]. Recently "p-type behavior" was shown also for plain and dye-sensitized nanostructured NiO electrodes [85]. However, as-prepared NiO is known to be p-doped [86]. Since nano-

structured p-type system are rare, the discussions in the following will be restricted to semiconductors with n-type behavior.

6.5.2.3 Scavengers in the Electrolyte

It was also clarified that electron scavengers in the electrolyte, energetically positioned to overlap with the semiconductor CB, substantially decreased the photocurrent. Oxygen (Fig. 6.4a) [82] and triiodide (Fig. 6.4b) [51] commonly used in the Grätzel cell was shown to collect electrons from the TiO_2 CB. These measurements again strongly indicated that the high currents collected at the back contact were driven by the interfacial kinetics, rather than by a potential gradient (in a depletion layer) inside the SC. A fast hole injection into the electrolyte, promoted by e.g. a fast oxidation of chemical species in the solution and a long life time of the electron in the conduction band, appeared to be the important factors for high yields. Trapping of the electron in intrinsic or surface states will increase the residence time of the electrons in the nanostructure, and thus also the probability of losses due to back reactions with components in the electrolyte. Consistent with the latter, it was also shown that the film thickness was a parameter of importance for the IPCE action spectra, particular for EE illumination [87].

On the basis of the action spectra analysis as described above, a first model for the charge separation and charge transport was proposed. It was applied to experi-

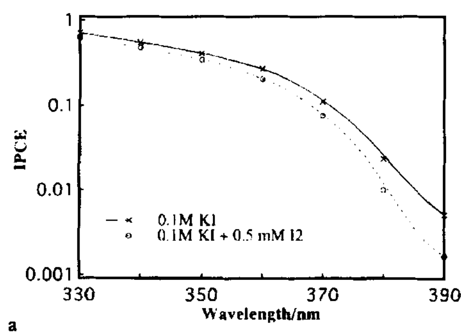

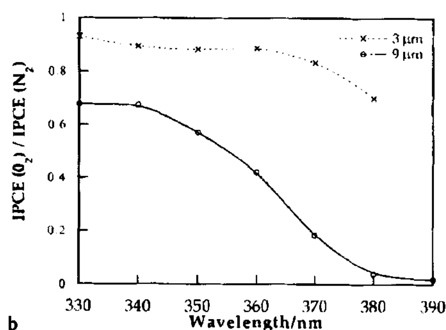

Fig 6.4 Action spectra obtained for SE illumination of a 6 µm thick porous nanocrystalline TiO_2, in 0.1 M KI (solid line) and 0.1 M KI + 0.5 mM I_2 (dashed line). Spectra recorded at 0.3 V relative to the SCE at pH 6.8. Note the logarithmic scale. (b) The ratio of the $IPCE_{SE}$ values, obtained in N_2- and O_2-saturated electrolyte (0.1 M KI at pH 6.6) at two porous nanocrystalline 9 µm (dashed upper line) and 3 µm (solid line) films. Spectra recorded at 0.3 V relative to the SCE [51, 82].

mental action spectrum data, and the current–voltage characteristics of nanostructured TiO_2 electrodes [88].

6.6 The Diffusion Model

As discussed in Section 4, the nanoparticles in typical porous SC films are too small to support a space charge layer. To explain charge separation, O'Regan et al. in one of their early papers [89] assumed that the clustering and interconnection of the particles can be expected to affect the potential distribution, so that a significant electrical field is likely to develop in the array of particles. The model proposed by Södergren et al. 1994 [2] abandoned the influence of any electrical field and assumed that the photogenerated electrons in the CB were driven solely by diffusion in a concentration gradient of electrons in the film. The diffusion length L of the *majority carrier* – the electron in the case of TiO_2 – was introduced as an important parameter, and it was shown that the L could be estimated from experimental data. The assumptions in the derivation of the "diffusion model" were: (i) The electron transport in the SC occurs via diffusion, and (ii) L is a constant through out the whole nanoporous film, (iii) the recombination losses is assumed to be of first order. The derivation of the spectral distribution of the IPCE and current-voltage characteristics started with equation:

$$Dn''(x) - [n(x) - n_0]/t + \Phi a e^{-ax} = 0 \tag{8}$$

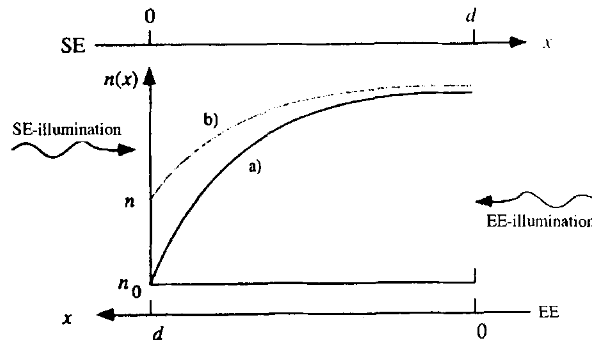

Fig. 6.5 Electron concentration profile in a nanostructured SC film during illumination. To obtain the boundary conditions for SE and EE illumination, the x-axis is in the direction of the incident light in the respective cases. Curve (a) displays the electron concentration when the cell is unloaded (short-circuit conditions), whereas for curve (b) the cell is loaded. The SC–back-contact interface is placed at the position of the y-axis for both SE and EE illumination. The boundary conditions for SE illumination: $n(0) = n_0$ and $dn(x)/dx|_{x=d} = 0$ respectively and for EE illumination: $n(d) = n_0$ and $dn(x)/dx|_{x=0} = 0$ [2].

where D is the diffusion constant of the electrons in the film, $n(x)$ the excess electron density, n_0 the electron density in the dark and t, Φ, and α are the same as in the equations given in the legend to Fig. 6.2.

Fig. 6.5 gives the electron concentration profile in the nanostructured SC electrode under short circuit and finite load conditions.

It also gives the boundary conditions and definitions of film thickness d under SE and EE illumination. With these boundary conditions and knowing the absorption coefficient, α, expressions for the photo-to-current efficiency as a function of wavelength can be derived (Eqs (6) and (10) in Ref. [2]). Fig. 6.6a gives the best fit to experimental data for SE and EE action spectra. Similarly an equation for the current-voltage characteristics, expressed by

$$I = I_L - I_S \exp[(qV/kTm) - 1] \tag{9}$$

was derived. In Eq. (9), I_L is the photocurrent due to the incident light and I_S is the saturation current. Eq. (9) was fitted to I-V data for a dye-sensitized nanostructured film illuminated with monochromatic light close to the absorption maximum of the dye (520 nm). The agreement between data and the I-V curves was

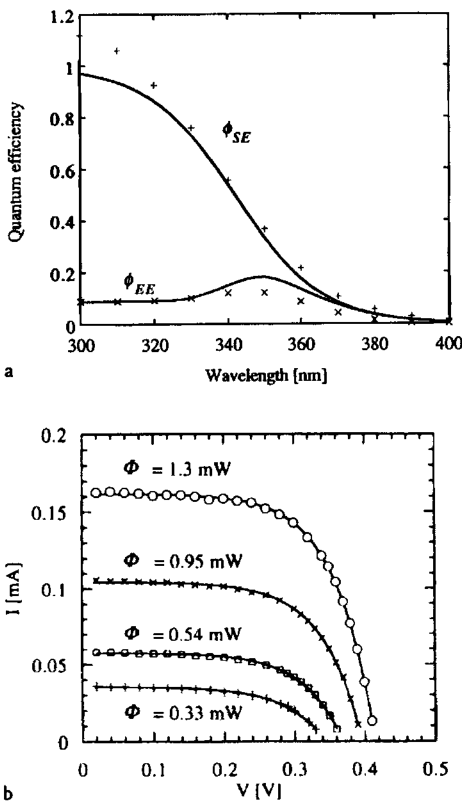

Fig. 6.6 (a) Experimental data for action spectra EE (ϕ_{EE}) and SE (ϕ_{SE}) illumination of a 2.5 μm thick nanostructured TiO_2 film electrode in 0.1 M KSCN ethanol. Theoretical curves (solid lines) to fit the experimental data have been calculated from Eqs (6) and (10) in Ref. [2] setting the diffusion length of the electron to 0.8 μm. (b) Current–voltage (I–V) characteristics of a 2 μm dye-sensitized nanostructured TiO_2 film electrode in a sandwich cell structure. Electrolyte: 0.4 M LiI and 0.1 M I_2 in a propylene–ethylenecarbonate mixture (1:4 by weight). The I–V curves were recorded at different monochromatic light intensities of 520 nm (FWHW = 10 nm). Solid lines are curves calculated from Eq. (9) in Ref. [2] for best fit to the experimental points. Both I_S and m in Eq. (9) were constant at all light intensities (within experiment error).

excellent and both the ideality factor m and I_S were constant within experimental error at four different light intensities (Fig. 6.6b).

6.7 Laser-pulse-induced Current Transients

Another way to study the charge transport through nanostructured electrodes is by pulse-induced current transients. The film electrode is excited with a short light pulse with a defined penetration depth, and the photocurrent transient collected at the back contact is registered. Potential dependent transient measurements can conveniently be performed in a conventional three-electrode cell.

Hoyer and Weller used this technique on nanostructured ZnO electrodes [90]. The injection of electrons into the CB was performed by illuminating the electrode from the EE side with a fast nanosecond excimer laser pulse of 308 nm wavelength. At this wavelength, the penetration depth of the light, $1/a$, in ZnO is small and, for the films studied, almost negligible compared to the thickness of the electrodes. The "flight time" to the back contact of the photogenerated electrons injected into the CB at the electrolyte side of the electrode could be measured. After a fast photocurrent transient in the micro- to millisecond regime, a slow current transient, peaking after a few milliseconds, was observed. These observed transit times (measured as the time between flash and the maximum transient current), decreased with increasing light intensity, and they were two to three orders of magnitude longer than expected from the mobility of the electrons in the bulk crystalline ZnO.

Other investigators used the same technique [27] on TiO_2 electrodes and a model for the electron transport was formulated [91–93]. The electron diffusion current was derived by solving the time-dependent diffusion equation (Fick's second law). Thus

$$n(x,t) = \frac{\Delta N}{2\sqrt{\pi D t}} \mathrm{e}^{-(x-d)^2/4Dt} \tag{10}$$

where t is time, x is the distance from the back contact, $n(x,t)$ is the concentration of electrons at time t at the position x, d the thickness of the film, D the chemical diffusion coefficient for the electron (coupled to its image charge in the solution), ΔN the number of photoexcited electrons after initial recombination (approximated by a square pulse of negligible width).

The diffusion current is given by the electron concentration gradient times D and the elementary charge q.

$$I_{\text{diff}} = \frac{qd\Delta N}{2\sqrt{\pi D} t^{3/2}} \mathrm{e}^{-d^2/4Dt} \tag{11}$$

From the fact that the current is at maximum when $\mathrm{d}I/\mathrm{d}t=0$, the current maximum appears when:

$$t_{peak} = d^2/6D \qquad (12)$$

An expression for an initial fast low-intensity current transient was added (for details see Solbrand et al. [92]) to give:

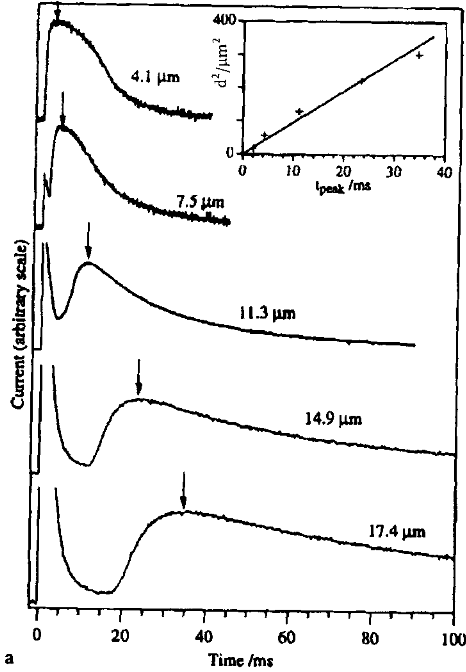

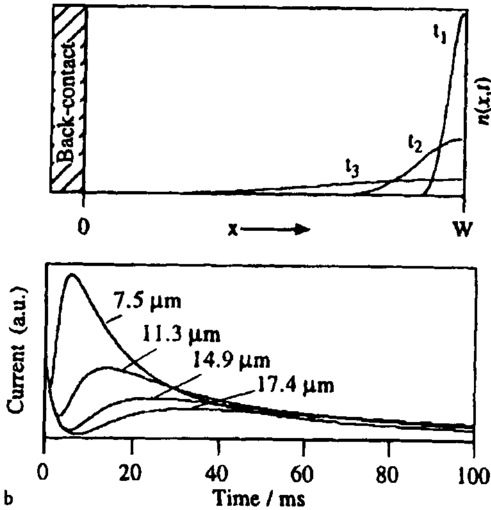

Fig. 6.7 (a) Induced photocurrent transients for five films with different thickness in the range 4–18 μm. The inset gives a best fit to Eq. (12). (b) The upper part shows the evolution of the electron concentration at three consecutive times, the lower part is a simulated transient from Eq. (13).

$$I = \frac{qd\Delta N}{2\sqrt{\pi D t^{3/2}}} e^{-d^2/4Dt} + \frac{q'}{\tau} e^{-t/\tau} \qquad (13)$$

The transit time for the electrons was studied as a function of the nanostructured film thickness. Fig. 6.7a shows the induced photocurrent transients for five films with different thickness in the range 4–18 μm. The inset gives a best fit to Eq. (12). Fig. 6.7b shows in the upper part the evolution of the electron concentration at three consecutive times and, in the lower part, a simulated transient from Eq. (13). The qualitative agreement between simulated (Fig. 6.7b) and experimentally determined curves (Fig. 6.7a) is striking.

The formulated model, again based on the assumption that the electron transport in the conduction band was controlled by diffusion, gave reasonable agreement between experiment and theory. The outcome of these studies was unambiguous: the charge transport is mainly controlled by a diffusive process. A general observation was that the estimated apparent diffusion constants were smaller, or of the same size as those for the ions in the solutions.

Further studies included detailed investigations of the effects of applied potentials [92, 94], conductivity and concentration of the supporting electrolyte in different solvents. Nanostructured TiO_2 and ZnO films were studied [93].

6.8 The Influence of Traps

An early paper by Schwarzburg and Willig [61] discussed the influence of trap filling on photocurrent in dye-sensitized polycrystalline TiO_2 electrodes. Unfortunately it is not possible to derive from their letter if the "polycrystalline electrode" was porous or not. The assumption of Schottky barrier-type contact may indicate that the authors assumed a solid close-packed compact and non-porous structure. They discuss the trapping-detrapping mechanism in terms of the Shockley-Read formalism and compare the experimental photocurrent response of their TiO_2 samples subject to square wavelight pulses at different incident photon flux, to numerical curves derived from their rate equations. The shape of the photocurrent transients at different light intensities provides evidence of a trap-filling controlled process. Photocurrent transient experiments on nanostructured TiO_2 electrodes show a similar behavior, indicating that, also in these electrodes, a trapping-detrapping mechanism should be considered.

Koenenkamp et al. [31, 95, 96] studied the transport kinetics and trapping processes in colloidal TiO_2 films using time-resolved photoconductivity techniques. They found that the transport process in the films was dispersive. Excess electrons induced by e.g. optical pumping or electrical injection was found to saturate the trap states and induce drastic changes in the trapping kinetics. Decay times on the millisecond range were reached, which results in correspondingly longer transport distances. Thus the transport properties were markedly improved when

excess carriers saturated deep trap states. They suggest that the success in using nanostructured films in DSCs may be due to the improved transport properties under high carrier injection.

In a preliminary model of dispersive transport based on the continuous-time random walk, Nelson [97] introduced traps. The model was applied to nanocrystalline TiO_2 electrodes. The basic idea is "that electrons perform a random walk on a lattice of trap states, each electron moving after a waiting time which is determined by the activation energy of the trap currently occupied". An exponential density of trap states, $g(E) \sim e^{a(Ec - E)/kT}$, was used. It was also shown that normal diffusive transport failed to explain the observed kinetic behavior.

6.9 Charge Transport in the Electrolyte

6.9.1 Liquid Electrolytes

As mentioned in Section 3 above, the properties of the liquid phase in the pores of the nanostructured electrode can be the limiting factor in the charge transport. It is easy to imagine and create systems in which the transport of the redox couple through the mesoscopic pores can be the limiting factor [12, 98–100]. In an n-type, nanostructured SC film subject to efficient injection of electrons into the CB, fast interfacial kinetics of the hole and a fast electron transport in the SC film, the photocurrent will be limited by the slow transport of the redox couples in the electrolyte. Such a limitation can be enhanced by physically obstructing the transport of the charged or neutral redox components with a polymer in the pores, increasing the viscosity of the solvent, or by decreasing the porosity by making the electrode more compact. Parameters of interest are well described in Ref. [36] and in references therein. Adsorption of redox components at the NSEI and thereby increased residence time in the nanostructure can also decrease the flux of redox component in the electrode. Most authors working on the transport properties of the redox couple(s) in the electrolyte deal with transport in a two-electrode sandwich solar cell sandwich structure [36, 101–104]. However, studies of the transport of redox species in nanostructured electrodes in bulk solutions in a three-electrode system have also been performed. In such a system, care must be taken to eliminate the concentration gradient outside the electrode by stirring. Control of the flux of component out to the electrode-electrolyte interface is best achieved in a rotating disk experiment [105]. For practical reasons, this method is rarely used for nanostructured electrodes. It is also important to note that, in a sandwich structure, the concentration of one of the redox components at high current densities will approach zero at the counter electrode. In a three-electrode measurement, on the other hand, the concentration outside a nanostructured electrode will be determined by the concentration in the bulk of the stirred solution. This means that the concentration gradient, and thus the driving force for flux of

redox components out of a nanostructured electrode in a sandwich structure, can be higher than for the same electrode in a three-electrode system.

Considering the huge interest in nanostructured electrodes, relatively few studies have been performed to elucidate the transport of the redox mediators and other chemical components in nanostructured electrodes. However, an extensive study on the relevance of mass transport in thin layer mesoporous PEC solar cells was made by Papageorgiou et al. [36, 102]. In these studies, analysis of the diffusion processes in the steady state operation of mesoporous dye-sensitized TiO_2 PEC solar cells was carried out. The influence of migration was also considered, but, for cells with normal operating current densities, was found to be of little importance. The I^-/I_3^- redox mediator served as the system of reference. The analysis gave information on the limiting or maximum possible currents in the nanostructured PEC devices. It showed that, for a nanostructured n-type sandwich solar cell in which charge transport is limited by the transport of the redox couple in the solution, EE (light incident on the cathode) rather than SE illumination should give the highest photocurrent yield. The derived equations were supported by experimental data. The mass transport limitation effect was amplified by using neat 1-hexyl-3-methylimidazolium iodide (MHImI) electrolyte and low concentration of the redox mediator. A high viscosity characterizes MHImI. Plots of photocurrent against photon flux showed ambiguously that, at high light intensities in a mass transport, limited nanostructured sandwich cell, EE illumination is more favorable than SE illumination. The generality in the underlying theory implicates that this could be used as a general method for the analysis of nanostructured solar cells. The paper also anticipated the mass transfer overpotential created by concentration changes in the cell.

Surprisingly Papageorgiou et al. [36] found that the effective diffusional coefficient, D_{eff}, of triiodide (I_3^-) in the investigated mesoporous films (porosity estimated to 64%) did not deviate significantly from the "free-stream" values of I_3^-, although their theoretical considerations, well described in their paper, suggested it should do so. The authors discuss the reason for this unexpected result in some detail, and give speculative explanations (best read in the paper) for the unimpaired diffusion of I_3^- through the porous network.

Kebede and Lindquist [106] prepared free standing nanostructured membranes from Degussa P25 TiO_2 nanoparticles at one of the ends of a small glass tube. When the tube was dipped into a beaker, they could, in a straightforward experiment, study the flux of I_3^- (in acetonitrile), in the concentration gradient formed over the membrane. The acetonitrile solution in beaker contained the same chemical ingredients as the solution in the tube, except for I_3^-. Consistent results were obtained for membranes of different thicknesses. The obstructed apparent diffusion coefficient in a 550 μm thick membrane with a porosity around 55%, and in a solution of 0.1 mM I_3^- and 0.1 mM I, was found to be around 3.4×10^{-6} cm^2 s^{-1}. This is almost an order of magnitude smaller than the diffusion coefficient for I_3^- in free solution. The apparent diffusion coefficient (corresponding to the effective diffusion coefficient, $D_{eff,}$ of Papageorgiou et al.) was, as expected, temperature dependent with a diffusional activation energy of 13.5 kJ mol^{-1}. This deviation in re-

sult from the electrochemical determination by Papageorgiou et al. [36] is interesting. One easily can think of reasons for a decrease of D_{eff} below the expected value. For example, D_{eff} could decrease due to adsorption-desorption equilibrium between I_3^- and the SC surface, since this would increase the residence time of I_3^- in the mesoscopic film. It is harder to understand the opposite behavior. Papageorgiou et al. suggested an influence of the mesoporosity on the transport mechanism involved [36]. Another and more immediate interpretation could be that, in the electrochemical experiments, there is a contribution of migration due to the electrical field, particularly in the vicinity of the counter electrode.

Kebede and Lindquist also discuss the relevance of their results in relation to what is needed for an efficient dye-sensitized nanostructured cell (DSNC). Under the assumption of a linear concentration gradient in the DSNC with 0.5 m I^- and 50 mM I_3^- (the most frequently used concentrations of the redox couple used in DSNC), they found that a D_{eff} value an order of magnitude smaller than that for free diffusion of I_3^-, could still carry a current density of 30 mA cm^{-2} – this even at 25 °C. This is more than expected from the DSNC. At 50 °C, which is a more realistic temperature for a solar cell in full sunlight, D_{eff} will increase to between 4–1.5 × 10^{-5} cm^2 s^{-1} and D_{eff} will be well above what is needed for a DSNC not current limited by diffusion in the electrolyte.

6.9.2
"Solid Electrolytes"

The problems of charge transport in the electrolyte are highlighted in the many attempts to make a "solid state" dye-sensitized solar cell [12, 98–100] by introducing a solid or highly viscous hole conductor. Interesting in this context is the work by U. Bach et al. [100]. They made a dye-sensitized mesoporous TiO_2 solar cell using the amorphous organic hole-transport material 2,2′,7,7′-tetrakis(*N*,*N*-di-*p*-methoxyphenylamino)-9,9′-spirobifluorene (OMeTAD). In this cell, the electron injection of the dye is immediately followed by a regeneration of the dye via hole-transfer from dye to OMeTAD. For the further transport through the OMeTAD, a hopping mechanism was assumed. A photon to electrical current efficiency of 30% with the sensitizer $Ru(II)L_2(SCN)_2$ (L=4,4′-dicarboxy-2,2′-bipyridyl) was achieved, but the short circuit photocurrent under white light at 9.4 mW cm^{-2} (less than 1/10 of a full sun) was only 0.3 mA cm^{-2}, indicating a severe limitation of charge transport in the OMeTAD. A number of different sensitized nanoporous solid-state cells was also investigated by Tennakone et al., using p-CuCNS, $4CuBr_3S(C_4H_9)_2$ and p-CuI as hole-collectors [107–113].

6.10
Intensity-modulated Photocurrent and Photovoltage Spectroscopy

Intensity-modulated photocurrent spectroscopy (IMPS) and intensity-modulated photovoltage spectroscopy (IMPV) has become a powerful tool to uncover the details concerning transport in nanostructures; see e.g. [4, 7, 8, 28, 64, 114, 115].

IMPS was used by de Jongh and Vanmaekelbergh to study the electronic transport properties of nanocrystalline particulate TiO_2 [7, 8]. By extending a model (used for nanoporous crystalline GaP prepared by etching single crystals) to include also recombination and a trapping-detrapping mechanism, they could satisfactorily describe their data. They suggested that the transport of photogenerated electrons through particulate TiO_2 electrodes is limited by electron trapping–detrapping states distributed in the band-gap and argue that these states are located at the TiO_2-electrolyte interface.

Light intensity-dependent measurements have revealed the complex nature of the charge transport in nanostructured materials. Major contributions to a deeper understanding of the charge transport phenomena in nanostructured electrodes has recently also been made by Peter et al. [64, 114] and Schlichthörl et al. [28, 115]. Peter et al. makes use of both IMPS and IMVS. These techniques made it possible to characterize the electron transport and back reactions over five orders of magnitude of light intensity. They studied a dye-sensitized nanostructured TiO_2 film in a Grätzel cell sandwich structure with iodide-triiodide redox couple as charge carrier in the electrolyte. In the evaluation of data they (similar to Södergren et al.) make use of the continuity equation:

$$\frac{\partial n}{\partial t} = \eta a I_0 e^{-a(\lambda)x} + D_n \frac{\partial^2 n}{\partial x^2} - \frac{n - n_0}{\tau_n} \tag{14}$$

which describes the injection, collection and back reaction of electrons in the DSNC in terms of the electron density n, the net electron injection efficiency η, the absorption coefficient of the dye-impregnated SC $a(\lambda)$, the intensity of light I_0, the electron diffusion coefficient D_n, and lifetime of the electron in the conduction band, τ.

Their results reveal that, while the diffusion length of the electron, L_n, is fairly constant, increasing only by a factor of about two over the five magnitudes of change in light intensity, τ and D_n vary over three orders of magnitude; τ decreasing and D_n increasing with increasing light intensity. The relatively small change in L_n can be understood considering that it is calculated from the relationship $L_n = (D_n \tau_n)^{1/2}$. According to the authors, the intensity dependence of D_n arises from the change in trap occupancy with intensity. At low intensities, electrons are exchanged between deep traps and the conduction band, and transport is slow. At higher intensities, the deep traps are filled and trapping-detrapping involves only shallower levels, so transport is faster [64, 114]. Consistent with the relative constancy of L_n, the measured IPCE values of the DSNC were found to be fairly independent of light intensity. Fig. 6.8 (from Ref. [64]) shows typical IMPS and IMVS

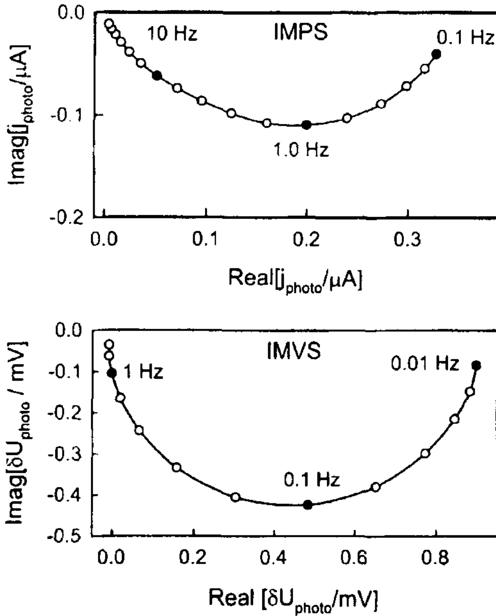

Fig. 6.8 (Figures 1 and 3 from Ref. [64].) Typical IMPS and IMVS plots for a DSNC at an intensity of $4 \times 10^{13}\ cm^{-2}\ s^{-1}$.

plots for a DSNC at an intensity of $4 \times 10^{13}\ cm^{-2}\ s^{-1}$, and Fig. 6.9 the dependence of τ_n, D_n and L_n as a function of the photocurrent density. Peter et al. [64] (and Ref. [115]) argues for a second order recombination process. The treatment of Peter et al. deals with the transport of the electrons in the nanostructure and assuming that limiting processes are primarily related to the particulate matrix of the SC. This implies that the transport in the studied cell is not limited by slow kinetics at the counter electrode or by diffusion limitations in the electrolyte.

Similarly Schlichthörl et al. [28] used IMVS and IMPS to evaluate the charge-collection efficiency in dye-sensitized nanostructured semiconductor cells (DNSC). Three comparable models were developed for relating the charge collection efficiency to the time constants for charge recombination at open circuit, τ_{oc}, and the combined process of charge collection and charge recombination τ_{sc}. The second and third model take as their starting point the assumption that the electron transport through the TiO_2 film occurs by diffusion, that electrical fields are negligible and that free and trapped electrons are in thermal equilibrium. The third, and most elaborate model, takes into account the observation that the rate of recombination does not depend linearly on the electron concentration. Interestingly, this third model results in an electron diffusion length, L, which depends on the distance from the back contact. Furthermore, the continuity equation is modified to account for charge trapping and detrapping. The validity of the method is demonstrated for the second model from which the exact IMPS and IMVS responses are calculated. A simple expression is derived for calculating the charge-collection efficiency from the measured values of τ_{oc}/τ_{sc} and the light intensity dependence of τ_{oc}.

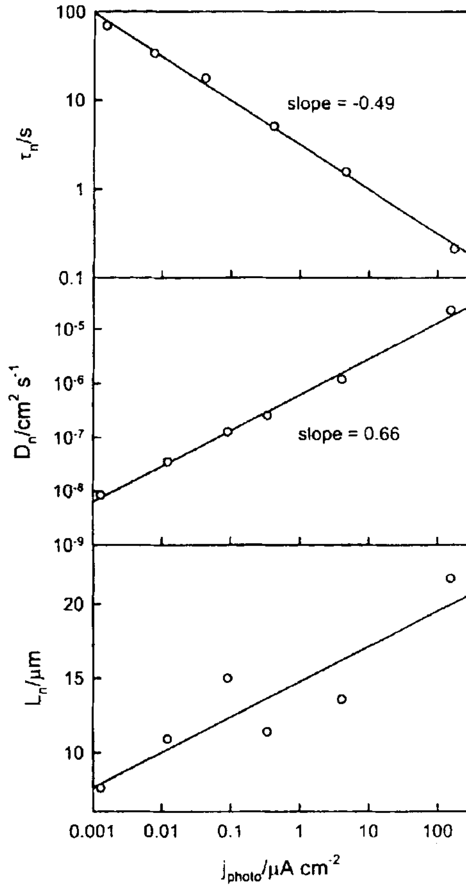

Fig. 6.9 Dependence of τ_n, D_n and L_n respectively on the photocurrent density.

Cao et al. [4] studied the photocurrent response of dye-sensitized, porous nanocrystalline TiO_2 cells as a function of light intensity. Photocurrent transient measurements and IMPS were used. They claim that the transient response of the DSNC was dominated by the electron transport in the nanocrystalline (porous) TiO_2 film. Their results were consistent with a diffusion model as proposed by Södergren et al. [2]. However, the apparent diffusion coefficient for electrons in the particle network was found to be a function of the light intensity.

As a comment to light intensity IMPS and IMVS measurement described above we could also note the following: Based on the fact that, at steady-state and in full sunlight, the carrier concentration in the photoactive electrode of a DNSC is about one electron per particle [115], Hagfeldt and Grätzel calculated a resistance for the illuminated nanocrystalline film which is at least 1000 times higher than experimentally observed. A light-induced change in conductivity, as earlier observed in polycrystalline TiO_2 films by Lindquist [116] and by Zaban et al. in nanostructured electrodes [117], was proposed by Augustynski [118] to explain the discrepancy.

6.11
Ambipolar Diffusion of Carriers Nanostructures

The effects of electron concentration in the conduction band [64] and the conductivity (or the concentration of ions) in the electrolyte [92] have been clearly demonstrated. However, models presented so far [2, 64, 97] describe only the transport of *one* charge carrier – the carrier in the SC. An elegant way to involve diffusion of carriers both in the SC and the electrolyte was recently suggested by Kopidakis et al. [32] by introducing the ambipolar diffusion coefficient. This concept was first introduced by Scher et al. to describe charge carrier transport in highly disordered solid materials such as amorphous chalcogenides. The ambipolar diffusion coefficient was then expressed by

$$D_{amb} = (n + p)/[(n/D_p) + (p/D_n)] \tag{15}$$

where n and D_n are the electron density and diffusion coefficient respectively, and p and D_p are the hole density and diffusion coefficient. According to the authors, ambipolar diffusion occurs when an electrical carrier is injected into a sea of oppositely charge mobile carriers; under these conditions the injected charge is referred to as the minority carrier. They point out that this description, in which a "packet" of the excess minority carriers is generated by light (or by contact injection) and confined to the nanoparticle matrix, undoubtedly applies to the photocarriers in the electrolyte-filled, nanoporous TiO_2 film electrodes they studied. The "packet" will diffuse naturally along with a cloud of positive charge (in the electrolyte) so that the entire package remains neutral. There can be only modest deviations from electrical neutrality and such deviations occur on the scale of the Debye length.

6.12
The Electrical Field at the Nanostructured SC-Back-contact Interface

The studies referred to so far have discussed the charge transport in the nanostructured electrodes in terms of diffusion, neglecting the possibility of the influence of any electrical field in the porous SC electrode. However, it is well established that when a liquid electrolyte or metal is brought into intimate contact with a macroscopic SC, the equilibration between the two phases results in transfer of charge between them and (in most cases, particularly for an electrolyte-SC junction) formation of a Schottky junction [119].

Generally, to collect the generated photocurrent in a nanostructured electrode, the predominant configuration is a nanocrystalline porous SC thin film in contact with a transparent (by heavy doping) conducting oxide (TCO) such as $SnO_2(F)$, $In_2O_3(Sn)$ or $ZnO(Al)$ (dopants in parenthesis). So we may ask: what happens at the junctions at the interface between the nanostructure and the back contact material? Several workers have addressed this question both theoretically and experimentally [13, 117, 120–123].

As pointed out by Schwarzburg and Willig [122] it is quite clear that, according to general thermodynamic rules, a difference in chemical potential of any two materials in contact will be balanced by an exchange of charges and/or the formation of a dipole layer in the vicinity of the interfacial contact [119]. The metal-SC or liquid-SC junctions discussed above are familiar examples of this. It is obvious that, in a nanostructured film in vacuum, such a junction can be expected at the interface between each SC particle and the TCO back contact. However, in contrast to a compact SC solid state-metal or a single crystal-liquid junction, the situation in a nanostructured film electrode, including electrodes in a DNSC, is further complicated by the fact that only a small fraction of the surface of the porous film is in contact with the TCO. In the presence of an electrolyte, the pores between the particles will be filled with a solution containing ions and dipoles, which will screen any charges in the nanoparticles and in the TCO back contact. It is well established that at high ion strength – the condition normally used in the DSNC – this potential drop is almost entirely over the Helmholtz layer in the electrolyte. Regarding these interfacial conditions, the questions now arise: What electrical field (if any) is present in the region where the TCO, the SC nanoparticles and electrolyte connect? If of significance, how large and how deep into the nanostructured film does the field penetrate, and how does this field affect the charge transport and the collection of charges at the back contact?

Schwarzburg and Willig [122] discuss in a recent paper the origin of the photovoltage and the photocurrent in nanoporous electrochemical solar cells and emphasize the essential role of the dark equilibrium potential for the charge separation and the photovoltaic action in these cells. To obtain a minimum electrostatic element to work with, they approximate the TiO_2 network immersed into a strong electrolyte by a hollow conducting cylinder where the base (connected to the TCO) is at a different potential than all the other surface elements of the cylinder. The cylinder corresponds to a chain of sintered nanoparticles. The analytical solution for potential distribution, as derived for the model element and transformed to the nanostructured TiO_2 network, predicts that the total potential drop for 10–20 nm diameter particles extends a few tens of nm into the nanostructure, that is, only over one or two particles. Schwarzburg and Willig also consider the screening of photogenerated electrons in the nanostructure and they point out that both electrons injected into the CB and the positive charge left behind are effective over a few nanometers in 0.5 M LiI solution. The major part of the screening is controlled by the relaxation time of the ions in the solution, i.e. within nanoseconds. The expected sharp potential drop at the interfacial region is used, when arguing for a general analogy between the DSNC and a solid state p-n junction solar cell. According to the authors the charge transport is conditionally dependent on such a p-n junction at the interface of the nanostructure electrode and the back contact material. Consistent with the findings of Schwarzburg and Willig, Levy et al. [120] demonstrated the presence of a contact potential between lightly sintered colloidal nanocrystalline TiO_2 films deposited on transparent highly conductive tin oxide films degenerately doped with fluorine, $SnO_2(F)$, using time-resolved photocharge (TRPC) measurements.

Zaban et al. [117] investigated the potential distribution and short-range screening in nanoporous TiO_2 electrodes on conducting SnO_2 films by impedance spectroscopy. They found that the capacitance of the nanoporous electrodes in the dark was potential dependent. While the capacitance at high potentials (above – 0.5 V relative to the SCE in 0.3 M tetra-ammonium hexafluorophosphate) was low and constant and comparable to the values of the bare SnO_2 back contact, it increased continuously below that potential up to a plateau at ca. –1.4 V. Depending on film thickness, the increase at –1.4 V was 2–3 orders of magnitude larger than in the potential range above –0.5 V. Simple dye desorption was used to correlate the capacitance of the nanoporous films to the real surface area of the film. The capacitance, C_{HL}, which they attributed to the Helmholtz double layer, scaled linearly with this surface area. The interpretation of the experimental results was that, at positive potentials, the TiO_2 is practically insulating and therefore little or no contribution from the large surface area of the TiO_2 film was observed. The overall capacitance was due mainly to the C_{HL} (capacitance of the Helmholtz layer) over the exposed SnO_2 film and the first few monolayers of the TiO_2 film. Only when the film was "doped" by injecting electrons into the CB (by applying a negative bias), the TiO_2 film became conducting and therefore could access the C_{HL} at the porous TiO_2 interface. The low doped film (~10^{16} cm^{-3}) became, on electron injection, more metal-like. Further proof of this interpretation was collected by comparing the C_{HL} as a function of potential in the dark and under UV illumination, inducing transition of electrons from the VB to the CB. The onset of increased C_{HL} with applied potential was now shifted about 1 V in the positive direction, showing that also the photogenerated electrons in the CB increase the conductivity of the porous TiO_2. According to the authors, the results provide a rationale for a dispersive transport. Because of the porous nature of the nanostructured films, ions can migrate through the film over very short distances to neutralize any electrical field, including those caused by photo-injected electrons. Therefore under the normal operating conditions of a DSNC, there should be no essential macroscopic field in the TiO_2 film. Thus, during steady state illumination, the injected electrons will experience little or no electrical field, so their transport will be governed primarily by concentration gradients in the film, i.e., it will be diffusional.

In a more recent paper Pichot and Gregg [121] investigated the potential drop at the nanostructured TiO_2-back contact interface in some more detail to find experimental proof for one of the two models – the "kinetic model" and the "junction model" – the latter which assumes that a flux of electrons in a nanostructure electrode can only occur with the assistance of an electrical field at the interface of the nanostructured electrode-back contact. Thus, TiO_2 nanostructured electrodes with back contact work functions varying over a range of 1.4 eV were prepared. The back contact materials used were ITO, SnO_2, Au, and Pt with the work functions were 4.3, 4.8, 5.1, and 5.7, respectively. In spite of the different back contact materials, the photovoltage of the assembled DNSC measured (in 0.5 M LiI in acetonitrile) at different light intensities were practically unchanged. Only with Pt as back contact the photovoltage was noticeable lower (~100 mV at one sun). This relatively small deviation could be explained by the high catalytic activ-

ity of Pt for the reductive back reaction $2e + I_3^- = 3I^-$. Contrary to Schwarzburg and Willig [122], Pichot and Gregg stated that the open circuit photovoltage of the DSNC is independent of any interfacial potential created by the difference in work function of the nanostructured TiO_2 and the back contact materials, to separate the screened electron from its image charge in the solution. Therefore the junction model is incorrect. A charge separation controlled by the interfacial kinetics and diffusional transport of charge carriers seems to be valid also for their experimental data. Pichot and Gregg suggest that the interfacial potential barrier may be smaller than expected and/or too thin to have a significant influence on the cell performance.

6.13 Ballistic Electron Transport

In a recent paper, Tennakone et al. discuss the possibility of ballistic electron transport in nanostructured electrodes [124]. They studied a dye-sensitized cell with photoanodes of various compositions made from mixtures of SnO_2 (ca. 15 nm diameter) and ZnO (ca. 1 μm) particles.

At a ZnO content of ~53%, optimum photocurrent (~22 mA cm^{-2}) and photovoltage (635 mV) were observed. Since at this composition, the total surface area of the SnO_2 is more than 60 times larger than that of the ZnO, they concluded that light absorption, and therefore the photocurrent generation, occur predominantly at the dye-coated SnO_2. They further calculated that the SnO_2 crystals should form a layer of ~100 nm on the ZnO crystals. Although the CB of SnO_2 is well below that of the ZnO, the dye pumps electron into the ZnO, raising the quasi-Fermi level of the ZnO well above the CB of SnO_2. From this they conclude: "it is inevitable that the energetic electrons in SnO_2 (i.e. ballistic electrons that have not relaxed to the conduction band of SnO_2) have been transported to ZnO". This phenomenon has certain similarities with the hot carrier injection from surface-adsorbed dye molecules to a semiconductor as discussed by Nozik and others [59]. However, the distance over which the ballistic electron transport takes place is one to two orders of magnitude larger. The overall transit time for the electron over the 10 μm film was not measured. Although such ballistic electron transport through the SnO_2 may occur, the overall electron transport through the film may still be diffusive.

6.14 Charge Transport and Applications of Nanostructured Electrodes

Although the nanostructured thin-film electrodes today, most commonly are discussed for their potential applications in the dye-sensitized solar cells, they are frequently used as electrodes in sensors, displays, super capacitors and batteries and even smart windows [125]. They may also be useful in photosynthetic cells for,

e.g., water splitting, or photocatalytic systems for air or water purification. In these latter applications, knowledge of the mechanisms of charge transport are equally of interest. In the solar cell prototypes, the most frequently used SC is TiO_2, but other oxides with large band-gap such as ZnO, Nb_2O_5, SnO_2 and NiO are currently under investigation. Recently a dye-sensitized solar cell based on a photoanode of nanostructured ZnO with 5% solar energy efficiency was prepared [126].

6.15 Summary

Many articles devoted to theoretical consideration and interpretation of the mechanism of charge transport in nanostructured electrodes have appeared during the last 5 years [6–8, 97, 108, 117, 127].

Except for some conflicting opinions concerning the potential drop in the interfacial region between the nanostructured porous large band-gap SC electrode and its conducting substrate, there seems to be a growing consensus about experimental results and, from these, derived concepts and ideas about charge transport in nanostructure materials. These are:

- the transport is mainly diffusional;
- the electrons are mainly driven by a one-dimensional concentration gradient of electrons normal to conducting substrate. If the photocurrent is not limited by diffusion in the electrolyte, the charge transport is limited by the electron transport in the nanoparticle network;
- the SC and electrolyte must be looked upon as one effective medium. There is an image charge in the electrolyte at the NSEI screening charges inside the nanostructure and charges in the back contact;
- the redistribution of ions and dipoles between the solution in the pores and the surface of the nanostructured SC strongly affect charge separation and kinetics at the NSEI as well as the charge transport;
- trapping and detrapping of electrons is of importance and may be the main cause of the slow transport.

As noted above, the unresolved questions seem to concern mainly the existence and importance of an electrical field at the back contact. Another question to be addressed is: Is it a matter of coincidence that the proposed trapping-detrapping mechanism leads to an upper limit of D_{eff} of the same size as the diffusion coefficient of the ions in solution? Concerning this question, the introduction of the ambipolar diffusion coefficient may be a step in the right direction [32]. The dependence of D_{eff} on the conductivity of the solution as measured by photocurrent measurement [92] points to another explanation: The reorganization of the image charge as the electron moves between traps and particles may be limited by diffusion of the screening ions from and to the NSEI.

References

1 A. HAGFELDT, Thesis, Uppsala, **1993**.

2 S. SÖDERGREN, A. HAGFELDT, J. OLSSON, S. E. LINDQUIST, *J. Phys. Chem*, **1994**, *98*, 5552–5556.

3 A. SOLBRAND, Dissertation from the Faculty of Science and Technology Thesis 320, Uppsala University, **1998**.

4 F. CAO, G. OSKAM, P. C. SEARSON, *J. Phys. Chem.* **1996**, *100*, 17021–17027.

5 L. M. PETER, E. A. PONOMAREV, G. FRANCO, N. J. SHAW, *Electrochimica Acta* **1999**, *45*, 549–560.

6 D. VANMAEKELBERGH, P. E. DE JONGH, *J. Phys. Chem. B* **1999**, *103*, 747–750.

7 P. E. DE JONGH, D. VANMAEKELBERGH, *J. Phys. Chem. B* **1997**, *101*, 2716–2722.

8 P. E. DE JONGH, D. VANMAEKELBERGH, *Phys. Rev. Lett.* **1996**, *77*, 3427–3430.

9 L. M. PETER, D. VANMAEKELBERGH, in: *Advances in Electrochemical Science and Engineering; Vol. 6*, edited by R. C. Alkire, D. M. Kolb (Wiley-Interscience, New York, **1999**).

10 B. MILLER, S. L. LICHT, M. E. ORAZEM, P. C. SEARSON, *Crit. Rev. Surf. Chem.* **1993**, *3*, 29–47.

11 A. HAGFELDT, M. GRÄTZEL, *Accounts of Chemical Research* **2000**, *33*, 269–277.

12 J. HAGEN, W. SCHAFFRATH, P. OTSCHIK, R. FINK, A. BACHER, H.-W. SCHMIDT, D. HAARER, *Synth. Met.* **1997**, *89*, 215–220.

13 D. CAHEN, G. HODES, M. GRÄTZEL, J. F. GUILLEMOLES, I. RIESS, *J. Phys. Chem. B* **2000**, *104*, 2053–2059.

14 B. O'REGAN, M. GRÄTZEL, *Nature (London)* **1991**, *353* 737–740.

15 H. GERISCHER, F. WILLIG, *Top. Curr. Chem.* **1976**, *61*, 31–84.

16 H. GERISCHER, H. TRIBUTSCH, *Ber. Bunsenges. Phys. Chem.* **1968**, *72*, 437–445.

17 H. TRIBUTSCH, *Berichte der Bunsengesellschaft* **1969**, *73*, 582–590.

18 H. TRIBUTSCH, H. GERISCHER, *Berichte der Bunsengesellschaft* **1968**, *72*, 437–445.

19 H. TRIBUTSCH, H. GERISCHER, *Berichte der Bunsengesellschaft* **1969**, *73*, 850–854.

20 R. MEMMING, H. TRIBUTSCH, *J. Phys. Chem.* **1971**, *75*, 562–570.

21 W. GÄRTNER, *Phys. Rev.* **1959**, *116* 84–87.

22 N. VLACHOPOULOS, P. LISKA, J. AUGUSTYNSKI, M. GRÄTZEL, *J. Am. Chem. Soc.* **1988**, *110*, 1216–1220.

23 M. MATSUMURA, S. MATSUDAIRA, H. TSUBOMURA, M. TAKATA, H. YANAGIDA, *Ind. Eng. Chem. Prod. Res. Dev.* **1980**, *19*, 415–421.

24 G. HODES, I. D. J. HOWELL, L. M. PETER, *J. Electrochem. Soc.* **1992**, *139*, 3136–3140.

25 A. HAGFELDT, U. BJOERKSTEN, S. E. LINDQUIST, *Sol. Energy Mater. Sol. Cells* **1992**, *27*, 293–304.

26 L. DLOCZIK, O. ILEPERUMA, I. LAUERMANN, L. M. PETER, E. A. PONOMAREV, G. REDMOND, N. J. SHAW, I. UHLENDORF, *J. Phys. Chem. B.* **1997**, *101*, 10281–10289.

27 G. OSKAM, F. CAO, P. C. SEARSON, *Electrochemical Society Proceedings* **1999**, *95*, 98–106.

28 G. SCHLICHTHÖRL, N. G. PARK, A. J. FRANK, *J. Phys. Chem. B* **1999**, *103*, 782–791.

29 J. VAN DE LAGEMAAT, N. G. PARK, A. J. FRANK, *J. Phys. Chem. B* **2000**, *104*, 2044–2052.

30 N. W. DUFFY, L. M. PETER, R. M. G. RAJAPAKSE, K. G. U. WIJAYANTHA, *Electrochemisty Communications* **2000**, *2*, 658–662.

31 R. KOENENKAMP, R. HENNINGER, P. HOYER, *J. Phys. Chem.* **1993**, *97*, 7328–30.

32 N. KOPIDAKIS, E. A. SCHIFF, N. G. PARK, J. VAN DE LAGEMAAT, A. J. FRANK, *J. Phys. Chem. B* **2000**, *104*, 3930–3936.

33 J. MOSER, S. PUNCHIHEWA, P. P. INFELTA, M. GRÄTZEL, *Langmuir* **1991**, *7*, 3012–3018.

34 A. HAGFELDT, S.-E. LINDQUIST, M. GRÄTZEL, *Solar Energy Materials and Solar Cells* **1994**, *32*, 245–257.

35 H. LINDSTRÖM, S. SÖDERGREN, A. HAGFELDT, S.-E. LINDQUIST, in: *Patent application 9901866-3*, Submitted (Sweden, **1999**).

36 N. PAPAGEORGIOU, C. BARBÉ, M. GRÄTZEL, *J. Phys. Chem. B* **1998**, *102*, 4156–4164.

37 J. J. KELLY, D. VANMAEKELBERGH, *Electrochimica Acta* **1998**, *43*, 2773–2780.

38 L. VAYSSIERES, Thesis, Université Pierre et Marie Curie, **1995**.

39 L. VAYSSIERES, A. HAGFELDT, S. E. LINDQUIST, *Pure Appl. Chem.* **2000**, *72*, 47–52.

40 N. Beermann, L. Vayssieres, S.-E. Lindquist, A. Hagfeldt, *Journal of The Electrochemical Society* **2000**, *147*, 2456–2461.

41 M. Gómez, E. Magnusson, E. Olsson, A. Hagfeldt, S.-E. Lindquist, C. G. Granqvist, *Solar Energy Materials & Solar Cells* **2000**, *62*, 259–263.

42 S. Doherty, D. Fitzmaurice, *J. Phys. Chem.* **1996**, *100*, 10732–10738.

43 L. Cusack, R. Rizza, A. Gorelov, D. Fitzmaurice, *Angew. Chem., Int. Ed. Engl.* **1997**, *36*, 848–851.

44 A. Hagfeldt, L. Walder, M. Grätzel, *Proc. SPIE-Int. Soc. Opt. Eng.* **1995**, *2531*.

45 R. Cinnsealach, G. Boschloo, S. Nagaraja Rao, D. Fitzmaurice, *Solar Energy Materials & Solar Cells* **1999**, *57*, 107–125.

46 R. Cinnsealach, G. Boschloo, S. N. Rao, D. Fitzmaurice, *Solar Energy Materials and Solar Cells* **1998**, *55*, 215–223.

47 A. Hagfeldt, N. Vlachopoulos, M. Grätzel, *J. Electrochem. Soc.* **1994**, *141*, L82–L84.

48 A. Hagfeldt, N. Vlachopoulos, S. Gilbert, M. Grätzel, *Proc. SPIE-Int. Soc. Opt. Eng.* **1994**, *2255*.

49 A. Hagfeldt, L. Walder, M. Grätzel, *Proc. Electrochem. Soc.* **1995**, *8*.

50 M. Mayor, A. Hagfeldt, M. Grätzel, L. Walder, *Chimica* **1996**, *50*.

51 H. Rensmo, H. Lindström, S. Södergren, A.-K. Willstedt, A. Solbrand, A. Hagfeldt, S.-E. Lindquist, *J. Electrochem. Soc.* **1996**, *143*, 3173–3178.

52 B. Burfeindt, T. Hannappel, W. Storck, F. Willig, *J. Phys. Chem.* **1996**, *100*, 16463–16465.

53 R. Eichberger, F. Willig, *Chem. Phys.*, **1990**, *141*, 159–173.

54 T. Hannappel, B. Burfeindt, W. Storck, F. Willig, *J. Phys. Chem. B* **1997**, *101*, 6799–6802.

55 T. Hannappel, C. Zimmermann, B. Meissner, B. Burfeindt, W. Storck, F. Willig, *J. Phys. Chem. B* **1998**, *102*, 3651–3652.

56 H. Tributsch, F. Willig, *Solar Energy Materials and Solar Cells* **1995**, *38*, 355–366.

57 N. J. Cherepy, G. P. Smestad, M. Grätzel, J. Z. Zhang, *J. Phys. Chem. B* **1997**, *101*, 9342–9351.

58 Y. Tachibana, J. E. Moser, M. Grätzel, D. R. Klug, J. R. Durrant, *J. Phys. Chem.* **1996**, *100*, 20056–20062.

59 R. J. Ellingson, J. B. Asbury, S. Ferre, H. N. Ghosh, J. R. Sprauge, T. Lian, A. Nozik, *Zeitschrift für Physicalische Chemie* **1999**, *212*, 77–84.

60 R. J. Ellingson, J. B. Asbury, S. Ferre, H. N. Ghosh, J. R. Sprauge, T. Lian, A. Nozik, in: *Sub-picosecond Injection of Electrons from Excited Ru(2,2'*-bipy-4,4' dicarboxy)$_2$(SCN)$_2$ into TiO_2 Using Transient Mid-Infrared Spectroscopy; Berlin, Germany, **1998** (Oldenbourg Verlag, München, Germany), pp. 79–85.

61 K. Schwarzburg, F. Willig, *Appl. Phys. Lett.* **1991**, *58*, 2520–2522.

62 G. K. Boschloo, A. Goossens, *J. Phys. Chem.* **1996**, *100*, 19489–19494.

63 F. Cao, G. Oskam, P. C. Searson, *J. Phys. Chem.* **1995**, 99, 17071–17073.

64 L. M. Peter, K. G. U. Wijayantha, *Electrochemistry Communications* **1999**, *1*, 576–580.

65 M. A. Butler, *J. Appl. Phys.* **1977**, *48*, 1914–1920.

66 S. E. Lindquist, B. Finnström, L. Tegner, *J. Electrochem. Soc.* **1983**, *130*, 351–358.

67 A. J. Bard, *J. Phys. Chem.* **1982**, *86*, 175.

68 G. Hodes, M. Grätzel, *Nouv. J. de Chimie* **1984**, *8*, 509.

69 L. Kronik, N. Ashkenasy, M. Leibovitch, E. Fefer, Y. Shapira, S. Gorer, G. Hodes, *J. Electrochem. Soc.* **1998**, *145*, 1748–1755.

70 A. Hagfeldt, M. Grätzel, *Chem. Rev.*, **1995**, *95*, 49–68.

71 G. Hodes, A. Albu-Yaron, F. Decker, P. Motisuke, *Phys. Rev. B: Condens. Matter* **1987**, *36*, 4215–4221.

72 S. Hotchandani, I. Bedja, R. W. Fessenden, P. V. Kamat, *Langmuir* **1994**, *10*, 17–22.

73 P. Hoyer, H. Weller, *Chem. Phys. Lett.* **1994**, *221*, 379–384.

74 L. Kavan, T. Stoto, M. Grätzel, D. Fitzmaurice, V. Shklover, *J. Phys. Chem.* **1993**, *97*, 9493–9498.

75 R. Vogel, K. Pohl, H. Weller, *Chem. Phys. Lett.* **1990**, *174*, 241–246.

76 R. Vogel, P. Hoyer, H. Weller, *J. Phys. Chem.* **1994**, *98*, 3183–3188.

77 L. Spanhel, H. Weller, A. Henglein, *J. Am. Chem. Soc.* **1987**, *109*, 6632–6635.

78 M. Grätzel, *Platinum Met. Rev.* **1994**, *38*, 151–159.

79 M. Grätzel, "Light Energy Harvesting and Conversion by Mesoporous Thin Film Devices," **(1997)**.

80 S.-E. Lindquist, A. Hagfeldt, H. Lindström, H. Rensmo, U. Björksten, S. Södergren, *Proc. SPIE-Int. Soc. Opt. Eng.* **1993**, *2017*, 240–251.

81 S.-E. Lindquist, H. Lindström, H. Rensmo, S. Södergren, A. Solbrand, H. Pettersson, in: *Electron Transport Properties in Nanoporous TiO_2 from Analysis of Action Spectra of Dye Sensitized Electrodes*, Freiburg, **1994**.

82 H. Lindström, H. Rensmo, S. Södergren, A. Solbrand, S.-E. Lindquist, *J. Phys. Chem.* **1996**, *100*, 3084–3088.

83 H. Rensmo, H. Lindström, S. Södergren, S. E. Lindquist, *Proc. Electrochem. Soc.* **1995**, 6161–6374.

84 G. Hodes, I. D. J. Howell, L. M. Peter, Beijing, **1993** (International Academic Publishers), p. 331.

85 J. He, H. Lindström, A. Hagfeldt, S.-E. Lindquist, *J. Phys. Chem. B* **1999**, *103*, 8940–8943.

86 Y.-M. Chiang, I. Dunbar, P. Birnie, W. D. Kingery, *Physical Ceramics, Principles for Ceramic Science and Engineering* (John Wiley & Sons, Inc., New York, Chichester, Toronto, Brisbane, Singapore, **1997**).

87 H. Lindström, A. Hagfeldt, H. Rensmo, A. Solbrand, S. Södergren, S.-E. Lindquist, *Proc. SPIE-Int. Soc. Opt. Eng.*, **1995**, *2531*.

88 S. Södergren, H. Siegbahn, H. Rensmo, H. Lindström, A. Hagfeldt, S.-E. Lindquist, *J. Phys. Chem. B* **1997**, *101*, 3087–3090.

89 B. O'Regan, J. Moser, M. Anderson, M. Grätzel, *J. Phys. Chem.* **1990**, *94*, 8720–8726.

90 P. Hoyer, H. Weller, *J. Phys. Chem.* **1995**, *99*, 14096–14100.

91 A. Solbrand, A. Henningsson, S. Södergren, H. Lindström, A. Hagfeldt, S.-E. Lindquist, *J. Phys. Chem. B* **1999**, *103*, 1078–1083.

92 A. Solbrand, H. Lindström, H. Rensmo, A. Hagfeldt, S. E. Lindquist, S. Södergren, *J. Phys. Chem. B* **1997**, *101*, 2514–2518.

93 A. Solbrand, K. Keis, S. Södergren, H. Lindström, S.-E. Lindquist, A. Hagfeldt, *Solar Energy Materials & Solar Cells* **2000**, *60*, 181–193.

94 A. Solbrand, A. Henningsson, S. Södergren, H. Lindström, A. Hagfeldt, S.-E. Lindquist, *J. Phys. Chem. B* **1999**, *103*, 1078–1083.

95 R. Koenenkamp, R. Henninger, *Appl. Phys. A* **1994**, *1*, 87–90.

96 R. Koenenkamp, A. Wahi, P. Hoyer, *Thin Solid Films* **1994**, *246*, 13–16.

97 J. Nelson, *Physical Review B* **1999**, *59*, 15374–15380.

98 B. O'Regan, T. D. Schwartz, *Chem. Mater.* **1998**, *10*, 1501–1509.

99 K. Murakoshi, R. Kogure, S. Yanagida, *Chem. Lett.* **1997** *5*, 471–472.

100 R. Bach, D. Lupo, P. Comte, J. E. Moser, J. Weissörtel, J. Salbeck, H. Spreitzer, M. Grätzel, *Nature* **1998**, *395*, 583–585.

101 P. Papageorgiou, P. Liska, A. Kay, M. Grätzel, *J. Electrochem. Soc.* **1999**, *146*, 898–907.

102 N. Papageorgiou, M. Grätzel, P. P. Infelta, *Sol. Energy Mater. Sol. Cells* **1996**, *44*, 405–438.

103 N. Papageorgiou, Y. Athanassov, M. Armand, P. Bonhote, H. Pettersson, A. Azam, M. Graetzel, *J. Electrochem. Soc.* **1996**, *143*, 3099–3108.

104 Y. Liu, A. Hagfeldt, X.-R. Xiao, S.-E. Lindquist, *Solar Energy Materials and Solar Cells* **1998**, *55*, 267–281.

105 Z. Kebede, S.-E. Lindquist, *Bull. Chem. Soc. Ethiop.* **1998**, *12*, 57–67.

106 Z. Kebede, S.-E. Lindquist, *Solar Energy Materials and Solar Cells* **1998**, *51*, 291–303.

107 K. Tennakone, G. R. R. A. Kumara, I. R. M. Kottegoda, V. P. S. Perera, G. M. L. P. Aponsu, *J. Phys. D: Appl. Phys.* **1998**, *31*, 2326–2930.

108 K. Tennakone, G. K. R. Senadeera, D. B. R. A. De Silva, I. R. M. Kottegoda, *Appl. Phys. Lett.* **2000**, *77*, 2367.

109 K. Tennakone, G. R. R. A. Kumara, I. R. M. Kottegoda, K. G. U. Wijayantha, V. P. S. Perera, *J. Phys. D: Appl. Phys.* **1998**, *31*, 1492–1496.

110 K. Tennakone, G. R. R. A. Kumara, I. R. M. Kottegoda, V. P. S. Perera, P. S. R. S. Weerasundara, *J. Photochem. Photobiol. A: Chemistry* **1998**, *117*, 137–142.
111 K. Tennakone, G. R. R. A. Kumara, I. R. M. Kottegoda, K. G. U. Wijayantha, *Semicond. Sci. Technol.* **1997**, *12*, 128–132.
112 K. Tennakone, K. P. Hewaparakkrama, M. Dewasurendra, A. H. Jayatissa, L. K. Weerasena, *Semicond. Sci. Technol.* **1998**, *3*, 382–387.
113 K. Tennakone, G. R. R. A. Kumara, A. R. Kumarasinghe, K. G. U. Wijayantha, P. M. Sirimanne, *Semicond. Sci. Technol.* **1995**, *10*, 1689–1693.
114 G. Franco, J. Gehring, L. M. Peter, E. A. Ponomarev, I. Uhlendorf, *J. Phys. Chem. B* **1999**, *103*, 692–698.
115 G. Schlichthörl, S. Y. Huang, J. Sprague, A. J. Frank, *J. Phys. Chem. B* **1997**, *101*, 8139–8153.
116 S.-E. Lindquist, H. Vidarsson, *J. Mol. Catal.* **1986**, *38*, 131–155.
117 A. Zaban, A. Meier, B. A. Gregg, *J. Phys. Chem. B* **1997**, *101*, 7985–7990.
118 A. Wahl, J. Augustynski, *J. Phys. Chem. B* **1998**, *102*, 7820–7828.
119 S. M. Sze, *Physics of Semiconductor Devices* (Wiley-Interscience, New York, London, Sydney, Toronto, **1969**).
120 B. Levy, W. Liu, S. E. Gilbert, *J. Phys. Chem. B* **1997**, *101*, 1810–1816.
121 F. Pichot, B. Gregg, *J. Phys. Chem. B*, **2000**, *104*, 6–10.
122 K. Schwartzburg, F. Willig, *J. Phys. Chem. B* **1999**, *103*, 5743.
123 J. Bisquert, G. Garacia-Belmonte, F. Fabregat-Santiago, *J. Solid State Electrochem.* **1999**, to be published.
124 K. Tennakone, I. R. M. Kottegoda, L. L. M. de Silva, V. P. S. Perera, *Semicond. Sci. Technol.* **1999**, *14*, 975–978.
125 C. Bechinger, S. Ferrere, A. Zaban, J. Sprague, B. A. Gregg, *Nature* **1996**, *383*, 608–610.
126 K. Keis, H. Lindström, E. Magnusson, S.-E. Lindquist, A. Hagfeldt, *J. Phys. Chem.*, Submitted,.
127 J. Ferber, R. Stangl, J. Luther, *Sol. E. Mat.* **1998**, *53*, 29.

Electrochemistry of Nanomaterials
by *Gary Hodes (Ed.)*
© WILEY-VCH Verlag GmbH, 2001

7
Dye-sensitized Solar Cells: Principles of Operation

David Cahen, Michael Grätzel, Jean Francois Guillemoles, and *Gary Hodes*

7.1
General Description of DSSC Systems

7.1.1
Solar Cells, How do They Work?

7.1.1.1 General

One way to understand the unique aspects of a dye-sensitized solar cell (DSSC) is to contrast it with normal, solid state, solar cells. The latter function because of the photovoltaic effect, by which supra-bandgap illumination causes a difference in the electrochemical potential of the two electrodes through which the photoeffect is measured. To help us understand the DSSC we will first explain the photovoltaic effect in normal cells.

While in a bulk semiconductor the excess of free carriers created by supra-bandgap illumination will quickly decay because of recombination, and produce heat, in good photovoltaic (PV) cells such recombination is suppressed and, in the best, virtually eliminated under short circuit. This happens because of the existence of an electric field in the device. Given such a field, optimization of the efficiency by which photon energy is converted into electrical energy depends on additional factors, including minimization of the density of recombination centers, that are due mostly to bulk defects and surfaces. The origin of the internal electric field can be understood as follows.

When the two components with different electrochemical potential of the electrons, that form the photovoltaically-active junction, are brought into electronic contact, a redistribution of free charge carriers occurs as the electronic carriers seek to establish electronic equilibrium between the components. While overall the system remains electrically neutral, this is not so locally, around the junction, because the electronic carriers that balanced the charged dopants are now spatially removed from them. This is the process of space charge formation, which, by Poisson's relation, implies the formation of a gradient in the electrical potential, i.e., an electric field. The field extends over the space charge layer. In electron energy band diagrams this is expressed as the bending of the (conduction and valence) bands.

The external performance of a PV cell is mostly measured by way of three primary parameters: I_{sc}, the short circuit current (infinite load); V_{oc}, the open circuit voltage (zero load) and *FF*, the fill factor, which is the ratio of the maximum power that can be obtained from the device and the product $V_{oc}I_{sc}$.

7.1.1.2 p/n Solid-state Cells

In a p/n type PV device, the photogenerated charge carriers are separated by the electric field in the space charge layer. These charge carriers include also those that are created in field-free regions, but still within a distance that electronic carriers can diffuse (their diffusion length) from the boundaries of the space charge region.

For what follows it is important to stress that while just differences in diffusion between the photogenerated carriers of opposite sign can lead to photovoltages (Dember voltages), such photovoltages are very small (several millivolts) in normal PV devices. This is so because these are ambipolar devices, where that concept here means primarily the presence of two types of electronic charge carriers with opposite charge in the semiconductor phases of the device.

In terms of electron energies, the PV action of a semiconductor p/n junction results from the separation of the Fermi levels (note: this is an ambipolar device, i.e. a device in which both positive and negative electronic charge carriers participate!) because of the supra-bandgap illumination (Fig. 7.1). As is common, we use here the term Fermi level as synonym for the chemical potential of the electron. Since, strictly speaking, that level, even as a virtual one, is defined only for an equilibrium situation, the term quasi-Fermi level is used to describe the situation under illumination.

The photovoltage that is measured is given by [1, 2]:

$$q\Delta V(\text{measured}) = \Delta\eta_e = \Delta\mu_e + q\Delta\phi \tag{1}$$

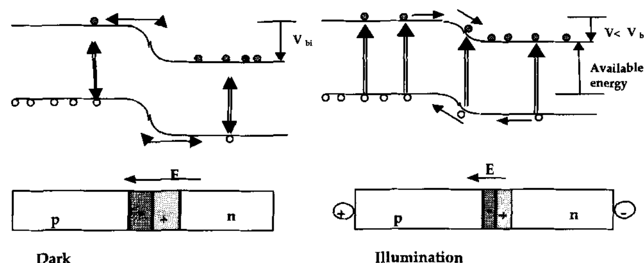

Fig. 7.1 Top: one-electron energy band diagrams of a p/n junction in the dark (left) and under illumination (right). Vertical double-headed arrows indicate thermal excitation and de-excitation processes; vertical, single-headed arrows indicate thermal excitation; horizontal arrows represent electronic charge transport processes. V_{bi} is the built-in voltage. Bottom: real-space schemes of the p/n junction, with the space charge regions and built-in electric field (E; horizontal arrows) indicated.

where ΔV is the difference between the two leads of the voltmeter, η_e and μ_e are the electrochemical and chemical potential of the electron, ϕ is the electrical (Galvani) potential, and q is the electron charge. In non-degenerate semiconductors

$$\mu_e = \mu_e^0 + kT\ln(n_e) \tag{2}$$

where μ_e^0 is the electron's standard chemical potential, n_e is the electron density, k is Boltzmann's constant, and T is the temperature (in Kelvin). In a p/n junction in equilibrium in the dark, $\Delta V = 0$, because $\Delta\mu_e = -q\Delta\phi$, with variations in their values along the electrochemical chain. The light-induced change in n_e changes $\Delta\mu_e$ to $\Delta'\mu_e$, which brings about a change in $\Delta\phi$ (as dictated by the Poisson relation), until a steady state is established. Then $\Delta'\mu_e \neq -q\Delta'\phi$ between the two halves of the cell, resulting in ΔV. Ultimately, the voltage is measured between two leads of the same material, and ΔV(measured) = $\Delta\phi_{leads}$, where $\Delta\phi_{leads}$ is the inner electrostatic potential difference between the leads.

7.1.1.3 **Photoelectrochemical Cells**

A special PV device is the photoelectrochemical cell (PEC), which is based on the junction between a semiconductor and an electrolyte, i.e. an ionic rather than electronic conductor. Mostly the electrolyte is a liquid one. The most striking difference between the PEC and a p/n or metal-semiconductor junction-based PV cell is that it contains two interfaces at which charge transport has to switch from electronic to ionic and vice versa, as in a common electrochemical cell (e.g. a battery). In contrast to a common electrochemical device, though, at least one of these interfaces is semiconductor/electrolyte, rather than the more common metal/electrolyte. Even though relatively efficient devices can be made, they are mostly plagued by stability problems because of the ease of corrosion of the semiconductor by the electrolyte under the strongly oxidizing or reducing conditions present at the interface. Among several notable exceptions are devices that use wide bandgap (mostly oxide) semiconductors, but those are inefficient solar energy converters. This can be understood by the rule of the thumb that the width of the optical bandgap is a measure of the chemical bond strength.

7.1.1.4 **Photogalvanic Cells**

Another type of PV converter, also an electrochemical cell variant, is the photogalvanic cell. In this device, the solution contains a chromophore that is photoexcited. The photoexcited chromophore oxidizes the reduced form of a redox species in solution. Instead of a semiconductor, both electrodes in a photogalvanic cell are metallic, but with different selectivity to the redox reaction. These cells have only given very low efficiency-stability performance. For example, a recent paper on photogalvanic cells gives a conversion efficiency of about half a percent for half an hour [3]. The issue of contact selectivity is important for the DSSC as it presents some analogy with the photogalvanic cell. In the DSSC system, two SnO_2 elec-

trodes are in contact with the redox couple; one is covered by TiO_2/dye and the other by Pt.

7.1.1.5 **Summary**

We summarize the important characteristics of a p/n or photoelectrochemical solar cell:

- light absorption occurs in the semiconductor; this leads to photogeneration of electronic charge carriers in the semiconductor (*);
- both minority and majority carriers are present in the semiconductor (*);
- charge separation occurs in the electric field in the space charge region (*);
- the photovoltage is equal to the reduction of the built-in electric potential (*);
- the recombination rate at and near the photovoltaically active junction should be minimized; and
- therefore, grain surfaces and boundaries need to be avoided (*).

In the above features that are different in a DSSC are marked by an asterisk. This then leads to the question of how such a device can work at all as a photovoltaic cell. This will become clear from the following.

7.1.2
Comparison of Dye-sensitized Solar Cells with Other Types

7.1.2.1 **Description of DSSC**

Commonly, this type of cell is composed of two surfaces of transparent conductor (mostly a conducting oxide on glass), onto one of which a few μm thick film of wide bandgap semiconductor has been deposited in the form of a self-connected network of nm-sized particles, with a network of similarly or larger-sized self-connected pores in between the particles. The semiconductor that is most widely used is the anatase form of TiO_2. Onto the semiconductor dye molecules are chemisorbed, forming close to a monolayer. This dye-semiconductor assembly is in contact with a redox electrolyte that serves to close the electrical circuit with the second transparent conducting electrode (counter electrode). A catalyst is deposited on the counter electrode to facilitate the redox reaction that has to occur on it to close the electrical circuit.

7.1.2.2 **General Model of Cell Action**

Fig. 7.2 shows the basic operating principles of a DSSC.

The heart of the device is the mesoporous oxide layer composed of a network of nanoparticles which have been sintered together to establish electronic conduction. Attached to the surface of the nanocrystalline film is the monolayer of the charge transfer dye. Photoexcitation of the latter ($h\nu$) results in the injection of an electron into the conduction band of the oxide (a). If it does not recombine (b), the electron is subsequently transferred to the electrode and the external circuit

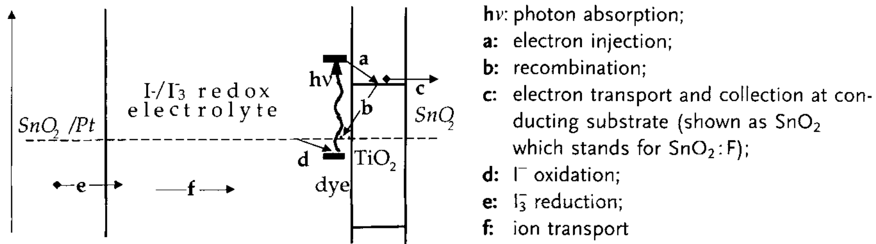

Fig. 7.2 Basic processes in a DSSC. Illumination is from the right. The vertical arrow indicates one-electron electron energy and the dashed horizontal line the Fermi level/redox potential/electro-chemical potential of the electron. For further discussion see text.

(c). The original state of the dye is restored by electron donation from the electrolyte (d), usually an organic solvent containing the iodide-tri-iodide redox system. The iodide is regenerated in turn by reduction of tri-iodide at the counterelectrode (e; $I_3^- + 2e^- \rightarrow 3I^-$), the circuit being completed by diffusion of the I^- back to the dye-sensitized electrode (f) and electron transport through the external load. The voltage measured under illumination corresponds to the difference between the quasi-Fermi level of the electrons in the two SnO_2 electrodes. At open circuit, this photovoltage can be identified with the voltage generated in the active part of the device, i.e., the difference between the quasi-Fermi level of the electrons in the solid (if it is uniform, that is in practical devices) and the redox potential of the electrolyte (the Fermi level at the ideally non-polarized counter electrode). Overall, electric power is generated without permanent chemical transformation.

7.1.2.3 What are the Special Features of a DSSC?

An important property of the nanocrystalline semiconductors used in the DSSC is that they function as a unipolar component, i.e., in the case described above there will be virtually no holes in the semiconductor. This is the case because in the DSSC the semiconductor is not photoexcited directly, in contrast to the case for the p/n or photoelectrochemical PV cells, discussed above. This is possible because a wide gap semiconductor is used, which does not absorb the photon energies that excite the dye. Thus, photocarrier generation and transport are well separated. Because of this spatial and material (phase) separation, the chances of recombination can be drastically reduced. Electrons can spend long periods of time in the semiconductor film without recombination. This is somewhat simplistic in that the electrons can be re-injected into the electrolyte and recombine in this way; however, also that pathway involves two phases and is much less probable than direct electron-hole recombination.

Another special feature of the DSSC is the essentially total depletion of the semiconductor, due to the small size of the nanoparticles [4] and porous structure. The Fermi level in the dark is therefore near the bandgap center, allowing genera-

tion of large photovoltages upon illumination. This aspect will be considered in more detail below.

7.2
Detailed Description of Dye-sensitized Solar Cells

7.2.1
Dye Chemistry and Photochemistry: General Presentation

The first panchromatic film, able to render the image of a scene realistically into black and white, followed on the work of Vogel in Berlin after 1873 [5] in which he associated dyes with silver halide grains. The first sensitization of a photoelectrode was reported shortly thereafter, using similar chemistry [6]. However, a clear recognition of the parallel between the two procedures, the realization that the same dyes can function in both [7] and verification that the operating mechanism is by injection of electrons from photo-excited dye molecules into the conduction band of the semiconductor substrates [8] date to the 1960s. In subsequent years the idea developed that the dye could function most efficiently if chemisorbed on the surface of a semiconductor [9, 10]. As the concept emerged to use dispersed particles to provide a sufficiently large interface [11], particulate photo-electrodes were employed [12]. The raison d'être for porous cells was to allow strong light absorption by the adsorbed dye. The DSSC has been around for a long time, but attained only very low conversion efficiencies, since a relatively thick layer of dye was necessary to absorb the incident light. This then led to very poor electron injection into the semiconductor. Most of the photogenerated electrons recombined in the dye layer. The major breakthrough was the use of a high surface area layer that was so well accessible (to the electrolyte) – the nanoporous TiO_2 – that a single monolayer (or less) of the dye on the semiconductor surface was sufficient to absorb essentially all the incident light in a reasonable thickness (several μm) of the semiconductor film. This is clearly a critical issue, although by itself it would not guarantee the efficient operation of these cells. Indeed, as discussed further in Section 2.4, other properties that derive from the porous nature of the nanocrystalline films appear to be no less important. These include efficient electron injection from the dye into the semiconductor, screening the injected electrons to facilitate their transport to the back contact and strong depletion of the semiconductor layer for the control of the maximum photovoltage.

Titanium dioxide became the semiconductor of choice [13]. The material has many advantages: it is cheap, abundant, non-toxic and biocompatible, and is widely used in health care products as well as in paints. The standard dye at the time was tris(2,2′-bipyridyl-4,4′-carboxylate)ruthenium(II), the function of the carboxylate being the attachment by chemisorption of the chromophore to the oxide substrate [12, 13]. In 1991 [14] the first dye-sensitized nanocrystalline solar cell (DSSC) with a conversion yield of 7.1% was announced and presently the certified efficiency is over 10% [15].

The ideal sensitizer for a photovoltaic cell converting standard global AM1.5 sunlight to electricity should absorb all light below a threshold wavelength of about 900 nm which is equivalent to a semiconductor with a band-gap of 1.4 eV. For a single-junction device this presents the optimal threshold energy where the solar to electric power conversion efficiency reaches its maximum of 33%. In addition, it must also carry attachment groups such as carboxylate or phosphonate to firmly graft it to the semiconductor oxide surface. Upon excitation it should inject electrons into the solid with a quantum yield of unity. The energy level of the excited state should be well matched to the lower bound of the conduction band of the oxide to minimize energetic losses during the electron transfer reaction. Its redox potential should be sufficiently high that it can be regenerated via electron donation from the redox electrolyte or the hole conductor. Finally, it should be stable enough to sustain about 10^8 turn-over cycles corresponding to ca. 20 years exposure to natural light.

Much of the research in dye chemistry is devoted to the identification and synthesis of sensitizers matching these requirements, while retaining stability in the photo-electrochemical environment. The attachment group of the dye ensures that it spontaneously assembles as a molecular layer upon exposing the oxide film to a dye solution. This molecular dispersion ensures a high probability that, once a photon is absorbed, the excited state of the dye molecule will relax by electron injection to the semiconductor conduction band. However, the optical absorption of a single monolayer of dye is weak, a fact which originally was cited as ruling out the possibility of high efficiency sensitized devices, as it was assumed that smooth substrate surfaces would be imperative in order to avoid the recombination loss mechanism associated with rough or polycrystalline structures in solid-state photovoltaics.

This objection was invalidated by recognizing that, by the injection process, the electron finds itself in the semiconductor lattice, separated spatially and by a dipole potential barrier from the dye. The surface dipole is generated by proton transfer from the carboxylate groups of the sensitizer to the oxide, charging the solid positively and leaving an excess negative charge on the dye. The resulting electric field promotes electron injection into the solid while impairing the reverse process. Further retardation arises from the large driving force of the back reaction which exceeds significantly its reorganization energy ("inverted Marcus region"). The energy released during the electron transfer is absorbed by vibrational excitation of the ambient. The higher the driving force, the less likely it is that such a resonant phonon coupling will occur. Recapture of an electron by the oxidized dye is therefore highly unlikely, given that the kinetics of its reduction by the contacting electrolyte is much faster. Equally, capture of conduction band electrons by the redox electrolyte is kinetically disfavored. For these reasons the external quantum yield of photocurrent generation in the DSSC is close to one if the optical losses in the conducting glass are accounted for. The basis for the insensitivity of dye-sensitized electrochemical interfaces to parameters such as surface texture is now obvious, and the use of nanocrystalline thin film structures with a roughness factor of over 1000 has become standard practice.

7.2.1.1 Dye Molecules

The best photovoltaic performance both in terms of conversion yield and long term stability has so far been achieved with polypyridyl complexes of ruthenium and osmium. Sensitizers having the general structure ML_2X_2 where L stands for 2,2'-bipyridyl-4,4'-dicarboxylic acid M is Ru or Os and X presents a halide, cyanide, thiocyanate or water substituent, are particularly promising. Thus, the ruthenium complex *cis*-$RuL_2(NCS)_2$, known as N3 dye, has become the paradigm of heterogeneous charge transfer sensitizers for mesoporous solar cells. The fully protonated N3 has absorption maxima at 518 and 380 nm, the extinction coeffi-

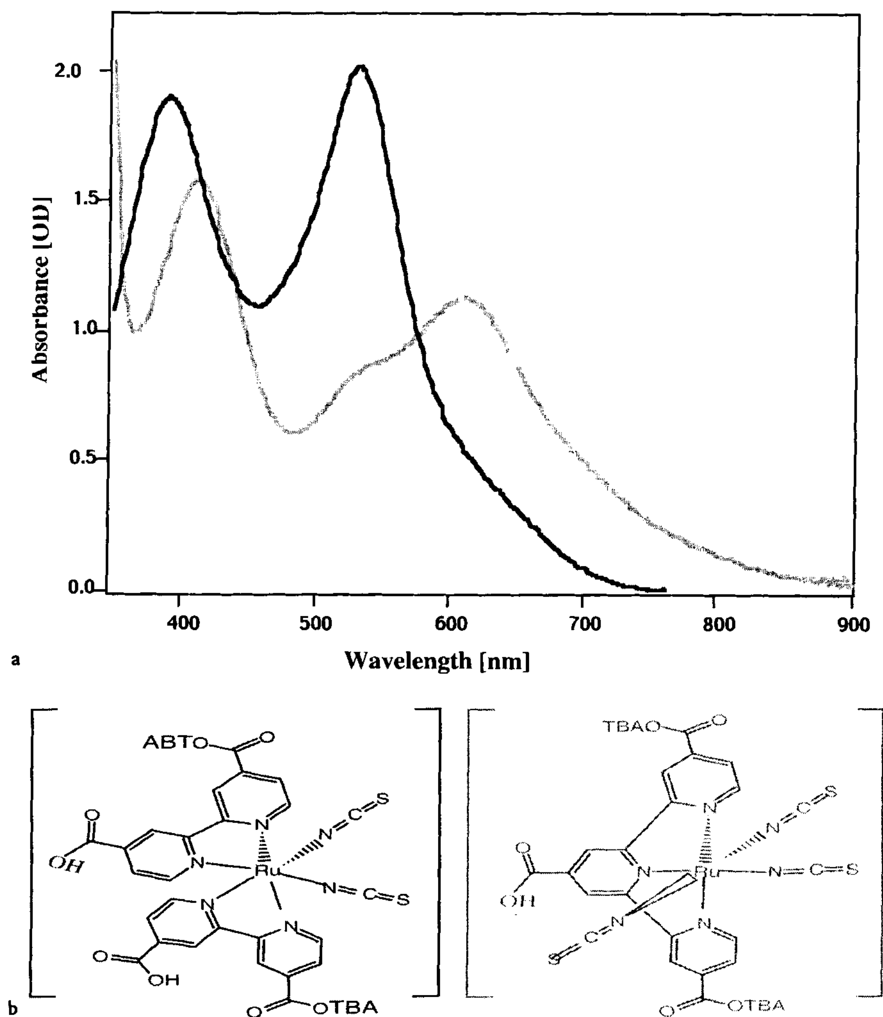

Fig. 7.3 Absorption spectra (a) and chemical structure (b) of the N3 sensitizer (dark gray) and the black (cf. text) dye (light gray). TBA is tetrabutyl ammonium.

cients being 1.3 and 1.33×10^4 $M^{-1} cm^{-1}$, respectively. The complex emits at 750 nm with a lifetime of 60 ns. The optical transition has MLCT (metal-to-ligand charge transfer) character: excitation of the dye involves transfer of an electron from the metal to the π^* orbital of the surface-anchored carboxylated bipyridyl ligand from where it is released within less than 100 fs into the conduction band of TiO_2, generating electric charges with unit quantum yield.

Discovered in 1993 [16] the photovoltaic performance of N3 has been unmatched by virtually hundreds of other complexes that have been synthesized and tested since then. Only recently a credible challenger has been identified with the "black dye" tri(cyanato)-2,2′,2″-terpyridyl-4,4′,4″-tricarboxylate)Ru(II) [15]. Fig. 7.3 compares the absorption spectra of the two sensitizers.

The response of the black dye extends 100 nm further into the IR than that of the N3. The gain in photocurrent expected from such a shift is about 6 mA cm^{-2}. Both chromophores show high incident photon-to-current conversion efficiencies (IPCE) values in the visible range. For the black dye, the photocurrent onset is close to 920 nm, i.e. near the optimal threshold for single junction converters. From there on the IPCE rises gradually until at 700 nm it reaches a plateau of ca. 80%. If one accounts for reflection and absorption losses in the conducting glass, the conversion of incident photons to electric current is practically quantitative over the whole visible domain. From the overlap integral of the photocurrent action spectrum under AM 1.5 solar radiation, one predicts the short circuit photocurrents of the N3 and black dye-sensitized cells to be 16 mA cm^{-2} and 20.5 mA cm^{-2} respectively, in agreement with experimental observations.

7.2.2 Nanocrystalline Semiconductor Film

Significant advances in the fields of colloid and sol-gel chemistry in the last two decades now allow fabrication of micro- and nanometer-sized structures using finely divided monodispersed colloidal particles [17–24]. As we enter the 21st century, there is a growing trend to apply these concepts to develop systems of smaller dimensions. Homogeneous solid electronic devices (3D) are giving way to multilayers with quasi 1D structures and quasi 0D structures, such as nanowires or clusters in an insulating matrix and finally to porous nanocrystalline films.

In recent years, nanocrystalline materials have attracted increasing attention from the scientific community because of their extraordinary physical and chemical properties. These result from the ultra-fine structure (i.e. grain size <50 nm) of the materials. It is useful to distinguish effects related to bulk properties, such as quantum confinement [25] and mono-domain grains [26], from surface effects. The latter arise from the high grain boundary to volume ratio allowing, e.g., for the fabrication of ductile [27] or super-plastic ceramics [28] as well as highly porous membranes [29] and electrodes [30].

Nanocrystalline electronic junctions are constituted by a network of mesoscopic oxide or chalcogenide particles, such as TiO_2, ZnO, Fe_2O_3, Nb_2O_5, WO_3, Ta_2O_5, or CdS and CdSe, which are interconnected to allow for electronic conduction to take

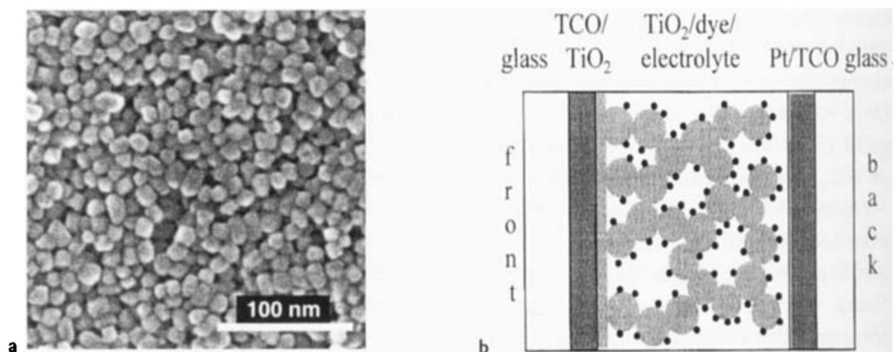

Fig. 7.4 (a) Secondary electron image of the surface morphology of several nanocrystalline TiO_2 (anatase) layers deposited on a transparent conducting oxide (TCO) glass. (b) Schematic cross-section of the DSSC (not to scale), emphasizing the porous character of the anatase film and dye adsorption on it.

place. Typically a paste containing the nanocrystalline semiconductor particles is applied by screen printing or doctor-blading on a conducting support usually a glass coated with a transparent conducting oxide layer. Subsequent sintering produces a mesoporous film whose porosity varies from about 20 to 80%. The pores form an interconnected network which is filled with an electrolyte, or, in a few studies, with a solid charge transfer material, such as an amorphous organic hole transmitter or a p-type semiconductor, such as CuI [31] or CuSCN [32]. In this way an electronic junction of extremely large contact area is formed displaying very interesting and unique optoelectronic properties.

The oxide material of choice for many of these systems has been TiO_2. Its properties are intimately linked to the material content, chemical composition, structure and surface morphology. Preparation of mesoporous semiconductor films consists of two steps: first a colloidal solution containing nanosized particles of the oxide is formed and this is used subsequently to produce a few micron thick film with good electrical conduction properties. Because of great advances in colloid chemistry in the last two decades, it is now possible to control the processing parameters such as precursor chemistry, hydrothermal growth temperature, binder addition and sintering conditions to optimize key parameters of the film viz., grain size, porosity and pore size distribution in order to control physical properties of the film such as light scattering and electron percolation. From the point of view of the material content and morphology, two crystalline forms of TiO_2 are important, anatase and rutile (the third form brookite is difficult to obtain). Anatase is the low-temperature stable form and gives mesoscopic films that are transparent and colorless.

The preparation of nanocrystalline TiO_2 films involves controlled hydrolysis of a Ti(IV) salt, usually an alkoxide such as titanium isopropoxide or a chloride followed by peptization [33]. In order to obtain particles of desired size, the hydrolysis and condensation kinetics must be controlled. Ti alkoxides with bulky groups

such as butoxy hydrolyze slowly, allowing slow condensation rates. Autoclaving of these sols (heating at 200–250 °C for 12 h) allows controlled growth of the primary particles and also to some extent control of the crystallinity. During this hydrothermal growth, smaller particles dissolve and fuse to form large particles by a process known as "Ostwald ripening". After removal of solvent and addition of a binder the sol is now ready for deposition on the substrate. For the latter, a conducting glass sheet is often used and the sol is deposited by doctor-blading or screen printing and fired in air to sinter. The film thickness is typically 1–20 μm and the film mass about 1–2 mg cm^{-2}. Analysis of the porous films shows the porosity to be about 50%, the average pore size being 15 nm. Fig. 7.4a shows a SEM micrograph of a typical TiO_2 film used in the DSSC. The morphology of the particles is controlled by the temperature of the hydrothermal treatment used for film preparation [33]. Interestingly, self-organization of the nanoparticles is observed below 240 °C. The prevailing morphologies of the anatase nanoparticles are square bipyramidal, pseudo-cubic and stab-like. According to HRTEM measurements [34], the face that is mostly exposed is the (101) one, followed by the (100) and (001) surface orientations.

7.2.3 Electron Injection from Dye to TiO_2

As can be understood from Fig. 7.2, electron injection from the dye into the TiO_2 is the primary charge separation step in the photovoltaic process of the DSSC. Electron transfer occurs from the first electronically excited state of the dye (its LUMO, in electron energy diagrams) to the semiconductor. Under normal conditions, this requires that the conduction band (CB) edge of the semiconductor is more negative (farther in energy from the vacuum level) than the LUMO. However, recent results suggest that electron injection is possible also if the LUMO is lower than the CB edge, apparently via higher vibrational and/or electronic states. The process has been measured to be very fast, in the range of tens of femtoseconds. This leads to the occurrence of wavelength-dependent quantum yields. With lower energy photons, electronic states are reached which can not inject into the conduction band of the semiconductor. Conversely photons of higher energy excite the molecules to levels from which the injection is readily possible.

7.2.4 The Importance of the Porous Nanocrystalline Structure of Semiconductor Film

The extremely large internal surface area (the roughness factor is >1000 for a film thickness of 8 μm) which is made possible by the porous and nanocrystalline nature of the semiconductor film, is of crucial importance for the functioning of DSSCs for a number of reasons. Several of these have already been mentioned. To summarize, it enables:

- sufficient adsorption of (partial) monolayers of dye molecules, to effect efficient light absorption;

- this huge surface to be electronically addressable, thus making charge carrier percolation across the nanoparticulate network possible by screening of the electrons in the film, via the adsorbed ionic solution species;
- the production of intrinsic or weakly doped semiconductors, by depleting each grain completely; and
- very rapid and highly efficient interfacial charge transfer between the oxide and each and every one of the dye molecules anchored to the particle surface.

We will now discuss two of these, lack of space charge and reduced charging in electron transport, in more detail.

7.2.4.1 **Space Charge Layer Effects**

The DSSC works because the semiconductor that is used is intrinsic, due to depletion of the nanometer-sized particles upon immersion in the electrolyte (a size effect). As the particle size shrinks, the chance that a particle will be completely dopant-free becomes increasingly greater: nanoparticles are more likely to be close to intrinsic than bulk semiconductors. However, maybe more important is that, in the common DSSC, individual crystallites are surrounded (at least to a large extent) by liquid electrolyte. This means that the crystallites will probably be totally depleted. This would occur even if the crystals were microns long, as long as electrolyte surrounds individual crystals of sufficiently small (typically tens of nanometers) cross-section. This depletion means that the semiconductor acts as a dye-sensitized photoconductor. Injection of electrons into the conduction band (or traps – we will treat the two cases later, separately) increases its conductivity. In other words, the Fermi level changes to an extent dependent on the electron injection rate. This change in Fermi level upon illumination is what enables efficient transfer of the photovoltage to the SnO_2 contact.

The extent of the depletion in semiconductor grains was first studied for a planar geometry [35] and then for spherical or cylindrical particles [36–38]. In the strong depletion regime, the band bending (difference between the electrostatic potential at the particle center and at the surface) is:

$$\Delta\phi = \mathrm{k}T/6q(R/L_\mathrm{d})^2 \tag{3}$$

where R ist the particle radius and L_d is the Debye screening length. For $L_\mathrm{d} \approx 40$ nm and $R \approx 10$ nm, the band bending will be in the range of a few millivolts. The grain size or the bulk doping would have to increase significantly (a factor of 10) to change that picture. The variation of the dimensionless reduced barrier height:

$$\phi_\mathrm{B} = 4\Phi_\mathrm{B}\varepsilon/(qRN_\mathrm{s}) \tag{4}$$

as a function of the reduced doping level of the grain (also dimensionless),

$$n = 2RN_\mathrm{d}/N_\mathrm{s} \tag{5}$$

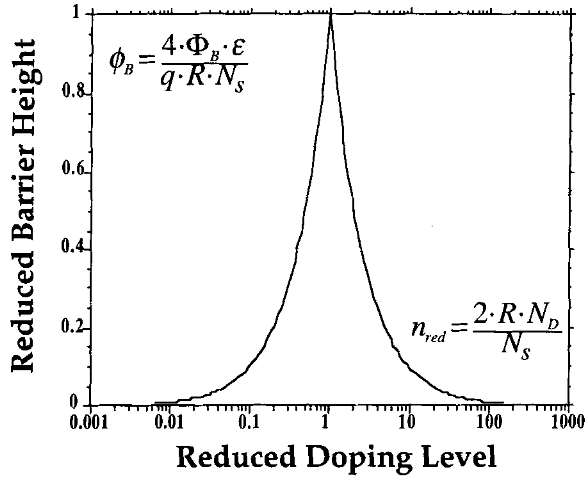

Fig. 7.5 The variation of the dimensionless reduced barrier height as a function of the dimensionless reduced doping level of a semiconductor grain.

is illustrated in Fig. 7.5. Here Φ_B is the actual barrier height (which gives the band bending), N_d is the bulk donor density (for n-type materials) of the particle, and N_s is the surface state density. The figure shows that band bending will be negligibly small for very small and for very large reduced doping densities. The physical reasons are different: for a particle without dopants (intrinsic and/or very small) the Debye screening length $L_D >> R$, while, for a particle with very high doping density, the material will become degenerate.

Although Eq. (3) is normally used to estimate the electrostatic potential band bending in semiconductor systems, for the nanocrystalline ones the issue of discrete effects, nearly always neglected in semiconductor physics, arises. As the system tends, under normal insolation and in steady state, towards one charge per TiO_2 particle [38], the continuum model (which considers a doping charge distributed in a continuous fashion over the volume) becomes questionable. Possibly, in some cases the continuum model greatly underestimates the band bending.

The Fermi level position in the particle in the dark is a fundamental quantity for the model presented below. Classically, it can be calculated by solving the electroneutrality equation (EN) for the semiconductor. In the following, n is the TiO_2 conduction band electron concentration, N_d is approx. 10^{16} cm^{-2}; cf. [14, 39] and N_d^+ is its ionized fraction, N_s is about 10^{12} cm^{-2}, N_s^- is the concentration of those having trapped an electron, E_s is their energy, R approx. 10 nm. We will show this for three limiting cases [23].

Bulk TiO_2

With a net ionized donor density N_d^+ (if the donor levels are shallow ones, $N_d^+ = N_d$), and if the semiconductor is non-degenerate, the electroneutrality condition is:

$$n = N_d^+ \approx N_d \text{ or, equivalently, } E_F = E_c + kT \ln(N_d/N_c) \quad (6)$$

where E_F is the Fermi level and N_c is the density of states in teh conduction band.

If we take $N_c \approx 10^{21}$ cm^{-3} and $N_d \approx 10^{17}$ cm^{-3}, $E_c - E_f = 0.23$ eV.

The value of N_d can be taken as an upper value [40]. The Fermi level will drop by 60 meV for every order of magnitude drop in N_d.

Isolated TiO_2 Colloid with Surface Traps

For a colloid of radius R, having N_s (acceptor) surface states per unit surface, in addition to its bulk doping density, the EN is:

$$n + N_s^-(3/R) = N_d^+ = N_d \tag{7}$$

In the case of interest, $N_s/R >> N_s^-/R \approx N_d >> n$, i.e., most surface acceptors are empty because, on average, there are not enough donors per particle to fill them (hence $E_F < E_s$) and most electrons released by donors are trapped. The converse case ($n \approx N_d^+ >> N_s^-/R$) would correspond to a small number of surface states near or below the Fermi level (a case treated above) a case that do not seem to fit the observations [41]. It is therefore reasonable to neglect n in the equation above. Using Boltzmann statistics for the donor and acceptor states:

$$E_f = E_s + kT \ln\{(R/3)(N_d/N_s)\} \tag{8}$$

With $E_c - E_s = 0.6$ eV [42], $R = 10$ nm, and $N_s = 10^{12}$ cm^{-2}, $E_c - E_f \approx 0.7$ eV (and even more if $N_d < 10^{17}$ cm^{-2}).

TiO_2 Colloid with Surface Traps Immersed in an Electrolyte

In this case, the colloid will transfer some charge to the electrolyte so as to equilibrate its Fermi level with the redox level of the electrolyte. If N_e is the net number of electrons transferred to the electrolyte (not being necessarily > 0) then it is determined by the global EN balance, i.e.:

$$N_e = N_d^+ - n - 3N_s^-/R \tag{9}$$

The quantities on the right side, n, N_d, N_s, are determined by the Fermi statistics, i.e. by the position of the Fermi level, with respect to the bands of TiO_2, a quantity that can be estimated experimentally, as shown below.

The redox level is ~ 4.85 eV below vacuum. The measured E_c position of dry anatase is –4.45 eV (vs. vacuum energy level), shifted to –3.9 eV when exposed to electrolyte, because of specific adsorption of ions and/or solvent [43], i.e., the TiO_2 levels are shifted upwards some 0.55 eV prior to charge transfer. From the respective position of E_F and the bands, we calculate $E_c - E_{redox} = 0.95$ eV and $E_s - E_{redox} = 0.35$ eV. The former value indicates that $N_{d+} = N_d$ and $n << N_d$, and from the latter one can compute N_s^- from

$$N_s^- = N_s(1 + \exp((E_s - E_F)/kT))^{-1} \tag{8}$$

so that $N_s^-/R = 10^{12}$ cm^{-3} $<< N_d$ and $N_e = N_d$.

The E_F shift can therefore be achieved with further depletion of the TiO_2 particle (depletion of the surface states), the electric potential drop due to this electron transfer (less than one e^- per particle) being very small thanks to electrolyte screening (see below): most of the shift in E_F is due to concentration changes in the colloid and to surface dipoles (ions/solvent adsorption) rather than electric fields due to interface charge transfer.

7.2.4.2 **Particle Charging**

Another consequence of the ability of the electrolyte to contact most of the real surface of the nanocrystals is efficient screening of the photo-injected electrons in the semiconductor by positive ions (cations, protons). Without this screening, charges might face a Coulomb barrier ("Coulomb blockade") of up to 50 meV in crossing from one crystal to an adjacent one (depending on the contact between crystals). Electrolyte screening would reduce this barrier, if it exists, to well below thermal energies, both due to free ions and, even if no free ions were present, due to polarizable solvent molecules at the semiconductor–electrolyte interface. Brus has shown that such effects can strongly reduce the energy required by an electron to jump from particle to particle when the particles are surrounded by a liquid [44].

7.2.5
Traps and Discrete Charge Effects

When the dopant is at the center of a spherical colloid, with the compensating surface charge spread uniformly, the potential distribution $\phi(r)$ can be easily calculated ($\phi = q/(4\pi\varepsilon\varepsilon_0 r)$), but the potential difference between the center and the edge of the particle $\{q\Delta\phi = q(\phi(R) - \phi(0))\}$ does not give the "band bending" (BB). BB here represents the energy needed to move an electron from inside the particle to its surface. Formally, as $r \to 0$, $\phi \to \infty$, and $q\Delta\phi$ is infinite, which can be best interpreted as a failure of the continuum model. The BB is best evaluated considering the neutral dopant as a hydrogen-like atom. The BB can here be identified with the ionization energy of the impurity (more accurately, with the energy difference between the ground state energy of the electron on the neutral dopant and the energy of the electron in an orbit located on the surface of the particle). Using a hydrogen-like model for the donor atom yields a pseudo-BB $\approx$ 4 meV (with an electronic effective mass of 5 and a dielectric constant of 130 in TiO_2, giving a Bohr radius of ca. 1.5 nm), a value not significantly different numerically from the one obtained with the continuum model, but with a different dependence on particle radius.

Actually, very few particles have a single dopant atom in the middle (because there is more volume near the surface than in the center: the probability distribution is $P(r) = 3r^2/R^3$). In that case, the potential distribution is anisotropic and has a minimum that can be significantly lower than the above-given value, somewhere on the surface.

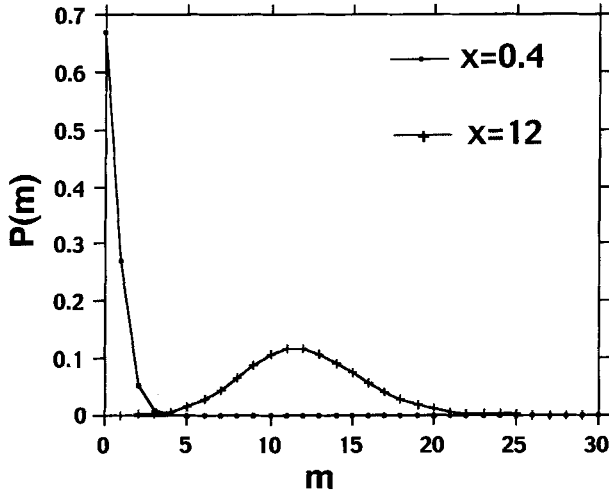

Fig. 7.6 Poisson law for the charge distribution: circles (•), one charge per particle on average ($x = 0.4$); crosses (+), ten charges per particle on average ($x = 12$).

Because the number of dopants per particle is small (approx. 0.4 on average, based on $N_d = 10^{17}\,cm^{-3}$), we should also consider how this affects the above picture from the statistical point of view. Assuming a completely random (non-correlated) dopant distribution, the probability law followed by the number of dopants per particle is a Poisson law ($P(m) = x^n/m!(\exp(-x))$, where x is the average number of dopants per particle). For $x \approx 0.4$, about 67% of the particles have no dopant, 27% have one, 5% have 2, and so on (cf. Fig. 7.6).

The same evaluation can be done for the surface states, with $x \approx 10$ (for r = 10 nm and $N_s = 10^{12}\,cm^{-2}$). Then the fluctuation is much less important (~ 80% of the particles will have between seven and fifteen surface states). In that case we also can not be sure that their distribution is Poisson-like, so that we will neglect the fluctuation in surface states concentration here.

Putting N_d values obtained for $x = 0.4$ in the equations above that determine the E_F position, we see that we can expect important fluctuations for electrically unconnected colloids. Because E_F will equilibrate by changing its position with minute charge transfer, this will not create an inter-grain barrier between connected particles.

In polycrystalline semiconductors, the mobility of carriers is often limited by the inter-grain barrier [35]. Having grains completely depleted, with a vanishingly small band bending ensures that inter-grain carrier transport is not impeded by a significant barrier (Fig. 7.7, top).

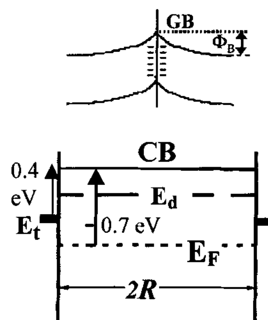

Fig. 7.7 Schematic energy diagrams of a grain boundary (GB). Top: in a polycrystalline semiconductor with a grain boundary potential ϕ_B. Bottom: of a nm-sized grain with a radius R, less than the exciton/Bohr radius In the latter a trapping level (E_t) and a doping level (E_d) are indicated.

7.2.5.1 Trapping

There is plenty of evidence that electrons in the semiconductor spend most of their time in traps and that conductivity occurs by trap hopping. This is logical, taking into account the long times (often ms) needed typically for electrons to traverse the film. If trapping did not occur, the injected electrons would need to spend this long time in the conduction band. Based on what is known of semiconductor nanocrystals in general, trapping of photogenerated electrons usually is a very fast process (sometimes sub-ps). The trapping also gives light-dependent mobility of electrons. These phenomena have been well studied and have been described in more detail in the previous chapter.

Because the trap states affect the way the quasi-Fermi level in the TiO_2 particle can change upon illumination, they may also affect the maximum photovoltage achievable in the DSSC. This is discussed further below.

7.2.6 Importance of Redox Potential and of the HOMO Level of the Dye

It is often stated that the redox level in the electrolyte needs to be above the level of the HOMO (on the electron energy scale, i.e. closer to the vacuum level), to be efficient in collecting the photogenerated holes from the excited dye molecules, but not too high in energy so as not to lose too much voltage. These considerations are inspired by experience with photoelectrochemical cells with a bulk electrode, where the electron energy level diagram at equilibrium leads easily to that under illumination.

The usual point of view is that the same holds for the DSSC, i.e., that the electrostatic barrier height is the limit for the photovoltage: in this point of view the photovoltage is equal to the neutralization of some built-in field. Therefore it is preferred to have a redox level in the solution as oxidizing as possible, i.e. very close to (but above, so as to enable hole transfer) the HOMO level of the dye. Any difference between the HOMO level and the dye then appears as a loss in cell voltage.

Actually, the opposite view can be held. The maximum achievable voltage is obtained for the most reducing electrolyte, as then, the recombination current (pro-

portional to the oxidant concentration) is minimal. This confusion comes about because two different effects are mixed up. One is that the difference in energy between redox potential and HOMO level of dye should be (energetically speaking) as small as possible and the other is that minimization of the back reaction (recombination) depends largely on minimizing the concentration of the oxidized species rather than on energetics. The latter agrees with the trend that is experimentally observed [45, 46], and which is also expected from first principles (V_{oc} is related to the ratio of the generation to recombination current, see e.g. [45, 47]). The limit to the lowering of the oxidant species concentration in solution actually comes from problems of current transport in the electrolyte. When comparing different redox couples, one has to take into account the different reaction rates (that depend on steric effects as well as wave function overlap). The best results have been obtained so far using an I^-/I_2 electrolyte with a large I^- concentration (at least 0.1 M) and a minimal I_2 concentration (ca. 10 mM).

7.3 DSSC Output Parameters

Up to now, we have discussed the main features of the DSSC in terms of its components. We will now consider the DSSC from a different perspective – the output parameters (photocurrent, photovoltage, fill factor) and how these parameters depend on the cell components. This approach requires a certain amount of duplication of information on the one hand, and for that reason will be given in a brief, outline manner. On the other hand, such a treatment widens the utility and comprehensiveness of this chapter.

7.3.1 Photocurrent

The photocurrent can be maximized as follows:
- The rate of electron injection from dye to semiconductor should be very high compared to the rate of back electron transfer from the semiconductor to the electrolyte (in particular, to the tri-iodide), so as to minimize recombination.
- Injected electrons should be removed as quickly as possible by the back contact (to prevent excessive electron built-up and, as a consequence, potential recombination).
- The Helmholtz field at the semiconductor/electrolyte interface should be of the right polarity so as to reduce recombination (cf. Section 3.4, below, and ref. [42]).
- If the hole carrier is negatively charged (as is the case for tri-iodide), this can reduce recombination significantly by electron repulsion (increased scattering cross-section).

The energy of the dye absorption edge should be as low as possible (to allow maximum photon absorption). However, under illumination, the dye HOMO level must

be below the actual redox level at the semiconductor surface while its LUMO level must be above the conduction band level [27] (cf. Fig. 7.10). Also, the difference between the HOMO and redox levels as well as that between the LUMO and conduction band level represent driving forces for charge separation, and therefore should never be zero. In other words, the dye absorption edge is always larger than the maximum achievable photovoltage, so that the dye absorption edge cannot be too small.

7.3.2 Photovoltage

The photovoltage can be maximized as follows:

The Fermi level of the semiconductor in the dark should be as far as possible from the conduction band (maximum possible depletion). This holds for electron injection into an electron conductor. An analogous argument holds for hole injection into a hole conducting material. In principle, injecting electrons into a p-type material should give even higher voltages. However, there are some practical problems, such as the poor electron mobility in a hole conductor, in part due to the presence of negative scattering centers (charged acceptors) [19].

As in any photovoltaic cell, the requirements from the light absorber for maximum photocurrent (see above) and photovoltage are conflicting. For maximum photovoltage, the energy of the dye absorption edge should be as *high* as possible. Since the dye HOMO level must be below the redox level while its LUMO level must be above the conduction band level for cell operation, the redox electrolyte should be chosen so that, under operating conditions (i.e., under illumination), E_{redox} is only slightly higher in energy than the dye HOMO while the dye LUMO should only be slightly higher than the semiconductor conduction band edge. This would be the ideal operating situation for maximum photovoltage.

Electrolyte diffusion should be optimized. This is problematic because of the porous semiconductor structure, which will tend to increase the concentration of the oxidized redox species at the photoelectrode, resulting in a shift of its potential (reduction in photovoltage). This effect would also increase recombination, thereby affecting all cell parameters.

In general, any factor that decreases recombination will increase the photovoltage and the fill factor.

7.3.3 Fill Factor

The fill factor will be optimized by considering the following:

- Reduce recombination. Several factors involved in recombination were already discussed above. In particular, as the Fermi level in the semiconductor approaches the conduction band, the charge distribution at the surface of the semiconductor particles will change and, as a result (cf. Section 4, below), the potential will be affected in such a way so as to decrease its efficacy in decreasing recombination.

- The counter electrode should be a good electrocatalyst for the oxidation reaction (to prevent increasing loss of photovoltage because of overpotential at the counter electrode as the photocurrent increases).

7.3.4 DSSCell Performance

The overall efficiency (*eff*{global}) of the photovoltaic cell is calculated from the integral photocurrent density (i_{ph}), the open-circuit photovoltage (V_{oc}), the fill factor of the cell (*FF*) and the intensity of the incident light (I_s = 100 mW cm^{-2})

$$eff\{global\} = i_{ph} \times V_{oc} \times FF / I_s \qquad (9)$$

At this stage the confirmed efficiency obtained with the black dye is 10.4% as shown in Fig. 7.8 [15]. Further development will concentrate on the enhancement of the photoresponse in the near IR region. Judicious molecular engineering of the black dye structure may increase the extinction coefficient substantially in the 700–900 nm region. The goal is to obtain a DSSC having optical features similar to GaAs. A nearly vertical rise of the photocurrent close to the 920 nm absorption threshold would increase the short circuit photocurrent from currently 20.5 to about 28 mA cm^{-2}. With the V_{oc} and *FF* values of Fig. 7.8, this would raise the overall efficiency to 14.2%.

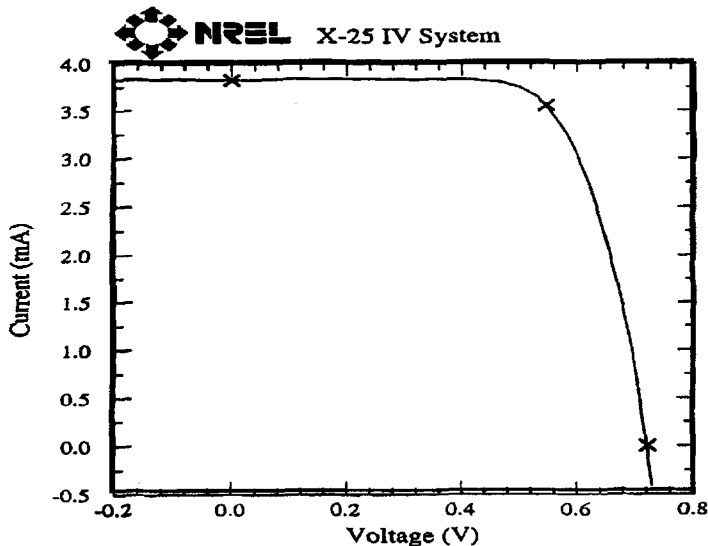

Fig. 7.8 Photocurrent-voltage characteristic of a nanocrystalline solar cell sensitized with the panchromatic "black" dye. The results shown were obtained at the NREL (CO, USA) calibration laboratory. A light source simulating AM 1.5 global insolation was used, with 100 mW cm^{-2} incident intensity.

An advantage of the DSSC with respect to most of the competing technologies is that its performance is remarkably insensitive to temperature change. Thus, raising the temperature from 20 to 60 °C has practically no effect on the power conversion efficiency. The loss in open circuit voltage due to the increase in the dark current is compensated by the improved mobility of the hole carrier (tri-iodide) in the electrolyte as well as the decrease of the charge transfer resistance of the counter electrode, augmenting the photocurrent and the fill factor of the cell. As these opposing effects cancel each other, the effect of temperature on cell performance is small. In contrast, conventional silicon cells exhibit a significant decline in the overall conversion yield amounting to ca. 20% over the range between 20–60 °C. Since the latter temperature is readily attained under full sunlight this feature of the injection cell is particularly attractive for power generation under natural conditions. Stability studies have shown the DSSC to sustain temperatures of 85 °C without loss of performance.

7.4
Further Comments on the Mode of Action of the DSSC

The origin and the limits of the photovoltage of a DSSC have been the subject of considerable discussion and some degree of controversy [43, 48–51]; see also Chapter 6.

In agreement with earlier work (cf. e.g. [52]), and as in all photovoltaic devices, we argue that the basic reason for the photovoltage of a DSSC is the shift in the semiconductor E_F under illumination. This shift leads to a $\Delta\eta_e$ (as the result of a $\Delta\mu_e$) at the electrolyte-semiconductor interface.

This mechanism requires an intrinsic semiconductor. Even if the dry semiconductor is not intrinsic, this will be the case in the DSSC, due to depletion of the nanocrystalline, mesoporous structure upon immersion in the electrolyte (because of the small particle size). In bulk form, transport of injected charge through an intrinsic material will be by way of drift in a strong electric field (cf. a-Si:H p/i/n structures). The absence of such a field in the mesoporous, nanocrystalline film of the active DSSC electrode excludes such a mechanism. There is, however, the added difficulty of charging, which can occur because of the small size of the nanocrystallites. It is the mesoporosity of the system that dictates both the absence of a significant electric field across the film and the insignificance of charging upon carrier injection. This mesoporosity allows for effective screening by electrolyte ions of any charged species in the nanoparticles. Given that, diffusion due to the gradient in the density of electrons allows charge transport to proceed. The possible existence of an electrical ($\Delta\phi$) or chemical ($\Delta\mu_e^0$) potential drop at the back contact helps to maintain the necessary $\Delta\mu_e$ by allowing the charge transfer to SnO_2 to be non-limiting.

Alternative models have been suggested, all depending on the concept of neutralization of an existing (dark) electric potential difference, which is used to explain PV action in normal p/n junction and photoelectrochemical solar cells. Ac-

cording to one model, the photovoltage results from neutralization of a potential drop at the semiconductor/electrolyte interface. Indeed it has been argued convincingly that, in the case of the common anatase- and Ru dye-based DSSC, there does exist an electrical field at the electrolyte/semiconductor interface, although not one due to space charge in the semiconductor [40, 52, 53]. It results from cation and dye adsorption on the surface. The dyes that are normally used are acids and release protons upon binding to an oxide surface. These protons, together with other cations in the electrolyte, become part of the oxide surface region (for example, by converting terminal oxide into hydroxide groups). A dipole is formed across the Helmholtz layer between the negatively charged (iodide and dye) species and the cations. The (Galvani) electrical potential drop across the Helmholtz layer, $\Delta\phi(H)$, (which we estimate at ~ 0.3 eV; cf. also Ref. [52]), will help to separate the charges and reduce recombination. A straightforward calculation shows that illumination cannot generate sufficient charges to neutralize $\Delta\phi(H)$ completely. Indeed, it has been argued that while dye excitation reduces $\Delta\phi(H)$, as a result of electron injection and charge rearrangement in the layer and at the surface, the change is too small to account for the photovoltage [52]. Charge separation, however, is aided by the interfacial Helmholtz dipole field that occurs at the semiconductor/electrolyte interface.

It has recently been argued that light-induced neutralization of an accumulation voltage at the back contact is equal to the photovoltage [49]. While this can indeed occur, it must be realized that a photovoltage can be generated without neutralization of an accumulation layer. This means that the photopotential cannot be limited by the Galvani potential difference at the back contact and a photovoltage is generated, independent of the possible presence of accumulation/depletion layers at the semiconductor/back contact interface. Neutralization of such layers can occur as the result of the E_F shift that is the cause for the photovoltage. Recently, Pichot and Gregg have presented experimental evidence to that effect [48]. Still, if this concept [49] were to be correct, it would have important consequences in terms of orienting research towards better cells: these could be obtained principally by selecting carefully the back contact material to obtain the largest potential drop achievable.

To put things in perspective, we evaluate the maximum photovoltage and efficiency achievable in theory in a perfect DSSC device.

Photon energy is first converted into electrical potential energy in the dye molecules where light absorption occurs, creating an electron-hole pair having a free energy at most equal to the dye absorption edge (1.8 eV). From this point on, all processes are dissipative and lead to a reduction of the output energy collected. When the losses are minimal, in the radiative recombination limit (the only losses that are unavoidable), the maximum achievable photovoltage (Schockley) is $V_{oc} \approx 0.9$, for $E_G \approx 1.6$ V. Using a more realistic value obtained from the luminescence efficiency of the dye, $V_{oc} \approx 1.3$ V, and in real devices non-radiative recombination, intrinsic to the dye, limits the achievable efficiency [51]. The actual V_{oc} is further lowered due to additional recombination processes such as:

$$2e^-_{TiO_2} + I_3^- \rightarrow 3\ I^- \qquad (10)$$

Charge separation occurs at the semiconductor/electrolyte interface and is aided by an interfacial Helmholtz dipole. High open circuit voltages and fill factors are possible because of very low recombination rates, due to the spatial and phase separation between electron and hole transport, the charge of the hole carrier (I_3^-), the direction of the interfacial dipole, screening of the electron by the adsorbed cations and the nature of surface traps. Screening furthermore assists the transport of electrons to the back contact. There the electrons are collected because of the drop in standard chemical potential of the electrons between the anatase and SnO_2:F, used as transparent conductor and because of the existence of a small electric potential drop across an accumulation layer. While light-induced neutralization of such an accumulation voltage at the back contact can occur, this neutralization is not essential for generating a photovoltage.

We can now summarize how the DSSC differs from a p/n or photoelectrochemical solar cell:

- light absorption occurs in the dye and *not* in the semiconductor; this leads to charge injection from the dye into the semiconductor;
- as a result *only* majority carriers are present in the semiconductor;
- charge separation occurs primarily due to chemical rather than electrical potential gradients;
- additional electrical effects can be involved due to the electrical potential difference across the Helmholtz layer;
- recombination is minimized, notwithstanding the enormous surface area of the photovoltaically active semiconductor + dye-electrolyte interface, because of: (i) the unipolar character of the charge transport; (ii) the absolute negative charge of the hole carrier (I_3^-); and (iii) the Helmholtz potential.

7.5 Modeling the DSSC

7.5.1 Energy Diagrams

A simplified band diagrammatic model of a DSSC can now be given schematically, as shown in Fig. 7.9. Upon illumination and if no current flows, the light-induced carriers split the quasi-Fermi levels, where the electron Fermi level, $E_{F,n}$, is essentially that in the TiO_2, while the hole Fermi level, $E_{F,p}$, is the redox potential of the solution, which is the potential taken on by the platinized SnO_2 counter electrode. If the system is short-circuited there will be a gradual variation in $E_{F,n}$ and $E_{F,p}$ across the absorber, which, in this picture, is the mesoporous TiO_2 film with adsorbed dye and intervening redox solution.

To model this more quantitatively, several options exist. One is noted here.

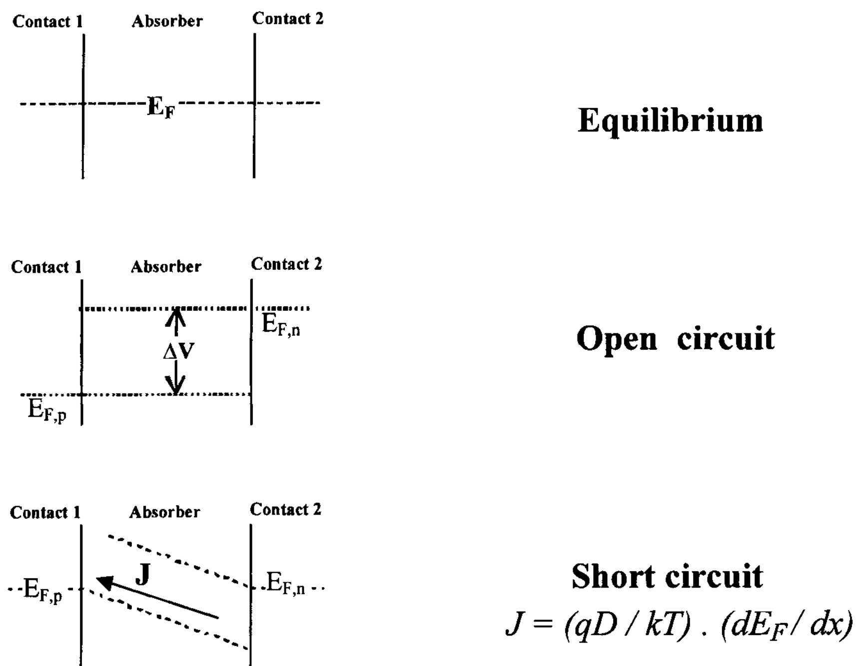

Fig. 7.9 Simplified schematic of the (pseudo)Fermi level positions of a DSSC at equilibrium in the dark and under illumination at open circuit and short circuit.

7.5.1.1 Effective Medium Picture [43, 54]: Advantages, Limitations and Uses

In the mesoporous nanocrystalline system with dye molecules adsorbed on the nanocrystallites system various phenomena occur on three distinct length scales: the atomic scale (0.1 nm), the colloid scale (10 nm), and the macroscopic scale (μm).

One of the important questions in the study of nanoporous media is that of knowing how phenomena occurring on these different scales are related. As the local picture is very complex, one is in need of a global picture that is simplified as compared to the local one.

When considering macroscopic phenomena, in homogeneous solids (that is, solids that are homogeneous above the atomic scale), one uses material characteristics that are local averages (atomic scale). Similarly, one can consider quantities averaged on scales larger than that of a colloid to obtain practical macroscopic information from microscopic data.

Many quantities can be simply averaged to give useful macroscopic quantities: the optical absorption coefficient, the electronic conductivity, the ionic conductivity (each conductivity can be meaningfully averaged because each medium (TiO_2, electrolyte) is percolating).

We can picture this schematically as shown in Fig. 7.10, where the TiO_2 plus electrolyte are given as one effective medium. Upon illumination and absorption of a photon by the dye, an electron is excited to the LUMO. Injection of the elec-

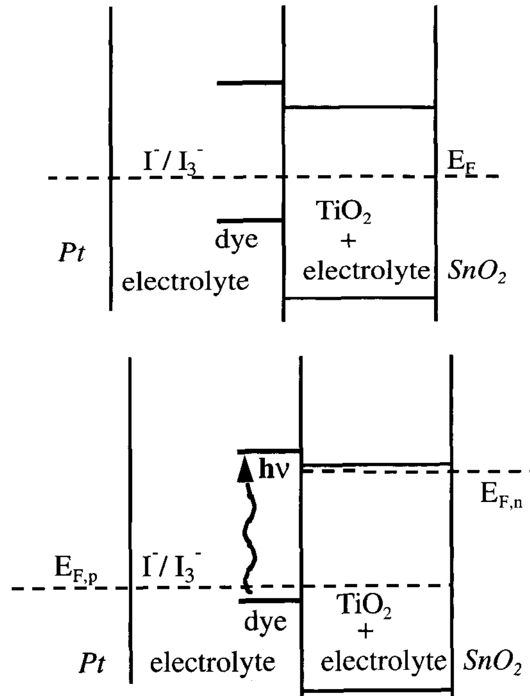

Fig. 7.10 Energetics of the DSSC in the dark (top) and under open circuit conditions with (TiO_2 + electrolyte) considered as one effective medium (bottom).

tron into the TiO_2 cum electrolyte and hole transfer to the electrolyte leads to the quasi-Fermi level splitting that is the origin of the photovoltage.

One of the complex question that arises is that of determining the electrical field in the system, but looking on the macroscopic scale at the composite system with an effective medium theory enables one to get important parts of its physics. Using such a model of effective medium one can estimate the effective screening length. Assuming that all of the particles' surfaces are exposed to charged species and taking an ionic concentration in solution of about 0.5 M, a medium at 50% porosity will have an effective charge carrier density of 1.4×10^{20} cm^{-3} (the dielectric constant of TiO_2 being around 100 and the particle radius around 10 nm). This gives a Debye screening length of 5–20 Å. As a consequence, there are no electric fields on a scale larger than a colloid.

Microscopically, this means that the electrons, injected in TiO_2, "hug" the surface as screening by electrolyte decreases their electrostatic energy. This fits the optical and electrical data (hopping, surface traps) obtained by several groups [42, 49, 55, 56]. This has important consequences for the cell operation, and specially for the recombination process between electrons and I_3^- that must take place at the microscopic solid/liquid interface. Because the electron must be within tunneling distance, d, of the tri-iodide (assume $d \ll R$), the probability of recombination is proportional to the specific surface area, S, which, to a first approximation, is proportional to $1/R$.

The process is influenced by two factors that counteract each other:

- Whereas the high dielectric constant of TiO_2 helps to confine the electron inside the particle, electrostatic screening brings it to the surface. Given an actual surface area, some 10^3 times larger than the geometric one, this increases recombination accordingly; and
- The negative charge of tri-iodide repels the electron and keeps it from getting to within tunneling distance. In semiconductors the capture cross-sections for like charges are some 10^4 times smaller than for oppositely charged carriers (cf. discussion in ref. [43]). Thus, the negative charge on the hole acceptor keeps the recombination rate to acceptable values (approx. $0.5–1 \times 10^{-3}$ s^{-1} [54]).

As already noted, the electron transport can be described in terms of the small polaron model [41, 48, 54, 55]. Assuming that the traps are essentially on the surface, the large S will reduce D_n (10^{-2} cm^2 s^{-1} [54]), in agreement with values derived from experimental data.

In addition the original reason for a large value of S remains, viz., an increase in optical absorption as the absorption coefficient is proportional to it. The value of L necessary to absorb most of the light thus decreases (exponentially) with increasing S.

7.6 Comparison of Liquid Electrolytes and Solid-state DSSCs

Because of the encapsulation problem posed by the use of an organic liquid in the common DSSC, much work is being done to make an all-solid state DSSC [57, 58]. Early work focussed on use of CuI instead of the I^-/I_3^- liquid electrolyte. The reason behind this is severalfold: CuI is a solid state ionic (Cu) conductor, and a very good one at > 150 °C. In addition it is a p-type electronic conductor and finally it can be prepared by precipitation from an acetonitrile solution at room temperature. Cells made in this way gave solar efficiencies of several percent, but their stability is relatively poor, because of the lability of CuI in air and light [57]. Possibly hermetic sealing can solve that problem. Other work along these lines is that of O'Regan and colleagues, using CuSCN [32, 59] and that of Bach et al., who used a hole conducting, amorphous organic solid, deposited by spin-coating [58]. Semi-solid solutions, such as use of gel electrolytes, are also explored. It is fair to say, though, that there is still a wide gap between the truly solid state devices and the best liquid electrolyte ones. Possible reasons for that can be gotten from what has been said above.

7.7 Potential Applications

The original application for the material covered in this chapter is, of course, for solar cells, and it is to this end that most effort has been expended. However, other possible applications have been presented and it is clear that the wide range of research aimed at understanding the mode of operation of the solar cell will benefit these other applications as well. Among such potential applications are those involving conversion of light to chemical energy (rather than to electrical energy), including photo(electro)catalytic reactions. The dual applicability of porous semiconductors for batteries and photovoltaic cells suggests that a photovoltaic cell with built-in storage may be possible (although the often conflicting demands of a photovoltaic cell and a battery may make this goal far from simple). A very different application is that of electrochromic materials for windows and displays, particularly because of the non-absorbing nature of the semiconductor itself and the ability to tailor redox dyes with different spectral characteristics.

Acknowledgements
We thank Prof. Ilan Riess (Technion) for useful discussions, as reflected in part in ref. [42].

References

1 N. W. Ashcroft, N. D. Mermin, *Solid State Physics* (Saunders, Philadelphia, 1976).
2 I. Riess, *Solid State Ionics*, **1997**, *95*, 327.
3 K. M. Gangotri, C. Lal, *Int. J. Energy Res.* **2000**, *24*, 365–371.
4 L. Kronik, N. Bachrach-Ashkenasy, M. Leibovich, E. Fefer, Y. Shapira, S. Gorer, G. Hodes, *J. Electrochem. Soc.* **1998**, *145*, 1748.
5 W. West, *Photogr. Sci. Eng.* **1974**, *18*, 35.
6 J. Moser, *Monatsh. Chem.* **1887**, *8*, 373.
7 S. Namba, Y. Hishiki, *J. Phys. Chem.* **1965**, *69*, 774.
8 H. Gerischer, H. Tributsch, *Ber. Bunsenges. Phys. Chem.* **1968**, *72*, 437.
9 M. P. Dare-Edwards, J. B. Goodenough, A. Hamnet, K. R. Seddon, R. D. Wright, *Faraday Disc. Chem. Soc.* **1980**, *70*, 285.
10 H. Tsubomura, M. Matsumura, Y. Noyamaura, T. Amamyiya, *Nature* **1976**, *261*, 402.
11 D. Duonghong, N. Serpone, M. Grätzel, *Helv. Chim. Acta* **1984**, *67*, 1012.
12 J. de Silvestro, M. Grätzel, L. Kavan, J. Moser, J. Augustynski, *J. Am. Chem. Soc.* **1985**, *107*, 2988.
13 N. Vlachopoulos, P. Liska, J. Augustynski, M. Grätzel, *J. Am. Chem. Soc.* **1988**, *110*, 1216–1220.
14 B. O'Regan, M. Grätzel, *Nature* **1991**, *353*, 737–740.
15 A. Hagfeldt, M. Grätzel, *Acc. Chem. Res.* **2000**, *33*, 269–277.
16 M. K. Nazeeruddin, A. Kay, I. Rodicio, R. Humphry-Baker, E. Muller, P. Liska, N. Vlachopoulos, M. Grätzel, *J. Am. Chem. Soc.*, **1993**, *115*, 6382–6390.
17 C. J. Brinker, C. W. Scherer, *Sol–Gel Science: The Physics and Chemistry of Sol–Gel Processing* (Academic Press, San Diego, **1990**).
18 L. C. Klein, *Sol-Gel Optics – Processing and Applications* (Kluwer, Boston, 1994).
19 H. D. Gesser, P. C. Goswami, *Chem. Rev.* **1989**, *89*, 765–788.
20 *Sol-Gel Technology for Thin Films, Fibres, Preforms, Electronics and Speciality Shapes;*

Vol., edited by L. C. Klein (Noyes, New Jersey, **1988**).
21 E. Matijevic, *Mater. Res. Soc. Bull.* **1989**, *4*, 18.
22 E. Matijevic, *Mater. Res. Soc. Bull.* **1990**, *5*, 16.
23 E. Matijevic, *Chem. Mater.*, **1993**, *5*, 412–426.
24 E. Matijevic, *Langmuir* **1994**, *10*, 8–16.
25 L. Brus, *J. Phys. Chem. Solids* **1998**, *59*, 459.
26 J. S. Foresi, *Mater. Res. Soc. Proc.* **1992**, *256*, 77.
27 T. G. Nieh, J. Wadsworth, F. Wakai, *Int. Mater. Rev.* **1991**, *36*, 146–161.
28 M. M. Boutz, R. J. Olde-Schulthuis, A. J. Winnubst, in: *Nanoceramics,; Vol. 51*, edited by R. Freer (British Ceramics Proceedings, London, **1993**).
29 Q. Xu, M. A. Anderson, *J. Am. Ceram. Soc.* **1994**, *77*, 1939.
30 A. Hagfeldt, N. Vlachopoulos, M. Grätzel, *J. Electrochem. Soc.* **1994**, *141*, L82–L84.
31 K. Tennakone, G. Kumara, A. R. Kumarasinghe, K. G. U. Wijayantha, P. M. Sirimanne, *Semicond. Sci. Technol.* **1995**, *10*, 1689–1693.
32 B. O'Regan, D. T. Schwartz, *Chem. Mater.*, **1995**, *7*, 1349–1355.
33 C. J. Barbe, F. Arendse, P. Comte, M. Jirousek, F. Lenzmann, V. Shklover, M. Grätzel, *J. Am. Ceram. Soc.* **1997**, *80*, 3157.
34 V. Shklover, M.K. Nazeeruddin, S.M. Zakeerudin, C. Barbe, A. Kay, T. Heubach, W. Steurer, R. Hermann, U.U. Nissen, M. Grätzel, *Chem. Mater.* **1997**, *9*, 430–439.
35 J. Y. W. Seto, *J. Appl. Phys.* **1975**, *46*, 5247.
36 W. Albery, *J. Electrochem. Soc.* **1984**, *131*, 315.
37 A. Goossens, *J. Electrochem. Soc.* **1996**, *143*, L131–L133.
38 J. Bisquert, G. Garcia-Belmonte, F. Fabregat-Zantiago, *J. Solid State Electrochem.* **1999**, *3*.
39 B. van der Zanden, A. Goossens, *J. Phys. Chem. B* **2000**, *104*, 7171–7178.
40 A. Zaban, A. Meier, B. Gregg, *J. Phys. Chem. B* **1997**, *101*, 7985.
41 G. Boschloo, D. Fitzmaurice, *J. Phys. Chem. B* **1999**, *103*, 2228–2231.
42 G. Boschloo, A. Goossens, J. Schoonman, *J. Electroanal. Chem.* **1997**, *428*, 25.
43 D. Cahen, G. Hodes, M. Grätzel, J. F. Guillemoles, I. Riess, *J. Phys. Chem. B* **2000**, *104*, 2053–2059.
44 L. Brus, *Phys. Rev. B* **1996**, *53*, 4649.
45 S. Y. Huang, G. Schlichthörl, A. J. Nozik, M. Grätzel, A. Frank, *J. Phys. Chem. B* **1997**, *101*, 2576–2582.
46 Y. Liu, A. Hagfeldt, X.-R. Xiao, *Sol. En. Mater. Sol. Cells* **1998**, *55*, 267.
47 A. Hagfeldt, M. Grätzel, *Chem. Rev.* **1995**, *95*, 49–68.
48 F. Pichot, B. A. Gregg, *J. Phys. Chem. B* **2000**, *104*, 6–10.
49 K. Schwarzburg, F. Willig, *J. Phys. Chem. B* **1999**, *103*, 5743–5746.
50 D. Vanmaekelbergh, P. E. de Jongh, *J. Phys. Chem. B* **1999**, *103*, 747–750.
51 G. Smestad, *Sol. En. Mater. Sol. Cells* **1994**, *32*, 273.
52 G. Schlichthörl, S. Y. Huang, J. Sprague, A. Frank, *J. Phys. Chem. B* **1997**, *101*, 8141–8155.
53 A. Zaban, S. Ferrere, B. Gregg, *J. Phys. Chem. B* **1998**, *102*, 452.
54 J. Ferber, R. Stangl, J. Luther, *Sol. En. Mater. Sol. Cells* **1998**, *53*, 29–54.
55 R. Koenenkamp, Henninger, Hoyer, *J. Phys. Chem.* **1993**, *97*, 7328.
56 P. E. de Jongh, D. Vanmaekelbergh, *Phys. Rev. Lett.* **1996**, *77*, 3427.
57 K. Tennakone, G. R. R. A. Kumara, I. R. M. Kottegada, K. G. U. Wijanthana, P. S. Perera, *J. Phys. D: Appl. Phys.* **1998**, *31*, 1492.
58 U. Bach, D. Lupo, P. Comte, J. E. Moser, F. Weissörtel, J. Salbeck, H. Spreitzer, M. Grätzel, *Nature* **1998**, *395*, 583.
59 B. O'Regan, D. T. Schwartz, S. M. Zakeeruddin, M. Grätzel, *Adv. Mater.* **2000**, *12*, 1263–1266.

Electrochemistry of Nanomaterials
by *Gary Hodes (Ed.)*
© WILEY-VCH Verlag GmbH, 2001

8 Electrochromic and Photoelectrochromic Aspects of Semiconductor Nanostructure-Molecular Assembly

Prashant V. Kamat

8.1 Introduction

The emerging field of semiconductor and metal nanoparticles has stimulated much interest in recent years because of their size- and shape-dependent electronic properties [1–5]. The functional properties of such materials can be greatly improved by assembling these nanoparticles as thin films on electrode surfaces. Development of thin nanostructured semiconductor films using chemical or sol-gel methods has potential applications in chemical sensors, microelectronics, electro-optics, imaging science, photovoltaics and photocatalysis. Of particular interest is the possibility to design electrochromic and photochromic display devices using nanostructured semiconductor films.

Compared to the ultrahigh vacuum deposition techniques (e.g. chemical vapor deposition or molecular beam epitaxy) chemical and electrochemical approaches of casting thin films are relatively simple and inexpensive [6–10]. Efforts have been made in recent years to synthesize and characterize the properties of thin semiconductor films prepared from colloidal semiconductor suspensions [11–26]. These films are highly porous and can easily be surface-modified with sensitizers, redox couples and other nanostructured semiconductors. For example, nanostructured TiO_2 films prepared from colloidal suspensions have been sensitized with dyes [7, 27–29], short-band-gap semiconductors [13, 19, 30], and metal nanoparticles [31]. Photoconversion efficiencies in the range of 10–12% are obtained for the sensitized photocurrent generation using nanostructured TiO_2 films modified with a ruthenium complex [27, 28].

By controlling the preparative conditions of semiconductor colloid precursors it is possible to tailor the properties of these semiconductor films. These thin metal oxide films exhibit interesting photochromic, electrochromic, photocatalytic and photoelectrochemical properties that are inherited from the native colloids. This chapter presents an overview of the recent developments in the area of electrochromic and photoelectrochromic aspects of nanostructured semiconductor films. The discussion on the semiconductor nanostructures and molecular assembly provides the basis for designing novel electrochemical and electroluminescent display devices.

8.2 Preparation and Characterization of Nanostructured Semiconductor Thin Films

8.2.1 From Colloidal Suspensions

Although the synthesis involved in casting of thin nanostructured films may vary in actual procedure, most of these methods use preformed colloidal suspensions. For example, a variety of different colloidal metal oxide suspensions have been employed to prepare nanostructured semiconductor films (0.1–10 μm thick) of SnO_2 [18], ZnO [14, 15, 32–39], TiO_2 [16, 17, 22, 24, 28, 40–47], WO_3 [48, 49], and Fe_2O_3 [23].

The synthetic procedure involves preparation of ultra-small semiconductor particles (particle diameter 2–30 nm) in aqueous or ethanolic solutions by controlled hydrolysis. Colloidal suspension of metal oxides such as SnO_2 (particle diameter ca. 10 nm) can also be obtained commercially (Johnson-Matthey). One of the most common methods employed for TiO_2 colloids involves aging the colloids at high temperature and pressure. Hydrothermal synthesis has been adopted to ob-

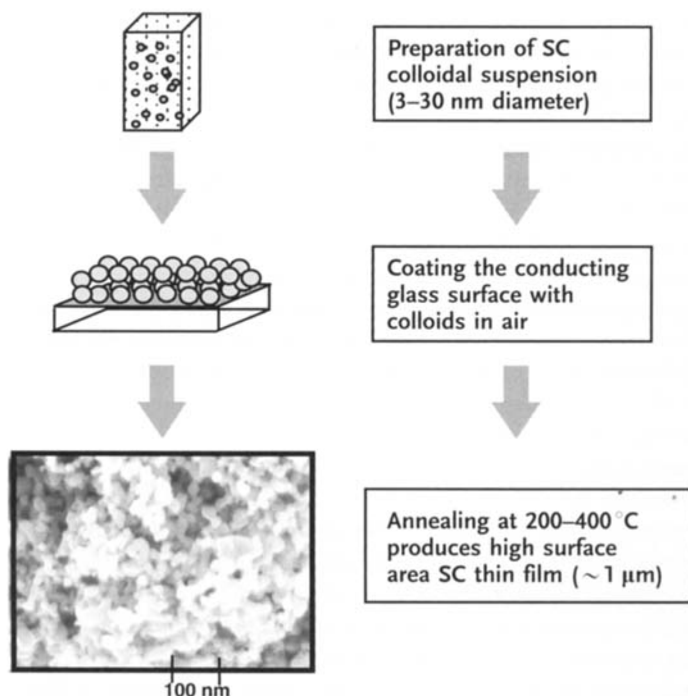

Fig. 8.1 Methodology adapted for preparing nanostructured semiconductor (SC) thin films. A scanning electron micrograph of nanostructured TiO_2 film is also shown.

tain desired size and phase of TiO_2 colloids [50]. TiO_2 colloids prepared in acetic acid medium had more {101} face compared to those prepared in nitric acid.

The colloidal suspension of the metal oxide semiconductor (~1%) is coated on to a conducting glass plate (referred as optically transparent electrode, OTE) and dried in air. The film is then annealed at 200–400 °C in air for about 1–2 h. The conducting surface facilitates direct electrical contact to the nanostructured semiconductor thin films. The schematic diagram in Fig. 8.1 illustrates the methodology of preparing thin film from colloidal suspensions.

This simple approach of coating preformed colloids on a desired surface and annealing produces a thin semiconductor film that is robust with excellent stability in both acidic and alkaline media (pH range 1–13). Usually one can achieve a thickness in the range of 0.1–1 μm. It may be necessary to optimize the concentration of precursor colloid for a particular application since higher colloid concentrations lead to cracking of the film. The above-mentioned procedure can be repeated several times to cast thicker films. (For example, see corresponding references for the methodology of preparation of SnO_2 [18], ZnO [15], TiO_2 [51], and WO_3 [49] films.)

Transmission electron micrographs of nanostructured films prepared from colloidal suspensions show a three-dimensional network of metal oxide nanocrystallites of particle diameter <5 nm [18]. No significant aggregation or sintering effects could be seen during the annealing process. XRD analysis has also confirmed in many instances the crystallinity of these nanostructured films. A similar approach that consists of mixing two or more components prior to casting films has been considered to prepare composite films. For example, thin films of SnO_2/TiO_2 composite semiconductors [52] have been synthesized. These composite films exhibit improved charge separation properties compared to single component semiconductor films.

Preparation of semiconductor nanoclusters in polymer films [53–65] and LB films [11, 42, 66–68] has also been considered. Sol-gel technique has been found to be useful in developing nanostructured semiconductor membranes with either 2D [69] or 3D configuration [70–75]. Organic template mediated synthesis has been employed to develop nanoporous tin(IV) sulfide materials [76, 77].

8.2.2 Electrochemical Deposition

Electrochemical deposition is a convenient technique for casting thin films of II–VI compound semiconductors, viz., CdS, CdSe, CdTe [6, 12, 26, 78]. Quantum size TiO_2 crystallites have been deposited on conductive surfaces by anodic oxidative hydrolysis of $TiCl_3$ [41]. Electrodeposition of WO_3 films has also been carried out from a solution of Na_2WO_4 at a constant current density of 0.1–0.24 mA cm^{-2} [79]. Electrochemically deposited semiconductor films are strongly adherent to the substrate and are comprised of aggregated nanocrystallites [6]. The nanocrystal size distribution (isolated or aggregated) can be controlled by the deposition current and temperature [80]. Presence of dye molecules such as Eosin Y in solution was found to bring dra-

matic changes in the growth of electrodeposited ZnO nanocrystals [81, 82]. Ordered surface of inorganic crystals and chemical interaction with the dye molecules in these examples facilitated ordering of dye molecules during the electrodeposition process.

8.2.3 Self-assembled Layers

The surface-assembled layers of functionalized molecules that interact with the solid surface (e.g., thio compounds on gold surfaces) have been successively used to cast thin semiconductor films [83]. Fendler and his coworkers [84, 85] have constructed ordered nanostructured films using layer-by-layer self-assembly of cationic poly(diallylmethylammonium chloride) and negatively charged solid particles on a variety of substrates. More details on this procedure can be found elsewhere [85]. Mono- and multilayers of CdS-nanoparticles prepared using a self-assembled monolayer of alkanedithiols on gold has been shown to exhibit photoelectrochemical effects [86–88]. Although the self-assembly approach is useful to obtain an ordered array of semiconductor nanoparticles in the film, it does not provide robust coverages on the electrode surfaces. Since high coverage of semiconductor particles is an important parameter in electrochromic or photoelectrochemical devices, this technique has very limited applications.

8.3 Photochromic Effects

Reversible electrochromic and photochromic effects are observed when thin films made from metal oxide colloids such as WO_3, SnO_2 and TiO_2 are subjected to band-gap excitation [40, 46, 48, 49, 89–91]. A blue coloration quickly develops, as the electrons are stored within the nanoparticles when subjected to UV irradiation. This effect can also be induced by radiolysis [92] and sonolysis [93]. The aqueous electrons as well as reductive radicals are capable of injecting electrons into the semiconductor nanoparticles and produce the coloration effects. Similarly, sonochromic effect observed for WO_3 colloidal suspension has been attributed to the binding of $H^{\bullet}$ atoms followed by electron injection into trap sites [93]. Photosensitized blue coloration in TiO_2 particles has also been observed by exciting surface-bound $Ru(bpy)_3^{2+}$ molecules [94].

The changes in the absorption observed at a nanostructured WO_3 film following the UV photolysis are shown in Fig. 8.2. The film turns blue as we irradiate the WO_3 film with UV-light. The increase in the absorption at wavelengths greater than 500 nm with increasing irradiation time indicates that charges get trapped at the color centers to induce the photochromic effect.

The principle behind the photochromic effect observed in the metal oxide nanostructure following the band-gap excitation could be summarized as in Fig. 8.3.

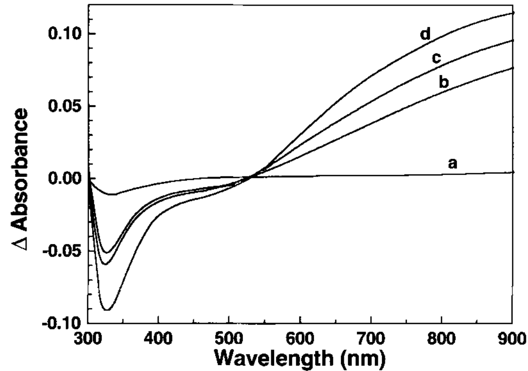

Fig. 8.2 Effect of band-gap excitation on the absorption of WO_3 particulate film cast on an OTE glass plate. Difference absorption spectra were recorded: (a) before photolysis, (b) 5, (c) 10, and (d) 30 s after UV-photolysis. The film was pre-annealed at a temperature of 423 K. (From Ref. [49]. Reprinted with permission from the American Chemical Society.)

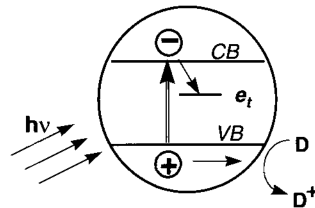

Fig. 8.3 Photoinduced charge separation and electron trapping processes leading to photochromic effect in metal oxide semiconductor nanocrystallites. *CB* and *VB* refer to conduction and valence band of the semiconductor, e_t refers to electron trap, and D refers to hole scavenger.

The band-gap excitation of WO_3 particulate film leads to charge separation followed by trapping of charge carriers (Eq. 1a):

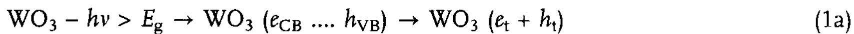

$$WO_3 - h\nu > E_g \rightarrow WO_3\ (e_{CB} \ldots h_{VB}) \rightarrow WO_3\ (e_t + h_t) \quad (1a)$$

$$WO_3\ (e_t + h_t) + D \rightarrow WO_3\ (e_t) + D^+ \quad (1b)$$

where e_{CB} and h_{VB} refer to free charge carriers in the conduction and valence bands, e_t and h_t represent trapped electrons and holes, and D is a hole scavenger respectively. In the presence of a sacrificial electron donor such as oxalic acid the photogenerated holes are quickly scavenged (Eq. 1b), thus reducing the possibility of charge recombination. Similar stabilization of trapped electrons have been observed for other metal oxide colloids such as TiO_2, ZnO and WO_3. These electrons trapped at the metal ion sites (e.g., Ti^{4+} in TiO_2 or W^{6+} in WO_3) are known to exhibit characteristic broad absorption in the red-IR region. XPS analysis of electrodeposited and vacuum-deposited WO_3 films has also confirmed the presence of mixed valent states in the colored film [79]. The photochromic effect observed with WO_3 particulate film was reversible. When the UV irradiation was stopped, the blue color slowly disappeared in air and the original color of the film was restored. The recovery in air was rather slow (10–20 min) since the reduction potential of O_2 is slightly more negative than the flat band potential of WO_3 ($E_{fb} \approx -0.2$ V relative to the NHE).

Spectroelectrochemical and microwave absorption experiments suggest that trapped electrons are the major species responsible for the blue coloration of the film [21, 49]. The biphotonic dependence of microwave conductivity indicated that the free carriers in the conduction band of the semiconductor can only be achieved by re-exciting the trapped charge carriers with a second photon. Since the trapped electrons have a long lifetime, it provides a convenient method to store electrons. Investigations of the trapping process by picosecond laser flash photolysis indicate that this trapping process occurs in a subnanosecond timescale [48]. The electron storage effects in such semiconductor nanostructures have potential applications not only in electrochromic devices, but also in building electronic devices such as microcapacitors. Such a concept has also been demonstrated recently by employing a WO_3 electrode as a counter electrode in a photochemical cell [95].

8.4 Electrochromic Effects

8.4.1 Nanostructured Metal Oxide Films

Efforts have been made in the past to investigate electrochemically induced chromic effects in WO_3 films [89, 96–99]. When deposited as thin films (amorphous or polycrystalline) on to a conducting glass substrate, these metal oxides are capable of undergoing color changes under applied potential and in the presence of alkali metal ions. Intercalation of metal ions becomes a limiting factor as the rate of transport of these ions become slower in thicker metal oxide films. This in turn controls the rate of coloration and recovery of the electrochromic effects. In addition the transport of ions in and out of the metal oxide films is intimately linked to lifetime issues in these devices, as cyclic intercalation leads to residual coloration and irreversible changes in film structure. Limited efforts have also been made to employ mixed TiO_2/WO_3 [100], WO_3/V_2O_5 [101], and WO_3/MoO_3 [102] systems for enhancing the efficiency of electrochromic effects. The beneficial aspect of these nanostructured semiconductor films in electrochromic devices is yet to be explored in a systematic way.

Fig. 8.4 shows the absorption changes in a nanostructured WO_3 film at different applied negative potentials. At positive potentials (0 V or higher), no change in the absorption is seen, but with increasing negative potentials an increase in the IR absorption is observed. Switching the electrode to positive bias can reverse the blue color observed in these films. At potentials more negative than –1.2 V the color changes to brown.

The onset potential at which the electrochromic effect is observed corresponds to the flat band potential of the corresponding semiconductor and is dependent on the pH of the medium. With increasing pH the onset of electrochromic effect was found to shift to more negative potentials [40, 103]. By monitoring the optical

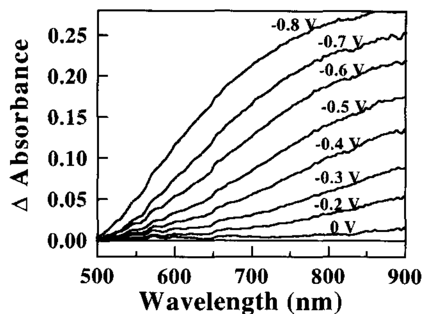

Fig. 8.4 Dependence of electrochromic effect of WO_3 particulate film on the charging potentials. (From Ref. [49]. Reprinted with permission from the American Chemical Society.)

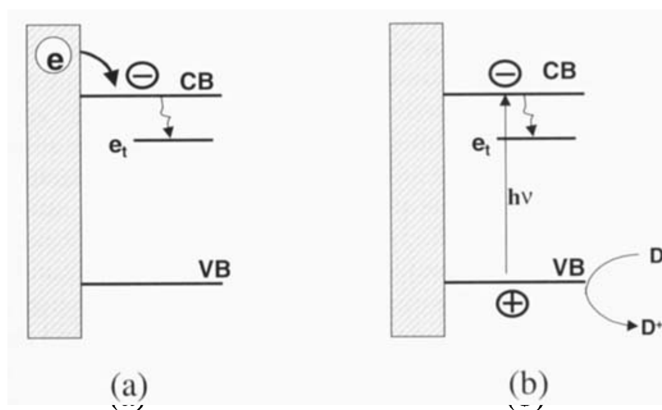

Fig. 8.5 (a) Electrochemically induced and (b) photoinduced charge separation and electron trapping processes leading to color changes in metal oxide semiconductor nanocrystallites. *CB* and *VB* refer to conduction and valence bands of the semiconductor, and e_t refers to surface traps and D refers to hole scavenger.

absorbance, Fitzmaurice and his coworkers [40, 103–106] have determined the flat band potentials of nanostructured films of TiO_2 and GaAs and the extinction coefficient of the trapped electrons. On the other hand ZnO [36], SnO_2 [18], and CdS [107] films exhibit bleaching at potentials more negative than the flat band potential.

Controversy still exists regarding the mechanism of coloration proposed to explain electrochromic effects in WO_3 films [89]. Some of these proposed mechanisms include formation of a blue colored oxide product [108], simultaneous injection of electrons and cations into interstitial sites in the WO_3 atomic lattice [109], intervalence transfer absorption [110], and polaron absorption [111]. Both intervalence transfer and polaron models attribute coloration to the tight localization of conduction band electrons to W^{5+} sites, although a recent electron resonance study has argued against such a strong localization [112]. Electrochromic efficiency has also been shown to increase with increasing oxygen deficiency [99]. As confirmed from the spectroelectrochemical study of TiO_2 particulate films [40, 103] the inherent semiconductor properties such as trapping of electrons at the

defect sites is responsible for the coloration effects (Fig. 8.5). In an earlier study we have considered both electrochemical and photoelectrochemical approaches to probe the mechanism of coloration in WO_3 colloids [48], and nanostructured films [49]. The net color change was found to be spectrally similar whether we employed direct band-gap excitation of WO_3 nanoparticles or subjected them to a negative electrochemical bias. The semiconducting behavior of these WO_3 films was also confirmed by carrying out photoelectrochemical experiments [21].

8.4.2 Nanostructured Oxide Films Modified with Dyes and Redox Chromophores

Oxide nanoparticles (e.g. SnO_2 or TiO_2) can be readily modified with dyes and electroactive molecules that have been functionalized with reactive groups such as carboxylic acid or phosphonate. These functional groups chemically bind to the oxide surface, thus creating a semiconductor-organic dye assembly. Similarly, one can use electrostatic interactions to bind the cationic or anionic dye molecules to the particle surface of SnO_2 or TiO_2. The schematic diagram presented in Fig. 8.6 illustrates the principle of surface modification of oxide nanoparticles.

The same approach can be extended to bind redox chromophores directly to a nanostructured semiconductor film and induce color changes under applied potentials (Fig. 8.7). The oxide nanoparticles in the film merely act as a high surface area support for anchoring these molecular assemblies and stabilize the redox species. As a result of such high coverage one can achieve 2–3 orders of magnitude enhancement in the color changes associated with the oxidation or reduction of an adsorbed molecular monolayer. For example, a phosphonate linkage has been used to bind viologen compounds to nanostructured TiO_2 films and construct electrochromic windows [113, 114]. Under an applied negative bias the viologens are reduced to develop a blue coloration. Long-term stability and high coloration efficiencies ($\sim 200\ cm^2\ C^{-1}$) have been reported in these studies.

Alternatively, one can bind a dye that absorbs in the visible and/or IR region to the nanostructured semiconductor films, but becomes colorless (or changes to another color) upon undergoing reduction (or oxidation) under the influence of an electrochemical bias. Feasibility of this concept has already been demonstrated in our laboratory by binding a thiazine dye to nanostructured SnO_2 film [115]. Re-

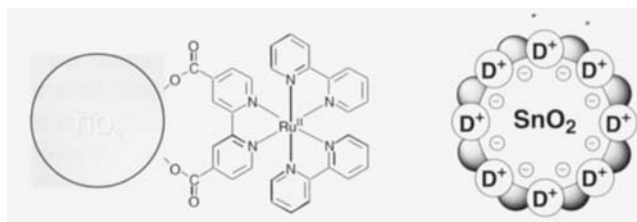

Fig. 8.6 Binding of redox chromophores to oxide nanoparticles via charge transfer and electrostatic interactions.

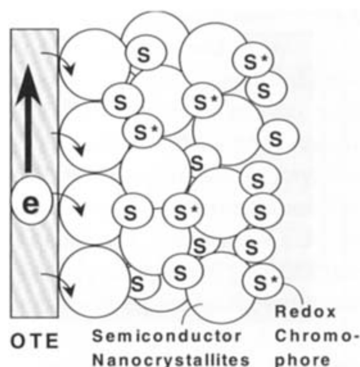

Fig. 8.7 Schematic diagram of nanostructured semiconductor–redox chromophore assembly for electrochromic applications.

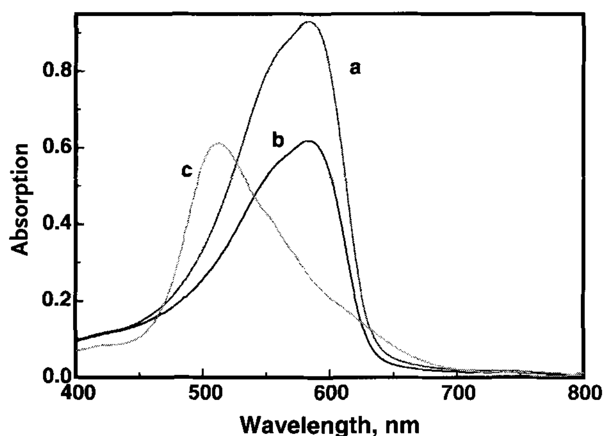

Fig. 8.8 Absorption spectra of dye-modified SnO_2 film. The absorption spectra of the dye in aqueous solution (a) before and (b) after immersing the OTE/SnO_2 film shows the decrease in dye concentration as it is adsorbed on the SnO_2 nanocrystallites (spectrum c). (From Ref. [116]. Reprinted with permission from the American Chemical Society.)

verse electrochromism obtained using such systems provides an alternative approach for electrochromic devices.

The technique of binding dye molecules to semiconductor nanostructures is especially convenient for extending the photoresponse of large-band-gap semiconductors and/or for making the nanostructured films electrochemically active [18, 28, 115]. Because of the high porosity large amounts of the sensitizing molecules (up to 0.1 M) can be incorporated in a nanocrystalline film of thickness of ca. 1 μm. Fig. 8.8 shows deposition of cresyl violet on nanocrystalline SnO_2 film by the adsorption technique.

Significant interaction between the adsorbed molecules often leads to the aggregation effects, thus broadening the absorption in the visible region. The deposition of monomeric and aggregate forms of chlorophyll and chlorophyllin on ZnO, TiO_2 and SnO_2 films have also been carried out [13, 20, 117].

8.4.2.1 From Colorless to Colored Films under the Application of an Electrochemical Bias

Viologen compounds are among the most suited organic molecules for achieving blue colored electrochromic windows under applied bias. They have also been shown to be useful for fabricating electrochromic optical diffraction gratings using lithography techniques [118]. The one-electron reduction product which exhibits an intense blue color ($\lambda_{max} \approx 600$ nm) can be formed when an electrochemical bias of ca. –0.5 V is applied. The early attempt to bind viologen to a semiconductor surface was made by Bard and coworkers [119]. The binding of viologen derivatives to nanostructured TiO_2 film provided a new approach to develop electrochromic display devices [113, 114, 120]. This approach is very useful for utilizing semiconducting oxides such as SnO_2 or ZnO that usually do not exhibit electrochromic effect.

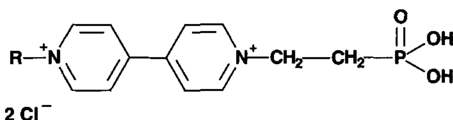

Phosphonate derivative of viologen compound (from Ref. [113])

Nanocrystalline TiO_2 thin films on conductive glass electrodes have been modified with monolayers of different electrochromic moieties (mono-, di- and trimeric *N,N'*-dialkyl- or diphenyl-4,4'-bipyridinium salts) functionalized with TiO_2 anchoring groups such as benzoate, salicylate, phosphonate [121, 122]. The type of anchoring group and the viologen moiety influenced the electrochemically active coloring centers on TiO_2. The transmittance changes from 79 to 11% in less than 1 s, which in turn indicates a fast response time of these electrodes [122]. An attempt has also been made to prepare electrochromic material by electropolymerizing *N,N'*-bis[*p*-(trimethoxysilyl)benzyl]-4,4'-bipyridinium dichloride ($BPQ^{2+} \cdot 2Cl^-$) on top of a reductively conducting film of tungsten trioxide [123]. The resulting composite film responds to a potential step from 0.9 to –0.65 V by turning from colorless to blue in two steps: the absorbance due to one-electron reduction of each monomer unit in poly(BPQ^{2+}) increases quickly (in <4 s), and is followed by a slower development of the absorbance due to the WO_3 reduction (>1 min). Metal hexacyanoferrates constitutes another class of redox species that can be coupled with semiconductor nanostructure for designing electrochromic hybrid assemblies. For example TiO_2-metal hexacyanoferrate has recently been shown to possess excellent electrochromic properties [124].

8.4.2.2 From a Colored to Colorless Window using Reverse Bias

The metal oxide semiconductor films modified with organic dyes are capable of absorbing light at selective wavelengths of the visible-IR spectrum. One can make use of this phenomenon beneficially to design electrochromic windows that display intense coloration under normal use, but colorless upon application of an electrochemical bias. Examples of these substrates include thiazine and oxazine dyes that absorb strongly in the 500–700 nm region [115]. These dyes are ther-

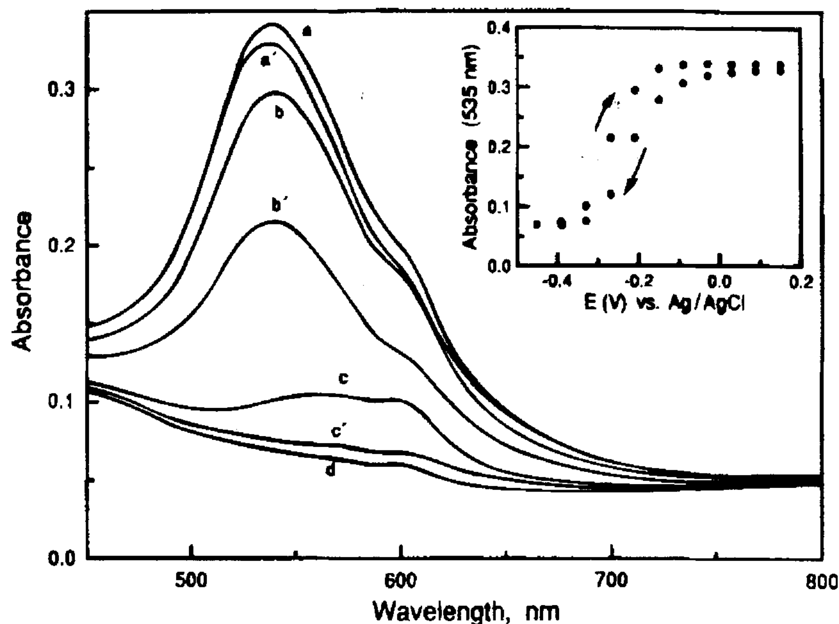

Fig. 8.9 Absorption changes of a thionine-modified SnO_2 film at applied potentials of (a,a') 0.09 V; (b,b') −0.21 V; (c,c') −0.33 V and (d) −0.45 V relative to the SCE. Insert shows the reversibility of maximum absorption response during forward and reverse bias. (From Ref. [115]. Reprinted with permission from the Electrochemical Society.)

mally and photochemically stable. They readily bind to the nanostructured semiconductor films and exhibit reversible cyclic voltammogram when cycled between 0 and 0.8 V relative to the SCE (Saturated Calomel Electrode). Under applied negative potentials these dyes undergo two-electron reduction to yield a colorless *leuco* product. Spectroelectrochemical studies carried out with a thionine-modified SnO_2 film show complete bleach at −0.5 V (Fig. 8.9). A total recovery of the color can be achieved by simply reversing the applied bias to 0 V relative to the SCE. The feasibility of modulating the color changes using an applied bias shows the importance of semiconductor nanostructure-molecular assemblies in electrochromic applications.

8.4.3 Surface-Bound Fluoroprobes

Engineering of the nanocluster surfaces with photoactive molecules have potential applications in designing electrochromic devices of nanometric dimension. Both semiconductor and metal nanoparticles are potential candidates for producing such photoactive hybrid nanoparticles. For example, the ability of the gold surface to bind with specific functional groups (-NH_2, -SH, or -SCN) has made it suitable for optoelectronic applications such as fluorescence patterning. Researchers have

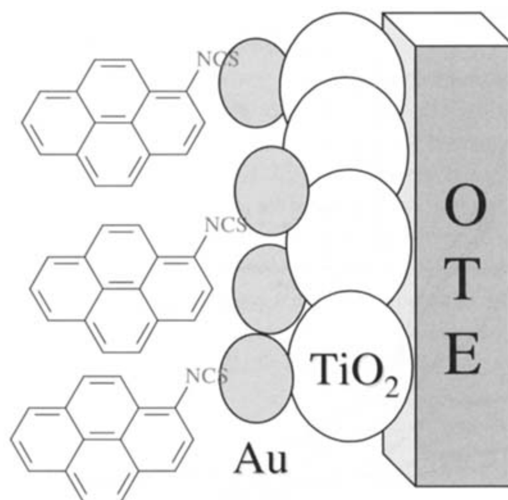

Fig. 8.10 Binding of a fluoroprobe to TiO_2-Au film.

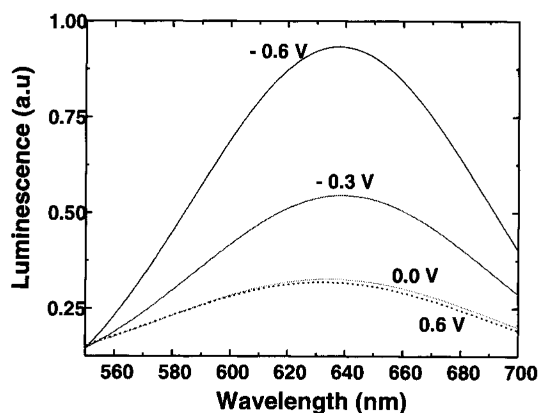

Fig. 8.11 Emission spectra of $OTE/SnO_2/Ru(bpy)_3^{2+}$ recorded at different applied potentials. Excitation was at 460 nm. The spectra were recorded in a front face configuration and are corrected for instrument response (CE: Pt; RE: Ag/AgCl; Electrolyte: 0.1 M tetrabutylammonium perchlorate in acetonitrile) (From Ref. [131]. Reprinted with permission from the American Chemical Society.)

often used functional groups such as thiols, amines, or silanes to attach electroactive or photoactive molecules to the gold surface [125–129]. Recently we have succeeded in organizing pyrene chromophores around gold nanoparticles through surface binding of an amine moiety, thus producing highly fluorescent hybrid nanoparticles [130]. Surface binding of the amine group to the gold surface suppresses the intramolecular photoinduced electron transfer process from the lone

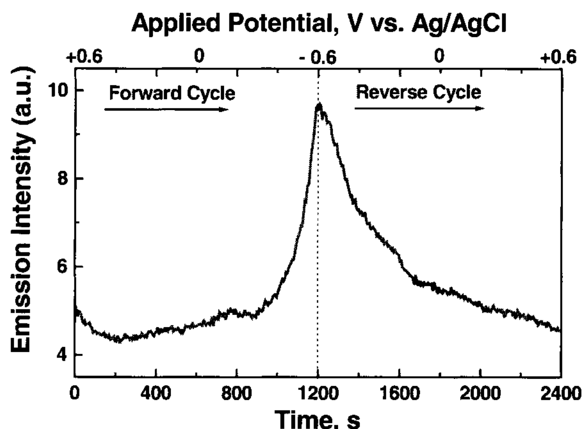

Fig. 8.12 Dependence of relative emission yield of OTE/SnO_2/Ru(II) on the applied potential. The emission was monitored at 640 nm during the electrochemical cycle (scan rate 1 mV s^{-1}; CE: Pt; RE: Ag/AgCl; electrolyte: 0.1 M tetrabutylammonium perchlorate in acetonitrile; excitation at 460 nm) (From Ref. [131]. Reprinted with permission from the American Chemical Society.)

pair of the amine to the pyrene chromophore and increases the efficiency of radiative conversion of the singlet excited state pyrene. Electroluminescent windows can thus be developed by first casting thin films of semiconductor nanoclusters and noble metal nanoclusters and then modifying the surface with a fluoroprobe (Fig. 8.10). The electrochemical bias can then be used to modulate the fluorescence emission.

Nanostructured SnO_2 films modified with $Ru(bpy)_3^{2+}$ [131] or chlorophyll *a* [132] molecules have been shown to exhibit fluorescence properties that are dependent on the applied electrochemical bias. $Ru(bpy)_3^{2+}$ complex has a strong emission in the red region with a maximum around 630 nm. The emission behavior of Ru(II)* is dependent on the electronic properties of the support material. The molecules are fluorescent on inert oxides such as SiO_2 and Al_2O_3, but are readily quenched on semiconductor (TiO_2, SnO_2) surfaces [94, 133, 134]. Nearly 95% quenching observed on TiO_2 or SnO_2 surface is the result of an efficient charge injection from excited $Ru(bpy)_3^{2+}$ into the conduction band of the semiconductor.

The emission spectra of excited $Ru(bpy)_3^{2+}$ bound to nanostructured SnO_2 film were recorded at various bias potentials (Fig. 8.11) [131]. The emission spectra recorded at 0 V and +0.2 V showed very weak emission. However, a dramatic increase in the emission yield is seen with increasing negative bias without any changes in the emission maximum. At a bias potential more negative than –0.6 V most of the emission of excited Ru(II) can be restored. The emission-quenching phenomenon could be seen again by reversing the applied potential to positive bias. The emission at 640 nm, which was monitored continuously during an electrochemical scan, is shown in Fig. 8.12.

The dependence of emission yield on the applied potential demonstrates the possibility of modulating the sensitized charge injection process by means of an external electrochemical bias. It is evident from Figs. 8.11 and 8.12 that the deactivation of the excited state on nanostructured semiconductor film is controlled by the applied potential. The energy difference, ΔE, between the pseudo-Fermi level of SnO_2 and the oxidation potential of the excited sensitizer acts as a driving force for the heterogeneous electron transfer. Since the pseudo-Fermi level of the SnO_2 nanocrystalline film can be varied by an externally applied electrochemical bias it is possible to alter ΔE and hence the kinetics of heterogeneous electron transfer. With increasing ΔE as in the case of applied positive bias, one sees efficient quenching of the sensitizer by the semiconductor. The sharp increase observed in the relative emission yield at negative applied potentials shows (Fig. 8.12) the suppression of the electron transfer quenching and dominance of radiative decay for deactivating the excited sensitizer.

The example discussed here shows how one can design a semiconductor nanocluster-dye molecule assembly for electroluminescent application. This new area of designing inorganic-organic hybrid assemblies for electrochromic and electroluminescent applications will bring us many new challenges to pursue in the future.

8.5 Concluding Remarks

The salient features of the nanostructured semiconductor films described here show that these semiconductor films possess many unique properties. The chemical approach of designing thin semiconductor films is a simple technique with many possible applications in the microelectronics and opto-electronics devices as well. The method of developing inorganic-organic hybrid systems has an added advantage that the mass transport and intercalation of metal ions no longer becomes a limiting factor. This in turn enhances the switching time of electrochromic devices. Another advantage of such a system is the tuning ability of the electrochromic device. By choosing the appropriate molecular assemblies, one can design a wide array of colored devices in the visible-infrared region. By carefully assembling semiconductor nanoparticle-molecular hybrids, it should be possible to design wavelength-selective and fast switching display devices. The modulation of luminescent displays using an electrochemical bias is another area that should draw significant attention in future.

To date, applications to architectural glazes as well as the fast switching displays have driven the research and development of electrochromic technologies worldwide. The switchable mirror employed in automobiles is just an example of rising success of electrochromic devices in commercial applications [135]. Replacement of liquid crystal displays with fast switchable electrochromic systems remains to be the challenge for the future. Molecular level engineering of electrochromic systems will play an important role in the development of such systems.

Acknowledgment

The work described herein was supported by the Office of Basic Energy Sciences of the US Department of Energy. This is contribution No. 4266 from the Notre Dame Radiation Laboratory.

References

1 P. V. Kamat, D. Meisel, *Studies in Surface Science and Catalysis;* Elsevier Science, Amsterdam, **1997**, p. 474.
2 P. Alivisatos, *J. Phys. Chem. 100,* **1996**, 13226.
3 A. Henglein, *J. Phys. Chem. 97,* **1993**, 5457.
4 M. L. Steigerwald, L. E. Brus, *Acc. Chem. Res. 23,* **1990**, 183.
5 S. Link, M. A. El-Sayed, *J. Phys. Chem. B 103,* **1999**, 8410.
6 G. Hodes, *Isr. J. Chem. 33,* **1993**, 95.
7 G. J. Meyer, P. C. Searson, *Interface* **1993**, 23.
8 P. V. Kamat, *Chemtech. June* **1995**, 22.
9 A. Hagfeldt, M. Grätzel, *Chem. Rev.* 95, **1995**, 49.
10 P. V. Kamat, in: J. Meyer (Ed.): *Molecular level artificial photosynthetic materials. Progress in Inorganic Chemistry Series, Vol. 44,* John Wiley and Sons, New York **1997**, p. 273.
11 J. H. Fendler, *Chem. Rev. 87,* **1987**, 877.
12 G. Hodes, I. D. J. Howell, L. M. Peter, *J. Electrochem. Soc. 139,* **1992**, 3136.
13 S. Hotchandani, P. V. Kamat, *Chem. Phys. Lett. 191,* **1992**, 320.
14 S. Hotchandani, P. V. Kamat, *J. Electrochem. Soc. 139,* **1992**, 1630.
15 S. Hotchandani, P. V. Kamat, *J. Phys. Chem. 96,* **1992**, 6834.
16 N. Uekawa, T. Suzuki, S. Ozeki, K. Kaneko, *Langmuir 8,* **1992**, 1.
17 D. Liu, P. V. Kamat, *J. Electroanal. Chem. Interfacial Electrochem. 347,* **1993**, 451.
18 I. Bedja, S. Hotchandani, P. V. Kamat, *J. Phys. Chem. 98,* **1994**, 4133.
19 R. Vogel, P. Hoyer, H. Weller, *J. Phys. Chem. 98,* **1994**, 3183.
20 I. Bedja, S. Hotchandani, R. Carpentier, R. W. Fessenden, P. V. Kamat, *J. Appl. Phys. 75,* **1994**, 5444.
21 I. Bedja, S. Hotchandani, R. Carpentier, K. Vinodgopal, P. V. Kamat, *Thin Solid Films 247,* **1994**, 195.
22 K. Vinodgopal, U. Stafford, K. A. Gray, P. V. Kamat, *J. Phys. Chem. 98,* **1994**, 6797.
23 U. Bjorksten, J. Moser, M. Grätzel, *Chem. Mater. 6,* **1994**, 858.
24 A. Hagfeldt, S. E. Lindquist, M. Grätzel, *Sol. Energy Mater. Sol. Cells 32,* **1994**, 245.
25 S. Hotchandani, S. Das, K. George Thomas, M. V. George, P. V. Kamat, *Res. Chem. Intermed. 20,* **1994**, 927.
26 D. Liu, P. V. Kamat, *J. Phys. Chem. 97,* **1993**, 10769.
27 B. O'Regan, M. Grätzel, *Nature (London) 353,* **1991**, 737.
28 M. K. Nazeeruddin, A. Kay, I. Rodicio, B. R. Humphry, E. Mueller, P. Liska, N. Vlachopoulos, M. Grätzel, *J. Am. Chem. Soc. 115,* **1993**, 6382.
29 A. C. Khazraji, S. Hotchandani, S. Das, P. V. Kamat, *J. Phys. Chem. B 103,* **1999**, 4693.
30 R. Vogel, K. Pohl, H. Weller, *Chem. Phys. Lett. 174,* **1990**, 241.
31 N. Chandrasekharan, P. V. Kamat, *J. Phys. Chem. B 104,* **2000**, in press.
32 C. Liu, H. Pan, M. A. Fox, A. J. Bard, *Science (Washington, D.C.) 261,* **1993**, 897.
33 P. Hoyer, R. Eichberger, H. Weller, *Ber. Bunsenges. Phys. Chem. 97,* **1993**, 630.
34 H. Hada, Y. Yonezawa, H. Inaba, *Ber. Bunsenges. Phys. Chem. 85,* **1981**, 425.
35 S. Sakohara, L. D. Tickanen, M. A. Anderson, *J. Phys. Chem. 96,* **1992**, 11086.
36 G. Redmond, A. O'Keeffe, C. Burgess, C. MacHale, D. Fitzmaurice, *J. Phys. Chem. 97,* **1993**, 11081.
37 G. Redmond, D. Fitzmaurice, M. Grätzel, *Chem. Mater. 6,* **1994**, 686.
38 Y. Harima, Y. D. Wang, K. Matsumoto, K. Yamashita, *J. Chem. Soc., Chem. Commun.* **1994**, 2553.
39 H. Yoshiki, H. K. A. Fujishima, *J. Electrochem. Soc. 142,* **1995**, 428.

40 B. O'Regan, M. Grätzel, D. Fitzmaurice, *Chem. Phys. Lett. 183*, **1991**, 89.
41 L. Kavan, T. Stoto, M. Grätzel, D. J. Fitzmaurice, V. Shklover, *J. Phys. Chem. 97*, **1993**, 9493.
42 D. V. Paranjape, M. Sastry, P. Ganguly, *Appl. Phys. Lett. 63*, **1993**, 18.
43 X. Marguerettaz, D. Fitzmaurice, *J. Am. Chem. Soc. 116*, **1994**, 5017.
44 D. D. Dunuwila, C. D. Gagliardi, K. A. Berglund, *Mater. Lett. 6*, **1994**, 1556.
45 N. A. Kotov, F. C. Meldrum, J. H. Fendler, *J. Phys. Chem. 98*, **1994**, 8827.
46 A. Hagfeldt, N. Vlachopoulos, M. Grätzel, *J. Electrochem. Soc. 141*, **1994**, L82.
47 D. H. Kim, M. A. Anderson, *Environ. Sci. Technol. 28*, **1994**, 479.
48 I. Bedja, S. Hotchandani, P. V. Kamat, *J. Phys. Chem. 97*, **1993**, 11064.
49 S. Hotchandani, I. Bedja, R. W. Fessenden, P. V. Kamat, *Langmuir 10*, **1994**, 17.
50 A. Zaban, T. Aruna, S. Tirosh, B. A. Gregg, Y. Mastai, *J. Phys. Chem. B 104*, **2000**, 4130.
51 K. Vinodgopal, S. Hotchandani, P. V. Kamat, *J. Phys. Chem. 97*, **1993**, 9040.
52 K. Vinodgopal, I. Bedja, P. V. Kamat, *Chem. Mater. 8*, **1996**, 2180.
53 Y. Wang, in: P. V. Kamat, D. Meisel (Eds.): *Semiconductor Nanoclusters – Physical, Chemical and Catalytic Aspects*, Elsevier Science, Amsterdam **1997**, p. 277.
54 M. Krishnan, J. R. White, M. A. Fox, A. J. Bard, *J. Am. Chem. Soc. 105*, **1983**, 7002.
55 A. W. H. Mau, C. B. Huang, N. Kakuta, A. J. Bard, A. Campion, M. A. Fox, J. M. White, S. E. Webber, *J. Am. Chem. Soc. 106*, **1984**, 6537.
56 J. P. Kuczynski, B. H. Milosavljevic, J. K. Thomas, *J. Phys. Chem. 88*, **1984**, 980.
57 Y. Nosaka, K. Yamaguchi, H. Yokoyama, H. Miyama, *Photoresponsive Materials, MRS Int. Meet. Adv. Mater.*, Formation of ultrafine semiconductor particles and their photoresponsive characteristics in polymer film, **1989**, pp. 155.
58 F. R. F. Fan, H. Y. Liu, A. J. Bard, *J. Phys. Chem. 89*, **1985**, 4418.
59 K. Honda, A. Kuwano, K. Chiba, A. Ishikawa, H. Miyama, *Chem. Lett.* **1988**, 195.
60 M. Kaneko, T. Okada, S. Teratani, K. Taya, *Electrochim. Acta 32*, **1987**, 1405.
61 D. Gningue, G. Horowitz, J. Roncali, F. Garnier, *J. Electroanal. Chem. Interfacial Electrochem. 269*, **1989**, 337.
62 R. Tassoni, R. R. Schrock, *Chem. Mater. 6*, **1994**, 744.
63 O. V. Salata, P. J. Dobson, P. J. Hull, J. L. Hutchison, *Thin Solid Films 251*, **1994**, 81.
64 K. R. Gopidas, P. V. Kamat, *Mater. Lett. 9*, **1990**, 372.
65 M. Gao, Y. Yang, B. Yang, F. Bian, J. Shen, *J. Chem. Soc., Chem. Commun.* **1994**, 2779.
66 K. C. Yi, J. H. Fendler, *Langmuir 6*, **1990**, 1519.
67 N. J. Geddes, R. S. Urquhart, D. N. Furlong, C. R. Lawrence, K. Tanaka, Y. Okahata, *J. Phys. Chem. 97*, **1993**, 13767.
68 R. Rafaeloff, Y. M. Tricot, F. Nome, J. H. Fendler, *J. Phys. Chem. 89*, **1985**, 533.
69 I. Moriguchi, H. Maeda, Y. Teraoka, S. Kagawa, *J. Am. Chem. Soc.* **1995**, 1139–1140.
70 L. Spanhel, M. A. Anderson, *J. Am. Chem. Soc. 112*, **1990**, 2278.
71 Q. Xu, M. A. Anderson, *J. Mater. Res. 6*, **1991**, 1073.
72 S. Tunesi, M. Anderson, *J. Phys. Chem. 95*, **1991**, 3399.
73 J. Sabate, M. A. Anderson, M. A. Aguado, J. Gimenez, M. S. Cervera, C. G. J. Hill, *J. Mol. Catal. 71*, **1992**, 57.
74 G. Dagan, M. Tomkiewicz, *J. Phys. Chem. 97*, **1993**, 12651.
75 M. N. Kamalasanan, N. D. Kumar, S. Chandra, *J. Appl. Phys. 74*, **1993**, 679.
76 T. Jiang, A. L. Lough, G. A. Ozin, D. Young, *Chem. Mater. 7*, **1995**, 245.
77 Neeraj, C. N. R. Rao, *J. Mater. Chem. 8*, **1998**, 279.
78 K. Rajeshwar, R. O. Lezna, N. R. de Tacconi, *Anal. Chem. 64*, **1992**, 429.
79 J. N. Yao, P. Chen, A. Fujishima, *J. Electroanal. Chem. 406*, **1996**, 223.
80 Y. Golan, L. Margulis, G. Hodes, I. Rubinstein, J. L. Hutchison, *Surface Science 311*, **1994**, L633.

81 T. Yoshida, H. Minoura, *Adv. Mater.* *12,* **2000**, 1219.

82 T. Yoshida, K. Terada, D. Schlettwein, T. Oekermann, T. Sugiura, H. Minoura, *Adv. Mater.* *12,* **2000**, 1214.

83 R. Rizza, D. Fitzmaurice, S. Hearne, G. Hughs, G. Spoto, E. Ciliberto, H. Kerp, R. Schropp, *Chem. Mater.* *9,* **1999**, 2969.

84 J. H. Fendler, *Chem. Mater.* *8,* **1996**, 1616.

85 J. H. Fendler, in: P. V. Kamat, D. Meisel (Eds): *Semiconductor Nanoclusters – Physical, Chemical and Catalytic Aspects.*, Elsevier Science, Amsterdam **1997**, p. 261.

86 T. Nakanishi, B. Ohtani, K. Uosaki, *J. Phys. Chem. B* *102,* **1998**, 1571.

87 V. L. Colvin, A. N. Goldstein, A. P. Alivisatos, *J. Am. Chem. Soc.* *114,* **1992**, 5221.

88 S. Ogawa, K. Hu, F.-R. F. Fan, A. J. Bard, *J. Phys. Chem. B* *101,* **1997**, 5707.

89 C. M. Lampert, *Solar Energy Mater.* *11,* **1984**, 1.

90 J. N. Yao, K. Hashimoto, A. Fujishima, *Nature* *355,* **1992**, 624.

91 T. Torimoto, R. J. Fox III, M. A. Fox, *J. Electrochem. Soc.* *143,* **1996**, 3712.

92 M. T. Nenadovic, T. Rajh, O. I. Micic, A. J. Nozik, *J. Phys. Chem.* *88,* **1984**, 5827.

93 P. V. Kamat, K. Vinodgopal, *Langmuir* *12,* **1996**, 5739.

94 K. Vinodgopal, X. Hua, R. L. Dahlgren, A. G. Lappin, L. K. Patterson, P. V. Kamat, *J. Phys. Chem.* *99,* **1995**, 10883.

95 C. Bechinger, S. Ferrere, A. Zaban, J. Sprague, B. A. Gregg, *Nature* *383,* **1996**, 608.

96 T. Oi, *Ann. Rev. Mater. Sci.* *16,* **1986**, 185.

97 C. G. Granqvist, *Solar Energy Mater. Solar Cells* *60,* **2000**, 1993.

98 C. G. Granqvist, *Electrochim. Acta* *44,* **1999**, 3005.

99 S. H. Lee, H. Cheong, M. C. E. Tracy, A. Mascarenhas, A. W. Czanderna, S. K. Deb, *Appl. Phys. Lett.* *75,* **1999**, 1541.

100 S. Hashimoto, H. Matsuoka, *J. Electrochem. Soc.* *138,* **1991**, 2403.

101 N. Ozer, C. M. Lampert, *Thin Solid Films* *349,* **1999**, 205.

102 S. Papaefthimiou, G. Leftheriotis, P. Yianoulis, *Thin Solid Films* *344,* **1999**, 183.

103 B. O'Regan, M. Grätzel, D. Fitzmaurice, *J. Phys. Chem.* *95,* **1991**, 10525.

104 G. Redmond, D. Fitzmaurice, M. Grätzel, *J. Phys. Chem.* *97,* **1993**, 6951.

105 G. Redmond, D. Fitzmaurice, *J. Phys. Chem.* *97,* **1993**, 1426.

106 L. Butler, G. Redmond, D. Fitzmaurice, *J. Phys. Chem.* *97,* **1993**, 10750.

107 C. Liu, A. J. Bard, *J. Phys. Chem.* *93,* **1989**, 3232.

108 A. Howe, S. Sheffeld, P. Childs, M. Shilton, *Thin Solid Films* *67,* **1980**, 365.

109 R. Hurditch, *Electron Lett.* *11,* **1975**, 142.

110 R. Faughnan, R. S. Crandall, P. M. Heyman, *RCA Rev.* *11,* **1975**, 4201.

111 O. F. Schirmer, K. W. Blazey, W. Berlinger, *Phys. Rev.* *11,* **1975**, 4201.

112 J. H. Pfifer, E. K. Sihel, *J. Electron. Mater.* *9,* **1980**, 129.

113 R. Cinnsealach, G. Boschloo, S. N. Rao, D. Fitzmaurice, *Sol. Energy Mater. Sol. Cells* *57,* **1999**, 107.

114 R. Cinnsealach, G. Boschloo, S. N. Rao, D. Fitzmaurice, *Sol. Energy Mater. Sol. Cells* *55,* **1998**, 215.

115 D. Liu, P. V. Kamat, *J. Electrochem. Soc.* *142,* **1995**, 835.

116 D. Liu, R. W. Fessenden, G. L. Hug, P. V. Kamat, *J. Phys. Chem. B* *101,* **1997**, 2583.

117 A. Kay, M. Grätzel, *J. Phys. Chem.* *97,* **1993**, 6272.

118 K. S. Schanze, T. S. Bergstedt, H. B. T., C. S. P. Cavalaheiro, *Langmuir* *16,* **2000**, 795.

119 B. Reichman, F. R. F. Fan, A. J. Bard, *J. Electrochem. Soc.* *127,* **1980**, 333.

120 M. Felderhoff, S. Heinen, N. Molisho, S. Webersinn, L. Walder, *Helv. Chim. Acta* *83,* **2000**, 181.

121 P. Bonhote, E. Gogniat, F. Campus, L. Walder, M. Grätzel, *Displays* *20,* **1999**, 137.

122 F. Campus, P. Bonhote, M. Grätzel, S. Heinen, L. Walder, *Solar Energy Mater. and Solar Cells* *56,* **1996**, 281.

123 N. Leventis, Y. C. Chung, *J. Mater. Chem.* *3,* **1993**, 833.

124 N. R. DE TACCONI, K. RAJESHWAR, R. O. LEZNA, *Electrochim. Acta 45*, **2000**, 3403.

125 A. C. TEMPLETON, D. E. CLIFFEL, R. W. MURRAY, *J. Am. Chem. Soc. 121*, **1999**, 7081.

126 D. FITZMAURICE, S. N. RAO, J. A. PREECE, J. F. STODDART, S. WENGER, N. ZACCHERONI, *Angew. Chem. Int. Ed. Engl. 38*, **1999**, 1147.

127 W. HAN, S. LI, S. M. LINDSAY, D. GUST, T. A. MOORE, A. L. MOORE, *Langmuir 12*, **1996**, 5742.

128 N. R. JANA, T. PAL, T. K. SAU, *Rad. Phys. Chem. 49*, **1997**, 127.

129 O. V. MAKAROVA, A. E. OSTAFIN, H. MIYOSHI, J. R. NORRIS, D. MEISEL, *J. Phys. Chem. B 103*, **1999**, 9080.

130 K. GEORGE THOMAS, P. V. KAMAT, *J. Am. Chem. Soc. 122*, **2000**, 2655.

131 P. V. KAMAT, I. BEDJA, S. HOTCHANDANI, L. K. PATTERSON, *J. Phys. Chem. 100*, **1996**, 4900.

132 I. BEDJA, P. V. KAMAT, S. HOTCHANDANI, *J. Appl. Phys. 80*, **1996**, 4637.

133 I. BEDJA, S. HOTCHANDANI, P. V. KAMAT, *J. Electroanal. Chem. 401*, **1996**, 237.

134 R. ARGAZZI, C. A. BIGNOZZI, T. A. HEIMER, F. N. CASTELLANO, G. J. MEYER, *Inorg. Chem. 33*, **1994**, 5741.

135 D. K. BENSON, H. M. BRANZ, *Sol. Energy Mater. Solar Cells 39*, **1995**, 203.

Electrochemistry of Nanomaterials
by *Gary Hodes (Ed.)*
© WILEY-VCH Verlag GmbH, 2001

9
Electron Transfer and Charge Storage in Ultrathin Films Layer-by-layer Self-assembled from Polyelectrolytes, Nanoparticles, and Nanoplatelets

Thierry P. Cassagneau and *Janos H. Fendler*

9.1
Introduction

9.1.1
Importance of Electron Transfer and Charge Storage

Electron transfer and charge storage are vital to daily life. We owe our very existence to photosynthetic and biochemical electron transfer events and could not function well without the myriad of electronic devices based on transistors which control and amplify the current flow. Transistors are, of course, the basic subunits of the personal computer; and with the progressive decrease of the size of the transistor the computer has become more and more powerful. Indeed, the prediction of Gordon Moore that the number of transistors on a chip would double every two years (Moore's Law) has so far been realized. Intel's Pentium III chip contains over 9.5 million transistors with a minimum feature size of 180 nm. The Semiconductor Industries Association has published a road map for future developments which predicts that in 2010 over 40 billion devices will be integrated with feature sizes in the ranges of 50 nm [1]. The exponential increase of the cost of fabrication facilities is an important consequence of this progress. It is now recognized that the cost of manufacturing of computer chips by current technology will increase exponentially with decreasing size to the point that fabrication by alternative technologies becomes a must. Chemical self-assembly offers a viable alternative for device fabrication. Self-assembly also offers a potential approach for increasing the charge storage densities of batteries, employed in portable computers, camcorders, mobile phones and related consumer electronic appliances.

9.1.2
Principles of the Layer-by-layer Self-assembly

Self-assembly of alternating layers of oppositely charged polyelectrolytes and nanoparticles (or nanoplatelets) is deceptively simple (see Fig. 9.1). A well cleaned substrate is immersed into a dilute aqueous solution of a cationic polyelectrolyte, for a time optimized for adsorption of a monolayer (ca. 2 nm thick), rinsed and dried.

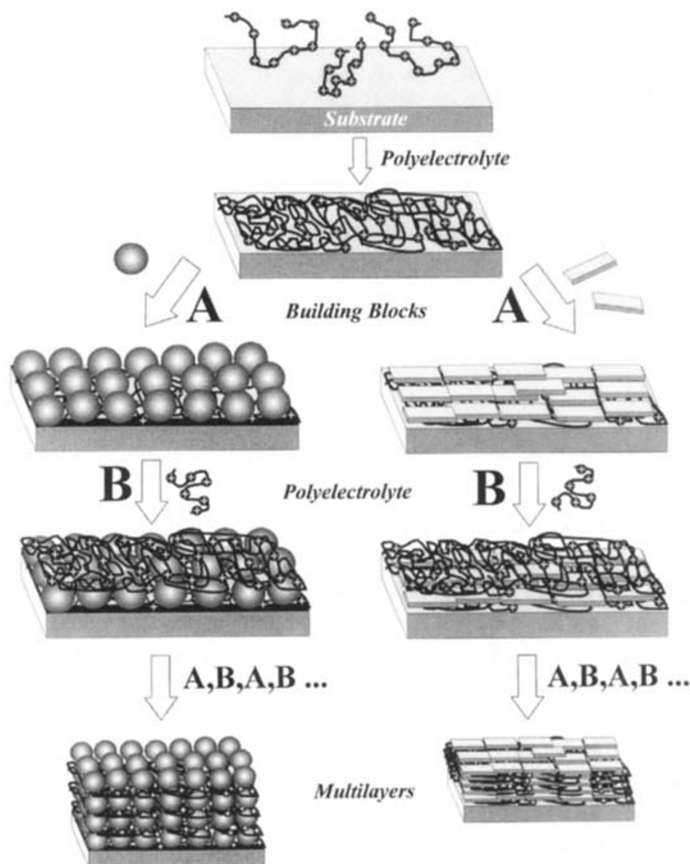

Fig. 9.1 Schematic representation of the principles of electrostatic layer-by-layer self-assembly.

The next step is the immersion of the polyelectrolyte monolayer-covered substrate into a dilute dispersion of negatively charged nanoparticles (or nanoplatelets or any other species with appropriate sizes and charge distributions!), also for a time optimized for adsorption of a monoparticulate layer, rinsing and drying. These operations complete the self-assembly of a polyelectrolyte monolayer and monoparticulate layer of nanoparticle (or nanoplatelet or any other species) sandwich unit on to the primed substrate. Subsequent sandwich units are self-assembled analogously.

Self-assembly is governed by a delicate balance between adsorption and desorption equilibria. In the self-assembly of nanoparticles, for example, the efficient adsorption of one (and only one) monoparticulate layer of nanoparticles on to the oppositely charged substrate surface is the objective of the immersion step. Desorption of nanoparticles forming a second and additional layers (and preventing the desorption of the first added layer) is the purpose of the rinsing process. The

optimization of the self-assembly in terms of maximizing the adsorption of nanoparticles from their dispersions and minimizing their desorption on rinsing requires the judicious selection of stabilizer(s) and the careful control of the kinetics of the process.

Forces between nanoparticles (or nanoplatelets) and binder nano-layers (polyions or dithiols, for example) govern the spontaneous layer-by-layer self-assembly of ultrathin films. These forces are primarily electrostatic and covalent (for self-assembled monolayers, SAMs, of dithiol derivatives on to metallic surfaces) in nature, but they can also involve hydrogen bonding, π-π interactions, van der Waals attractions, hydrophobic and epitaxial or other types of interactions. It is important to recognize that polyionic binders must have *displaceable* counterions in order to electrostatically bind them to the oppositely charged surface. The use of dithiols is only relevant with building blocks which incorporate accessible metal atoms, M (Au and Ag nanoparticles, for example), or semiconducting nanoparticles (MS and MSe, for example where M=Cd, Zn, Pb) in which covalent M-S bonds can be formed. The properties of the self-assembled multilayers depend primarily on the choice of the building blocks used, their rational organization and integration along the axis perpendicular to the substrate.

Sequential adsorption of oppositely charged colloids was reported in a seminal paper in 1966 [2]. Self-assembly was subsequently "rediscovered" and extended to the preparations of multilayers of polycations and phosphonate anions [3], as well as to the layering of polyelectrolytes [4, 5]. Construction of electrodes coated by polyelectrolytes, clays and other materials often involved self-assembly [6], albeit the method had not been called as such. Self-assembly are now routinely employed for the fabrication of ultrathin films from charged nanoparticles (metallic, semiconducting, magnetic, ferroelectric, insulating, for example) nanoplatelets, (clays or graphite platelets, for example), proteins, pigments, and other supramolecular species [7–9]. That any of these species in any order can be layer-by-layer adsorbed is the greatest advantage of self-assembly. The oppositely charged species are held together by strong ionic bonds and form long lasting, uniform and stable films which are often impervious to solvents. No special film balance is required for the self-assembly; indeed the method has been referred to as a "molecular beaker epitaxy" [10]. Furthermore, self-assembly is economical (dilute solutions and dispersions are used and the materials can be recovered) and readily amenable to scaling-up for the fabrication of large area defect-free devices on virtually any kind and shape of surfaces.

9.1.3
Scope of the Review

Self-assembly is defined as the spontaneous liquid-phase adsorption of materials on to a surface. This definition includes the formation of self-assembled monolayer (SAMs) on coinage metals (Au and Au, for example) when immersed into solutions containing thiols or dithiols. SAMs have found a variety of applications including soft lithography and chemical microcontact printing (μCP) [11] and will

not be discussed in this review. Attention will be focused on the layer-by-layer self-assembled films and electron transfer and charge storage therein. In particular we shall survey recent results on the nanofabrication of rectifiers (Zener diodes, Schottky diodes, light-emitting diodes or LEDs), single and cascade electron-transfer devices and lithium storage batteries. Space limitation has also precluded the treatment of self-assembled sensors and biosensors [12–23] and the use of self-assembled films for electro-optical applications [24, 25].

9.2
Self-assembled Light-emitting Diodes (LEDs) and Photochromic and Electrochromic Display Devices

The potential of fabricating low cost, light weight and flexible flat-panel display devices [26] and solid state lasers [27] has prompted the exploration of polymeric light emitting diodes (LEDs) and photochromic and electrochromic devices. Low operational voltages (<5 V), high brightness, fast speed and large viewing angle are the basic requirements for flat-panel display devices. The demonstrated electroluminescence [28] and the structural versatility of polymers allows, at least in principle, the constructions of LEDs with desired and tunable light emission [29–33], quantum and conversion efficiencies, lifetimes and stabilities [34, 35]. Unfortunately, the limited lifetime of the polymeric display devices precluded, to date, their use instead of liquid crystals. Clearly a greater understanding of the underlying chemical and photophysical properties of the polymers are required. For example, in single-layer electroluminescence (EL) devices, it is now well established that the electrode/polymer interfaces play an important role as hole injection is very sensitive to the quality of the indium tin oxide (ITO)-coated glass anodes [28d]. ITO constitutes a source of oxygen that can oxidize the semiconducting polymer film emitter (poly(2-methoxy-5-(2′-ethylhexyloxy)-*p*-phenylenevinylene, MEH-PPV, for example), and thereby decrease the quantum efficiency of EL [36, 37]. Attempts to overcome this problem included the use of polyaniline [38] or fluorine tin oxide [39] electrodes instead of ITO or to improve the performance of the ITO electrode by plasma etching [40, 41]. Interposing a Langmuir-Blodgett film of poly(methyl methacrylate) [42], a layer of a derivative of polyaniline or polythiophene [43], a doped (by 3,4-ethylene dioxythiophene, for example) [41], or sequentially chemisorbed and hydrolyzed layers of a dielectric "capping" octachlorotrisiloxane [44], between ITO and MEH-PPV (or PPV) was found to reduce the rate of oxidative degradation, increase the quantum efficiency of EL and extend the lifetime of the diodes.

9.2.1
LEDs Based on Nanostructured Polymers Films

Self-assembly enables the interposition of a well-defined and continuous ultrathin layer (or layers) of the desired material between the electrode and the polymer

emitter. In a recent study the influence of the nature and the thickness of a self-assembled interlayer, composed of conducting (self-doped polyaniline), semiconducting (polymer with oligo-*p*-phenylenevinylene sequences) or insulating poly(styrenesulfonate), PSS, and poly(allylammonium chloride), PAH, polymers, on the light-emitting properties of a spin-coated MEH-PPV film has been investigated [45]. The results clearly showed that introducing an interlayer between an ITO electrode, derivatized by a silyl coupling layer and MEH-PPV film, gave a significant improvement of the quantum efficiency and luminance (i.e. 500 cd m^{-2} as compared with 100 cd m^{-2} obtained on using a conventional ITO/MEH-PPV device). Importantly, improvement in device brightness was also obtained in systems supporting a high current density; best results were found for polymers having high resistivity and interlayer thicknesses in the order of 1.0 to 2.0 nm [45]. Thin-film light-emitting devices, with an external quantum efficiency of $\eta_{ext} \equiv$ 0.2%, have been also prepared by combining anionic and cationic water-soluble poly(*p*-phenylene)s, PPPs, polyelectrolytes [46]. Self-assembled multilayers of PPV precursor and poly(methacrylic acid), PMA, exhibited luminance levels of 10–50 cd m^{-2} with external device efficiency of about 0.002%, after annealing the films at 210 °C [47]. Interestingly, it was found that both the luminance levels and η_{ext} could be increased by self-assembling hetero structures (consisting of multibilayer combinations). The system ITO/$(PSS/PPV)_5$/$(PMA/PPV)_{15}$/Al showed, for example, luminance levels of 100–150 cd m^{-2} and were two to four times more efficient than that fabricated from PMA and PPV only. This better performance was attributed to the unique hole transport capabilities occurring in the bilayers PSS/PPV and to the "polyanion-type doping" induced on the conjugated backbone of PPV [48]. Additionally, this multibilayer system was used as a hole conducting layer in a composite hetero-structure comprising CdSe nanocrystals as inorganic electroluminescent materials but only weakly contributed to the overall performance of the devices [49]. Attempts to use negatively charged particles, to locally modify the electric field at the ITO/MEH-PPV interface, were carried out by interposing SiO_2 particles between a MEH-PPV film and a NH_2-terminated self-assembled monolayer bound to the ITO surface (Ca was used as the cathode). This simple procedure allowed to increase η_{ext}, from 0.8–1.0%, for devices devoid of particles, to 2.5%, for devices incorporating SiO_2 particles. This effect was interpreted in terms of enhanced hole injections, due to the reversing of the local field across the device, or to the reversing of the dipole moment, across the interface [50].

Tunable light emission has been demonstrated in ultrathin films layer-by-layer self-assembled from anionic (polyacrylic acid, PAA, or polystyrene sulfonate, PSS) and cationic (phenylene vinylene, PV, polymerized with different chromophores) copolymers on to ITO and coated by aluminum (Fig. 9.2) [51, 52]. One of the remarkable observations was the dependency of the blue-shift of the photoluminescence on the thickness of the anionic polyelectrolyte layer. Substituting a 10 Å thick layer of PSS for a 40 Å thick PAA layer resulted in an almost 50 nm shift of the emission (Fig. 9.2). Similar shifts were observed on increasing the ionic strength of the PSS solution (thereby obtaining a thicker layer of it). Increasing

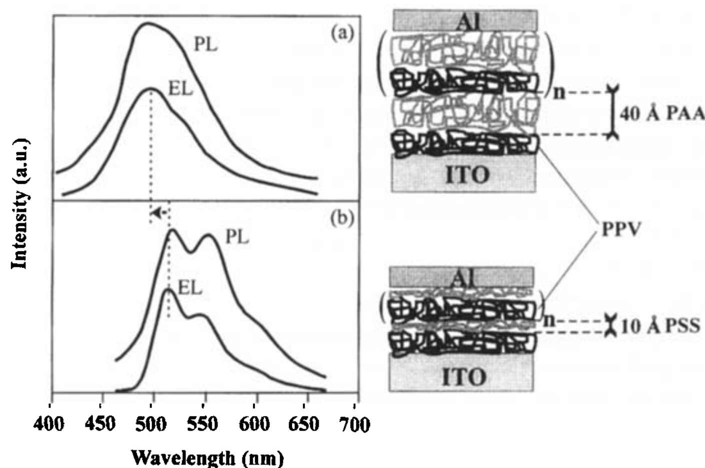

Fig. 9.2 Photoluminescence and electroluminescence spectra of two series of multilayers made from bilayers of polyphenylene vinylene (PPV) and a polyanion, differing by the nature of the polyanion; poly(acrylic acid) (PAA) in (a) and polystyrene sulfonate sodium salt (PSS) in (b). All films were 30 nm thick and submitted to a thermal treatment to convert the PPV-precursor to PPV (reproduced from Ref. [51b]).

the ionic strength of a film self-assembled from thirteen layers of PPV and PSS on quartz, quartz$(PPV/PSS)_{13}$, have been also shown to result in a blue-shift of the photoluminescence spectra [53]. These results have been rationalized in terms of better compartmentalization of the semiconducting layers, and improved spatial confinements of the excitons in the thicker than in the thinner layers. When the copolymer contained pH-sensitive moieties (for example pyridine groups), the emission spectrum became sensitive to the pH which modified the electron density by protonation. It has been shown that the system PPV/polycation, particularly PPV grafted with PEI [54b] or triethylenetetramine [54c] and loaded with transition metal ions, increased the device lifetime and the electroluminescence intensity [54b]. PPV-based electroluminescent ultrathin film hetero structures have also been prepared by the sequential adsorption of a semiconducting polymer (sulfonated polyaniline) and protonated poly(*p*-pyridylvinylene) [54a]. Other devices were based on the use of poly(4-vinylpyridine) adsorbed with transport layers such as polyvinylcarbazole and 2-(4-biphenylyl)-5-(4-terbutylphenyl)-1,3,5-oxadiazole [55].

9.2.2
LEDs Based on Redox Polymer Films

The concept of a rectifying bilayer (diode-like bilayer) has been demonstrated in electrochemical liquid cells employing an electrode coated by two redox polymers (a $Ru(bpy)_3^{2+}$-based polymer and polyvinylferrocene, for example) in the early eighties [56, 57]. Polymers were used to avoid the intermingling and to create a well-

defined interface between the two redox species. In this configuration, the outer film underwent electron transfer reactions with the electrode via electron transfer mediated by the redox states of the inner film. The resulting interface between the inner and outer films exhibited an unidirectional (vectorial) flow of electrons which was not the consequence of semiconducting characteristics or space-charge effects. Indeed, the conduction of electrons within the films was only possible at the energies of the film's redox levels; insulating characteristics were observed at other energies. The rectifying action of the inner/outer-film interface was attributed to the existence of discrete levels of redox conductivity associated with the insulating regions [56b].

Because the Ru(II) chelates (typically $Ru(bpy)_3^{2+}$ complexes) exhibit a $d_{\pi*}$ metal-to-ligand charge transfer-excited state that can be electrochemically (or chemically) produced via reduction of the complexes, an electrogenerated chemiluminescence (ECL) can be also observed in a single film of Ru(II) chelates or (Ru-II) polymers, adsorbed on to a conductive electrode in a suitable solvent [58]. Solid films of $Ru^{2+}(bpy)_3$ complexes and derivatives, sandwiched between ITO and Al electrodes [59–61] or incorporated in frozen molten salts [62], have only recently been shown to function as electroluminescent devices (functioning by the same principles as that in a liquid cell; see Fig. 9.3). This implies that the film must be both electronically and ionically conductive, since the liquid electrolyte is absent. Upon the application of a voltage, the redox polymer film undergoes oxidation at the anode, Ru(II) is converted to Ru(III), and reduction at the cathode, Ru(II) is converted to Ru(I). If the diffusion of the redox products is prevented, a steady state concentration gradient appears between the electrodes, and electron hopping constitutes the only possible route for bringing the Ru(III) and Ru(I) species together in order to generate the Ru(II)*-excited state. Depending on the nature of the ruthenium derivatives the emitted light is red or red-orange which can be exploited for the construction of LED-based flat panel display devices [59–61, 63–66]. The recent elucidation of the mechanisms of charge injection and transport in solid-state devices based on Ru(II) complexes clearly indicated that redox conduction is facilitated by the formation of serial concentration gradients of Ru(III/II) and Ru(II/I) couples, ultimately leading to a voltage gradient-driven charge transport process [62, 67, 68]. Fig. 9.3 depicts the principle of the functioning of such an LED.

Recent developments of these electrochemically driven systems have involved the use of polyester containing Ru(II) complexes as emitters and the control of the ionic conductivity in the device and of the nature of the interfaces by different techniques of layering (spin-coating and sequential electrostatic layering) [59–61, 63–66]. It has been reported that a blend of small molecules of Ru(II) complexes dispersed in a matrix of poly(ethylene oxide), PEO, and spin-coated on to an ITO electrode with an aluminum top contact, produced luminance levels of 100 cd m^{-2} at 6 V but operated with a very low external device efficiency, 0.02% [63]. Complexes of $Ru(bpy)_3(PF_6)_2$ and its derivatives have been also spin-coated with pyridine on to ITO anodes with an aluminum cathode thermally evaporated on top of the films [65]. Luminance as high as 1000 cd m^{-2} at 5 V and 200 cd m^{-2} at 3 V were realized, with unprecedented external quantum efficiencies of 1%, meeting

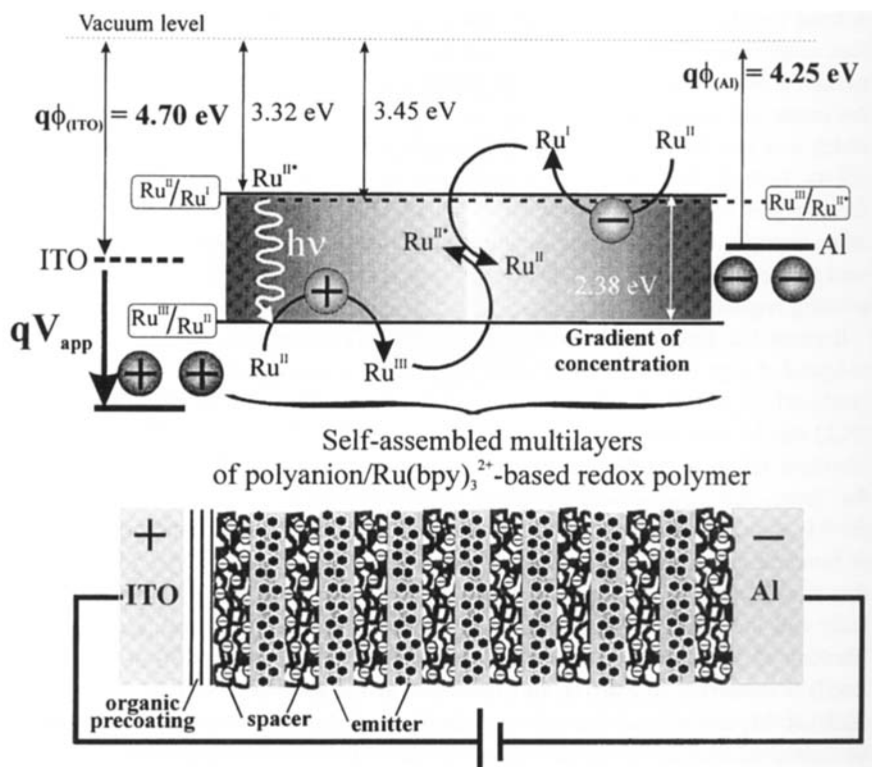

Fig. 9.3 Principle of fabrication and functioning of a light-emitting diode based on a $Ru(bpy)_3^{2+}$ polymer sequentially layered with a polyanion (i.e., poly(acrylic acid)) as a spacer. At a forward bias, the applied voltage V_{app} increases the work function Φ(ITO) of the ITO electrode, allowing the oxidation of Ru(II) to Ru(III). Concomitantly, at the cathode (Al lead), Ru(II) is reduced to Ru(I). Two gradients of concentration of reduced and oxidized species are established within the film, near the cathode and anode, respectively. At the interface where Ru(I) and Ru(III) are the predominant species, one electron from Ru(I) is transferred to Ru(III) leading to a Ru(II*) with an electron in the excited state at an energy level of 3.45 eV below the vacuum level. The electroluminescence occurs when this electron reaches the redox level Ru(III)/Ru(II) located at 5.70 eV (3.45 eV + 2.38 eV) below the vacuum level, releasing a photon of energy *hν*.

the needs of solid-state $Ru(bpy)_3^{2+}$-based devices operating at high brightness, high efficiency, low voltage (<6 V) and minimal delay time [65]. Using this approach it was demonstrated that, on employing small molecules, an applied bias close to the redox potential of the emitter is sufficient to both induce the counterion migration and affect the required redox reactions.

Because redox polymers are charged, they can be layer-by-layer self-assembled in place of employing the traditional film processing techniques (spin-coating, for example). There are several advantages of the self-assembly. First, the 3D and 2D diffusion of electrogenerated species is expected to be diminished, if not alleviated, thus

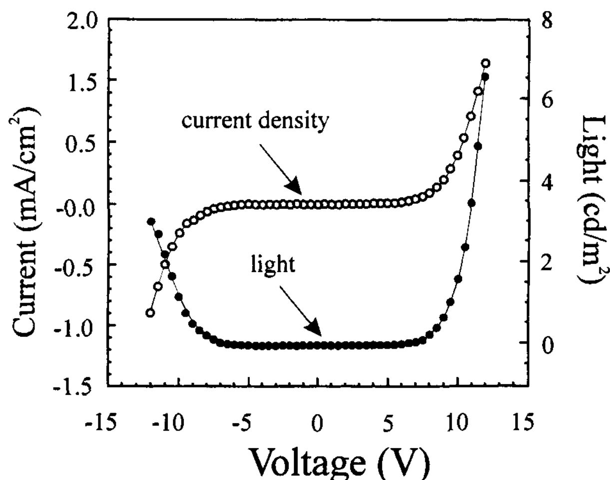

Fig. 9.4 Current-voltage and light-voltage characteristics of a device composed of 20 bilayers of the 46% $Ru(bpy)_3^{2+}$ polyester and 54% poly(acrylic acid) (reproduced from Ref. [66]). The electroluminescence is reported in candela per meter square.

a potential-mediated concentration gradient is readily obtainable in the direction perpendicular to the electrodes. Second, the thickness and the amount of active materials incorporated in the junction as well as their level of blending are readily controllable [69]. Third, self-quenching can be reduced by judiciously controlling the average site-to-site distance of the Ru(II) complexes in the redox polymer itself and in the multilayer films [66]. Fourthly, and most importantly, the versatility and ease of self-assembly permit the convenient variation of experimental parameters necessary for the detailed elucidation of the mechanisms involved [64].

LED devices with quantum efficiencies in the 2–3% range have recently been fabricated by layer-by-layer molecular-level assembly [66]. In one experiment, poly(acrylic acid) (PAA) was used to control the degree of layer interpenetration and the relative amounts of $Ru(bpy)_3^{2+}$-polyester and PAA by a simple adjustment of the pH of the polymer-dipping solutions. The luminance level, at a given thickness of the films (typically 110 nm), increased up to 3%, as the $Ru(bpy)_3^{2+}$ polyester contents decreased from 80 to 46%. This effect was partly due to a reduction of self-quenching and it became comparable at a forward and a reverse bias (Fig. 9.4). The layer-by-layer processing have allowed the design of complex systems, in which compositionally graded structures were obtained by varying the amount of $Ru(bpy)_3^{2+}$ polyester across the multilayer films. With suitable compositional grading of the multilayer structure, devices with higher luminance and emitting either in forward or reverse bias have been fabricated by reversing the grading order relative to the metal leads [66].

Several advantages of the layer-by-layer processing stems from the fact that dilution of the redox species in a polyelectrolyte matrix (PAA) is beneficial to the photoluminescence (by a factor 7–9 times relative to spin-coated films) and to the

device efficiency. Relatively high voltages (10 V and more) are required to drive the device because of the increased bulk resistance of the films, and the maximum light output is generally lowered. This reflects the very low ionic conductivity. As expected, during the sequential layering process, most of the small counterions associated with the polyelectrolytes are entropically displaced to allow the formation of polymer-polymer contact ion pairs. Such films have been found to be three orders of magnitude less conductive than the spin-cast films [66]. However, this drawback can be satisfactorily circumvented by using a polyelectrolyte with non-ionized acidic moieties. It has been proposed that in addition to the low level of small ions present in the films, non-ionized acid groups of PAA may act as potential donors of mobile protons to restore the charge neutrality as the voltage is applied. Compared to PPV-based LEDs, this nanofabrication method offers the advantage of avoiding the use of low work function metals (Ca, Mg, for example) which are very reactive with air and producing amazingly high luminance levels (comparable to or higher than the PPV-based devices) [65, 66].

9.2.3
Photochromic and Electrochromic Display Devices

Photo- or electrochromism manifest themselves as reversible color changes of materials upon exposure to light or to the passage of an electric current (or change of potential), respectively. Colored redox molecules (polymers, oxides and heteropolyanions incorporating transition metal atoms such as W, Mo, Ti, V) exhibiting different coloration in their oxidized and reduced states are generally used for the fabrication of electrochromic coatings which are employed in smart windows for the modulation of incoming light and in flat-panel display devices.

Electrochromic complexes and polyoxometallates have the property required for the layer-by-layer construction of composite electrochromic films electrodes. An im-

Tab. 9.1 Self-assembled photo- and electrochromic devices.

Polyoxometallate	*Cationic layer*	*Coverage (mol heteropolyanion cm^{-1})*	*Ref.*
$Na_3PW_{12}O_{40}$	$Ru(bpy)_3^{2+}$, $Fe(phen)_3^{2+}$, CuPEI, $PVPH^+$	–	70
$Na_4SiW_{12}O_{40}$	CTA, DTA, $PVPH^+$	1.5×10^{-10} to 3×10^{-10}	70
$H_4SiW_{12}O_{40}$	CTA, DTA, $PVPH^+$	1.5×10^{-10} to 3×10^{-10}	70
$H_3PW_{12}O_{40}$	$Ru(bpy)_3^{2+}$, $Fe(phen)_3^{2+}$, CuPEI, $PVPH^+$	–	70
Isopolymolybdate	CTA, CP, $PVPH^+$	1.5×10^{-10}	70
$(NH_4)_6[P_2Mo_{18}O_{62}]$	$Os(bpy)_3^{2+}$, $Ru(bpy)_3^{2+}$	2×10^{-11}	71
$K_6P_2W_{18}O_{62}$	$Os(bpy)_3^{2+}$, $Ru(bpy)_3^{2+}$	–	71
$Na_4W_{10}O_{32}$	PDDA	2×10^{-10}	72
$(NH_4)_4[Mo_6O_{26}]$	PEI, PAH	–	73
$(NH_4)_6[V_{10}O_{28}]$	PEI, PAH	0	73
$H_5SiMo_{11}VO_{40}$	$PVPH^+/Os(bpy)_3^{2+}$	–	74
$H_3(PMo_{12}O_{40})\cdot xH_2O$	PyC6BPC6Py	–	75

portant feature of Keggin- or Dawson-type polyoxotungstate and polyoxomolybdate anions is their ability to undergo a rapid reversible reduction accompanied by coloration and leading to a so-called heteropolyblue. Polyoxometallate anions have been self-assembled on to ITO, and glassy carbon electrodes with a variety of water-soluble cationic species, including transition metal complexes [70, 71], cationic surfactants (CTA, DTA) [70], polycations [70, 72–74] and bipolar pyridine [75] (Table 9.1).

The use of large cationic surfactants has been found to increase the surface coverage during the alternate immersions [70], while polycations were preferred for providing overall stability (prevention of decomposition and desorption upon repetitive cycling) [70, 72]. A multicomponent electrochromic film has been prepared by self-assembling protonated poly(4-vinylpyridine), $PVPH^+$, with silicotungstate (inner film) and isopolymolybdate (outer film) to create a bi-stable switching device [70]. $Os(bpy)_3^{2+}$ was used in combination with $[P_2Mo_{18}O_{62}]^{6-}$ to build-up seven bilayers on to an ITO electrode [71]. Repeatedly stepping the electrode potential between 0.8 and 0.34 V (relative to Ag/AgCl) allowed to cycle between $Os(bpy)_3^{3+}$ and $Os(bpy)_3^{2+}$ in the coating while leaving the $[P_2Mo_{18}O_{62}]^{6-}$ unchanged, with a corresponding repetitive absorbance change at 450–480 nm. When the potential step was between 0.34 and –0.30 V (relative to Ag/AgCl), the heteropolyanion was cycled between its oxidized and fully reduced forms, leading to absorbance changes at 680–750 nm.

The layering of polyoxometallates with polycations is critically affected by the pH of the solutions. The presence of protons in the adsorption solution is known to significantly enhance the quantity of anion that is irreversibly adsorbed. The pH has generally been adjusted to be between 2.0 and 3.5 in order to prevent the desorption of the species [70, 72, 73]. Very stable electrochromic coatings have been obtained by layering CTA with silicotungstate [70], $Fe(phen)_3^{2+}$ and phosphotungstate [70], and PDDA and sodium decatungstate (W) [72]; they could be cycled 60 to 400 times. The PDDA/W films were layer-by-layer self-assembled on to quartz, mica and ITO-electrode substrates (S). The color of the self-assembled films were found to change from dark blue to colorless upon the application of a negative potential. The observed color change of W in aqueous acidic solution is due to the presence of an intervalence charge-transfer band (W^V-O-W^{VI} $\leftrightarrow$ W^{VI}-O-W^V) which is readily influenced by an applied potential and/or light and hence it manifests itself in electrochromism and/or photochromism [76, 77]:

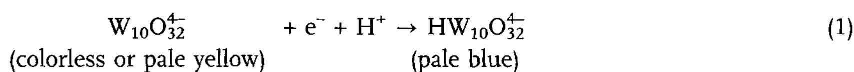

$$\underset{\text{(colorless or pale yellow)}}{W_{10}O_{32}^{4-}} + e^- + H^+ \rightarrow \underset{\text{(pale blue)}}{HW_{10}O_{32}^{4-}} \quad (1)$$

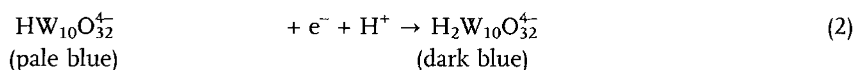

$$\underset{\text{(pale blue)}}{HW_{10}O_{32}^{4-}} + e^- + H^+ \rightarrow \underset{\text{(dark blue)}}{H_2W_{10}O_{32}^{4-}} \quad (2)$$

Typical time courses of absorbances of the S-$(PDDA/W)_6$/PDDA film, at 780 nm and 650 nm, during potential-step chronoamperometry (0 V → –0.4 V, 0 V → –0.8 V) are illustrated in Fig. 9.5. The potential steps could be recycled over 60 times with ± 5% reproducibility [72].

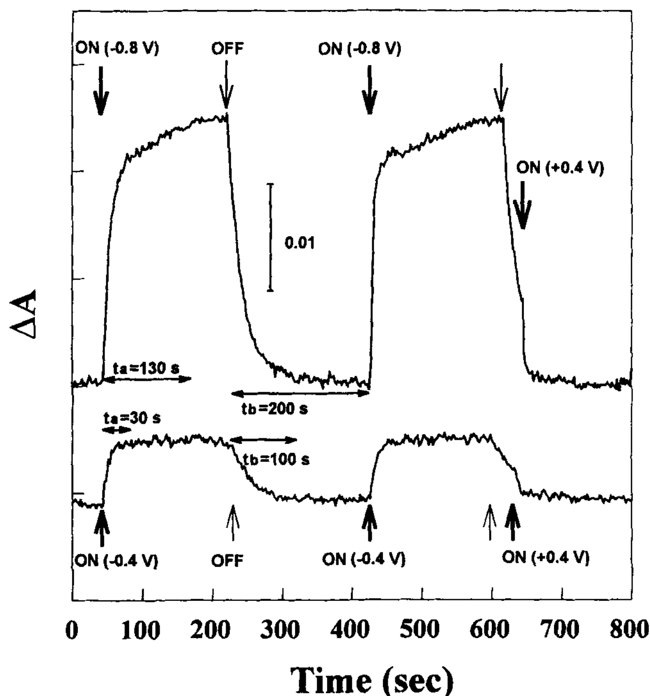

Fig. 9.5 Absorbance changes at 650 nm (−0.8 V relative to the SCE) and 780 nm (−0.4 V) in a self-assembled S-(PDDA/W)$_6$/PDDA film accompanying the potential steps of 0 → −0.4 V; 0 → −0.8 V; 0 → +0.4 V; and 0.8 → +0.4 V. t_a and t_b are response times for coloration and bleaching, respectively. (from Ref. [72])

Recently, a potentiodynamically driven layer-by-layer assembly has been employed for the improvement of the uniformity of the multilayer assemblies having relatively weak charge densities, and for diminishing competitive adsorption of electrolytes [74]. Drying and curing the multilayers at moderate temperatures (70 °C) has also been reported to enhance the stability of the films [70].

9.3 Self-assembled Rectifying Diodes

A typical p-n junction, leading to a pronounced increase of the current with a slight voltage variation, is set up at the interface between a hole conductor (p-type) and an electron conductor (n-type) semiconductor. Rectification is described by the Schottky diode equation or by the Fowler-Nordheim law. For p-n junction devices obeying the Schottky equation, the operating voltage is typically equal to, or lower than, the semiconductor band-gap. Due to the Fermi level mismatch, a space charge layer is created at the rectifying interface and the current is gener-

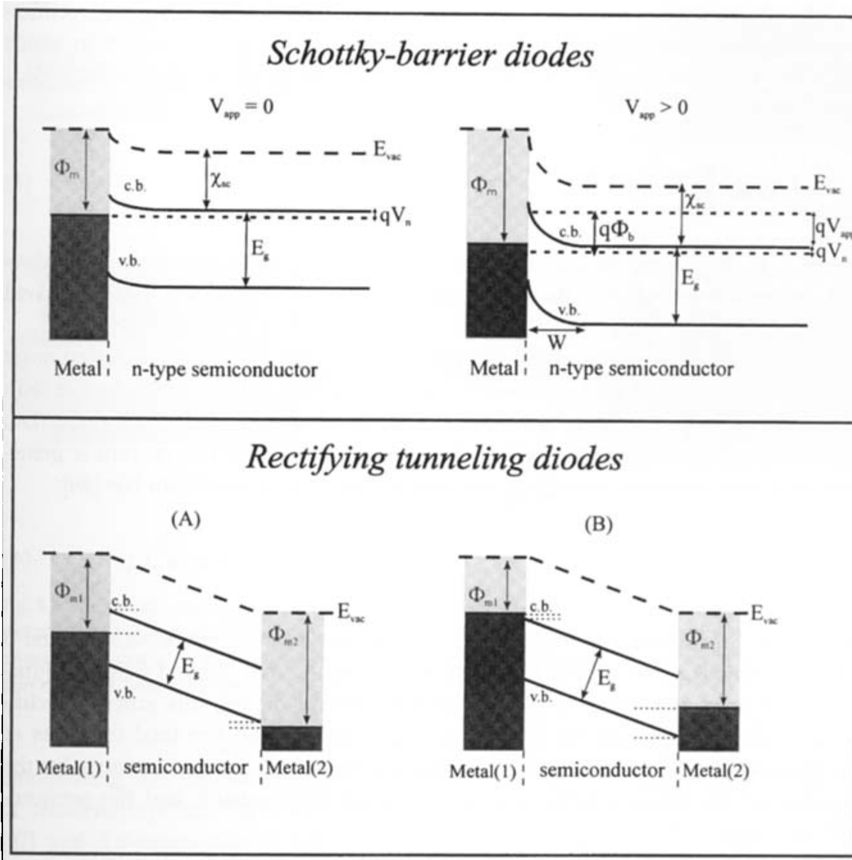

Fig. 9.6 Schematic energy level diagram of a Schottky junction composed of a metal with a high work function Φ_m and a n-type semiconductor of electroaffinity χ_{sc} and band-gap energy E_g. As a positive bias V_{app} is applied to the metal layer, the Fermi level and the conduction band of the n-type semiconductor (close to the conduction band edge, c.b.) moves upward by (ideally) qV_{app}. The rectification occurs due to a depletion layer (of width W). V_n is the depth of the Fermi level relative to the conduction band. ϕ_b is the barrier height. W is the width of the depletion layer. The lower diagram shows two rectifying metal/semiconductor/metal tunneling junctions under bias (with work functions Φ_{m1} and Φ_{m2} for the cathode and anode, respectively), obeying the Fowler-Nordheim law. Because of a low concentration of carriers in the semiconductor, the rectification is best described by a field emission tunneling mechanism. A rigid band model accounts for the charge injection. In (A), as the barrier is lower at the cathode than the anode, the majority carriers are holes, and the *i-V* characteristics will reflect the tunneling current at this interface. Note that the device efficiency, on the other hand, will be determined by the minority carriers injected through the heights of the barriers (here electrons). In (B) the reverse situation is observed, the majority carriers are electrons at the anode.

ated by thermionic emission inside the junction. As a consequence the rectification is temperature-dependent, as indicated by the Mott-Schottky equation which describes the evolution of the current as a function of the applied voltage V_{app} [78]:

$$I = I_0\left[\exp\left(\frac{qV_{app}}{nk_B T}\right) - 1\right] \tag{3}$$

where I_0 is the reverse saturation current, k_B the Boltzmann constant, T the absolute temperature and n is the diode quality factor ($n=1$ for the ideally-behaved junction).

When the materials composing the junction have a low carrier concentration, it is commonly observed that a current begins to flow at a voltage much higher than their band-gap. In this case, the junction does not follow the Schottky equation, and a tunneling mechanism controls its characteristics [79]. The current is generated by a field-emission tunneling and follows the Fowler-Nordheim law [80]:

$$I = V^2 \exp\left(-\frac{\beta d}{V}\right) \tag{4}$$

where d is the thickness of the device sandwiched between the electrodes and β has the dimensions of electric field [78], and is related to a "critical field" for junction breakdown. Note that, in contrast to the Schottky diodes, this junction rectification is independent on the temperature and depends on the total thickness of the film. A rigid-band model with a triangular tunneling barrier accounts for the injection of the charges at the interface between the electrode and the semiconducting material (Fig. 9.6).

9.3.1
p-n Junctions

The current method of fabrication of p-n junctions relies on doped silicon materials and on energetically costly procedures. The layer-by-layer self-assembly (or assembly) of doped semiconducting polymers and semiconducting nanoparticles offer an alternative, and potentially economically, viable approach for the fabrication of rectifying junctions. A convenient way to fabricate self-assembled p-n junctions is to use a p-doped semiconducting polymer and n-type II–VI semiconductor nanoparticles (see Fig. 9.7).

Several procedures have been published for layering ultrathin poly(pyrrole)/polyanion and polyaniline/polyanion films [81, 82]. For example, poly(pyrrole), Ppy, films can be conveniently deposited in controllable thickness (in the subnanometer range) by repeatedly dipping the substrate into a freshly prepared aqueous solution of Ppy (pyrrole solution oxidized by $FeCl_3$) and rinsing it with water [83, 84].

Composite diodes have been fabricated by incorporating semiconductor nanoparticles into (or on to) semiconducting polymers which had been prepared by

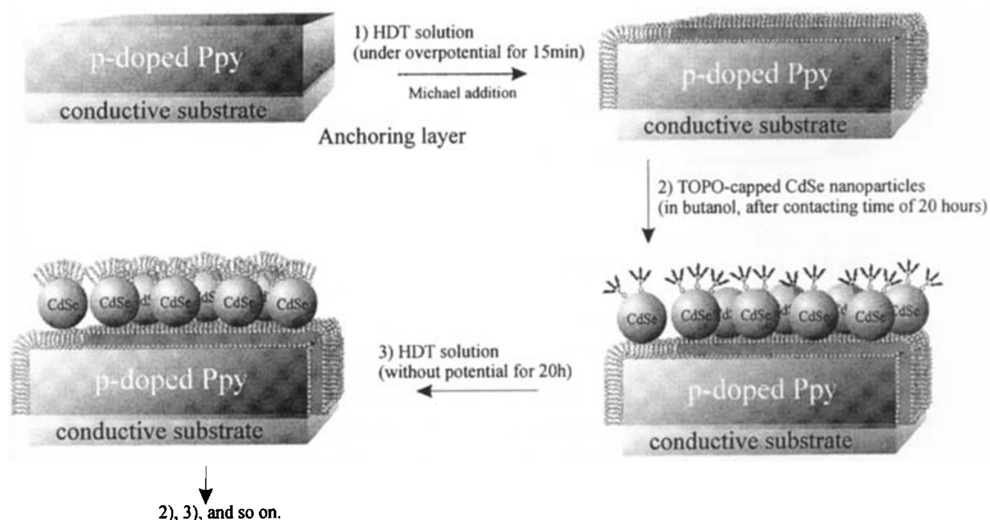

Fig. 9.7 Schematic representation of the derivatization of a p-doped polypyrrole (Ppy) layer under overpotential in alcoholic medium solution of 1,6-hexanedithiol (HDT), followed by the sequential adsorption of TOPO-capped n-type CdSe nanoparticles and HDT to create a p^{+}-n type junction. (from Ref. [83]).

spin-coating [85], electrochemical synthesis [83], or self-assembly [83, 86]. A variety of rectifying systems have been self-assembled from CdSe nanocrystals (n-type) [87] and 1,6-hexanedithiol, HDT (as a binder) in the past few years [83, 86]. Approaches to create an electroactive interface included the Langmuir-Blodgett transfer of the CdSe nanoparticles to glass slides precoated with a sulfonated polystyrene film [88] or spin-coating mixtures of CdSe nanoparticles, polyvinylcarbazole (a hole conducting polymer) and an oxadiazole derivative, t-Bu-PBD (an electron transporting material) [85]. The sequential deposition of CdSe nanocrystals with HDT on to a film of poly(*p*-phenylenevinylene), PPV, allowed the observation of rectification and enhanced EL [86]. Similar properties were reported more recently for a device made from a CdS nanoparticle layer, deposited by a wet chemical process on to a PPV film [89]. However, the *i-V* characteristics of these junctions incorporating II–VI semiconducting nanocrystals did not originate in a p-n junction, but in a Schottky-diode junction.

Ultrathin films assembled layer-by-layer from conducting polymers and CdSe nanoparticles have recently been shown to function as Zener diodes (p-n junctions with a disymmetrical level of doping) [83]. The ultrathin films have been prepared by self-assembling trioctylphosphine oxide, TOPO, capped n-type 20–40 Å diameter CdSe nanoparticles and 1,6-hexadecanethiol, HDT, on to p-doped semiconducting polymers, chemically deposited poly(3-methylthiophene), PMeT, and electrochemically deposited poly(pyrrole), Ppy. The semiconducting polymers have, in turn, been

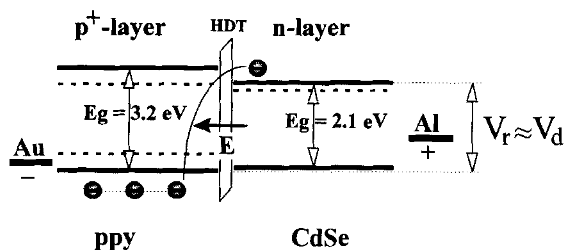

Fig. 9.8 Zener breakdown created at the interface between a p^+-type poly(pyrrole), Ppy, film and multilayers of n-type CdSe nanoparticles and 1,6-hexanedithiol (HDT). As the p-type film is negatively biased, electrons of the valence band undergoes a strong electric field triggering a breakdown at a potential corresponding to the difference of energy between the conduction band edge of CdSe and the valence band edge of Ppy (the width of the space charge layer is not represented) (taken from Ref. [83]).

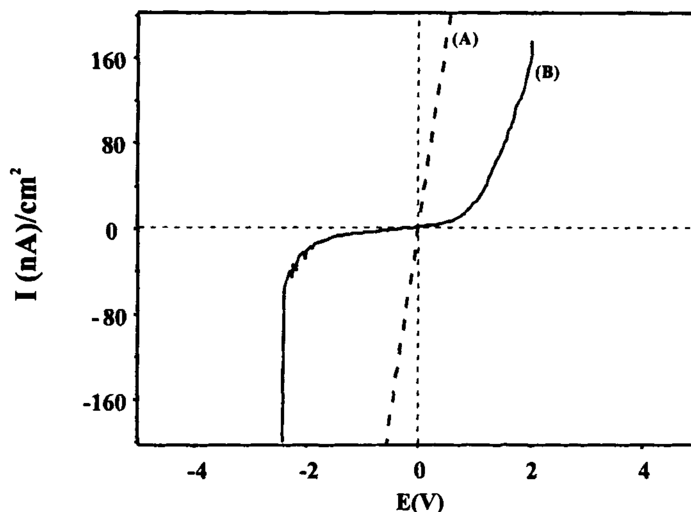

Fig. 9.9 *i*-V characteristics obtained for (A) a system Au/Ppy (ca. 100 Å)/(Al_2O_3)-Al and (B) a system Au/Ppy (ca. 100 Å)/(HDT/CdSe$)_3$/(Al_2O_3)-Al. A Zener breakdown is clearly seen at negative bias (taken from Ref. [83]).

electrochemically layered or sequentially assembled on to derivatized conducting substrates. Ultrathin films of ITO/Ppy/(HDT/CdSe$)_3$/Al and ITO/PMeT/(HDT/CdSe$)_3$/Al were shown to exhibit a Zener breakdown at reverse bias [83].

The principle of operation of the layer-by-layer assembled Zener diode is depicted in Fig. 9.8.

The level of doping inside the polymer film is electrochemically or chemically promoted to a much higher value than that exists in the CdSe layer, creating a p^+-n

junction. As the applied bias is reversed, the electric field is at the maximum at the interface between the p- and n-type material and varies as:

$$E_0 = \frac{eN_d W_n}{\varepsilon} \quad \text{with } W_n = \left(\frac{2\varepsilon}{eN_d}(V_d + V_r)\right)^{1/2} \tag{5}$$

where N_d and W_n are, respectively, the donor density and the width of the space charge layer in the p-type material, V_d is the difference of potential between the two regions, and V_r is the reverse voltage. Thus, for $V_r = V_d$:

$$E_0 = 2\left(\frac{eN_d}{\varepsilon}\right)^{1/2} V_r^{1/2} \tag{6}$$

If the electric field, E_0, is high enough, the binding forces between electrons in the valence band of the p-type region and nuclei are overcome, and these electrons of the valence band are promoted to unoccupied states of the conduction band of the n-type region. The material becomes a conductor and the voltage V_r stabilizes. The limit of V_r is dependent upon both the width of the depletion layer and the level of doping in the semiconductor. The limit observed for the reverse voltage is also called the Zener voltage V_z. The electron-hole pairs created by ionization are drained off by the electric field and generate an important reverse current. Electrons are directly emitted, by tunneling through the space charge layer, from the valence band of the p-doped conducting polymer to the conduction band of CdSe nanocrystals. The voltage cannot increase beyond V_z, leading to the *i-V* characteristics reported in Fig. 9.9. Typically, this effect is observed for heavily doped asymmetric p–n junction, having a very narrow space charge layer (ca. 500 Å) for $V_z < 5$ V [90]. In the forward direction, the observed rectification followed the Fowler-Nordheim equation (Eq. 4) which describes the field emission tunneling current, *I*, as a function of the bias voltage [80].

Ultrathin electroactive junctions have been fabricated by the chemical grafting of a monoparticulate film of nanosized silicon crystallites on to derivatized silicon wafer [91]. The method involved the preparation of colloidal 1–10 nm diameter silicon nanocrystallites, Si-nc, by the sonication of anodically etched porous silicon (PS), produced from p- or n-type silicon waters, in toluene and their covalent attachment to derivatized silicon wafers (p-Si-D or n-Si-D) or quartz. The substrate derivatization consisted of three steps: (i) self-assembly of dimethyloctadecylmethoxysilane (DOMS) on to given substrates, followed by (ii) bromination and (iii) subsequent hydroxylation of the brominated terminal methyl groups to give 18-hydroxydimethyloctadecylsiloxane monolayers covalently attached to the silicon wafers [92], p-Si-D or n-Si-D (Fig. 9.10).

Evidence for the covalent attachment of the Si-nc to the 18-hydroxydimethyloctadecylsiloxane monolayers was obtained by UV-visible absorption, surface plasmon spectroscopic and atomic force microscopic measurements on quartz-, gold-, and silicon substrates, respectively. The thickness of the Si-nc layer on the 18-hydroxydimethyloctadecylsiloxane monolayer was determined to be 12 ± 0.5 nm.

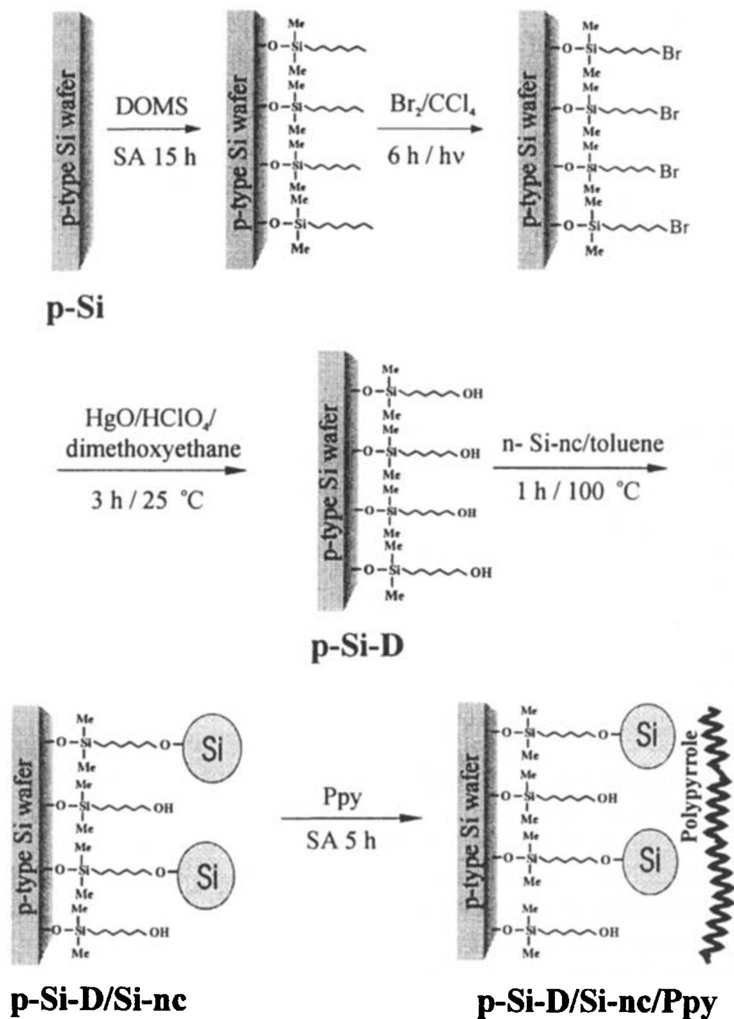

Fig. 9.10 Schematic depiction of the derivatization of a p-type silicon wafer, p-Si, by a monolayer of 8-hydroxydimethyloctadecylsiloxane to produce a p-Si-D substrate; the subsequent grafting of silicon nanocrystallites (n-Si-nc); and coating by a layer of p-type poly(pyrrole), Ppy, of the p-Si-D substrate to produce a p-Si-D/n-Si-nc/Ppy-rectifying junction (reproduced from Ref. [91]).

Ultrathin junctions were constructed by coating the Si-nc layer by a 40 nm thick p-type chemically prepared Ppy film [81, 83] on to which gold was sputtered. Rectification behavior was examined for the following films: (p- or n-)Si-D/Si-nc/Ppy/Au, (p- or n-)PS/Ppy/Au, and (p- or n-)Si/Ppy/Au. As a control, a (p- or n-)Si-D/Si-nc/Au film, expected to function as Schottky diodes, was constructed (see Table 9.2 and Fig. 9.11). Rectification properties were assessed by estimating the asymmetry ratio and the current density at voltages of 2 V (Table 9.2). At this range of

Tab. 9.2 Electrical characteristics of the different junctions.

Junction		Polarization of the back contact electrode[a]	Asymmetry ratio[b]	Current density at + 2 V ($\mu A\ cm^{-2}$)	Barrier height (eV)[c]
p-Si/Ppy/Au	(curve a)[d]	+	1	20	–
p-PS/Ppy/Au	(curve b)	+	1.8	0.16	–
p-Si-D/p-Si-nc/Ppy/Au	(curve c)	+	93	18	0.026
p-Si-D/p-Si-nc/Au	(curve e)	+	0.08	0.30	–
p-Si-D/n-Si-nc/Au		+	0.06	0.50	–
p-Si-D/n-Si-nc/Ppy/Au	(curve d)	+	13	268	0.132
n-Si/Ppy/Au	(curve f)	–	0.7	1.10	–
n-PS/Ppy/Au	(curve g)	–	1.5	2	–
n-Si-D/n-Si-nc/Ppy/Au	(curve h)	–	138	490	0.207

[a] The back contact electrode consisted of a nickel wire connected to a p- or n-type silicon substrate (ohmic contact) and the sign of the polarization refers to the forward bias.
[b] The asymmetry ratio was calculated by dividing the measured current at +2 V by the current measured at –2 V.
[c] The barrier height was calculated from a Fowler-Nordheim equation fit (see text), by extending the potential range to +10 V.
[d] See curves in Figure 9.11.

voltages the serial resistance of PS-based devices does not dominate the *i-V* curve [93].

When p-type substrates (p-Si, p-PS and p-Si-D) were used, the forward bias condition corresponded to the application of a negative voltage to the Ppy film with respect to the back contact on the Si substrate. For the simple p-Si/Ppy/Au junction, the *i-V* plot was almost symmetrical. The observed rectification in the p-PS/Ppy/Au films originated in the interface between the PS and the p-Si substrate which behaved like an n-type silicon [93, 94]. Consequently, a p-n-like junction was formed with the bulk p-Si (under the PS-layer). The rectification observed with the p-Si-D/n-Si-nc/Ppy/Au junction was caused by the p-Si-D/n-Si-nc interface while the Ppy film assisted the Si-nc in the electron injection.

The role the Si-nc size quantization plays in affecting the rectification of the different junctions constructed can be visualized by considering the approximate energy level diagrams drawn (Fig. 9.12). Interestingly, (p- or n-)Si-D/Si-nc/Ppy/Au junctions were not regulated by the thermionic emission beyond an applied forward bias of 1 volt. However, a good fit was found on using the Fowler-Nordheim law (Eq. 4) indicating that the charge injection into the junction was governed by a tunneling mechanism. Values of the barrier height, ϕ, were calculated for the three most rectifying junctions (curves c, d and h in Fig. 9.11; and Table 9.2). At forward bias, electrons are injected into the conduction band of the quantized Si-nc at the cathode (via the Ppy layer), while holes flow along the valence band of the p-doped Si substrate at the anode. Therefore, rectification occurs at the p-Si/Si-nc interface. It should be noted that the reactivity and/or the electronic proper-

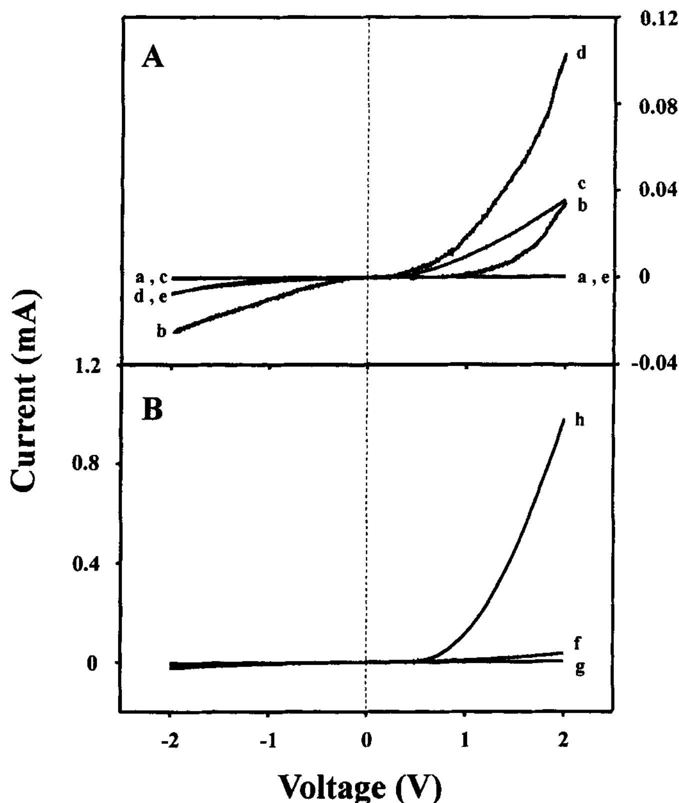

Fig. 9.11 Electrical characteristics of the different junctions investigated: A) all devices with a back contact to p-type silicon wafers polarized positively under a forward bias: a) p-Si/Ppy/Au; b) p-PS/Ppy/Au; c) p-Si-D/p-Si-nc/Ppy/Au; d) p-Si-D/n-Si-nc/Ppy/Au; e) p-Si-D/p-Si-nc/Au. B) all devices with back contact polarized negatively under a forward bias: f) n-Si/Ppy/Au; g) n-PS/Ppy/Au; h) n-Si-D/n-Si-nc/Ppy/Au (reproduced from Ref. [91]).

ties of Si-nc made from p-Si and n-Si was observed to be different in these devices.

Specifically, the asymmetry ratio was higher while the current density was lower for Si-nc obtained from p-Si than those prepared from n-Si (Table 9.2). These differences suggest that sizes, size distributions, surface defects, and reactivity toward the OH-terminated monolayer of Si-nc play an important role in the properties of the junctions constructed. Reversing the bias led to the injection of electrons into the conduction band of p-Si and their rapid recombination with the holes already present in the valence band (see curves c and d in Fig. 9.11 A). Size-quantized Si-nc at the p-Si-D/Ppy interface dramatically improved the rectifying properties of the junctions (compare curves b and d in Fig. 9.11 A). The conduction band shifts upward about half as much as the downward shift of the valence band in Si-nc up size quantization [95], which is negligible for Si particles larger

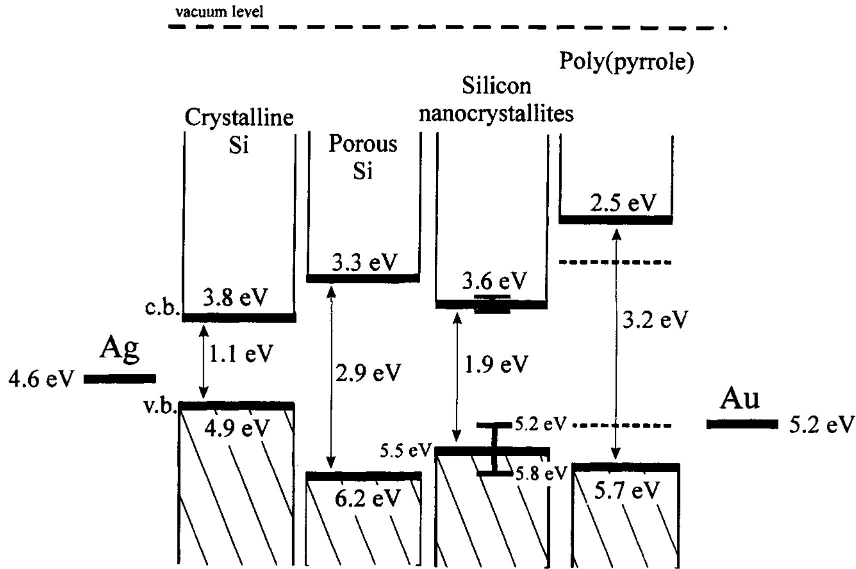

Fig. 9.12 Schematic energy level diagram for the four types of materials used to fabricate the junctions. Values of the electron affinity and the band-gap are indicated for each of them. Energy levels refer to the vacuum level. The vertical error bars set on the valence and conduction band edges of Si-nc are related to the dispersity of the Si-nc deposited on to (p- or n-type) Si-D in the early stages of the reaction, as evaluated by AFM (from Ref. [91]).

than 5 nm [96]. The conduction band edge of Si-nc is located at almost the same level than the conduction band edge of PS. This may explain why both the p-PS/Ppy/Au and p-Si-D/Si-nc/Ppy/Au film were rectifying at forward bias. It also justifies this method of construction of electroactive junctions by the layer-by-layer self-assembly of silicon nanocrystallites.

n-Type substrates in n-Si/Ppy/Au, n-Si-D/Si-nc/Ppy/Au and n-Si-D/Si-nc/Au films were also tested (see Table 9.2). For these films, the polarity of the back contact electrode was made negative relative to the gold contact, under a forward bias. The n-Si/Ppy/Au (see curve f in Fig. 9.11 B) and n-Si-D/Si-nc/Au junctions (not shown) did not exhibit rectification at +2 V and the current was negligible. Introducing a layer of Si-nc (made from etching of n-Si) between n-Si-D and Ppy (n-Si-D/Si-nc/Ppy/Au) led to a dramatic change in the *i*-*V* curve (see curve h in Fig. 9.11 B). An asymmetry ratio of 138 was found, with the highest current densities determined (490 $\mu A\ cm^{-2}$ at +2 V, see Table 9.2). The valence band edge of size-quantized Si-nc can be located at lower energy (5.5 eV and below) [96] than that of Ppy (5.7 eV) [83] thereby favoring hole injection, while the valence band edge of PS (6.2 eV) [95b] is at much higher energy (see Fig. 9.12). The meager rectification in the n-PS/Ppy/Au film (curve g in Fig. 9.11 B) at forward bias, in contrast to pronounced rectification on employing size-quantized Si-nc at the interface n-Si-D/Si-nc (curve h in Fig. 9.11 B) is rationalized analogously. The barrier height to overcome tunneling was observed to increase proportionally to the cur-

rent density at a given voltage, i.e. +2 V (Table 9.2). Higher energy barriers are expected to induce a greater charge accumulation in the depletion layer, leading to an enhanced current once the applied electric field induces tunneling.

9.3.2 Schottky Diodes

A Schottky junction is generally formed at the interface between a p-type semiconductor and a metal of low work function, or a n-type semiconductor and a metal

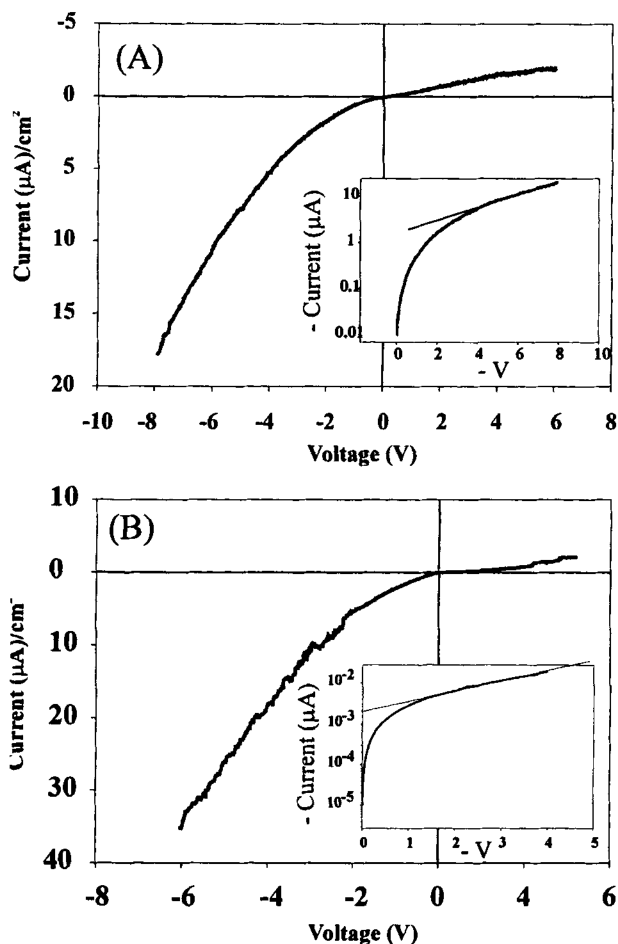

Fig. 9.13 *i*-*V* characteristics of the systems $ITO/(PDDA/TiO_2)_{10}/Au$ (A), and $ITO/(PDDA/TiO_2)_{10}/(PDDA/GO)_{30}/Au$ (B). In both films a Schottky diode is obtained as evidenced by the insets showing the existence of a linear dependence of Log(*I*) on *V*. The barrier heights were found to be 0.80 eV in (A) and 0.42 eV in (B) (from Refs. [98, 99]).

of high work function. The space charge layer field allows charge to flow in only one direction (the low work function metal at negative polarity for a p-type semiconductor and the high work function metal positive for n-type one). Fig. 9.6 describes the case of a Schottky diode made from a n-type semiconductor and metallic anode. The *i-V* characteristics are described by the Schottky-Mott equation (Eq. 3).

A Schottky diode can be readily made at the interface between a multilayer of semiconducting nanoparticles (capped by polyelectrolytes or dithiols as binders) and a metallic conductor deposited on to it. Schottky behavior of the layer-by-layer-assembled ITO/PPV/$(HDT/CdSe)_n$/metal [86, 87], the multilayers of PDDA/TiO_2 nanoparticles (capped and uncapped) [97–99], and the ITO/(PDDA/TiO_2 nanoparticles$)_{10}$/(PDDA/graphite oxide$)_{30}$/PDDA/Au films has been demonstrated [99]. In the last case, the interface TiO_2/graphite oxide (GO) was found to be rectifying, suggesting that GO (oxidized at 25%) was still graphitic enough to behave as a metallic-like material. Fig. 9.13 shows the *i-V* characteristics obtained by using TiO_2 nanoparticles of 2.3 nm in diameter as a n-type semiconductor. These junctions, made of 3–10 nanoparticle/binder bilayers generally exhibit a barrier height of 0.4 to 1 V when using ITO and Au as the cathode and anode, respectively. Another type of composite-layered rectifier has been recently developed from a $Ru(bpy)_3^{2+}$ polymer, TiO_2 nanoparticles, GO and polyelectrolytes as a binder [99]. Sequential deposition of these materials in an appropriate order resulted in double rectifications (i.e., both at negative and positive bias), due to the interface TiO_2/GO at a negative voltage and due to the electrochemistry of the redox polymer at a positive voltage.

9.4
Single-electron Conductivity – Self-assembled Coulomb Blockade Devices

There is a considerable current interest in the theoretical understanding and practical exploitation of single electron conductivity [100]. Single electron conductivity implies, by definition, the controllable charge transport by individual electrons. There are two stringent requirements for the observation of single electron events. First, the electrostatic energy of introducing an electron into an isolated conductor, E_c, has to be larger than the thermal fluctuation, k_BT:

$$E_c = e^2/2C >> k_BT \quad (7)$$

(where C is the effective capacitance of the conductor, e the charge of the electron, k_B the Boltzmann constant, and T the absolute temperature). This can be accomplished by reducing the temperature or the capacitance or, indeed, decreasing both of these parameters. The capacitance is determined by the size of the conductor and its distance from the surrounding electrodes (gates). A simple calculation shows that charging a macroscopic capacitor (having capacitance in the 10^{-12} F range) by a single electron would require a potential of 10^{-8} V and a temperature in the milli-Kelvin range to avoid thermal fluctuations. Single electron events

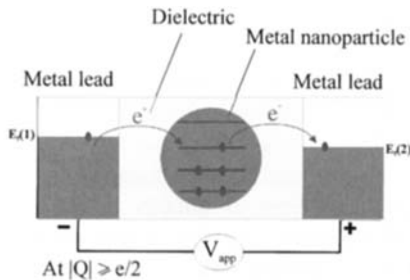

Fig. 9.14 Schematic representation of a metal-insulator-nanoparticle-insulator-metal Coulomb blockade junction. As the voltage is applied a charge Q is first accumulated on one side of the metal lead. Owing to the presence of an insulating barrier between the metal electrode and the nanoparticle (typically Au or CdSe), electrons cannot flow. This charge Q will increase with the applied voltage unless a tunneling event occurs allowing the transfer of one electron to the opposite metal electrode via the nanoparticle. This event will appear each time $|Q|$ will be greater or equal to $e/2$.

become observable at room temperatures, however, if the junction capacitance is lowered to the 10^{-18}–10^{-19} F range. This can be best achieved by entrapping a conducting nanoparticle (with a diameter <5 nm) into an appropriate tunneling barrier [101] (Fig. 9.14) or by placing a highly ordered and closely packed monodispersed (σ<10%) array of conducting nanoparticles (with diameters <5 nm, each of which are protected by an insulating surfactant monolayer) between macroscopic electrodes [102].

The second requirement for realizing single electron events is that the dielectric constant of the barrier which surrounds the conducting nanoparticle should have a tunneling resistance R_T which exceeds the resistance quantum, R_Q ($R_T >> R_Q$, $R_Q = h/e^2 \approx 25.8$ kΩ). This requirement can be met by selecting an insulating barrier which ensures the localization of the electron in (or on) the nanoparticle.

Single electron trapping and flow manifest themselves in an observable Coulomb blockade, Coulomb staircase and sometimes differential negative resistance in contrast to the classical ohmic behavior of a macroscopic capacitance device. Thus, application of a bias voltage of $e/2C$ (or an odd multiple of $e/2C$) to a monolayer-protected nanoparticle (by the conducting tip of the AFM, for example) is required in order for current to flow through the circuit. When the charge, $|Q|$, on the junction is smaller than $e/2$ ($|Q| < e/2$) the potential energy barrier of the trapped single electron, already present in (or on) the nanoparticle, cannot be overcome; that is to say the entry of the next incoming electron is Coulomb blockaded. When the junction is biased at a constant current, I, at $|Q| > e/2$, electrons will tunnel in increments with a frequency of I/e. The incremental electron tunneling manifests itself in the appearance of steps in the current-voltage plots, i.e., in the set-up of a Coulomb staircase (see Fig. 9.15). Oscillations at the steps in the current–voltage plots sometimes become observable as differential negative resistance regions. For single electron transport there is a linear relationship between the current and the frequency of the voltage signal. Superimposing a sinu-

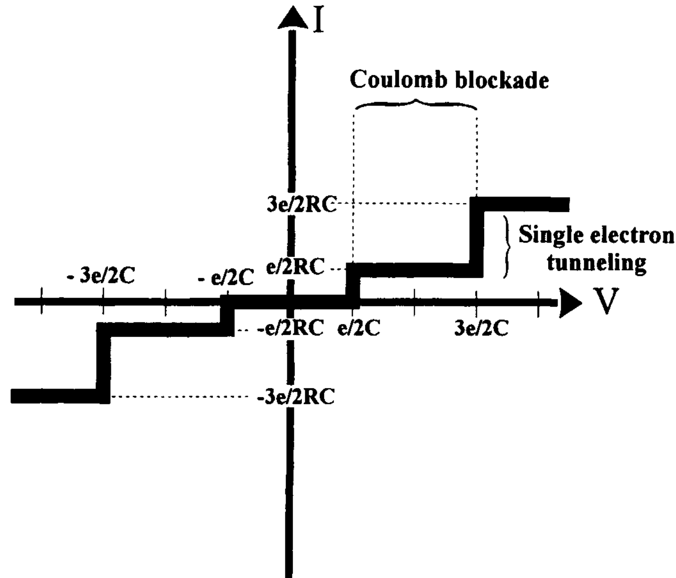

Fig. 9.15 Ideal staircase *i-V* characteristics of a single electron tunneling junction. As the junction is biased by a constant current I, at $|Q| > e/2$, a tunneling event takes place, making $|Q|$ jump to $-e/2$ and a new charging cycle restarts. The junction is Coulomb blockaded as long as $|Q| < e/2$ or the voltage $V < e/2C$ (plateau of the current), while single electron tunneling is characterized by a jump of the current at $|Q| > e/2$. Since the current is proportional to the reciprocal of the resistance R of the junction times the voltage, each single electron tunneling generates a jump of e/RC in the current.

soidal signal on to the bias voltage, the amplitude of the measured current through the conducting nanoparticle is proportional to the signal frequency. Furthermore, the ratio of the current to the frequency is equal to the electron charge.

Single electron tunneling, at low temperatures, has been observed by scanning tunneling microscopy [101]. Evidence has been obtained for a Coulomb staircase behavior, for example, on charging a 1,10-phenanthroline ligand (phen)-stabilized 2.1 nm diameter platinum cluster, $Pt_{309}phen_{36}O_{20}$, by an STM tip, on a gold substrate at 4.2 K (Fig. 9.16) [103]. Single electron transfer events have been observed at room temperature in polymer spin-coated (35 nm thick polymethylmethacrylate, PMMA) highly ordered arrays of 2–4 nm diameter silver nanoparticles between Al electrodes [104], and in organized and surface-capped gold nanoparticles [105]. Single electron tunneling has also been observed on placing in situ prepared PbS nanoparticles between the gold-coated STM tip and the HOPG substrate [106]. Particularly interesting is the recently observed single electron transfers in monolayer-protected gold cluster dispersions by differential pulse voltammetry; these experiments have been likened to "doing redox chemistry with quantum capacitors' [107].

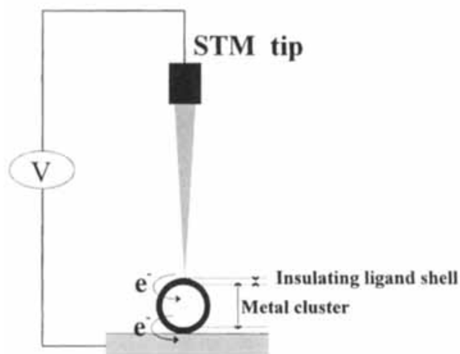

Fig. 9.16 Schematic representation of a tunneling junction made upon applying a voltage between a ligand-stabilized metal cluster and a STM tip. Both the tip and the substrate are conductive and the ligand shell is the tunneling barrier between these two electrodes and the metallic core of the cluster.

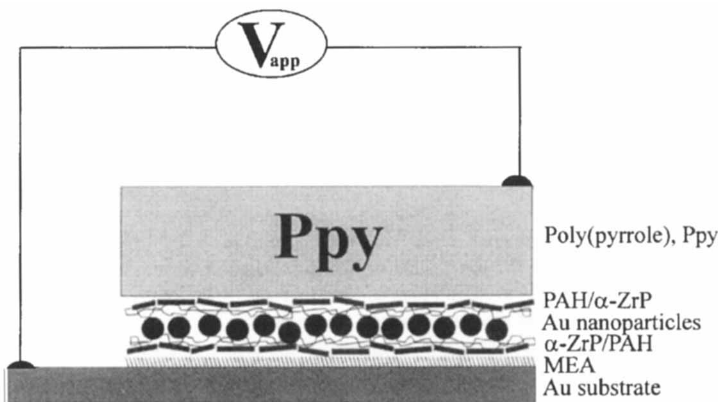

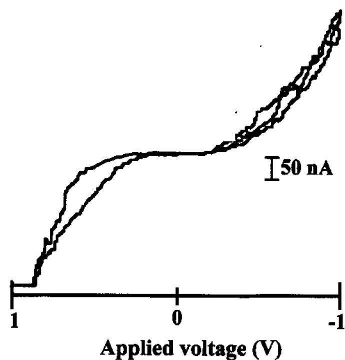

Fig. 9.17 Schematic depiction of the MINIM structure created by layer-by-layer self-assembly. The gold nanoparticles are separated from the two conductive electrode on each side by a thin bilayer of α-ZrP/PAH. The *i*-V curve (taken at room temperature) shows a staircase profile at potentials ranging from –1 V to +1 V, assumed to be characteristic of a Coulomb-blockaded junction (adapted from Ref. [108]).

To the best of our knowledge there is only one published report on single electron charging of a layer-by-layer self-assembled ultrathin film [108]. Sequential self-assembly of anionic exfoliated zirconium phosphate, α-$Zr(HPO_4)_2H_2O$ (α-ZrP), poly(allylamine hydrochloride) (PAH), negatively charged gold nanoparticles (Au), PAH, α-ZrP and poly(pyrrole) (Ppy) on to a mercaptoethylamine hydrochloride (MEA)-treated gold substrate leads to the formation of a metal-insulator-gold nanoparticle-insulator-metal, MINIM ultrathin film, Au-MEA/α-ZrP/PAH/Au/PAH/α-ZrP/PPy. Current-voltage curves of this MINIM device displayed tunable Coulomb gaps (Fig. 9.17) [108].

These investigations have been largely motivated by the perceived possibility of constructing a memory storage device based on the presence or the absence of a single electron on a nanoparticle. Fabrication of single electron transistors will also open the door to a large variety of nanoelectronic applications.

9.5 Photoinduced Energy and Electron Transfer in Self-assembled Multilayers

Natural photosynthetic systems are characterized by remarkable efficient and sustained mechanisms in converting visible light into chemical energy. This is accomplished by broadly tuned light-harvesting chromophoric systems and vectorial energy and electron transfer reactions involving molecules which have appropriate redox potentials and geometries and are localized at precisely defined intermolecular distances from each other. Mimicking natural photosynthesis in artificial chemical systems has provided a significant insight into the organization imperative and the kinetics and mechanisms involved [109]. It is known, for example, that, for efficient energy transfer, the different molecular antennas have to be separated from each other only by a fraction of a nanometer to remain within the range of the Förster radius (1.5 to 4.0 nm, depending on the chromophores considered) and to be able to mediate the required energy cascades with high quantum efficiency. Similarly, the importance of well placed spacer molecules has been recognized in alleviating the interpenetration of the redox species and in controlling the undesirable back electron-transfer reactions.

Aspects of photosynthesis have been mimicked by the self-assembly of cyanine dyes (J-aggregates) and poly(diallyldimethylammonium chloride), PDDA [110], or polyethylenimine, PEI [111], coumarin [112–114], rhodamine and fluorescein derivatives [112–115], congo red, acid red and indigo carmine [116]. Layer-by-layer self-assembly has been proposed to control the degree of mixing of the different layers and to create bidimensional dyads or triads of organic polycations separated by an inorganic lamellar layer, typically α-zirconium phosphate (α-$Zr(HPO_4)_2 \cdot H_2O$) [112, 117]. The use of α-ZrP both as a spacer and a host has been also proposed to promote rapid photoinduced electron transfers within supramolecular assemblies of donor and acceptor metal complexes at the galleries of n-butylammonium salt of α-ZrP in solution, typically between tris(2,2′-bipyridyl)ruthenium(II) and tris(2,2′-bipyridyl)cobalt(III) [118]. The polycation, poly(allylamine hydrochlor-

ide), PAH, was tagged with a dye, typically fluorescein or rhodamine B, to build-up a solid state photon antenna by layer-by-layer self-assembly with α-ZrP as a spacer. It was successfully demonstrated that a Förster mechanism accounts for the energy transfer between these two dyes in these multilayers. Quantum yields as high as 0.89 were achieved (close to the theoretical limit) for systems which typically contained one dye molecule for 50 PAH monomers. Photoinduced charge separation, with a quantum efficiency of almost 0.3, has been also reported for multilayer "onion-like" redox thin films, grown by the sequential adsorption of polyelectrolytes and redox polymers on spherical silica particles [119].

In some cases the interaction between polymers containing donor and acceptor groups is sufficient to drive the self-assembly to fruition. Recently, charge transfer interactions have been proposed to mediate self-assembly [120]. In this approach two polymers, bearing respectively an electron-accepting and electron-donor groups at the end of their side chains, were sequentially adsorbed on to a substrate, to form periodic layers of charge transfer complexes. These types of multilayers may also be used as layered photonic antennas in electron transfer cascades. Imperfections [121] and interpenetrations [122] in the layer-by-layer self-assembly of oppositely charged polyelectrolytes have been inferred, in fact, from steady-state Förster energy transfer measurements. In one set of experiments, for example, a layer of poly(p-phenylene vinylene) (PPV) was used as a donor, several layers of poly(styrene sulfonate) (PSS) and poly(allylamine hydrochloride) (PAH) functioned as transparent spacers, and a single layer of dye (rhodamine B and fluorescein)-labeled PAH acted as an acceptor. Steady state fluorescence intensity of PPV decreased regularly with increasing spacer thicknesses at large spacer thicknesses as theoretically predicted for ideal two-dimensional layers. At short distances a different behavior was observed. A good agreement between the experimental data and computer simulations was obtained under the assumption of a Gaussian distribution of both donor and acceptor molecules, in the direction normal to the film plane with a width of 2.5–3.0 nm. However, a poor agreement was found between the spectroscopically determined Förster radius and that obtained from the layer-to-layer energy transfer [121].

The layer-by-layer assembly of an antenna (1), a photosensitizer electron donor (2), an antenna (3), a spacer (4), and an electron-acceptor (5) five component thin film on to a support (an α-ZrP-precoated, amine-derivatized glass substrate) has recently been shown to mimic well aspects of natural photosynthesis (Fig. 9.18) [114]. Negatively charged coumarin- and fluorescein-tagged PAH functioned as the antennas (1 and 3), positively charged palladium(II)tetrakis(4-sulfonatophenyl)porphyrin ($PdTSPP^{4-}$) served as the electron donor (2), $HTiNbO_5$ acted as a semiconducting spacer (4) which separated the polyviologen electron acceptor (5) from (4). The thickness of each layer was in the nanometer range and the coverage for layers 1, 2, 3 and 4 was calculated to be 5.0, 1.3, 3.5, 1.3 and 3.5 mol $cm^{-2} \times 10^{11}$. Photoexcitation into the coumarin absorption (450 nm), emissions of both the coumarin and fluorescein were significantly quenched while the emission of the porphyrin (at 720 nm) was found to greatly increase. Interestingly, a higher quantum efficiency for the electron transfer ($\chi = 0.82$) was found for films

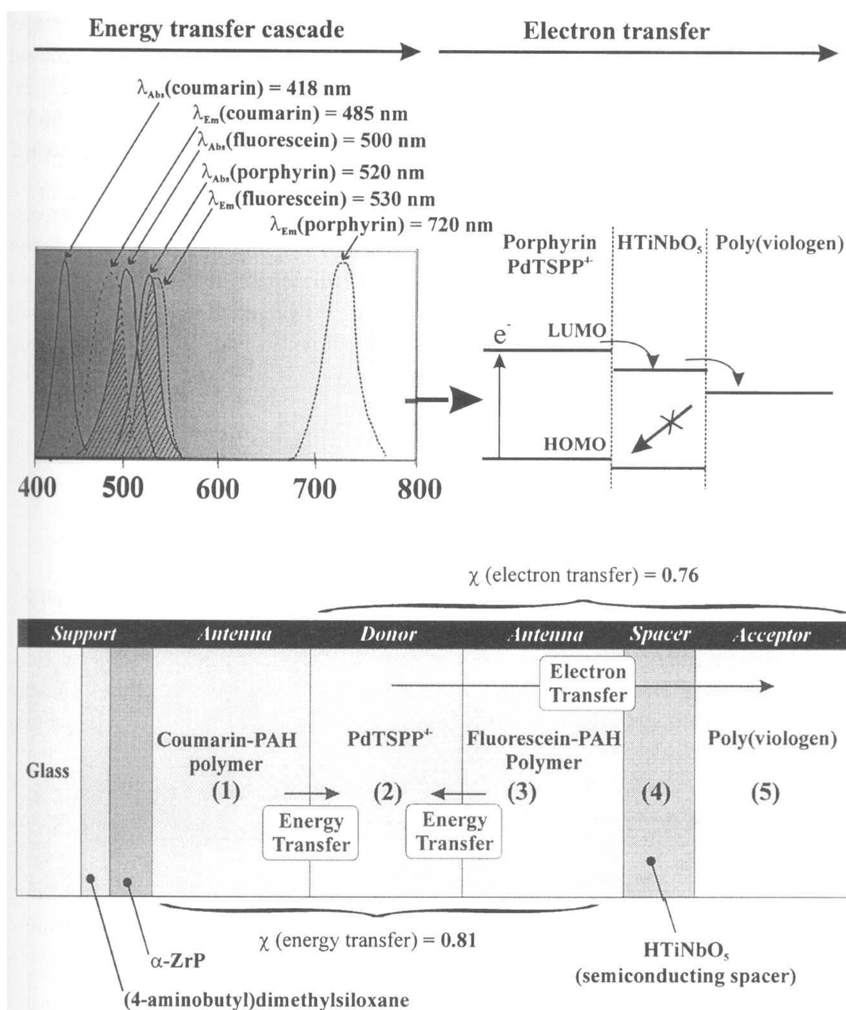

Fig. 9.18 Self-assembled five-component energy and electron transfer cascade consisting of an antenna composed of coumarin-tagged PAH (1) and fluorescein-tagged PAH (3), sandwiching a donor electron layer of $PdTSPP^{4-}$ (2), and separated from the acceptor layer of polyviologen (5) by a semiconducting thin layer of titanoniobate sheets, $HTiNbO_5$ (4). The arrows indicate the direction of energy and electron transfers through the system. Note that an exceptionally high quantum yield of energy/electron transfer cascade is observed with this combination, $\chi=0.61$ [114].

in which the two antennas and the donor were co-adsorbed rather than layer-by-layer assembled ($\chi=0.65$). Very likely, in the co-adsorbed films the different chromophores were close to each other, favoring a fast energy transfer cascade. Transient diffuse reflectance spectroscopy established that a porphyrin-viologen charge-separated state was formed upon photoexcitation of the photon antenna multi-

layer, with an exceptionally long-lived component with the titanoniobate sheets as a spacer ($\tau \approx 900$ μs). This result was attributed to the fact that $HTiNbO_5$ behaved as a semiconductor with a flat-band potential (–0.66 V relative to the SCE) [123], lying between the formal potentials of $PdTSPP^{4+}$ (–0.77 V) and polyviologen (–0.56 V), and can, therefore, mediate electron transfer for a fraction of the $PdTSPP^{4+}$-excited states.

It should be emphasized that this five-component energy/electron-transfer cascade could be efficiently triggered even in the absence of covalent bonds between the different chromophores and well-defined orientations. However, the quantum efficiency was found to substantially decrease in the absence of a spacer between the donor and acceptor. Constructing covalently linked components of the photosynthetic apparatus constitutes an alternative approach for the replacement of the protein matrix.

9.6 Self-assembled Electrodes for Lithium Storage Batteries

Lithium batteries are the recognized choice for high energy density power supply [111]. On discharge, the metallic anode of a lithium battery supplies Li^+ ions to the Li^+ ion electrolyte and electrons to the external circuit; the cathode is an electronically conducting host into which Li^+ ions are inserted as guest species and the charge is compensated by electrons from the external circuit (Fig. 9.19). The chem-

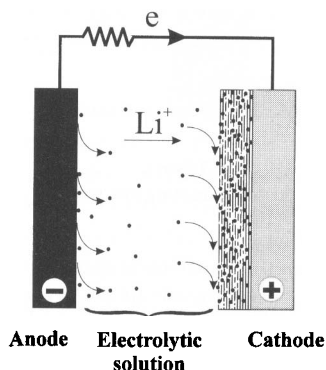

Fig. 9.19 Principle of operation of a lithium battery in a liquid electrolytic medium. Upon discharge (as shown here) the metallic anode supplies Li^+ to the surrounding electrolyte while electrons flow to the external circuit toward the cathode. The cathode is an electronically conducting host into which Li^+ ions are inserted as guest species and charge is compensated by electrons from the external circuit. The chemical reactions at the anode and cathode of a lithium secondary battery must be reversible. In that case, on charge, removal of the electrons from the cathode is achieved by applying an external opposite current to restore the difference of chemical potential between the anode and the cathode. During the charge, lithium ions are released back into the electrolyte with the concomitant formation of metallic lithium at the negative electrode.

ical reactions at the anode and the cathode of a secondary (rechargeable) battery must be reversible. On charge, the removal of the electrons from the cathode by an external field releases Li^+ ions back into the electrolyte to restore the parent host structure and the addition of the electrons to the anode by the external field attracts charge-compensating Li^+ ions back to the anode. A battery is said to be rechargeable when charging is complete (or quasi complete) even after a large number of discharge and charge cycles (typically, 1000 times for commercial uses [124]).

Lithium is a good material for the anode because of its intrinsic high negative potential and its low density and graphite and carbonaceous hosts have often constituted the cathode. Batteries based on Li^+ ion intercalation into graphite or carbonaceous hosts have the highest specific energies (energy per unit weight) and energy densities (energy per unit volume). While the specific capacity of graphite does not exceed 372 mA h g^{-1} (LiC_6), high-capacity carbonaceous materials, prepared by thermal treatment of organic precursors (epoxy or phenolic resins, sugars, petroleum pitch, polymers) between 550 °C to 1000 °C, show reversible specific charges of 400 mA h g^{-1} ($1.2 \leq x \leq 5$ in Li_xC_6) [125b].

A correlation was shown to exist between the H/C atomic ratio and the capacity of the carbonaceous materials [126]. Alternatively, high charging capacities have been rationalized in terms of disordered carbons in the carbonaceous materials [127, 128]. Two different sites for Li^+ ion intercalation have been suggested based on ^7Li NMR investigations [127]. The first site was believed to be restricted by the graphite intercalation carbon stoichiometry ("ionic" site). The second site was proposed to be restricted only by the geometrical limit of the host and the formation of Li_2 was believed to act as a capacity reservoir in this type of site [127]. These results suggested that the presence of hydrogen and oxygen atoms in the carbonaceous material as well as defects and disorders was likely to increase the charging capacity of lithium batteries.

Additional sites for Li^+ ion insertion could also be generated by the oxidation of graphite. Graphite oxidation is usually carried out by heating in a mixture of $NaClO_3/HNO_3$ or $KMnO_4/H_2SO_4$ [129, 130]. Cathodes have been then fabricated by simply blending the graphite oxide with a polymer, poly(vinylidenefluoride), PVDF, to prevent the direct exposure of the graphite to the electrolytic liquid [131]. Layer-by-layer self-assembly of graphite oxide (GO), polyethylene oxide (PEO), and poly(diallyldimethylammonium chloride), PDDA, on to an ITO substrate has recently been demonstrated to provide an efficient Li^+ ion intercalation cathode in an experimental lithium cell consisting also of a metallic lithium anode and $LiAsF_6$ electrolyte, dissolved in a mixture of ethylene carbonate and methyl formate (Fig. 9.20) [132]. An open circuit voltage (typically of 2.3 V) between the electrodes triggers the flow of electrons from the anode (lithium metal) to the cathode (the ultrathin film self-assembled on to ITO) and the concomitant intercalation of lithium ions into the self-assembled films to compensate for the charges. The rate of charge transfer can be also controlled by the application of an appropriate current to the cathode, allowing further quantitative and qualitative studies of the intercalation reactions and charging properties. As electrons flow toward the cathode, the electromotive force decreases and the cell undergoes a dis-

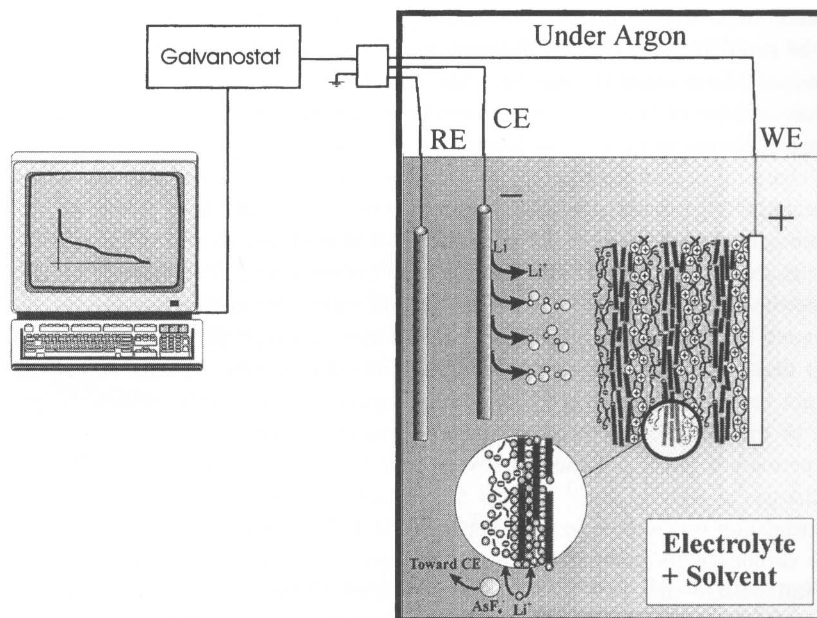

Fig. 9.20 Schematic diagram of the electrochemical cell used. A multilayer formed by the sequential adsorption of polyelectrolyte (PDDA), graphite oxide nanoplatelets (GO) and poly(ethylene oxide) (PEO) constitutes the cathodic film in the cell. Metallic lithium is used as reference and counter electrodes. The cell is isolated and under an inert atmosphere.

charge. To restore the initial electromotive force a current must be applied, leading to recharge of the cell.

Graphite oxidation is crucial to produce carboxyl or hydroxyl groups with exchangeable protons at the surfaces and the edges of the graphitic platelets. These groups allow the swelling of the graphitic sheets in a saline solution (0.1 M) and their exfoliation occurs when the cationic exchange capacity (CEC) of the platelets is high enough. Graphite oxidized by Staudenmaier's method ($HNO_3/NaClO_3$) [133] has been recently shown to exhibit charge density as high as 6 mmol exchangeable proton per gram [132c]. These levels of CEC are favorable for exfoliation and the resulting colloidal GO nanoplatelet dispersions have been successfully used for the layer-by-layer self-assembly of polyelectrolyte/GO/polymer ultrathin films [132c, 134]. Hummers' method of oxidation ($H_2SO_4/KMnO_4$) [130] was also recently used to produce large unilamellar GO colloids (150 nm to 9 μm) for self-assembly with different polycations and conducting polymers [135].

The influence of the thickness of the GO layers and the interface PEO/nanoplatelets (graphitic and non-graphitic) as well as the role of PEO on charging and discharging of the electrochemical cell shown in Fig. 9.21 has been investigated. Different cathodes were tested: ITO-$(PDDA/GO)_{10}$ (Film I), ITO-PDDA/$(GO/PEO)_{10}$ (Film II), ITO-$(PDDA/GO/PEO)_{10}$ (Film III), ITO-$(PDDA/PEO)_{10}$ (Film

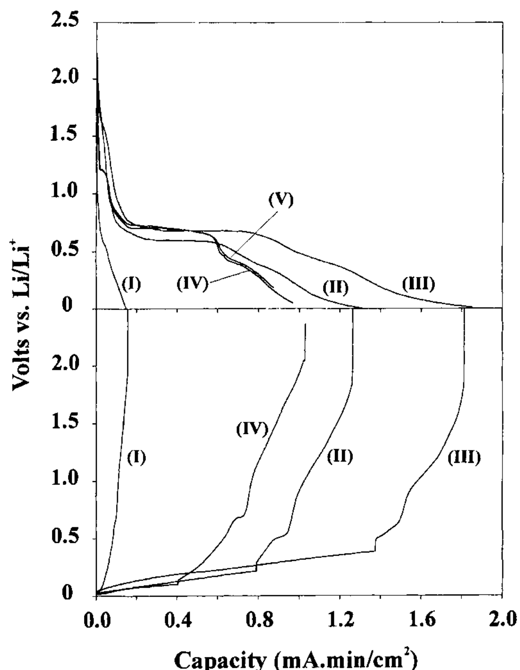

Fig. 9.21 Chronopotentiometric curves, discharge (A) and charge (B), obtained for Film I (S-(PDDA/GO-33)$_{10}$, Curve I); Film II (S-PDDA/(GO-33/PEO)$_{10}$, Curve II); Film III (S-(PDDA/GO-33/PEO)$_{10}$, Curve III); Film IV (S-(PDDA/PEO)$_{10}$, Curve IV) and Film V (S-(PDDA/MO/PEO)$_{10}$, Curve V) (taken from Ref. [132a]).

IV), ITO-(PDDA/MO (montmorillonite)/PEO)$_{10}$ (Film V) and characterized by surface plasmon spectroscopy, optical absorption and atomic force microscopy, in order to determine precisely the thickness and the amount of the different materials laid down after each adsorption cycle [132]. Table 9.3 summarizes the main charging characteristics of the multilayers and indicates the effective thickness of the GO layers in the different films.

Fig. 9.21 shows the chronopotentiometric curves obtained on discharging and charging the different films with a current density of 50 μA cm^{-2}. It can be seen that although Film I contained the largest amount of GO, the capacity (number of charge equivalent taken by the system per unit time and surface area of electrode) was the lowest in the series. This result indicated that self-assembled PDDA/GO films were poor ionic conductors, preventing the penetration of Li^+ ions into the film and their further intercalation into GO. This issue was addressed by introducing PEO into the self-assembled films. In Film II, a thin layer (0.5 nm) of PEO, self-assembled on to the GO layers, is seen to have greatly improved the specific capacity of battery. To precisely determine the contribution of the GO layers in Film II, it was necessary to subtract the lithium uptake due to PEO layers. Film IV did not contain GO, therefore, the capacity difference between Film II and Film IV provided the contribution due to GO and was characteristic of a lithium intercalation compound LiC_2. Introducing an inert layer of clay platelets (montmorillonite, MO) between PDDA and PEO, in Film V, did not change the chronopotentiometric profile, overlapping with the profile obtained with Film IV.

Tab. 9.3 Properties of the different self-assembled electrodes.

Self-assembled film	*Q (C cm^{-2}) (charging)*[a]	*Q (C cm^{-2}) (discharging)*	*Thickness of the GO layers (Å)*			*LiC$_n$ (graphite)*[c]	*Specific capacity*[d] *(mA h g^{-1})*
			From AFM data		*From UV-visible absorption*[b] *$T_{GO\ film}$*		
			Coverage of the GO layer	*$T_{GO\ seq}$*			
Film I:	0.009	0.009	80%	80 Å[e]	–	n=11.98	–
S-(PDDA/GO)$_{10}$	0.009	0.009	–	–	653 Å	n=12.22	182
Film II:	0.078	0.075	45%	20 Å[f,g]	–	n=1.36[h]	–
S-PDDA/(GO/PEO)$_{10}$	0.078	0.075	–	–	194 Å	n=1.80[h]	1232
Film III:	0.109	0.105	80%	70 Å	–	n=1.90[h]	–
S-(PDDA/GO/PEO)$_{10}$	0.109	0.105	–	–	555 Å	n=1.89[h]	1174
Film IV:							
S-(PDDA/PEO)$_{10}$	0.060	0.061	–	–	–	–	–
Film V:							
S-(PDDA/MO/PEO)$_{10}$	0.060	0.060	–	–	–	–	–

[a] Calculated values based on thicknesses determined by AFM (top) and by absorption spectroscopy (bottom).
[b] Calculated from absorption spectra, taking $\varepsilon_{230\ nm}$=21412.
[c] Calculated from the charging process.
[d] Calculated for the graphitic layers only, by taking into account the amount of carbon deduced from absorption spectroscopy.
[e] In good agreement with the AFM image histogram of a window of 1 μm^2, indicating a maximum distribution at 85 Å.
[f] This thickness corresponds to a GO layer sandwiched between PEO layers only.
[g] In good agreement with the AFM image histogram of a window of 1 μm^2, indicating a maximum distribution at 25 Å.
[h] By assuming that PEO layers contribute 0.060 C cm^{-2}.

However, substituting GO for MO allowed a twofold increase in capacity, as more GO platelets were present in these films than in Film II, but the intercalation compound was also found to be LiC_2. This last result indicates that the existence of well-defined interfaces PEO/GO into the films was crucial in discharging the platelets, with the ability to convey lithium ions into GO layers of at least 5.5–6.0 nm thick. Film III were electronically and ionically conductive enough to undergo a significant discharge, though the GO layer was thicker than in Film II. These intercalation compounds corresponded to a specific capacity of about 1200 mA g h^{-1} (for the graphite oxide only) and were comparable to the values measured for polyacenic compounds (PAS) materials, 1100 mA g h^{-1} [136]. However the PAS-based cells suffer from pronounced hysteresis (similarly to the self-assembled systems) and/or important irreversible capacity [136b]. The approach developed here allows to minimize the surface of GO in direct contact with the solution, avoiding the formation of a so-called chemically bonded solid electrolyte interface (CB-SEI film) [137], consuming part of the electrons and lithium ions in a side reaction involving the carboxyl and alkoxyl moieties attached to GO surface and leading to the formation of stabilizing salts containing irreversible reduction products of solvent at first cycle [138]. The efficient isolation of graphite with a polymeric binder, poly(vinylidenefluoride) (PVDF), has been recently observed by using a mixture of 14 wt% in PVDF [131]. In that case, an irreversible capacity of only 4% was measured at first cycle, quite comparable to the negligible values obtained in these self-assembled multilayers [132]. Further work has been devoted to the understanding of this exceptional high capacity by varying the degree of oxidation of the starting materials, and by conducting chronocoulometry experiments to determine the activation energy of Li^+-ion intercalation into these nanostructured films. These studies have shown that the oxidation plays also an important role in the charging mechanism [132c].

9.7 Conclusions and Perspectives

The layer-by-layer self-assembly of polyelectrolytes nanoparticles and nanoplatelets has been demonstrated, in this review, to provide a viable approach for the fabrication of electron transfer and charge storage devices. We have applied only a small part of our chemical knowledge and experience to this inherently interesting and potentially rewarding investigations. Many challenges remain. We shall have to develop methodologies for the larger scale preparation of the desired monodispersed nanoparticles and nanoplatelets and for their self-assembly in geometrically preferred orientations with greater uniformity and long term stability. Advantage could be taken of the precise and versatile electrodepositions, recently reported [139]. It would also be desirable to obtain a better control over the construction of composite and core/shell type nanoparticles, particularly those in which a metallic (or a magnetic or a ferroelectric) nanoparticle could be completely coated by an ultrathin (e.g. a few Angstroms thick) insulator. We shall also have to improve our

fundamental understanding of the forces which govern self-assembly. Nevertheless, we are confidently looking forward to the fabrication of many functional nanostructured electronic devices by the layer-by-layer self-assembly.

Acknowledgments
We thank the New York State Science and Technology Foundation and Clarkson University's Center for Advanced Materials Processing (CAMP) for support of this research.

References

1 Semiconductor Industry Association, *The National Technology Roadmap for Semiconductors*, Semiconductor Industry Association, San Jose, CA, **1994**.

2 R. K. Iler, *J. Colloid Interface Sci.* **1996**, *21*, 569.

3 (a) H. Lee, L. J. Kepley, H.-G. Hong, S. Akhter, T. E. Mallouk, *J. Phys. Chem.* **1988**, *92*, 2597; (b) H. Lee, L. J. Kepley, H.-G. Hong, T. E. Mallouk, *J. Am. Chem. Soc.* **1988**, *110*, 618.

4 (a) G. Decher, J. D. Hong, *Makromol. Chem. Macromol. Symp.* **1991**, *46*, 321; (b) G. Decher, J. D. Hong, *Ber. Bunsenges. Phys. Chem.* **1991**, *95*, 1430.

5 G. Decher, *Science* **1997**, *277*, 1232.

6 (a) J. C. Brumfield, C. A. Goss, A. E. Irene, R. W. Murray, *Langmuir* **1992**, *8*, 2810; (b) A. J. Bard, T. E. Mallouk, Electrodes modified with clays, zeolites, and related microporous solids, in: *Molecular design of electrode surfaces* (Ed. R. W. Murray), John Wiley & Sons, New York, **1992**, Vol. XXII, pp. 270–312.

7 (a) J. H. Fendler, *Membrane-Mimetic Approach to Advanced Materials*, Springer, Berlin **1994**; (b) J. H. Fendler, *Chem. Mater.* **1996**, *8*, 1616.

8 T. E. Mallouk, H.-N. Kim, P. J. Ollivier, S. W. Keller, in: *Comprehensive Supramolecular Chemistry* (Ed. G. Alberti, T. Bein); Pergamon Press, Oxford UK, **1996**, *7*, pp. 189–217.

9 G. Decher, in: *Comprehensive Supramolecular Chemistry* (Ed. J.-P. Sauvage); Pergamon Press, Oxford, UK, **1996**, *9*, pp. 507–528.

10 S. W. Keller, H. N. Kim, T. E. Mallouk, *J. Am. Chem. Soc.* **1994**, *116*, 8817.11; (a) Y. Xia, G. M. Whitesides, *Angew. Chem. Int. Ed.* **1998**, *37*, 550; (b) S. Whitesides, G. M. Whitesides, *Langmuir* **1999**, *15*, 826.

12 D. Q. Li, B. I. Swanson, *Langmuir* **1993**, *9*, 3341.

13 G. Decher, B. Lehr, K. Lowack, Y. Lvov, J. Schmitt, *Biosens. Bioelectr.* **1994**, *9*, 677.

14 E. R. Kleinfeld, G. S. Ferguson, *Chem. Mater.* **1995**, *7*, 2327.

15 L. M. Tender, R. L. Worley, H. Y. Fan, G. P. Lopez, *Langmuir* **1996**, *12*, 5515.

16 X. Yang, S. Johnson, J. Shi, T. Holesinger, B. Swanson, *Sens. Act. B: Chem.* **1997**, *45*, 87.

17 F. Caruso, D. N. Furlong, K. Ariga, I. Ichinose, T. Kunitake, *Langmuir* **1998**, *14*, 4559.

18 Y. M. Lvov, G. N. Kamau, G. N., D. L. Zhou, J. F. Rusling, *J. Coll. Interf. Sci.* **1999**, *212*, 570.

19 A. Bardea, F. Patolsky, A. Dagan, I. Willner, *Chem. Commun.* **1999**, 21.

20 C. Danilowicz, J. M. Manrique, *Electrochem. Commun.* **1999**, *1*, 22.

21 L. M. Goldenberg, M. R. Bryce, M. C. Petty, *J. Mater. Chem.* **1999**, *9*, 1957.22; (a) Y. M. Lvov, Z. Lu, J. B. Schenkman, X. Xu, J. F. Rusling, *J. Am. Chem. Soc.* **1998**, *120*, 4073; (b) Y. M. Lvov, Electrostatic layer-by-layer self-assembly of proteins and polyions, in: *Protein Architecture: Interfacing Molecular Assemblies and Immobilization Biotechnology* (Eds. H. Möhwald, Y. Lvov), Marcel Dekker, New York, **1999**, pp. 125–167; (c) J. F. Rusling, Electroactive and enzyme-active protein-polyion films assembled layer by layer, in: *Protein Architecture: Interfacing Molecular Assemblies and Immobilization Biotechnology* (Eds. H. Möhwald, Y. Lvov), Marcel Dekker, New York, **1999**, pp. 337–354.

23 F. Caruso, Fabrication of immunoglobulin mono- and multilayers and their application for immunosensing, in: *Protein Architecture: Interfacing Molecular Assemblies and Immobilization Biotechnology* (Eds. H. Möhwald, Y. Lvov), Marcel Dekker, New York, **1999**.

24 S. A. Asher, J. Weissman, H. B. Sunkara, G. Pan, J. Holtz, L. Liu, R. Kesavamoorthy, *ACS Symp. Ser.: Photonic and Optoelectric Polymers* **1997**, *672*, 495.

25 K. M. Lenahan, Y. J. Liu, Y.X. Wang, R. O. Claus, in: *Smart structures and materials 1999: smart materials technologies*, Proc. SPIE (Ed. M. Wuttig); *SPIE-Int. Soc. Opt. Eng.*, **1999**, pp. 104–112.

26 (a) D. Braun, A. R. Brown, E. Staring, E. W. Meijer, *Synthetic Metals* **1994**, *65*, 85; (b) P. May, *Phys. World* **1995**, *8*, 52.

27 (a) N. Tessler, G. J. Denton, R. H. Friend, *Nature* **1992**, *382*, 695; (b) S. V. Frolov, A. Fujii, D. Chinn, M. Hirohata, R. Hidayat, M. Taraguchi, T. Masuda, K. Yoshino, Z. V. Vardeny, *Adv. Mater.* **1998**, *10*, 869.

28 (a) J. H. Burroughes, D. D. C. Bradley, A. R. Brown, R. N. Marks, K. Mackay, R. H. Friend, P. L. Burn, A. B. Holmes, *Nature* **1990**, *347*, 539; (b) M. Granström, M. Berggren, D. Pede, O. Inganas, M. R. Andersson, T. Hjertberg, O. Wennerstrom, "Self-Organizing Polymer-Films – A Route to Novel Electronic Devices Based on Conjugated Polymers"; Supramolecular Science; The Boulevard, Langford Lane, Kidlington, Oxford OX5 1GB, Oxon, England, **1997**; (c) M. Logdlund, W. R. Salaneck, *Nature* **1999**, *397*, 121; (d) Y. Cao, I. D. Parker, G. Yu, C. Zhang, A. J. Heeger, *Nature* **1999**, *397*, 414.

29 N. C. Greeham, R. H. Friend, *Solid State Physics* (Eds. H. Ehrenreich, F. Spaepen); Academic Press, San Diego, CA, **1995**, *49*, 1.

30 For recent reviews see for example: A. Kraft, A. C. Grimsdale, A. B. Holmes, *Angew. Chem. Int. Ed.* **1998**, *37*, 402; And a special issue of *Acc. Chem. Res.* **1999**, *32*, pp. 191–276.

31 (a) A. W. Grice, A. Tajbakhsh, P. L. Burn, D. D. C. Bradley, *Adv. Mater.* **1997**, *9*, 1174; (b) Z. He, G. H. W. Milburn, A. Danel, A. Puchala, P. Tomasik, D. Rasala, *J. Mater. Chem.* **1997**, *7*, 2323; (c) Z. Peng, Z. Bao, M. E. Galvin, *Adv. Mater.* **1998**, *10*, 680; (d) Z. Peng, Z. Bao, M. E. Galvin, *Chem. Mater.* **1998**, *10*, 2086.

32 (a) M. Strukeji, R. H. Jordan, A. Dodabalapur, *J. Am. Chem. Soc.* **1996**, *118*, 1213; (b) J. Kido, W. Ikeda, M. Kimura, K. Nagai, *Jpn. J. Appl. Phys.*, Part 2, **1996**, *35*, L394; (c) Z. Y. Xie, J. S. Huang, C. N. Li, S. Y. Liu. Y. Wang, Y. Q. Li, J. C. Shen, *Appl. Phys. Lett*, **1999**, *74*, 641; (d) Z. Y. Xie, J. S. Huang, C. N. Li, S. Y. Liu, Y. Wang, Y. Q. Li, J. C. Shen, *Appl. Phys. Lett.* **1999**, *74*, 641.

33 V. Savvateev, A. Yakimov, D. Davidov, *Adv. Mater.* **1999**, *11*, 519.

34 T. Tsutsui, *MRS Bulletin* **1997**, *22*, 39.

35 (a) X. Z. Jiang, Y.Q. Liu, Q.L. Li, X.Q. Song, D.B. Zhu, *Synthetic Metals* **1997**, *85*, 1237; (b) T. P. Nguyen, P. Jolinat, P. Destruel, R. Clergereaux, J. Farenc, *Thin Solid Films* **1998**, *325*, 175.

36 J. S. Scott, J. H. Kaufman, P. J. Brock, R. DiPietro, J. Salem, J. A. Goitia, *J. Appl. Phys.* **1996**, *79*, 2745.

37 M. Yan, L. J. Rothberg, F. Papadimitrikapoulos, M. E. Galvin, T. M. Miller, *Phys. Rev. Lett.* **1994**, *73*, 744.

38 (a) Y. Yang, A. J. Heeger, *J. Appl. Phys.* **1994**, *64*, 1245; (b) Y. Yang, E. Westerweele, C. Zhang, P. Smith, A. J. Heeger, *J. Appl. Phys.* **1995**, *77*, 694.

39 A. Andersson, N. Johansson, P. Bröms, N. Yu, D. Lupo, W. R. Salaneck, *Adv. Mater.* **1998**, *10*, 859.

40 M. Matsumura, K. Furukawa, Y. Terasaka, H. Ueda, *Synthetic Metals* **1997**, *91*, 99.

41 J. S. Kim, M. Granström, R. H. Friend, N. Johansson, W. R. Salaneck, R. Daik, W. J. Feast, F. Cacialli, *J. Appl. Phys.* **1998**, *84*, 6859.

42 Y.-E. Kim, H. Park, J.-J. Kim, *Synthetic Metals* **1997**, *85*, 1191.

43 (a) Y. Yang, E. Westerweele, C. Zhang, P. Smith, A. J. Heeger, *J. Appl. Phys.* **1995**, *77*, 694; (b) J. Gao, A. J. Heeger, J. Y. Lee, C. Y. Kim, *Synthetic Metals* **1996**, *82*, 221; (c) J. C. Scott, S. A. Carter, S. Karg, M. Angelopoulos, *Synthetic Metals* **1997**, *85*, 1197.

44 J. E. Malinsky, G. E. Jabbour, S. E. Shaheen, J. D. Anderson, A. G. Richter, T. J. Marks, N. R. Armstrong, B.

KIPPELEN, P. DUTTA, N. PEYGHAMBARIAN, *Adv. Mater.* **1999**, *11*, 227.

45 P. K. H. HO, M. GRANSTRÖM, R. H. FRIEND, N. C. GREEHAM, *Adv. Mater.* **1998**, *10*, 769.

46 J. W. BAUR, S. KIM, P. B. BALANDA, J. R. REYNOLDS, M. F. RUBNER, *Adv. Mater.* **1998**, *10*, 1452.

47 O. ONITSUKA, A. C. FOU, M. FERREIRA, B. R. HSIEH, M. F. RUBNER, *J. Appl. Phys.* **1996**, *80*, 4067.

48 A. C. FOU, O. ONITSUKA, M. FERREIRA, M. F. RUBNER, B. R. HSIEH, *J. Appl. Phys.* **1996**, *79*, 7501.

49 H. MATTOUSI, L. H. RADZILOWSKI, B. O. DABBOUSI, E. L. THOMAS, M. G. BAWENDI, M. F. RUBNER, *J. Appl. Phys.* **1998**, *83*, 7965.

50 V. BLIZNYUK, B. RUHSTALLER, P. J. BROCK, U. SCHERF, S. A. CARTER, *Adv. Mater.* **1999**, *11*, 1257.

51 (a) H. HONG, Y. AVNY, D. DAVIDOV, H. CHAYET, E. FARAGGI, R. NEUMANN, *Adv. Mater.* **1995**, *7*, 846; (b) H. HONG, D. DAVIDOV, M. TARABIA, H. CHAYET, I. BENJAMIN, E. Z. FARAGGI, Y. AVNY, R. NEUMANN, *Synthetic Metals* **1997**, *85*, 1265; (c) M. TARABIA, H. HONG, D. DAVIDOV, S. KIRSTEIN, R. STEITZ, R. NEUMANN, Y. AVNY, *J. Appl. Phys.* **1998**, *83*, 725.

52 E. Z. FARAZZI, G. COHEN, R. NEUMANN, Y. AVNY, D. DAVIDOV, *Adv. Mater.* **1996**, *8*, 234.

53 J.-D. HONG, D. KIM, K. CHA, J.-I. JIN, *Synthetic Metals* **1997**, *84*, 815.

54 (a) M. ONODA, T. YAMAUE, K. TADA, T. KAWAI, K. YOSHINO, *Synthetic Metals* **1997**, *84*, 983; (b) I. BENJAMIN, Y. AVNY, V. N. SAVVATE'EV, D. DAVIDOV, R. NEUMANN, *J. Chem. Mater.* **1999**, *9*, 138; (c) H. HONG, I. BENJAMIN, S. KIRSTEIN, Y. AVNY, R. NEUMANN, D. DAVIDOV, *Synthetic Metals* **1999**, *102*, 1215.

55 H. HONG, R. SFEZ, S. YITZCHAIK, D. DAVIDOV, *Synthetic Metals* **1999**, *112*, 1217.

56 (a) P. DENISEVICH, K. W. WILLMAN, R. W. MURRAY, *J. Am. Chem. Soc.* **1981**, *103*, 4727; (b) H. D. ABRUA, P. DENISEVICH, M. UMAA, T. J. MEYER, R. W. MURRAY, *J. Am. Chem. Soc.* **1981**, *103*, 1.

57 G. P. KILLELSEN, H. S. WHITE, M. S. WRIGHTON, *J. Am. Chem. Soc.* **1985**, *107*, 7373.

58 W. L. WALLACE, A. J. BARD, *J. Phys. Chem.* **1979**, *83*, 1350.

59 J.-K. LEE, D. S. YOO, E. S. HANDY, M. F. RUBNER, *Appl. Phys. Lett.* **1996**, *69*, 1686.

60 D. S. YOO, J.-K. LEE, M. F. RUBNER, *Mater. Res. Symp. Proc.* **1996**, *413*, 395.

61 J.-K. LEE, D. YOO, M. F. RUBNER, *Chem. Mater.* **1997**, *9*, 1710.

62 K. M. MANESS, H. MASUI, R. M. WIGHTMAN, R. W. MURRAY, *J. Am. Chem. Soc.* **1997**, *119*, 3987.

63 C. H. LYONS, E. D. ABBAS, J.-K. LEE, M. F. RUBNER, *J. Am. Chem. Soc.* **1998**, *120*, 12100.

64 A. WU, J. LEE, M. F. RUBNER, *Thin Solid Films* **1998**, *327–329*, 663.

65 E. S. HANDY, A. J. PAL, M. F. RUBNER, *J. Am. Chem. Soc.* **1999**, *121*, 3525.

66 A. WU, D. YOO, J.-K. LEE, M. F. RUBNER, *J. Am. Chem. Soc.* **1999**, *121*, 4883.

67 K. M. MANESS, R. H. TERRILL, T. J. MEYER, R. W. MURRAY, R. M. WIGHTMAN, *J. Am. Chem. Soc.* **1996**, *118*, 10609.

68 Y. ATHANASSOV, F. P. ROTZINGER, P. PÉCHY, M. GRÄTZEL, *J. Phys. Chem. B* **1997**, *101*, 2558.

69 D. YOO, S. SHIRATORI, M. F. RUBNER, *Macromolecules* **1998**, *31*, 4309.

70 D. INGERSOLL, P. J. KULESZA, L. R. FAULKNER, *J. Electrochem. Soc.* **1994**, *141*, 140.

71 A. KUHN, F. C. ANSON, *Langmuir* **1996**, *12*, 5481.

72 I. MORIGUCHI, J. H. FENDLER, *Chem. Mater.* **1998**, *10*, 2205.

73 I. ICHINOSE, H. TAGAWA, S. MIZUKI, Y. LVOV, T. KUNITAKE, *Langmuir* **1998**, *14*, 187.

74 L. CHENG, S. DONG, *Electrochem. Commun.* **1999**, *1*, 159.

75 S. SUN, J. ZHANG, *Electrochim. Acta* **1998**, *43*, 943.

76 T. YAMASE, N. TAKABAYASHI, M. KAJI, *J. Chem. Soc., Dalton Trans.* **1984**, 793.

77 B. KEITA, L. NADJO, *J. Electroanal. Chem.* **1994**, *33*, 1064.

78 S. M. SZE, *Physics of Semiconductor Devices*, Wiley, New York, **1981**.

79 I. D. PARKER, *J. Appl. Phys.* **1994**, *75*, 1656.

80 R. H. FOWLER, L. NORDHEIM, *Proc. Roy. Soc. London Ser. A* **1928**, *119*, 173.

81 J. H. CHEUNG, A. F. FOU, M. F. RUBNER, *Thin Solid Films* **1994**, *244*, 985.

82 A. C. FOU, M. F. RUBNER, *Macromolecules* **1995**, *28*, 7115.

83 T. Cassagneau, T. E. Mallouk, J. H. Fendler, *J. Am. Chem. Soc.* **1998**, *120*, 7848.

84 I. Ichinose, H. Miyauchi, M. Tanaka, T. Kunitake, *Chem. Lett.* **1998**, 19.

85 B. O. Dabbousi, M. G. Bawendi, O. Onitsuka, M. F. Rubner, *Appl. Phys. Lett.* **1995**, *66*, 1316.

86 (a) V. L. Colvin, M. C. Schlamp, A. P. Alivisatos, *Nature* **1994**, *370*, 354; (b) J. E. Bowen-Katari, V. L. Colvin, A. P. Alivisatos, *Biomimetic Materials Chemistry* (Ed. S. Mann); VCH, **1996**, Chapter 8, pp. 221–248.

87 C. B. Murray, D. J. Norris, M. G. Bawendi, *J. Am. Chem. Soc.* **1993**, *115*, 8706.

88 B. O. Dabbousi, C. B. Murray, M. F. Rubner, M. G. Bawendi, *Chem. Mater.* **1994**, *6*, 216.

89 N. D. Kumar, M. P. Joshi, C. S. Friend, P. N. Prasad, R. Burzynski, *Appl. Phys. Lett.* **1997**, *71*, 1388.

90 H. Mathieu, *Physique des Semiconducteurs et des Composants Electroniques*, Masson, 3rd ed, **1996**, p. 147.

91 B. Sweryda-Kraviec, T. Cassagneau, J. H. Fendler, *Adv. Mater.* **1999**, *11*, 659.

92 M. V. Baker, J. D. Watling, *Langmuir* **1998**, *13*, 2027.

93 A. K. Ray, M. F. Mabrook, A. V. Nabok, S. Brown, *J. Appl. Phys.* **1998**, *84*, 3232.

94 N. J. Pulsford, G. L. J. A. Rikken, Y. A. R. R. Kessener, E. J. Lous, A. H. J. Venhuizen, *J. Appl. Phys.* **1994**, *75*, 636.

95 (a) T. van Buuren, T. Tiedje, *Appl. Phys. Lett.* **1993**, *63*, 2911; (b) P. H. Hao, X. Y. Hou, F. L. Zhang, X. Wang, *Appl. Phys. Lett.* **1994**, *64*, 3602.

96 S. Y. Ren, J. D. Row, *Phys. Rev. B* **1992**, *45*, 6492.

97 N. A. Kotov, I. Dékány, J. H. Fendler, *J. Phys. Chem.* **1995**, *99*, 13065.

98 T. Cassagneau, J. H. Fendler, T. E. Mallouk, *Langmuir* **2000**, *16*, 241.

99 T. Cassagneau, J. H. Fendler, S. A. Johnson, T. E. Mallouk, *Adv. Mater.* **2000**, *12*, 1363.

100 (a) D. Goldhabergordon, M. S. Montemerlo, J. C. Love, G. J. Opiteck, J. C. Ellenbogen, *Proceed. IEEE* **1997**, *85*, 521; (b) K. F. Goser, C. Pacha, A. Kanstein, M. L. Rossmann, *Proceed. IEEE* **1997**, *85*, 558; (c) D. L. Feldheim and C. D. Keating, *Chem. Soc. Rev.* **1998**, *27*, 1; (d) G. Schmid, L. F. Chi, *Adv. Mater.* **1998**, *10*, 515.

101 (a) B. Alperson, S. Cohen, I. Rubinstein, G. Hodes, *Phys. Rev. B* **1995**, *52*, R17017; (b) R. P. Andres, T. Bein, M. Dorogi, S. Feng, J. I. Henderson, C. P. Kubiak, W. Mahoney, R. G. Osifchin, R. Reifenberger, *Science* **1996**, *272*, 1323.

102 (a) K. von Klitzing, *J. Appl. Phys.* **1999**, *85*, 3374; (b) D. M. Schaadt, E. T. Yu, S. Sankar, A. E. Berkowitz, *Appl. Phys. Lett.* **1999**, *472*, 74; (c) S. H. M. Persson, L. Olofsson, L. Gunnarsson, *Appl. Phys. Lett.* **1999**, *74*, 2546.

103 A. Bezryadin, C. Dekker, G. Schmid, *Appl. Phys. Lett.* **1997**, *71*, 1273.

104 G. Markovich, D. V. Leff, S. W. Chung, H. M. Soyez, B. Dunn, J. R. Heath, *Appl. Phys. Lett.* **1997**, *70*, 3107.

105 M. Y. Han, L. Zhou., *Chem. Phys. Lett.* **1998**, *287*, 47.

106 P. Jiang, Z. F. Liu, Y. C. Wang, S. M. Cai, *Mol. Cryst. Liq. Cryst. Sci. Technol. A – Mol. Cryst. Liq. Cryst.* **1999**, 317.

107 (a) S. W. Chen, R. W. Murray, *Langmuir* **1999**, *15*, 682; (b) S. Chen, R. W. Murray, *J. Phys. Chem. B*, in press.

108 D. L. Feldheim, K. C. Grabar, M. J. Natan, T. E. Mallouk, *J. Am. Chem. Soc.* **1996**, *118*, 7640.

109 See for example: a) R. V. Bensasson, E. J. Land, A. L. Moore, R. L. Crouch, G. Dirks, T. A. Moore, D. M. Gust, *Nature* **1981**, *290*, 32; (b) M. Grätzel, *Acc. Chem. Res.* **1981**, *14*, 376. (c) M. A. Fox, *Photochem. Photobiol.* **1990**, *52*, 617; (d) D. Gust, T. A. Moore, A. L. Moore *Acc. Chem. Res.* **1993**, *26*, 198; (e) M. C.Feiters, M. C. T. Fyfe, M. V. Martinez-Diaz, S. Menzer, R. J. M. Nolte, J. F. Stoddart, P. J. M. van Kan, D. J. Williams, *J. Am. Chem. Soc.* **1997**, *119*, 8119; (f) A. A. C. Benniston, P. R. Mackie, A. Harriman *Angew. Chem. Int. Ed.* **1998**, *37*, 354.

110 H. Fukumoto, Y. Yonezawa, *Thin Solid Films* **1998**, *327–329*, 748.

111 T. Cassagneau, J. H. Fendler, unpublished results.

112 D. M. Kaschak, T. E. Mallouk, *J. Am. Chem. Soc.* **1996**, *118*, 4222.

113 J. Kerimo, D. M. Adams, P. F. Barbara, D. M. Kaschak, T. E. Mallouk, *J. Phys. Chem. B* **1998**, *102*, 9451.

114 D. M. Kaschak, J. T. Lean, C. C. Waraksa, G. B. Saupe, H. Usami, T. E. Mallouk, *J. Am. Chem. Soc.* **1999**, *121*, 3435.

115 F. Caruso, E. Donath, H. Möhwald, *J. Phys. Chem. B* **1998**, *102*, 2011.

116 K. Ariga, Y. Lvov, T. Kunitake, *J. Am. Chem. Soc.* **1997**, *119*, 2224.

117 D. M. Kaschak, S. A. Johnson, C. C. Waraksa, J. Pogue, T. E. Mallouk, *Coord. Chem. Rev.* **1999**, *185–186*, 403.

118 C. V. Kumar, Z. J. Williams, R. S. Turner, *J. Phys. Chem. A* **1998**, *102*, 5565.

119 S. W. Keller, S. A. Johnson, E. S. Brigham, E. H. Yonemoto, T. E. Mallouk, *J. Am. Chem. Soc.* **1995**, *117*, 12879.

120 Y. Shimazaki, M. Mitsuishi, S. Ito, M. Yamamoto, *Langmuir* **1997**, *13*, 1385.

121 B. Richter, S. Kirstein, *J. Chem. Phys.* **1999**, *111*, 5191.

122 J. W. Baur, M. F. Rubner, J. R. Reynolds, S. Kim, *Langmuir* **1999**, *15*, 6460.

123 Y. I. Kim, S. J. Atherton, E. S. Brigham, T. E. Mallouk, *J. Phys. Chem.* **1993**, *97*, 11802.

124 (a) O. Kazunori, M. Yokokawa, *Cycle performance of lithium ion rechargeable battery*, 10th International Seminar of Primary and Secondary Battery Technology Applications, Deerfield Beach, Florida Educational Seminars, Boca Raton, Florida, **1993**.

125 (a) J. R. Owen, *Chem. Soc. Rev.* **1997**, *26*, 259; (b) M. Winter, J. O. Besenhard, M. E. Spahr, P. Novák, *Adv. Mater.* **1998**, *10*, 725.

126 T. Zheng, J. S. Xue, J. R. Dahn, *Chem. Mater.* **1996**, *8*, 389.

127 K. Sato, M. Noguchi, A. Demachi, N. Oki, M. Endo, *Science* **1994**, *264*, 556.

128 N. Takami, A. Satoh, T. Ohsaki, M. Kanda, *Electrochem. Acta* **1997**, *42*, 2537.

129 Z. Wu, U. Pittman Jr., S. D. Gardner, *Carbon* **1995**, *33*, 597.

130 W. Hummers, R. Offeman, *J. Am. Chem. Soc.* **1958**, *80*, 1339.

131 Y. Ein-Eli, S. R. Thomas, R. Chadha, T. J. Blakley, V. R. Koch, *J. Electrochem. Soc.* **1997**, *144*, 823.

132 (a) T. Cassagneau, J. H. Fendler, *Adv. Mater.* **1998**, *10*, 877; (b) T. Cassagneau, F. Guérin, J. H. Fendler, *Langmuir* **2000**, *16*, 1318; (c) T. Cassagneau, J. H. Fendler, in preparation.

133 L. Staudenmaier, *Ber. Deutsch. Chem. Ges.* **1898**, *31*, 1484.

134 N. A. Kotov, I. Dékány, J. H. Fendler, *Adv. Mater.* **1996**, *8*, 637.

135 N. I. Kovtyukhova, P. J. Ollivier, B. R. Martin, T. E. Mallouk, S. A. Chizhik, E. V. Buzaneva, A. D. Gorchinskiy, *Chem. Mater.* **1999**, *11*, 771.

136 (a) S. Yata, H. Kimoshita, M. Komoi, N. Ando, T. Kashiwamura, T. Harada, K. Tanaka, T. Yamabe, *Synthetic Metals* **1994**, *62*, 153; (b) S. Yata, Y. Hato, H. Kimoshita, N. Ando, A. Anekawa, T. Hashimoto, M. Yamaguchi, K. Tanaka, T. Yamabe, *Synthetic Metals* **1995**, *73*, 273; (c) H. Ago, K. Tanaka. T, Yamabe, K. Takegoshi, , T. Terao, S. Yata, Y. Hato, N. Ando, *Synthetic Metals* **1997**, *89*, 141.

137 E. Peled, C. Menachem, D. Bar-Tow, A. Melman, *J. Electrochem. Soc.* **1996**, *143*, L4.

138 (a) D. Aurbarch, O. Yougman Chusid, Y. Carmeli, M. Babai, Y. Ein-Eli, *J. Power Sources* **1993**, *43*, 47; (b) D. Aurbarch, Y. Ein-Eli, O. Chusid; M. Babai, H. Yamin, *J. Electrochem. Soc.* **1994**, *141*, 603; (c) D. Aurbach, Y. Ein-Eli, B. Markovsky, A. Zaban, *J. Electrochem. Soc.* **1995**, *142*, 2882.

139 (a) J. A. Switzer, B. M. Maune, E. R. Raub, E. W. Bohannan, *J. Phys. Chem. B* **1999**, *103*, 395; (b) J. A. Switzer, M. G. Shumsky, E. W. Bohannan, *Science* **1999**, *284*, 293.

Electrochemistry of Nanomaterials
by *Gary Hodes (Ed.)*
© WILEY-VCH Verlag GmbH, 2001

Index

absorbed photon to current efficiency (APCE) 177
absorption layers 127
absorption spectra
– dye-modified tin dioxide 237
– sensitizers 208
acceptors
– porous silicon 145
– solar cells 214
accumulation layers 123
acetate complexation 81
acetic acid 231
action spectra analysis 176 f
affinities, semiconductor quantum dot films 35
aggregation
– semiconductor assemblies 237
– ultrathin films 273
alkyl reagents 160
alloys, quantum dot films 47
aluminum arsenides 69
ambipolar diffusion 192
amines 240
amorphous semiconductors 26
anchoring groups 238
annealing 230
anodic deposition 80
anodic etching 103, 141
anodic oxidation 231
anatases 204, 210
applications
– porous silicon 161 f
– semiconductor quantum dot films 62
– semiconductors 20, 134 f
– solar cells 227
– thin-film electrodes 195 f
atomic layer epitaxy (ALE) 79
Auger depth profiling 76, 85
avalanche breakdown 106

back contacts
– solar cells 222
– thin-film electrodes 169 ff, 177 f, 183, 192
backwall photocurrent 177
ballistic electron transport 195
band bending
– porous silicon 144
– porous-etched semiconductors 122 f, 127 f
– solar cells 201 f, 215 f
band edge mismatch 131
bandgap materials 68 f
bandgaps
– porous silicon 142, 156
– semiconductor assemblies 229 ff
– semiconductor quantum dot films 28 ff, 51 ff
– size-tunable 3
– solar cells 201
– thin-film electrodes 170, 176
– ultrathin films 258
barrier heights 212 f, 265
batteries 276
benzoates 238
bias applications, semiconductor assemblies 238
bilayer thickness, superlattices 67
binders 249
bixbyite structure 84
blue oxide products 235, 238
blue shift
– semiconductor quantum dot films 26, 29
– semiconductor nanocrystals 18
– superlattices/multilayers 85
see also: color changes
Bohr radius 18, 217
Boltzmann constant 149, 223, 260
Boltzmann statistics 214
bonds, ultrathin films 249
borofluorides 31

boron nitride 69
Bragg mirrors 153, 161
Bragg peaks 88, 91, 95
branching 108
Bravais lattice 84
Brownian dynamics 9 f
bulk effect, titanium dioxide 213

cadmium 2, 7, 41
cadmium perchlorate 32
cadmium selenide
– codeposition 79
– gold cadmium alloy film 48
– gold films 37, 42 f
– gold-palladium alloy film 47
– lattice parameters 41, 69
– palladium films 45
– quantum dots 29, 155
– solar cells 209
– thin-film electrodes 179
cadmium sulfide 1 ff
– films 26
– gold films 43
– lattice parameters 41, 69
– palladium films 47
– quantum dots 155
– semiconductor quantum dot films 29
– semiconductor nanocrystals 20
– solar cells 209
– thin-film electrodes 179
cadmium telluride
– codeposition 79
– gold films 42
– lattice parameters 41, 69
– porous-etched semiconductors 120
– quantum dots 155
– semiconductor quantum dot films 33
capacitance ranges, porous-etched semiconductors 125
capping 31, 155
carbon, lattice parameters 69
carboxilates 206 f
carboxylic acids 31, 151, 160
carboxylic groups 236
carriers
– porous silicon 143
– porous-etched semiconductors 105, 123, 126
– solar cells 202
– superlattices/multilayers 68
– thin-film electrodes 173
casting, thin films 229
cathodic deposition 80
cationic exchange capacity (CEC) 278
cationic layers 256
cationic polyelectrolytes 247
cations, porous-etched semiconductors 131
cavity effects, porous silicon 154
ceramic multilayers/superlattices, electrodeposition 78, 83 f
chalcogenides
– compound semiconductor films 79
– quantum dot films 37
– solar cells 209
– thin-film electrodes 192
chalcogens 26 ff
charge carriers *see:* carriers, electrons, holes
charge separation, thin-film electrodes 177
charge storage, ultrathin films 247–286
charge transport
– porous silicon 144
– thin-film electrodes 169–200
charging, semiconductor quantum dot films 53
chemical etching 107
chemisorption 206
chlorides 32
chlorine solution 115
chlorophyll 237
chromic properties 229 246
chromophores 206, 233, 273
clusters, porous silicon 155

coatings
– semiconductor thin films 230
– superlattices/multilayers 71
codeposition 79
colloidal suspensions
– porous-etched semiconductors 104
– semiconductor assemblies 229 ff
colloids, titanium dioxides 214
color changes
– quantum dot films 42
– semiconductor assemblies 232 ff, 238 f
– ultrathin films 256
composite semiconductors 231
compound semiconductor films 79
conduction band
– gallium arsenides 119
– porous silicon 145
– solar cells 201 f, 211, 219
– superlattices/multilayers 68
– thin-film electrodes 169, 173
conductivity, ultrathin films 269
conversion processes, semiconductor nanocrystals 13 f
copper 7
copper alloy layers 71, 76, 94
copper/cuprous layers 86, 90
β copper iodide 1 ff
corrosion 147
Cottrell equation 8, 74
Coulomb blockade devices 269
Coulomb charging 53
coumarin 275
counter electrodes 205, 220
coupling matrix, enzymes 134
covalent attachement 160
covalent bonds 249
coverage, display devices 256
cracks, superlattices/multilayers 94
crystal diameter 27
current-voltage characteristics, diffusion model 181
cyanides 208
cyanine dyes 273

dangling bonds 154
dark etching 115 ff
dark field transmission 29
Debye–Scherrer equation 27
Debye screening 213
deep holes, indium phosphides 120
defects
– gallium arsenides 117
– porous-etched semiconductors 107
– solar cells 201
Dember voltages 202
depletion
– minority carriers 112
– porous silicon 144
depletion layers
– gallium arsenides 119
– porous-etched semiconductors 123 f, 127
– solar cells 212 f, 219
– thin-film electrodes 175
depostion techniques
– quantum dot films 25–65
– semiconductor nanocrystals 1 ff, 9
diamond, lattice parameters 69
diffraction gratings 238
diffraction pattern, porous silicon 155
diffuse layers, porous silicon 144
diffusion 126, 202, 219
diffusion control, porous-etched semiconductors 108
diffusion controlled growth 8
diffusion model, thin-film electrodes 181, 192
dimensional control, electrodeposition 2
dimethyl sulfoxide (DMSO) 26, 29 ff, 42
diodes 250 ff, 258 ff
dipcoating 104
discrete charge effects, solar cells 215
dislocations
– gallium arsenides 117
– porous-etched semiconductors 107
– superlattices/multilayers 94

dispersivity 3 f
display devices, ultrathin films 250, 256
dithiol derivatives 249
doctor blading 210
donors
– porous silicon 145
– solar cells 214
doping
– porous silicon 142 ff
– porous-etched semiconductors 106, 112
– solar cells 212 f
– thin-film electrodes 192
– ultrathin films 260
dual bath electrodepostion 72 f
dye sensitized nanostructured semiconductor cells 190
dye sensitized solar cells (DSSC) 201–228
dyes
– semiconductor assemblies 236
– ultrathin films 273

efficiencies, solar cells 220 ff
electrical characteristics
– junctions 265
– self-assembled electrodes 280
electrical fields 192
electrical impedances 122
electrical properties, porous silicon 158
electrochemical atomic layer epitaxy (ECALE) 2, 79
electrochemical deposition, semiconductor thin films 231
electrochemical formation, porous silicon 141–167
electrochemical functionalization, porous silicon 160 f
electrochemical quartz crystal microbalance (EQCM) 85
electrochromic properties, semiconductor assemblies 229–246
electrodeposition 25–65
– porous-etched semiconductors 104
– superlattices/multilayers 67–101
electrodes, thin film 169–200
electrogenerated base method 82
electroless etching 106
electroluminescence 141, 158, 250
electrolyte–electrode interface 177
electrolyte scavengers 180
electrolytes 214, 219, 226
electron diffraction 27
electron generation 126
electron–hole pair recombination
– porous silicon 156
– porous-etched semiconductors 130
see also: recombination
electron injection 211
electron photogeneration 18
electron repulsion 218
electron transport
– porous silicon 144
– porous-etched semiconductors 132
– self-assembled multilayers 273
– thin-film electrodes 173 ff, 186, 195
– ultrathin films 247–286
electron trapping 53
electroneutrality equation 213
electropolishing, porous silicon 142
energy barriers, semiconductor quantum dot films 52
energy diagrams, solar cells 223
Eosin Y 232
epitaxial films 95
epitaxial layer transfer (ELTRAN) 134
epitaxy 36
etching, porous 103–139
ethanolic solutions 230
excitations, semiconductor assemblies 232
excitons 217

Fabry–Pérot equation 152
Faradaic efficiency 122

Faraday law 25 f, 38, 74
Fermi level pinning 114, 146
Fermi levels
– porous silicon 143 ff, 158
– porous-etched semiconductors 132
– rectifying diodes 258
– semiconductor quantum dot films 51 ff
– solar cells 202 ff, 212 ff, 219, 225
– superlattices/multilayers 70
– thin-film electrodes 174
ferromagnetic materials 70
Fick law 183
fill factor, solar cells 202, 219
film electrodes 169–200
films
– semiconductor quantum dot 25–65
– thin *see:* thin films
– ultrathin *see:* ultrathin films
flat band condition, porous-etched semiconductors 122
flat band potentials, porous silicon 145
fluorescein 274 f
fluorides 32
fluororescence patterning 239
Formvar films 20
Förster radius 273 f
Fourier transform 89
Fowler–Nordheim law 258
Frank–van derMerve growth 36
fringes 152
frontwall photocurrent 179
full width at half maximum (FWHM)
– porous silicon 153
– semiconductor quantum dot films 27
– superlattices/multilayers 78
functional groups, semiconductor assemblies 240
functionalization, porous silicon 160

gallium arsenide
– lattice parameters 69
– porous-etched semiconductors 104, 116 f, 129
– superlattices/multilayers 68
gallium nitride 72, 120
gallium phosphide 115, 129
Galvani potential 203
Gärtner–Butler approximation 170, 174
Gärtner model 127, 130
gas phases 4
germanium 69, 142
giant magnetostrictive (GMR) devices 70, 77
glasses 37
gold
– lattice parameters 41
– semiconductor assemblies 240
– sulfur affinity 35
– ultrathin films 249, 272
gold cadmium alloys 48
gold palladium alloys 47
gold surfaces 2
grain boundaries 217
grain growth 25 f
graphite 1–25
graphite oxide 277
gratings 238
Grätzel cell 180
Grignard reagents 160
grooves
– gallium arsenide 119
– indium phosphide 120
group II–VI compound semiconductors 79
group II–VI materials
– porous silicon 157
– porous-etched semiconductors 103, 109, 120
group III–V materials, porous-etched semiconductors 103, 109, 115
group IV–IV materials 103, 109, 113
growth
– gallium arsenide 117
– semiconductor films 36
– Volmer–Weber 6

halides 31, 208
Helmholtz layers 125, 143 f, 218, 222
hexanedithiol (HDT) 261
high-electron mobility transistor (HEMT) 68
high-resolution transmission electron microscopy (HRTEM) 29, 40
highest occupied molecular orbital (HOMO) 173, 217
hole generation 126
hole photogeneration 18
hole transfer
– porous silicon 144
– thin-film electrodes 173 ff, 186
holes
– indium phosphide 120
– porous silicon 159
– porous-etched semiconductors 104
– semiconductor assemblies 233
– solar cells 218
hybrid electrochemical/chemical synthesis, semiconductors 1–25
hydride termination 160
hydrofluoric acid (HF) solution
– porous silicon 141 f, 146 f, 151 f
– silicon, etching 103, 109
hydrogen 155
hydrogen bonding 249
hydrolysis 230
hydrosylation 160

illumination
– porous silicon 151
– porous-etched semiconductors 109 ff
– solar cells 223
– thin-film electrodes 177
impact ionization 106
impedances, porous-etched semiconductors 122 f, 125 f
incident photon to current efficiency (IPCE)
– solar cells 209
– thin-film electrodes 174 f, 178, 181
indium arsenide 69
indium phosphide 119
integrated circuits 141
intensity modulated photocurrent spectroscopy (IMPS) 133, 170, 189 f
intensity modulated photovoltage spectroscopy (IMVS) 170, 189 f
intercalation 234
interdiffusion 72
interfaces
– electrolyte/electrodes 173, 192
– solar cells 218
interferometer films 152
intergrain barriers 216
intermediates, semiconductor nanocrystals 13
isolated nanocrystal deposition 35

J-aggregates 273
junctions
– porous silicon 143, 158
– solar cells 201 f
– ultrathin films 260 f, 265 f

kink sites 117

lactate complexation 81
Langmuir–Blodgett growth 172
laser pulse induced transients 183
lattice mismatch
– porous silicon 155
– quantum dot films 41
– superlattices/multilayers 68, 96
lattice parameters
– quantum dot films 39 ff
– superlattices/multilayers 69
lattice spacing 89
layer thickness 73
layer-by-layer self-assemblies 247–286
layers
– gallium arsenide 119

– porous silicon 142 ff, 152
– porous-etched semiconductors 103, 107, 123, 127
– semiconductor assemblies 232
– semiconductor nanocrystals 1 ff
– solar cells 206 f, 212 f, 218
– thin-film electrodes 175
lead sulfide 69
lead titanium oxygen films 83
lead titanium oxygen superlattice 75, 83, 92
Lennard–Jones potential 15
Lewis acids 160
light emitting diodes (LED) 250 ff
linear sweep voltammograms 73
liquid phases, semiconductor nanocrystals 4
liquid electrolytes
– solar cells 226
– thin-film electrodes 170, 186
lithium storage batteries 276 f
lithographic techniques
– semiconductor assemblies 238
– ultrathin films 249
lowest unoccupied molecular orbital (LUMO) 173, 211, 219
luminescence 113, 129, 156

macromorphology, porous-etched semiconductors 111
magnetic oxides 96
magnetoresistance 78
majority carriers
– porous-etched semiconductors 126
– thin-film electrodes 181
Marcus region 207
mass transport, thin-film electrodes 187
mass transport controlled deposition 73
mechanical properties, layers 71
mesomorphology, porous-etched semiconductors 111
mesoporous systems 123
metal chalcogenides 79
metal organic vapor phase epitaxy 36
metal oxide ceramic films 78, 81 f
metal oxide films 234
metal oxide semiconductors (MOS) 160
metal salts 1 f, 14 f, 26 ff
metallic ferromagnets 70
metallic multilayers/superlattices 76
methanol solutions 115
methylsulfonates 31
methylviologen radicals 131
mica substrate 37
microcavities, porous silicon 161
microcontact printing 249
microelectromechanical systems (MEMS) 134
micromorphology, porous-etched semiconductors 111
microporous systems 123
migration, porous-etched semiconductors 126
minoritiy carriers 105, 123, 126
mismatch *see:* lattice mismatch
mobility 216
modulation wavelength 67
molecular beam epitaxy (MBE) 2
– porous-etched semiconductors 113
– semiconductor quantum dot films 36
monodispersivity 3, 7, 22
monolayers, ultrathin films 247 f
Moore's law 247–286
morphology
– porous silicon 142
– porous-etched semiconductors 111
– thin-film electrodes 171
– titanium dioxide 121
Moss–Burstein shift 85
Mott–Schottky equation 123, 150 f, 260
multilayers
– electrodepositions 67–101
– porous silicon 152
– ultrathin films 248 f, 273

n-type semiconductors 105
nanoparticles 247–286
negative differential resistance (NDR) 87
Nernst potential 144
nickel alloy layers 71, 76, 94
nitric acid 231
noble metals
– quantum dot films 37 ff, 47
– semiconductor nanocrystals 2, 7 f
– sulfur affinity 35
– ultrathin films 249
nonaqueous deposited semiconductor quantum dot films 35
nonbonding oxygen hole center (NBOHC) 159
noncontact atomic force microscopy (NC-AFM) 6
normal hydrogen electrode (NHE) 145
nucleation controlled growth 7 f

on-line fabrication, thin-film electrodes 170
open circuit etching 119
optical absorption, semiconductor quantum dot films 27
optical properties, porous silicon 156
optically transparent electrodes (OTE) 231 ff
organo-iodides/bromides 161
orientations, superlattices 67
osmium 208
output parameters, solar cells 218
overpotentials
– porous silicon 160
– semiconductor nanocrystals 8
– superlattices/multilayers 73
oxalic acid 233
oxazine dyes 238
oxidation, semiconductor nanocrystals 1 ff
oxidative dissolution, porous-etched semiconductors 105
oxide films 236
oxidizing agents 131, 142
oxygen 159, 180

p-n junctions 159
p-type semiconductors 105
palladium 41
particle charging, solar cells 215
particle self-assemblies, ultrathin films 247–286
passivating films 117
passivation, porous silicon 156
pellets, titanium dioxide 121
penetration depth, porous-etched semiconductors 126 f
peptization 210
perchlorates 31
percolation
– solar cells 210 ff, 225
– superlattices/multilayers 86
peroxydisulfate 131
phase transitions
– quantum dot films 48
– semiconductor nanocrystals 4
phonon loss lines 18
phosphonates 207, 236 ff
photoanodic dissolution 114
photochemistry, solar cells 206 f
photoconversion efficiencies, semiconductor assemblies 229
photocurrent 126, 218
photocurrent action spectra 179 f
photocurrent spectra 30
photoelectrochemical cells 203
photoelectrochemical characterization, porous-etched semiconductors 122
photoelectrochemical photocurrent spectroscopy 58
photoelectrochemically patterned porous silicon 151
photoelectrochromic properties, semiconductor assemblies 229–246
photoetching 120, 122
photoexcitation, solar cells 205

photogalvanic cells 203
photoluminescence 113, 129, 141 f
photoluminescence spectroscopy 17
photovoltaic conversion 80
photovoltaic effect 201 f
pinning, porous silicon 145
pitting 107, 117
plateless self-assemblies 247–286
plating, semiconductor nanocrystals 6
platinum 35
p-n junctions 260 f, 265 f
Poisson equation 203, 216
polaron model 226
polyacrylic acid (PAA) 251, 255, 274
poly(allylammonium chloride) 251, 274
polydispersivity 11
polyelectrolytes 247–286
poly(ethylene oxide) (PEO) 253, 277
polyionic binders 249
polymer films 250 ff
polyoxometallates 256
polyphenylene vinylene (PPV) 252, 274
polypyrrole 261, 272
poly(styrenesulfonate) (PSS) 251, 274
pores 107
– gallium arsenides 117
– silicon 142
porous electrodes 170
porous etching 103–139
porous silicon 141–167
porphyrin viologen 275
Pourbaix diagrams 13 f
precursors, ceramics electrodepostion 81
press molding 121
protective coating 71
proton transfer, solar cells 207
pyrene chromophores 240

quantum confinement 68, 142
quantum dot films 25–65
quantum dots
– porous silicon 155 ff
– semiconductor nanocrystals 1 ff
– thin-film electrodes 170, 175
quantum efficiency, porous-etched semiconductors 126
quantum well lasers 68
quantum yields
– solar cells 207
– thin-film electrodes 177
– ultrathin films 274
quenching 131

recombination
– porous silicon 156
– porous-etched semiconductors 105, 126, 130 ff
– semiconductor assemblies 233
– semiconductor nanocrystals 19
– solar cells 201 f, 218 f
– thin-film electrodes 179
rectifying diodes 258
redox change method, ceramics electrodepostion 81
redox chromophores 233, 236 f
redox couples 144, 186
redox molecules, display devices 256
redox polymer films, light emitting diodes 252
redox potentials, solar cells 217
reducing agents, porous silicon 146
reduction, semiconductor nanocrystals 4
retrieval length 128
rhodamine B 274
rocksalt 48
roughness 117
roughness factor, solar cells 211
ruthenium 208

sacrificial layers, porous-etched semiconductors 103, 134
salicylate 238

salts 1 f, 14 f
  see also: metal salts
satellites 88
saturated colomel electrodes (SCE) 239
scanning force microscopy (SFM) 50
scanning probe current voltage spectroscopy 50
scanning tunneling microscopy (STM) 50, 84, 93
scattering factor, superlattices/ multilayers 89
scavengers 180, 233
Schottky barrier
– porous-etched semiconductors 113
– thin-film electrodes 170, 174 ff, 185, 192
Schottky diode
– porous silicon 149
– ultrathin films 250 ff, 258 f, 268 f
Scotch tape 20
screen printing 210
selected area electron diffraction (SAED) 1, 13, 37
selenides 32
self-assembled layers, semiconductor assemblies 232
self-assembled monolayers (SAMs) 249
self-assemblies, ultrathin films 247–286
semiconductor-electrolyte interface (SEI) 176, 218
semiconductor multilayers/ superlattices 78
semiconductor quantum dot films 25–65
semiconductor synthesis, on graphite 1–25
semiconductor cells, back contact interface 192
semiconductors
– solar cells 204, 209 f
– thin-film electrodes 169 ff
sensitizers 229
sensitizing, dye solar cells 201–228
Shockley–Read formalism 185
Shockley potential 223
side branching, porous-etched semiconductors 108
silanes 240
silica 69
silicon
– energy levels 267
– lattice parameters 69
– porous 141–167
– porous-etched semiconductors 103, 109, 131, 134
silicon carbide 114
silicon germanium alloys 113
silicon on insulator (SOI) 103, 134
silicontungstase 257
silver 249
silver plating 6
silyl esters 151
single bath electrodepostion 72 f
single crystals 170
single-electron conductivity 269
sintered pellets, titanium dioxide 121
size quantization, semiconductor quantum dot films 28 ff
size-selective electrodeposition 5
Södergren model 181
solar cells, dye-sensitized 201–228
solid electrolytes 188
solid-state dye sensitized solar cells 226
space layers
– porous silicon 144
– solar cells 212
spacing
– quantum dot films 39, 47
– superlattices/multilayers 89
spark erosion process 142
spin coated ITO glass 253
spin coating 104
spin dependent transport 70
splitting, solar cells 220
sputtered indium oxide 158
stacking 67

stain etching
– porous semiconductors 109, 113
– porous silicon 142
staircase, coulomb 270
standard carbon electrode (SCE) 75, 83
standard deviation 9
standard dyes 206
standard hydrogen electrode (SHE) 83
stoichiometric semiconductor quantum dot films 34
Stranski–Krastanow growth 36
strong interactions, semiconductor nanocrystals 12
structural properties, porous silicon 155
substrate-electrode interface, thin-film electrodes 177
substrate variations, gold films 45
substrates
– deposited films 35
– porous silicon 142
– solar cells 206
– superlattices/multilayers 67
– ultrathin films 265
sulfides 32
sulfur affinity 35
sulfuric acid solutions 121
superlattices 67–101
superperiodicity 88
supra-bandgap 58, 201 f
surface area
– solar cells 201, 206
– thin-film electrodes 172
surface bonds 104
surface bound fluoroprobes 239
surface modifications, porous silicon 151
surface passivating layers 107
surface roughness 117
surface states
– semiconductor quantum dot films 53
– solar cells 214
surfactants 257
suspensions 229
sylanol groups 159
synthesis, porous silicon 142

Tafel plot 84, 150
tartrate complexation 81
tellurium layers 2
thermal fluctuations, ultrathin films 269
thiazine dyes 238
thick films 29
thickness
– semiconductor quantum dot films 61
– superlattices/multilayers 67
thin film electrodes 169–200
thin films 229
thiols 240
thionine 239
time-resolved photocharge (TRPC) 193
tip contacts, semiconductor quantum dot films 50
titanium dioxide-gold film 240
titanium dioxide
– porous-etched semiconductors 103, 109, 121 ff
– semiconductor assemblies 229 ff
– solar cells 204 ff
– thin-film electrodes 171, 177 ff, 185
topography, semiconductor quantum dot films 55
transit time
– porous-etched semiconductors 132
– thin-film electrodes 185
transmission electron microscopy (TEM) 27, 93, 115
transparent conducting oxide (TCO) 192
trapping
– porous silicon 156
– semiconductor assemblies 233

– semiconductor quantum dot films 53
– semiconductor nanocrystals 19
– solar cells 213 ff, 217 f
– thin-film electrodes 173, 179 f, 185 ff
tri-iodides
– solar cells 205 ff, 218
– thin-film electrodes 180, 187
tri-*n*-butylphosphine (TBP) 33
tunnel barrier 70
tunneling diodes 68, 259

ultrathin films 247–286
ultrathin semiconductor quantum dot films 35
under-potential deposition (UPD)
– compound semiconductor films 79
– semiconductor nanocrystals 2

V grooves 119
valence band
– porous silicon 145
– porous-etched semiconductors 104
– solar cells 201 f
– superlattices/multilayers 68
– thin-film electrodes 173

van der Waals attractions 249
Vegard law 42
viologen compounds 236 ff, 275
Volmer–Weber growth 6, 36
voltage tunability, porous-etched semiconductors 131

wafers 151
weak interactions, semiconductor nanocrystals 12
wide bandgap oxide semiconductors 170
wurtzite 41

X-ray diffraction (XRD)
– semiconductor quantum dot films 26 f
– superlattices/multilayers 84, 88

Zener diodes 250, 261
zinc 7
zinc oxide 1 ff, 69
zinc perchlorates 32
zinc selenides 41, 43
zinc telluride 120

© WILEY-VCH Verlag GmbH, 2001

List of Symbols

Chapter 1

ε_0	L–J 6–12 potential
ν_{fluor}	fluorescence emission frequency
σ_{dia}	standard deviation of the particle diameter
σ_R	standard deviation of the particle radius
$\langle dia \rangle$	mean particle diameter
r	particle radius
t	time
A	area
E	interaction energy
E_{BG}	bandgap energy
N	number of particles

Chapter 2

a	absorption coefficient
λ	X-ray wavelength
θ	peak position
$\Delta(2\theta)$	peak full width at half maximum (FWHM) in radians
C	capacitance of the material
e	electronic charge
i	current
K	constant
V	potential

Chapter 3

χ	tilt angle
ϕ	azimuthal angle
λ	wavelength

λ_a	thickness of layer a
λ_b	thickness of layer b
θ	Bragg angle
θ_i and θ_j	angles corresponding to the positions of the satellites
ρ	density
ρE	displacement of the bound state of the conduction band or valence band
ω	rocking angle
Λ	modulation wavelength
$\langle d \rangle$	average d spacing of layers
i	current
i_L	limiting current
k	wavevector (or reciprocal lattice vector)
m	effective mass of electron or hole (dimensionless)
m_0	mass of free electron (9.109×10^{-31} kg)
v	volume
A	electrode area
C^*	bulk concentration of diffusion-limited component
D	diffusion coefficient
E_g	bandgap energy
F	Faraday's number
J	valence band
L	confinement dimension
L_i and L_j	satellite orders
M	formula weight
Q	charge
Q	charge of the individual layers
$\mathbf{Q}$	scattering vector
$\mathbf{Q}^{+n}$ and $\mathbf{Q}^{-n}$	harmonics
V	potential

Chapter 4

a	instability parameter
$a(\lambda)$	absorption coefficient for light of wavelength λ
ε	dielectric constant of the solid
$\phi(0)$	photon flux at the electrode surface
$\phi(x)$	photon flux at a depth x
$\tilde{\Phi}(\omega)$	modulated light intensity
κ	ratio of the rate of radiative recombination to the total recombination rate
τ_d	average transit time of electrons
λ	wavelength
d	width of the porous layer

$\tilde{j}(\omega)/e\tilde{\Phi}(\omega)$	opto-electrical transfer function
$\tilde{j}(\omega)$	modulated photocurrent
k_B	Boltzmann constant
n_s	carrier concentration at the surface
n_b	carrier concentration in the bulk
q	perturbation wavenumber
$p_s n_s$	concentration of holes at the surface
n_s	concentration of electrons at the surface
x	depth
C_{sc}	space-charge layer capacitance
D	dimensions of the porous structure
E_F	Fermi level
I_{max}	maximum photoluminescence intensity
I_{PL}	photoluminescence intensity
$L(\lambda)$	penetration depth of light of wavelength λ
L_p	diffusion length of holes
N_D	donor density
Q	quantum efficiency
T	temperature
U	electrode potential
U_{fb}	flat-band potential
U_{sc}	potential drop across the space charge layer
W	width of the depletion layer

Chapter 5

a	power coefficient for size dependent quantum confinement
β	fitting parameter
ε_s	dielectric constant of the semiconductor
λ	wavelength of light
Δa	lattice mismatch
$\Delta a/a$	lattice expansion
$2nL$	effective optical film thickness
i	current
j	current density
j_0	reverse-bias saturation current density
k	Boltzmann constant
m	integer corresponding to the spectral order of a fringe
q	charge of an electron
A	diode quality factor
A_s	electrode area
C_{sc}	junction capacitance
D	diameter of nanocrystallite
E_b	band-bending energy

E_c	quantum confinement energy
E_{CB}	energy of the conduction band edge
E_f	Fermi energy in the semiconductor
E_{fb}	flat band potential
E_g	bandgap of bulk semiconductor
$E_{g'}$	bandgap of quantum confined semiconductor
E_{ss}	surface state energy
E_{VB}	energy of the valence band edge
F	Faraday constant
L	thickness of a film
L_x, L_y and L_z	three dimensions in a nanocrystal
N_D	dopant density in a semiconductor
R	ideal gas constant
T	temperature Kelvin
V	voltage
Y	intensity of reflected light

Chapter 6

a	absorption coefficient
$a(\lambda)$	the absorption coefficient
τ	lifetime of the electron in the conduction band
ε	relative dielectric constant
ε_0	permittivity of free space
η	the net electron injection efficiency
λ	wavelength
ϕ_λ	incident photon to current efficiency
ϕ_{inj}	quantum yield for injection of electrons or holes
Φ_0	photon flux
η_{esc}	charge separation probability
τ_{oc}	time constant for charge recombination at open circuit
τ_{sc}	time constant for the combined process of charge collection and charge recombination
d	film thickness
i	net photocurrent
i_{ph}	photocurrent
m	ideality factor
n	electron density
$n(x)$	excess electron density
$n(x,t)$	concentration of electrons
n_0	electron density in the dark
n_D	donor concentration in the semiconductor
p	hole density
q	elementary charge

x	distance from the back contact
t	time
A_λ	absorption
$APCE$	absorbed photon to current efficiency
C_{HL}	capacitance
D	chemical diffusion coefficient for an electron
D_{amb}	ambipolar diffusion coefficient
D_{eff}	effective diffusional coefficient
D_n	electron diffusion coefficient
D_p	diffusion coefficient
E_F	Fermi level
I	current
I_0	intensity of light
I_L	photocurrent
$IPCE$	incident photon to current efficiency
I_S	saturation current
L	diffusion length
LHE	light harvesting efficiency
L_n	diffusion length of the electron
L_p	diffusion length
U	electrode potential
U_{FB}	flat band potential
V	voltage
W	film thickness

Chapter 7

ε	dielectric constant
ε_0	permittivity of vacuum
ϕ	electrical (Galvani) potential
$\Delta\phi$	electrical potential difference
$\Delta'\phi$	$\Delta\phi$ for illuminated cell
$\Delta\phi(H)$	(Galvani) electrical potential drop across Helmholtz layer
$\phi(r)$	potential distribution
ϕ_B	reduced barrier height (dimensionless)
Φ_B	barrier height
μ_e^0	standard chemical potential of electron
$\Delta\mu_e^0$	difference in μ_e^0
$_\mu_e$	difference in μ_e
$_'\mu_e$	difference in μ_e for illuminated cell
η_e	electrochemical potential of electron
$\Delta\eta_e$	difference in η_e
d	tri-iodide tunneling distance
i_{ph}	integral photocurrent density

k	Boltzmann constant
n	conduction band electron concentration
n_e	electron density
q	electron charge
r	variable distance parameter
x	average number of dopants per particle
D_n	electron diffusion coefficient
E_d	doping level
E_F	Fermi level
$E_{F,n}$	electron quasi-Fermi level
$E_{F,p}$	hole quasi-Fermi level
E_G	bandgap
E_{redox}	redox potential
E_s	energy of surface states
FF	fill factor of solar cell
I_s	intensity of the incident light
I_{sc}	short circuit current (infinite load)
L_D	Debye screening length
N_c	density of states in conduction band
N_d	bulk donor density
N_d^+	ionized fraction of the donor concentration
N_e	net number of electrons transferred to electrolyte
N_s^-	concentration of surface states having trapped an electron
N_s	surface state density
$P(r)$	probability distribution of dopant in particle
R	particle radius
S	specific surface area
T	temperature (in degrees Kelvin)
V_{bi}	built-in voltage
V_{oc}	open circuit voltage

Chapter 8

λ_{max}	wavelength maximum
e_t	trapped electron
h_t	trapped hole
D	hole scavenger
E_{fb}	flat band potential

Chapter 9

β	has the dimensions of electric field
χ	quantum efficiency for the electron transfer

χ_{sc}	electroaffinity
ε	semiconductor permittivity
ϕ_b	barrier height
η_{ext}	external quantum efficiency
σ	polydispersivity index of nanoparticles
τ	luminescence lifetime
Φ_m	work function
Φ_{m1}	work function for the cathode
Φ_{m2}	work function for the anode
d	thickness of the device sandwiched between the electrodes
e	charge of the electron
i	current
k_B	Boltzmann constant
k_BT	thermal fluctuation
n	diode quality factor
t_a	response time for coloration
t_b	response time for bleaching
C	effective capacitance
E_0	electric field
Ec	electrostatic energy of introducing an electron into an isolated conductor
E_g	bandgap energy
I_0	reverse saturation current
N_d	donor density
Q	charge
R_Q	resistance quantum
R_T	tunneling resistance
T	absolute temperature
V	potential
V_{app}	applied voltage
V_d	difference between the potential of two regions
V_n	depth of the Fermi level relative to the conduction band
V_r	reverse voltage
V_z	Zener voltage
W	width of depletion layer
W_n	width of space charge layer in p-type material

© WILEY-VCH Verlag GmbH, 2001

List of Abbreviations

α-ZrP	α-$Zr(HPO_4)_2 \cdot H_2O$
μCP	microcontact printing
AFM	atomic force microscopy
ALE	atomic layer epitaxy
APCE	absorbed photon to current efficiency
CB	conduction band
CB-SEI	chemically bonded solid electrolyte interface
CD	chemical deposition
CEC	cationic exchange capacity
CP	cetylpyridinium
CTA	cetyltrimethylammonium
CuPEI	solutions of copper complex with polyethylenimine
DEG	diethyleneglycol
DL	diffuse layer
DMSO	dimethyl sulfoxide
DNSC	dye-sensitized nanostructured semiconductor cells
DOMS	dimethyloctadecylmethoxysilane
DOS	density of states
DSNC	dye-sensitized nanostructured (solar) cell
DSSC	dye-sensitized solar cell
DTA	dodecyltrimethylammonium
E/C	electrochemical/chemical
ECALE	electrochemical atomic layer epitaxy
e_{CB}	free charge carrier in the conduction band
ECL	electrogenerated chemiluminescence
ED	electrodeposition OR electron diffraction
EE	light incident on the electrode interface (front wall illumination)
EL	electroluminescence
ELTRAN	epitaxial layer transfer
EN	electroneutrality equation
EQCM	electrochemical quartz crystal microbalance
e_{VB}	free charge carrier in the valence band
$Fe(phen)_3^{2+}$	tri(1,10-phenanthroline)iron(II)

FF	fill factor
FWHM	full width at half maximum
GB	grain boundary
GMR	giant magnetoresistance
GO	graphite oxide
HDT	1,6-hexanedithiol
HEMT	high electron mobility transistor
HL	Helmholtz layer
HOMO	highest occupied molecular orbital
HRTEM	high resolution transmission electron microscopy
IMPS	intensity-modulated photocurrent spectroscopy
IMPV	intensity-modulated photovoltage spectroscopy
IMVS	intensity-modulated voltage spectroscopy
IPCE	incident photon to current efficiency
ITO	indium tin oxide
LCAO	linear combination of atomic orbitals
LED	light-emitting diode
LHE	light harvesting efficiency
LUMO	lowest unoccupied molecular orbital
MBE	molecular beam epitaxy
MEA	mercaptoethylamine hydrochloride
MEH-PPV	poly(2-methoxy)-5-(2′-ethylhexyloxy)-*p*-phenylenevinylene
MEMS	microelectromechanical systems
MHImI	1-hexyl-3-methylimidazolium iodide
MINIM	metal-insulator-nanoparticle-insulator-metal
MO	montmorillonite
MOCVD	metal oxide chemical vapor deposition
MOS	metal-oxide semiconductor
NBOHC	non-bonding oxygen hole center
NC-AFM	non-contact atomic-force microscopy
NDR	negative differential resistance
NHE	normal (standard) hydrogen electrode
n-PS	n-type porous silicon
NREL	National Renewable Energy Laboratory
NSEI	nanostructured semiconductor electrode-electrolyte interface
n-Si-D	n-type silicon wafer derivatized with a covalently attached 18-hydroxydimethyloctadecylsiloxane monolayer
n-Si-nc	silicon nanocrystallites prepared from n-type silicon wafers
OMeTAD	2,2′,7,7′-tetrakis(*N*,*N*-di-*p*-methoxyphenylamino)-9,9′-spirobifluorene
$Os(bpy)_3^{2+}$	tris(2,2′-bipyridine)osmium(II)
OTE	optically transparent electrode
PAA	poly(acrylic acid)
PAH	poly(allylamine hydrochloride)
PAS	polyacenic compounds
PDDA	poly(dimethylammonium chloride)

$PdTSPP^{4-}$	palladium(II)tetrakis(4-sulfonatophenyl) porphyrin
PEC	photoelectrochemical
PEI	polyethylenimine
PEO	poly(ethylene oxide)
PL	photoluminescence
PMA	poly(methacrylic acid)
PMeT	poly(3-methylthiophene)
PPP	poly(*p*-phenylene)
p-PS	p-type porous silicon formed by the electrochemical etching of p-type silicon wafer
PPV	poly(*p*-phenylenevinylene)
Ppy	poly(pyrrole)
p-Si-D	p-type silicon wafer derivatized with a covalently attached 18-hydroxydimethyloctadecylsiloxane monolayer
p-Si-nc	silicon nanocrystallites prepared from p-type silicon wafers
PSS	poly(styrene-4-sulfonic acid), sodium salt
PV	phenylenevinylene OR photovoltaic
PVDF	poly(vinylidenefluoride)
$PVPH^+$	protonated poly(4-vinylpyridine)
PyC_6BPC_6Py	bipolar pyridine salt
QD	quantum dot
RHEED	reflection high-energy electron diffraction
RS	rock salt
RSD	relative standard deviation
$Ru(bpy)_3^{2+}$	tris(2,2′-bipyridine)ruthenium(II)
SAD	selected area diffraction
SAED	selected area electron diffraction
SAMs	self-assembled monolayers
SC	semiconductor
SCL	space charge layer
SE	light incident on the substrate-electrode interface (back wall illumination)
SEI	semiconductor-electrolyte interface
SFM	scanning force microscopy
Si-nc	silicon nanocrystallites
SOI	semiconductor-on-insulator
STM	scanning tunneling microscopy
TBP	tri-*n*-butylphosphine
t-Bu-PBD	electron-transporting oxadiazole derivative
TCO	transparent conducting oxide
TEM	transmission electron microscopy
TOPO	trioctylphosphine oxide
TRPC	time-resolved photocharge
UHV	ultrahigh vacuum
UPD	underpotential deposition

UV	ultraviolet
VB	valence band
W	sodium decatungstate OR wurtzite
XPS	X-ray photoelectron spectroscopy
XRD	X-ray diffraction
ZB	zinc blende